Frontiers in Low Temperature Plasma Diagnostics III

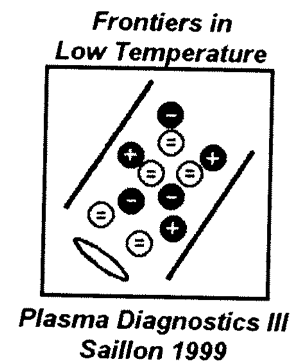

Papers

Saillon, Switzerland
15.02.99 - 19.02.99

Centre de Recherches en Physique des Plasmas
Ecole Polytechnique Fédérale de Lausanne
LRP 629/99 February 1999

EPFL
ÉCOLE POLYTECHNIQUE
FÉDÉRALE DE LAUSANNE

Frontiers in Low Temperature Plasma Diagnostics III

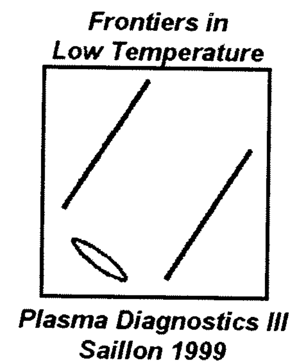

Papers

Saillon, Switzerland
15.02.99 - 19.02.99

Centre de Recherches en Physique des Plasmas
Ecole Polytechnique Fédérale de Lausanne
LRP 629/99 February 1999

Frontiers in Low Temperature Plasma Diagnostics III

Saillon, Switzerland, 15. - 19.2.1999

Book of Papers

LRP 629/99 February 1999

This volume includes the abstracts of all contributions.

Scientific/Industrial Committee

Prof. R. d'Agostino, University of Bari (Italy)
Prof. M. Boulos, University of Sherbrooke (Canada)
Prof. F.Döbele, Universität GH Essen (Germany)
Dr. P. Fayet, Tetrapak Suisse SA, Romont (Switzerland)
Dr. A. Garscadden, Wright Patterson AFB (USA)
Prof. B. Graham, The Queen's University of Belfast (Northern Ireland)
Dr. G. Kroesen, Eindhoven University of Technology (The Netherlands)
Prof. N. Sadeghi, Université Joseph Fourier de Grenoble (France)
Dr. A. Salito, Sulzer Metco, Wohlen (Switzerland)
Prof. D. Schram, Eindhoven University of Technology (The Netherlands)
Prof. K. Tachibana, Kyoto University (Japan)
Dr. E. Turlot, Balzers Process Systems SA, Palaiseau (France)
Prof. J. Winter, Ruhr-Universität Bochum (Germany)

Organizing Committee

Dr. Ch. Hollenstein (chairman)
Dr. A. A. Howling
Dr. J.-L. Dorier
Dr. Ch. Nieswand
Prof. M.Q. Tran
Centre de Recherches en Physique des Plasmas (CRPP)
Ecole Polytechnique Fédérale de Lausanne

Centre de Recherches en Physique des Plasmas (CRPP)
Association EURATOM - Confédération Suisse
Ecole Polytechnique Fédérale de Lausanne
PPB, CH-1015 Lausanne, Switzerland
phone: +41 21 693 34 82 / 7
fax: +41 21 693 51 76

Sponsors

CRPP
Centre de Recherches en Physique des Plasmas
Ecole Polytechnique Fédérale de Lausanne
CH-1015 Lausanne
Switzerland
Tel.: +41-21-693 34 82 / 7
Fax.:+41-21-693 51 76
E-mail: Edith.Grueter@epfl.ch
http://crppwww.epfl.ch/

International Union for Vacuum Science, Technique, and Applications (IUVSTA)
Plasma Science Division

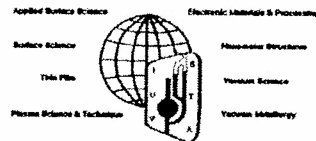

Swiss Vacuum Society (SGV)

GMP SA Laser/Photonics/Telecom.
19, av. des Baumettes
CH-1020 Renens
Switzerland
Tel.: +41-21-634 81 81
Fax: +41-21-635 32 95
E-mail: laser@gmp.ch
http://www.gmp.ch/

Sulzer Metco AG (Switzerland)
Rigackerstrasse 16
CH-5610 Wohlen
Switzerland
Tel: +41 56 618 81 81
Fax: +41 56 618 81 00
E-mail: info@sulzermetco.ch
http://www.sulzermetco.com/

Balzers Process Systems
P.O.Box 1000
FL-9496 Balzers
Liechtenstein
http://www.bps.balzers.net/bps0/homepage.htm

Sauerstoffwerk Lenzburg AG
Hauptsitz und Produktionsstandort
Seonerstrasse 75
CH-5600 Lenzburg
Switzerland
Tel: +41 (62) 886 41 01
Fax: +41 (62) 886 41 41
E-Mail: webmaster@slgas.ch
http://www.slgas.ch/

Table of Contents

Page

Foreword 1

Workshop Schedule 3

Invited Lectures 5

I.1 **Diagnostics of Thermal Plasmas** 7
M. Boulos

I.2 **Potential and Limitations of Thomson Scattering in Reactive Plasmas** 9
H. Soltwisch, M. Kaczor

I.3 **Laser based diagnostics of sputtered atoms and molecules** 17
A. Goehlich, N. Niemöller H.F. Döbele

I.4 **In situ Powder Diagnostics in Low Temperature Plasmas** 27
E. Stoffels, W.W. Stoffels, G.M.W. Kroesen

I.5 **Control of Plasma Spray Processes** 37
A. Vardelle

I.6 **Cavity Ring Down Spectroscopy** 39
R. Engeln, G. Berden, R. Peeters, G. Meijer

I.7 **Real time plasma etch diagnostics by plasma monitoring system Hercules** 51
A. Steinbach et al.

I.8 **The Black Box Illuminated** 61
R.A. Gottscho, D. Cooperberg, V. Vahedi

I.9 **Present and Future Diagnostics in Industrial RF Reactors** 71
J. Schmitt

I.10 **Diagnostics on the cascaded arc generated downstream plasma** 73
M.C.M. van de Sanden, G.J.H. Brussaard, W.M.M. Kessels, A. de Graaf, M.F.A.M. van Hest, K.G.Y. Letourneur, D.C. Schram

Page

Oral Contributions 83

O.1 **Imaging Diagnostics and Process Control in Plasma Spraying** 85
E. Hämäläinen, T. Korhonen, J. Vattulainen, R. Hernberg

O.2 **Electron Density Measurements in a Microwave Plasma by the Plasma Oscillation Method** 89
A. Brockhaus, A. Schwabedissen, Ch. Soll, J. Engemann

O.3 **Quantification of the ion flux by measurements of mass resolved ion energy distributions in RF/VHF plasmas** 93
E.A.G. Hamers, J. Bezemer, W.F. van der Weg

O.4 **Characterization of Electron Parameters in Inductively/ Capacitively Coupled RF Discharges by Use of Ar Line Emission** 97
S.A. Moshkalyov, W.G. Graham, C.M.O. Mahony, P.G. Steen, S. Gomez

O.5 **Continuous Temperature Measurement of Transparent Plates in Low-Pressure Plasma using Laser Interferometric Technique** 101
S.V. Merkulov, A.N. Magunov

O.6 **Correlation between an optical plasma diagnostic (OES) and an in-situ optical thin film diagnostic (SE)** 105
C. Vallée, K. Aumaille, A. Granier, A. Goullet, G. Turban

O.7 **Interaction of SiH_3 radicals with a-Si:H film surfaces, monitored by in-situ real time infrared absorption spectroscopy** 109
A. von Keudell, J.R. Abelson

O.8 **"IRMA" a Tunable Infrared Multi-Component Acquisition System for Plasma Diagnostics** 113
J. Röpcke, M. Käning, J. Anders, F.G. Wienhold, D. Nelson, M. Zahniser

O.9 **Ion flux and electron temperature measurements with an insulator-covered planar electrostatic probe** 117
J.P. Booth, N.St.J. Braithwaite, A. Goodyear, F. Neuilly, J.-M. Francou

Page

Poster Session I 121

P.I.1 **Experimental study of the recombination of atomic oxygen on fused silica** 123
G. Carty, L. Magne, G. Cernogora

P.I.2 **Electron Density Measurements using the Microwave Cavity Technique Applied to Large Area PECVD Industrial Reactors** 127
L. Chevalley, L. Sansonnens, A.A. Howling, C. Monard, Ch. Hollenstein

P.I.3 **Toward a fully monitored Fourier Transform Infrared Spectroscopic Ellipsometry** 131
J.-C. Cigal, G.M.W. Kroesen

P.I.4 **Diagnostics of Plasma Torch Fluctuations** 135
J.-L. Dorier, Ch. Hollenstein, A. Salito, M. Loch, G. Barbezat

P.I.5 **Remote Silane Plasma Chemistry Studied by Mass Spectrometry and Langmuir Probes** 139
W.M.M. Kessels, C.M. Leewis, M.C.M. van de Sanden, D.C. Schram

P.I.6 **Mie Scattering from Zirconia Evaporating in an Inductively Coupled Plasma** 143
G. Lins, D.W. Branston

P.I.7 **Characteristics of a Pulsed Microwave Oxygen Plasma** 147
M. Baeva, X. Luo, J. Uhlenbusch

P.I.8 **Complementarity of in-situ IR absorption spectroscopy and mass spectrometry for diagnostics in organosilicon plasmas** 151
D. Magni, Ch. Deschenaux, C. Courteille, Ch. Hollenstein, P. Fayet

P.I.9 **TDL Absorption Diagnostics and Chemical Modelling of Microwave Plasmas Containing Hydrocarbons** 155
L. Mechold, J. Röpcke, M. Käning, D. Loffhagen, P.B. Davies

P.I.10 **Optical Emission Study of Plasma-Surface Interaction in Reactive Plasmas** 159
S.A. Moshkalyov

P.I.11 **Diagnostics of a Planar Magnetron Sputter Source by Langmuir Probe and Optical Emission Spectroscopy** 163
A. Neuffer, A. Lunk

Page

		Page
P.I.12	**Modelling of the Composition of the Ion Flux Emanating from a Methane Electron Cyclotron Resonance Plasma** P. Pecher	167
P.I.13	**Diagnostics and modelling of an ICP discharge** P. Scheubert, P. Awakowicz, R. Schwefel, G. Wachutka	171
P.I.14	**Determination of the absolute density of F_2 formed in a CF_4 plasma by time-resolved threshold-ionization mass spectrometry** W. Schwarzenbach, J. Derouard, N. Sadeghi	175
P.I.15	**Charged Particles Fluxes and Energy Distributions Diagnostics in PECVD-Reactor During the Growth of Silicon- and Carbon-Based Films** A.S. Smirnov, A.I. Kosarev, M.V. Shutov, K.E. Orlov, T.V. Chernoiziumskaya	179
P.I.16	**Application of triple probe for volume-resolved monitoring of internal plasma parameters during industrial plasma polymerization process** P. Spatenka, J. Krumeich, J. Blazek, H.-J. Endres, R.W. Cook	183
P.I.17	**Test function for detection of parameters in electropositive and electronegative plasmas** E. Stamate, G. Popa, K. Ohe	187
P.I.18	**Pulsed Discharge at High Overvoltages: Diagnostic, Basic Features and Possibility of Applications** N.B. Anikin, S.V. Pancheshnyi, S.M. Starikovskaia, A. Yu Starikovskii	191
P.I.19	**Monitoring a single micrometer size particle by angle resolved light scattering** W.W. Stoffels, E. Stoffels, G.H.P.M. Swinkels, G.M.W. Kroesen	195
P.I.20	**Measuring the Temperature of Dyed Dust Particles in RF Plasmas** G. Swinkels, G. Kroesen	199
P.I.21	**Time resolved Langmuir probe measurements in medium pressure Ar-H_2 microwave plasma** E. Teboul, A. Rousseau, P. Leprince	203

Page

Poster Session II 207

P.II.1 **Thomson scattering in fluorescent lamps** 209
L.P. Bakker, G.M.W. Kroesen

P.II.2 **Atomic Lithium Beam Spectroscopy for N_e and T_e in Reactive Plasmas** 211
M. Böke, G. Himmel, B. Schweer, J. Winter

P.II.3 **Cavity Ring Down detection of neutral hydrogen atoms and negative hydrogen ions in plasmas** 215
M.G.H. Boogaarts, A.H.M. Smets, M.C.M. van de Sanden, D.C. Schram

P.II.4 **Absolute Concentrations of Reactive Species in Etching Plasmas by High-Sensitivity UV Absorption Spectroscopy** 219
J.P. Booth, D. Romanini, A. Katchanov, L. Biennier, G. Cunge

P.II.5 **Photo-detachment Technique Applied to High-Frequency Produced Plasmas** 223
F.M. Dias, E. Tatarova

P.II.6 **Time-resolved absorption and emission measurements of rotational temperatures and concentrations of C_2 and CH in a H_2/CH_4 microwave pulsed plasma** 227
X. Duten, A. Rousseau, A. Gicquel, Ph. Leprince

P.II.7 **Detection of atomic fluorine concentrations in discharges by two-photon absorption laser induced fluorescence spectroscopy (TALIF)** 231
A. Francis, U. Czarnetzki, H.F. Döbele

P.II.8 **Investigation of Pulsed Reactive Microwave Plasmas by Time-Resolved Laser-Induced Fluorescence** 233
A. Georg, Ch. Soll, St. Behle, A. Brockhaus, J. Engemann

P.II.9 **Applications of the Cavity Ring-Down Technique to a Large Area RF-Plasma Reactor** 237
F. Grangeon, C. Monard, J.-L. Dorier, A.A. Howling, Ch. Hollenstein, D. Romanini, N. Sadeghi

P.II.10 **Thomson scattering applied to a large volume ECR discharge** 241
D. Hemmers, A. Beck, S. Brezinsek, S. Meier, H. Kempkens, H.B. Schweer, J. Stanco, J. Uhlenbusch

Page

P.II.11 **Diagnostics and modeling of SiH_2 density in Ar/H_2SiH_4 deposition plasmas** 245
M. Hertl, J. Jolly

P.II.12 **Light Scattering Diagnostic System for Investigation of Reactive Plasmas in a Capacitively Coupled RF-Discharge** 249
M. Kaczor, H. Soltwisch

P.II.13 **Time Behaviour of Various Emissions in a Modulated Hydrogen Microwave Discharge** 253
N. Lang, M. Kalatchev, M. Käning, B.P. Lavrov, J. Röpcke

P.II.14 **Diagnostic studies of a capacitively coupled RF plasma containing CH_4-H_2-Ar**
Part II: On CH_4 dissociation and hydrocarbon plasma chemistry 257
M. Käning, J. Röpcke, C. Lukas, T. Kawetzki, V. Schulz-von der Gathen, H.F. Döbele

P.II.15 **Diagnostic Studies of a Capacitively Coupled RF Plasma Containing CH_4-H_2-Ar**
Part I: On radial species concentrations and temperature distributions 261
C. Lukas, T. Kawetzki, V. Schulz-von der Gathen, H.F. Döbele, M. Käning, J. Röpcke

P.II.16 **A 2-photon LIF study on the expansion behaviour of a plasma beam generated from a mixture of Ar and H_2** 265
S. Mazouffre, M.G.H. Boogaarts, I.S.J. Bakker, J.A.M. van der Mullen, D.C. Schram

P.II.17 **Concentrations of molecular species in a CH_4/O_2-plasma: a simple numerical model and measurements by infrared absorption spectroscopy** 269
C. Busch, I. Möller, H. Soltwisch

P.II.18 **Thomson Scattering Using ICCD Detectors in Photon Counting Mode for Low-Temperature, Low-Density Plasma Diagnostics** 273
S.A. Moshkalyov, C. Thompson, T. Morrow, W.G. Graham

P.II.19 **Reactive Species densities measured by optical emission and absorption spectroscopy in a chlorine inductively coupled plasma** 275
F. Neuilly, J.P. Booth, N. Sadeghi, L. Vallier

Page

P.II.20 **On Use of Rational Intensity Distribution in $GK^1\Sigma_g^+ \rightarrow B^1\Sigma_u^+$ bands of H_2 for Diagnostics of Non-equilibrium Plasmas** 279
S.A. Astahkevich, M.V. Kalachev, B.P. Lavrov, V.L. Ovtchinnikov

P.II.21 **Measurement of Quenching Rates for Short-Lived States in the Afterglow of Nanosecond Discharge** 283
S.V. Pancheshnyi, S.M. Starikovskaia, A. Yu Starikovskii

P.II.22 **LIF diagnostic of NO removal in a high pressure photo-triggered discharge** 287
F. Fresnet, G. Baravian, S. Pasquiers, C. Postel, V. Puech, A. Rousseau, M. Rozoy

P.II.23 **Time and Space Resolved LIF-Spectroscopy of O- and N-Atoms in a Dielectric Barrier Discharge** 291
M. Spaan, Ch. Lukas, V. Schulz-von der Gathen, H.F. Döbele

Contributions without Presentations 295

N.1 **The RF electric field and current density measured in an inductive discharge with a B-Dot probe: anomalous skin effect and collisionless power absorption** 297
G. Cunge, B. Crowley, D. Vender, M.M. Turner

N.2 **Spectroscopy Diagnostics of the Multicomponent Arc Plasma in Metal Vapours** 301
A.N. Veklich, I.L. Babich

Post-Deadline Papers 305

I.1 **Diagnostics of Thermal Plasmas** 307
M. Boulos

P.I.22 **Diagnostic Studies of Processing Plasmas Involving Electronegative Gases** 315
P.A. Read, J.A. Rees, C.L. Greenwood

List of Participants 319

Author Index 327

Foreword

WORKSHOP ON
FRONTIERS IN LOW TEMPERATURE PLASMA DIAGNOSTICS III

Organised by the
Centre for Research in Plasma Physics (CRPP),
Swiss Federal Institute of Technology Lausanne, Switzerland.

This is the third biennial workshop in the series following Les Houches, France (1995) and Bad Honnef, Germany (1997). The present workshop is principally devoted to:

DIAGNOSTICS OF INDUSTRIAL PLASMAS

Plasmas are an important tool in industry for a large number of different applications. Industrial processes require not only new and sophisticated plasma diagnostics for R&D purposes but also simple and effective plasma diagnostics for process monitoring and control.

ELECTRONIC VERSION

Extended abstracts which were submitted in electronic form are also available on the workshop web server http://crppwww.epfl.ch/LTPD99/ in pdf version. Contributions can be submitted to the workshop E-mail account plasma@epfl.ch .

REFERENCING

If required, the workshop papers can be referenced as:
Centre de Recherches en Physique des Plasmas, EPFL, Lausanne Report LRP 629/99 "Workshop on Frontiers in Low Temperature Plasma Diagnostics III", Switzerland, 15-19 February 1999.

SCHEDULE

Time	MONDAY 15	TUESDAY 16	WEDNESDAY 17	THURSDAY 18	FRIDAY 19
09:00 - 09:30	WELCOME	INVITED #3	PRESENTATION OF	INVITED #7	INVITED #10
09:30 - 10:00	INVITED #1	**A. Goehlich**	POSTER SESSION #2	**A. Steinbach**	**R. van de Sanden**
10:00 - 10:30	**M. Boulos**	INVITED #4	(23 x 5 min.)	INVITED #8	ORAL #8, 9
10:30 - 11:00	INVITED #2	**E. Stoffels**		**R. Gottscho**	**J. Röpcke**
11:00 - 11:30	**H. Soltwisch**	INVITED #5	POSTER	INVITED #9	**J.-P. Booth**
11:30 - 12:00		**A. Vardelle**	SESSION #2	**J. Schmitt**	CONF. CLOSING
12:00 - 12:30	LUNCH				
12:30 - 13:00		LUNCH		LUNCH	LUNCH
13:00 - 13:30	PRESENTATION OF		LUNCH		
13:30 - 14:00	POSTER SESSION #1	INVITED #6		ORAL #5, 6	
14:00 - 14:30	(21 x 5 min.)	**R. Engeln**		**S. Merkulov(to be conf.)**	
14:30 - 15:00		ORAL #1		**Ch. Vallée**	
15:00 - 15:30	COFFEE BREAK	**R. Hernberg**	FREE AFTERNOON	COFFEE BREAK	
15:30 - 16:00		COFFEE BREAK		ORAL #7	
16:00 - 16:30		ORAL #2, 3, 4		**A. von Keudell**	
16:30 - 17:00	POSTER	**A. Brockhaus**		OPEN DISCUSSION	
17:00 - 17:30	SESSION #1	**E. Hamers**		WITH PANEL	
17:30 - 18:00		**S. Moshkalyov**		"Industry-University	
18:00 - 18:30				collaboration and	
18:30 - 19:00				technology transfer"	
19:00 - 20:00	DINNER	DINNER	DINNER	DINNER "raclette" at Saillon village	

Invited Lectures

Diagnostics of Thermal Plasmas

Maher I. Boulos
Plasma Technology Research Centre (CRTP)
Université de Sherbrooke, Department of Chemical Engineering
2500 blvd. Université, Sherbrooke (Québec) Canada J1K 2R1

1. Introduction

Thermal plasmas are characterized by their high particle densities, high specific enthalpies and high flow velocities. These are often combined with the presence of steep property gradients and the simultaneous presence of particulate matter. Plasma diagnostic under these conditions offers quite a challenge which has been at the center of systematic study for the past two or three decades. Numerous techniques have been developed and are used on a regular basis for the measurements of the plasma and/or particulate parameters for the purpose of fundamental research, model validation, and process on-line controls. In the following, a brief over-view is given of the principal plasma and particulate diagnostics techniques currently used in thermal plasma studies giving for each; their potential, limitations and areas of applications. A number of general review papers have been published in the field [1-5]. Details about the individual techniques can be found in the vast literature on the subject.

2. Thermal plasma sources

A critical discussion of diagnostic techniques require a clear identification of the different plasma sources which would be the subject of study using these techniques. These can be classified for the purpose of the present review as direct current (d.c.), or inductively coupled, radio frequency (r.f.) discharges. The basic energy coupling mechanism and plasma flow configuration for each of these types of thermal plasma generators are presented schematically in Figure 1. These are discussed in the following.

2.1 D.C. plasma torches

As shown in Figure 1a, standard, plasma-spraying type, d.c. plasma torches operate with a central Thoriated Tungsten cathode and a water-cooled annular copper anode. The plasma gas is injected into the gap between the two electrodes and serves to keep the arc root in a continuous motion over the surface of the anode. Typical torch currents are in the range of a few hundred amps up to 1000 A or more. The torch voltage depends largely on the nature of the plasma gas and can vary between 25 to 30 V for pure argon operation up to 80 or 100 V when operating with molecular gases (Ar/H_2), N_2, ... As the gases pass around the arc through the anode nozzle constriction, they are heated and partially ionized emerging from the anode nozzle as a high velocity plasma jet with mean temperature of the order of 12 000 K and centerline plasma velocities that can be as high as 1000 m/s. Higher velocities can also be reached when discharging the plasma jet at low pressures 6.6 - 13.4 kPa (50 to 100 torr). The anode nozzle discharge diameter is typically of the order of 5 to 8 mm giving rise to steep property gradients in the fringes of the plasma jet. These can reach as high as a (10^3 K/mm) or hundreds ((m/s)/mm). The fringes of the plasma jet are also characterized by a rather complex turbulence structure which results from the interaction of the plasma jet with the cold ambient gas (air) surrounding it. When used for materials processing and thermal spraying applications, powders ($5 < d_p < 100$ μm) are injected into the plasma jet either internally into

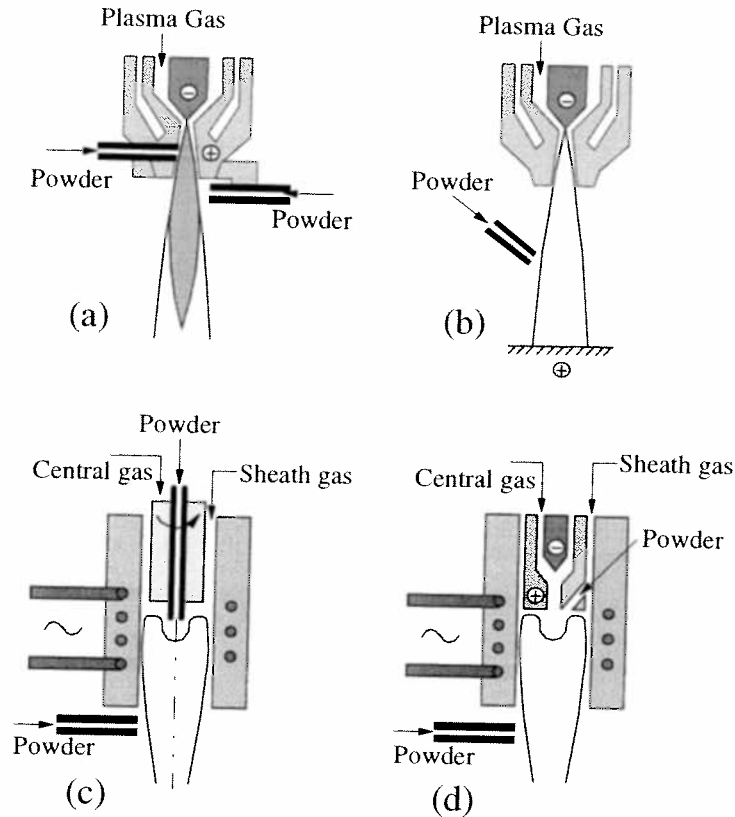

Figure 1: *Schematic of thermal plasma generation devices (a) d.c. plasma torch (b) d.c. transferred arc (c) r.f. induction plasma torch (d) d.c./r.f. hybrid plasma torch.:*

the anode nozzle, or externally as shown on either sides of Figure 1a. Typical material residence time in the plasma is less than one ms.

2.2 D.C. transferred arc plasmas

As shown in Figure 1b, transferred arcs differ from the standard d.c. plasma torches by the fact that they operate with an external anode which can be at a distance of a few centimeters up to 30 or 40 cm from the cathode. Typical arc currents are of the order of a few hundred amperes up to 1000 A or more. Arc voltages can vary between 20 to 30 V up to a few hundred volts depending on the arc length and the nature of the plasma gas. The plasma gas is injected in this case into the annular region between the cathode and an auxiliary nozzle which is usually kept at a floating potential. Typical conditions in the arc column are temperatures in the range of 12 000 K to 20 000 K though temperatures up to 26 000 K have been reported near the cathode tip. Gas velocities are of the order of a few tens of m/s. When used for material processing, transferred arcs are often used with a molten metal pool as anode in which the material in powder or chuck form is injected.

Due to late submission, this paper reproduced in full at the end of the book.

Potential and Limitations of Thomson Scattering in Reactive Plasmas

H.Soltwisch, M.Kaczor
Institut für Experimentalphysik V, Ruhr-Universität Bochum
Germany

Introduction

Scattering of electromagnetic radiation from free electrons in a plasma leads to a spectral broadening of the radiation due to the Doppler effect. Provided that the wavelength and the angle of observation are properly chosen, the spectrum of the scattered light represents a direct image of the electron velocity distribution, and the scattered light intensity is directly proportional to the electron density. This straightforward signal interpretation and the (conceptually) simple set-up needed to perform such measurements have made incoherent Thomson scattering the favored diagnostic tool for determining electron temperatures and densities in many plasma experiments. For glow discharges used in industrial applications, however, the technique is still far from being routine. Here the main obstacles are the low density of free electrons (resulting in very low signal levels) and the richness of spectral emission and absorption lines due to the presence of molecules and radicals. Under these conditions a flexible Thomson scattering system requires a tunable laser which allows the wavelength to be shifted to appropriate gaps in the spectra. In addition, the detection system should be capable to resolve the temporal behavior of the scattered light in order to track down possible contributions of weak laser-induced fluorescence. Moreover, the laser must not perturb the plasma (for example by affecting the composition of complex gas mixtures or reducing the content of negative ions due to photodetachment), which excludes, in many cases, the application of high-energy pulses and necessitates the use of photon counting techniques. In the following we will briefly summarize the principles of Thomson scattering, describe experimental systems and special features that have been tried to cope with the aforementioned problems, and finally discuss some new approaches and developments.

Basics of Incoherent Thomson Scattering

Using the classical picture of a free electron oscillating in the electric field of a linearly polarized laser beam, the radiated power into the full solid angle of 4π is found to be $P_s = \sigma_T I_0$, where $\sigma_T = 6.65\times10^{-29}$ m^2 is the total Thomson scattering cross-section and I_0 is the laser beam intensity in Wm^{-2}. The power is not uniformly distributed but shows the familiar $\sin^2\varphi$-dependence of an oscillating dipole (with φ being the angle between the direction of electron motion and the direction of observation). The power per unit solid angle radiated in a certain direction is therefore given by

$$\frac{dP_s}{d\Omega} = \frac{3\sigma_T}{8\pi} I_0 \sin^2\varphi. \qquad (1)$$

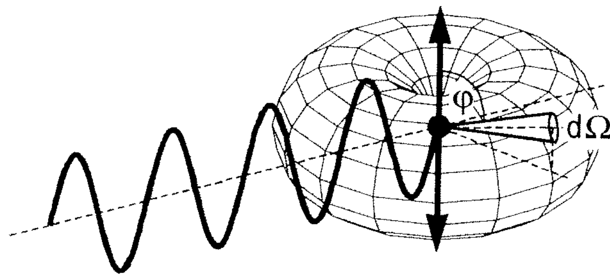

Figure 1: *Spatial distribution of the power radiated by a free electron which oscillates in the field of a linearly polarized electromagnetic wave.*

If the electron is not initially at rest but has a velocity **v** with components v_0 and v_s in the directions of the laser beam and of observation, the scattered light will be

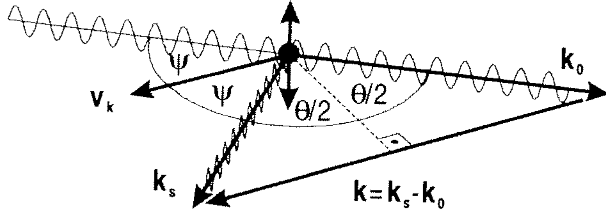

Figure 2: *Illustration of the wave vectors* $\mathbf{k}_0$ and $\mathbf{k}_s$ *of the incident and the scattered wave, respectively, and of the electron's relevant velocity component* $\mathbf{v}_k$.

frequency-shifted due to the Doppler effect. Defining a scattering vector $\mathbf{k} = \mathbf{k}_s - \mathbf{k}_0$ as the difference between the wave vectors of the scattered and the incident waves, the frequency shift can be expressed as (see, e.g. [1], [2])

$$\Delta\omega = \mathbf{k} \bullet \mathbf{v} = 2\frac{\omega_0}{c} v_k \sin(\theta/2), \qquad (2)$$

where v_k is the electron's velocity component parallel to $\mathbf{k}$, and θ denotes the angle between $\mathbf{k_0}$ and $\mathbf{k_S}$.

From eq. (2) it is obvious that an ensemble of scattering electrons will broaden the observed frequency spectrum in accordance with their velocity distribution along $\mathbf{k}$, provided that the phases of the scattered waves are random and the scattered power can be obtained as an incoherent sum of radiated powers from individual electrons. In a plasma this condition is satisfied if the Debye length λ_D is much larger than the inverse of the scattering vector $|\mathbf{k}|$:

$$\alpha = \frac{1}{|\mathbf{k}|\,\lambda_D} = 1.07\times 10^{-14}\cdot\frac{\lambda_0\,[\mathrm{nm}]}{\sin(\theta/2)}\cdot\sqrt{\frac{n_e\,[\mathrm{m}^{-3}]}{T_e\,[\mathrm{eV}]}} << 1 \qquad (3)$$

($\lambda_0 = 2\pi c/\omega_0$ is the wavelength of the incident laser beam, and n_e and T_e are the electron density and temperature; for typical parameters of reactive plasmas α is in the order of 10^{-3}).

In case of a Maxwellian electron velocity distribution the line shape of the scattered spectrum is a Gaussian with a (full) halfwidth at half maximum of

$$\frac{\Delta\lambda_{\mathrm{FWHM}}}{\lambda_0} = 4\sin(\theta/2)\sqrt{\frac{2\,k_B T_e}{m_e\,c^2}\ln 2} = 6.588\times 10^{-3}\cdot\sin(\theta/2)\cdot\sqrt{T_e\,[\mathrm{eV}]}\,. \qquad (4)$$

The total scattered intensity as given by the area under the line profile is proportional to the total number of electrons in the scatter volume and hence to the density n_e. In practice, the constant of proportionality depends on the transmission of the optical system, the length of the scatter volume, the solid angle of the direction of observation and other factors. These data are difficult to calculate and have to be determined experimentally. For this purpose a set-up is normally calibrated by a scattering process which has identical dependencies on the system parameters as the Thomson scattering process and where the density of scattering particles and the scattering cross-section are well known. A frequently used method of calibration is Rayleigh scattering from a cold gas at a given pressure. If infrared wavelengths are employed, the Rayleigh cross-sections become too small ($\sigma_R \propto \lambda_0^{-4}$), and liquids or crystals have to be used instead of gases.

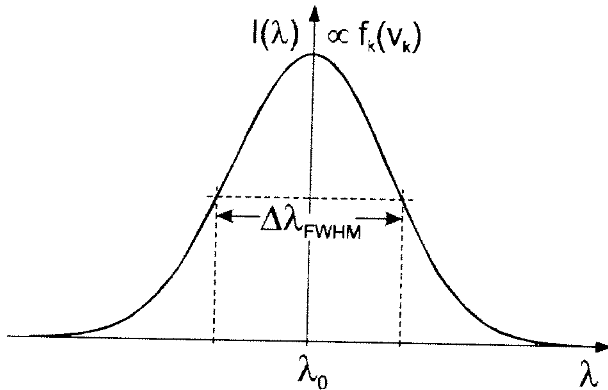

Figure 3: *Scattered spectrum for a one-dimensional Maxwellian electron velocity distribution* $f_k(v_k)$*; the area under the profile is proportional to* n_e *and the halfwidth is proportional to* $T_e^{1/2}$.

Thomson Scattering Experiments on Plasmas of Low Electron Density

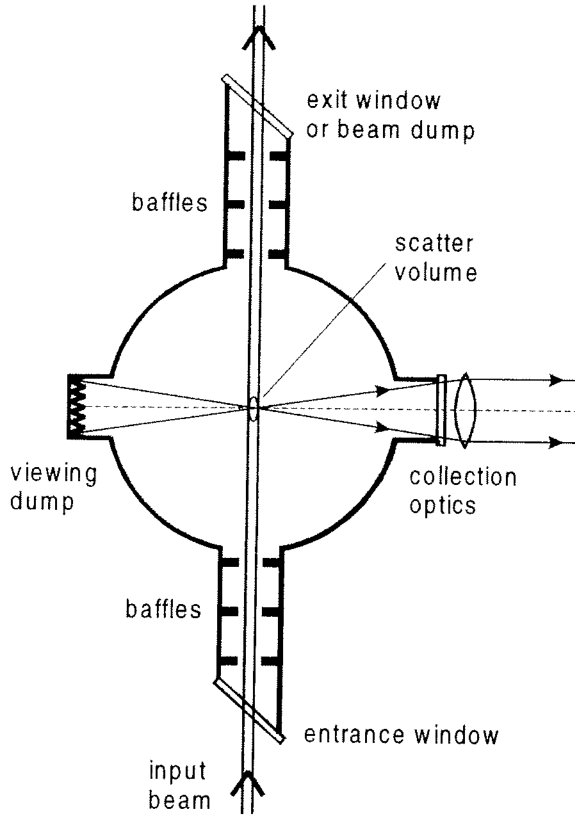

Figure 4: *Typical configuration for an incoherent Thomson scattering experiment (after* [3]; *note that the windows should be rotated by 90° along an axis parallel to the laser beam in order to allow for maximum transmission).*

The major problem in designing a functional Thomson scattering system is the smallness of the cross-section σ_T which requires high input power to obtain a reasonable number of scattered photons. According to eq. (1) the power radiated by N electrons into a solid angle $\Delta\Omega$ at φ=90° amounts to

$$\Delta P_s = N \cdot \frac{3\sigma_T}{8\pi} \cdot I_0 \cdot \Delta\Omega. \qquad (5)$$

Substituting $N = n_e A_s L_s$ and $I_0 = P_0/A_s$ (where A_s is the cross-section of the laser beam and L_s is the length of the scatter volume) and expressing the powers P_0 and ΔP_s in terms of injected (N_0) and scattered (N_T) photons per laser pulse, we arrive at

$$N_T = \frac{3\sigma_T}{8\pi} \cdot L_s \cdot \Delta\Omega \cdot n_e \cdot N_0. \qquad (6)$$

Taking typical values L_s = 1 cm, $\Delta\Omega$ = 0.2 sr, and $n_e = 10^{11}$ cm^{-3}, we find $N_T/N_0 = 1.6\times10^{-15}$. To make eq. (6) more tractable, the number of injected photons can be related to the pulse energy W_0 or to the average power $\overline{P}_0$ of a repetitively pulsed laser according to

$$N_0 = \frac{\lambda W_0}{hc} = \frac{\lambda \overline{P}_0}{hc f_{rep}}. \qquad (7)$$

For a high-repetition-rate laser (f_{rep} = 1 kHz, λ= 500 nm) with an average power of 1 W we have $N_0 = 2.5\times10^{15}$ photons/pulse, yielding under our assumed conditions just 4 scattered photons in each laser shot. To make things worse, this small number is further reduced by the transmission factor of the optical system and by the quantum efficiency of the detector. The use of a laser with high pulse energy in the order of 1 J (ruby or Nd:YAG at a repetition rate of 10 Hz or less) would increase N_0 (and hence N_T) by a factor of 10^3. On the other hand, high-energy pulses are likely to alter the composition of a reactive plasma by photodissociation of molecules and/or photo-detachment of electrons from negative ions. In addition, the laser could heat the scattering electrons, thus affecting the quantity to be measured [4].

Until now Thomson scattering measurements have only been performed on glow discharges of simple gas composition (mainly noble gases like He or Ar) where laser-induced perturbations of the plasma have played a minor role (see [5] for a recent review). Consequently, in most experiments high-pulse-energy, low-repetition-rate lasers have been used, and the efforts have been concentrated on improving the detection of the sparsely scattered photons and on optimizing the optical system. In order to suppress parasitic stray light (i.e. that part of the incoming laser light which reaches the detection system without any plasma scattering process through reflections at windows, vessel walls, etc.), entrance and exit tubes for the laser beam have been developed which are sealed by high-quality Brewster windows and which contain apertures that are carefully tailored to match the beam diameter. The purpose of these apertures is to cut off light which has been scattered at small angles by

anterior components. In addition, the background of the observation path has been made to appear deep black by installing a so-called viewing dump. It usually consists of a stack of razor blades or blackened pyramids viewed onto the edges and tips, or of polished color glass filters positioned at Brewster angle. By taking these measures, the residual level of stray light has been brought down to values which are well below the inevitable level of Rayleigh scattering from bound electrons in the atoms and ions. Since the spectral distribution of the stray light is very narrow and centered at the laser wavelength λ_0, a further reduction is possible by placing a suitable narrow-band notch filter in the observation path. However, such a filter would prevent a convenient absolute calibration of the set-up since it would also block the light due to Rayleigh scattering. In practice, therefore, a double monochromator is used which offers a sufficient rejection of monochromatic light next to its pass band (10^{-7} over a spectral separation of 0.6 nm, as reported in [4]). Another important aspect in designing a Thomson scattering diagnostic concerns the optics for collecting the scattered light and relaying it to the spectrometer. The acceptance cone $\Delta\Omega$ and the overall transmission should be made as large as possible in compliance with the specific limitations and boundary conditions at a given experiment.

The standard detector for Thomson scattering measurements on low-density plasmas is a photomultiplier tube (PMT) because of its low noise, high current gain (up to 10^7) and reasonable quantum efficiency (between 10 and 20% in the visible). Depending on the number of photons reaching the PMT per laser shot, it can be operated in an analogue or in a counting mode. In the first case, the output current I_{PMT} is recorded as a function of time, and the integral $\int I_{PMT}\,dt$ over the pulse duration provides a direct measure of the number of scattered photons (after subtraction of a background due to plasma radiation). If on average less than one photon per laser shot is scattered onto the PMT, the counting method has to be used. It is based on the high gain of a PMT which produces a large current pulse if a photon hits the cathode and releases an electron. By putting the output signal through a discriminator, noise components below a properly adjusted threshold are blocked and the remaining spikes, which are considered to represent individual photons, are fed into a counter. Since multiple photons striking the cathode simultaneously are regarded as a single event, this technique can only be applied at very small signal levels.

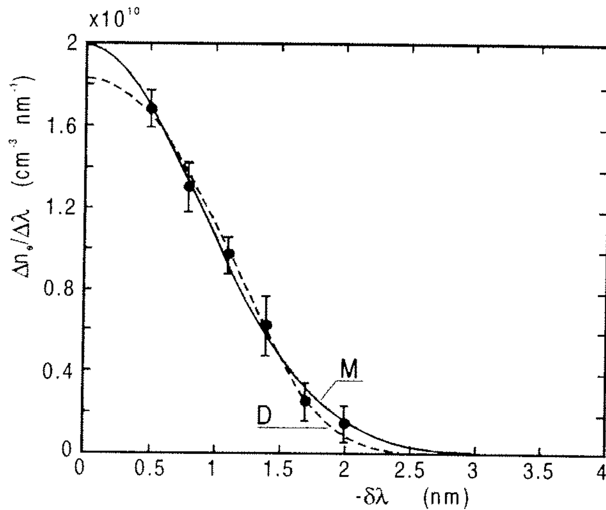

Figure 5: *Thomson scattering spectrum from a capacitive rf discharge in helium as published in* [4] (*see text for details*).

To conclude this short survey of relevant experimental features, we want to present two examples of actual measurements. The first one was aimed at investigating the α-γ transition of a capacitive rf discharge in helium ([4], [6]). In order not to falsify the electron temperature, a low-pulse-energy laser in combination with photon counting was employed. Figure 5 shows a measured Thomson scattering spectrum where the ordinate gives electron densities Δn_e per wavelength resolution interval $\Delta\lambda$ as a function of the wavelength separation $\delta\lambda$ to the laser line at 532 nm. The error bars of the data points not only represent statistical uncertainties but also include errors due to background subtraction and corrections of instrumental effects (for details see [4]). For this experiment a single PMT was used, and the spectral points were measured one after the other. The time necessary to collect all data was

about 10 hours with the laser running at a repetition rate of ~1 kHz with pulse energies of a few mJ. The resolution of the double monochromator was $\Delta\lambda \cong 0.3$ nm, meaning that the outermost point in Fig. 5 at $\delta\lambda = -2$ nm represents a velocity group of just 5×10^8 electrons per cm^3. The lines denoted by *M* and *D* are fit curves based on a Maxwellian and a Druyvestein velocity distribution. Both are compatible with the experimental data points and yield nearly the same electron density and temperature of about 5×10^{10} cm^{-3} and 0.6 eV, respectively.

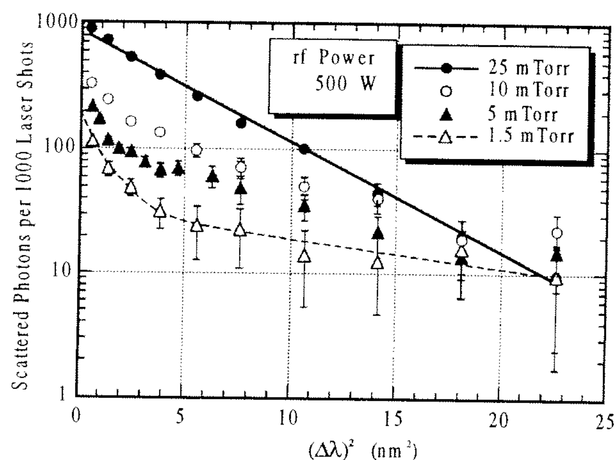

Figure 6: *Thomson scattering spectra from inductive rf discharges in argon as published in* [8] (*see text for details*).

The second example is an experiment which was performed to study deviations from a Maxwellian distribution function in inductively coupled rf discharges ([7], [8]). The laser used was again a Nd:YAG operated at the second harmonic wavelength $\lambda_0 = 532$ nm but at a repetition rate of 10Hz and with pulse energies of 0.5 J. The scattered light was detected by a single PMT at different spectral positions with a maximum distance of 5 nm away from λ_0 (corresponding to an energy of the scattering electrons of 11 eV). Photon counting was used here, too, in order to enable reliable measurements especially in the far wings of the scattered light spectrum. Figure 6 shows some results for the discharge operated in argon at various filling pressures and at a constant rf input power of 500 W. In this semi-logarithmic representation of the count rates vs. the square of the wavelength separation, a Gaussian line shape (corresponding to a Mawellian distribution) appears as a straight line. The data clearly indicate significant departures for pressures below 10 mTorr which were attributed, at least in part, to the influence of the rf magnetic field on the electron motion (a detailed discussion may be found in [8]). The electron density in the discharge varied linearly with pressure from 2×10^{11} cm^{-3} at 1.5 mTorr to 1.5×10^{12} cm^{-3} at 25 mTorr. The temperature in the high-pressure case was found to be ~2.5 eV, whereas at low pressure two components of ~0.5 and ~5 eV were obtained.

New Approaches and Developments

The examples given in the previous section show that fairly accurate Thomson scattering measurements are feasible in low-pressure, low-temperature plasmas with electron densities down to a few times 10^{10} cm^{-3}. Moreover, these measurements can be done with lasers of low pulse energy to minimize perturbations. It must be emphasized, though, that the experiments have been performed on discharges of very simple gas composition only. Reactive plasmas are characterized by complex mixtures of atoms, ions, molecules, and radicals, and they often exhibit slowly evolving chemical reactions and processes such as dust formation and surface coating. The problems posed by these additional complications call for a further improvement of existing techniques as well as for the introduction of new concepts.

To begin with, ten hours or more for collecting a sufficient number of scattered photons is barely acceptable in view of maintaining a reactive plasma stationary (and keeping the windows and other in-vessel components sufficiently clean) for such a long time. A reduction by an order of magnitude is readily achieved if the spectral points are measured simultaneously rather than one by one. In our group [9] we are using an eight-channel fiber

optics aperture with a height of 8 mm and a channel width of 0.8 mm (corresponding to a wavelength interval of 0.6 nm) to transmit the spectrally resolved light to an eight-channel PMT (Hamamatsu R6665) designed for photon-counting applications. Bowden et al. [10] employ a high performance image-intensified CCD camera (Princeton Instruments) to record the entire spectrum in every laser shot. The device is equipped with hardware and software to allow for photon counting, too. In addition, these authors have developed a multipass cell for reflecting the laser beam through the discharge many times in order to make more effective use of the beam energy. Disadvantages of this approach are the increased level of stray light, the deterioration of spatial resolution, and, most severely, the loss of ability to follow the temporal behavior of the scattered light.

Weßeling and Kronast reported in Ref. [4] that even in their extremely clean helium discharges it was necessary to record the time dependence of the received light because of weak laser-induced fluorescence (LIF), which caused a faint afterglow also in spectral channels well separated from the laser line (Weßeling [6] studied this effect in detail and attributed it to an electronic transition in the He_2 molecule in combination with changes of its rotational state). In their experiment they employed a multichannel scaler being capable of recording photon counts in 512 intervals of 5 ns each with every laser pulse. As an example we show in Fig. 7 the count rates as a function of time measured with similar equipment in our laboratory (details of our experimental set-up may be found elsewhere in these proceedings). Filling gas and discharge parameters were the same as in [4], but our impurity level was probably higher since we could change the amount of LIF by baking the vessel. In order to apply the technique of time resolved photon counting to all the eight channels of our PMT in every laser shot, we serialized the output signals by feeding them through delay units with staggered delay times. The resulting train of PMT signals had a total length of typically ~10 µs, requiring ~2000 intervals of 5 ns each for registration, which was well within the capacity of our multichannel scaler (EG&G Ortec T914). Figure 7 also indicates how the signals can be separated into contributions due to Thomson scattering and LIF. The shape of the Thomson scattering signal is identical to that of the laser pulse and is well known from Rayleigh scattering. The shape of the laser pulse also determines the rising edge of the LIF signal. From the slow decay during the afterglow it is then possible to calculate the contribution of LIF to the total signal as a function of time, leaving after subtraction a Rayleigh signal scaled to the size of the Thomson contribution.

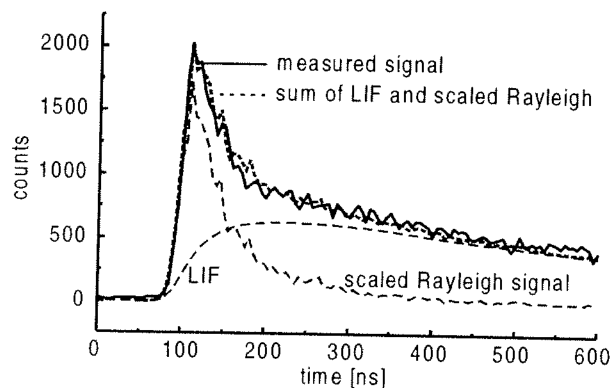

Figure 7: *Time resolved scattering signal from a capacitive rf discharges in helium measured in the interval 0.6±0.3 nm away from the laser line at 532 nm.*

The occurrence of laser-induced fluorescence already in a fairly standard helium discharge points to another necessity: the application of a tunable laser which allows to shift the wavelength away from atomic or molecular resonances into a region of lowest possible background radiation. Since the pulse energy and repetition rate should be comparable to those of proven frequency-doubled Nd:YAG systems, the choice is presently limited to either a Ti:S laser or a Dye laser. Recently, a Dutch group at Eindhoven University of Technology has embarked on setting up a Thomson scattering system based on a Dye laser [11]. However, the high level of Amplified Spontaneous Emission (ASE) typical for these devices constitutes

a serious problem since it produces a broadband background of stray light that is not filtered out by the spectrometer. Therefore the spectral purity of the laser beam has to be improved before entering the plasma chamber by means of a rather elaborate arrangement of prisms and pinholes. In our group we have started to use a Ti:S laser pumped by an upgraded version of the Nd:YAG that had been employed in previous experiments. It offers a range of tunability from 425 nm to 480 nm (after frequency doubling) which matches the range of maximum quantum efficiency of our eight-channel PMT.

Summary

In the last decade much progress has been made in lowering the detection limit of incoherent Thomson scattering. Efficient techniques of stray light suppression and the accumulation of data from a large number of laser pulses have made it possible to perform accurate measurements on glow discharge plasmas with electron densities $<10^{17}$ m^{-3}, albeit under favorable conditions of simple plasma composition and long-term stability. Reactive plasmas containing a large variety of atomic and molecular species pose additional problems which have prevented a successful application of Thomson scattering so far. Improvements necessary to cope with the extra demands are (i) a significant reduction of the time required for data collection, (ii) the application of time-resolved photon counting methods to keep track of weak laser-induced fluorescence, and (iii) the ability to adapt the laser wavelength to very complex emission and absorption spectra. Appropriate modifications are presently being developed, and there is hope that Thomson scattering will become a practicable and reliable tool to diagnose the electron component also in those types of plasmas which are used in technological applications such as plasma etching and deposition.

Acknowledgement

This work was supported by SFB191 of the “Deutsche Forschungsgemeinschaft”.

References

[1] H.J. Kunze; *The Laser as a Tool for Plasma Diagnostics* (in W. Lochte-Holtgreven: *Plasma Diagnostics*), North Holland Publishing Company, Amsterdam (1968).

[2] J. Sheffield; *Plasma Scattering of Electromagnetic Radiation,* Academic Press, London (1975).

[3] I.H. Hutchinson; *Principles of Plasma Diagnostics,* Cambridge University Press, Cambridge (1987).

[4] H.J. Weßeling, B. Kronast; J. Phys. D: Appl. Phys., **29**, 1035-1039 (1996).

[5] K. Muraoka, K. Uchino, M.D. Bowden; Plasma Phys. Contr. Fusion, **40**, 1221-1239 (1998).

[6] H.J. Weßeling; *PhD Thesis*, Ruhr-Universität Bochum, Germany (1994).

[7] M.D. Bowden, T. Hori, M. Kogano, K. Uchino, K. Muraoka; *Proc. 8th Int. Symp. Laser-Aided Plasma Diagnostics*, Doorwerth, Netherlands, 229-234 (1997).

[8] T. Hori, M. Kogano, M.D. Bowden, K. Uchino, K. Muraoka; J. Appl. Phys., **83**, 1909-1916 (1998).

[9] C. Busch, H. Soltwisch; *Proc. Frontiers in Low Temp. Plasma Diagnostics II*, Bad Honnef, Germany, 107-109 (1997).

[10] M.D. Bowden, Y. Goto, K. Uchino, K. Muraoka; *Proc. 8th Int. Symp. Laser-Aided Plasma Diagnostics*, Doorwerth, Netherlands, 259-264 (1997).

[11] L.P. Bakker; *private communication* (1998).

Laser based diagnostics of sputtered atoms and molecules

A.Goehlich, N. Niemöller and H.F. Döbele

Institut f. Laser- und Plasmaphysik, Universität-GH Essen, 45117 Essen, Germany

I. a. Introduction

The modification of solid surfaces by plasmas or ion beams and the deposition of thin films are based on the erosion of a surface by energetic particles. A precise knowledge of the underlying fundamental sputtering mechanisms and a detailed knowledge of the energy and angular distribution are therefore of great importance. In ion beam experiments for the study of plasma wall interaction well defined bombarding conditions e.g. a mono energetic beam and a well defined angle of incidence can be established. As the main fraction of the erosion products are neutrals, the diagnostics of the neutral products is an important issue. In this contribution we report on measurements of energy and angular distributions of sputtered particles with two different laser based methods: First, we report on laser induced fluorescence measurements (LIF) of the velocity distribution of sputtered metal atoms. In this case the velocity distribution is measured by scanning narrow bandwidth laser radiation over the Doppler broadened absorption line. Our experimental set-up allows to change the observed angle of emission independently of the angle of incidence in order to study anisotropy effects as described in section II of this article. The sensivity of laser induced fluorescence is limited by false light. High current ion guns are therefore required in general which generate a sufficient high density of particles. Methods which rely on the detection of ionized particles are much more sensitive, however. This higher sensitivity is based on the possibility to collect practically all photo-ionized particles e.g. with the aid of electrostatic lenses and to detect them by high efficiency particle detectors. In part III of this contribution first results of a set-up which recently started operation are reported. Energy distributions of atoms and molecules are determined by a time-of-flight technique. Non-resonant ionization for the detection of metal atoms (W,Al,Ti) as well as resonant enhanced ionization (REMPI) for the detection of atomic oxygen are used.

b. Standard theory

Physical sputtering is a well known process in principle. The underlying basic mechanism may be described as follows: An energetic ion (say with keV energy for the moment) hitting the solid surface is stopped by a series of binary collisions and penetrates the solid to a depth of typically a few nm. Target atoms are set in motion as a result of this stopping

process, which are able to collide with further target atoms, and a more or less extended recoil cascade develops. If the density of the recoiling atoms is not too high (most of the target atoms in the cascade volume are at rest, no collisions among moving atoms) the cascades superpose linearly ("linear cascade regime"). A fraction of the recoiling atoms in a surface-near layer receives enough momentum normal to the surface to overcome the surface barrier and leave the solid as a sputtered particle. The energy distribution of sputtered particles was calculated by Thompson [1] with the aid of simple physical assumptions (see below) and by Sigmund [2] on basis of transport theory.
The essential assumptions for the applicability of the Thompson formula are:

1.) an "amorphous" solid (this often realized in a polycrystalline target by averaging over many crystallites).
2.) binary collisions through a screened Coulomb potential (often approximated by a power potential of the form $R^{-1/m}$).
3.) an isotropic distribution of momentum of the recoil atoms.
4.) a planar surface potential of height E_b. The heat of sublimation is often used for E_b.

The flux energy distribution then assumes for not to high emission energies ($E << \frac{4M_1M_2}{(M_1+M_2)^2}E_p$, E_p projectiles energy) the following form:

equu. 1

$$\Gamma \propto \frac{E}{(E+E_b)^{3-2m}}$$

The validity of the Thompson formula is experimentally proven in many contributions (e.g.[3]) and often serves the purpose as a reference standard. Deviations from equ. 1 arise, however, for oblique incidence of the ion beam and/ or small energy transfer in the collisions (e.g. by "low" bombarding energy or small projectile-to-target mass ratio). In this case in addition to the "isotropic" part (equ. 1) anisotropic contributions to the energy distribution appear, which are caused by recoil atoms of a low generation of recoil cascades. The deviation of the energy distribution from the isotropic limit is of the order of $\sqrt{M_1E/M_2E_p}$ [4]. In this case the motion of the recoiling atoms which lead to sputtering are decoupled from the motion of the ion and the energy distribution of the sputtered particles depends, in contrast to equ. 1, on the energy , the mass and the angle of incidence of the impinging ion.
Simulation codes like the Monte Carlo program TRIM.SP [5] include these anisotropy corrections. In the following section measurements of velocity distributions of metal atoms are described and deviations from the isotropic limit are discussed. A part of the measurements is compared to TRIM-calculations.

II. Determination of angular resolved velocity distributions of sputtered tungsten and aluminum atoms by laser induced fluorescence.

a. Experimental set-up

The basic arrangement is shown in figure 1.

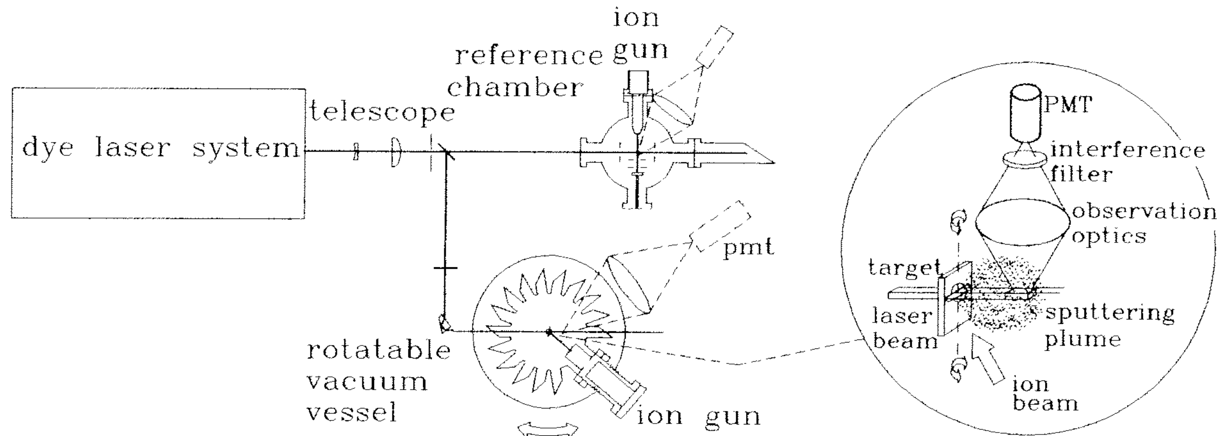

Fig. 1. Experimental set-up for angle resolved laser induced fluorecence measurements

The laser pump radiation is generated by an excimer pumped dye laser which is equipped with an intracavity etalon and a second harmonic generator. The linewidth of the laser amounts to 0.04 cm^{-1} in the visible. The laser frequency is changed by variation of the pressure in the oscillator chamber of the dye laser. The frequency shift is monitored by an external etalon. For the detection of tungsten atoms the transition 0->34342 cm^{-1} at $\lambda=291$ nm is pumped, the fluorescence radiation around $\lambda=403$ nm is observed. Aluminum atoms are detected by pumping the transition $3p\ ^2P_{3/2} \rightarrow 4d\ ^2D_{3/2}$ and observing a subsequent transition at $\lambda = 396$ nm.
A fraction of the generated UV-radiation is adjusted through a rotatable vacuum chamber (base pressure 5 10^{-8} mbar) which is equipped with 15 Brewster windows with an angular displacement of 20°. A stainless steel target holder is mounted in the center of the vessel. The target mount may be rotated with the aid of a vacuum stepper motor. For the main part of the measurements a target mount with a slit was used through which the laser beam was adjusted. Thin pure polycrystalline metal foils were clamped inside. The free target diameter limited by a stainless steel mask amounts to 8 mm (see insert in figure 1). The target is bombarded by rare gas ions (argon or xenon) from a Kaufmann type ion source with energies in the range (0.2-1 keV). The current density amounts to approximately 0.15 to 0.4 mA/cm^2. The diameter of the ion beam is limited by apertures to a diameter of 10 mm. The scattering volume (placed about 20 mm in front of the target surface) is imaged

by a large aperture lens (spatially fixed with respect to the laser beam) on the cathode of a photomultiplier tube (see insert in fig. 1). The emission angle of interest can be chosen by aligning a Brewster-window parallel to the laser beam through a rotation of the vacuum chamber. A rotation of the target allows a change of the angle of incidence. Since the velocity distribution is asymmetric a separate LIF set-up is used to determine zero velocity. In a reference vessel atoms are also generated by sputtering. The atoms are excited with a fraction of the pump radiation perpendicular to their emission direction. In this case a symmetric profile results.

In order to avoid saturation effects the laser radiation is attenuated to a level near the small signal regime. For the registration of a velocity distribution the pressure in the oscillator chamber is varied in distinct steps. Typically 30-50 pulses are summed up - depending on the signal intensity. The fluorescence pulses obtained from the main chamber and the reference vessel are stored together with a monitor signal supplied by a fast UV-diode (for normalization) and the signals of a diode behind the monitor etalon.

b. Results and discussion

Deviations of the velocity distribution from the isotropic case are caused by incomplete randomization of the recoil cascades e.g. at low bombarding energy. In fig. 2 a,b a comparison of the velocity distributions of sputtered tungsten atoms for 5 keV and 0.3 eV argon bombardment is presented. The data were taken for normal incidence and emission. At the lower energy a stronger high energy fall-off of the distribution is obvious. The Thompson distribution and the corresponding TRIM-simulation are also shown for comparison.

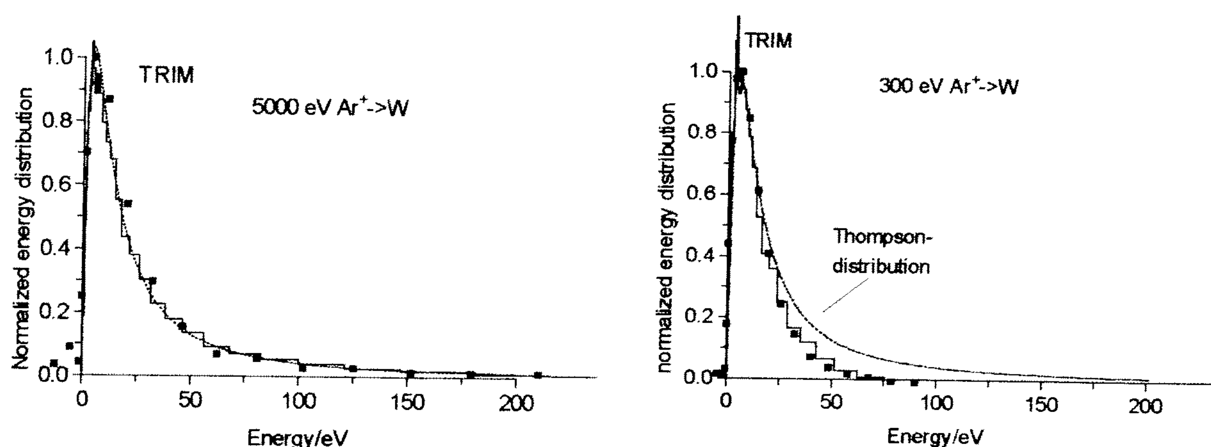

Fig. 2 a,b: Energy distributions of sputtered tungsten toms for 5000 and 300 eV argon bombardment at normal incidence

The lack of high energetic atoms at 300 eV is connected to the larger energy loss in the large angle deflections of recoil atoms which lead to sputtering in the low bombarding

energy case. The dependence of the distribution on the angle of emission is small, however. The experimental distributions presented in figure 3 exhibit no pronounced influence of the emission angle on the velocity distribution.

A small angular effect was observed for the low energy bombardment of aluminum with 250 eV argon ions, however. In figure 4 energy distributions for normal emission and emission under 60° are shown. The latter exhibits a somewhat smoother decay towards higher energies. This may be explained by the fewer large angle collisions which are necessary for oblique emission as compared to normal ejection. For oblique incidence anisotropy may dominate. An illustrative example is the oblique (70°) bombardment of aluminum with 500 eV xenon ions (figure 5). The energy distribution for emission in the backward direction (on the side of the incident ion beam) exhibits an "under-Thompson" behavior, which is caused by weakly developed recoil cascades. In forward direction ($\phi=30°$) a clear broadening and a shift of the peak is observable. The mean energy increases from 5 eV ($\phi=-50°$) to 24.1 eV ($\phi=30°$). The distributions could not be approximated with a single Thompson distribution with E_b taken as the heat of sublimation (3.4 eV of Al). As a trial the energy distribution in forward direction is approximated by a superposition of two Thompson-distributions with E_b =3.4 eV and E_b=12.9 eV respectively.

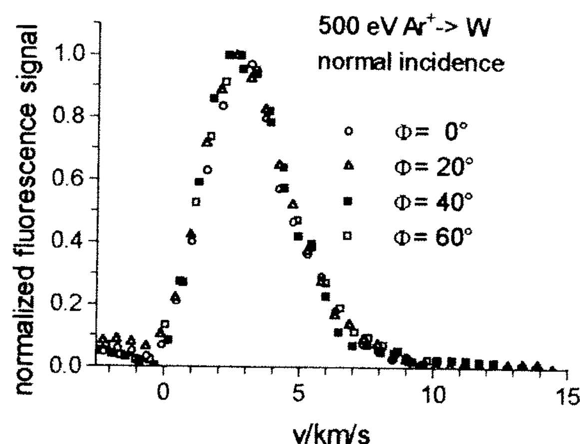

Fig. 3 Velocity distributions of sputtered tungsten atoms for different emission angles (ϕ)

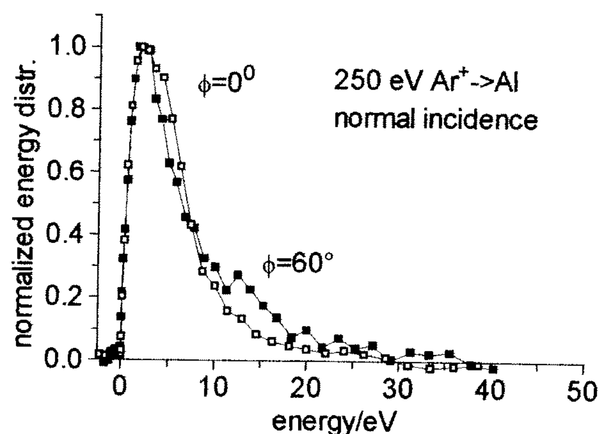

Fig. 4. Energy distribution of aluminum atoms for normal and oblique emission.

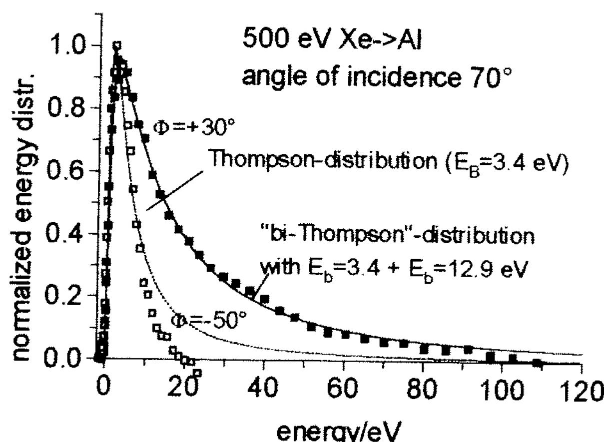

Fig. 5 Anisotropic effect on the energy distributions for oblique bombardment of aluminum with 500 eV argon ions. Note the considerable broadening of the distribution in forward direction.

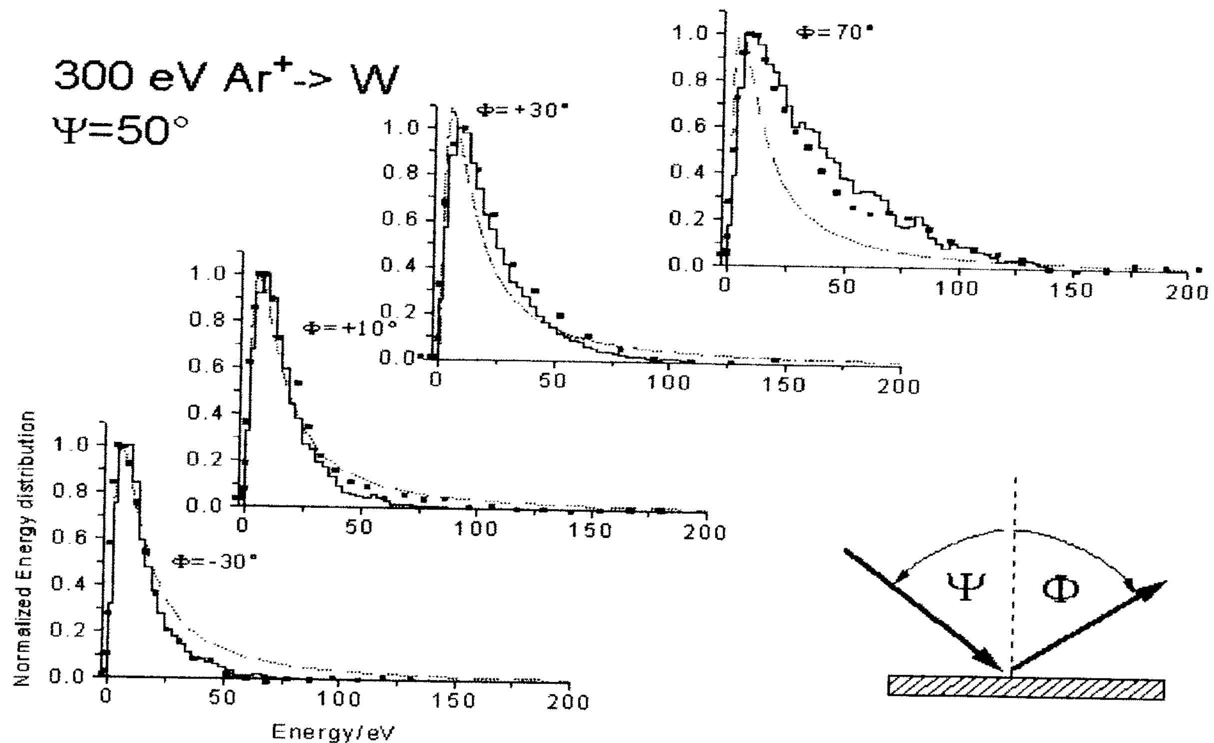

Fig. 6. Change of energy distributions of sputtered tungsten atoms at 300 eV bombardment and oblique incidence. Note the shift of the distributions with respect to the standard theory (dashed). The TRIM.SP simulation is drawn as a step function.

The high energetic contribution may be interpreted as the anisotropic component.
Energy distributions for lower bombarding energy (300 eV) and an angle of incidence 50° are shown in figure 6 and compared with the TRIM.SP-simulation. Note the systematic change of the data as a function of the emission angle with respect to the isotropic limit. The effect of the anisotropy causes a shift and a broadening of the distribution.
The last example in this section is devoted to the possibility of our set-up to determine relative angular distributions. The relative flux of the sputtered particles is calculated by integrating a fluorescence profile and multiplying with the mean velocity obtained from the first moment of the distribution. The result is presented in figure 7 as a function of the polar angle. The emission is peaked in forward direction near the specular angle. The agreement with TRIM.SP is satisfactory.

It can be summarized that anisotropy is important especially at oblique incidence. The influence of anisotropy may be used to control the yield and the mean energy of the erosion products. The measurements show satisfactory agreement with the simulation. Details of the distribution, e. g. direct recoil peaks, are smeared out, however. This is ascribed to the relatively high fluences which are applied for the measurements. For low

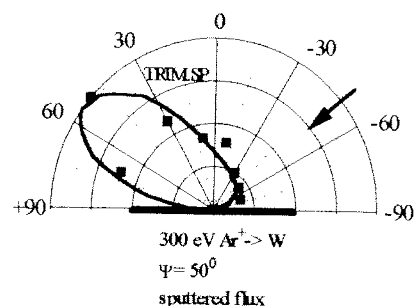

Fig. 7. relative angular distribution for oblique bombardment of tungsten

dose measurements the more sensitive laser post-ionization method in connection with a pulsed ion gun is more suitable. In the following section first measurements of an experiment which recently started operation are communicated.

III. Determination of time-of-flight distributions of sputtered atoms and molecules by resonant and non-resonant ionization.

a. Experimental set-up and data acquisition procedure

A sketch of the set-up is depicted in figure 8 below.

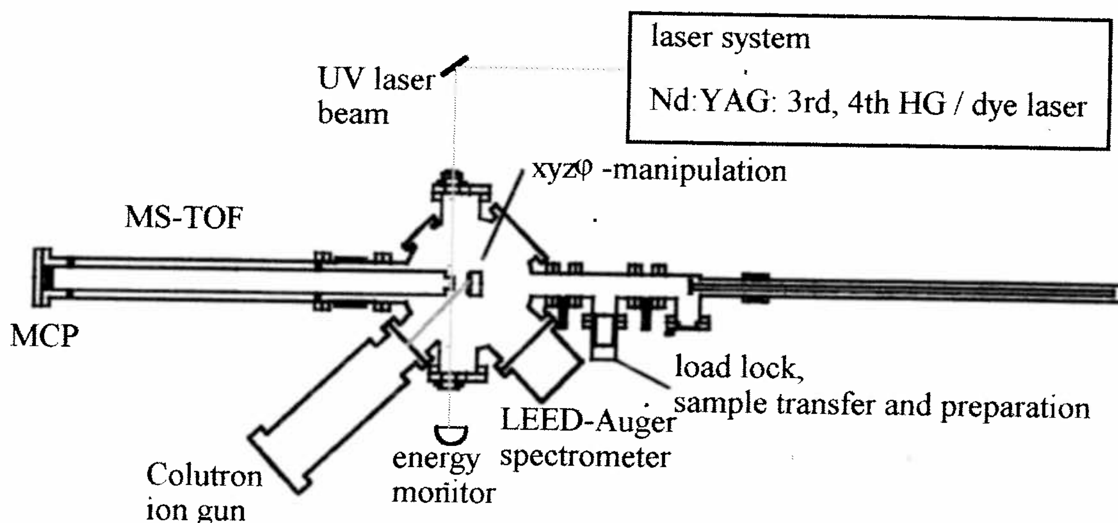

Fig. 8 UHV-apparatus for the determination of time-of-flight distributions of sputtered particles

In the case of non-resonant ionization the tripled ($\lambda=355$ nm) or quadrupled radiation ($\lambda=266$nm) of a Nd:Yag laser system is used (Continuum PL 9020: repetion rate 20 Hz, pulse duration 5 ns). For resonance enhanced ionization tunable UV-radiation is generated by a frequency doubled dye laser which is pumped by the aforementioned Nd:Yag laser.
The vacuum system consists of a load lock and sample transfer system including a separate preparation chamber with an argon sputtering gun, and the UHV-main chamber (base pressure 5 10^{-10} mbar). The samples are transferred on a heatable xyz-ϕ manipulator . A mass separated ion gun (Colutron) is attached to the main chamber. The measurements reported in the following were performed with 6 keV argon ions. An einzel lens focuses the beam on the target surface (spot diameter < 1mm). Ion pulses with an amplitude of a few microamps and pulse duration in the range of 0.5 and 2 μs are generated by pulsing a pair of deflection pairs.

Sputtered particles are detected by a linear time-of-flight mass spectrometer (MSTOF). The neutral particles are ionized by the focused (f=300 mm) laser beam, accelerated into the drift tube which is biased with -2 kV and detected by a pair of microchannel plates. The signal of the channel plates is fed to a multi channel scaler (SR430) and is averaged over typ. 200 laser shots. A time-of-flight distribution is determined by varying the time delay between the laser and ion pulse. The velocity of the detected ions is calculated by the drift distance (38 mm) and the time delay.

b. Results

The first example refers to the bombardment of a tungsten sample and subsequent ionization of the particles with radiation around $\lambda=355$ nm. This wavelength was chosen to take advantage of the spectral vicinity to a 1-Photon transition of the tungsten atom and the resulting enhancement of the ionization cross section. The mass spectrum essentially exhibits two peaks (besides a background generated by reflected argon) (fig. 9). Both mass peaks exhibit the isotope structure of tungsten. The first peak is ascribed to tungsten atoms. Using the isotopic structure of the first peak for mass calibration the second peak is ascribed to sputtered WO-molecules.

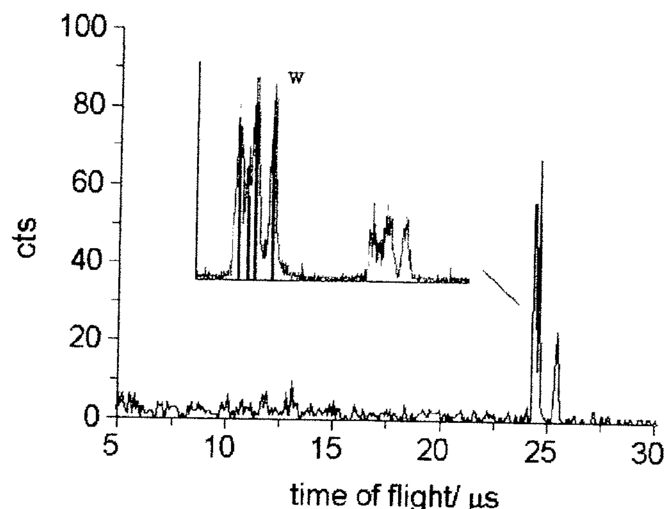

Fig. 9 Mass spectrum of products sputtered from a tungsten foil. The first peak is identified as tungsten atoms. The second peak is attributed to a surface contamination (see text).

The contamination peak may also be removed by continuous bombardment of the target. The time-of-flight distribution (fig. 10) as well as the corresponding energy distributions are shown in figures 10 and 11. The energy distribution is approximated by a Thompson distribution with a surface energy of 10 eV (in accordance with previous LIF-results). The distribution of the surface contamination - reduced in the plot by a

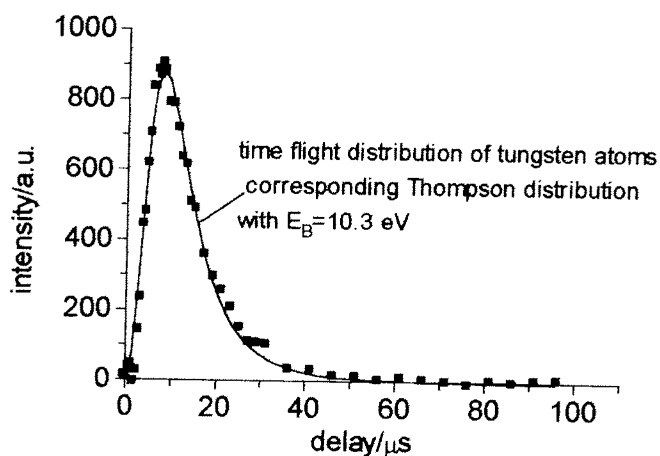

Fig. 10 Time-of-flight distribution of sputtered tungsten atoms. The fitted line corresponds to a time-of-flight distribution transformed according to the Thompson formula.

factor of ten for clarity- has a similar shape and can be also approximated by a Thompson-distribution with a somewhat smaller value of the surface binding energy.

Figure 12 shows the results of the bombardment of an aluminum foil and subsequent ionization with radiation around $\lambda=355$ nm. The monomer and the dimer are detected. The energy distribution of the atom is well described by the linear cascade model with a value for the surface binding energy near the heat of sublimation. The distribution of the dimer is not described by a Thompson distribution. The fall-off of the energy distribution with an exponent near $n=2$ indicates the sputtering of the dimer as an unit by a cascade mechanism , however.

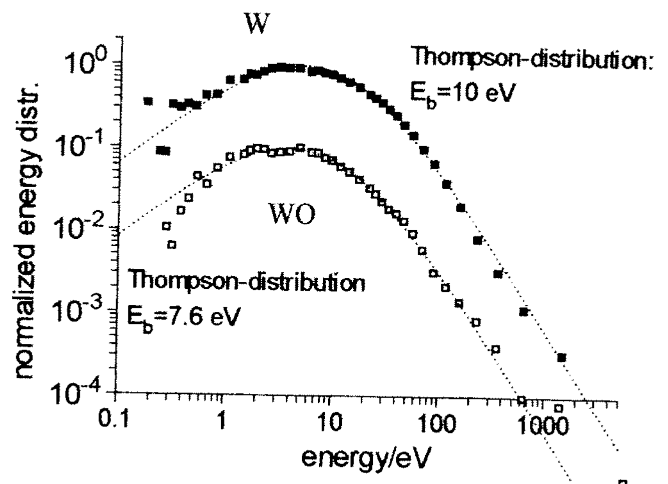

Fig. 11 Energy distributions of tungsten atoms and WO-molecules sputtered from a polycrystalline tungsten surface.

The last example reported here refers to the detection of atomic oxygen by REMPI. As a result of the comparatively high ionization potential it is not possible to detect oxygen atoms by non-resonant ionization. In this case advantage was taken of the enhancement of the ionization rate by a resonant excitation step. In figure 13 the ionization signal as a function of the dye laser wavelength is presented.

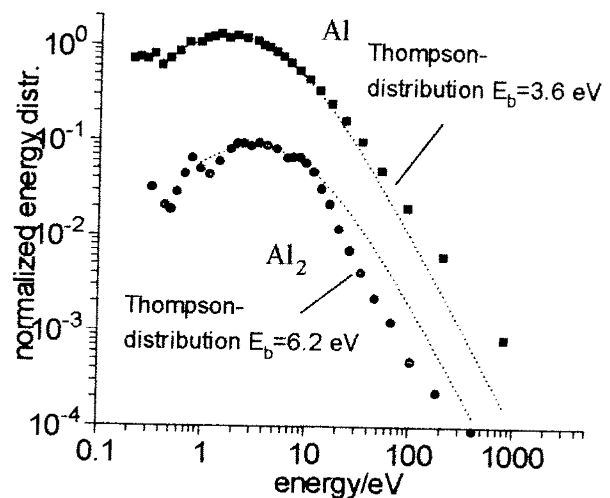

Fig. 12 Energy distributions af sputtered aluminum atoms and dimers.

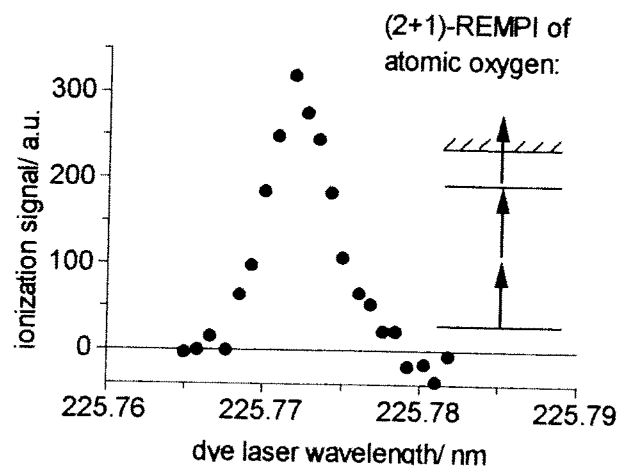

Fig. 13. Relative atomic oxygen ionization signal as a function of the dye laser wavelength. The two photon transition 2p $^3P_2$-> 3p $^3P_2$ is excited by absorption of two photons near $\lambda=226$ nm. The upper level is subsequently ionized with a photon of the same wavelength (single color scheme).

In figure 14 a the time-of-flight distribution of resonantly ionized oxygen atoms is shown along with the distribution of non-resonantly ionized titanium atoms sputtered from an oxidized titanium surface (figure 14b). For completeness the distribution of TiO-molecules is also depicted. The oxygen distribution is approximated by a superposition of two Thompson time-of-flight distributions.

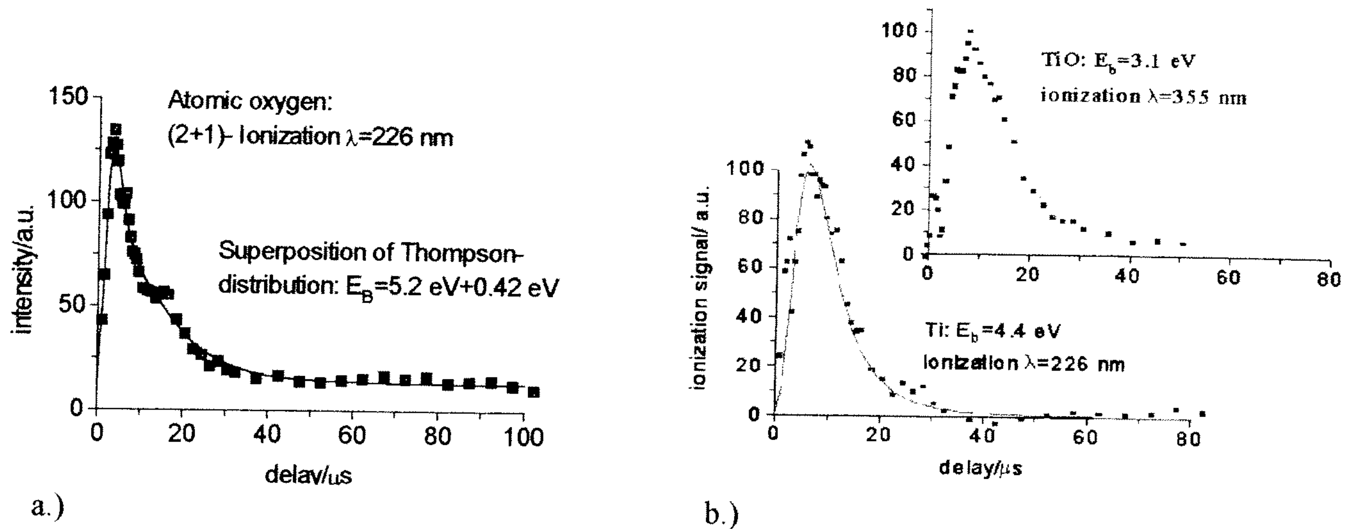

Fig. 15 Time-of-flight distributions of particles sputtered from an oxidized titanium surface. Atomic oxygen is resonantly ionized (a.), titanium atoms are non-resonantly ionized by radiation around 226 nm and TiO molecules are non-resonantly ionized by radiation around λ=355 nm (b.).

It can not be excluded at this point that the distribution of oxygen atoms is influenced by photo-dissociation of sputtered oxides by the strong radiation around λ=226 nm. The complication may be avoided by a multi color ionization scheme e.g. using a part of the pump radiation at 355 nm for the ionizing step.

For the further future it is planned to improve the set-up e.g. by attachment of a reflectron mirror to the time-of-flight mass spectrometer in order to suppress background due to reflected neutralized projectiles. Our measurements will be extended in the direction of the study of the interaction of reactive ion beams with surfaces.

We thank Dr. Wolfgang Eckstein from the IPP Garching for giving us the opportunity to use the TRIM code.

References:

[1] M.W. Thompson, Phys. Rep. 69, 335 (4) 1981.

[2] P. Sigmund, Phys. Rev. 184, 383 (1969).

[3] H.Bay, NIM B 18, 430 (430).

[4] P. Sigmund in : "Sputtering by particle bombardment", Vol. 1, ed. R. Behrisch Springer, (Berlin) 1981.

[5] W. Eckstein: "Computer Simulation of Ion-Solid Interactions", Springer (Berlin) 1991.

IN SITU POWDER DIAGNOSTICS IN LOW TEMPERATURE PLASMAS

E. Stoffels, W.W. Stoffels, G.M.W. Kroesen.
Eindhoven University of Technology, P.O. Box 513,
5600 MB Eindhoven, The Netherlands.

Abstract

We present a survey of diagnostics developed for dust particles, present in low pressure, low temperature plasmas. Formation of microscopic particles is an extensively studied phenomenon, and its complexity requires specific experimental methods. The most valuable information about the properties and behaviour of powders is obtained *in situ* in the plasma. Various interactions of photons with dust particles offer a variety of in situ diagnostic techniques, which allow characterising a wide category of particles. Here we shall concentrate on classification of photon-induced processes in dusty plasmas and demonstrate their diagnostic possibilities. Methods to determine physical and chemical properties of particles, dust density and size from nanometer to micrometer scale, will be described and illustrated with examples.

Introduction

Dusty plasmas are a hot topic in contemporary plasma physics, due to their interesting fundamental aspects as well as industrial relevance. The interest in low-pressure dusty plasmas has grown together with the development of plasma surface processing. Dust formation is a widely recognised process in many chemical systems, related to Reactive Ion Etching (RIE) or Plasma Enhanced Chemical Vapor Deposition (PECVD). Especially in the technology of plasma-enhanced dry etching of semiconductor elements dust contamination has posed a serious problem. Initially the dust contamination was thought to be due to handling of the samples outside the plasma reactor. The design of dust free chambers ("cleanrooms") did indeed bring some improvements for the cleanliness of fabricated elements. However, soon it appeared that the plasma itself is a source of contaminating dust particles. In the commonly used radio frequency (rf) discharges applying chemically active gases, particles are readily formed and trapped in the plasma glow. Thus, the contaminants accumulate above the processed surface and eventually deposit on it. Examples of chemistries are numerous: fluorocarbon (C_2F_6, CHF_3), CCl_2F_2 and SF_6 etching plasmas, silane (SiH_4) plasmas, used for deposition of amorphous silicon in solar cell fabrication technology, methane plasmas for deposition of graphite or diamond layers. Nowadays, the development of the semiconductor industry requires higher quality and purity of the fabricated elements, so the tolerated level of contamination is lowered. The desired size of the etched structures has decreased down to the sub-micrometer region and will soon be reduced to below 100 nm. This implies that even nanometer scale particles must be removed from the plasma. The need of contamination control has resulted in development of sensitive diagnostics for monitoring nanometer size particles.

Recently, a more positive approach to dust particles has arisen. The new research lines concentrate on applications of dust particles, produced in the plasma. These particles can have valuable properties, which make them suitable in coating

technology, ceramic industry and catalysis. A new development is the fabrication of composite materials, for example coatings seeded with small particles. Co-deposition of nanometer scale silicon particles can lead to major improvements in the stability of solar cells [1]. Hard coatings of titanium nitride containing small lubricant particles are shown to be particularly wear-resistant and therefore extremely valuable for coating of tools for metal processing [2]. New technologies using plasma-produced particles pose high requirements on the particle quality. Thus, advanced diagnostics is needed for the characterisation of particle properties.

Following the development of dusty plasma research, numerous diagnostics have been designed. These methods suit the particular needs of various investigators and manufacturers. In fundamental research they help to understand the phenomena in dusty plasmas, and in industry they can decide whether a technological process has been successful. The demands range from a simple particle detection system in the pumping line of the reactor to sophisticated methods for the determination of specific particle and plasma properties. But in any case, the first approach in the study of dusty plasmas is the visualisation of particles in situ. In this stage the most relevant issues to the investigator are checking the particle presence, determining their density, size and location in the discharge.

The most favoured in situ methods involve photon interactions with particles. There are of course many other techniques, based on monitoring electric properties of the plasma, using electric probes or mass spectrometry. However, a major difficulty in the *in situ* investigation is the access to the vacuum reactor, in which the particles are present. Thus, most of the electric techniques are either indirect or intrusive. The same is valid for mass spectrometry, although this technique has been proven indispensable in studying the particle formation process [3]. Optical techniques are most convenient, as most research reactors have good optical access. Optical methods generally do not disturb the plasma and are not destructive for the particles.

Light Scattering Diagnostics

Light scattering technique is one of the oldest techniques for the detection of particles, and its applications reach far beyond the plasma physical research. Light scattering is experimentally easy and it yields qualitative data directly. Therefore it is widely used as a side diagnostics to check the presence of dust particles. Extracting quantitative information from the measurements is however a difficult exercise. In the beginning of this century, Rayleigh and Mie developed complete theories of light scattering by objects much smaller than the scattering wavelength (Rayleigh scattering) and comparable with the wavelength (Mie scattering). Detailed treatment of light scattering is beyond the scope of this review. A full description of the standard theories can be found in excellent monographs by van der Hulst [4] and Bohren [5]. Here we will merely address some practical aspects of light scattering. Shortly, the intensity of the light scattered by a particle is related to the particle size, shape and (complex) refraction index, as well as to the wavelength and polarisation state of the light. The scattered intensity I_{sca} is proportional to the particle concentration N_p in the detection volume ΔV and the incident light intensity I_0:

$$I_{sca} = N_p \, \Delta V \, Q_{sca} \, I_0$$

The scattered intensity is angle dependent. Another parameter which is relatively easy to determine experimentally is the extinction of the incident intensity I(l) along the path length l:

$$I(l) = I_0 \exp(-N_p \pi r_p^2 Q_{ext} \, l).$$

Extinction is due to absorption and scattering by particles with a radius r_p:
$Q_{ext} = Q_{abs} + Q_{sca}$.
The expressions for the scattering and absorption efficiencies are generally very complicated, so the determination of particle properties is a numerical task.

We will show how different approaches, like laser light scattering (LLS), white light scattering, angle-resolved measurements, extinction and polarisation sensitive techniques have been used to tackle specific physical problems. The method will be illustrated by various examples of applications in the dusty plasma research. Finally, the drawbacks and limits of light scattering will be discussed.

White light scattering

Broad band light sources, such as halogen lamps, have been used successfully for recording images of the spatial distribution of particles in discharges. Dust clouds dynamics has been analysed by using these light sources and video camera recordings of the scattered light. This technique has been used by A.A. Howling et al [6] to characterise powders generated in a silane discharge. A more sophisticated version of white light scattering is spectroscopic scattering. From the Mie theory it follows that the scattering intensity is a sensitive function both of the light wavelength and of the particle size. When white light is used, the color distibution in images collected at a given angle contains information about the particle size. Howling et al. employed spectroscopic scattering to probe the particle size distribution in the dust cloud. Qualitative data, as size segregation in space, are available but a full quantitative exploitation of this method is not a straightforward task. As the irradiated intensity of continuum sources is much lower than that of monochromatic sources (lasers), this method is restricted to reasonably large particles (> 100 nm).

Laser light scattering

Starting with the pioneering works of G. S. Selwyn [7], laser light scattering have been extensively used to evidence the presence of the particles in a wide variety of situations including low pressure etching, sputtering and deposition [8]. The LLS method is now developed as a ready-to-use diagnostic, commercially available. These devices have been used to measure for example the size and concentration of the aerosol particles and to monitor the contamination levels in the cleanrooms.

In the studies of nucleation and growth phenomena, more precise information on as particle size and concentration is required. Recording a scattering signal at one laser wavelength, one polarisation state and one angle of detection is not sufficient to obtain the desired information. Typically, LLS is used to determine the density once the particle size is known. The latter can be determined by other means, e.g. by SEM or TEM. A broad size distribution of plasma-produced particle sizes makes the interpretation of scattering signals more difficult. In some cases, like a silane discharge, a narrow size distribution exists for a restricted time of particle growth [9]. LLS together with electron microscope data are proven very useful for determining the particle size and density in this system. Thanks to the LLS data, the formation mechanism of clusters in a silane discharge has been clarified. In Figure 1 the evolution of particle size and density as a function of plasma operation time is given. At a given stage, a characteristic jump in particle size and density can be detected. This shows that there is a coalescence phase in particle evolution, during which the size increases rapidly at the same time the density drops.

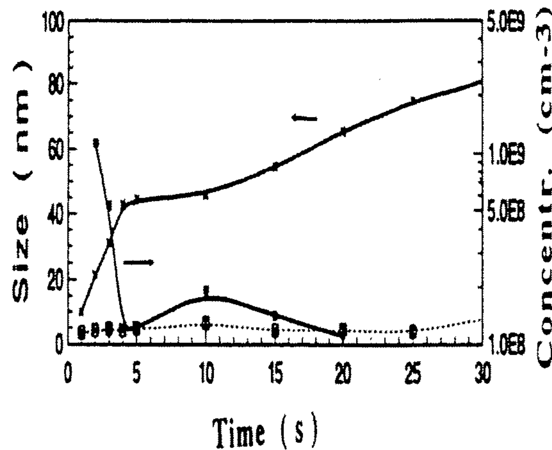

Figure 1. Particle size and particle density as a function of plasma operation time in a silane discharge. (after Boufendi et al [9])

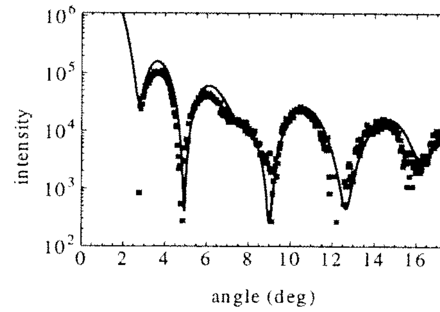

Figure 2. Angle-resolved Mie scattering data of a single melamine-formaldehyde particle (squares), trapped in a radio-frequency oxygen plasma. The data are fitted by a theoretical scattering curve for a particle of 5.90μm radius and 1.68 refractive index.

The problem for any quantitative use of LLS is that the scattered intensity is a complex convolution of particle size, shape, concentration and refractive index. Different methods have been developed for the de-convolution of these parameters. A spherical shape is generally assumed for the scattering particles in order to fit experiments and the scattering theory. One of the approaches is recording the signal at several angles. In the Mie scattering regime, when the particle size is in the order of the scattering wavelength, the scattered intensity displays a characteristic angular pattern (see Figure 2). Stoffels et al.[10] has fitted the fringes with a numerical model in order to achieve very accurate particle sizing and to monitor size changes in the order of 1%. For less accurate sizing it is sufficient to record the intensity at few angles. Alternatively, Hollenstein et al. [11] combined scattering with extinction measurements. Multi-wavelength LLS is basically similar to spectroscopic scattering, but the signal is recorded only at few wavelengths. Polarisation sensitive diagnostic studies offer a convenient method for determining the particle size. Figure 3 shows the ratio σ of scattered intensities when the incident beam is polarised parallel and perpendicular to the scattering plane. This ratio is a function of the particle size and has been used by Shiratani et al. [12] to map the particle size and distribution in the discharge.

Some other versions of LLS have been applied. Mie scattering ellipsometry is a very sensitive technique for particle sizing, and it has been applied by Hayashi and Tachibana [13] to determine the size evolution of particles in a methane plasma.

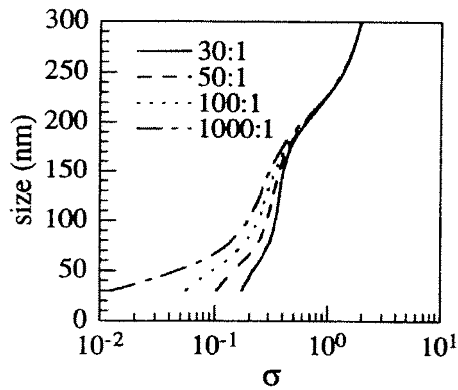

Figure 3, Particle size as a function of the scattering ratio σ for several polarisation degrees of the incident light. (after Shiratani et al [12]

Limitations of light scattering

When the particle radius is much smaller than the wavelength, the scattered intensity is described by Rayleigh theory. The absorption and scattering parameters within the Rayleigh approximation are:

$Q_{abs} = -4x\ \mathrm{Im}[(m^2-1)/(m^2+2)]$

$Q_{sca} = 8/3\ x^4\ |(m^2-1)/(m^2+2)|$,

where m the complex refraction index and x the scattering parameter: $x=2\pi r_p/\lambda$, with λ the incident wavelength and r_p the particle radius. The scattering efficiency varies as r_p^6/λ^4, which implies that the scattered intensity decreases rapidly with decreasing particle size. This forms a serious problem in detection of very small particles (nanometer size), which are otherwise very interesting in a study of nucleation mechanisms. Detection of nanoparticles requires using UV photons, which is experimentally difficult. In practical situations, the detection limit for particle size is about 20 nm [9,11]. On the other hand, the absorption efficiency varies as r_p^3/λ, which is much more favourable for small particles. This means that all techniques based on absorption of photons, like extinction measurements, fluorescence, etc., are potentially interesting for detection of very small particles.

Other Photon-Induced Processes

Infrared absorption

In the past years many new techniques based on photon interactions with particles have been introduced. Infrared absorption is a commonly used and well-established technique in molecular physics, but its application to dusty plasmas is relatively new. This technique is especially useful in studies of the chemical nature of the particles. It allows monitoring *in situ* changes in the gas chemistry and at the same time to study the particle composition. The absorption bands of the particles can be easily distinguished in the spectrum, as they are solid state-like and thus much broader than the absorption bands of gas phase species. Figure 4 shows some absorption spectra of particles formed in a CCl_2F_2 radio-frequency plasma during etching of a silicon substrate. The particle size is in the order of micrometers. These measurements have been done using a Fourier Transform Infrared Absorption Spectrometer. Kroesen et al. [15] applied the same technique to monitor particle formation in silane discharges. Depletion of the source gas was found and solid-state absorption bands SiH and SiH_2 in the particles were detected. These bands were visible only for particles larger than 50 nm.

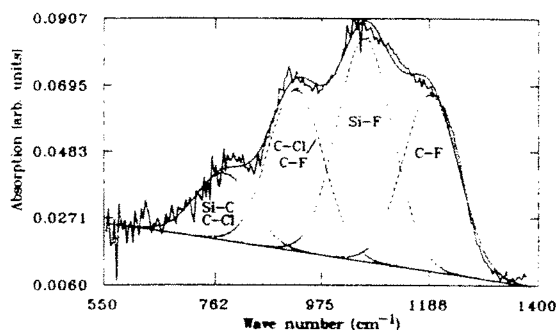

Figure 4, Infrared spectrum of particles formed during dry etching of Si in a CCl_2F_2/Ar plasma. The particle size is about 1 μm. (after Stoffels et al. [14])

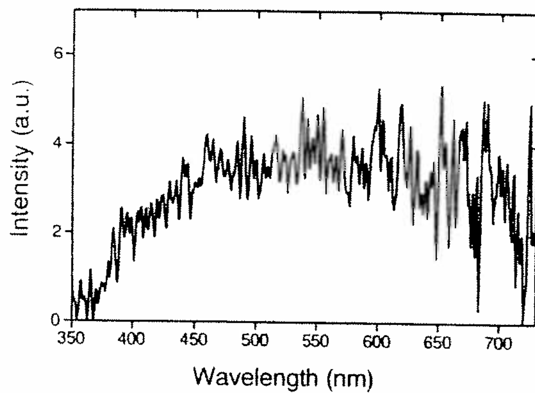

Figure 5. A typical LIPEE spectrum of nanoparticles in a silane discharge. (after Boufendi et al. [16])

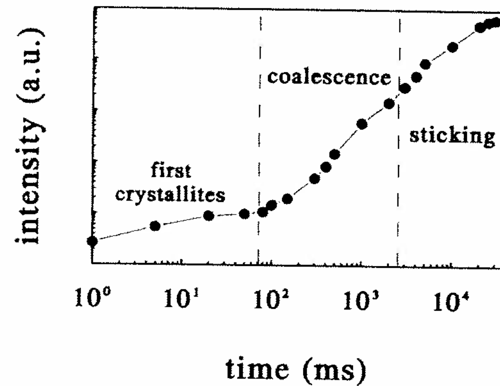

Figure 6. Time evolution of the LIPEE signal as a function of plasma operation time. Particle formation in SiH_4 is monitored. Different phases (nanoparticle formation, coalescence and sticking) are described by Boufendi et al. (after Boufendi et al. [16])

"Inelastic scattering"

From the point of view of understanding particle formation mechanisms there is a need for an experimental method to detect particles in the nanometer range. Nanometer size particles produced in the plasma also find some applications in industry, so their detection is essential for a good process control. Photon absorption has a favourable dependence on the particle size: for large or very opaque objects the absorbed intensity scales as r_p^2 (surface absorption), while for smaller objects it scales as r_p^3 (volume absorption). However, direct extinction measurements require significant absorption, which can be obtained either for large particles or at very high particle densities. Therefore, in spite of the convenience and informational value of infrared techniques, they are generally not practical for the detection of nanometer size clusters. Thus, other techniques involving photon absorption have been designed. Physical base of these techniques can be figuratively described as "inelastic scattering", i.e. absorption of a photon and emission of a photon of different wavelength. Typically, a high power laser is applied. The radiation emitted by particles during interaction with a high power laser can be of different nature, depending on particle size and properties: black-body radiation (relatively large particles), fluorescence, photoluminescence (nanocrystalline materials), etc.

a. LIPEE

Boufendi et al. [16] used UV excimer laser pulses (XeCl, 308 nm) to detect nanometer size particles in a silane discharge. The presence of nanoparticles was predicted in previous studies as being a critical initial step for dust formation. This technique is based on evaporation and ionisation of particles during their irradiation by a laser (LIPEE – laser-induced particle explosive evaporation). It is known from laser-material interaction studies that the hot vapour, produced by high intensity pulsed laser irradiation of solid targets, is already ionised when ejected from the surface. This so-called "erosion plasma" is characterised by atomic line emission of vapour atoms and ions and also by continuum emission due to recombination and

Bremsstrahlung [17]. Boufendi et al. [16] recorded laser-induced continuum emission to evidence nanoparticles in the discharge. In Figure 5 a typical continuum spectrum is shown, and in Figure 6 one can see the evolution of the signal as a function of the plasma operation time. Clearly, the LIPEE technique is more powerful for the detection of small particles than the LLS, and it allows to study the initial phase of particle formation.

b. Laser heating

Another version of "inelastic scattering" has been developed by Stoffels et al. [18,19] and applied for micrometer size particles. A high power Nd:YAG laser was used to heat the teflon-like clusters formed in a CCl_2F_2 etching discharge. Irradiated particles emit very intense white light, which spectrum can be very well approximated by a black-body curve (see Figure 7). Laser heating technique has an additional advantage in the detection of larger, opaque clusters. The laser heating dynamics and emitted light intensity can be easily modelled and information about particle size and density can be obtained. For opaque structures only surface absorption occurs and the heat is transported inside the cluster it is clear, that the time needed to heat the particle is proportional to its size. A simple energy balance, in which the absorbed power is used to heat the particle yields the following relation between the heating time τ_{heat} and the particle size r_p:

$\tau_{heat} = 4/3\ r_p\ \rho\ C\ \Delta T/(Q_{abs}\, I)$.

Some material constants, like solid state density ρ, heat capacity C must be known or found by fitting the experimental data. The size can be thus determined from the time-resolved measurements of particle black-body emission. In Figure 8 laser-induced emission from the particles is shown as a function of time during laser heating. The time dependence of the Nd:YAG laser intensity is shown for comparison. The delay of the particle emission with respect to the laser pulse (τ_{heat}) is clearly visible. The effect was verified by varying the laser intensity I. As expected, the heating time is also inversely proportional to the laser power. The particle temperature ($\Delta T = T - T_0$, where T_0 is the initial room temperature) can be determined from the black-body spectra. Once the particles are heated to a certain temperature, evaporation or decomposition of the material occurs. The particle size decreases, which leads to gradual decay of the emission signal. A detailed treatment of the heating and decomposition kinetics is given elsewhere. As shown in Figure 9, the time dependent signal can be fully simulated by the developed model. From the decomposition kinetics, some additional information about the particle size can be deduced. The time evolution of the emission signal gives the particle size while the height of the signal is proportional to the particle density. Thus, the laser heating method yields both the particle size and density from a single time-resolved measurement. Another interesting aspect of heating and decomposition of particles using high power lasers is the possibility of particle destruction. If the particle density is not too high and the formation rate is slow, laser-induced evaporation offers a good means of contamination control in a surface-processing reactor. Particles can be visualised by laser light scattering and afterwards destroyed by high-power laser evaporation. This is particularly useful to free etching discharges from small amounts of contaminants.

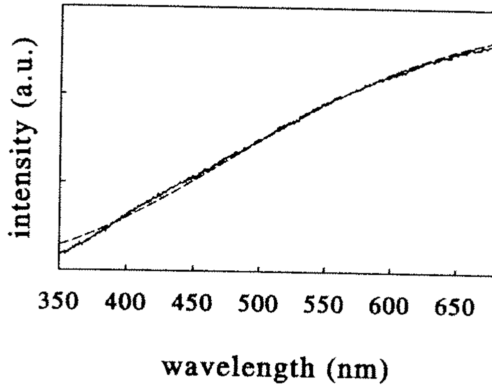

Figure 7. A typical black body spectrum of laser heated particles in a CCl2F2 discharge (solid line) and a black body fit for 3600 K (dotted line).

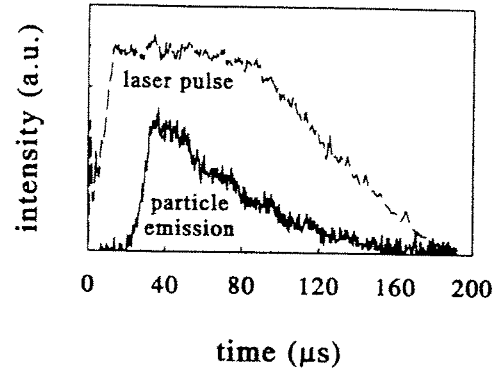

Figure 8. Time evolution of the laser pulse and the spectrally integrated particle emission (300-1000 nm). The delay between the laser pulse and the particle emission signal is a measure for the particle size.

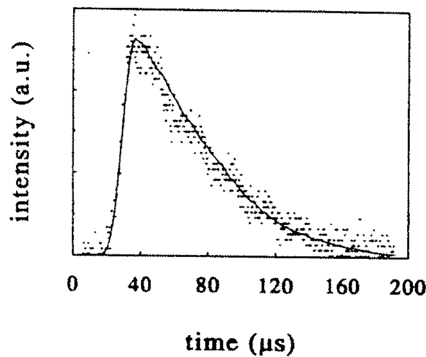

Figure 9 Wavelength integrated laser induced emission (dots, cf. fig 8) and a numerical fit (solid curve). The calculations are performed for a 1 µm particle. The onset of the laser pulse is at t = 0 s.

Conclusions

We have presented a number of *in situ* optical diagnostics used in dusty plasma research and discussed their applicability in solving particular problems related to dust. Finally, in Table I we give an overview of the treated methods, their advantages and drawbacks. Naturally, the use of a diagnostics must be adapted to specific needs and it is up to an experimentalist to make a proper choice for a given problem. Detailed information about the presented methods is contained in the book "Dusty Plasmas" [20], which will be issued soon.

Acknowledgements

The "dusty research" in the framework of a cooperation program between various European research groups has been supported by the European Commission under the contract numbers BRE2-CT94-0944 and BRPR-CT97-0438. The authors wish to acknowledge the contributions from the BRITE-EURAM partners from Switzerland: Dr. Ch. Hollenstein at Ecole Polytechnique Federale de Lausanne, France: Prof. A. Bouchoule at CNRS/Universite d'Orleans, Dr. J.-C. Bertolini at Institut de Recherches sur la Catalyse, Villeurbanne, Dr. P. Roca i Cabarrocas at CNRS/Delegation Regionale "Ile de France", Gif-sur-Yvette, Dr. J.-P. Boeuf at Universite de Toulouse, Spain: Dr. E. Bertran at Univesidad de Barcelona, and Portugal: Prof. R. Martins at New University of Lisbon. One of the authors (W.W. Stoffels) wishes to acknowledge the support of the Royal Dutch Academy of Science (KNAW).

Table I. A list of parameters, which are of interest in dusty plasma research and the corresponding diagnostics to determine these parameters experimentally.

Parameter	Experimental technique	Remarks
presence, density	particle counters,	easy, convenient.
	light scattering:	experimentally easy.
	-white light scattering	cheap but not sensitive.
	-LLS	good for studying trends; good spatial resolution.
	laser heating/LIPEE	expensive high power lasers needed; good timing of data acquisition needed; can be used for removing particles
density, size, size distribution, shape	light scattering:	requires absolute intensity measurements; interpretation of data difficult; numerical modelling needed; *a priori* knowledge of particle shape and size distribution needed.
	-angle resolved scattering	provides very accurate sizing.
	-spectroscopic scattering,	good sizing; requires a strong white light source.
	-polarisation scattering	a simple way of sizing; may be used to investigate the particle shape.
	-scattering ellipsometry,	complicated numerical simulations involved; good knowledge of optical properties required.
	laser heating	size&density from a single measurement; applicable for small particles.
	LIPEE	suitable for detection of nanoparticles; sizing difficult.
chemical composition	IR absorption	applicable for large particles; experimetally easy, interpretation straighforward; gives absolute densities.
morphology, structure	photoluminescence	applicable to nanocrystalline materials.

References

[1] P. Roca i Cabarrocas, P. Gay, A. Hadjadj, J. Vac. Sci. Technol A14, 655, 1996.
[2] E. Stoffels, W.W. Stoffels, G. Ceccone, F. Rossi, to be published in J. Appl. Phys. 1999.
[3] A.A. Howling, J.-L. Dorier, Ch. Hollenstein, Appl. Phys. Lett. 62, 1341-1343, 1993.
[4] H.C. van de Hulst, Light scattering by small particles, John Wiley & Sons, New York, 1957.
[5] C.F. Bohren, D.R. Huffman, Absorption and scattering of light by small particles, John Wiley & Sons, New York, 1983.
[6] A.A. Howling, Ch. Hollenstein, P.-J. Paris, Appl. Phys. Lett. 59, 1409-1411, 1991.
[7] G. S. Selwyn, J. Singh, R.S. Bennett, J. Vac. Sci. Technol. A7, 2758-2765, 1988.
[8] NATO Advanced Workshop on the Formation, Transport and Consequences of Particles in Plasmas, Chateau de Bonas, Castera-Verduzan, France, August 30-September 3 1993, proceedings published in special issue of Plasma Sources: Science and Technology 3, 239-451, 1994.
[9] L. Boufendi, A. Bouchoule, Plasma Sources Sci. Technol. 3, 262-267, 1994.
[10] W.W. Stoffels, E. Stoffels, G. H.P.M. Swinkels G.M.W. Kroesen, Contribution to this conference.
[11] Ch. Hollenstein, J.-L. Dorier, J. Dutta, L. Sansonnens, A.A. Howling, Plasma Sources Sci. Technol. 3, 278-285, 1994.
[12] M. Shiratani, H. Kawasaki, T. Fukuzawa, Y. Watanabe, J. Vac. Sci. Technol. A14, 603, 1996.
[13] Y. Hayashi, K. Tachibana, Jpn. J. Appl. Phys.33, L476-L478, 1994.
[14] W.W. Stoffels, E. Stoffels, M. Haverlag, J.H.W.G. den Boer, G.M.W. Kroesen, F.J. de Hoog, Plasma Sources Sci. Technol. 3, 320-324, 1994.
[15] G.M.W. Kroesen, J.H.W.G. den Boer, L. Boufendi, F.Vivet, M. Khouli, A. Bouchoule, F.J. de Hoog, J. Vac. Sci. Technol. A14, 546, 1996.
[16] L. Boufendi, J. Hermann, A. Bouchoule, B. Dubreuil, E. Stoffels, W.W. Stoffels, M.L. de Giorgi, J. Appl. Phys. 76, 148-153, 1994.
[17] J. Hermann, C. Boulmer-Leborgne, I.N. Mihailescu, B. Dubreuil, J. Appl. Phys. 73, 1091, 1993.
[18] E. Stoffels, W.W. Stoffels, D. Vender, G.M.W. Kroesen, F.J. de Hoog, IEEE Trans. Plasma Sci. 22, 116, 1994.
[19] W.W. Stoffels, E. Stoffels, G.M.W. Kroesen, F.J. de Hoog, J. Vac. Sci. Technol. A14, 588-594, 1996.
[20] E. Stoffels, W.W. Stoffels, L. Boufendi, "Diagnostics of dusty plasmas", in *Dusty plasmas*, ed. A. Bouchoule, to be published by Wiley & Sons, 1999.

Control of Plasma Spray Processes

A. Vardelle
Ecole Nationale Superieure d'Ingenieurs de Limoges
France

Cavity Ring Down Spectroscopy

Richard Engeln[1], Giel Berden[2], Rudy Peeters[2] and Gerard Meijer[2]

[1] *Department of Applied Physics, Eindhoven University of Technology,, P.O. Box 513, 5600 MB Eindhoven, The Netherlands*

[2] *Department of Molecular and Laser Physics, University of Nijmegen Toernooiveld, 6525 ED Nijmegen, The Netherlands*

In recent years the Cavity Ring Down absorption technique has emerged as a versatile and sensitive optical detection technique, that has been applied e.g. for trace gas detection and for combustion and plasma diagnostics. In this contribution we will first give a brief overview of various CRD detection schemes and their applications. Secondly, two of these schemes, i.e. the Fourier Transform CRD and the Cavity Enhanced Absorption scheme, will be described in more detail.

1. Introduction

Cavity Ring Down (CRD) spectroscopy is a direct absorption technique that combines a good detection sensitivity with a rather simple and straightforward experimental setup. Application of direct absorption techniques is advantageous in a variety of research fields, since quantitative concentration data as well as absolute frequency dependent absorption cross-sections can be extracted from the measurements. For these reasons, sensitive absorption spectroscopic techniques are still gaining in interest. Among the variety of techniques that have been developed, the Cavity Ring Down (CRD) absorption technique has proven to be a valuable addition to other detection techniques like Laser Induced Fluorescence (LIF), Infrared Laser Absorption Spectroscopy (IRLAS) or Resonance Enhanced Multi Photon Ionisation (REMPI). The CRD technique is based on the measurement of a *rate* of absorption rather than the *magnitude* of absorption of a light pulse confined in a closed optical cavity with a high Q factor [1]. The advantage over normal absorption spectroscopy results from (i) the intrinsic insensitivity of the CRD technique to light source intensity fluctuations, and (ii) the extremely long effective path-lengths (many kilometers) that can be realized in stable optical cavities.

Use of CRD for sensitive absorption measurements with pulsed lasers was first demonstrated by O'Keefe and Deacon in 1988 [2]. Since then, trace gas detection by means of CRD absorption spectroscopy has been demonstrated via the measurement of OH and CH_3 in flames and discharges [3, 4] and via the detection of trace amounts of atomic mercury vapour and ammonia in ambient air [5], to just name a few. Successful application of CRD for the measurement of absolute oscillator strengths of weak (forbidden) transitions of stable molecules has, for instance, been demonstrated on overtone transitions of HCN in the visible region of the spectrum [6] and on the Herzberg bands of molecular oxygen in the near UV [7, 8]. The CRD technique has also been used to determine predissociation lifetimes of the $A^2\Sigma^+(v'=1)$ state of the SH radical [9] and to determine the rotational level dependent predissociation of $OH(A^2\Sigma^+ v'=3))$ [10]. In the latter experiment, the CRD absorption spectrum was measured simultaneously with the LIF excitation spectrum, and relative predissociation rates were determined from the ratio of the CRD to

the LIF signal. The CRD detection technique is also shown to be a viable diagnostic for the detection of neutral hydrogen atoms and negative hydrogen ions in a capacitively coupled RF H_2 plasma [11], as well as for density measurements of SiH_2 in a argon-silan DC discharge [12].

In other experiments, explicit use has been made of the pulsed nature of the CRD detection method, due to which the absorbing species only need to be present in the ringdown cavity for a short period of time. CRD is therefore well suited for absorption measurements in repetitive sources like pulsed molecular beams [13, 14, 15, 16], laser vapourization sources [17] and pulsed discharges [18, 19]. Quandt *et al.* have shown the application of the CRD technique to the study of dynamical processes via a time-resolved absorption measurement of H^- in a pulsed magnetic multipole source [20].

In all the CRD experiments reported to date polarized laser radiation has been used for absorption measurements. By putting a polarization selective optical element in front of the detector, it should in principle be possible to measure the optical rotation of the plane of polarization of the incoming beam upon passage through the ring down cavity. With a polarization analyzer that selects radiation polarized parallel to that of the incoming beam placed in front of the light detector, in addition to the 'normal' absorption, rotation of the plane of polarization in the ring down cavity will be detected as an apparent absorption, i.e. as a shortening of the ring down time [21]. With the analyzer rotated (almost) 90 degrees relative to the plane of polarization of the incoming beam, there will still be shortening of the cavity decay time due to absorption but optical rotation will cause a time-dependent *increase* in the detected signal, i.e. it will appear as an apparent lengthening of the ring down time ('cavity ring up'). When both signals are measured simultaneously, one can discriminate between the effects of absorption and optical rotation [21]. In contrast to most other schemes for polarization spectroscopy, the PD-CRD scheme is not completely background-free, and is therefore not overly sensitive to slight deterioration of the degree of polarization upon multi-passing through the cavity. In the PD-CRD detection scheme, the *rate* of polarization rotation is measured, which enables the rotation to be quantitatively determined, and noise-equivalent polarization rotation of 10^{-8} rad./cm has been demonstrated [21].

There is no intrinsic limitation to the spectral region in which CRD can be applied, provided mirrors with a sufficiently high reflectivity, detectors with a sufficiently fast time-response, and tunable (pulsed) light sources are available. The above mentioned detection of ammonia [5] and the detection of CO on the spin-forbidden Cameron band [22] showed the applicability of CRD spectroscopy down to 200 nm. Using a state-of-the-art narrow band tunable infrared laser system, Rakestraw and co-workers reported the first CRD experiment in the IR spectral region out to 3500 nm [23]. Using a free-electron laser, CRD absorption experiments were performed at even longer wavelengths, and the detection of ethylene in the 10-11 μm region was demonstrated [24].

Quantitative information is most readily extracted from the CRD measurements when the line width of the light source can be neglected relative to the width of the absorption line. If this is no longer valid, one can still extract the correct absorption coefficient from the measured transients, provided the spectral intensity distribution of the light source is known [5, 25, 26]. As a consequence, one does not necessarily need a narrow band laser to perform a CRD experiment. One might just as well use a polychromatic light source and extract the spectral information after spectrally dispersing the light exiting the cavity. For this the temporal shape of the ring down transient for a specific frequency-(interval) has to be recorded and analyzed. A monochromator with suitable detector or a time-resolved

optical multi-channel analyzer could for instance be used. Another possibility, i.e. to couple the polychromatic pulsed light exiting the cavity into a Michelson interferometer, will be explained in section 2 of this contribution [27].

In view of the limited duty cycle, the pulsed nature of the CRD detection method is actually a drawback when absorption measurements are performed on static samples; in a typical CRD experiment with a 10–50 Hz repetition rate laser and cavities with ring-down times of 1–50 μs, one effectively measures only during a small fraction of the time. For this reason, as well as for the reason of compactness, the use of continuous (diode) lasers has been experimented with in a variety of experimental schemes [28, 29, 30]. As in these experiments the spectral resolution is in principle only limited by the width of the longitudinal cavity modes [31], i.e. the spectral resolution can even be better than the band width of the laser, (extremely) high resolution CRD absorption spectroscopy can be performed in these cw-CRD detection schemes.

In section 3 we report on the use of narrow band cw light sources to perform Cavity Enhanced Absorption (CEA) spectroscopy. The radiation from a scanning narrow band cw laser is coupled into the cavity via the accidental coincidences of the laser frequency with the frequency of one of the multitude of modes of the cavity. The absorption information is extracted from a measurement of the *time-integrated* light intensity that leaks out of the cavity. From a plot of the inverse of this intensity versus wavelength, the direct absorption spectrum is obtained [32].

Although not at the focus of attention at first, CRD absorption can also be performed on transparent solid samples. An obvious way to proceed is to place a transparent solid sample, containing for instance a thin film of the material to be studied, at Brewster's angle in the ringdown cavity, thereby minimizing reflection losses. An approach that is experimentally found to be superior is to place the transparent solid sample in the cavity in such a way that all separate cavities are optically stable. Although there will be a significant reflection at each interface, these are not experienced as overall cavity losses; with a 3 mm thick optically flat ZnSe window placed in the ringdown cavity, we found the losses per passage through the sample to be below 340 ppm around 8.5 μm, even though the reflection per surface is on the order of 20 %. With a 20–30 nm thick C_{60} film deposited on this ZnSe window, the absorption line (one of the four F_{1u} IR fundamental absorptions) centered at 8.46 μm was recorded with a free electron laser using the CRD detection scheme [33].

2. Fourier Transform Cavity Ring Down Spectroscopy

In a standard Fourier Transform absorption spectroscopy experiment, one uses a broad band light source in combination with a Michelson interferometer, and one records the intensity $I(\Delta)$ of the light that passes through the interferometer as a function of the optical path length difference Δ, between the two arms of the interferometer. The desired intensity as function of ν is obtained by Fourier transformation of $I(\Delta)$. To detect the frequency and time dependence of a certain process simultaneously, time-resolved Fourier transform spectroscopy can be performed. In this case one detects the temporal dependence of the spectrally integrated intensity as a function of Δ, i.e. one measures $I(\Delta, t)$. The time dependence of the intensity at frequency ν ($I(\nu, t)$) is obtained after Fourier transformation of $I(\Delta, t)$. Various FT spectrometers are equipped with the required hardware and software to move the mirrors of the interferometer in such a way that time-resolved FT-spectroscopy can be performed.

In the FT-CRD spectrometer a time-resolved FT-spectroscopic measurement of the broad band light exiting a ringdown cavity is performed [27]. In this case the measured quantity $I(\Delta, t)$ is generally not an exponentially decaying function of time. After Fourier transformation of $I(\Delta, t)$, the ring down transient per frequency (interval), $I(\nu, t)$, is obtained. This can be written as $I(\nu, t) = I(\nu, 0) \exp(-t/\tau(\nu))$ and $\tau(\nu)$, and thereby the absorption coefficient $\kappa(\nu)$, can be determined over the complete spectral range covered by the light source.

In a standard CRD experiment, in which a narrow band pulsed laser is used, the absorption information is deduced from the temporal shape of the ring down transient recorded at a certain frequency and is independent of the absolute intensity of the ring down signal. It suffices, therefore, to record normalized ring down transients at each laser frequency. In the FT-CRD spectrometer the absorption information is deduced from the temporal shape of the ring down transient that is now recorded as a function of the path-length difference Δ in the interferometer. Also in this case it is sufficient to only record normalized transients. These transients $I_{norm}(\Delta, t)$, normalized to have the same maximum value at $t = 0$ for all values of Δ, can be written as

$$I(\Delta, t) = I_{norm}(\Delta, t) \times I(\Delta, 0) \tag{1}$$

The Fourier transform of the left-handed side of this expression yields the required $I(\nu, t)$, from which the absorption spectrum can be deduced. According to the convolution theorem of Fourier analysis, the Fourier transform of a product of two functions is identical to the convolution of their individual Fourier transforms. This implies that $I(\nu, t)$ can also be obtained by taking the convolution of the Fourier transform of the normalized interferograms with the Fourier transform of $I(\Delta, 0)$. The latter is nothing else than the spectral intensity distribution of the light at the time it enters the ringdown cavity. So provided the spectral intensity distribution of the light source is known and is constant during the measurements, a measurement of $I_{norm}(\Delta, t)$, an intensity independent measurement, suffices to obtain the absorption spectrum. It is noted that also in the standard CRD experiment the spectral intensity distribution has to be known and has to be constant during the measurement to be able to extract accurate absolute absorption values [5, 25, 26].

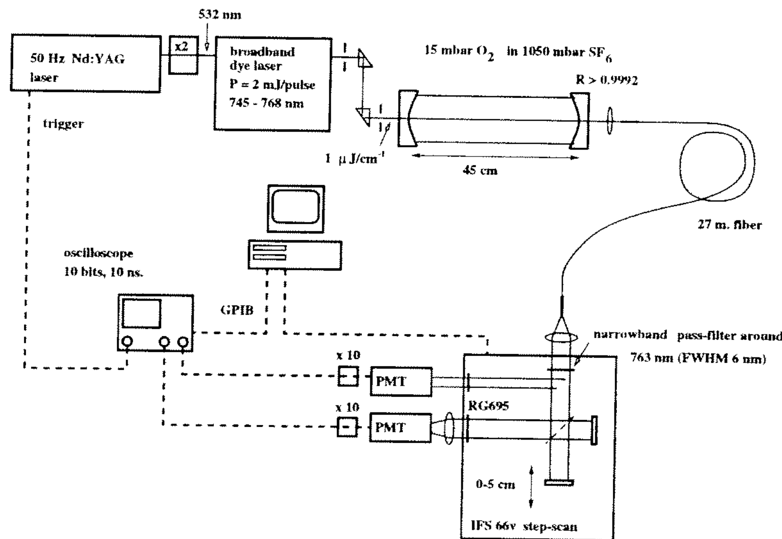

Figure 1: Schematic view of the FT-CRD spectrometer.

2.1 Experimental setup and measurement procedure

The FT-CRD spectrometer shown in Figure 1, consists of a Nd:YAG pumped broad-band dye laser, which produces a 5 ns light pulse with an energy of 2 mJ over a spectral width of about 400 cm^{-1}. After passing through two pinholes, a light pulse with a spectral energy density of approximately 1 $\mu J/cm^{-1}$ is directed toward the ringdown cavity. The ringdown cavity is formed by two highly reflecting plano-concave mirrors, with a radius of curvature of -25 cm and a reflectivity better than 0.999, placed 45 cm apart. No mode matching is performed to allow a near continuum of modes to build up in the cavity [3, 31, 34, 35]. The light that leaks out of the cavity is focused onto a multi-mode fiber and directed to the entrance port of the FT-spectrometer. The multi-exponentially decaying curves are measured at every mirror position Δ with a photo multiplier tube, are amplified, and are digitized by means of a fast (10 ns) and deep (10 bits) oscilloscope. About 100 transients recorded at the same mirror position Δ are summed in the on-board memory of the oscilloscope to improve the measurement statistics. A PC controls the FT-spectrometer and reads out the averaged ring down transients from the oscilloscope. The data analysis involves the Fourier transformation of the interferograms measured at each time-point, and the determination of the decay time τ at each frequency (interval) from the corresponding single exponentially decaying transients. Plotting $1/c\tau$ versus frequency results in the cavity loss spectrum, i.e. the molecular absorption spectrum superimposed on a baseline, where the latter is determined by the finite mirror reflectivity and the length of the cavity.

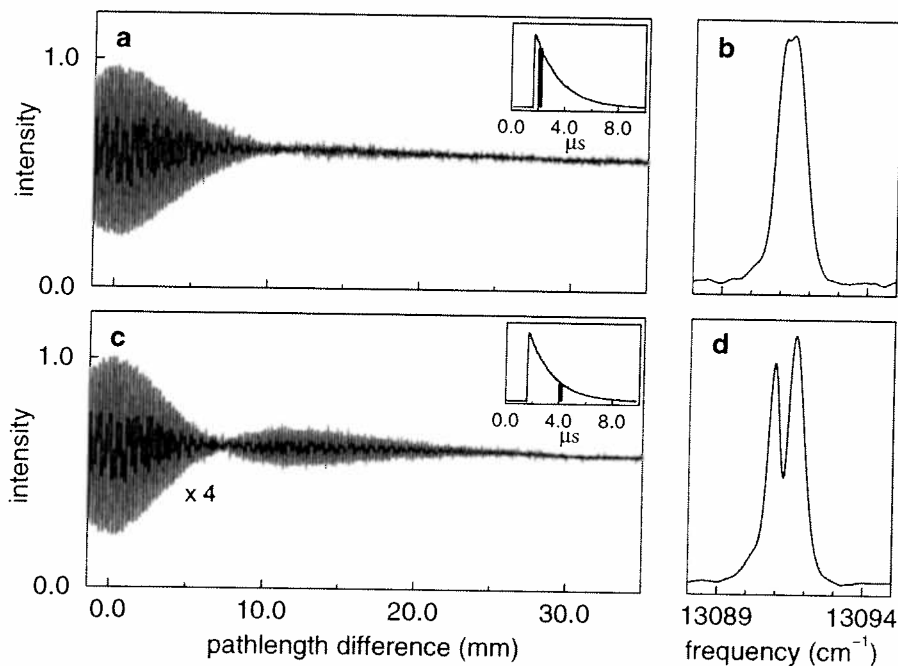

Figure 2: Interferograms, measured with the FT-CRD spectrometer depicted in Figure 1, taken at the beginning of the ring down transient (a) and after 2 μs (c) with their corresponding Fourier transforms (resp. (b) and (d)). Note that the spectral full-width at half-maximum of the light pulse is only 1.1 cm^{-1} in this example.

In order to illustrate the working principle of the FT-CRD spectrometer, we performed an experiment using a light pulse with a spectral full-width at half-maximum of 1.1 cm^{-1}.

In Figure 2a and 2c two interferograms are shown, measured at $t = t_0$ and $t = t_0 + 2\mu s$ (as depicted in the insets), after excitation of the ringdown cavity with this light pulse. The cell is filled with molecular oxygen, and the frequency of the laser is centered on the ${}^{P}P_2(9)$ line of the spin-forbidden magnetic dipole $\mathrm{b}^1\Sigma_g^+(\mathrm{v}'=0) \leftarrow \mathrm{X}^3\Sigma_g^-(\mathrm{v}''=0)$ transition. After Fourier transformation of $I(\Delta, t_0)$, the spectral intensity distribution of the light pulse at the beginning of the transient is obtained (Figure 2b). This spectral intensity distribution is mainly determined by the pulsed laser, although the molecular absorption that occurs during the first 100 ns can already be recognized. After 2 μs the spectrum as shown in Figure 2d is obtained, in which the oxygen absorption is readily visible. Dividing these two spectra would be equivalent to a two-point CRD measurement. In the actual experiments many time points are recorded and the frequency dependent absorption coefficient is determined using all these data points. In [27] the FT-CRD spectrum of 15 mbar O_2 in 1050 mbar SF_6 is shown, after excitation of the cavity with a light pulse with a spectral FWHM of 400 cm^{-1}, centered around 763 nm. The complete vibrational band of molecular oxygen (the oxygen A band) is recorded at once using the multiplex CRD detection scheme.

3. Cavity Enhanced Absorption Spectroscopy

When using narrow band cw lasers for CRD spectroscopy, one might at first think that thereby one of the biggest advantages and probably the main reason for the enormous success of CRD spectroscopy, i.e. the simplicity of the highly sensitive absorption detection setup, is thrown overboard, as now the cavity will have to be frequency-locked to the laser (or *vice versa*). Although various schemes for locking of narrow band cw lasers to optical cavities have been successfully implemented in the past and although it is therefore well-known how to proceed, the resulting experimental setup will certainly always be more involved than the 'conventional' pulsed CRD setup.

In a 'standard' cw CRD experiment, the absorption information is deduced from the time-dependence of the intensity build-up and/or decay of an optical cavity when tuned into and/or away from resonance with the laser frequency. For this, a triggering system is required that actively controls when data taking has to start, together with fast detection electronics [29, 30, 36]. From the observed time-dependence the absolute value of the 'ring-down' time $\tau(\nu)$ is determined, which can be expressed as

$$\tau(\nu) = \frac{d}{c(1 - R + \kappa(\nu)d)} \tag{2}$$

In an experiment, the total cavity loss $1/c\tau(\nu)$ is plotted as a function of frequency, as this is directly proportional to the absorption coefficient $\kappa(\nu)$, apart from an offset which is mainly determined by the finite reflectivity of the mirrors. To record a complete spectrum, the laser is slowly scanned or stepped from one frequency to the other, much like in a pulsed CRD experiment.

In the Cavity Enhanced Absorption method reported here, the laser is rapidly scanned in time and the signal on the detector is integrated over a time that, with a given scanning-rate of the laser, is matched to the expected width of the spectral lines. Scanning the laser over 1 cm^{-1} at a 10 Hz repetition rate with an integration time of 1 ms, corresponds to a spectral integration over only 0.01 cm^{-1}. Several identical scans are summed on the oscilloscope to improve the measurement statistics. The data on the scope are transferred via GPIB to a PC for further analysis. When the inverse of the *time-integrated* detector

signal is plotted versus the wavelength of the laser (*vide infra*) absorption spectra over the full scanning range, spectra that are of comparable quality to those obtained via 'conventional' pulsed or cw CRD spectroscopy, appear directly on the screen in a fraction of a second!

In choosing the optimum experimental parameters several considerations are important. The width of the individual cavity modes, $\Delta\nu_{cavity}$, is rather small (in the tens of kHz range) for the high-Q optical cavities used in these experiments, and is actually considerably smaller than the width of the spectral profile of the scanning laser. We assume in the following that the spectral profile of the laser is a block-function with a width $\Delta\nu_{laser} \gg \Delta\nu_{cavity}$ and is scanned linearly in time. When the laser is slowly scanned into resonance with a cavity mode, light intensity will gradually build up in the cavity. The exact time-dependence of this process can be described using, for instance, the formalism as outlined by Zalicki and Zare in Appendix B of their paper [25]. The maximum intensity that can be reached inside the cavity is proportional to the spectral overlap of the laser profile with the profile of the cavity mode. As the spectral profile of the cavity mode is well-approximated by a Lorentzian profile with a width proportional to the total cavity losses, i.e. proportional to $1/\tau$, and with an intensity proportional to τ^2, the maximum intensity in the cavity is directly proportional to the 'ring-down' time τ. The light intensity inside the cavity will converge to this limiting value, provided that the laser stays in resonance with the cavity mode sufficiently long, i.e. provided that the scanning-rate is small compared to the ratio of $\Delta\nu_{laser}$ to τ. When the laser is tuned out of resonance, the intensity in the cavity will exponentially decay in time, again governed by the time-constant τ.

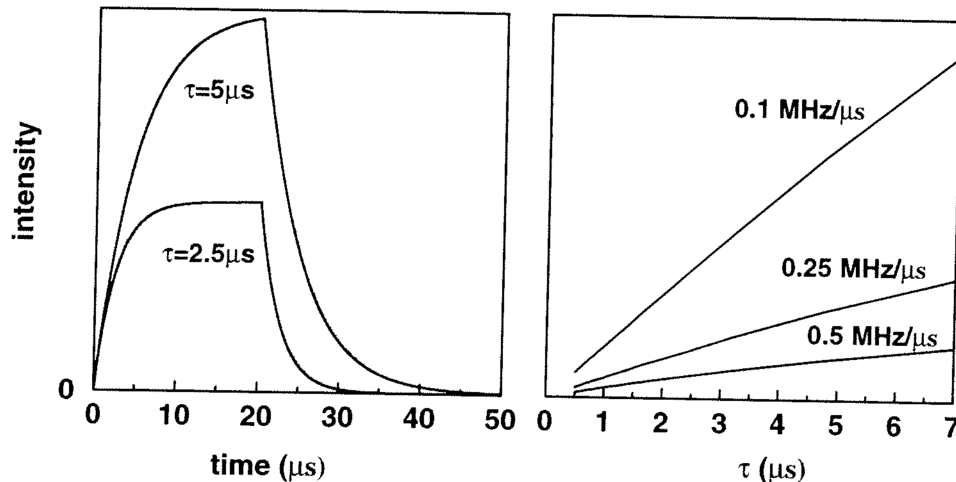

Figure 3: Left part: Calculated light intensity at the exit of a 15 cm long optical cavity as a function of time.
Right part: Calculated integrated light intensity exiting the 15 cm long cavity as a function of the photon lifetime τ in the cavity, for three different values of the scanning-rate of the laser.

In the left part of Fig. 3 the calculated time dependence of the light intensity behind a 15 cm long cavity, having round trip losses of either $2 \cdot 10^{-4}$ ($\tau = 5$ μs) or $4 \cdot 10^{-4}$ ($\tau = 2.5$ μs), is shown. For these calculations a block-profile with a width of 5 MHz and a scanning rate of 0.25 MHz/μs (≈ 8 cm^{-1}/s) is assumed for the laser. As the intensity-decay when the laser is tuned out of resonance with the cavity mode follows a strict $\exp(-t/\tau)$

time-dependence, it is evident that the time-integrated signal behind the cavity would be exactly proportional to τ if the intensity build-up would follow a (1− exp(−t/τ)) dependence. Although the latter is not strictly true, it is explicitly shown in the right part of Fig. 3 that the time-integrated intensity nevertheless follows a linear τ-dependence to a good approximation, and that this approximation gets better with lower scanning-rates. Experimentally there is also a lower limit to the scanning-rate, which is set by the requirement that all cavity modes should be in resonance with the laser more-or-less equally long, as otherwise large intensity fluctuations will occur. This implies that the scanning-rate has to be significantly higher than the rate at which the cavity modes are jittering, or, alternatively, that one has to stabilize the cavity sufficiently to fulfill this requirement also for lower scanning rates. Even with the unstabilized optical cavities we used, there is a large 'window' of scanning-rates available in which both requirements are fulfilled. It is evident from the curves in the left part of Fig. 3 that the light is actually coupled into the cavity as efficient as when the cavity is actively locked to the laser. This, combined with the strongly relaxed requirements on the light intensity behind the cavity as now the total time-integrated signal is used to extract the absorption information from, makes that the power levels of commercially available diode lasers are more than sufficient for these experiments.

3.1 Experimental setup and measurement procedure

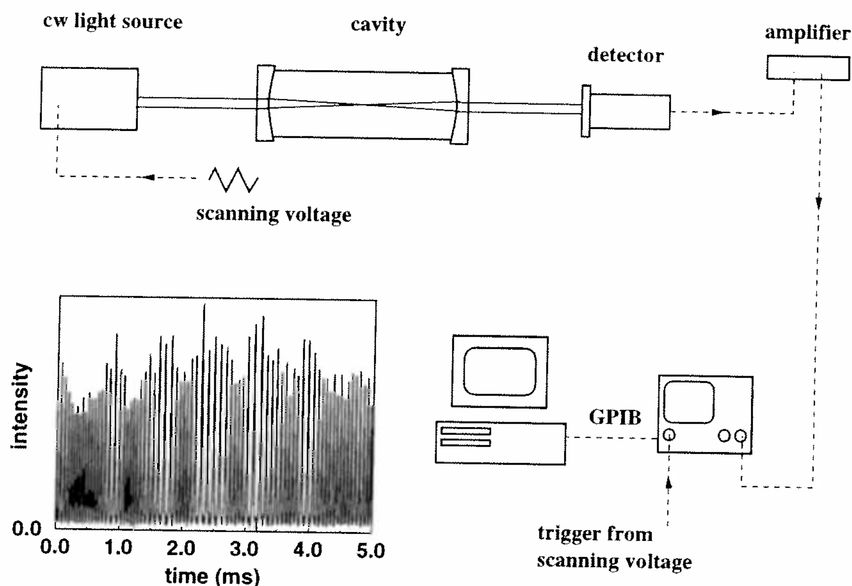

Figure 4: Cavity Enhanced Absorption detection scheme.

A scheme of the experimental setup is depicted in Fig. 4. As a light source we have used two single-frequency cw diode lasers as well as an Ar^+-laser pumped single-frequency cw ring dye laser. The diode modules covered the 750–780 nm region (up to 15 mW) and the 1506–1595 nm region (5 mW maximum power), the ring dye laser, operated on DCM, covered the spectral region of the γ-band of molecular oxygen around 628 nm and delivered typically 200 mW. Both diode lasers have an external cavity and can be scanned mode-hop free by piezo tuning the end mirror. The ring dye laser is scanned mode-hop free by changing the cavity length with two galvo-driven plates. During all the experiments the

lasers were repeatedly scanned over a spectral range of typically 1 cm^{-1} at a rate on the order of 5–100 Hz.

The narrow band cw laser radiation is coupled into a high finesse stable optical cavity, formed by two plano-concave mirrors with a diameter of 25 mm and a radius of curvature of -1 m and a specified optimum reflectivity of typically R=0.9999. In the cell experiments, the mirrors act as windows for the cell. When using short cells (5–20 cm), the mirrors are directly flanged onto a stainless steel tube and no further alignment of the mirrors relative to each other is needed. Obviously, the cell as a whole is adjusted such as to couple in the laser-light efficiently. To avoid optical feedback from the cavity to the laser, the cell is positioned under a small angle with respect to the incoming laser beam or a Faraday isolator is used. When using longer cavities (25–90 cm), independent alignment of the two mirrors is required. The light that leaks out of the cavity is detected by either a photodiode or a photo multiplier tube (PMT). The detector signal is amplified and displayed on a digital oscilloscope. To record wavelength spectra, the oscilloscope is used in x-y mode, in which the horizontal axis is triggered by the voltage ramp used to scan the laser and is therefore proportional to the laser wavelength. In the inset of Fig. 4 the light intensity leaking out of a 45 cm long empty cavity is shown as a function of the wavelength of the diode laser (around 765 nm; bandwidth several MHz). The horizontal axis corresponds to a total frequency range of 0.115 cm^{-1}, which is about ten Free Spectral Ranges (FSRs) of the optical cavity. During the wavelength scanning, which is linear in time, different transverse cavity modes are excited. As the (unstabilized) cavity will drift during scanning, the observed mode pattern is not expected to repeat perfectly. It is observed that light is coupled into the cavity at an approximate rate of 10^4 times per second. This rate strongly depends on the detailed mode-structure of the cavity [3], in combination with the scanning rate of the laser and the frequency-jitter of the cavity modes, i.e. the 'unstability' of the cavity.

If one were to make a single scan, and were to probe the absorption spectrum of species inside the cavity that way, it is evident from the inset, and it has been pointed out by others [25, 31, 34], that spectral features that are narrower than the spacing between the modes (approximately 50 MHz in this particular example) would escape observation. In repeating this procedure over the same spectral region, and summing up the observed results, these 'gaps' in the spectrum can be filled up, however, via 'random interleaved sampling'.

In Fig. 5 a part of the absorption spectrum of the $b^1\Sigma_g^+(v'=2) \leftarrow X^3\Sigma_g^-(v''=0)$ band of $^{16}O_2$ (γ-band), showing the bandheads of the ^RR and ^RQ branches, is shown as recorded with the cw ring dye laser in a 12 cm long cell filled with 200 mbar of molecular oxygen at room temperature. The spectrum is a compilation of three partly overlapping measurements, each covering about 1.5 cm^{-1} averaged over 100 scans. With a scanning rate of the laser of around 5 Hz, this implies an effective recording time of one minute. In the vertical direction, the inverse of the time-integrated intensity behind the cavity is plotted, with the baseline denoted as zero. The value of the baseline is proportional to (1-R)/d, but, contrary to CRD experiments, the absolute value of this quantity is not directly determined in this experiment. Therefore, the intensity scale of the spectrum is expressed relative to the baseline intensity. This relative absorption spectrum can obviously be put on an absolute scale if the ring-down time of the empty cavity is known via some other way. If we do the reverse, and extract the effective mirror reflectivity R from the measured spectrum using the calculated population distribution of ground-state molecular oxygen and the known absorption cross-sections for these transitions, we deduce a reflection

coefficient R=0.9998, in good agreement with independent CRD measurements [21]. It is worth noting that the noise-level on the baseline of the spectrum is at the 10^{-3} level, as good as can be obtained in standard CRD experiments. As mentioned previously, the time axis of the digital oscilloscope which is used to average the traces is triggered by the ramp voltage used for scanning the laser. To accurately determine the absolute frequency position as well as to be able to correct for possible non-linearities in the scanning, the well-known absorption spectrum of I_2 is recorded simultaneously.

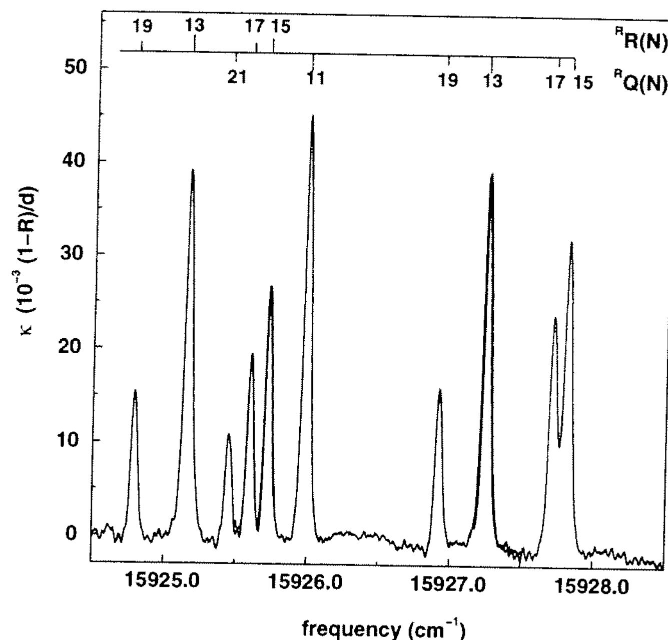

Figure 5: Cavity Enhanced Absorption spectrum of 200 mbar molecular oxygen.

Acknowledgments

This work is part of the research program of the 'Stichting voor Fundamenteel Onderzoek der Materie (FOM)', which is financially supported by the 'Nederlandse Organisatie voor Wetenschappelijk Onderzoek (NWO)', and receives direct support by the NWO via PIONIER-grant # 030-66-89.

Literature Cited

[1] *Cavity-Ringdown Spectroscopy: An Ultratrace-Absorption Measurement Technique*, eds. K.W. Busch and M.A. Busch (in press at Oxford University Press)

[2] A. O'Keefe and David A.G. Deacon, Rev. Sci. Instrum. **59**, 2544 (1988)

[3] G. Meijer, M.G.H. Boogaarts, R.T. Jongma, D.H. Parker, and A.M. Wodtke, Chem. Phys. Lett. **217**, 112 (1994)

[4] P. Zalicki, Y. Ma, R.N. Zare, E.H. Wahl, J.R. Dadamio, T.G. Owano, and C.H. Kruger, Chem. Phys. Lett. **234**, 269 (1995)

[5] R.T. Jongma, M.G.H. Boogaarts, I. Holleman, and G. Meijer, Rev. Sci. Instrum. **66**, 2821 (1995)

[6] D. Romanini and K.K. Lehmann, J. Chem. Phys. **99**, 6287 (1993)

[7] D.L. Huestis, R.A. Copeland, K. Knutsen, T.G. Slanger, R.T. Jongma, M.G.H. Boogaarts, and G. Meijer, Can. J. Phys. **72**, 1109 (1994)

[8] T.G. Slanger, D.L. Huestis, P.C. Cosby, H. Naus, and G. Meijer, J. Chem. Phys. **105**, 9393 (1996)

[9] M.D. Wheeler, A.J. Orr-Ewing, M.N.R. Ashfold, and T. Ishiwata, Chem. Phys. Lett. **268**, 421 (1997)

[10] J.J.L. Spaanjaars, J.J. ter Meulen, and G. Meijer, J. Chem. Phys. **107**, 2242 (1997)

[11] see the contribution of M.G.H. Boogaarts *et al.* at this workshop

[12] A. Campargue, D. Romanini, and N. Sadeghi, J. Phys. D: Appl. Phys. **31**, 1168 (1998)

[13] A. O'Keefe, J.J. Scherer, A.L. Cooksy, R. Sheeks, J. Heath, and R.J. Saykally, Chem. Phys. Letters **172**, 214 (1990)

[14] J.J. Scherer, J.B. Paul, C.P. Collier, and R.J. Saykally, J. Chem. Phys. **102**, 5190 (1995)

[15] M.G.H. Boogaarts and G. Meijer, J. Chem. Phys. **103**, 5269 (1995)

[16] J.B. Paul, J.J. Scherer, C.P. Collier, and R.J. Saykally, J. Chem. Phys. **104**, 2782 (1996)

[17] D. Kraus, R.J. Saykally, and V.E. Bondybey, Chem. Phys. Lett. **295**, 285 (1998)

[18] M. Kotterer and J.P. Maier Chem. Phys. Lett. **266**, 342 (1997)

[19] H. Linnartz, T. Motylewski, and J.P. Maier, J. Chem. Phys. **109**, 3819 (1998)

[20] E. Quandt, I. Kraemer, and H.F. Döbele, *Europhysics Lett.* (accepted)

[21] R. Engeln, G. Berden, E. v.d. Berg, and G. Meijer, J. Chem. Phys. **107**, 4458 (1997)

[22] R.T. Jongma, M.G.H. Boogaarts, and G. Meijer, J. Mol. Spectrosc.**165**, 303 (1994)

[23] J.J. Scherer, D. Voelkel, D.J. Rakestraw, J.B. Paul, C.P. Collier, R.J. Saykally, and A. O'Keefe, Chem. Phys. Lett. **245**, 273 (1995)

[24] R. Engeln, E. van den Berg, G. Meijer, L. Lin, G.M.H. Knippels, and A.F.G. van der Meer, Chem. Phys. Lett. **269**, 293 (1997)

[25] P. Zalicki and R.N. Zare, J. Chem. Phys. **102**, 2708 (1995)

[26] J.T. Hodges, J.P. Looney, and R.D. van Zee, Applied Optics **35**, 4112 (1996)

[27] R. Engeln and G. Meijer, Rev. Sci. Instr. **67**, 2708 (1996)

[28] R. Engeln, G. von Helden, G. Berden, and G. Meijer, Chem. Phys. Lett. **105**, 262 (1996)

[29] D. Romanini, A.A. Kachanov, N. Sadeghi, and F. Stoeckel, Chem. Phys. Lett. **264**, 316 (1997)

[30] B.A. Paldus, J.S. Harris, J. Martin, J. Xie, and R.N. Zare, J. Appl. Phys. **82**, 3199 (1997)

[31] K.K. Lehmann and D. Romanini, J. Chem. Phys. **105**, 10263 (1996)

[32] R. Engeln, G. Berden, R. Peeters, and G. Meijer, Rev. Sci. Instrum. **69**, 3763 (1998)

[33] R. Engeln, G. von Helden, A.J.A. van Roij, and G. Meijer, J. Chem. Phys. **110** (1 February 1999)

[34] J.T. Hodges, J.P. Looney, and R.D. van Zee, J. Chem. Phys. **105**, 10278 (1996)

[35] J. Martin, B.A. Paldus, P. Zalicki, E.H. Wahl, T.G. Owana, J.S. Harris, C.H. Kruger, and R.N. Zare, Chem. Phys. Lett. **258**, 63 (1996)

[36] Y. He, M. Hippler, and M. Quack, Chem. Phys. Lett. **289**, 527 (1998)

Real time plasma etch diagnostics by plasma monitoring system Hercules

A. Steinbach et al
Siemens Microelectronics Center Dresden
Germany

Introduction

The semiconductor technology is one of the major applications of low temperature plasmas. The Semiconductor production is characterized today by a fast change to higher integration levels. Critical structure dimensions of 0.2 µm to 0.17 µm are used in high volume production already, and structures of 0.15 µm to 0.12 µm are the target of the next shrink steps. Parallel to this technology shrink, semiconductor industry switches over to larger wafer diameter. Currently the Si wafers have a diameter of 200 mm usually. The first European 300 mm semiconductor fab, a joint venture of Siemens and Motorola in Dresden, has already started production.
These efforts are made to achieve an effective production of semiconductor devices with higher complexity. In memory production 64 M DRAM´s are produced in high volume now. The production of 256 M DRAM´s has been started already and 1 G DRAM´s are expected during the next two years.
In contrast to this fast development of the integration level and the wafer size, the production strategy is developing slowly. For the process development, experience and statistical methods are used mainly. Tool control is performed by means of many test wafers and a lot of time. For control of the process results additional in – line measurements are necessary. Statistical Process Control is widely used. The costs of tools and wafers are increasing rapidly. Therefore the established methods of process development, tool control, and process control become more and more expensive and ineffective.
The way out is to use in – situ measuring techniques for real time process monitoring on product wafers. In this way it is possible to save test wafers and time and to improve process stability. Thus a higher yield and a reduction of the costs of production can be achieved.
Plasma process steps are a very important part of semiconductor technology. But especially in plasma processing, the in – situ process control is still very poorly developed. The plasma monitoring system HERCULES, presented here, is one example of new in – situ real time measuring techniques, which are ready for use in semiconductor production.

Why is In – situ plasma monitoring necessary

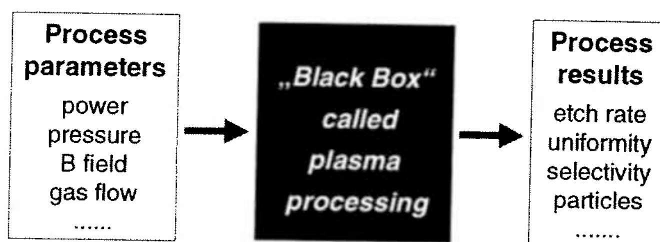

Figure 1: *Figure caption should be in Times, 10pts, italics and positioned under the corresponding figure*

Plasma processes, used in semiconductor industry, are usually treated as “black box”, see Figure 1. Process parameters, e.g., power output of the rf generator, discharge pressure, B – field, and gas flows, are measured at the tool. Etch results are measured on test or product wafers. In this way the process conditions should be kept constant to achieve

the same etch results on all product wafers.
But, in fact, these "process" parameters, are more tool parameters, not real process parameters. And these measurements can have relevant errors or provide only a small amount of information ! The rf power measurement is a typical example. It is measured at the output of the rf generator. There are power losses on the cable between the generator output and the rf matchbox input, inside the match box, and at the connector from the output of the match to the wafer electrode in the chamber. These power losses are unknown and they vary from tool to tool and from process to process. But even if we could guarantee a constant power input into the chamber, the rf power is not a true measure for well known process conditions, e.g. because of secondary plasmas and changes of the chamber conditions as polymers on the chamber wall.
Etch rates, uniformities, and particle densities are usually measured on blank test wafers. But, even in case of the same tool parameters, the etch chemistry differs in the plasma between blank oxide test wafer and product wafers, which are covered with photo resist, except a few percent. Test wafers are often less sensitive against changes of the process conditions than product wafers. That is why the test results can be constant, while the product yield decreases.
Experience and statistical methods, e.g., designs of experiments, are used to develop and optimize processes. We can not transfer a process directly from one tool to another different one, because we do not know the real important process parameters in the plasma. In fact, every time we have to develop the process again.
If we look into the "black box", we find many interacting phenomena, compare Figure 2.

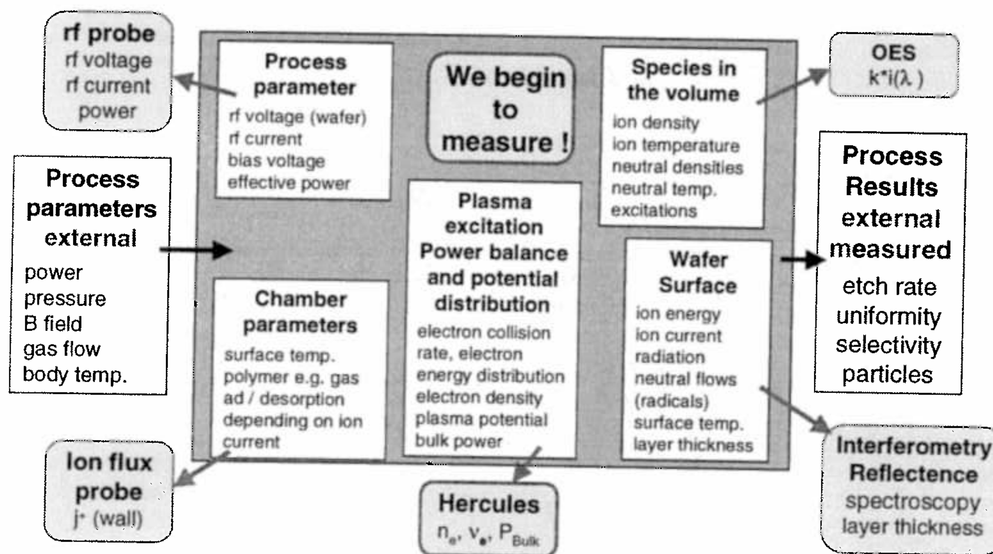

Figure 2: Measuring techniques for in – situ real time plasma monitoring

The plasma excitation, power balance, and potential distribution depend on external process parameters, which are measured at industrial tools, and on other process parameters, e.g., rf voltage, rf current, bias voltage and effective power, which are usually not measured. Plasma excitation and process parameters impact the species in the discharge volume. Finally the conditions on the wafer surface are responsible for the etch result. They depend very much on the plasma excitation and the species in the volume. To some extent, unknown chamber parameters, such as surface temperature, adsorption and desorption of process gases, and gaseous etch products in polymer layers on the chamber wall, have a strong impact as well.
Constant etch results can be only obtained by stable conditions at the wafer surface. To reach this final goal is a tricky thing. Therefore several measuring techniques have been developed

to measure at "different corners" of the "black box". Optical methods are well known, e.g. for endpoint detection. New electrical methods have been developed. The plasma monitoring system Hercules is based on the **S**elf **E**xcited **E**lectron plasma **R**esonance **S**pectroscopy (SEERS). Hercules can measure important plasma parameters, such as electron collision rate, electron density, and bulk power. Therefore we can expect information about the reactions on the wafer surface and about the tool conditions.

Theoretical background and experimental setup

The **S**elf **E**xcited **E**lectron plasma **R**esonance **S**pectroscopy (SEERS) is based on the non-linearity of the space charge sheath at the rf electrode, which provides harmonics with the modulated sheath width and high-frequency oscillations in the bulk plasma.
In order to include the nonlinear sheath capacitance, the fundamental relation of the temporal derivative of sheath voltage u, sheath width s[u] and displacement current i:

$$\frac{du}{dt} = \frac{s[u(t)]\, i(t)}{A_0 \epsilon_0} \tag{1}$$

is used and indicates the nonlinear properties of the sheath. A_0 denotes the rf electrode area. The degree of the nonlinearity depends on the ion density distribution within the sheath and results basically in a saw tooth shaped current.
Using a hydrodynamic approach for the electrons, the known equation for the permittivity of the cold plasma can be expressed as

$$\frac{\epsilon}{\epsilon_0} = 1 - \frac{\omega_e^2}{\omega(\omega - j\nu)} , \quad \omega_e^2 = \frac{e^2 n}{\epsilon_0 m_e} \tag{2}$$

where ω_e is the electron plasma (Langmuir) frequency. When the collision rate ν vanishes, Eq. (2) is known as Eccles relation.
Bearing in mind the relation between electrostatic field and current density $J = j\omega\epsilon E$ for $(\omega_e/\omega)^2 >> 1+(\nu/\omega)^2$, the conductivity can be written as

$$\sigma_p = \frac{n e^2}{m_e (j\omega + \nu)} , \tag{3}$$

and the potential drop of the bulk plasma in the time domain as

$$u_p = \frac{m_e l}{A_0 n e^2}\left(\nu i + \frac{d}{dt} i \right) . \tag{4}$$

The effective length of the plasma body is obtained by a separate treatment of rf current distribution given boundary conditions. Neglecting the conduction currents of ions and electrons in the sheath, however, one obtains

$$\frac{d}{dt} u_{rf} + \frac{\bar{s} - s[u(t)]}{A_0 \epsilon_0} i = \frac{\bar{s}}{A_0 \epsilon_0} i + \frac{m_e l}{A_0 n e^2}\left(\nu \frac{d}{dt} i + \frac{d^2}{dt^2} i \right) \tag{5}$$

for the whole discharge driven by the voltage u_{rf} at the rf electrode, see Figure 3.
This is a nonlinear, inhomogeneous, and stiff differential equation of second order. On the right hand side of the equation above is a linear oscillation term with the geometric resonance frequency $\omega_p^2 = \omega_e^2\, s/l$ for a plasma with small damping, where l denotes the effective geometric length of the plasma.
The dependence of the sheath width on the displacement current involves a special approach and usually requires a numerical solution of the differential equation (5).

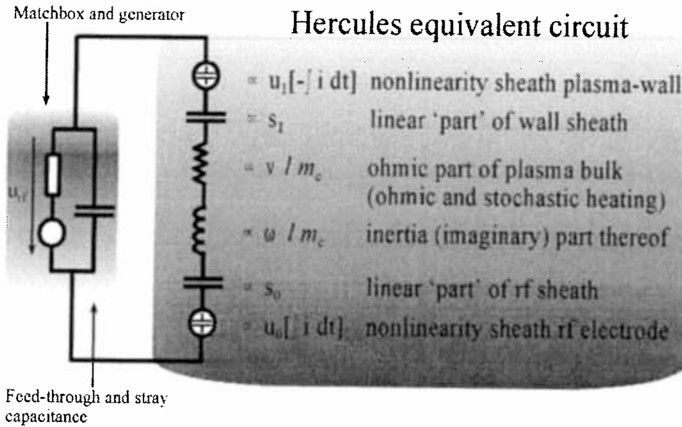

Figure 3: *Equivalent circuit of radio frequency discharge*

This differential equation can be interpreted using an equivalent circuit, compare Figure 3. On the left hand side, we have the external excitation - the matchbox including the rf generator. The discharge is treated as a damped oscillating circuit as suggested by the right hand side of Eq. (5).
Finally we have the nonlinear phenomena, given by the second term on the left hand side of Eq. (5). The nonlinearity of the sheath, compare with Eq. (1), provides harmonics exciting the oscillating circuit. This additional resonance can be observed measuring the discharge current.
SEERS allows the determination of the volume averaged electron density,

$$\tilde{n} \approx \left(\frac{1}{V} \int_V n^{-1} dV \right)^{-1} \qquad (6)$$

$$\tilde{\nu} \approx \frac{\tilde{n}}{V} \int_V \frac{\nu}{n} dV \qquad (7)$$

electron collision rate,
and bulk power dissipated in the plasma body:
Using a fast numerical algorithm, the plasma monitoring system Hercules provides a temporal resolution better than a second and performs SEERS measurements automatically.
The experimental setup is shown in Figure 4. Because of unavoidable stray and feedthrough capacitances at the powered electrode, a direct measurement of the discharge current is very

$$P_B \propto \frac{\tilde{\nu}}{\tilde{n}} \sum_{(k)} \left[I^{(k)} \right]^2 \qquad (8)$$

difficult in commercial systems. Hercules uses a special sensor in a coaxial geometry (50 Ω) inserted into the wall (flange) of the recipient as a virtual part of the wall. By means of the nonlinear model, the current pitch ratio of the current measured and the real discharge current can be determined. Therefore, calibration depending on the sensor position is not necessary.

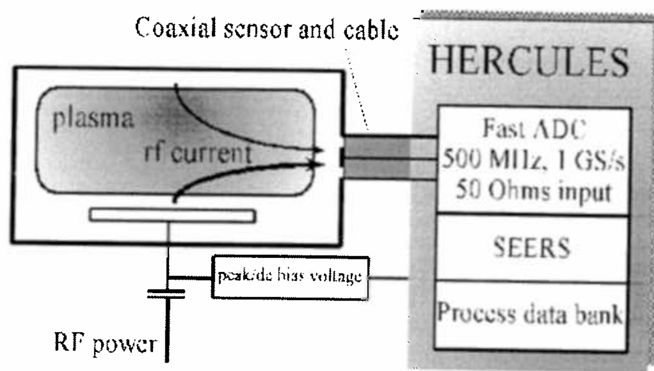

Figure 4: *Experimental setup*

An insulating layer up to a thickness of 100 µm on the sensor can be treated as a capacitance adding a very small series impedance (<< 50 Ω) and therefore can be neglected. The measured discharge current is converted using a fast ADC (analog / digital converter) with a bandwidth of 500 MHz and a sampling rate of 2 GS/s.
The peak voltage of the substrate is measured by using a capacitive voltage divider. At many industrial tools the peak voltage and even the bias voltage are not available. In this case, the sheath thickness is estimated to be constant. As a result of this simple approximation, electron density, bulk power and the calculated bias voltage have a systematic deviation.
Many plasma processes use a rotating magnetic field. Here the measurement is triggered by a Hall sensor. In a process data base, the measuring results are stored together with logistical data, e.g. date, time, chamber, lot name and recipe step. The size data file of one lot (25 wafers) is about 100 kByte. In comparison to other methods, these files are small and easy to handle.

Basic experiments – Sensitivity to process parameter variations

The measurements were done at a LAM TCP 9600 SE for Al etch with Cl chemistry and at Applied Materials Centura MxP+ and P 5000 MxP chambers for oxide and nitride etch with CF_4, CHF_3, Ar, and O_2. Basic experiments were done for oxide etch with blank BPSG wafers and test wafers with contact mask (structure).
Typical examples of the results are shown in Figure 5 and Figure 6.

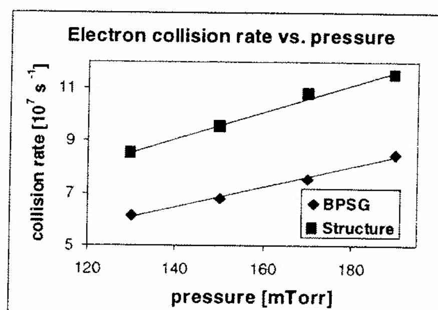

Figure 5: *Electron collision rate depending on pressure at Oxide etch in AMAT MxP+ chamber*

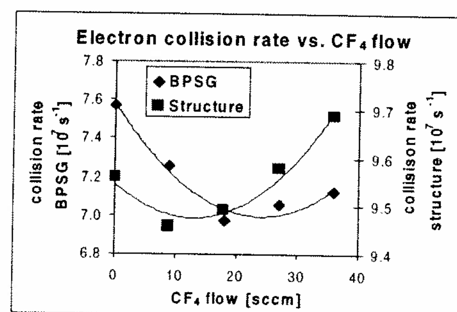

Figure 6: *Electron collision rate depending on and CF_4 flow at Oxide etch in AMAT MxP+ chamber*

Variations of "physical" process parameters, e.g. rf power or pressure cause continuos, and partly linear correlations between the measured plasma parameters and the process parameters. Variations of the "plasma chemistry", e.g. of the CF_4 or O_2 flow, result in often strong nonlinear effects. Electron collision rate, electron density and bulk power depend significantly on all process parameter changes and on the wafer surface.

Correlation between plasma parameters and etch results

It would be very useful, to be able to conclude from the measured plasma parameters on the etch results directly. The following examples demonstrate, that such conclusions can be maid partly, see Figure 7 and Figure 8.

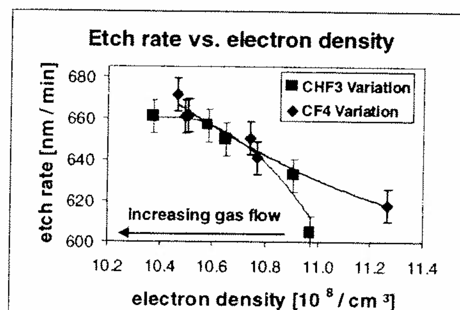

Figure 7: *Correlation between BPSG etch rate and electron density*

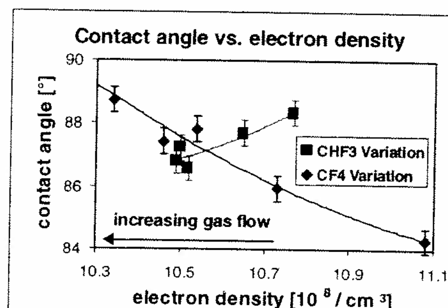

Figure 8: *Correlation between contact whole angle and electron density*

In a typical oxide or nitride etch gas mixture, consisting of CF_4, CHF_3, Ar, and O_2, an increasing CF_4 - or CHF_3 - flow causes a lower electron density. But the effects of both reactive gases on the discharge chemistry are completely different. CF_4 delivers particularly CF_2 and F – radicals and ions, which are the main etch species. On the contrary, the main result of the CHF_3 dissociation are CHF_x components, causing polymerisation. Therefore, an increasing flow of both gases provides a higher BPSG etch rate, while the contact hole angle varies opposite. A higher CHF_3 –flow increases the polymerisation, gives a better side wall passivation and a lower contact angle. A higher CF_4 – flow creates a higher concentration of F etch species and therefore a steeper contact angle. It follows that a one – to – one conclusion from the electron density to the contact angle is not possible.
But generally, a change of the electron density, or any other measured parameter indicates a variation of the discharge conditions.

Long term process monitoring and tool stability

A mixture of oxide and nitride etch processes has been monitored at an Applied Materials MxP+ chamber for more than 450 rf hours to characterise the long term stability of these processes. Figure 9 shows the trend of the electron collision rate at oxide etch during 5 wet clean cycles (WC).

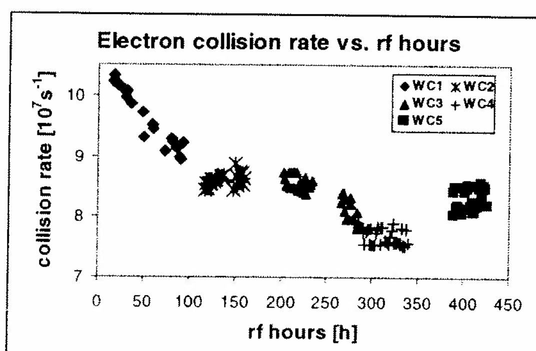

Figure 9: *Electron collision rate depending on rf hours at oxide etch during 5 wet clean cycles (WC,), one point one lot*

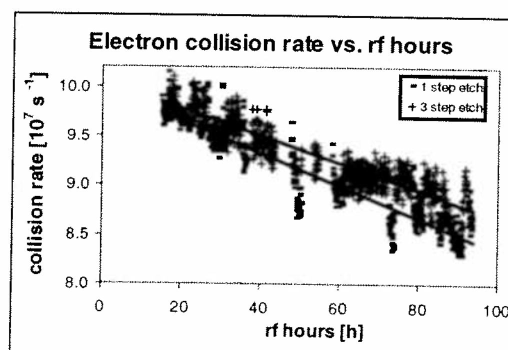

Figure 10: *Electron collision rate of an oxide etch process, used in two different recipies, WC1, one point one wafer*

During WC1 and WC3 a continuos shift was observed, while the electron collision rate was comparatively constant on different levels during WC2, WC4 and WC5.
To make the wet clean as fast as possible, the MxP+ chamber is covered by removable liner parts inside. During the wet clean, all liner parts are changed for external cleaning. It seems, that the long term process stability depends on the wet clean, including the kind of liner set, reassembled in the chamber. Different spare part sets were used, new, regenerated, and already many times used. The reason for the differences could not be found in detail, because the spare parts were not tracked individually. Therefore we could not correlate between the measurements and the hardware, used inside the chamber.
Figure 10 compares the electron collision rate of the same oxide etch process at a one step recipe and at a three step recipe, during WC1. The other steps of the three step recipe cause a deconditioning of the polymer inside the chamber. Therefore, the difference of the electron collision rate increases by time. Electron collision rate is the most sensitive of all measured plasma parameter.

First wafer effect and short term process stability

First wafer effects were detected at both tools. During the main etch step of the first wafer (Al etch), see Figure 11, the electron density was significantly higher, compared to the next wafers. This is connected with a lower etch rate.

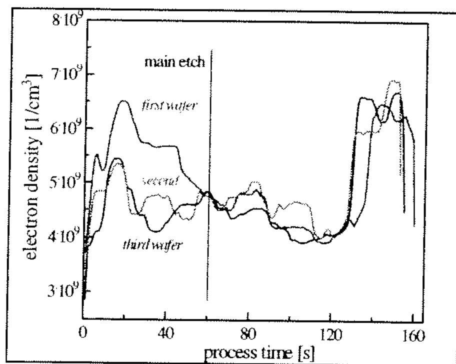

Figure 11: *First wafer effect at Al etch in LAM TCP*

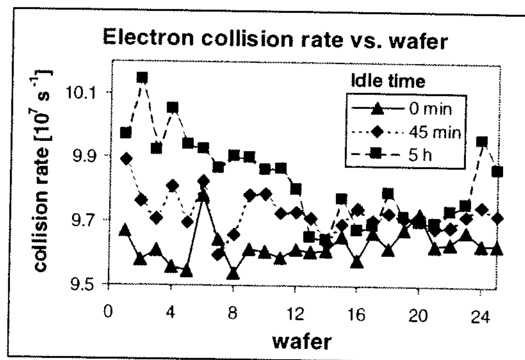

Figure 12: *First wafer effect at oxide etch in MxP+, one point one wafer*

In the MxP+ chamber, depending on the idle time, a drift of the electron collision rate was found up to more than ten wafers, compare Figure 12.The drift effect increases with the idle time before processing the lot. This can be explained by a temperature drift of the liner cylinder and gas adsorption effects at the polymer layers inside the chamber.

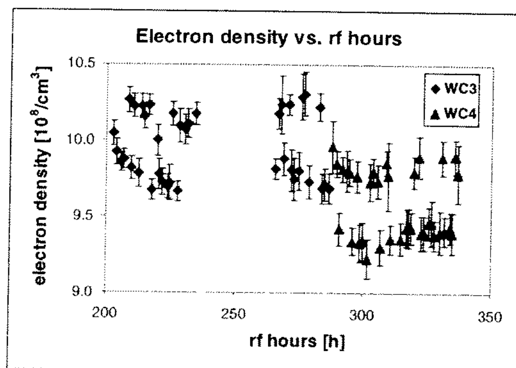

Figure 13: *Wafer depending process instability at oxide etch, one point mean of one lot*

Wafer effects

During the long term process monitoring of oxide etch, lot depending, see Figure 13, and wafer depending process instabilities were found, see also Figure 14. The optical intensities of the CO – and CN – emission line varied as well, see Figure 15. These variations are caused by wafer processing before this etch step. The actual reason

could not be found. There was not any significant correlation to regular in – line measurements or yield.

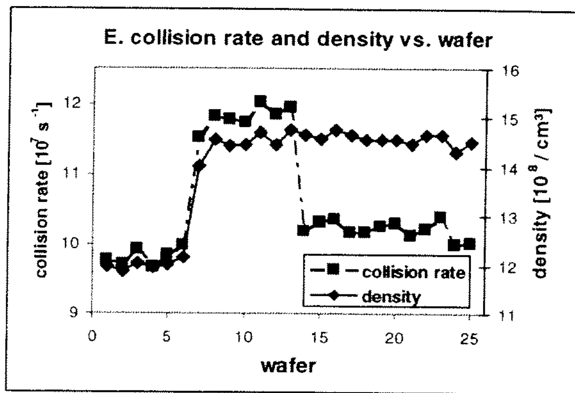

Figure 14: *Wafer depending process instability at oxide etch at one lot, one point one wafer*

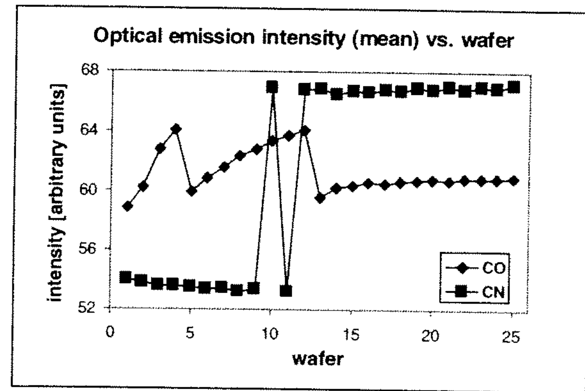

Figure 15: *Wafer depending process instability at oxide etch, one point mean of one lot*

Hercules is a very sensitive plasma monitoring system, and can detect process variations, which are still tolerated by the process itself. In future on higher integration levels the process windows will become smaller. The importance of tools tolerances will increase. Partly it will be necessary to adapt the processes to the tolerances. This can be done only with real time in – situ process and, in particular, plasma monitoring.

End point detection

The Al etch process consists of three steps, a break through, the main etch and the over etch. Below the Al layer there is a stack of Ti and TiN. During the Al etch process at a LAM TCP at an etch time of about 75 s, a peak in collision rate appeared, if the stack contained a Ti layer. By using a set of special test wafers, it was verified, that this peak was caused by 15 nm thick Ti layer. The reason is probably the large cross section of Ti. Therefore Hercules can be used for endpoint detection as well. At contact etch processes it was less sensitive, than optical systems. In case of comparatively large open area and processes with a strong polymerization, this endpoint detection method can be more successful, than an optical one.

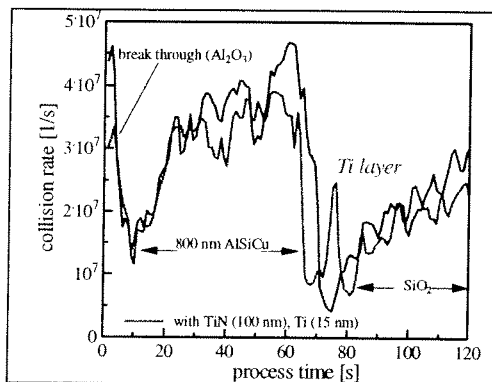

Figure 16: *Layer detection at Al etch*

Optimization of conditioning procedures

The impact of a wet clean on electron collision rate and electron density is shown in Figure 17 and Figure 18. After the wet clean at 110.7 rf hours, resist wafers are used for chamber conditioning. Using this etch process, about 10 wafers are necessary to reach stabile process conditions after the wet clean. Obviously, the plasma monitoring system Hercules can be used to optimise conditioning procedures and to reduce the costs in this way.

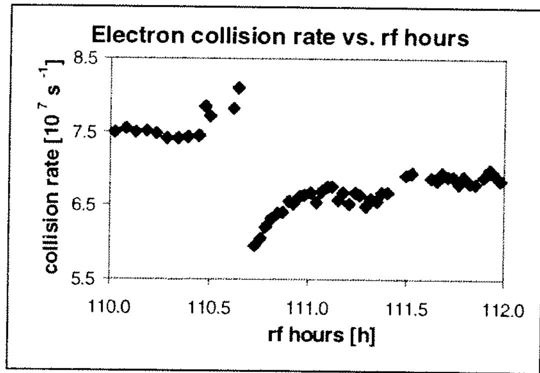

Figure 17: *Electron collision rate before and after wet clean, oxide etch, MxP+ chamber, one point per wafer*

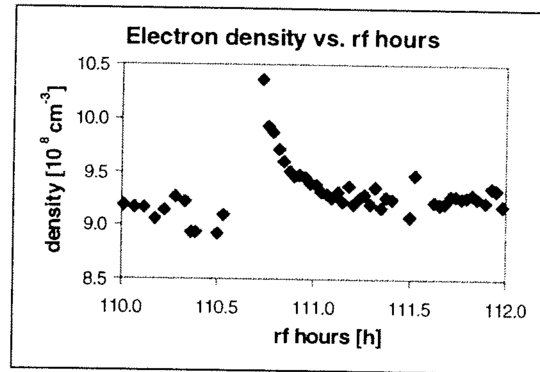

Figure 18: *Electron density before and after wet clean, oxide etch at MxP+ chamber, one point per wafer*

Power density measurement

To improve the uniformity of a nitride etch process at a MxP chamber, several shadow rings, were tested, located around the wafer electrode and behaving like a virtual part of it. While the rf power was kept constant, the etch rate varied, depending on the shadow ring material. Figure 19 shows the bulk power, measured at a two step process with a high permittivity shadow ring and a low permittivity shadow ring. The two etch steps can be distinguished very well. The bulk power, and the electron collision rate, too, measured with the low permittivity shadow ring, are significantly higher. The values of bulk power and electron collision rate correlate with the etch rate and the wafer surface temperature. Because of its capacitive coupling to the wafer electrode, the high permittivity ring acts as a rf conducting part of the wafer electrode. As a result, the same rf power is spread on a "larger wafer" with a diameter of 260 mm. All measured parameters correlate very well with the calculated inverse area ratio of the rf conducting wafer electrode area.

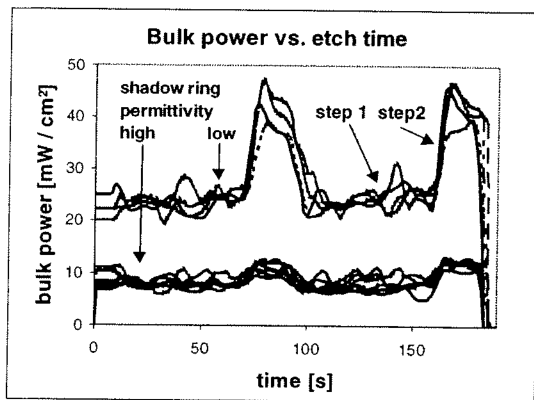

Figure 19: *Power dissipation in a MxP chamber at a two step process and depending on shadow ring permittivity*

Arcing detection

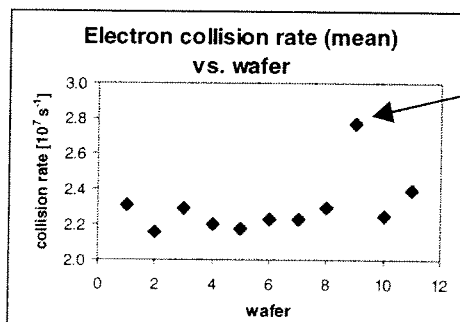

Figure 20: *Arcing detected at wafer 9*

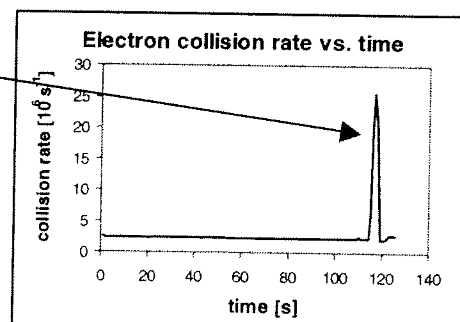

Figure 21: *Arcing detected at wafer 9*

During the conditioning of a new MxP+ chamber, a high wafer mean value of the electron collision rate was observed at wafer 9, see Figure 20. The time resolved curve of this wafer indicates a short and heavy arcing, see Figure 21. We found hot spots on the electrostatic chuck and at the back side of the wafer. In comparison to all measured tool parameters, e.g. reflected power, bias voltage, and load and tune of the matching network, the electron collision rate was the most sensitive parameter.

Summary

Because of the increasing integration level and larger wafer diameter in semiconductor industry, we will have to switch from **S**tatistical **P**rocess **C**ontrol to **A**dvanced **E**quipment **C**ontrol and **A**dvanced **P**rocess **C**ontrol during the next years. This is only possible by means of in – situ real time process monitoring.
Hercules is a powerful example of the recently developed plasma measuring techniques, which can be applied for in – situ real time process monitoring in semiconductor technology. It can be used for

- Development and optimization of processes
- Improvement of process transfer
- Measurement of long and short term process and tool stability
- Endpoint detection
- Control of tool matching
- Optimization of chamber cleaning and conditioning
- Measurement of power coupling into plasma
- Detection of process and tool failures
- Arcing detection

The new plasma measuring techniques are necessary tools to

- achieve higher yield
- reduce the costs of test wafers and maintenance.

There is still a large gap between the abilities of the new plasma measuring techniques and their industrial application today. High volume production is and has to be very conservative. "Never change a running production". To overcome this gap and to use the new measuring tools under industrial conditions, they have to be very reliable and robust, including the data handling. Otherwise they will not be accepted. It is our task to get over this gap.

[1] M. Klick, J. Appl. Phys. **79** 3445 (1996)

[2] M. Klick, M. Kammeyer, W. Rehak, W. Kasper, P. Awakowicz, G. Franz, 5th International Conference on Plasma Surface Engineering, Garmisch - Partenkirchen, 1996, Germany

[3] M. Klick, W. Rehak, M. Kammeyer, Jpn. J. Appl. Phys. **36** 4625 (1997)

[4] M. Klick, Frontiers in Low Temperature Plasma Diagnostics II, Bad Honnef, 1997, Germany

[5] S. Wurm, W. Preis, Ch. Köbl, M. Klick, D. Suchland, M. Kammeyer, A. Steinmetz, Proc. of the Plasma Etch Users Group, 4th Intern. Workshop on Adv. Plasma Tools

[6] A. Steinbach et al. SEMATECH AEC/APC Symposium X, Vail, Colorado, 1998, USA

The Black Box Illuminated

Richard A. Gottscho, David Cooperberg, and Vahid Vahedi

Lam Research Corporation

Fremont, CA 94538

Introduction

It has been more than 20 years since Winters, Coburn, and Kay [1] referred to the plasma reactor as a "black box" and described a phenomenological model relating concentrations of reactive species to etching rates. Since that time, our level of understanding has increased markedly as a result of systematic studies to elucidate etching mechanisms, plasma generation, and plasma transport. Today, we can see inside the "black box," understand in greater depth what takes place in plasma reactors, and assemble elements of the reaction pathways to predict outcomes on semiconductor wafers being processed into nano-scale devices.

This improved understanding stems from advances on several fronts (with representative references):

1. By irradiating surfaces with beams of reactive ions, molecules, atoms, and electrons and analyzing the resultant surface composition, the governing laws for ion-neutral synergistic effects have been uncovered.[2-12]
2. By simulating the dynamics of ions impacting surfaces with multi-layers of adsorbed reactant, we have witnessed how mixing, adsorption, reaction, and desorption occur during the etching process. [13]
3. By measuring the reactive plasmas employed to generate and transport etchants, inhibitors, and depositers to surfaces, the fluxes, energies, and angles of reactive species have been determined. All manner of techniques have been applied to the measurement of plasma properties: for example, ion sampling,[14-16] Thomson scattering,[17], Langmuir probes,[18], microwave interferometry,[18] laser-induced fluorescence,[19,20], photodetachment,[21-23], and infrared absorption spectroscopy.[24]
4. By simulating bulk plasma properties such as densities, energy distributions, power coupling, and dissociation we can fill in critical pieces of information that could not be measured. Spatial variations in plasma properties are also elucidated. [25-32]
5. By simulating the local transport of reactants and products as well as the surface itself, we gain prediction of the etched profile and can tailor it within the confines of the reactor design. [33-36].

In this talk, we outline how plasma diagnostic data[37] are combined with beam-surface data, reactor-scale simulations, and plasma etch data to enable etched profile simulation. Key to our approach is *semi-empirical* calibration of the simulator, which enables us to circumvent inadequacies in the input data set. In effect, we use etched profiles as an *ex situ* diagnostic.

We consider two etching reactions Al:Cu and SiO_2, used routinely in constructing the interlayer dielectric and interconnect structure of ultra-large-scale integrated circuits. The etching rate is described in terms of occupied sites, ion energy, and ion flux. Product desorption and etchant re-emission are described using a local transport model. The incoming particle trajectories and energies are selected at random from appropriate distribution functions. Similarly, the surface front is transported using Monte-Carlo techniques. Nano-

structure charging and the corresponding deflection of ions and electrons has also been modeled but these effects were found to be unimportant for both the Al and oxide etching simulations discussed here.

Note that effects such as aspect ratio dependent etching (ARDE) are implicitly captured in the model above. The fluxes of etchants, ions, and inhibitors are what depend on aspect ratio (depth/width for trench or depth/diameter for contact).[38,39]. Given the incident fluxes, whose determination will be discussed below, the variation in flux as the feature evolves will depend on the sticking coefficients, sputter yields, and evaporation rates.

Etching Models

We model Al stack etching with up to three mechanisms, ion-induced desorption, sputtering, and evaporation. The relative importance of each mechanism depends on the film being etched – photoresist, TiN anti-reflection coating, Al:Cu (5%), or Ti/TiN barrier layer.[40] The etch rate is expressed as a sum of these three terms,[41]

$$Etch\ Rate = \frac{1}{\rho^f}(\Gamma_i \eta_{ei}^f \theta_e + \Gamma_i \eta_s^f + \Gamma_{evap} \theta_e) \qquad (1)$$

where Γ_i is the ion flux and Γ_{evap} is the flux of products produced by thermal desorption. The ion-induced sputter yield coefficients are given by:

$$\eta = Y \int_{E,\varphi} (E^{1/2} - E_{th}^{1/2}) \Phi(\varphi) f_i(E,\varphi) \qquad (2)$$

where E is the incident ion energy, E_{th} is the threshold energy for sputter etching, $\Phi(\varphi)$ is the angular dependence to the sputter yield, and $f_i(E,\varphi)$ is the incident ion energy and angular distribution function. The sputter yield is normalized to Y, the number of atoms removed per incident ion after integration over all ion energies and angles. The subscripts ei and s denote yields for ion-induced etching, or chemical sputtering,[3] and physical sputtering, respectively, of the f film in the stack with density ρ^f. Physical and chemical sputtering are distinguished here by their dependence on etchant surface coverage, θ_e. Chemical sputtering is directly proportional to θ_e while physical sputtering is independent of θ_e.

In the case of rapid inhibitor deposition such that a new film begins to grow, chemical sputtering of the deposit can occur and the etch products may consist of a mixture of film, etchant, and deposition agent. This is the model we use for oxide etching. For highly selective dielectric etching using fluorocarbon plasmas, best results are achieved when etching and deposition occur simultaneously. Etching of the dielectric is believed to proceed through a steady-state fluorocarbon film that accumulates on the etching surface [42].

To account for net deposition that may occur in etching SiO_2, we modify the Eq. 1 phenomenologically:

$$Etch\,Rate = \frac{1}{\rho^d}\left[\Gamma_i \eta_{ei}^d \theta_e - \Gamma_d S_d^d\right] \qquad DR_{dep} > ER_{dep} \qquad (3a)$$

$$Etch\,Rate = \frac{1}{\rho^f}\left[\Gamma_i \eta_{ei}^f \theta_e + \Gamma_i \eta_s^f\right] \cdot \left(1 - \frac{\Gamma_d S_d^d}{\Gamma_i \eta_{ei}^d \theta_e}\right) \qquad DR_{dep} < ER_{dep} \qquad (3b)$$

When net deposition occurs, all that is etched is the deposited film (Eq. 3a). When net etching occurs, film etch rate is attenuated by the presence of the deposited film with the attenuation factor depending on the relative rates of deposition and etching of the deposited layer. We further assume the fluorocarbon polymer deposition rate depends solely on the deposition precursor flux and not the ion flux. The proportionality constant is the ion-flux-independent sticking coefficient. Finally, we consider the fluorocarbon polymer film to be chemically sputtered.

The equations above describe etching reactions in a plasma reactor in terms of several variables:

- Etchant, ion, and deposition fluxes
- Chemical or physical sputter yields
- Ion energy (distribution)
- Angular dependence of chemical or physical sputter yields
- Sticking coefficients

We now direct our attention to how these parameters are determined.

Ion Energy and Flux

The energy dependence of the yield in Eq. 2 is based on beam-surface studies[6] [5] and theoretical considerations.[13,43] While Al etches spontaneously at room temperature in the presence of Cl and the Al etching rate is, therefore, independent of ion energy,[44] photoresist and oxide etching are observed to follow the form of Eq. 2.[36,40] To determine

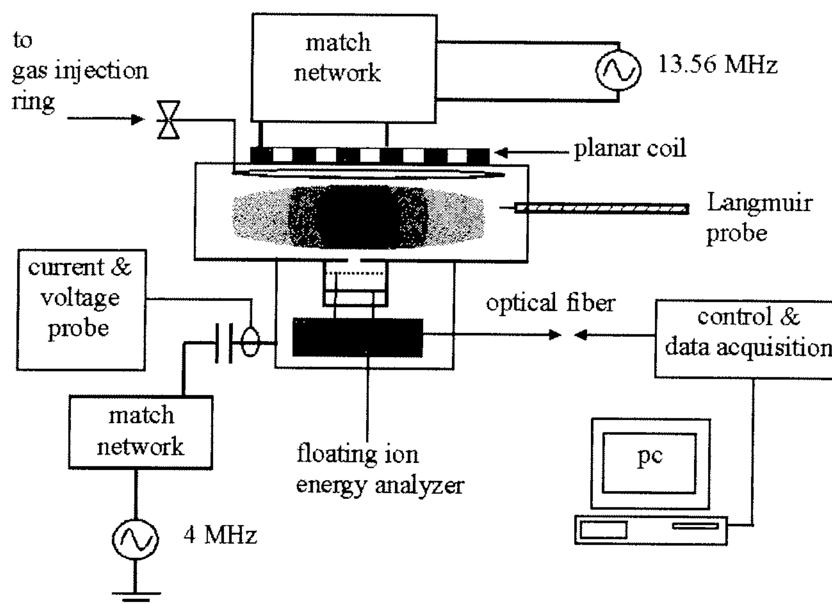

Figure 1. *Illustration of analyzer used to sample ion energies through a powered electrode in a transformer coupled plasma reactor[37].*

the energy distribution and average ion energy in TCP™ systems, Edelberg *et al.*[37] used an apparatus as illustrated in Fig. 1 to sample ions impinging onto an rf biased electrode. The plasma potential, electron temperature, and ion density were estimated from Langmuir probe data. An IV probe was also used to determine rf and dc potentials of the electrode relative to

ground (chamber walls). The total ion flux was estimated from the Langmuir probe data, reactor scale simulations and charge sensing wafer probes.

Typical energy distributions for an Ar plasma at different bias powers are shown in Fig. 2. In this case, the bias frequency was 4 MHz, sufficiently low to result in substantial energy

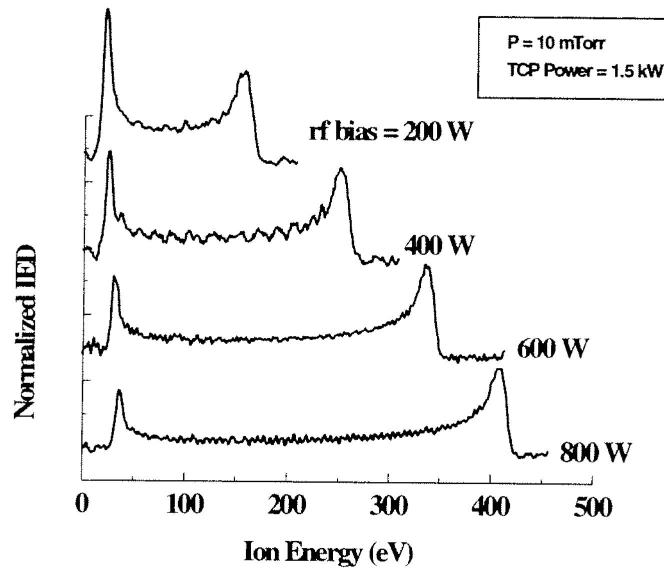

Figure 2. *Ion energy distributions from an Ar plasma as a function of the biased (bottom) electrode power [37].*

modulation of the incoming ions during an rf cycle. Clearly, the average ion energy is adjustable by tuning the bottom electrode power. On the other hand, as the data in Fig. 3 illustrate, the ion flux remains unchanged over this same range of bias powers. Thus, ion energy can be adjusted without affecting ion flux. The ion flux, in turn, can be adjusted by tuning the top (TCP) power while operating the bottom electrode in voltage control mode to maintain constant ion energy at the wafer surface.[45]

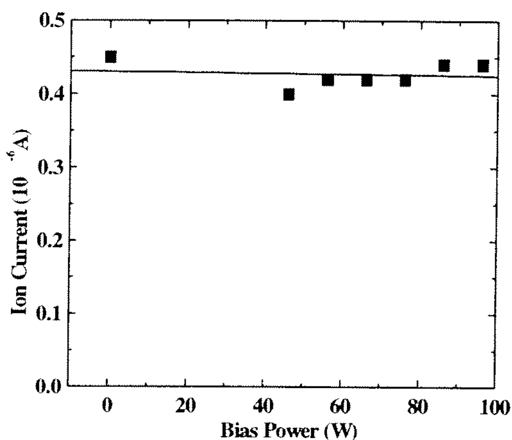

Figure 3. *Invariance of ion flux as bottom power and ion energy are tuned.[37].*

Despite the breadth of the ion energy distribution shown in Fig. 2, the ion energy scaling in Eq. 2 appears to be valid when the etching rate of oxide is considered as shown in Fig. 4.

Under the conditions shown in Fig.4, the ion flux was measured to be 7 mA/cm^2. At 1000W of bottom power, the average ion energy was measured to be 390eV, so the sputter yield is estimated to be $7.6 \times 10^{-3}\ eV^{-1/2}$.

Note that the exact value of the average ion energy is not critical to the simulator as the yield is calibrated against experiment.

Using an improper value of the average ion energy merely distorts the interpretation of the derived parameters. Because the yield and average ion energy are strongly correlated, the precise value of either one does not affect the accuracy of the simulation. The key input from the diagnostic measurements is the energy scaling.

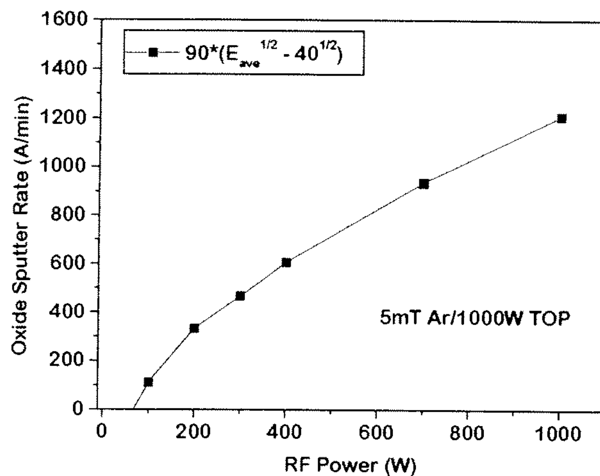

Figure 4. Oxide sputter rate as a function of bottom rf power. The data are fit to functions of the square root of average energy and average momentum. Both approximation are consistent with the data.

Angular Dependence of Etch Yield

We now turn to the angular dependence of the sputter yield, which is assumed to follow the form shown in Fig. 5 with α and β variable parameters that depend on ion and surface composition. Note that we assume the ions to be largely directional with a perpendicular energy distribution characteristic of a temperature of 0.2 eV. The angle of impact varies because the surface topography changes during the etch. For chemical sputtering, the angular dependence is typically a simple cosine function corresponding to $\beta = 1$ and $\alpha = 0$.[46] To determine α and β, we use a wafer probe - SEMs of etched and sputtered nano-structures.

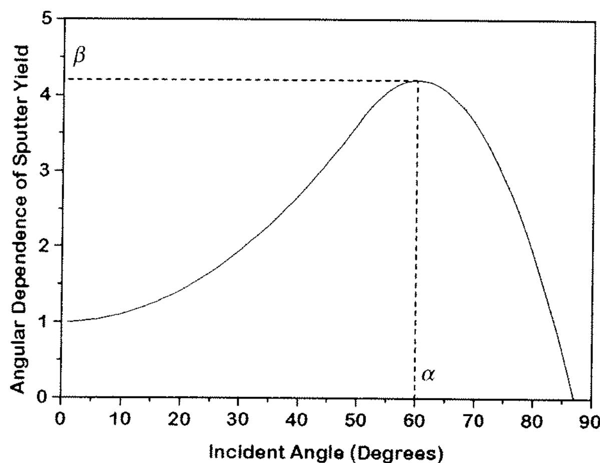

Figure 5. Schematic of the assumed angular dependence of the sputter yield.

For example, a previously etched contact is stripped of resist and re-exposed to plasma, this time containing only Ar. After 2mins of sputtering, the entrance to the contact narrows significantly as sputtered oxide is re-deposited as shown in Fig. 6. By matching the observed profile with the simulator output, we determine the sputtering angular parameters to be $\alpha = 60^o$ and $\beta = 4.2$. This calibration also leads to an estimate of the sticking coefficient for re-deposited sputtered oxide of $S_d = 0.7$.

Note that the aspect ratio of the feature before being sputtered in Fig. 6 was roughly 6 and that a 100-200V potential difference between the top and bottom of the feature is expected from electron shading effects. Clearly, such a potential drop would reduce the average ion energy at the bottom of the contact, thereby decreasing the sputter rate at the bottom relative to the top of the contact. However, the SEMs show no evidence of such a decrease in sputter

rate and we conclude that contact does not charge severely. Presumably surface migration of charge reduces the net charging and prevents a strong aspect ratio dependence to the sputter rate.

Etchant Surface Coverage

Now that we have estimates for the incident fluxes, the energy dependence of the sputter yield, and the angular dependence for the sputter yield, we only need to determine the etchant surface coverage to know the local etch rate. The etchant surface coverage, θ_e, is governed by a dynamic balance between adsorption and desorption of both etchant and inhibitor or deposition agent, *d*. Inhibition occurs when *d* blocks etching sites leading to surface coverage of inhibitors of θ_d. For the Al etching case (where net deposition does not occur), in steady state:

$$\frac{d\theta_e}{dt} = \Gamma_e S_e^f (1-\theta_e-\theta_d) - k_{ei}^f \Gamma_i \eta_{ei}^f \theta_e - k_{ev}^f \Gamma_{evap} \theta_e \cong 0 \quad (4a)$$

$$\frac{d\theta_d}{dt} = \Gamma_d S_d (1-\theta_e-\theta_d) - k_s \Gamma_i \eta_s^d \theta_d \cong 0 \quad (4b)$$

The *k*-factors are given by the stoichiometry of the removal processes. For example, if all Al atoms are removed in the form of Al_2Cl_6, then $k_{ei}^f = k_{ev}^f = 3$. Note that the rate at which etchants stick is directly proportional to a zero-coverage surface sticking coefficient, S_e^f, and the number of unoccupied sites. The film atom densities and the product stoichiometries appear as parameters but are not critical. Each is strongly correlated with overall etch yield and so the precise determination of these values matters little since we calibrate the simulator against measured rates.

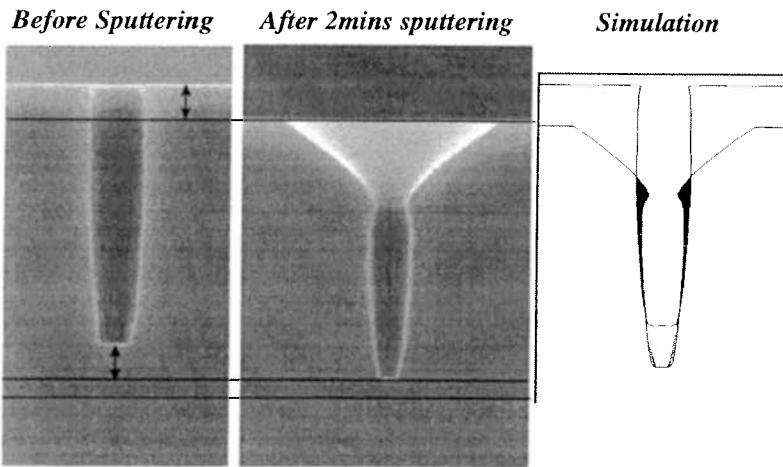

Figure 6. Comparison of simulation results with SEM photos of a 0.25μ contact in TEOS.

The site balance equations for oxide etching are similar to those used for Al etching.

Etch Profile Simulation

In Al stack etching, the inhibitor adsorption is assumed proportional to the number of unoccupied sites, but desorption is considered to occur solely by physical sputtering. In other words, there are no etch products containing the inhibiting species. The inhibitor is presumed to come from a flux of photo-resist-derived, carbonaceous material, which is estimated from the photoresist erosion rate.[40]

For Al, only spontaneous etching or evaporation is considered. Assuming the product stoichiometry is Al_2Cl_6, the evaporation rate is readily determined given the surface temperature.[47] The formation of Al_2Cl_6 is governed by the availability of Cl, which in turn

is determined by ion and neutral transport to the surface, the probability of sticking to the surface (depends on inhibitor concentration), and the rate of ion-induced desorption. By matching simulated profiles to those measured from partially etched structures, we determine an effective sticking coefficient for Cl to be 0.35, resulting in a Cl surface coverage of

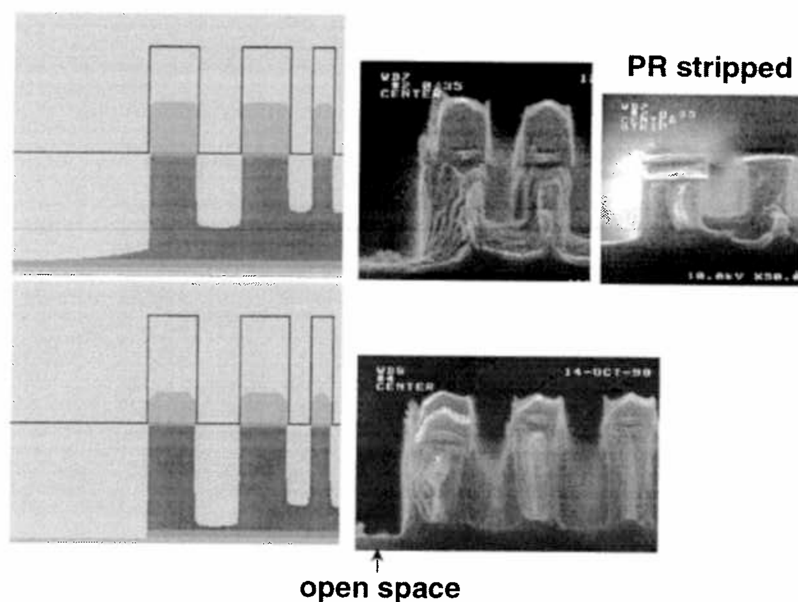

Figure 7. Comparison of simulated and actual etched lines and spaces. The upper figures show the etch structures resulting from stopping at end-point (open area just cleared). The lower picture corresponds to 30% over etch.

approximately 20%. Because the Cl coverage is small, ARDE is an important effect. From the etch rate and within the context of the model, the effective Cl flux is determined to be 10^{18} $cm^{-2}s^{-1}$, which compares favorably to that predicted from a reactor scale simulation.[40]

For the thin (50 nm) TiN and Ti layers physical sputtering alone is included. The details of etching these materials matter little to the overall profile since the layers are so thin.

For photoresist, we consider only chemical sputtering, ignore evaporation and sputtering, and assume the reaction to be uninhibited. Besides the etchant flux, we now need the ion flux and energy (see Eq. 2), which are estimated as outlined above. Note, however, that the simulation is tolerant of error in any given parameter because of the correlation between ion flux, average ion energy, and etch yield and their empirical determination.

A comparison between etched and simulated profiles is shown in Fig. 7.

In a similar fashion, the parameters for oxide etching are determined and the results for 0.5μ contacts in TEOS are shown in Fig. 8.

Conclusion

We have shown how a variety of data – from experiment and simulation – can be combined to produce semi-empirical prediction of etched structures in Al and oxide etching for nano-scale device fabrication. A novel diagnostic – the etched structure – is used to determine crucial surface parameters. We continue to improve these tools and are evaluating the range of applicability. Nonetheless, the results have provided crucial insights into etching mechanisms and are now being used in on-going process development.

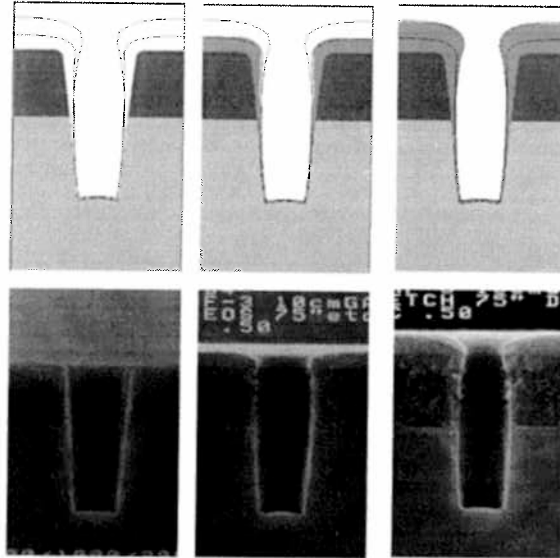

Figure. 8. *Simulated and measured etch profiles in oxide thin films. The etch times were constant for each profile. From left to right, the deposition dosage was increased monitonically. A constant depositer sticking coefficient of*

Acknowledgements

We are grateful to E. Edelberg, E. S. Aydil, A. Perry, N. Benjamin, S. Baldwin, N. Williams, R. Patrick, G. Goldspring, R. O'Donnell, and E. Bosch for stimulating discussion as well as sharing the results of their work prior to publication.

References

[1] H.F. Winters, J.W. Coburn, E. Kay, J.Appl.Phys. **48**, 4973 (1977).

[2] J.W. Coburn, H.F. Winters, J.Appl.Phys. **50**, 3189 (1979).

[3] H.F. Winters, J.W. Coburn, T.J. Chuang, J.Vac.Sci.& Technol. **B 1**, 469 (1983).

[4] U. Gerlach-Meyer, J.W. Coburn, E. Kay, Surf.Sci. **103**, 177 (1981).

[5] J.P. Chang, H.H. Sawin, J.Vac.Sci.& Technol. **15A**, 610 (1997).

[6] D.C. Gray, I. Tepermeister, H.H. Sawin, J.Vac.Sci.& Technol. **B 11**, 1243 (1993).

[7] R.A. Rossen, H.H. Sawin, J.Vac.Sci.& Technol. **45**, 860 (1984).

[8] T.M. Mayer, R.A. Barker, J.Vac.Sci.Technol. **21**, 757 (1982).

[9] R.A. Barker, T.M. Mayer, W.C. Pearson, J.Vac.Sci.Technol. **B 1**, 37 (1983).

[10] S.C. McNevin, G.E. Becker, J.Appl.Phys. **58**, 4670 (1985).

[11] G.S. Oehrlein, J.Vac.Sci.& Technol. **A 11** , 34 (1993).

[12] G.S. Hwang, C.M. Anderson, M.J. Gordon, T.A. Moore, T.K. Minton, K.P. Giapis, Phys.Rev.Lett. **77**, 3049 (1996).

[13] M.B. Barone, D.B. Graves, J.Appl.Phys. **78**, 6604 (1995).

[14] J. Liu, G.L. Huppert, H.H. Sawin, J.Appl.Phys. **68**, 3916 (1990).

[15] B.E. Thompson, K.D. Allen, A.D. Richards, H.H. Sawin, J.Appl.Phys. **59**, 1890 (1986).

[16] K. Kohler, J.W. Coburn, D.E. Horne, E. Kay, J.H. Keller, J.Appl.Phys. **57**, 59 (1985).

[17] M.D. Bowden, T. Okamoto, F. Kimura, H. Muta, K. Uchino, K. Muraoka, T. Sakoda, M. Maeda, Y. Manabe, M. Kitagawa, T. Kimura, J.Appl.Phys. **73**, 2732 (1993).

[18] F.F. Chen, *Plasma Diagnostic Techniques* (Academic Press, New York, 1965).

[19] R.A. Gottscho, T.A. Miller, Pure and Appl.Chem. **56**, 189 (1984).

[20] D.J. Trevor, N. Sadeghi, T. Nakano, J. Derouard, R.A. Gottscho, P.D. Foo, J.M. Cook, Appl.Phys.Lett. **57**, 1188 (1990).

[21] M. Bacal, G.W. Hamilton, A.M. Bruneteau, H.J. Doucet, J. Taillet, J.de Physique **40**, C7-791 (1979).

[22] K.E. Greenberg, G.A. Hebner, J.T. Verdeyen, Appl.Phys.Lett. **44**, 299 (1984).

[23] C.E. Gaebe, R.A. Gottscho, *Radiative Processes in Discharge Plasmas*, J.M. Proud and L.H. Luessen, Eds. (Plenum, 1986), p. 495.

[24] K. Kawaguchi, C. Yamad, Y. Hamada, and E. Hirota, J. Mol. Spectrosc. **86**, 5602 (1981).

[25] D.B. Graves, J.Appl.Phys. **62**, 88 (1987).

[26] D.B. Graves, K.F. Jensen, IEEE Trans.Plasma Sci **14**, 78 (1986).

[27] M. Surendra, D.B. Graves, I.J. Morey, Appl.Phys.Lett. **56**, 1022 (1990).

[28] M.J. Kushner, W.Z. Collison, M.J. Grapperhaus, J.P. Holland, M.S. Barnes, J.Appl.Phys. **80**, 1337 (1996).

[29] T.J. Sommerer, M.J. Kushner, J.Vac.Sci.& Technol. **B 10**, 2179 (1992).

[30] M.J. Kushner, J.Appl.Phys. **54**, 4958 (1983).

[31] J.-P. Boeuf, J.Appl.Phys. **63**, 1342 (1988).

[32] T. Makabe, N. Nakano, Y. Yukio, Phys.Rev.A. **45**, 2520 (1992).

[33] J. Ulacia, J.P. McVittie, J.Appl.Phys. **65**, 1484 (1989).

[34] T. Arikado, K. Horioka, M. Sekine, H. Okano, T. Horiike, Jpn.J.Appl.Phys **27**, 95 (1988).

[35] J. P. McVittie, J. C. Rey, A. J. Bariya, M. M. IslamRaja, L. Y. Cheng, S. Ravi, and K. C. Saraswat, *SPEEDIE: A profile simulator for etching and deposition,* **Dry Processing Symposium**, (Tokyo, Japan, 1990).

[36] V. Vahedi, D. J. Cooperberg, J. M. Cook, and R. A. Gottscho, *Study of dominant mechanisms in dielectric etching with a physically-based profile simulator,* **Dry Process Symposium**, (Tokyo, Japan, 1998).

[37] E.A. Edelberg, A.J. Perry, N. Benjamin, E.S. Aydil, J.Vac.Sci.& Technol., submitted (1999).

[38] R.A. Gottscho, C.W. Jurgensen, D.J. Vitkavage, J.Vac.Sci.Technol. **B 10**, 2133 (1992).

[39] D. Chin, S.H. Dhong, G.J. Long, J.Electrochem.Soc. **132**, 1705 (1985).

[40] D.J. Cooperberg, unpublished.

[41] U. Gerlach-Meyer, Surf.Sci. **103**, 524 (1981).

[42] N.R. Rueger, J.J. Beulens, M. Schaepkens, M.F. Doemling, J.M. Mirza, T.E.F.M. Standaert, G.S. Oehrlein, J.Vac.Sci.& Technol. **A15**, 1881 (1997).

[43] C. Steinbrüchel, Appl.Phys.Lett. **55**, 1960 (1989).

[44] D. Beale, S. Siu, and R. Patrick, J.Vac.Sci.& Technol. **B 16,** 1059 (1998).

[45] S. Baldwin, N. Williams, and R. Patrick, unpublished (1999).

[46] H. Okano, Y. Horiike, Jpn.J.Appl.Phys **20** , 2429 (1981).

[47] S.C. McNevin, J.Vac.Sci.& Technol. **B 8**, 1212 (1990).

Present and Future Diagnostics in Industrial RF Reactors

J. Schmitt
Balzers Process Systems
France

Diagnostics on the cascaded arc generated downstream plasma

M.C.M. van de Sanden, G.J.H. Brussaard, W.M.M. Kessels, A. de Graaf, M.F.A.M. van Hest, K.G.Y. Letourneur and D.C. Schram

Department of Applied Physics, Eindhoven University of Technology, P.O.Box 513, 5600 MB Eindhoven, The Netherlands, email: **m.c.m.v.d.sanden@phys.tue.nl**

In this paper we will review four plasma diagnostics which have over the years lead to a better understanding of the plasma chemistry that occurs in the downstream plasma generated by a cascaded arc. The diagnostics reviewed comprise Thomson-Rayleigh scattering, Langmuir probe, ion mass spectrometry, residual gas analysis and infrared gas phase absorption. From these diagnostics important source properties as ion fluence, electron density and temperature downstream, the presence of large cluster ions, consumption of the injected precursor gas and the generation of new stable gases under processing conditions is obtained.

Introduction

The expanding cascaded arc (fig. 1) can be characterized as a high density remote plasma source[1]. The patented method of deposition utilizing this source has demonstrated over the last decade a couple of successful applications. Among these are the fast deposition of hydrogenated amorphous silicon (a-Si:H)[2] and carbon (a-C:H)[3], oxydation of c-Si[4], etching of c-Si[5] and deposition of ZnO:Al as a transparant conductive oxide[6]. Especially the deposition of solar grade a-Si:H, which has been applied in a thin film silicon solar cell (initial efficiency of 3.3 %), at a rate of 10 nm/s has attracted considerable interest[2]. The latter rate is approx. a factor of fifty higher than rates obtained using conventional Plasma Enhanced Chemical Vapour Deposition[7]. Another remarkable observation made by Gielen et al.[3] is the improvement of a-C:H quality in terms of hardness with increasing growth rate. Recently, the deposition method based on the expanding cascaded arc has been licensed to two companies involved in plasma processing of polymer and semiconductor substrates.
Important questions related to the processing capability of the plasma source (fig. 1) are the basics of the plasma chemistry and dynamics taking place using different precursor gases. For this reason good diagnostics which can be used in a processing environment are needed. As a spin-off of these investigations important "industrial" questions related to plasma source optimization such as the gas efficiency of, e.g., SiH_4 during a-Si:H deposition in relation to the useful deposition area, film homogeneity, etc. are addressed too. In the latter the specific role of the plasma in connection with plasma-wall processes is the key issue. This usually makes good in situ film diagnostics indispensable. Closely connected to the questions mentioned is the still open issue of the growth mechanism of e.g. a-Si:H and a-C:H. Also in this respect the expanding cascaded arc has demonstrated potential in that it is capable of an independent controle of radical and ion fluxes striking the growth surface[8].
This paper is organized as follows. In the next section four different diagnostics will be reviewed which have led to essential information in the understanding of the principle of operation of the expanding cascaded arc. Part of the discussion will be a short recapitulation of the paper by Schram et al.[9] on the Bad Honnef "Frontiers" meeting in 1997. The main guideline will be one of the essential properties of the expanding cascaded arc: the truly remote character of the downstream plasma. This enables a separate treatment of arc source properties and downstream plasma properties, the latter including precursor gases used for processing.

Experiment

In fig. 1 an overview is given of a typical expanding cascaded arc set up. The plasma source is a so-called cascaded arc which generates a DC thermal plasma in mixtures of gases such as Ar, N_2 and H_2 mixture at high pressure (typ. 0.5 bar) and high power (typ. 3 kW at 50 A). Typically the total flow through the arc is in the range 50-100 sccs. The thermal plasma expands through a conically shaped anode nozzle into a vessel at low pressure (typ. 0.2 mbar) where precursor gases, e.g. SiH_4, C_2H_2, O_2

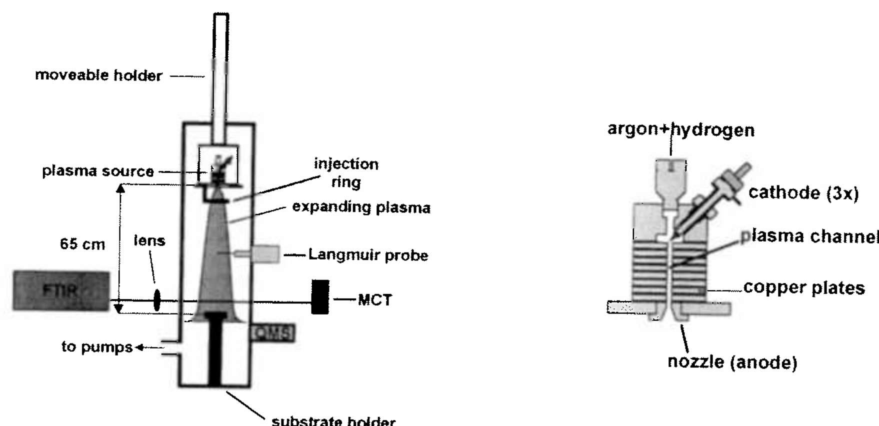

Figure 1 The expanding cascaded arc set up and the cascaded arc (explanation see text). Another example with different diagnostics attached can be found in the contribution by Kessels et al.[30].

etc., are injected by means of an injection ring. Usually the set up is equipped with a load lock (base pressure 10^{-7} mbar) to transfer samples (Corning glass, stainless steel and crystalline silicon) under defined vacuum conditions in and out the low pressure vessel (base pressure 10^{-6} mbar). At approx. 30-60 cm from the arc nozzle a substrate holder can be mounted. Thomson-Rayleigh scattering experiments are performed on a slightly different set up in which axial scans can be made by moving the cascaded arc in axial sense[10]. The set up can be equipped with a Langmuir probe and a mass spectrometer at the position of the substrate holder to measure radicals, stable gases and positive ions. A residual gas analyzer, located at one of the flanges on the side of the expansion vessel analyses stable gases (H_2, SiH_4, Si_2H_6 etc.) from the background. Finally, single pass gas phase infrared absorption utilizing a Fourier Transform infrared (FTIR) spectrometer are performed just in front of the substrate holder. A more detailed description of the set up used can be found in the different publications[1,2,3,4,5,10].

Thomson-Rayleigh scattering

Very accurate measurements of the electron and neutral particle density and electron temperature using Thomson-Rayleigh scattering (TRS) on the expanding cascaded arc in pure argon were performed by van de Sanden et al.[11]. Important aspects of the TRS set up used are a good sensitivity (the detection limit is about 10^8 electrons in the detection volume 0.25 mm^3, leading to a detection limit for n_e as low as 5×10^{17} m^{-3}), good sub-millimeter spatial resolution, a low stray light level and the utilization of a gated light amplified photodiode array enabling the measurement of the full Thomson-spectrum with good signal to noise ratio[10]. In fig. 2 the electron density as function of the axial position is given for different background pressures[11]. Due to the high spatial resolution the stationary shock front can be clearly seen. Also it is clear from fig. 2 that the first part of the expansion is supersonic, (as was also demonstrated by velocity measurements by Kroesen et al. [12]) and a strong expansion in which the electron density decreases by three orders of magnitude is observed. The background pressure leads to a shift of the stationary shock front towards the exit of the cascaded arc in agreement with the relation as derived by Ashkenas et al.[13]. Under the same conditions as displayed in fig. 2 the electron temperature, which also showed a shock structure, was determined to be in the range of 0.2-0.4 eV[11]. The latter is an essential result and has big consequences for the plasma chemistry downstream where precursor gases are injected. Another important consequence of the measurement of the electron density follows from the comparison with a recombination free expansion model. It was shown by van de Sanden et al.[14] that recombination in a pure argon expansion can be neglected at the densities and temperature measured.

The low electron temperature downstream and the absence of significant recombination of the argon ions and electrons emanating from the arc is a characteristic of the expanding cascaded arc plasma which makes it distinctly different from other type of remote plasmas. For an arc operating in pure argon this means for instance that, due to this low electron temperature, the dissociation of injected

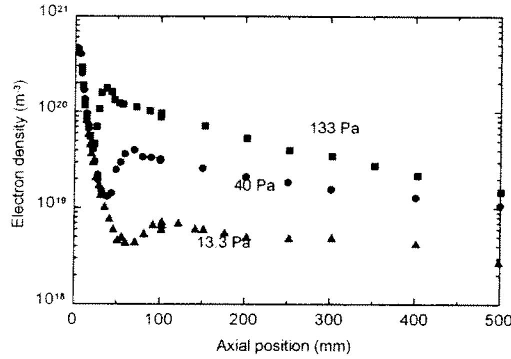

Figure 2. The electron density as function of the axial position: Ar-flow=58 sccs, I_{arc}=45 A, p_{vessel}=13.3, 40, 133 Pa.

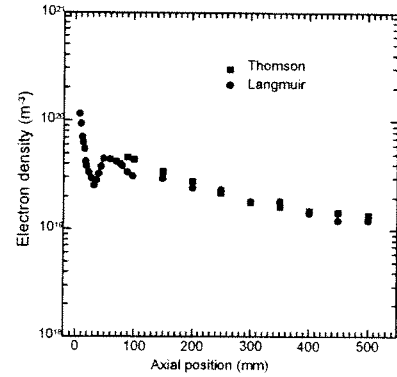

Figure 3. Comparison between the electron density as determined from Thomson scattering and Langmuir probe[22].

precursor gases downstream is not by means of electron collisions as is usually the case but by means of collisions with argon ions[15,16]. Furthermore, since recombination can be neglected, the chemical activity contained in the ions is limited by the arc source and can be characterized by measuring the ion fluence in the downstream region. In fact the high pressure difference between arc source and downstream region makes the expanding cascaded arc the ultimate remote source since no precursor gas or other species generated downstream can flow back into or influence the arc region.
An anomalous recombination of the ions and electrons occurs if small amounts of hydrogen are added to the argon flow in the arc[17]. Initially this was a big surprise since the small amount of hydrogen added is fully dissociated and ionized in the arc leading to H^+. Since we did not expect the behavior of H^+ to be very different from Ar^+ the explanation for the strong recombination of ions and electron lies in the fact that the walls in the downstream region are effective in the association of the atomic hydrogen[17,18]. Molecular hydrogen then quenches the ions

$$Ar^+ + H_2 \rightarrow ArH^+ + H \qquad (1)$$

followed by

$$ArH^+ + e \rightarrow Ar + H^* \qquad (2)$$

a reaction sequence which is much faster than the three particle recombination of Ar^+ or H^+. It should be noted that in general similar reaction sequences, i.e. charge exchange followed by dissociative recombination of the molecular ion formed, occur for precursor gases injected in a pure expanding argon plasma. Examples of the latter are the injection of C_2H_2 for the fast deposition of a-C:H (rates as high as 70 nm/s have been obtained)[3,16] and oxygen to strip photoresist or oxidize c-Si[4].
The decrease of the electron density when molecules are added to a pure argon plasma, either in the arc or in the downstream region, lead to electron densities well below 10^{18} m^{-3}. This requires either a more sensitive TRS set up or another method to determine the electron/ion density and temperature. Moreover, a more simpler, cheaper and robust technique is required to measure the electron density and temperature under real processing conditions. Langmuir probes fulfill these demands and the next section will be devoted to the results obtained using this plasma diagnostic technique.

Langmuir probe measurements
The first application of Langmuir probe measurements on an expanding cascaded arc plasma in argon/hydrogen mixtures were performed by de Graaf et al.[17]. He discovered the anomalous loss of ionization leading to ion densities as low as a few times 10^{15} m^{-3}. The theory used to analyze the probe data was the theory developed by Langmuir in the early thirties[19]. Since we usually have relatively

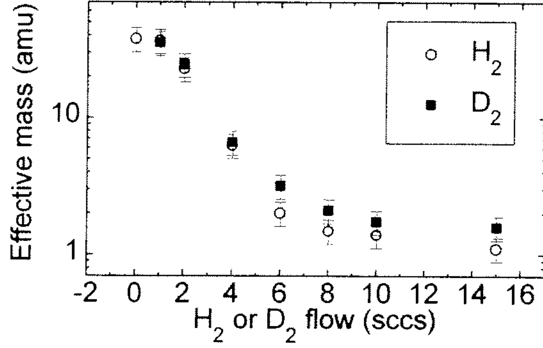

Figure 4. The effective mass vs. the H_2/D_2-flow as determined from Langmuir probe. Ar-flow=55 sccs, I_{arc}=45 A, p_{vessel}= 20-24 Pa.

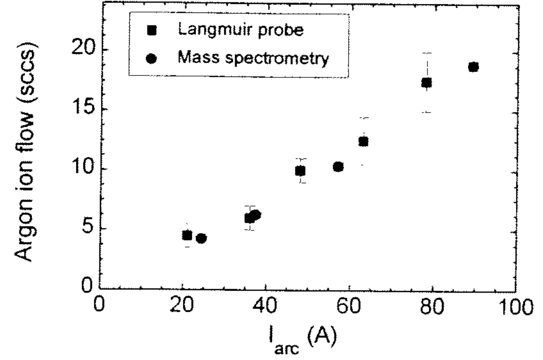

Figure 5. Ion fluence vs. arc current as obtained from Langmuir probe and mass spectrometry. Ar-flow=100 sccs, p_{vessel}= 18 Pa.

high electron densities (> 10^{16} m^{-3}), the Debye length is small in comparison with the typical mean free paths in the plasma and a typical dimension (usual the radius) of the probe. This requires a probe theory in between the simple Langmuir probe theory and orbital limited motion theory. Therefore in later work[20,21] we use the empirical relations developed by Peterson and Talbot and which are based on Laframboise's historical work[22]. Furthermore, we compared different geometries of the probe (planar and cilindrical, double and single). The results for the electron density and temperature were, in a wide range of electron densities, $10^{16} < n_e < 10^{19}$ m^{-3}, equal within a typical 10-20% error margin for the electron density and about 30% in the electron temperature. It is noteworthy to mention the fact that the differences in the measured ion saturation current were equal within an error margin of 10%. The electron temperature and density as determined using a cilindrical probe in a pure argon plasma were compared with Thomson scattering[23]. The result is shown in fig. 3 for the electron density. As can be seen the agreement is rather good and the difference is smaller than 10%. The electron temperature as determined from Thomson scattering and Langmuir probes differ significantly[23] which is not yet understood. The difference could be related to the fact that Thomson scattering is more sensitive to the bulk of the electron energy distribution (EED) while Langmuir probe measurements are also sensitive to the tail of the EED. The tail of the EED could be overpopulated due to the presence of high densities of metastables as discussed in a paper by Capitelli et al.[24]
Since the electron-ion coupling is very good (due to the relatively high electron density) and no power incoupling occurs in the downstream plasma, the ion and electron temperature are more or less equal. This means that the ions do not need to be accelerated to the Bohm velocity and the ratio between the ion and electron saturation current is given by[22]

$$I_{ion}/I_{electron} = (m_e/m_{ion})^{1/2} \qquad (3)$$

where m_e and m_{ion} are the electron and effective ion mass. Thus relation Eq. (3) can be used to determine the effective mass of the ions present in the downstream plasma. This method was first used by Brussaard et al.[25] to determine the dominant ion in a pure downstream nitrogen plasma. In fig. 4 the results of the effective ion mass as measured downstream in an argon-hydrogen and argon-deuterium mixture can be seen as function of the H_2/D_2 flow admixed in the arc[26]. As expected, the effective mass goes down from the value for argon (m_{Ar} = 40) to the value for hydrogen (m_H = 1) or deuterium (m_D = 2). Below we will show mass spectrometry measurements which confirm these results. The fact that H^+ (D^+) becomes dominant at high hydrogen flows is related to the principle of operation of the arc source. At the temperatures and electron density present in this high density source the dominant ion will be the ion with the lowest ionization potential[17,18]. Moreover, molecular ions emanated from the arc are quickly quenched downstream by the presence of the abundant low temperature electrons.

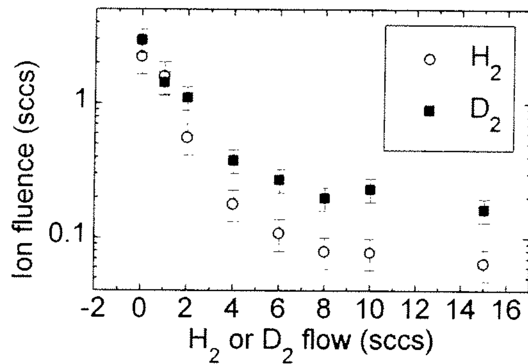

Figure 6. The ion fluence vs H_2/D_2-flow. Ar-flow=55 sccs, I_{arc}=45 A, p_{vessel}= 20-24 Pa.

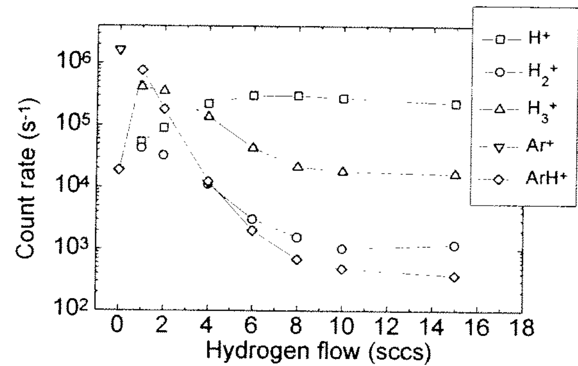

Figure 7. Ion composition vs. H_2 -flow. Ar-flow =55 sccs, I_{arc}=45 A, p_{vessel}= 20-24 Pa.

As we mentioned the downstream plasma is the ultimate remote source. Therefore we can characterize the chemical activity of the arc source by measuring the ion fluence, i.e. the ions and electrons that pass an area per unit of time. To determine the ion fluence radial profiles of the ion density are measured. This profile (which is usually Gaussian shaped) multiplied by the directed velocity as measured from e.g. Doppler TALIF measurements[27] is integrated over the beam area. A result for pure expanding argon plasma is given in fig. 5[28]. As can be seen the ion fluence (expressed in sccs) scales roughly linear with the arc current. Also, since the flow used is 100 sccs, we see that at 48 A about 10% of the argon flow is ionized (i.e. ion fluence 10 sccs). In fig. 6 the ion fluence emanating from the arc is given as function of the H_2 flow admixed (conditions similar to fig. 4). The ion fluence (as determined here from the electron saturation current because the effective mass is unknown; the total ion fluence equals the electron fluence since the transport in the downstream is ambipolar) decreases with increasing H_2/D_2 flow as expected[17].
To conclude this section, figs. 4-6 specify the ion chemical activity for the expanding cascaded arc in pure argon and argon-hydrogen mixtures. As we will see, this information can be used to understand the dissociation and consumption of SiH_4 and C_2H_2 under processing conditions, i.e. during deposition of respectively a-Si:H and a-C:H at high rates.

Ion mass spectrometry and residual gas analysis
As we discussed in the previous section the ion saturation current can be measured relatively easy and with a good accuracy. In simple molecular plasmas such as H_2/Ar and N_2 plasmas, the ratio of the saturation currents can be used to determine the effective ion mass. However, still other molecules, such as ArH^+ can be important in the ion chemistry (cf. Eq. (1)-(2)). To characterize the ion flux at the substrate position we used a Hiden Analytical EPIC 300 quadrupole mass spectrometer in the ion mode. In fig. 7 the ion composition is shown in a downstream Ar/H_2 plasma as function of the H_2 admixed. As can be seen the outcome of the effective ion mass (cf. fig. 4) agrees well with the results in fig. 7. However, the detailed ion chemistry is measured with a much higher sensitivity and conclusions about the details of operation of arc source in relation to the downstream plasma chemistry can be better addressed.
In processing plasmas the ion chemistry is even more complicated. This was shown by Kessels et al. for an Ar/H_2/SiH_4 plasma under actual processing conditions, see fig. 8[20,29,30]. As can be seen cationic clusters with up to 10 silicon atoms were observed. These cationic clusters are formed by charge exchange of ions emanating from the arc with silane and subsequent addition of silane molecules and elimination of hydrogen molecules[29]. Remarkably, the hydrogen content of the cluster ions is low, much lower than observed in other type of plasmas[31]. Furthermore, by determining the average silicon atom number from spectra such as fig. 8, Kessels et al. were able to estimate the absolute contribution of the silicon cluster ions to the a-Si:H growth by comparison with the absolute ion flux measurements using a Langmuir probe[20]. As can be seen in fig. 9 the contribution is 5-9 %, even under the condition

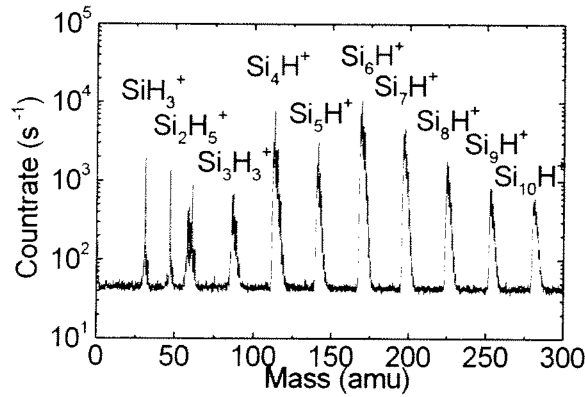

Figure 8. Ion mass spectrum in an argon-hydrogen-silane plasma. Ar-flow=55 sccs, H_2-flow=10 sccs, I_{arc}=45 A, p_{vessel}= 20 Pa.

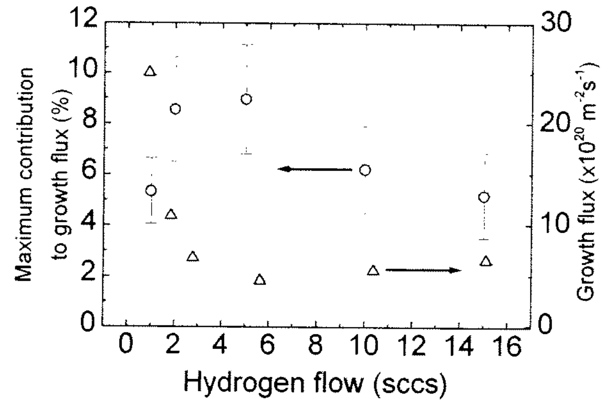

Figure 9 The relative contribution of the cluster ions to and the a-Si:H growth flux vs. H_2 flow. I_{arc}=45 A, Ar-flow 55 sccs, p_{vesel}= 20 Pa.

where solar grade material is grown[2,15]. This is an intriguing observation since it is widely believed that cluster ions are detrimental for the opto-electronic quality of a-Si:H[7].

In the background of the expanding plasma measurements of stable gases using a residual gas analyzer are relatively straightforward and can be done under processing conditions. In the case of a-Si:H deposition the consumption of silane (SiH_4) and the production of molecular hydrogen (H_2) and higher silanes (Si_nH_{2n+2}) can be monitored absolutely, if a proper calibration procedure is done. Since the typical diffusion times towards the wall (in the ms range) are much shorter than the residence time (typ. 0.5-1 s) at the flows and pressures used the reactor is fully mixed. Therefore, by comparing the plasma on and off situation the total silane consumed can be measured. It is important to stress here that radicals or ions usually do not influence the RGA signals due to their high reactivity and resulting low densities[15].

In fig. 10 the depletion (or consumption) of silane is given as function of the H_2 flow admixed. As can be seen a good correlation is observed with the ion fluence measurements as shown in fig. 6. The interpretation of fig. 10 is that at low hydrogen admixture silane is dissociated dominantly by ions emanating from the arc (only the dominant channels for both Ar^+ and H^+ are given, notice that $T_e < 0.3$ eV excluding significant electron induced dissociation or ionization, also we neglect SiH_4 dissociation by pyrolysis[15])

$$H^+ + SiH_4 \rightarrow SiH_3^{+,r,v} + H_2 \qquad (4)$$

$$Ar^+ + SiH_4 \rightarrow SiH_3^{+,r,v} + Ar + H \qquad (5)$$

in which $SiH_3^{+,r,v}$ is a possibly rovibrationally excited molecule. Reactions (4)-(5) are quickly followed by a dissociative recombination of the molecular ion leading to radicals SiH_x ($x<3$) and atomic and molecular hydrogen. If the electron density is well above 10^{17} m^{-3}, reactions (4)-(5) are the rate limiting step in the dissociation of SiH_4. When the hydrogen flow is increased and the ion flux emanating from the arc diminishes, the atomic hydrogen generated in the arc takes over the dissociation of SiH_4 by means of an abstraction reaction[15,30]

$$H + SiH_4 \rightarrow SiH_3 + H_2 \qquad (6)$$

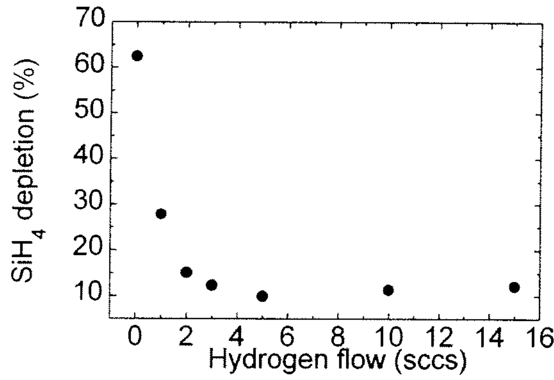

Figure 10. The depletion of silane vs. H_2-flow. Ar-flow=55 sccs, I_{arc}=45 A, p_{vessel}= 20 Pa.

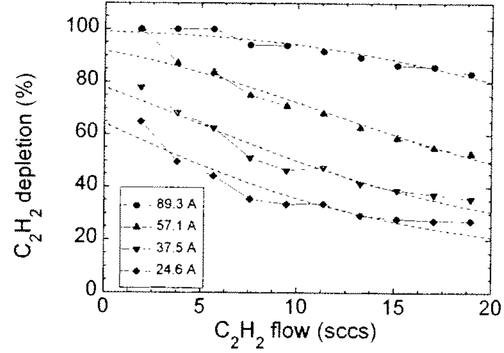

Figure 11. The depletion of acetylene vs. C_2H_2-flow for different arc currents. Ar-flow=100 sccs, I_{arc}=45 A, p_{vessel}= 18-25 Pa. Dashed lines fits according to Eq. (10).

A clear correlation with the quality of a-Si:H has been observed, i.e. the opto-electronic quality improves with H_2 mixture[2,15]. This is in line with the general accepted presumption that SiH_3 is the preferred radical rather than SiH_x (x<3)[2,30]. Note that this observation is rather paradoxial with the observation of the contribution of the silicon cluster ions (cf. fig. 8).
Since the levels of production of higher silanes were small the consumed silane flow should be directed correlated with the growth rate. Comparing fig. 9 and fig. 10 shows that this is indeed the case.
Another example of the strength of the combination of Langmuir probe measurements and RGA measurements is given in fig. 11[28]. In fig. 11 the consumption of C_2H_2 is given as a function of the acetylene flow admixed in a pure argon expanding plasma. Note that a complication occurs in the measurement of the depletion since other stable hydrocarbon gases can be produced which also lead to RGA signals at the position where usually acetylene is measured (around mass 26). During acetylene injection as the precursor gas, we could exclude generation of other hydrocarbon gases in the downstream plasma by infrared absorption in the gas phase (see next section).
As can be seen in fig. 11 full consumption is observed at high arc currents and low acetylene flows. As demonstrated by van de Sanden et al.[28], the depletion of acetylene can be modeled in a very simple model of the downstream plasma chemistry. The first step is a charge exchange reaction (note T_e is low, cf. Eq. (4))

$$Ar^+ + C_2H_2 \rightarrow Ar + C_2H_2^{+,r,v} \qquad (7)$$

which is followed by a dissociative charge exchange of the rovibrationally excited molecular ion

$$C_2H_2^{+,r,v} + e \rightarrow \text{products} \qquad (8)$$

Following reactions (7)-(8) the consumption of acetylene is proportional to the ion flow, i.e.

$$\frac{\partial}{\partial t}\Phi_{C2H2}(t) = -k\Phi_{C2H2}(t)\Phi_{Ar+}(t) \qquad (9)$$

Here $\Phi_{C2H2}(t)$ is the acetylene flow injected and $\Phi_{Ar+}(t)$ is the ion flow emanating from the arc. The constant k is determined by the reaction probability of an argon ion with acetylene and depends further on the diffusion profile and the directed velocity. By utilizing Eq. (9) we assume that acetylene is only consumed by interacting with argon ions and electrons. A similar equation as Eq. (9) is used for the

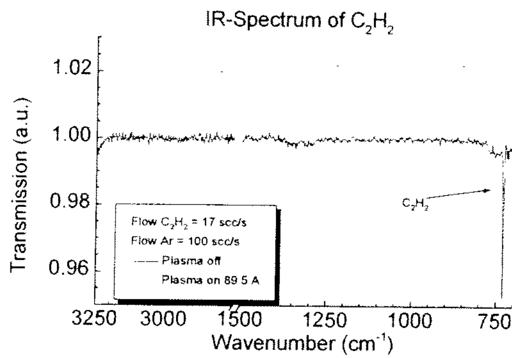

Figure 12a. Infrared absorption by C_2H_2 with plasma off and plasma on. Ar-flow=100 sccs, C_2H_2-flow=17 sccs, I_{arc}=89.5 A, p_{vessel}= 20 Pa.

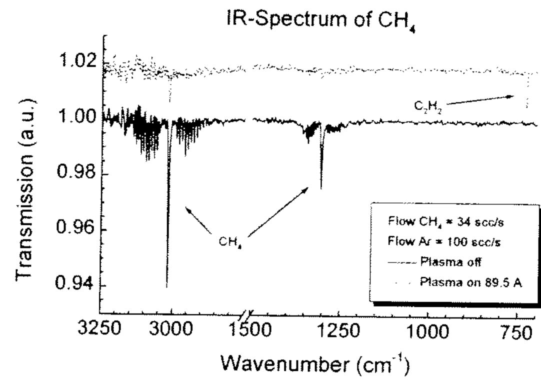

Figure 12b. Infrared absorption spectrum in an argon-methane plasma. Note the generation of C_2H_2 during plasma on. Ar-flow=100 sccs, CH_4-flow=34 sccs, I_{arc}=89.5 A, p_{vessel}= 20 Pa.

argon ions, i.e. we assume that argon ions are only lost by interaction with acetylene. The solution of both equations of the typ. Eq. (9) can be expressed in the initial flows of argon ions $\Phi_{Ar+,0}$ (emanated from the arc) and acetylene $\Phi_{C2H2,0}$ injected

$$\Phi_{C2H2}(t) = \frac{\Phi_{Ar+,0} - \Phi_{C2H2,0}}{(\Phi_{Ar+,0} / \Phi_{C2H2,0})\exp((\Phi_{Ar+,0} - \Phi_{C2H2,0})kt) - 1} \quad (10)$$

In fig. 11 the dashed lines represent the fits of the consumption of acetylene following from Eq. (10). The measurement at 89.3 A was fitted using expression Eq. (10), varying kt and fixing $\Phi_{Ar+,0}$. Than for the other arc current settings only $\Phi_{Ar+,0}$ was varied while the value for kt was kept fixed at the value found for I_{arc} = 89.3 A. The result for $\Phi_{Ar+,0}$ as obtained from these fits is also shown in fig. 5 together with the results for $\Phi_{Ar+,0}$ as obtained from Langmuir probe measurements. The good agreement suggests strongly the proposed acetylene consumption mechanism Eq. (7)-(8).

Infrared absorption spectrometry

A complementary diagnostic to the RGA and which can measure stable gases either injected or produced in the downstream plasma is infrared absorption in the gas phase[32]. The external beam of a FTIR spectrometer (Bruker Vector 22) is directed through the plasma and focused on an external MCT detector (type MCT D318). At specific wave numbers infrared absorption occurs for the different stable gases (C_2H_2, C_2H_4, C_2H_6, CH_4, etc.). The effect of plasma on and off for an Ar/C_2H_2 can be seen in fig. 12a: the plasma consumes C_2H_2 and no significant amounts of other hydrocarbon gases are produced. This is distinctively different from an Ar/CH_4 plasma, cf. fig. 12b. In this case significant amounts of C_2H_2 are generated. Figure 13 illustrates that although CH_4 is the primary feed gas, the influence of the other hydrocarbon gases generated can not be neglected. The results in fig. 13 were verified by RGA measurements although in this case the RGA signals need to be deconvoluted because the different hydrocarbon gases generate mass peaks in the same region.

There is also another important difference between RGA and infrared absorption measurements. As mentioned the RGA is not sensitive for temperature differences between plasma on and off because the gases are sampled from the background. Since the absorption measurement is a line of sight measurement through the downstream plasma (which has temperatures in the 0.1-0.3 eV range) the IR absorption is affected by the temperature change, even in the case that no consumption of the precursor gas occurs. Therefore, the depletion as measured using IR absorption is different from the band is the possibility to measure e.g. the C_2H_2 temperature by simulating the Q-branch around ν =

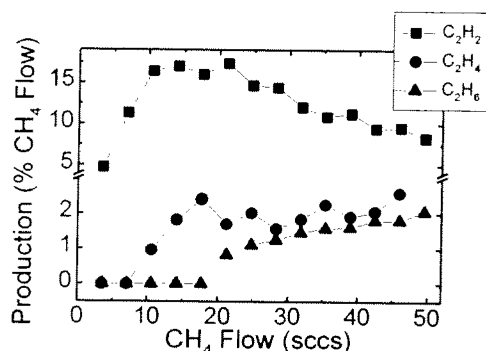

Figure 13. The production of hydrocarbon gases in an Ar/CH$_4$ plasma. Ar-flow=100 sccs, I_{arc}=75 A, p_{vessel}= 18-30 Pa.

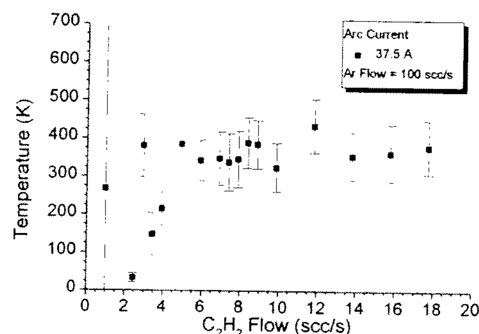

Figure 14. The C_2H_2 rotational temperature vs. C_2H_2 flow. Ar-flow=100 sccs, I_{arc}=37.5 A, p_{vessel}= 18-25 Pa.

730 cm^{-1} using a computer simulation program based on the HITRAN database. The results from this simulation for the temperature of C_2H_2 are shown for different acetylene flows in fig. 14. As can be seen the temperature is close to room temperature. This indicates that C_2H_2 is recycling in the background where the gas temperature is low.

Conclusions

A short overview is given of the diagnostics applied to understand the plasma chemistry in silane and acetylene containing downstream plasmas generated by a cascaded arc in argon and argon-hydrogen mixtures. What is particular clear is that even simple and robust diagnostics as Langmuir probe and mass spectrometry lead to a better understanding of the often complicated chemistry. Comparison with more advanced techniques such as Thomson scattering the results as obtained using these simple techniques can be verified and extrapolated to conditions under which simple, cheap and robust plasma diagnostics are needed.

In this paper we limited ourselves to the general questions usually asked in an industrial environment: what is the electron density and temperature (basic plasma parameters)?, what is the consumption of the precursor gas injected?, can we determine the aspects of the plasma chemistry occurring?, etc. From the combination of the different diagnostics, we have shown that for the particular case of the expanding cascaded arc plasma, answers can be given based on the fact that we are dealing with the ultimate remote plasma. Next we have to demonstrate, using advanced new plasma diagnostics, what the actual plasma chemistry is by measuring the different radical densities using e.g. appearance potential mass spectrometry[30], cavity ring down spectroscopy[33], two-photon laser induced spectroscopy[34], etc.. These measurements can then be used to address the question of the deposition mechanism of a-Si:H and a-C:H growth and further improve the use of the expanding cascaded arc source.

Acknowledgements

The authors gratefully acknowledge the support of the Netherlands Technology Foundation (STW), Royal Netherlands Academy of Arts and Sciences (KNAW), Netherlands Organization for Energy and Environment (NOVEM), Netherlands Foundation on Fundamental Research (FOM) and General Electric. The skillful technical assistance of Ries van de Sande, Bertus Hüsken and Herman de Jong is very much appreciated.

References

[1] D.C. Schram, J.A.M. van der Mullen and M.C.M. van de Sanden, Plasma Phys. Control. Fusion **36** B65 (1994), M.C.M. van de Sanden and J.A. Tobin, Plasma Sources Sci. Technol. 7 28 (1998)

[2] R.J. Severens, G.J.H. Brussaard, H.J.M. Verhoeven, M.C.M. van de Sanden, D.C. Schram, Mat. Res. Soc. Symp. Proc. **377** 33 (1995), R.J. Severens, M.C.M. van de Sanden, H.J.M. Verhoeven, J. Bastiaansen and D.C. Schram, Mat. Res. Soc. Symp. Proc. **420** 341 (1996)

[3] J.W.A.M. Gielen, M.C.M. van de Sanden and D.C., Appl. Phys. Lett. **69** 152 (1996), J.W.A.M. Gielen, P.R.M. Kleuskens, M.C.M. van de Sanden, L.J. van Ijzendoorn, D.C. Schram, E.H.A. Dekempeneer and J. Meneve, J. Appl. Phys. **80** 5986 (1996)

[4] K.G.Y. Letourneur, M. Schaepkens, G.J.H. Brussaard, M.C.M. van de Sanden and D.C. Schram, to be published

[5] J.J. Beulens, A.T.M. Wilbers, M. Haverlag, G.S. Oehrlein, G.M.W. Kroesen and D.C. Schram, J. Vac. Sci. Technol. B**10** 2387 (1992)

[6] M.C.M. van de Sanden, B. van Lierop, H. Linden and D.C. Schram, to be published

[7] G. Bruno, P. Capezutto and A. Madan,(Eds.), "Plasma deposition of amorphous silicon-based materials" (Academic Press, Boston, 1995)boeken PECVD

[8] M.C.M. van de Sanden, R.J. Severens, W.M.M. Kessels, F. van de Pas, L. van IJzendoorn and D.C. Schram, Mat. Res. Soc. Symp. Proc. **467** 621 (1997), W.M.M. Kessels, R.J. Severens, M.C.M. van de Sanden and D.C. Schram, J. Non-Cryst. Solids **227-230** 133 (1998)

[9] D.C. Schram et al., Proc. LTPD II, Bad Honnef 1997

[10] M.C.M. van de Sanden, G.M. Janssen, J.M. de Regt, D.C. Schram, J.A.M. van der Mullen and B. van der Sijde, Rev. Sci. Instrum. **63** 3369 (1992)

[11] M.C.M. van de Sanden, J.M. de Regt and D.C. Schram, Plasma Sources Sci. Technol. **3** 501 (1994), M.C.M. van de Sanden, R. van den Bercken and D.C. Schram, Plasma Sources Sci. Technol. **3** 511 (1994)

[12] G.M.W. Kroesen, D.C. Schram, A.T.M. Wilbers, and G.J. Meeusen, Contr. Plasma Phys. **31** 27 (1991)

[13] H. Ashkenas and F.S. Sherman, Proc. Rarefied Gasdynamics **4**, Ed. J.H. de Leeuw (Academic Press, New York, 1966)

[14] M.C.M. van de Sanden, J.M. de Regt and D.C. Schram, Phys Rev. E **47** 2792 (1993)

[15] M.C.M. van de Sanden, R.J. Severens, W.M.M. Kessels, R.F.G. Meulenbroeks and D.C. Schram, J. Appl. Phys. **84** 2426 (1998)

[16] J.W.A.M. Gielen, M.C.M. van de Sanden, P.R.M. Kleuskens and D.C. Schram, Plasma Sources Sci. Technol. **5** 492 (1996), J.W.A.M. Gielen, W.M.M. Kessels, M.C.M. van de Sanden and D.C. Schram, J. Appl. Phys. **82** 2643 (1997)

[17] M.J. de Graaf, R.J. Severens, R.P. Dahiya, M.C.M. van de Sanden and D.C. Schram, Phys. Rev. E **48** 2098 (1993), R.F.G. Meulenbroeks, A.J. van Beek, A.J.G. van Helvoort, M.C.M. van de Sanden and D.C. Schram, Phys. Rev. E **49** 4397 (1994), M.C.M. van de Sanden, R.J. Severens, R.F.G. Meulenbroeks, M.J. de Graaf, Z. Qing, D.K. Otorbaev, R.A.H. Engeln, J.W.A.M. Gielen, J.J.A.M. van der Mullen and D.C. Schram, Surface and Coatings Technology **74/75** 1 (1995)

[18] D.K. Otorbaev, M.C.M. van de Sanden and D.C. Schram, Plasma Sources Sci. Technol. **4** 293 (1995)

[19] H. Mott-Smith and I. Langmuir, Phys. Rev. **28** 727 (1926)

[20] W.M.M. Kessels, C.M. Leewis, M.C.M. van de Sanden and D.C. Schram, to be published

[21] G.J.H. Brussaard M.C.M. van de Sanden and D.C. Schram, to be published

[22] E.W. Peterson and L. Talbot, AIAA J. **8** 2215 (1970)

[23] R.F.G. Meulenbroeks, M.F.M. Steenbakkers, Z. Qing, M.C.M. van de Sanden and D.C. Schram, Phys. Rev. E **49** 2272 (1994)

[24] M. Capitelli, G. Colonna, A. Giquel, C. Gorse, K. Hassouni and S. Longo, Phys. Rev. E **54** 1843 (1996)

[25] G.J.H. Brussaard, M. van der Steen, M. Carrère, M.C.M. van de Sanden and D.C. Schram, Phys. Rev. E **54** 1906 (1996)

[26] W.M.M. Kessels, C.M. Leewis, M.C.M. van de Sanden and D.C. Schram, to be publ.. See also these procs.

[27] M.G.H. Boogaarts et al., G.J. Brinkman, H.W.P. van der Heijden, P. Vankan, S. Mazzouffre, J.A.M. van der Mullen, D.C. Schram and H.F. Döbele, Proc. 8th Inter. Symp., LAPD (Doorwerth, The Netherlands, 1997)

[28] M.C.M. van de Sanden, M.F.A.M. van Hest, A. de Graaf, A.H.M. Smets, K.G.Y. Letourneur, M.G.H. Boogaarts and D.C. Schram, accepted in Diam. Rel. Mater.

[29] W.M.M. Kessels, M.C.M. van de Sanden and D.C. Schram, Appl. Phys. Lett. **72** 2397 (1998)

[30] See contribution of W.M.M. Kessels et al. at this workshop

[31] A.A. Howling, L. Sansonnens, J.-L. Dorier and C. Hollenstein, J. Appl. Phys. **75** 1340 (1994)

[32] L. Sansonnens, A.A. Howling and C. Hollenstein, Plasma Sources Sci Technol. **7** 114 (1998)

[33] See contribution of M.G.H. Bogaarts et al. and R. Engeln et al. at this workshop

[34] See contribution of S. Mazouffre et al. at this workshop

Oral Contributions

Imaging Diagnostics and Process Control in Plasma Spraying

E. Hämäläinen, T. Korhonen, J. Vattulainen, R. Hernberg
Tampere University of Technology, Department of Physics, Plasma Technology Laboratory
P.O.Box 692, FIN-33101 Tampere, Finland

Introduction

In large-scale industrial applications of plasma spraying the need to improve quality control and to reduce the process costs have generated a need for objective criteria and methods for control of the process. The primary process control parameters are flow rates for plasma gas and carrier gas, plasma power and powder feed rate. The quality of the spray coating and the coating efficiency are also influenced by the powder quality and the condition of the nozzle of the spraygun. However, there is not a universal and unambiguous coupling between these control parameters and the spray result, which could be used to select the optimum process control under given conditions. Much research is therefore being devoted to the development of in-situ optical diagnostic methods to monitor the state of the spray process. Among the parameters of interest in monitoring of the spray process are spatial particle distribution, particle velocity distribution, particle temperature distribution and particle size distribution. The particles can be observed by their emitted light or scattered laser light. The relatively high particle speed of, typically, several hundred metres per second implies a time resolution requirement of the order one microsecond or better.

Imaging spray monitoring vs. point diagnostics

The recent development of CCD cameras of reasonable cost and yet sufficient time resolution make these instruments very attractive for the described industrial monitoring purpose. The possibility of *Passive Imaging Spray Monitoring* (PISM), i.e. to obtain a visual overview of the spray plume in combination with the quantitative evaluation of spray parameters using a CCD camera underlines its attractiveness in comparison with instruments providing essentially point information from the plume. The word "Passive" refers to the fact that self radiation only is used, whereas a method would be denoted as "Active", if an external light source were employed.

The strength of PISM lies in its capability to submit an overall indication of anomalies in the spray pattern, which could be misinterpreted or not understood at all by point diagnostics. For example, background radiation from bursts of plasma or fumes of the powder material may influence the total radiation emitted at a certain time and location in a way that is difficult to interpret if information of the radiation from a larger area is not available. Another advantage is that integrated information, e.g. number of particles or average particle speed, from an extended region of the spray plume gives a more reliable indication of the trend of operational parameters than a time average from one point of the plume only.

A prototype for PISM

Fig. 1 shows the principal set-up for a prototype instrument for PISM developed at Tampere University of Technology. In an early version an 8 bit PCO Flashcam® CCD camera was employed. In this camera the exposure time can be selected down to 1 μs and in the present application the effective pixel resolution of the CCD chip was 756 x 580 pixels of 11x22 μm^2 size each. A recent, more developed version employs a digital 12 bit PCO Sensicam® SVGA camera with 1280 x 1024 pixels of 6.7 x 6.7 μm^2 size.

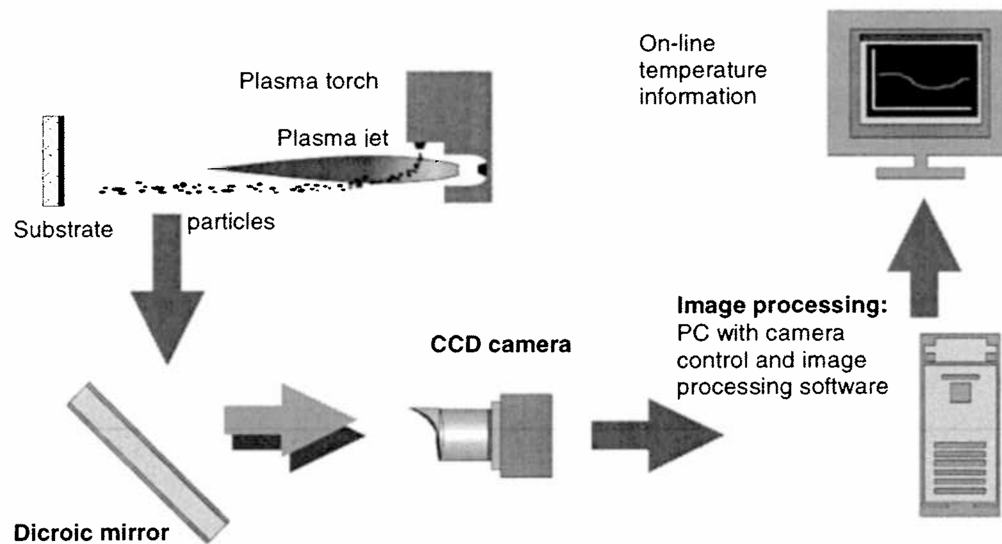

Fig. 1. Conceptual set-up of PISM system based on a CCD camera. Technical details are given in the text. The double dichroic mirror produces a bichromatic double image, which is used for two-colour pyrometric particle thermometry.

The basic principles of spray analysis are based on the identification of spray particles in the camera image using digital image processing and on determining light fluxes emitted by particles based on grayscale levels of the particle images. The developed version of the instrument is programmed on the Labview® interface.

Image formation and particle identification

The basic spray parameters studied so far are the number and spatial distribution of particles in the jet, the speed and direction of the particles and the particle temperatures.

The principle of image formation is illustrated in Fig. 2. The image on the left is taken with long exposure time and gives an overview of particle trajectories in the spray jet. On the right is a close-up detail of a small part of the jet. The exposure time is a microsecond, whereby the particle motion becomes almost frozen. The brightness and sharpness of the particle images depends on the temperature and location of the particle with respect to the focal plane.

Particles are identified from the images using digital image processing. The identification criteria are based on brightness and contrast. The sensitivity and dynamic range of state-of-the art CCD cameras are not yet high enough to avoid loss of particles in the formation of images. Hot particles will become registered from a larger volume than cold ones, and, therefore, the portion of hot particles tends to become overweighted in relation to cold ones in the population of observed particles.

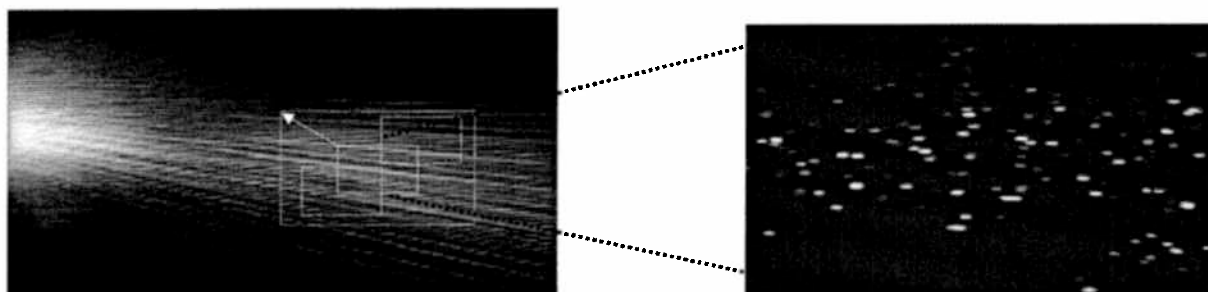

Fig. 2. Image formation in PISM. Using a high shutter speed images of a desired portion of the spray jet are formed with the CCD camera. Particle number distributions and speed distributions can be formed by digital image processing. Particle thermometry requires an additional technique explained in the text.

Distributions of particle number and speed

To deduce particle speeds and directions one increases the exposure time to produce elongated particle images, as shown in Fig. 3. An overall particle speed distribution deduced from a total population of over 30 000 particles is shown in Fig. 4. The data was compiled from 225 consecutive frames. Lateral distributions of average particle speeds across the jet can also be produced. Such distributions can give important information about the conditions of powder injection, for instance.

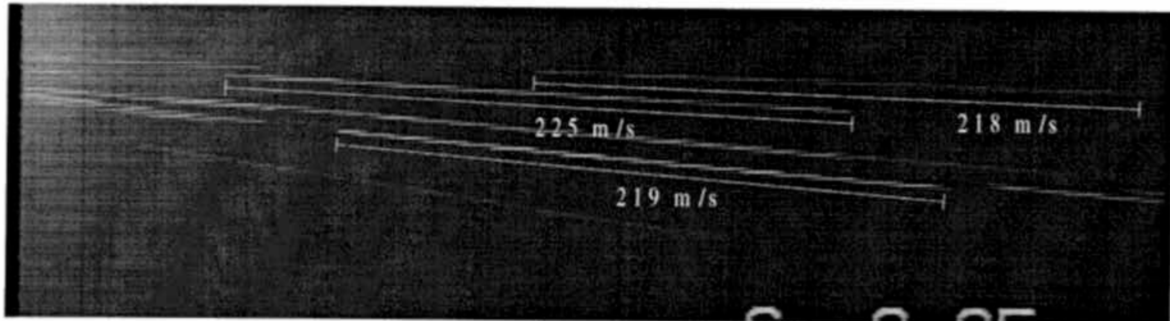

Fig. 3. Particle speeds and directions are deduced from long-exposure images of the particles.

For process control purposes it is useful to produce moving averages of spray parameters, which can provide the operator with information on trends affecting the spray process. An example of such a trend diagram based on a moving time average of the particle speed is shown in Fig. 5. The data and curve on the top show the mean speed vs. time and the bottom ones show the standard deviation. In this example conditions were steady, which is reflected by the absence of a trend.

The recording frame rate in Fig. 5 was 3 frames per second, but the processing of one frame takes at present about 3 seconds. It is, however, realistic on the basis of present day technology to project a processing rate of several frames per second. Thus, continuous on-line monitoring of plasma spray processes based on PISM is fully realistic today.

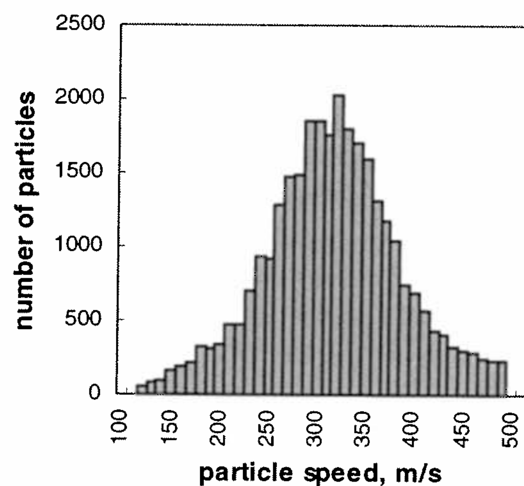

Fig. 4. Particle speed distribution in plasma spray jet as recorded by PISM from a total population of 30132 particles. Mean speed: 310.7 m/s,

Imaging two-colour pyrometric particle thermometry

PISM can also be used to deduce spray particle temperatures based on two-colour pyrometry. As in the case of particle speeds, global temperature distributions, lateral distributions of mean temperatures and temporal trends can be produced, all based on temperature measurements of single individual particles. The key element for imaging two-colour pyrometric particle thermometry is the double dichroic mirror (patent pending) shown in Fig. 1.

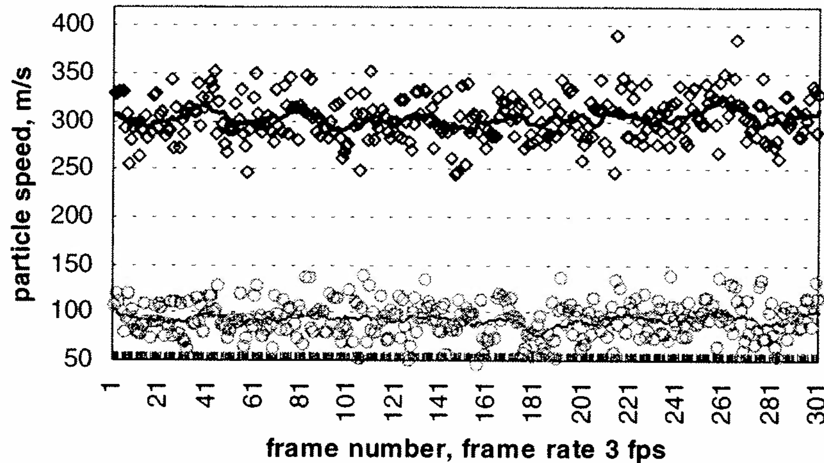

Fig. 5. Evolution of mean particle speed (top) and standard deviation vs. time (bottom) in plasma spraying.

The mirror consists of a glass plate with dichroic coatings on each side. The coatings are tailored to have different cut-off wavelengths, which both lie within the active spectral response band of the CCD chip. One image is formed by light reflected from the front surface of the mirror. A second one, spatially displaced with respect to the first one, is formed by reflection from the rear mirror surface. Due to the dichroic coatings, the light of the two images will be in different spectral bands. The particle temperature is obtained by taking the ratio of the brightnesses of the two images, following the principles of two-colour pyrometry.

Examples of bichromatic double images of particles taken in a plasma spray-jet are shown in Fig. 6. To obtain correct particle temperatures it is necessary to carefully consider the chromatic properties of the optics and the detailed distribution of light on individual pixels in the images. This work is in progress at present and the preliminary results obtained so far are promising.

Applications and general features

The instrument has been successfully tested on plasma spray jets at electrical powers up to 200 kW, on a detonation spray gun and on an HVOF spray gun.

An important property of a digital CCD camera is the possibility of binning of pixels to form super-pixels. This makes possible a trade-off between spatial resolution and sensitivity. Thereby, the instrument performance can be optimised for several different conditions of thermal spraying and for different parameters in a given spray application.

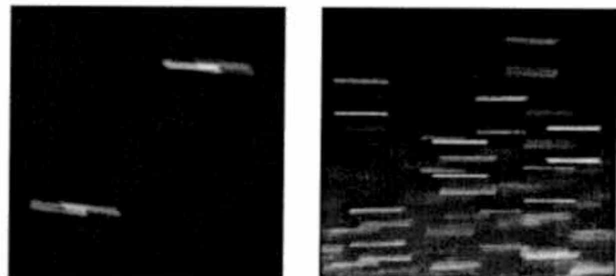

Fig. 6. Bichromatic particle images produced by the double dichroic mirror shown in Fig. 1. The images can be either laterally (right) or longitudinally displaced (left).

The versatility of PISM has also been demonstrated by observations of phenomena, like collisions between spray particles, fumes of nucleated particle vapour and particles bouncing back from the substrate. It is believed that besides providing wide possibilities for quantitative parameter studies and monitoring of the spray process, PISM also has much potential in visualising new phenomena both in the spray jet and on the substrate.

Electron Density Measurements in a Microwave Plasma by the Plasma Oscillation Method

A. Brockhaus, A. Schwabedissen, Ch. Soll, J. Engemann
Forschungszentrum für Mikrostrukturtechnik – fmt, University of Wuppertal
Germany

Introduction

The electron density is a key plasma parameter needed for any process control as well as for understanding and modelling. Therefore powerful diagnostic methods for the quantitative determination of the electron density have been developed, such as Langmuir probes [1], microwave interferometry [2], and Thomson scattering [3]. It is not appropriate to discuss their advantages and limitations here; we just want to point out one unpleasant pitfall all these methods share: their inability to reliably measure densities in deposition plasmas. On the other hand, in particular deposition plasmas are of primary industrial relevance due to their large number of applications.

In this paper we present measurements with a relatively new diagnostic method, the "plasma oscillation probe" (POP) which was first investigated in a radio-frequency discharge by Shirakawa and Sugai [4]. The working principle is as follows. A beam of electrons is injected into the plasma giving rise to the beam-plasma instability [5]. The frequency of the excited electrostatic plasma oscillation ν_{max} is very close to the plasma frequency ν_p if two conditions are met. Firstly, the electron density of the beam must be small as compared to the plasma density, e.g. $\eta := n_{beam}/n_e << 1$. In the framework of linear dispersion theory this leads to the expansion [5]:

$$\nu_{max} = \nu_p \left[1 - \frac{1}{2} \left(\frac{1}{2} \eta \right)^{1/3} + \ldots \right] \quad (1)$$

Secondly, the energy of the beam electrons should greatly exceed the mean energy of the plasma electrons. The plasma frequency in turn solely depends on electron density. Experimentally, a small antenna allows to detect the oscillation. At the high frequencies involved the coupling is capacitive; thus an insulating layer on the antenna does not prevent proper operation of the system.

The purpose of this paper is twofold. On one hand we demonstrate the capability of POP to determine electron densities in a deposition plasma. And we also extend the POP diagnostic to the regime of microwave-excited plasmas where the excitation frequency is near the plasma frequency. Where possible, POP results are compared to Langmuir probe measurements.

Experimental set-up

The plasma is generated by a SLAN type plasma source which is in detail described elsewhere [6]. Essentially a circular waveguide with ten slots is used to excite a plasma within a quartz bell jar of 20 cm length and 16 cm diameter. The source is powered by a 2.45 GHz magnetron delivering up to 6 kW. No external magnetic field is used. The SLAN is attached to a stainless steel vacuum chamber which can be evacuated by a turbomolecular pump and a rotary backing pump. Pressure and gas flow are controlled by a throttled valve and mass flow controllers, respectively. We use argon and oxygen as feedstock gases. In deposition experiments hexamethyldisiloxane (HMDSO) is added through a gas ring positioned 35 cm downstream from the center of the SLAN. For details about direct and remote plasma polymerization of HMDSO we refer to previous publications, e.g. [7].

The SLAN plasma has already been investigated extensively. For electron density measurements single and double Langmuir probes with a computerized system as well as microwave interferometry have been used [8]. Although at the centre of the SLAN plasma densities exceed 10^{13} cm^{-3} the experiments reported here were performed at a position 23 cm downstream. There the electron density has dropped down by three orders of magnitude which is more appropriate for deposition purposes.
The set-up of the POP diagnostic is similar to the one described in [9]. The electron beam is generated by a hot tungsten filament biased to a negative voltage with respect to the plasma potential. The excited electron oscillations are picked up by a small antenna, consisting of a 5 mm long straight metal wire of 0.25 mm diameter. Both the electron emissive filament and the detector antenna are mounted parallel to each other on the same vacuum flange, at a distance of 15 mm. The antenna is connected to the centre lead of a 50 ohms vacuum BNC cable. Outside the vacuum chamber the signal is transferred via a 50 ohms microwave SMA cable to a high-frequency spectrum analyzer (Advantest R3272, 9 kHz – 26.5 GHz) which allows for very sensitive detection and analysis of the oscillations.

Experimental results and discussion

From previous Langmuir probe measurements it is known that the plasma density in a rare gas SLAN plasma scales linearly with microwave power over a wide range. Thus it is possible to realize an underdense as well as an overdense plasma (where the density exceeds the critical density of 7.4×10^{10} cm^{-3} at 2.45 GHz) by simply changing the input power. In Figures 1 and 2 frequency scans obtained with the plasma oscillation probe are displayed for both cases.

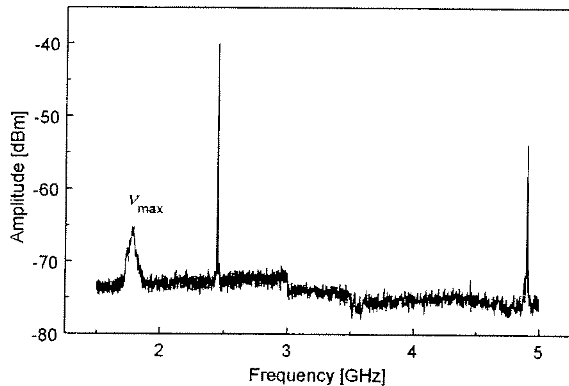

Figure 1: *Frequency spectrum in an underdense argon microwave plasma at 3 Pa and 800 W input power*

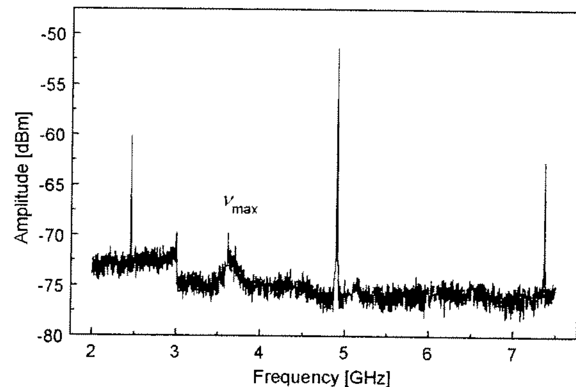

Figure 2: *Frequency spectrum in an overdense argon microwave plasma at 4 Pa and 1200 W input power*

The sharp peaks at 2.45, 4.9, and 7.35 GHz correspond to the driving frequency of the magnetron and its harmonics. The fundamental can be observed without plasma while the higher harmonics are a consequence of the plasma being a nonlinear load. Note also that in the case of an overdense plasma (Fig. 2) the amplitude of the 2.45 GHz fundamental is about 20 dB lower than in the underdense case. The plasma oscillation probe signals for the two conditions are seen at 1.8 GHz and 3.6 GHz, respectively, and are much broader.
From an experimental point of view two parameters have to be adjusted for the plasma oscillation probe to work: the kinetic energy of the beam electrons should be large as compared to the mean energy of the bulk plasma electrons. Typical conditions were energies in the range of 40-80 eV. A compromise is necessary for the electron beam density. On one hand the beam density must be high enough to raise the plasma oscillations above the noise level, on the other hand the density should be kept as low as possible because only then the

oscillation frequency closely resembles the plasma frequency. In our case the beam currents were around 10-50 mA corresponding to electron densities of about 10^8 cm^{-3}. Since the plasma density is in the range of 10^{10} cm^{-3} the "weak beam approximation" holds and the systematic error in electron density will be less than 15%. In principle, it should be possible to correct the systematically too low n_e value according to equation (1) by an independent measurement of the beam electron density.

Figure 3 displays the electron density as a function of microwave input power as measured by single Langmuir probe (SLP), double Langmuir probe (DLP), and POP. As expected, the plasma density increases with microwave power. However, the increase is not linear over the whole range, and the slope changes for power levels in excess of 1.3 kW. Under these conditions the SLAN operates in the surface wave mode. As a consequence, higher microwave power input will primarily increase the plasma volume and not so much the electron density. The calculated electron densities from the POP diagnostic generally lie in between the values obtained from DLP and SLP. It is assumed that the DLP results may be regarded as upper boundaries for plasma density [1].

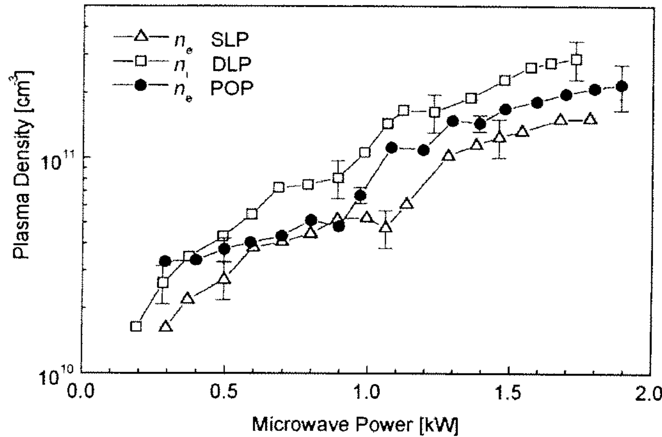

Figure 3: *Plasma densities in an argon SLAN plasma at 3 Pa as a function of input power*

The dependency of electron density on gas pressure is displayed in Figure 4. In agreement with earlier measurements [8] the electron density as measured by Langmuir probe exhibits a maximum at about 5 Pa and decreases with higher pressures. For pressures below 7 Pa the POP measurements are again between DLP and SLP results. However, for higher pressures the electron densities obtained from the plasma oscillation probe are significantly higher than both DLP and SLP values.

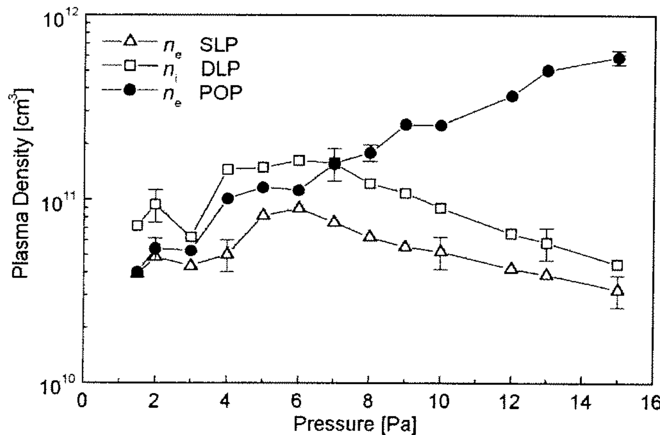

Figure 4: *Plasma densities by DLP, SLP and POP as a function of argon pressure for 800 W microwave power*

The reason for this discrepancy is not clear yet. At 15 Pa the ion mean free path is about 0.2 mm thus being still larger than the probe radius of 0.125 mm (DLP) or 50 μm (SLP). Therefore the Langmuir probes should operate in the collisionless regime. The effect of collisions on the plasma oscillation probe has been studied by Shirakawa and Sugai in the framework of linear theory [4]. Essentially the frequency ν_{max} of the most unstable electrostatic wave is nearly unchanged if the collision frequency is small as compared to the plasma frequency but the growth rate drops down at higher collision frequencies. We think that collisional damping is the reason why no POP signal could be observed for pressures above 15 Pa. However, since the frequency is still close to the plasma frequency in the investigated pressure range, it is concluded that the POP diagnostic should be accurate.

In order to investigate the possibility of POP measurements in deposition plasmas a gas mixture of argon and oxygen is used for the plasma and hexamethyldisiloxane (HMDSO) is added at a downstream position. Even at very low HMDSO flow rates (1 sccm) the Langmuir probes were coated with insulating layers in a few seconds. In contrast to this the plasma oscillation probe did not show degradation and gave long-term stable results. This could be verified also for higher flow rates at 10 sccm which are routinely used for high rate deposition processes.

It is known from experiments that the properties of the deposited film largely depend on the oxygen concentration in the plasma [8]. Therefore the variation of electron density with oxygen partial pressure was studied. The results are displayed in Figure 5. Argon and HMDSO flows were kept constant at 15 and 10 sccm, respectively. Microwave input power was 1400 W, and total pressure 8 Pa. It is seen that with increasing oxygen concentration the electron density drops down significantly. This regime is of particular practical importance because a high oxygen content is needed for the generation of hard quartz-like coatings.

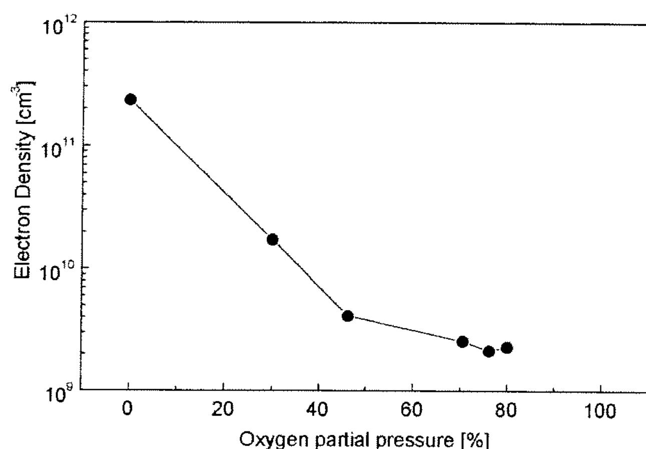

Figure 5: *Electron densities measured by POP as a function of oxygen partial pressure in an Ar:O_2:HMDSO plasma*

In summary, successful operation of the POP diagnostic could be demonstrated in a microwave deposition plasma for the first time.

This work was supported by the DFG under contract Br1407/3-1.

References

[1] J. D. Swift and M. J. R. Schwar: Electric Probes for Plasma Diagnostics; Iliffe Books, London (1971)

[2] M. A. Heald and C. B. Wharton: Plasma Diagnostics with Microwaves; Krieger Publishing, New York (1978)

[3] J. Sheffield: Plasma Scattering of Electromagnetic Radiation; Academic Press, New York (1975)

[4] T. Shirakawa and H. Sugai; Jpn. J. Appl. Phys. **32**, 5129-5135 (1993)

[5] J. R. Thompson; Phys. Fluids **14**, 1532-1541 (1971)

[6] F. Werner, D. Korzec, J. Engemann; Plasma Sources Sci. Technol. **3**, 473-481 (1994)

[7] D. Korzec, D. Theirich, F. Werner, K. Traub, J. Engemann; Surface and Coatings Technol. **74-75**, 67-74 (1995)

[8] A. Brockhaus, D. Korzec, F. Werner, Y. Yuan, J. Engemann; Surface and Coatings Technol. **74-75**, 431-442 (1995)

[9] A. Schwabedissen, E. C. Benck, J. R. Roberts; Plasma Sources Sci. Technol. **7**, 119-129 (1998)

Quantification of the ion flux by measurements of mass resolved ion energy distributions in RF/VHF plasmas

E.A.G. Hamers [1], J. Bezemer, and W.F. van der Weg

Debye Institute, Section Interface Physics, Utrecht University, P.O. Box 80.000, NL-3508 TA Utrecht, the Netherlands

In the plasma bulk electrons have sufficient kinetic energy to create radicals and ions. The radicals diffuse through the sheath towards the electrodes and the wall of the reactor. Their flux to the walls is larger than the flux of ions. However the ions are accelerated in the electric field that is present in the sheath. Therefore the kinetic energies of the ions at the electrode are much larger than the thermal energies of the neutrals. In order to understand the growth process, and especially the role of ions in this, it is important to quantify the ion flux and the amount of energy which the ions transfer to the growing surface.

In this article we will outline a method to characterize the sheath from mass resolved ion energy distributions (IEDs) measured at the position of the deposition substrate. This characterization will allow us to quantify, amongst others, the ion flux. The method is applicable in plasmas where charge exchange reactions occur in the sheath. We will show the strength of the method by studying silane plasmas under typical deposition conditions.

1 Charge exchange

In a charge exchange process an electron is exchanged between a neutral and an ion. A well known charge exchange process [1,2] occurs in argon plasmas between an Ar atom and its corresponding ion, Ar^+. In the plasma bulk this charge exchange process has no effect on the velocity of the particles, but in the sheath it leads to the formation of a fast neutral, denoted by the superscript (f) and an ion with thermal energy, denoted with the superscript (t):

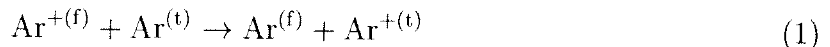

$$\mathrm{Ar}^{+(\mathrm{f})} + \mathrm{Ar}^{(\mathrm{t})} \rightarrow \mathrm{Ar}^{(\mathrm{f})} + \mathrm{Ar}^{+(\mathrm{t})} \quad (1)$$

In the case of argon the reaction is reversible and therefore the process is called a resonant charge exchange process. Such resonant charge exchange processes are very common, eg. in H_2, N_2, and O_2 discharges.

Charge exchange processes in the sheath of RF plasmas result in very characteristic peaks in the ion energy distribution [1,2]. The energy position ϵ_p of the pth peak in the ion energy distribution depends on the plasma potential V_{pl}, the RF period T, the mass m of the measured ions and the charge carrier density n in the sheath,

$$\epsilon_p = eV_{\mathrm{pl}} \left(1 - \left[\cosh \left(pT\sqrt{\frac{e^2 n}{m\epsilon_0}} \right) \right]^{-2} \right), \quad (2)$$

where e is the elementary charge, and ϵ_0 the permittivity of the vacuum. This formula is deduced with the assumption of a constant charge carrier density in the sheath. There

[1]Present Adress: LPICM, Ecole Polytechnique, F-91128 Palaiseau, France. E-Mail: hamers@poly.polytechnique.fr

are two unknowns in this equation: the time averaged plasma potential $V_{\rm pl}$ and the charge carrier density n. In practice the plasma potential is determined from the IED of an ion that does not collide in the sheath, and thus has its maximum intensity at an energy corresponding to $eV_{\rm pl}$. The charge carrier density n is then deduced from an IED with charge exchange maxima. It must must be stressed that the absolute intensity is not important, neither is the relative abundance of the measured ions.

A related parameter that depends on the plasma potential and the charge carrier density is for example the sheath thickness d_s: $d_s = \sqrt{2\epsilon_0 V_{\rm pl}/(en)}$.

In order to calculate the ion flux Γ from the plasma potential and the charge carrier density, we will assume that no collisions occur in the sheath. In that case the ion flux $\Gamma_{\rm max}$ at the electrode is:

$$\Gamma_{\rm max} = n v_{\rm max} = n\sqrt{2eV_{\rm pl}/m}. \qquad (3)$$

From the kinetic energy which ions gain in the sheath, we calculate the maximum *ion kinetic energy* flux of ions $(\epsilon\Gamma)_{\rm max}$, $(\epsilon\Gamma)_{\rm max} = eV_{\rm pl}\Gamma_{\rm max}$, where ϵ denotes the ion energy. The dimension of $(\epsilon\Gamma)_{\rm max}$ is $\mathrm{W\,m^{-2}}$. This parameter is important in describing the material properties as we will show.

In order to express the importance of the ions to the growth process quantitively, two related quantities are used in ion beam assisted deposition. The first one is the fraction of arriving *ions* per deposited *atom*, R_i. The second quantity of interest is the kinetic energy $E_{\rm max}$ transferred by *ions* per deposited *atom*:

$$E_{\rm max} = \frac{(\epsilon\Gamma)_{\rm max}}{\rho\, r_d}, \qquad (4)$$

where r_d is the growth rate. In the calculation of these quantities we will assume a density ρ of the network of 5×10^{28} $\mathrm{m^{-3}}$.

2 IEDs from a silane-argon plasma

The mass resolved ion energy distributions are measured with a Hiden EQP system, that is described extensively elsewhere [3-5]. Although most deposition plasmas are generated in mixtures of silane and hydrogen, we will show measured ion energy distributions from a silane-argon plasma. A silane-argon plasma is very illustrative, since no less than four different ions have charge exchange maxima in their ion energy distribution.

These ion energy distributions originate in a plasma that was created in a mixture of 13 sccm Ar, 13 sccm SiH_4, at a pressure of 10 Pa. The applied RF frequency was 13.56 MHz, at a power of 10 W. The self bias voltage that developed was -135 V. The substrate temperature was 250°C.

The measured IEDs of Ar^+, SiH_3^+, SiH_2^+, H_2^+ and $Si_2H_4^+$ are shown in Fig. 2.

The first 4 IEDs that are shown, have distinct peaks. The energy positions of these peaks are fitted with Eq. 2 with a value of the plasma potential of 21.8 V as deduced from the $Si_2H_4^+$ IED, and a charge carrier density n of $(1.66\pm0.05)\times10^{14}$ single charged charge carriers per cubic meter. We stress that only one value of the charge carrier density is needed to explain the different peak positions in all IEDs. The error in n is determined from the variation in the fitted value of n as obtained from the different ion energy distributions. The fitted energy positions of the maxima are indicated with the dotted vertical lines.

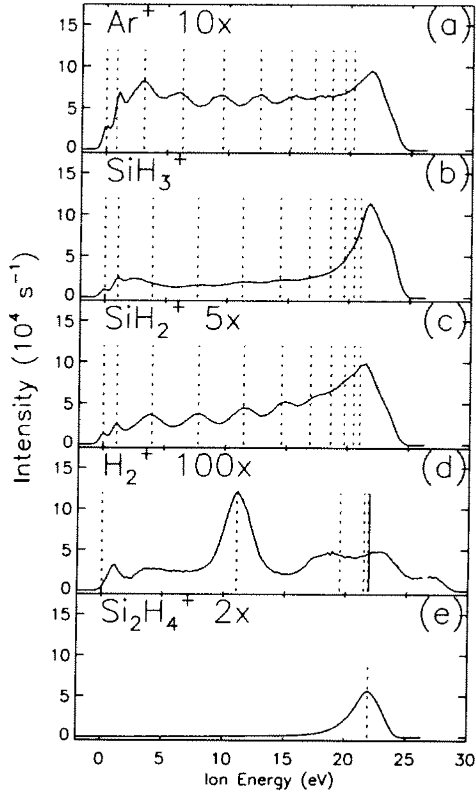

Figure 1: The ion energy distributions of (a) Ar^+, (b) SiH_3^+, (c) SiH_2^+, (d) H_2^+, (e) $Si_2H_4^+$ from a SiH_4-Ar plasma. The dotted lines in (a)..(d) indicate the position of the first 10 charge exchange peaks based on a plasma potential of 21.8 V and a charge carrier density n of $1.66\times10^{14}m^{-3}$. The dotted line in the IED of $Si_2H_4^+$ (e), indicates the value of the plasma potential. Note the different scaling factors of the various IEDs.

The charge exchange reactions that occur are resonant charge exchange reactions for Ar^+ and H_2^+ with their parent neutral. The reactions responsible for the charge exchange maxima in the SiH_3^+ and SiH_2^+ IEDs are dissociative charge exchange reactions between H_2^+ and SiH_4.

3 Ion bombardment and material structure

In an identical reactor as in which the IEDs are measured, hydrogenated amorphous silicon films are deposited at a similar position as where the IEDs are measured. This allows to correlate plasma properties, as deduced from the IEDs, with the properties of the deposited material.

Good structural properties, i.e. a refractive index of about 4.25 at a photon energy of 2 eV and a low number of SiH_2 bonds, are found when the ions transfer more than 5 eV kinetic energy per deposited atom to the growing surface, so E_{max} >5 eV. This is observed at a substrate temperature of 250°C [4], independent of process parameters as frequency, power, pressure, external bias and gas dilution. A temperature series at 200°C shows the same behaviour, whereas at a substrate temperature of 300°C the importance of ion bombardment for achieving a dense network is strongly reduced [5].

Another structural parameter that is studied is the internal stress in the a-Si:H film. The relation between stress and E_{max} is plotted in Fig. 2. The points of the 200 and 250°C substrate temperature series show the same relation, the stress increases linearly with E_{max}. The data points of the 300°C substrate temperature series follow the same slope, but exhibit a 600 MPa higher compressive stress at given E_{max}. A compressive stress of 600 MPa corresponds to a compression of about 1%, due to an excess of about

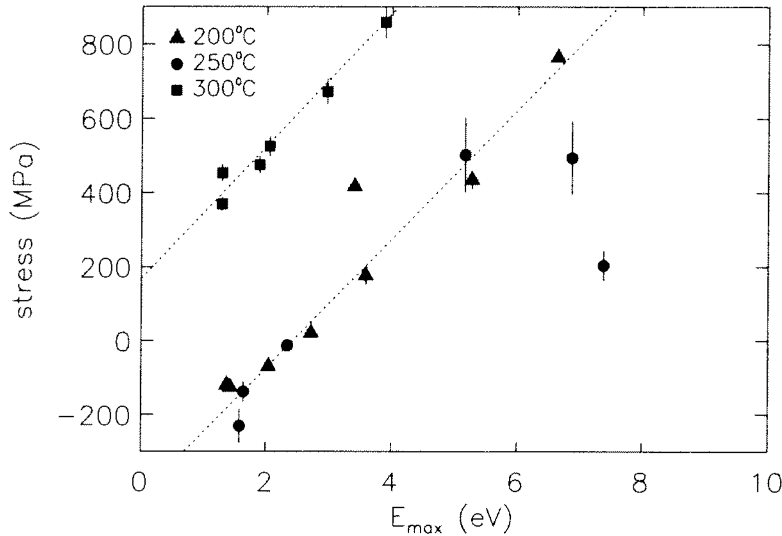

Figure 2: Internal stress as function of $E_{\rm max}$ in the pressure series at 50 MHz.

1% of Si-atoms in the network. Layers that were deposited at a higher value of $E_{\rm max}$ than 4.5 eV peeled off from the silicon substrate directly after exposure to air, and therefore the stress in these films could not be measured. The very fact that the layers peeled off indicates a high internal stress in these layers.

4 Conclusions

We shortly outlined the method to characterize plasmas by means of charge exchange maxima in mass resolved ion energy distributions. The relation between the transferred kinetic ion energy and the structural properties of the deposited material, in this case hydrogenated amorphous silicon, demonstrate the strength of this method to understand the interaction between plasma and material.

[1] C. Wild, and P. Koidl, J. Appl. Phys. **69**, 2909 (1991).
[2] M. Fivaz, S. Brunner, W. Schwarzenbach, A. A. Howling, and Ch. Hollenstein, Plasma Sources Sci. Technol. **4**, 373 (1995).
[3] E. A. G. Hamers, W. G. J. H. M. van Sark, J. Bezemer, W. J. Goedheer, and W. F. van der Weg, Int. J. Mass Spectrom. Ion Processes **173**, 91 (1998).
[4] E. A. G. Hamers, W. G. J. H. M. van Sark, J. Bezemer, H. Meiling, and W. F. van der Weg, J. Non-Cryst. Solids **226**, 205 (1998).
[5] E. A. G. Hamers, PhD thesis, Utrecht University, the Netherlands, 1998.

Characterization of Electron Parameters in Inductively/Capacitively Coupled RF Discharges by Use of Ar Line Emission

S.A.Moshkalyov, W.G.Graham, C.M.O.Mahony, P.G.Steen and S.Gomez
School of Mathematics and Physics, Queen's University of Belfast, Belfast, Northern Ireland, UK

Introduction

In reactive plasmas the use of electric probes for measurements of electron parameters is not always possible. In this case, optical emission spectroscopy with rare gases can provide information on electron parameters if the excitation mechanisms are well established [1,2]. In the present experiments, performed with a GEC reference cell, a comparative analysis of electric probe data and Ar line emission ($2p_x \rightarrow 1s_y$ transitions) was made. It is shown that at electron densities $\geq 10^{15}$ m^{-3} for the most lines (e.g., 811.5 nm), two-step excitation via metastable Ar states becomes an important channel, while the 750.4 nm line emission is mainly due to direct excitation from the ground state. Linear correlation is found between intensity ratios I (811.5 nm)/I(750.4 nm) and the density of "cold " electrons (with energies of a few eV). A simple model explaining this dependence has been developed.

Main mechanisms of Ar line excitation

In low-temperature, low-pressure plasmas, there are two major mechanisms of electron-impact excitation of atomic Ar line emission:

(i) direct excitation from ground state

$$Ar + e \rightarrow Ar^* + e$$

(ii) two-step excitation via metastable states:

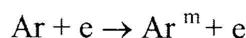

$$Ar + e \rightarrow Ar^m + e$$

$$Ar^m + e \rightarrow Ar^* + e$$

Cross-sections for excitation of metastables into higher levels can be 10^2 to 10^3 times as large as the cross-sections for excitation from the ground state [3]. The energy threshold for excitation out of metastables is much lower (~1.5 eV for Ar) than that for excitation of ground state atoms (~13 eV for Ar). Therefore in low-temperature plasmas metastable atoms can play an important (sometimes even dominant) role in Ar optical emission, and ionization too. For most Ar "red" lines ($2p_x \rightarrow 1s_y$ transitions, wavelength range ~ 700-800 nm) the two-step excitation becomes dominant at electron densities exceeding 10^{16} m^{-3} . The Ar I line 750.4 nm ($2p_1 \rightarrow 1s_2$ transition) is the only one which is excited mainly by the direct process from the ground state. The Ar I line 811.5 nm ($2p_9 \rightarrow 1s_5$) is the one most effectively excited from the metastable levels. It should be noted that the excitation out of metastable states is produced mainly by electrons with relatively small energies ("cold" electrons, with energies $\leq$ 3 eV), which represent the main body of electron population in the plasma. Only small fraction of "hot" electrons (with energies > 13 eV) is responsible for the direct excitation.

The ratio of intensities for these two lines (811.5 nm and 750.4 nm) is given by:

$$\frac{I(ArI,811nm)}{I(ArI,750nm)} = a\frac{N_{e,c}N_{A,m}K_{c,1} + N_{e,h}N_{A}K_{h,1}}{N_{e,h}N_{A}K_{h,2}} = a(\frac{N_{e,c}}{N_{e,h}}\frac{N_{A,m}}{N_{A}}\frac{K_{c,1}}{K_{h,2}} + \frac{K_{h,1}}{K_{h,2}})$$

where, respectively, the number densities for populations of "cold" and "hot" electrons in plasma are $N_{e,c}$ and $N_{e,h}$ ($N_{e,c} >> N_{e,h}$), K_c and K_h are the rate coefficients of excitation by "cold" and "hot" electrons, N_A and $N_{A,m}$ are the number densities of ground state and metastable Ar atoms, indexes 1 and 2 refer to the corresponding Ar levels, and a is the proportionality factor.

The fraction of metastables ($N_{A,m} / N_A$) is determined by the balance between their generation (by "hot" electron impact, with the rate coefficient $K_{h,3}$) and losses (by diffusion and quenching in collisions with electron and atomic particles). At low pressures we can neglect quenching by atoms, so that

$$\frac{N_{A,m}}{N_{A}} \approx \frac{N_{e,h}K_{h,3}}{k_{d} + N_{e,c}Q_{e}}$$

where k_d is the diffusion coefficient and Q_e is the electron quenching rate coefficient (here we take into account that quenching is produced mainly by "cold" electrons).

At low electron densities, diffusion losses are dominant, then $N_{A,m} / N_A \approx N_{e,h} K_{h,3} / k_d$ and the expression for the line ratio can be reduced to the form

$$\frac{I(ArI,811nm)}{I(ArI,750nm)} \approx a(N_{e,c}\frac{K_{c,1}}{k_{d}} + \frac{K_{h,1}}{K_{h,2}})$$

i.e., it depends linearly on the density of "cold" electrons. In another limiting case, where the quenching term becomes dominant (high electron density), the fraction of metastables is given by $N_{A,m} / N_A \approx N_{e,h} K_{h,3} / N_{e,c} Q_e$, and then the line ratio does not depend on the electron density (but it depends on electron energy distribution function). So, from the simple model presented here, it follows that this ratio rises linearly with ("cold") electron density until quenching of Ar metastables becomes important.

Experimental results and discussion

Comparative analysis of optical emission and electric probe data has been performed in experiments with an Ar plasma in a GEC reference cell. The cell can operate in both inductive (high density) and capacitive (low density) modes. Experiments were carried out with Ar pressures ranging from 5 to 50 mTorr at relatively low powers (30-40W), i.e., in the region where the capacitive /inductive transition occurs. Electric probes were used for measurements of electron energy distribution functions and densities in the center of the plasma. Optical emission from the same location in the plasma was analyzed using a grating spectrometer (dispersion 6.5 nm/mm) and ICCD detector.

In Figure 1 the ratios of intensities for several Ar lines are plotted against the gas pressure for the two discharge modes.

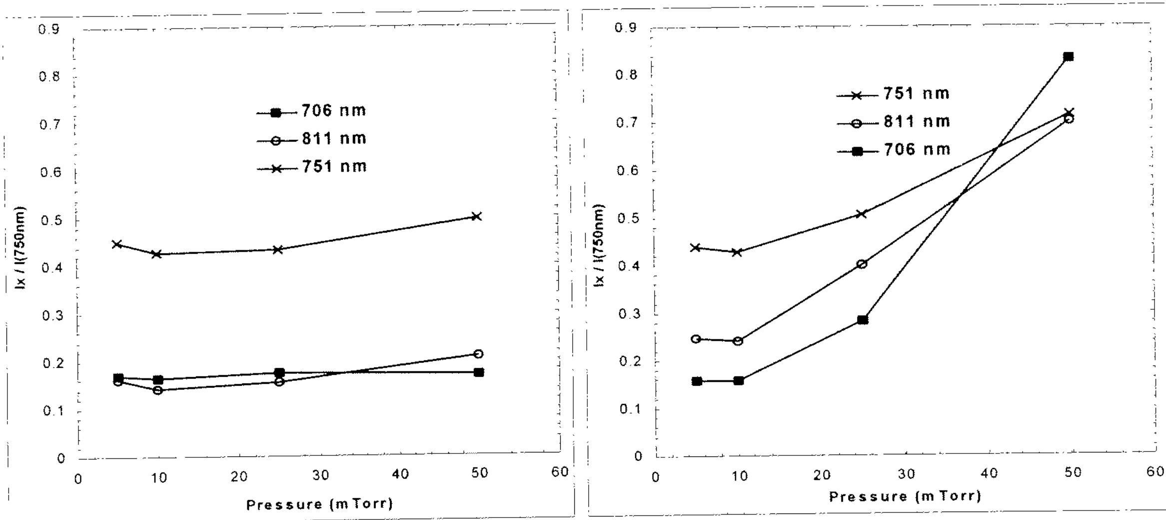

Figure 1: *The ratios of intensities for several Ar lines to 750.4 nm line vs Ar pressure, for capacitive (left) and inductive (right) modes.*

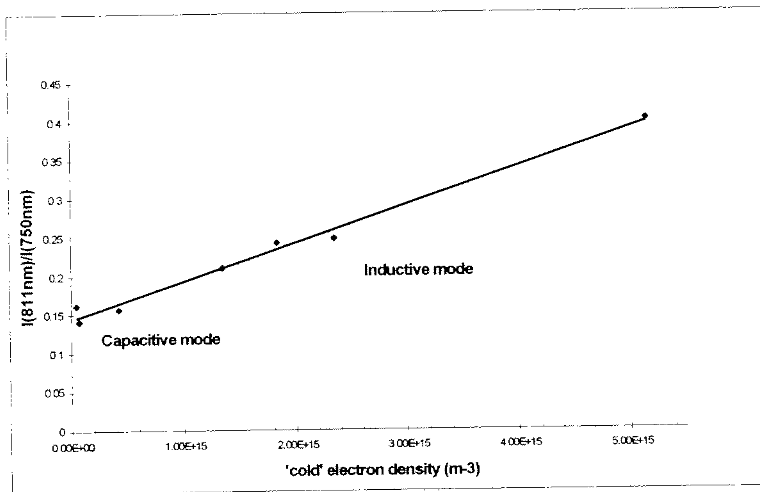

Figure 2: *The ratio of intensities for 811 nm and 750 nm Ar lines vs "cold" electron density.*

In Figure 2, the same data are plotted against the density of "cold" electrons (with energies

< 3 eV), determined from the probe measurements. As predicted by our simple model, a linear rise of the line ratio with density is observed in this density range ($\leq 5 \times 10^{15}$ m^{-3}). For densities higher than 10^{16} m^{-3}, the tendency for saturation of the line ratio was observed.

References

[1] M.V.Malyshev and V.M.Donnelly; J. Vac. Sci. Technol. A **15**, 550 (1997)

[2] S.A.Moshkalyov, J.A.Diniz, J.W.Swart, P.J.Tatsch and M.Machida; J. Vac. Sci. Technol. B **15**, 2682 (1997)

[3] G.A.Piech, J.B.Boffard, M.F.Gehrke, L.W.Anderson and C.C.Lin; Phys. Rev. Lett., **81**, 309 (1998)

CONTINUOUS TEMPERATURE MEASUREMENT OF TRANSPARENT PLATES IN LOW-PRESSURE PLASMA USING LASER INTERFEROMETRIC TECHNIQUE

S.V.Merkulov and A.N.Magunov

Institute of Microelectronics of Russian Academy of Sciences, Russia

Abstract

The technique for quasi-continuous temperature reading by the use of laser interferometric thermometry is developed for materials with small surface reflectance (similar to glass). At least thirty points (instead one point) within each interference half-period corresponding to about 15 K are used for temperature measurement of glass plate located at RF electrode in nitrogen plasma. Some potential applications are briefly discussed.

Introduction

The kinetics and mechanisms of the heat transfer from non-equilibrium plasmas to surfaces have only recently started to receive attention [1]. The greater part of information concerning the heat fluxes in plasma-surface interaction is associated with the derivatives of the transient temperature with respect to time. By the first differentiating the curve T(t), we obtain the temperature dependences of the heating rate dT/dt and the power density of the total heat flux onto the wafer surface $D(W/cm^2) = c\rho h(dT/dt)$, where c is the specific heat, ρ is the density, h is the wafer thickness. A more complicated structure of the integral heat flux can be reconstructed using the second differentiation of the function T(t). However, any traditional methods of thermometry are in general not applicable to the measurements in plasma conditions. The laser interferometric thermometry of semiconductors and dielectrics is rapidly becoming an accepted alternative to the conventional techniques in plasma processing (see review [2]).

At present the temperature reading is carried out only at the points of interference extrema at intervals $\Delta T \approx 2.6$ K for 0.5-mm-thick silicon single crystal at the wavelength of 1.15 μm and $\Delta T \approx 15.7$ K for 1-mm-thick fused quartz at λ=0.63 μm. Linear and other kinds of the interpolation of T(t) between two neighbouring points T_i and T_{i-1} are probably in poor agree with the real temperature evolution. This is observed after calculating dT/dt and d^2T/dt^2. Here we report the quasi-continuous temperature measurement using non-ideal actual interferograms obtained in heating the quartz wafer in gas discharge plasma.

Statement of the problem to be solved

To use the first and the second derivatives for the heat transfer analysis, it is necessary to perform a reading the temperature T(t) at small intervals ΔT. So, the way to improve the data handling technique is to use the quasi-continuous temperature reading instead the large discrete steps from one to the other interference extremum. To reach this goal, the temperature

quantization should be reduced to about $\Delta T \approx 0.01$ K. By this improvement, we can eliminate some errors connected with the numerical determination of the derivatives $\Delta T/\Delta t \approx (T_i - T_{i-1})/(t_i - t_{i-1})$ using experimental curve $T_i(t)$, where $i = 1,2,...,n$ (in our experiments, $n \approx 30 \div 50$ for silicon and $n \approx 5 \div 9$ for quartz wafers).

Due to non-ideal plane-parallel shape of wafers, the contrast V (or so-called "visibility") of the interference fringes is less then theoretically predicted by a factor of $1.1 \div 2$ [3]. Compared to the ideal interferogram having $R_{min} = 0$, the actual one has the non-zeroth reflectance at the interference minima. So, the approximation of ideal interferogram does not allow in this case to calculate the wafer temperature quasi-continuously due to different amplitudes and shapes of calculated and experimental Fabry-Perot resonances. Problem to be solved is to describe the interaction of the laser beam with real wafers and to develope the algorithm for continuous temperature reading.

Origin and description of non-ideal interferogram

There are three main reason for decreasing the interference contrast in heating the transparent plate which is illuminated by the narrow laser beam at the normal incidence:
a) specular reflectances of two opposite surfaces of a wafer are not equal each to the other (for example, a roughness on the front surface is less than on the backside surface; there is a thin film at the front surface, etc.); b) a non-zeroth angle ($\sim 10^{-5} \div 10^{-4}$ radians) between two surfaces leads to the partial or complete mutual compensation of interference maxima and minima at the photodetector; c) the same angle causes an angular separation of reflected beams of different orders of reflection, this results in the spatial separation of these beams on the detector.

Let us assume that total intensity registered by photodetector consists of two part, which may be called by convention as coherent and incoherent beams [4]. Then registered reflectance R may be described by the superposition of two terms:

$$R = fR_1 + (1-f)R_2 \qquad (1)$$

where f is the part of the laser beam area in which an overlapping the beams of of different orders takes place, $0 \le f \le 1$, R_1 is the reflectance taking the light interference into account, R_2 is the reflectance given by the approximation of multiple internal reflections without interference. The second term on the right-hand side is useless for the thermometry. This term could be eliminated fy the re-definition of coordinate axis if the shape of interference fringes is the same as for ideal interferogram. The quantitative characterization of ideal fringe's shape is given by finesse F [2]:

$$F = \pi\left[\arccos(2\sqrt{R_1 R_2} / (1 + R_1 R_2)\right]^{-1} \qquad (2)$$

where subscripts1 and 2 sign the face and the backside surface, respectively.Reflectance of the glass surface is small as compared to unity, $R_1 \approx R_2 \ll 1$. If $R_1 = R_2 \to 0$, we obtain $F \to 2$.

For the interference amplitude (i.e. contrast) we have [4]

$$V_R = \frac{2\sqrt{R_1 R_2}(1-R_1)(1-R_2)}{(R_1+R_2)(1+R_1R_2)-4R_1R_2} \quad (3)$$

When $R_1=R_2$, the contrast equals to unity.

In the limiting case of two-beam interference ($F \approx 2$) it is easy to describe the actual interferograms using the expression (1). To transform the interferogram from actual ($R_{min} > 0$) to ideal ($R_{min} = 0$) form, it is possible to replace the zeroth point at the reflectance axis along this axis up to reflectance minimum. This procedure is equivalent to increasing the value of f in (1) up to 1. The next steps are routine calculations for quasi-continuous function T(t) using the comparison between calculated dependence R(T) and measured dependence R(t) which is transformed to the ideal form. Analogous procedures for silicon crystals ($R_1 \approx R_2 \approx 0.31$ at wavelength $\lambda \approx 1.2$ μm) are impacting some difficulties due to the mixing on the photodetector about 4÷5 partially overlapping beams. This study is now under way.

Experimental

The study of the temperature kinetics of quartz plate was performed in an asymmetric diode RF etch system RDE-300 (Alcatel CIT). The RF discharge (at 13.56 Mhz) is excited at gas pressure of 10 Pa and power input from 50 W to 400 W. A quartz wafer is placed on the power electrode. The wafer temperature is measured using a laser interferometer at $\lambda = 0.633$ μm (the common using this interferometer is to measure the etch rate of transparent films on the silicon wafers). Laser beam 1 mm in diameter passes through the hole in upper electrode, hits the wafer, reflects backward to the same hole after interference within the wafer and is detected by the silicon photodiode. Interferogram processing is performed by the use of PC.

Results and discussion

Four interferograms were obtained in heating the wafer after discharge ignition in nitrogen at different levels of power applied. Performing the procedures described above, the quasi-continuous reflected light intensity reading was made. Within a half-period of interferogram corresponding to the phase shift by π we calculate the temperature at 30 points (this number may be increased by 10÷30 times). The evidence of agreement between ideal interferogram and transformed actual one is the absence of temperature oscillations (these imaginary oscillations may be observed due to some discrepance between the forms of ideal and experimental interferograms). The temporal dependences of wafer temperature consist of about 1,000 experimental points. This curve may be obtained almost in real time with negligible small time delay as compared to process itself.

Conclusion

We conclude, based on the experimental attemption to obtain the quasi-continuous temperature measurement with interferometric technique, that this task is solved for material with small index of refraction, i.e. quartz glass. Through this study, we have established that there is possible to increase essentially the information concerning a heating the solids in

plasmas. Data processing will be performed in real time in nearest future for monitoring the plasma chemical reaction on the surfaces and for end-point detection using sharp change of heating rate dT/dt of wafer as signal of reaching the interface of two different materials [5].

Acknowledgement

This work was supported by the Russian Foundation for Basic Research under grant No.96-02-18164 ("Mechanisms of heat transfer from non-equilibrium plasmas to surfaces").

References

1. A.N.Magunov // Plasma Phys.Repts. 1997. Vol.23, No.11. P.940.
2. A.N.Magunov // Instrum.Experim.Techniques. 1998. Vol.41, No.3. P.297.
3. A.N.Magunov and S.V.Merkulov // Technical Physics. 1999. Vol.68 (in press).
4. A.N.Magunov // Proc.SPIE. Refractometry. 1995. Vol.2208. P.103.
5. O.V.Lukin and A.N.Magunov // Rus.Microelectron. 1998. Vol. 27, No.6. P.378.

Correlation between an optical plasma diagnostic (OES) and an in situ optical thin film diagnostic (SE)

C. Vallée, K. Aumaille, A. Granier, A. Goullet and G. Turban
Laboratoire des Plasmas et des Couches Minces, IMN-CNRS-Université de Nantes
2 rue de la Houssinière, BP 32229, 44322 Nantes Cedex 3, France.

Introduction

This paper reports the monitoring of thin film growth and treatments by optical emission spectroscopy (OES) and spectroscopic ellipsometry (SE). The thin films are deposited from oxygen/TEOS (tetraethoxysilane Si-$(OC_2H_5)_4$) plasmas in a rf helicon reactor. According to the TEOS fraction (%TEOS) in the mixture, either inorganic SiO_2-like dielectric films (%TEOS<30%) or organic $SiO_xC_yH_z$ films (%TEOS>30%) are deposited. *Ex situ* analyses by X-ray photoelectron spectroscopy (XPS) and Fourier transform infrared (FTIR) spectroscopy have shown that the area of the infrared CH_x absorption band between 2800-3000 cm^{-1} is proportional to the C atomic ratio in the $SiO_xC_yH_z$ films [1] and thus is a good indicator of the evolution of the total carbon content in the films. In the first part of the paper, we investigate the *in situ* monitoring of the carbon content by ellipsometry and OES. In the second part, both OES and ellipsometry are used to gain insight into the surface reactions occurring during a post deposition treatment of an organic film by pure oxygen or argon plasmas.

Experimental

The low pressure rf helicon reactor used to create oxygen/TEOS plasmas is described in detail in [2]. It is operated at 2 mTorr, 300 W with a total gas flow rate of 16 sccm (including 0.8 sccm Ar added to the O_2/TEOS feed). The vapor of TEOS is injected through a dispersal ring, a few centimeters above the substrate.

The film growth is monitored *in situ* using a UVISEL spectroscopic phase-modulated ellipsometer (SE) (1.5-5 eV, i.e. 240-800 nm). The real time monitoring of the ellipsometric angles (ψ,Δ) yields the *in situ* monitoring of changes in the film.

The plasma is investigated using optical emission spectroscopy (OES). The light emitted by the plasma close to the film is analyzed in the 180-850 nm range by a UV-Visible monochromator (JY460) equipped with a Hamamatsu R928S photomultiplier. All the emission lines are normalized to the intensity of the 750 nm Ar* line, in order to get partly free from electron density or temperature variations.

Results

1-Monitoring of the carbon content in the film

The incorporation of carbon in a silicon dioxide film modifies its optical properties. Indeed, the simulation of the spectroscopic (ψ,Δ) curves evidences an increase of the refractive index n and the appearance of a weak absorption in the near UV range ($k\neq0$, k is the extinction coefficient). This latest effect has been used to monitor the carbon incorporation. Figures 1 and 2 show the Δ=f(ψ) trajectories recorded during the deposition of a transparent (k=0) SiO_xH_z film and an organic $SiO_xC_yH_z$ film, respectively. It is well known that the kinetic Δ=f(ψ) curve is cyclic when k=0. In addition, the analysis of the spectroscopic results show that carbon is incorporated during the growth whenever the recorded Δ=f(ψ) curve is not cyclic (case of figure 2).

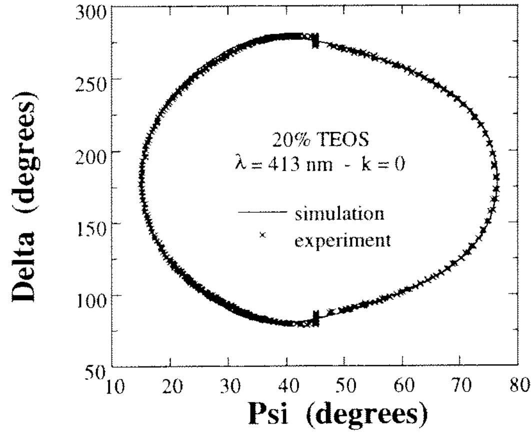

Figure 1: *Real time $\Delta=f(\psi)$ curve during the growth of a SiO_2-like film on Si, recorded at 413 nm, for 20% TEOS in the mixture.*

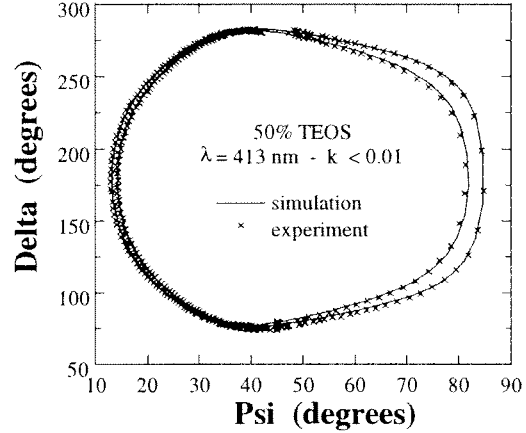

Figure 2: *Real time $\Delta=f(\psi)$ curve during the growth of a $SiO_xC_yH_z$ film on Si, recorded at 413 nm, for 50% TEOS in the mixture.*

It is also interesting to look for any emission from carbon containing species in the plasma which could be related to the incorporation of carbon in the film. Lamendola and Fracassi have shown in a O_2/HMDSO plasma that the CH* emission is related to the carbon content in the film [3]. But the CH* emission at 431.4 nm is very difficult to evidence in an oxygen/TEOS plasma since it is hidden by the CO triplet band, as can be seen in figure 3. In order to monitor the CH* intensity, the CO* system has to be subtracted to the spectrum $I(\lambda)$. Therefore, a CO* reference spectrum is recorded in an oxygen rich mixture and the CH* spectrum is assumed to be equal to :

$$I_{cor}(\lambda) = I(\lambda) - \alpha I_{ref}(\lambda),$$

where $I(\lambda)$ is a recorded spectrum, $I_{ref}(\lambda)$ the CO* reference spectrum and α a factor adjusted in order to cancel the emission in the 432-434 nm region where CO* is the only emitting species. Examples of different corrected spectra are given in figure 4.

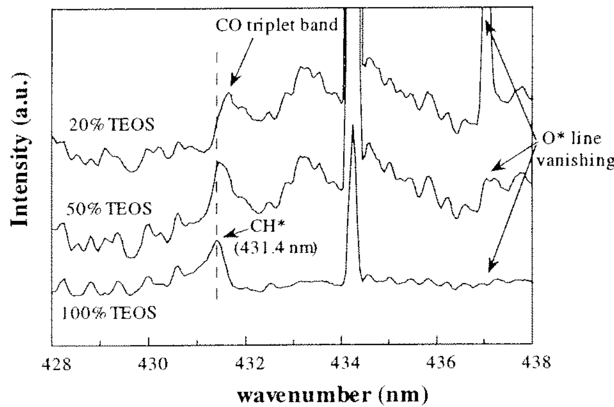

Figure 3: *Appearance of the CH* emission line at 431.4 nm when varying the TEOS fraction in the O_2/TEOS mixture*

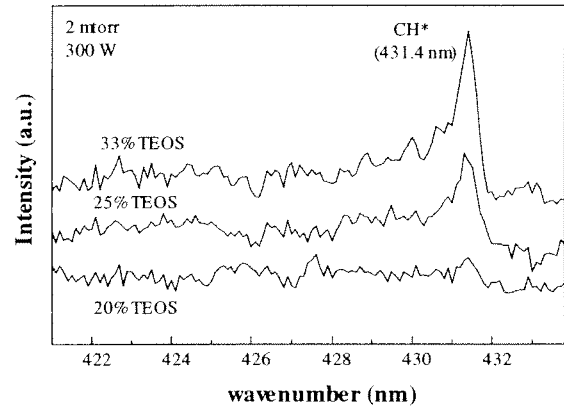

Figure 4: *View of the evolution of the CH* emitted line intensity when changing the mixture from 20% TEOS to 33% TEOS*

As can be seen in figure 5, the normalized intensity of the CH* line is well correlated to the infrared CH_x area. In this way, we evidenced a correlation between the CH* line emission and the incorporation of carbon during the growth so that this emission can be used to control the organic or inorganic nature of the growing film.

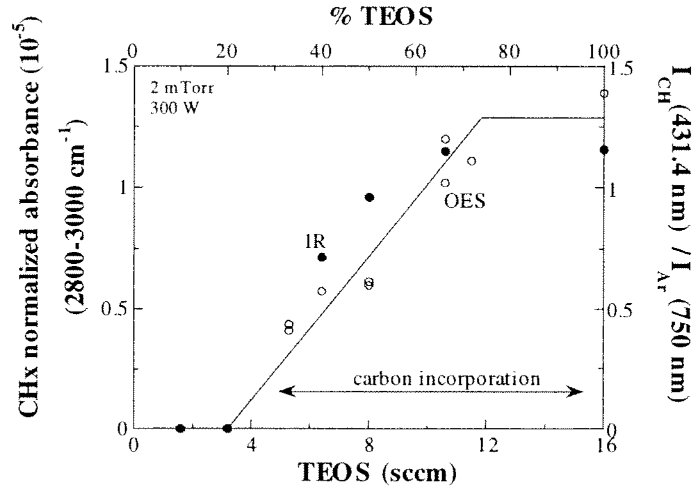

Figure 5: *Correlation between the CH* emitted line intensity and the CHx absorption band (2800-3000 cm^{-1})*

2-Monitoring of the modification of an organic film during its exposure to O_2 or Ar plasma

A freshly deposited organic film ($SiO_xC_yH_z$, 50%O_2/50% TEOS mixture) has been exposed to a pure oxygen plasma. During this post deposition exposure, the film and the plasma have been analyzed using SE and OES. As can be seen in figure 6, the real time $\Delta=f(\psi)$ curve, recorded during the deposition and the post-deposition exposure to the oxygen plasma, clearly evidences the etching of the $SiO_xC_yH_z$ film consecutive to its exposure to the oxygen plasma. Indeed, the $\Delta=f(\psi)$ curve obtained during the post-deposition exposure is running back the one relative to the deposition. The simulation of this trajectory evidences a fast etching in the first minutes. After a 5-min-exposure, the etching slows down and the $\Delta=f(\psi)$ trajectory moves away the deposition one which indicates some structural modifications of the film. OES has also been carried out during the post-deposition exposure of the organic film to the pure oxygen plasma. Hence, emissions from CO*, OH* and H* are evidenced. As shown in figure 7, the normalized intensities of CO* and Hγ* decrease sharply during the first 5 minutes before vanishing. This OES result agrees very well with the evolution of the kinetic $\Delta=f(\psi)$ curve obtained by ellipsometry and evidences an etching process mainly occurring during the first minutes.
Further to this treatment by an oxygen plasma, we exposed a freshly deposited organic film to a pure argon plasma. Again, we used both ellipsometry and OES to evidence any structural modifications of the film. This time, the Δ and ψ values remain almost stable (see figure 8). This is well correlated with the OES analysis which does not show any significant emissions from CO*, OH* or H* (see figure 9). Thus, only a very weak sputtering of the organic film has been evidenced, which has been confirmed by the simulation of the (Δ,ψ) spectroscopic curves.
So, we found a very good correlation between SE and OES for the analysis of the post deposition treatment of an organic film by different plasmas. The simulation of the (ψ,Δ) spectroscopic curves, completed with TEM and Auger analyses, have shown that a thick SiO_2 layer is formed on the top of the organic film treated by O_2 plasma [4]. This is due to the chemical etching the organic part of the $SiO_xC_yH_z$ film by O atoms.

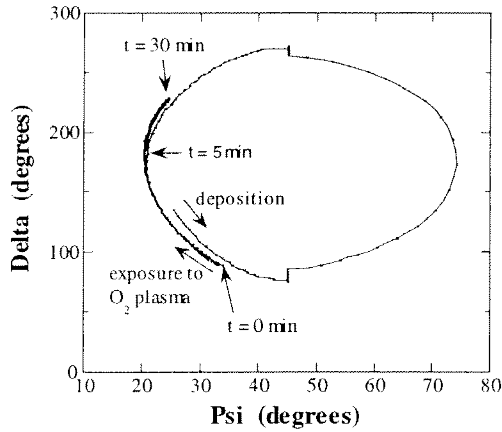

Figure 6: *Real time Δ=f(ψ) curve evolution, at 439 nm, during the deposition of a $SiO_xC_yH_z$ film and its exposure during 30 min to a pure oxygen plasma.*

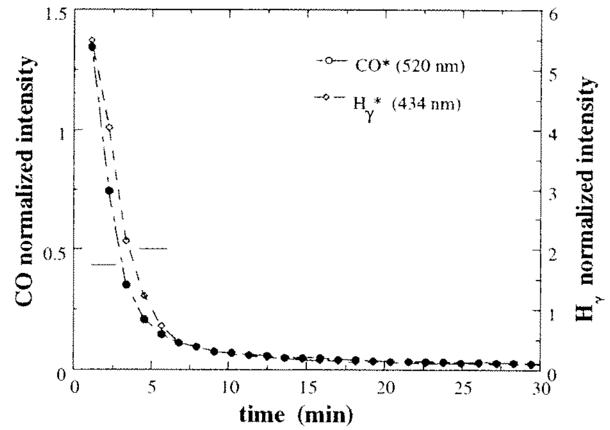

Figure 7: *Evolution of the normalized CO* (520 nm) and Hγ* (434 nm) intensities during the $SiO_xC_yH_z$ film exposure to a pure O_2 plasma*

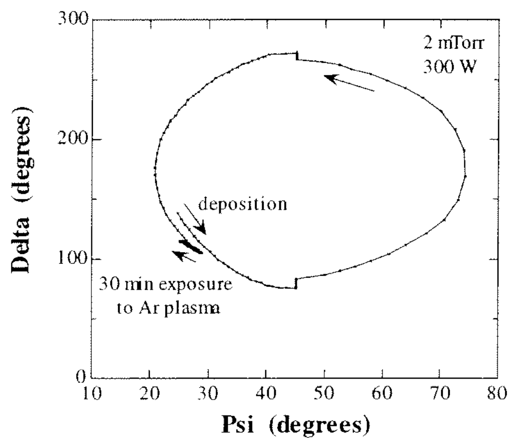

Figure 8: *Real time Δ=f(ψ) curve evolution, at 439 nm, during the deposition of a $SiO_xC_yH_z$ film and its exposure during 30 min to a pure argon plasma.*

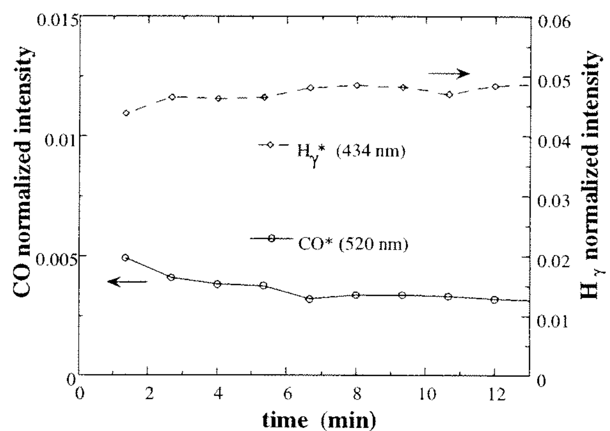

Figure 9: *Evolution of the normalized CO* (520 nm) and Hγ* (434 nm) intensities during the $SiO_xC_yH_z$ film exposure to a pure Ar plasma*

Conclusion

To conclude, we have shown that both optical emission spectroscopy (OES) and *in situ* ellipsometry are very suitable for the monitoring of growth and treatments. This was shown in the specific case of PECVD in O_2/TEOS plasmas, but is likely to be extended to other deposition processes.

References

[1] C.Vallée, A.Goullet, A.Granier, J.P.Deville, A. van der Lee, J.Durand and C.Marlière; submitted to J. Vac. Sci. Technol. A

[2] A.Granier, F.Nicolazo, C.Vallée, A.Goullet, G.Turban and B.Grolleau; Plasma Sources Sci. Technol., **6**, 147-156 (1997)

[3] R.Lamendola and R. d'Agostino; Proceeding of ISPC97, 1257-1258 (1997)

[4] C.Vallée, A.Granier, K.Aumaille, C.Cardinaud, A.Goullet, N.Coulon and G.Turban; Applied Surface Science, **138-139**, 57-61 (1999)

Interaction of SiH_3 radicals with a-Si:H film surfaces, monitored by in situ real time infrared absorption spectroscopy

Achim von Keudell[a] and John R. Abelson[b]
[a]*Max-Planck-Institut für Plasmaphysik, Boltzmannstr. 2, 85748 Garching,*
[b]*Coordinated Science Laboratory, University of Illinois at Urbana-Champaign, Urbana, Illinois 61801*

Introduction

Hydrogenated amorphous silicon films (a-Si:H) are generally prepared from low temperature plasma chemical vapor deposition (P-CVD) using silane [1,2]. Understanding the growth mechanism is important for predicting and controlling the resulting film properties, including hydrogen content, film morphology and defect density. The dominant growth precursor in silane discharges is the SiH_3 radical, if the dissociation of the SiH_4 source gas is kept below ~ 15 % [3-8]. It has been generally assumed that incoming SiH_3 radicals attach to the growing film surface via adsorption at dangling bonds [1-6]. It is well established that dangling bonds can be created by hydrogen abstraction from the film surface due to incoming atomic hydrogen, and it has been assumed that the analogous reaction occurs with incoming SiH_3 radicals; however, no direct evidence has been available.

In this paper we obtain quantitative information about the reaction of SiH_3 radicals with a hydrogenated amorphous silicon surface using in situ real time infrared (IR) spectroscopy. From the change in the IR spectra during exposure of a deuterated (a-Si:D) film to a SiH_3 radical source, we determine the temporal relationship between the loss of SiD groups and the creation of SiH groups. Thereby the creation of SiH surface groups should occur simultaneously with the removal of SiD surface groups during adsorption of the first monolayer of surface SiH, due to the formation of SiH_3D molecules.

In order to resolve the time dependence of the reactions at the growing film surface, the loss and creation of SiD/SiH groups has to be measured with submonolayer resolution. This resolution is usually achieved in IR spectroscopy by sampling over a long period of time (~ 1 h) and averaging the resulting spectra. However, during film growth the time for sampling an IR spectrum has to be smaller than the time for depositing a new Si:H monolayer (~ min). We obtain excellent IR signal enhancement for SiH and SiD vibrational modes using a multilayer 'optical cavity' substrate [13-16] which consists of a double-polished c-Si wafer with a thermal oxide thickness of 1040 nm on both sides and an Al backside coating [15,16].

Experiment

A remote dc plasma source using SiH_4 as source gas is used to generate SiH_3 radicals, as described in reference 10. The pressure in the discharge is ~100 mTorr at a flow rate of 5.5 sccm. Using these parameters at a low dc power, the depletion of the SiH_4 source gas in the discharge is small (~10%), as measured by mass spectrometry [10]. Consequently SiH_3 (silyl) is the dominant radical [3-8]. Through a small orifice (diameter 3 mm) in the grounded electrode, a directed radical beam effuses into a growth chamber which is equipped with an in situ Fourier transform infrared spectrometer. This directed beam can be blocked with a beam stop in order to reduce the growth flux towards the substrate, i.e., only radicals with low

sticking probability (SiH_3) can reach the substrate via multiple reflection off the Si-coated chamber walls.

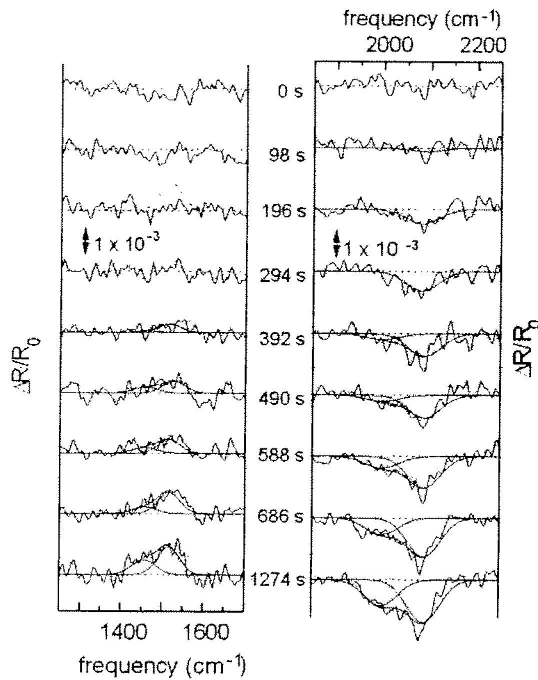

Fig. 1 Change in the reflectivity during exposure of the a-Si:D film surface to the radical beam source with beam stop (low flux). The SiH/SiD bulk and surface modes are fitted with Gaussian peaks.

To produce deuterated samples, a-Si:H films are deposited by the remote plasma source and then exposed to atomic deuterium, generated by a hot tungsten filament at a molecular D_2 pressure of 3 mTorr. The substrate temperature during exposure is also 230^0C. The abstraction and replacement of surface bonded H atoms by gas phase D atoms was detected at a level of 1.5 x 10^{14} atoms/cm^2.

IR absorption spectra are measured in reflectance mode using 500 scans which takes ~ 98 s. The signal to noise ratio is $\Delta R/R$ ~$5x10^{-4}$. The change in the extinction coefficient κ of the sample is calculated from the measured change in reflectance R during growth or exposure to atomic deuterium using a rigorous optical model [13]. An increase in reflectivity corresponds to the removal of SiH/SiD groups and a decrease in reflectivity corresponds to the creation of SiH/SiD groups. The change in the extinction coefficient $\Delta\kappa$ is plotted as $\Delta\kappa$ times film thickness in order to obtain a spectrum proportional to the areal density of hydrogen in the sample. From fitting the extinction coefficient to Gaussian peaks for the individual SiH vibrations, the integrated absorption coefficient for each vibrational mode is determined. The line positions for the SiH and SiD surface and bulk groups are taken from the literature [17-21]. From the integrated extinction coefficient the hydrogen areal density is calculated using known oscillator strengths [22].

Results

A fresh a-Si:D film is prepared by exposing an in situ grown a-Si:H film to atomic deuterium until saturation. This film is then exposed to the radical source. Fig. 1 shows the resulting changes in the reflectivity spectra The decrease in reflectivity at ~ 2090 cm^{-1} after 98 s indicates the creation of SiH surface groups consisting predominantly of monohydrides; the decrease in reflectivity at ~ 2000 cm^{-1} at 392 s indicates the creation of SiH bulk modes and corresponds to the onset of bulk film growth. The increase in reflectivity at 1515 cm^{-1} indicating the removal of SiD surface groups becomes visible only after 392 s, and saturates after 780 s. The reflectivity at 1455 cm^{-1} increases slightly during longer exposure times, indicating a slow release of SiD bulk groups.

The spectra are converted to $\Delta\kappa$ and fit with Gaussian peaks for the SiH and SiD bulk and surface modes. For this quantification we use only one Gaussian peak for the SiH(SiD) bulk mode and the sum of the SiH(SiD) surface modes. The resulting changes in the areal density of hydrogen(deuterium) are shown in Fig. 7. Initially, ~ 0.5 x 10^{15} cm^{-2} SiH surface groups are created before the onset of the formation of SiH bulk modes. Interestingly, the onset of the removal of SiD surface groups after 392 s occurs simultaneously with the creation of the SiH bulk modes, i.e., the onset of bulk film growth. The loss of SiD surface groups saturates

exponentially during film growth as illustrated by the solid line in Fig. 2: during exposure of an a-Si:D film to SiH_3 radicals, SiH surface groups are created *before* deuterium from SiD surface groups is released. In the following section, we present a reaction scheme which is able to explain this result as well as the consequences for a-Si:H film growth.

IV. Discussion

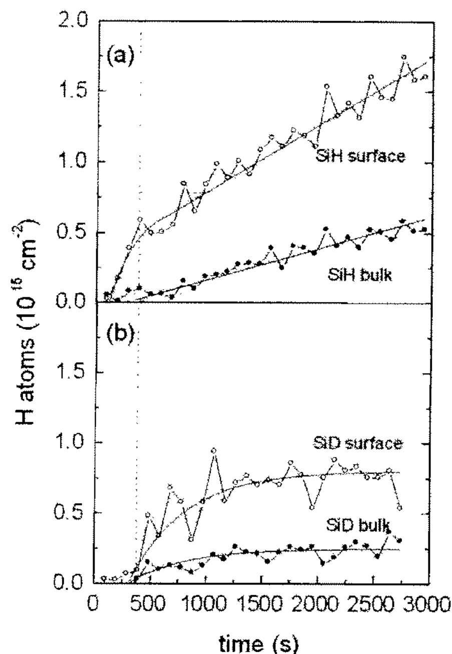

Fig. 2: Variation of the areal density of hydrogen during exposure of the deuterated film to a SiH_3 radical source. (a) Increase of the areal density of SiH surface groups and SiH bulk groups; (b) decrease in the areal density of SiD surface groups and SiD bulk groups

It has generally been assumed that the attachment of SiH_3 radicals to the growing film surface occurs via chemisorption at Si dangling bonds. These dangling bonds are thought to be created when incoming SiH_3 radicals abstract hydrogen [1-6]. However, the exact reaction mechanisms are unknown, due to the lack of detailed experimental data. The creation of one monolayer of SiH groups implies the removal of 1 monolayer of SiD, if it is necessary to create dangling bonds by deuterium abstraction from the initial film surface. The experimental results, as shown in Figs. 1 and 2, directly contradict the above assumption: SiH surface groups are created with no release of surface SiD groups. This asymmetry is illustrated in Fig. 2 for the spectrum taken after 294 s: 0.55 x 10^{15} cm^{-2} SiH monohydride groups are created and according to the reaction scheme 0.55 x 10^{15} cm^{-2} SiD groups should be released. This would lead to an increase in reflectivity at 1515 cm^{-1} as shown by the calculated dotted line, but the data show no such change well within the measurement uncertainty. Therefore the dominant mechanism for SiH_3 insertion during the initial exposure of an a-Si:D film does not require deuterium abstraction.

Therefore we propose an alternative reaction pathway for SiH_3 adsorption, namely, that *the preferred adsorption sites are strained Si-Si bonds at the film surface.* It is known that atomic hydrogen can easily insert into strained dimers at the 2×1 reconstructed Si(100) surface to form the 1×1 reconstruction [12]. At elevated substrate temperatures this 1×1 reconstruction transforms spontaneously back into the 2×1 reconstruction [12]. We propose that the incoming SiH_3 radical follows an analogous reaction pathway. The insertion of a SiH_3 radical into strained Si-Si bonds on the growing a-Si:H film surface will form at first a transition state consisting of a penta-coordinated SiH_3 site [23,24]: $SiH_{3(g)}$ + $Si\text{-}Si_{(s)} \rightarrow Si\text{-}SiH_3\text{-}Si_{(s)}$ (the indices (s) and (g) denote the surface and gas phase, respectively). We assume that the lifetime of the penta-coordinated SiH_3 transition state should be sufficient to lead to a nonzero steady state coverage at the growing film surface. We postulate further that neighboring SiH_3 sites can reconstruct by directly forming a surface monohydride and releasing 2 H_2 molecules: 2 $Si\text{-}SiH_3\text{-}Si_{(s)} \rightarrow Si_2\text{-}SiH\text{-}SiH\text{-}Si_{2(s)} + 2\ H_{2(g)}$. Overall this reaction pathway leads to the attachment of three SiH_3 radicals, the release of two H_2 molecules, and the relaxation of two strained bonds on the initial film surface. *No hydrogen abstraction from the film surface and no creation of dangling bonds is involved in this reaction scheme.* This reaction scheme has several consequences for the understanding of a-Si:H film growth which is thoroughly discussed in reference 25.

Conclusion

We analyzed the interaction of SiH_3 radicals, produced by a remote silane plasma source, with a deuterated a-Si:D film at 230 ^0C using in situ real time IR spectroscopy. 1-2 ML of SiH surface groups are created during adsorption of SiH_3 radicals before the removal of deuterium from the surface is observed. This experimental observation directly conflicts with the assumption that SiH_3 radicals abstract surface D atoms and leave open dangling bond sites on which other SiH_3 radicals attach. This experimental result is explained by postulating a reaction scheme based on insertion of SiH_3 radicals into strained Si-Si surface bonds forming metastable penta-coordinated Si-SiH_3-Si sites. These metastable sites can further reconstruct by the desorption of H_2 molecules. This reaction mechanism leads to a hydrogen rich overlayer present during film growth, which is observed in this work as well as in the literature. This reaction scheme forms a new basis for the development of realistic growth models for a-Si:H growth from low temperature silane discharges as well as for the evolution of microcrystallinity in H_2 diluted SiH_4 discharges.

References

[1] "*Hydrogenated amorphous silicon*", R. A. Street, Cambridge University Press, Cambridge (1992)

[2] J. R. Abelson, Appl. Phys. A **56**, 493 (1993)

[3] A. Matsuda, K. Nomoto, Y. Takeuchi, A. Suzuki, A. Yuuki, J. Perrin, Surf. Sci. **227**, 50 (1990)

[4] J. Perrin, Y. Takeda, N. Hirano, Y. Takeuchi, A. Matsuda, Surf. Sci. **210**, 114 (1989)

[5] J. Perrin, J. Non Cryst. Solids **137&138**, 639 (1991)

[6] K. Maeda, A. Kuroe, I. Umezu, Phys. Rev. B **51**, 10635 (1995)

[7] J. R. Doyle, D. A. Doughty, A. Gallagher, J. Appl. Phys. **68**, 4375 (1990)

[8] J. R. Doyle, D. A. Doughty, A. Gallagher, J. Appl. Phys. **71**, 4771 (1992)

[9] P. Kae-Nune, J. Perrin, J. Guillon, J. Jolly, Jpn. J. Appl. Phys. **33**, 4303 (1994)

[10] A. Nuruddin, J. R. Doyle, J. R. Abelson, J. Appl. Phys. **76**, 3123 (1994)

[11] S. Yamasaki, T. Umeda, J. Isoya, K. Tanaka, Appl. Phys. Lett. **70**, 1137 (1997)

[12] H. N. Waltenburg, J. T. Yates, Jr, Chem. Rev. **95**, 1589 (1995)

[13] M. Katiyar, J. R. Abelson, J. Vac. Sci. Technol. **A13**, 2005 (1995)

[14] M. Katiyar, Y. H. Yang, J. R. Abelson, J. Appl. Phys. 77, 6247 (1995)

[15] A. von Keudell, J. R. Abelson, Appl. Phys. Lett. **71**, 3832 (1997)

[16] A. von Keudell, J. R. Abelson, J. Appl. Phys. **84**, 489 (1998)

[17] M. H. Brodsky, M. Cardona, J. J. Cuomo, Phys. Rev. **B16**, 3356 (1977)

[18] G. Lucovsky, R. J. Nemanich, J. C. Knights, Phys. Rev. **B19**, 2064 (1979)

[19] D. V. Tsu, G. Lucovsky, J. Non Cryst. Solids **97&98**, 839 (1987)

[20] Y. Chabal, G. S. Higashi, K. Raghavachari, V. A. Burrows, J. Vac. Sci. Technol. **A7**, 2104 (1989)

[21] Y. Chabal Int. J. of Mod. Phys. **B7**, 1031 (1993)

[22] A. A. Langford, M. L. Fleet, B. P. Nelson, W. A. Lanford, N. Maley, Phys. Rev. **B45**, 13367 (1992)

[23] J. Xu, W. J. Choyke, J. T. Yates, Jr. , J. Phys. Chem. **101**, 6879 (1997)

[24] P. Avouris, F. Boszo, J. Phys. Chem. **94**, 2243 (1990)

[25] A. von Keudell, J.R. Abelson, Phys. Rev. B (1999) accepted

“IRMA“ a Tunable Infrared Multi-Component Acquisition System for Plasma Diagnostics

J. Röpcke[1], M. Käning[1], J. Anders[2], F. G. Wienhold[2], D. Nelson[3], M. Zahniser[3]
(1) *Institut f. Niedertemperatur-Plasmaphysik, 17489 Greifswald, R.-Blum-Str. 8-10, Germany*
(2) *FhG Inst. f. Physikalische Meßtechnik, 79110 Freiburg i. Br., Heidenhofstr. 8, Germany*
(3) *Aerodyne Research, Inc., 45 Manning Rd, Billerica MA 01821-3976, USA*

Introduction

The monitoring of transient or stable plasma reaction products, in particular the measurement of their ground state concentrations, is the key to an improved understanding of plasma chemistry and kinetics in molecular non-equilibrium plasmas, which are of increasing interest for plasma processing. Infrared tunable diode laser absorption spectroscopy (TDLAS) is a modern promising technique with specific capabilities for effective and reliable on-line process control in research and industry. For plasma diagnostics and control a compact and transportable tunable infrared multi-component acquisition system, “IRMA“, has been developed. The IRMA system contains 4 independent laser stations which can be temporally multiplexed. A multi-path cell is included for exhaust gas detection. Based on rapid scan software using direct absorption with sweep integration, the absolute concentrations of several molecular species can be measured simultaneously within milliseconds and used as digital output for process control. This contribution gives a survey of the optical subsytem, the data processing and the analysis technique. The flexibility and versatility of IRMA is demonstrated at an example of time-dependent species density measurement.

Optical Subsystem

The narrowband infrared emission of four lead-salt diode lasers is used to monitor the infrared absorption features of the target species. The arrangement of the instrument optical table (dimensions: 110 x 60 cm^2) is illustrated in Fig. 1. The four diode lasers are mounted in individual cold stations which are thermally coupled to the cold finger of a closed cycle cryostat (Model RGD 12/45, Leybold GmbH, Köln) by a wire structure etched in a 0.1 mm copper sheet. The temperature of each laser is controlled at milli-Kelvin precision in the range between 30 K and 100 K. A single cold station can be heated up to room temperature and decoupled from the main vacuum to allow laser replacement in typically 90 minutes time with the other laser stations remaining operative.

For each optical channel, the divergent laser emission is brought to an intermediate focus by an off-axis ellipsoidal mirror (OAE) and then collimated by an off-axis parabolic mirror (OAP). A fiber-coupled HeNe laser, an ocular or a reference pin-hole can be placed at the location of the intermediate focus for alignment purpose. During operation, the entrance slit of a grating monochromator, that serves as mode filter, is situated in this position. The blazed grating (90 lines/mm) is used in Littrow configuration with a lateral angle of 12^0 separating the incident and diffracted beam. The desired wavelength is selected by an adequate tilt of the grating towards the optical table.

The light of the four lasers is directed by plane steering mirrors to two combiner plates, each combining two beams. The two dual laser beams are then combined to a single quadruple beam by a third combiner. The two light paths emerging from this element are used for measurement and reference purpose, respectively. The measurement path can either be conducted through a measurement cell external to the optical table after traversing the

monochromator's exit slit in a focus formed by two OAPs, or through an internal multipath astigmatic Herriot cell (New Focus, model 5612). The Herriot cell entrance f-number is matched by an OAP-OAE combination with an intermediate focus which also provides the exit slit position. In the reference path, the spectral absorption from small optical cells containing the target gas at high concentration is monitored as input for a laser emission wavelength control loop (line-locking). In this path, too, a monochromator exit slit position is foreseen at the intermediate focus of an OAP-OAE mirror arrangement.

The two measurement beams and the reference beam are focused on photoconductive infrared detectors (Model FTIR-16, 1.0, Graseby Inc.) mounted in liquid nitrogen cooled dewars. The optical quality of the imagining elements is near the diffraction limit. To avoid unwanted etalon background structure wedge beam combiners and cell windows are used.

Data Processing and Analysis Technique

The data acquisition system for the four-channel tunable diode system consists of two 200 MHz Pentium computers combined with two high speed (300 kHz) boards (Scientific Solutions Lab Master AD boards) and two dual diode laser controllers (Laser Photonics, Model L5831) housed in a single transportable rack (comp. Fig. 4).

The data acquisition method is an advanced form of sweep integration which is carried out by a software package developed at Aerodyne Research, Inc. The software sweeps the laser frequency over the full infrared transition or group of transitions, then integrates the area under the transitions using nonlinear least squares fitting to the known spectral line shapes and positions. Frequency modulation (FM) techniques are not used, because the clear connection between the direct absorption spectrum and the species' concentration is preferred.

There are several advantages to this sweep integration approach. First, absolute species concentrations are returned from the nonlinear least squares fits so that external calibration is not required. The species concentrations may be determined from the absolute spectroscopic data available from the HITRAN or GEISA data bases or from user supplied data. Second, the line shape functions are known from theory and can be precisely calculated. Finally, this detailed understanding of the expected line shapes and positions allows the operator to easily monitor complex and overlapping spectral features using "fingerprint fitting". This is important because monitoring several transitions for one species can enhance sensitivity and is sometimes necessary - especially for larger molecules. In addition, fingerprint fitting allows one to monitor multiple species simultaneously, since overlapping lines can be used, and it even the fitting of unknown lines which overlap the desired spectrum as a method of removing background absorption from unknown species.

The basic functions of the program for controlling two laser diodes are as follows: The software creates a waveform which is used to modulate the frequency of the laser or lasers. The digital waveform is converted to an analog voltage at a rate of 300 kHz using a 12 bit digital to analog converter. Typically 150 points are used to represent the waveforms so that each frequency sweep is 500 μs in duration. The current is varied linearly for a given time period, which causes a variation of the frequency of the laser light that the diode emits. Then the current is lowered to a much lower value which is below the threshold for laser emission. This provides a measurement of detector output in the absence of laser light. Each laser is below its light emission threshold while the other is swept. Both lasers are below threshold at the end of the scan.

The detector output voltage is sampled by an analog-to digital converter using the same data acquisition board. The individual spectra are automatically transferred to the

computer's extended memory using direct memory access. The program divides the data in extended memory into individual sweeps and averages the sweeps to produce one resultant spectrum for each laser. The spectra are coaveraged using assembly language averaging routines in order to maintain a 100% duty cycle. The resultant spectra are analyzed spectroscopically to determine the concentrations or column densities of any species which absorb in that spectral window. The column densities are displayed to the operator, saved to disk and analyzed.

An example spectrum measured in a H_2-CH_4 plasma excited in a GEC reactor (see Refs. [1,2]) is shown in Fig. 2. In that specific case the signal intensity was too low to fully use the capabilities of time resolution, since we had to coaverage spectra about two seconds to get reasonable results. Acetylene and methane were measured by recording the change in absorption of individual rotational-vibrational lines at a frequency 1303 cm^{-1} (7.67 μm). The diode laser was scanned over a spectral region of 0.2 cm^{-1} by varying the laser current in order to obtain a baseline for the pair of spectral lines. The laser was turned off at the end of each scan to obtain the total laser intensity during the scan.

The spectra are analyzed in real-time using the Levenberg-Marquardt non-linear least-squares method to obtain the best fit to the Voigt line shape and a baseline polynomial. Nonlinearity in laser frequency as a function of laser current is described by the laser tuning rate $T = C_1 + C_2 \exp(-C_3 t)$, where t is time since the laser was turned on and the C_i are free parameters which are determined using a germanium etalon. The average CH_4 and C_2H_2 densities in the laser beam were calculated from the measured fractional absorption using the tabulated line strengths and pressure broadening coefficients from the HITRAN data base. The software will fit up to four species simultaneously using up to 45 individual spectral lines per species.

Figure 3 shows, as an example, the result of a stream mode data acquisition giving an example of online measurements useful especially for process control. In the graph one can see how the change of methane admixture to hydrogen and switching the plasma on/off influences the species densities of CH_4 and C_2H_2 (which were calculated using the lines shown in Fig. 2) in the laser beam path. Further details of these measurements can be found in references [1,2].

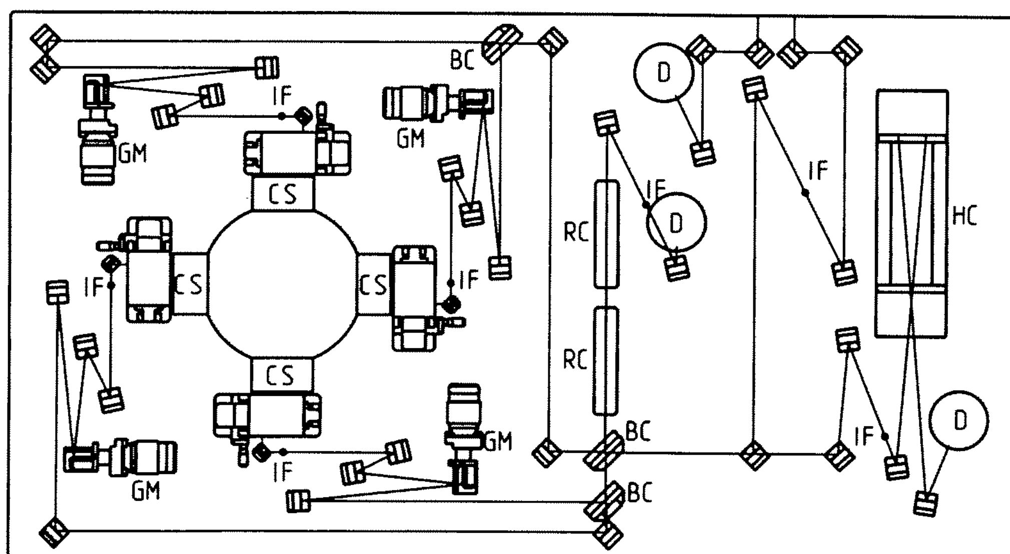

Figure 1: *Setup of the IRMA Optical Table, BC: beam combiner, CS: cold station, D: detector, HC: Herriot cell, IF: intermediate focus, GM: grating monochromator, RC: reference cell.*

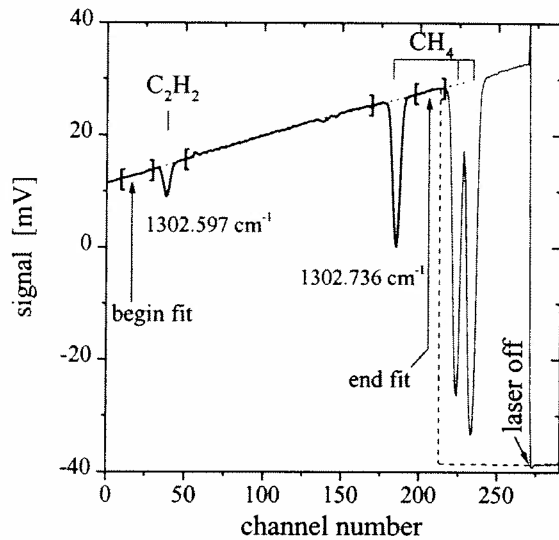

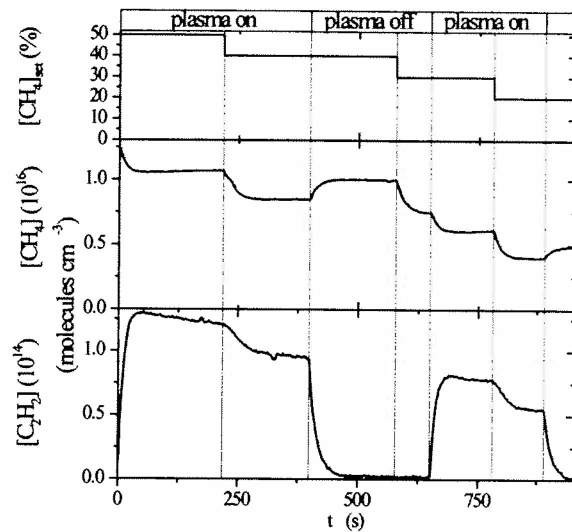

Figure 2: *Measured and fitted absorption spectrum of methane and acetylene in a H_2-CH_4 plasma ($[H_2]:[CH_4] = 1:1$, $\phi_{total} = 66$ sccm, p = 100 Torr, P = 50 W).*

Figure 3: *Results of stream mode data acquisition of species densities with varying methane admixture using the absorption lines from Fig. 2.*

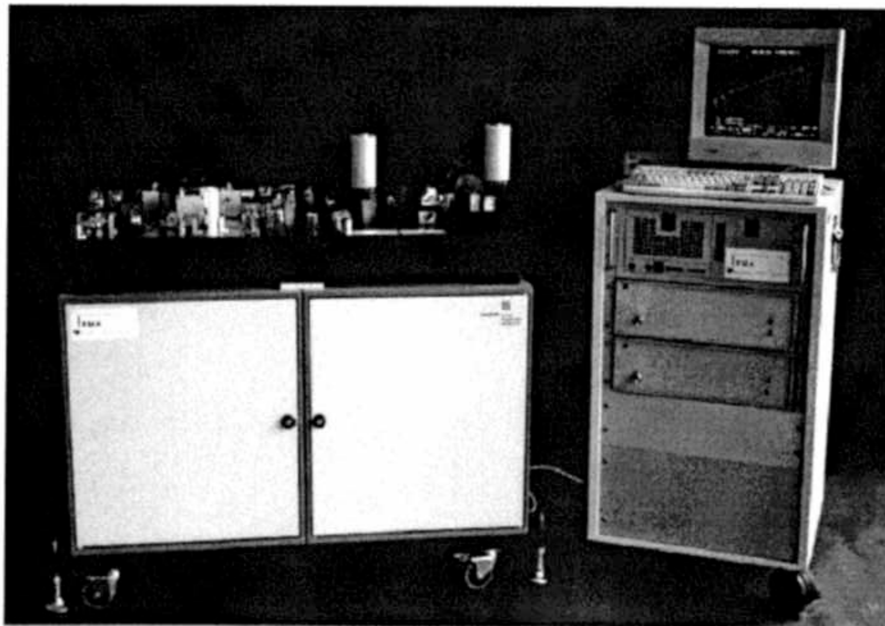

Figure 4: *Photograph of the "IRMA" system: left - optical table, right - data acquisition rack with diode laser controllers and industrial computers.*

Acknowledgments: The authors are indebted to J.P.F. Conrads for general support of the project and thankful to M. Tacke, M. Knothe and W.J. Riedel for their cooperation.

References

[1] C. Lukas et al, *"Diagnostic Studies of a Capacitively Coupled RF Plasma Containing CH_4-H_2-Ar, Part I: On the Radial distribution of Species and Temperature"*, same issue.
[2] M. Käning et al, *"Diagnostic studies of a capacitively coupled RF plasma containing CH_4-H_2-Ar, Part II: On CH_4 dissociation and hydrocarbon plasma chemistry"*, same issue.

Ion flux and electron temperature measurements with an insulator-covered planar electrostatic probe

J.P.Booth[1], N.St.J.Braithwaite[2], A.Goodyear[2], F.Neuilly[3] and J-M.Francou[3]

[1]Laboratoire de Spectrométrie Physique, Université Joseph Fourier-Grenoble, France
[2]The Open University, Oxford Research Unit, Foxcombe Hall, Boars Hill, Oxford, UK
[3]Centre Commun ST-Microelectronics-CNET, Rue Jean Monnet, Crolles, France

Introduction

The vast majority of electrostatic probe measurements are made with small (<< 1 mm diameter) cylindrical probes, which are often used for probing the Electron Energy Distribution Function (EEDF) in the low energy region without, in principle, excessively perturbing the system under investigation. Larger area *planar* probes have seen much less usage, despite the fact that they have certain advantages over cylindrical probes and give complementary information. They are particularly adapted for measuring the I/V characteristic in the positive ion current region. If careful attention is paid to ensuring that the sheath in front of the probe is truly planar (using a guard ring to suppress edge effects), then the positive ion flux to the surface, Γ_i, can be considered to be independent of the probe potential (at least for reasonable applied voltages that do not significantly perturb the plasma). In this case, when the applied voltage is sufficiently negative to repel all electrons, the net current collected saturates at a value equal to $e\Gamma_i$. A planar probe located in the reactor wall therefore gives a direct measurement of the ion flux to that wall, a parameter that can only be deduced from cylindrical probe characteristics by the use of one of several contradictory models. A further advantage of planar probes is that the probe characteristic in the electron retardation region gives a good measurement of the EEDF in the important high-energy tail region. This is due both to the fact that the larger probe area gives bigger signals in this low-flux region of the characteristic, and that the positive ion current, that must be subtracted, is well known (in contrast to cylindrical probes where $\Gamma_i(V)$ must be modelled).

A practical disadvantage (and possibly the reason why planar probes have been so little used) is that it is not possible to keep the large probe surface clean by the technique of intense electron current heating used routinely for smaller cylindrical probes. However, a novel technique has been proposed recently (1,2) that allows planar probe *I/V* characteristics to be determined even with dirty probe surfaces. The probe is capacitively coupled, and *transient* currents are measured through the capacitor (which can be the insulating film on the probe surface). The probe is biased negative with respect to floating potential by the application of a short burst of RF power via the capacitor, using the well known DC bias effect (3), and is swept back towards floating potential as the capacitor discharges. Consequently, only that part of the *I/V* characteristic more negative than the floating potential is accessible.

In this article we will look in more detail at how to extract accurate information about the plasma from the observed signals. In particular we will look at the effect of insulating films on the probe surface. The conditions necessary to observe correct saturation of the ion current were investigated, particularly the use of correct geometry and biasing for the guard ring. Information can also be obtained about the electrical properties (and, indirectly, the thickness) of these films.

The capacitively-coupled RF-biased planar probe technique

The experimental configuration is shown in Fig.1. A short RF impulsion (10 MHz, 60 V p-p, 1 ms) is applied to the probe surface via a capacitor, C_x, (a few nF). After the end of the impulsion, positive ion current flows to the probe surface and discharges the capacitor. As the impedance of the RF generator is small, the current flowing can be deduced simply from the observed voltage by

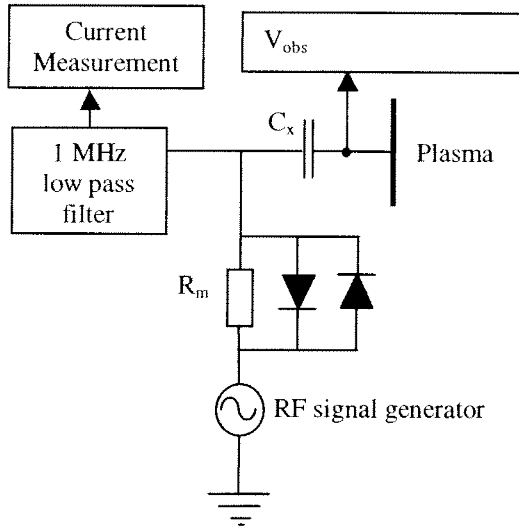

Figure 1 *The measurement circuit*

$$I_{obs}(t) = C_x \frac{dV_{obs}}{dt} \quad (1)$$

However, the differentiated signal is extremely noisy, particularly if there is a large 13.56 MHz signal from the plasma generator superposed on V_{obs}. An improved way to determine the current is also shown in Fig.1. Here the image current returning to the RF generator side of C_x is deduced from the voltage across a load resistor, R_m. The head-to-tail diodes are necessary to pass the high-amplitude RF signal during the RF biasing step. The value of R_m (~ 1kΩ) is chosen so as to give an adequate signal (~ 10-100 mV) without causing appreciable commutation of the diodes. This current measurement technique gives significantly cleaner measurements, $I(t)$, than those obtained by differentiating the voltage.

The effect of insulating layers on the probe surface

Now let us consider what happens when there is a dielectric film on the probe, of capacitance C_f. The high frequency RF signal used to bias the probe will be unaffected, provided the effective capacitance, given by

$$C_{eff} = \frac{C_x C_f}{C_x + C_f}, \quad (2)$$

does not become so small that it is comparable to the sheath capacitance, C_{sh}. Therefore, the initial potential seen by the plasma (at the film surface-plasma interface) at the end of the RF impulsion is unchanged, as is the initial current to the probe. However, the effective capacitance is now smaller than C_x, and therefore discharges more quickly. Furthermore, the observed voltage is no longer equal to the voltage seen by the plasma, V_{probe}, but is related to it by:

$$V_{probe} = V_{obs} \cdot \left(\frac{C_x + C_f}{C_f} \right) \quad (3)$$

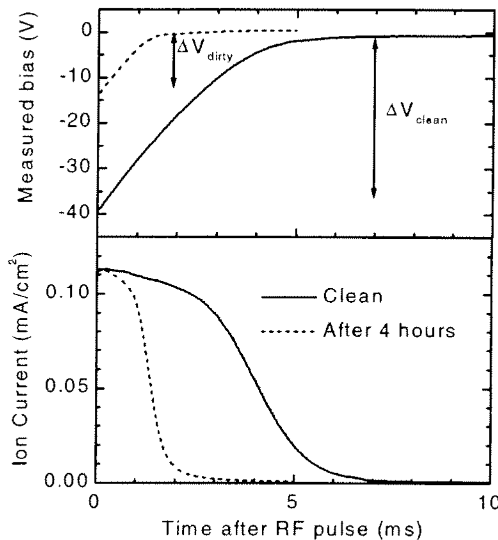

Figure 2 *Effect of an insulating layer on the probe: C_2F_6 RIE plasma, 50mTorr 100W, C_x = 10 nF, C_f = 5.2 nF ⇒ thickness = 400nm.*

Fig. 2 shows the corresponding signals observed in a C_2F_6 plasma, both with a clean probe, and after 4 hours plasma treatment, by which time a film several 100s nm thick has been deposited. The film capacitance can be estimated from the decrease in the observed

initial bias. Defining ΔV_{clean} as the difference between the initial observed bias and the observed floating potential when the probe is clean, and ΔV_{dirty} that observed when the probe is dirty, we obtain

$$C_{eff} = C_x \frac{\Delta V_{dirty}}{\Delta V_{clean}} \quad (4)$$

The film thickness, d, is then given by

$$d = \left[\frac{\Delta V_{clean}}{\Delta V_{dirty}} - 1 \right] \frac{\varepsilon_o \varepsilon_r A}{C_x}, \quad (5)$$

where A is the probe area and ε_o, ε_r are the permitivity of free space and the film dielectric constant, respectively. This technique is only possible, however, if it is possible to start with a strictly clean probe, or at least with a film of known capacitance.

Ion flux measurements

In order to obtain a good absolute measurement of the ion flux it is necessary to assure that edge effects are properly suppressed by using a guard ring of adequate size and biased to the same potential as the probe throughout the discharge period. The guard ring is designed to extend the probe sheath sideways at least as far as the maximum sheath thickness. This can be estimated on the basis of Poisson's equation: about one Debye length for every square-root of normalised potential (eV/kT). Failure to achieve this design limit is evident in the I-V plot as an incomplete saturation of the ion current at large bias. This effect can be investigated by plotting the I/V characteristic, obtained by eliminating time and plotting I_{obs} against V_{obs}. as seen in Fig. 3. Correct adjustment of the guard ring biasing is a delicate task. However, if only relative measurements are required the guard ring can be dispensed with entirely. Fig 4 shows results obtained in an industrial inductively-coupled etching reactor during silicon wafer processing. The probe consisted of a single 1-cm^2 anodised Al electrode, and is totally compatible with reactive chemical environments.

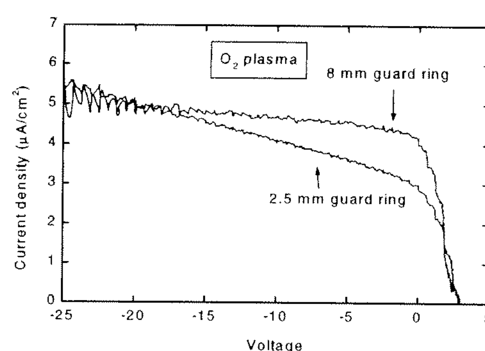

Figure 3 *Effect of the guard ring size on the I/V curve: 50 mT O_2, 50W RF.*

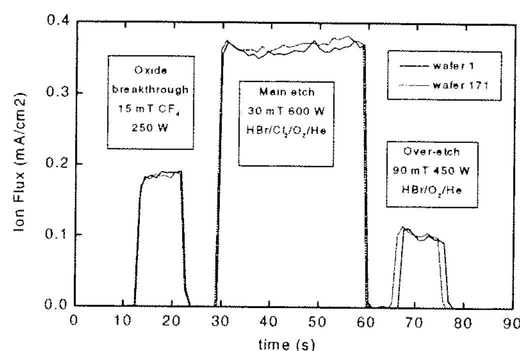

Figure 4 *Ion flux during an industrial etching.process*

Electron temperature measurements

Analysis of the I/V curve allows the EEDF to be determined in the important high-energy tail region, provided that edge effects are properly suppressed, and that the voltage is corrected according to equation (3). An example of an I/V curve obtained with an SiO_2 –coated probe, with a fit (assuming a single Maxwellian EEDF) to determine electron temperature, is shown in Fig. 5.

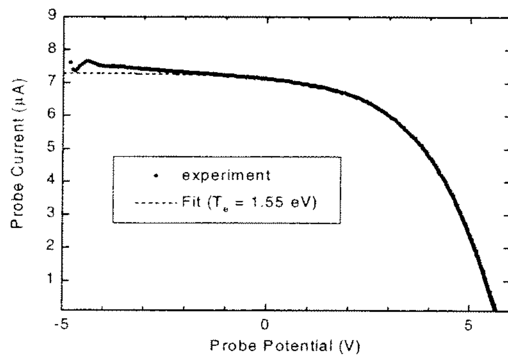

Figure 5. *I/V curve for a coated planar probe in a 100 mtorr 25 W argon plasma. The probe was coated with 400nm of SiO_2 by Applied Vision Ltd, UK.*

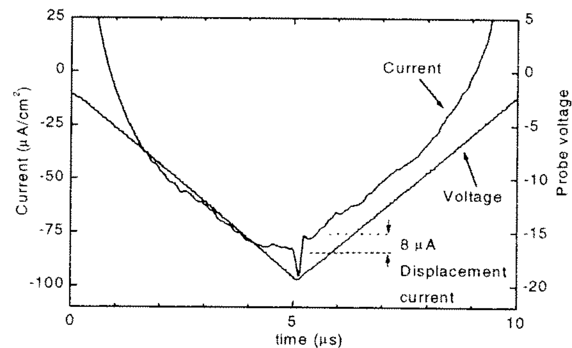

Figure 6. *Current to a DC-coupled clean planar probe with triangle wave biasing in an Ar plasma*

One further effect needs attention: thick films on the probe lead to rapid voltage sweep rates at the probe surface. This can ultimately lead to distortion of the I/V curve. Fig. 6 shows the current to a (clean) planar probe biased by a rapid DC-coupled triangle-wave voltage signal. Marked hysteresis is observed, due firstly to the displacement current that must be supplied to charge the sheath capacitance, and secondly due to the positive ion inertia in the collapsing sheath. These effects set a maximum film thickness that is acceptable on the probe surface during electron temperature measurements of the order of 10 μm (but depending on the insulating material and the plasma conditions).

Conclusion

The design and operation of an RF biased planar probe has been specified, particularly as a surface mounted diagnostic. The probe materials and configuration are compatible with a wide range of low pressure plasma processing systems. The probe gives real time information on ion flux and also provides a measure of the tail of the EEDF.

Acknowledgements

This work was supported in part by EPSRC grants GR/L78864 and GR/L82380. Pierre Barroy of ESPEO, Orleans is acknowledged for his assistance with the coated probe work done at the OU Oxford Research Unit during a 3 month training programme, as are Applied Vision Ltd for their provision of probe coatings.

References

(1) N. St. J. Braithwaite and J. P. Booth, Patent No. FR901451, France, 1995

(2) N. St. J. Braithwaite, J. P. Booth, and G. Cunge, Plasma Sources, Sci. Technol. **5,** 677 (1996).

(3) K. Kohler, J. W. Coburn, D. E. Horne, E. Kay, and J. H. Keller, J. Appl. Phys. **57,** 59 (1985).

Poster Session I

Experimental study of the recombination of atomic oxygen on fused silica

Cartry Gilles *, Magne Lionel *, Cernogora Guy **

* *Laboratoire de Physique des Gaz et des Plasmas*

Bât. 210, Université de Paris Sud

91405 Orsay cedex, France

** *Service d'Aéronomie CNRS*

Université de Versailles Saint Quentin

78035 Versailles cedex, France

Introduction

This work is devoted to the experimental study of the recombination of oxygen atoms on fused silica surface. The oxygen surface recombination takes on a particular interest in the study of Space Shuttle atmospheric re-entry. Actually, during the atmospheric re-entry phase at supersonic velocity, the created shock wave dissociates both the oxygen and nitrogen molecules. Atoms are then likely to recombine on the silicon dioxide based thermal protection tiles of the shuttle, leaving to the surface the excess energy and contributing to its heating. As the shuttle velocity is decreasing, only the oxygen molecules are dissociated [1]. Hence, studying alone the oxygen recombination on silica based surface is of practical and theoretical interest. Furthermore atomic oxygen sources are used in a wide range of industrial applications such as improvement of wettability and adhesion properties of polymer or as growth of superconductor materials. As the oxygen sources are often designed using quartz or Pyrex vessel, the study of atomic recombination is also of great interest in their optimisation. In the present work, oxygen atoms are created during a short pulsed discharge and are monitored in the time afterglow by VUV resonant absorption spectroscopy. It is well known that under our experimental conditions the main loss process of atomic oxygen is reaction at the wall. Therefore, the atomic density decrease in the time afterglow is directly correlated to the surface reaction processes.

Experimental set up

The absorption diagnostic and its calibration have already been presented in a previous work [2]. We briefly remind here the main features concerning the experimental device.

The experimental set up is shown in figure 1. The discharge tube, 50 cm long and 1.9 cm inner diameter, is made of fused silica and is closed at each extremities by MgF_2 windows allowing V.U.V radiation transmissions. The VUV resonant absorption spectroscopy diagnostic used here, requires the knowledge of the gas temperature because of the Doppler broadening of the absorption lines. Hence, the pulse duration is set as low as possible in order to avoid any heating of the gas (20 μs). A weak gas flow of 1 sccm is maintained in order to remove impurities. This flow rate is low enough to neglect the atomic loss by convection to the pumping device. The repetition frequency is set to 0.17 Hz in order to ensure that the gas is fully removed between two pulses. The current and the pressure during the pulsed discharges are set to respectively 400 mA and 1 Torr. The tube is lighted at one side by VUV

radiation emitted by a low-pressure (0.1 Torr) Penning discharge (Damany source). The three lines of the resonant atomic triplets $O(^3S^0) \rightarrow O(^3P_j)$ at 130.217 (j=2), 130.487 (j=1) and 130.604 (j=0) nm are emitted with a high intensity and a good stability. In order to minimise the self-absorption, the Damany source is working in a mixture of helium (98 %), nitrogen (1%) and oxygen (1%). The emitted lines are absorbed along the tube by oxygen atoms and the transmitted signal is analysed in wavelength by a 50 cm VUV focal length monochromator (ASM 50 Jobin Yvon). The transmitted light for the selected wavelength is detected by a Solar Blind photomultiplier (EMI 9413B). The cut off of this detector for high wavelengths (210 nm) allows working with the second order of the grating without any overlapping with the first order. The PM output signal is connected to a fast amplifier followed by a multi-channel scaler (SR 440). Incoming photons are counted by the analyser during 1.3 ms windows, and 4000 windows (5.2 s) are used to sample the time afterglow. The recorded signals are then transferred to a microcomputer in order to be analysed.

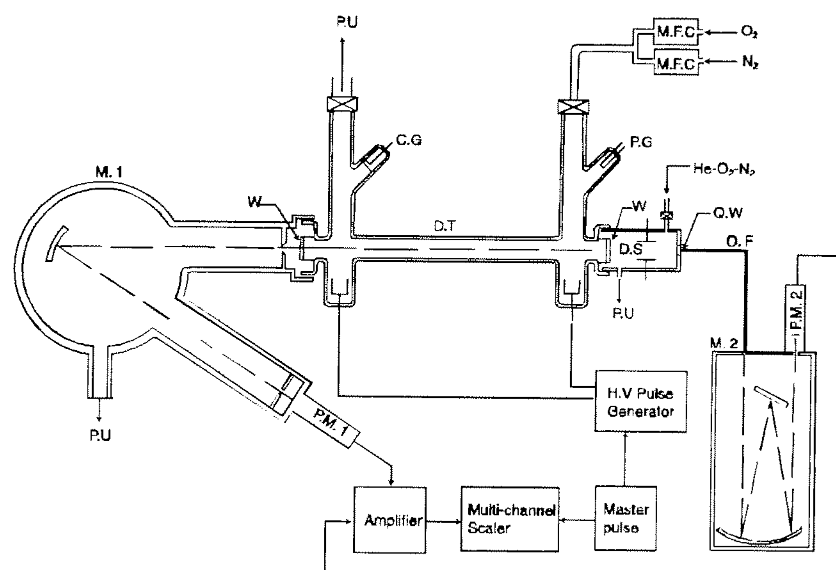

Fig.1: Experimental set up. P.U: Pumping units, C.G: Capacitance gauge, P.G: Pirani gauge, M.F.C: Mass flow controller, D.T: Discharge tube, W: MgF_2 window, Q.W: Quartz window, D.S: Damany source, O.F: Optical fibre, M.1: VUV monochromator, M.2: monochromator, P.M.1: Solar blind photomultiplier, P.M.2: Photomultiplier.

Experimental results

The surface state is a crucial parameter with respect to the loss of atoms. The presence of adsorbed species or impurities can strongly influence the oxygen interaction with the wall. In order to perform each experiment with the same surface state, a DC discharge in pure oxygen is maintained during 30 minutes before the measurements of atomic oxygen concentrations in pulsed discharges. Thirty minutes are sufficient to obtain a very good reproducibility of the experiments. As was shown by Cartry et al [3], the DC discharge can be used not only to ensure the cleanliness of the wall but also to prepare different initial surface states. Therefore, the DC discharge experimental conditions take on a particular importance.

For the results presented here the DC discharge was conducted under a pressure of 0.3 Torr, a flow rate of 10 sccm and a current of 60 mA. After the wall tube has returned to the room temperature, pulsed DC discharges are performed under a pressure of 1 Torr and for the conditions mentioned above. Each atomic measurement requires an accumulation of the signal on several afterglows to reduce the ratio noise/signal. The notation n° i-j on the figure 2

means that the signal has been accumulated between the pulses number i and j (usually j-i =5). The figure 2 presents the obtained results. For the first pulses, the atomic oxygen decrease is very fast (n° 1-5 on the figure). This decrease is going slower and slower as the number of pulses is increasing, and finally reaches a steady state condition for which no more evolution is measured, even after several hours of pulsed discharges. The final decrease is obtained for approximately 80 afterglows. The same experiment was also performed using a different preparation of the wall. The DC discharge conditions were: 2 Torr, 1 sccm and 60 mA. In that case, the final decrease is immediately reached and no evolution of the atomic loss at surface is observed.

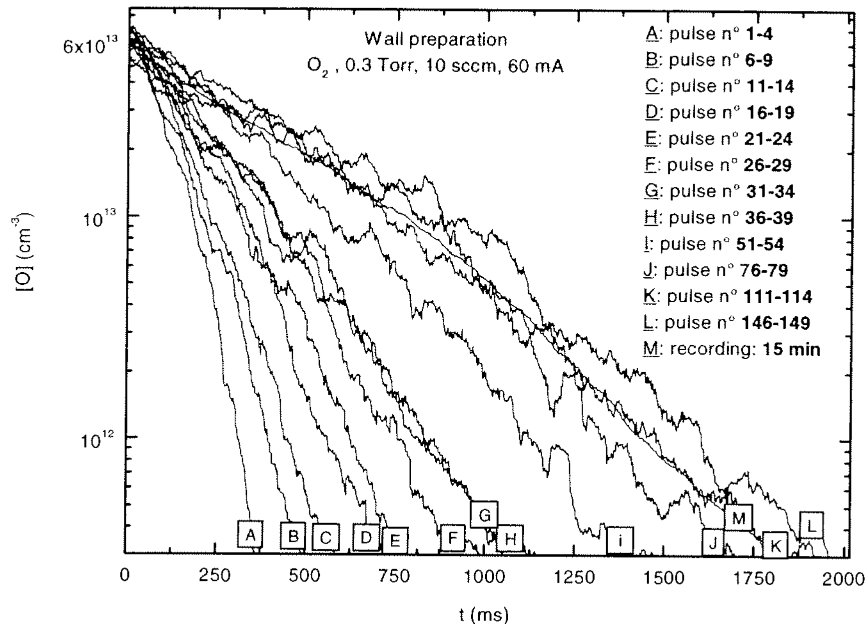

Fig.2: Atomic oxygen decrease in the afterglow

As was said above, under the present low-pressure experimental conditions, the main atomic loss process is reaction at the wall. Hence, an evolution of the oxygen loss probability can only be attributed to an evolution of the surface state and more precisely to an evolution of the coverage of the chemisorption sites. We have at the present time two hypothesis to explain the evolution of the atomic decrease.

Our first hypothesis is that after the wall treatment, most of the chemisorption sites are empty. Hence, we observed during the first pulses a very strong adsorption of oxygen atoms on vacant chemisorption sites. As a consequence, the oxygen decrease in the afterglow is very fast. The atomic oxygen flux being not sufficient to cover all the sites in one afterglow, this process is pursuing during the successive afterglows. The sites are filled gradually and we observe an evolution of the atomic decrease. When the evolution limit is reached, an equilibrium between adsorption on vacant sites and recombination on occupied sites is established. The coverage of the chemisorption sites is constant and does not change with the following pulses.

The second hypothesis is symmetrical about the first one. The chemisorption sites are assumed to be for their most part occupied by chemisorbed oxygen atoms after the wall treatment. In this way, the fast decrease during the first pulses is attributed to a strong recombination of oxygen atoms and the evolution is attributed to the cleaning of the chemisorption sites that modify the atomic interaction with the wall. The final decrease also

means here that an equilibrium between recombination and adsorption is reached. Nevertheless, for the second treatment (2 Torr and 1 sccm), the atomic concentration during the DC discharge is surely higher than for the first treatment, and it is expected that the coverage of the active sites will be higher. Therefore, the first hypothesis seems to be the most probable.

Whatever is the adopted explanation, the evolution is assumed to be the consequence of an evolution of the coverage of the active sites. The dependence of the oxygen atom surface reaction probability (β) with the coverage of the active sites is observed. The variation of β with temperature provides a lot information concerning the processes of surface recombination [4]. It is our opinion that the variation of β with the coverage of the active sites can also gives rise to a better knowledge of the basic processes governing atomic reactions at surface.

An exponential fit of the atomic decrease has been achieved in order to obtain the value of the surface reaction probability for oxygen on silica. Of course we do not obtain a single value but a range of variation of this probability. Table 1 shows the result obtained and compares it with published values. All the values presented are for 300 K. Our values are in good agreement with most of these values.

[4]	[5]	[6]	[7]	Present work
4.8×10^{-4}	1.6×10^{-4}	3.5×10^{-4}	5.1×10^{-4}	8.6×10^{-5} - 4×10^{-4}

Tab.1: Surface reaction probability of atomic oxygen on silica.

To conclude we would like to stress the importance of the experimental method and the diagnostic used. Actually, this study would have been very difficult or impossible using another diagnostic. Titration or thermocouple methods are adapted for spatial afterglow but are not for temporal afterglow. LIF or pulse reexcitation can be used in temporal afterglow but would not have allowed to observe the surface state evolution. Atomic decrease observation by these methods requires a long signal acquisition in order to sample the afterglow and to obtain an accurate signal. Furthermore absolute concentrations are not easily obtained by these diagnostics. On the contrary, the VUV absorption spectroscopy allows real time measurements of the absolute atomic oxygen concentration and of its evolution in the afterglow.

References

[1] Seward W A and Jumper E J 1991 *J. Therm.* **5** 284-291

[2] Magne L, Coitout H, Cernogora G and Gousset G 1993 *J. Phys. III France* **3** 1871-1889

[3] Cartry G, Magne L, Cernogora, Touzeau M and Vialle M 1997 *XXIII International Conference on Phenomena in Ionised Gases (Toulouse, France)* **II** 70-71

[4] Kim Y C and Boudart M 1991 *Langmuir* **7** 2999-3005

[5] Greaves J C and Linnett J W 1959 *Transactions of the Faraday Society* **55** 1355-1361

[6] Dickens P G and Sutcliffe M B 1964 *Trans. Faraday Soc.* **60** 1272-1285

[7] Diamy A M, Legrand J C, Al Andari J 1997 *New J. Chem.* **21** 177-185

Electron Density Measurements using the Microwave Cavity Technique Applied to Large Area PECVD Industrial Reactors

L. Chevalley, L. Sansonnens, A. A. Howling, C. Monard and Ch. Hollenstein
EPFL-Centre de Recherches en Physique des Plasmas, Switzerland

Introduction

The free electron number density n_e is a fundamental parameter for defining plasma conditions. A measurement of n_e would therefore be useful for industrial process monitoring provided that it could be made directly and reliably without requiring extensive interpretation, expensive hardware, or perturbation to the plasma process. A straightforward technique is to measure the shift in resonance frequency Δf of a microwave cavity in the presence of the plasma with respect to its value in vacuum. Typically, the plasma reactor is designed as a cylindrical cavity with a single resonant mode, and the measurement is a spatial average of the electron density profile weighted by the electric field power density [1]; the advantage of using a single eigenmode is that the distribution of the electric field is known. However, the form of industrial reactors is dictated by plasma process requirements, not by the cavity diagnostic. Large area PECVD reactors are flat rectangular boxes which, consequently, are strongly overmoded cuboid cavities presenting a complicated frequency spectrum of many superposed resonant modes. In this paper we show that, by selectively exciting only one mode across the RF electrode gap, the frequency product $f \cdot \Delta f$ of all the cavity modes is identical because the plasma is designed to be uniform over the planes parallel to the electrode surface. Therefore, the shift of any part of the frequency spectrum waveform can be measured, giving a simple routine diagnostic for n_e in large area industrial plasma reactors.

Experimental arrangement of the reactor and microwave cavity diagnostic

Figure 1 shows a modified version of the industrial KAI-S "plasma box" reactor commercialised by Balzers AG for thin-film deposition. It consists of a grounded box which encloses a RF electrode suspended 2.4 cm above the reactor floor. The plasma therefore completely fills a cuboid cavity of internal dimensions 47 cm width x 57 cm length x 2.4 cm height which is grounded on all sides except for the RF electrode. The process gases are introduced through a showerhead in the RF electrode, whose back-face centre is capacitively-coupled to the matching network and RF power source. The residual gases are pumped out through the back wall which is a coarse grid. The interelectrode RF voltage amplitude is constant, to within a few per cent, over the electrode area for RF frequencies up to 70 MHz [2], and the plasma is horizontally uniform as judged by light emission measured across its width, and by the uniform film thickness deposited on the 35 cm x 45 cm glass substrates placed centrally on the reactor floor.

A low power microwave signal from a sweep generator (Wavetek model 965) was coupled into the reactor through a sidewall via an X band (8.2 - 12.4 GHz) waveguide, whose height approximately matches the 2.4 cm electrode gap (Fig. 1). Electrical continuity at the reactor wall was maintained by means of a vertical grid, which is transparent to the horizontal electric field of the waveguide TE_{10} mode. If necessary, the waveguide exit can be protected by a thin dielectric window (high purity alumina). The cavity frequency response was monitored by an identical waveguide connected to a crystal square-law detector (Hewlett Packard HP 423B), whose DC output voltage is proportional to the microwave power level, connected to a digital oscilloscope triggered synchronously with the microwave sweep generator. The location of the launcher and detector waveguides is not critical, but the best signal level was obtained for opposite (Fig. 1), or adjacent, positions in the sidewalls perpendicular to the pumping grid.

The plasma reactor is installed inside a larger vacuum chamber, and so the microwave instruments are connected, via coaxial cable vacuum feedthroughs, to microwave adaptors mounted on the reactor sidewalls. To withstand the high temperatures (250 °C) and aggressive gases without deterioration or outgassing, the adaptors, cable and connectors were custom-built using aluminium and alumina, based on the design of the Hewlett Packard X281A model. Even simpler antennae than the adaptors could be envisaged, such as electrodes embedded in ceramic mounted in the sidewalls, according to industrial limitations of space and cost.

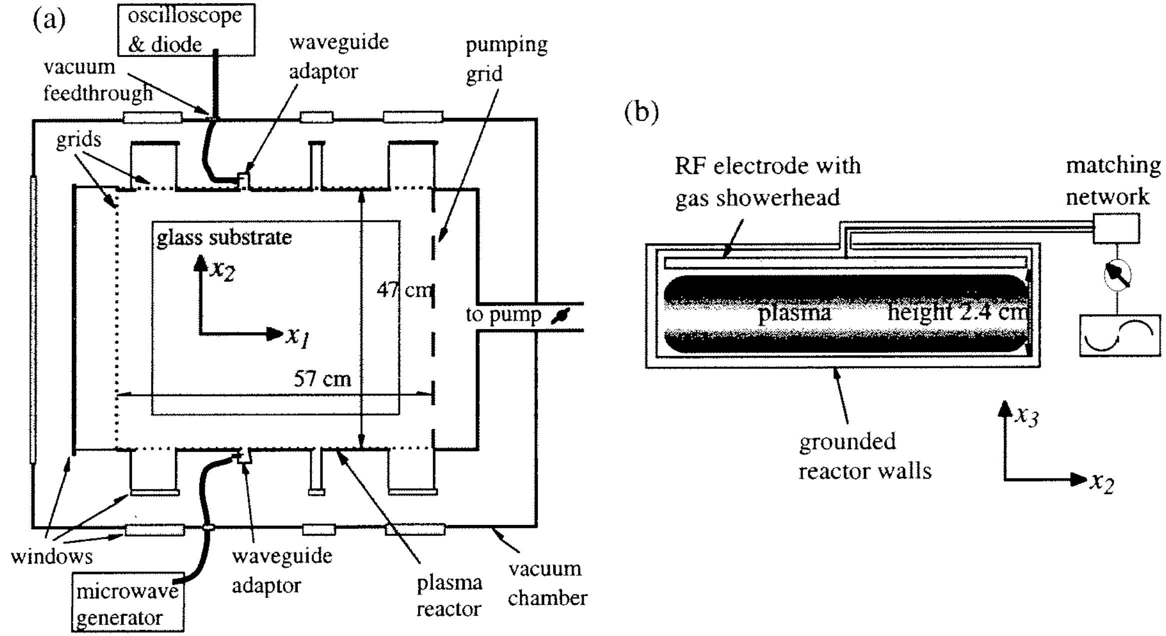

Figure 1: *Schematic of the experimental arrangement, a) plan view; b) side view.*

Basic relations used in the microwave cavity technique

Resonant cavities have discrete frequencies of oscillation with a definite field configuration for each resonance frequency. The shape and the size of the cavity impose the field configuration for a given mode, whereas its resonance frequency also depends on the permittivity of the medium inside the cavity. The frequency shift caused by a plasma is related to the free electron density by [1]:

$$n_{e0} = \frac{2m_e\varepsilon_0\omega^2}{e^2}\frac{\Delta\omega}{\omega_0} \tag{1}$$

where n_{e0} is weighted over the spatial electric field power distribution:

$$n_{e0} = \frac{\int_{cavity} n_e(\vec{x})E^2(\vec{x})d\vec{x}}{\int_{cavity} E^2(\vec{x})d\vec{x}} \tag{2}$$

Usually, the cavity technique employs only one spatially well-defined mode to determine the electron density [1]. Our experimental situation allows us to avoid this problem: In a cuboid cavity, the resonance frequencies are given by:

$$f_{n_1,n_2,n_3} = \frac{c}{2}\sqrt{\left(\frac{n_1}{L_1}\right)^2 + \left(\frac{n_2}{L_2}\right)^2 + \left(\frac{n_3}{L_3}\right)^2}\ , \ n_1,\ n_2,\ n_3 = 0,\ 1,\ 2,\ 3... \tag{3}$$

The TE_{10} mode in the waveguide launches an electric field oriented in the plane parallel to the electrodes. Using the X-band in our cavity where L_3 = 2.4 cm, the boundary condition of zero tangential electric field at the electrode surfaces means that only modes with n_3 = 1 can be excited. The resultant electric field of the allowed cavity modes is therefore an undetermined mixture of the modes $\vec{E} = E_0\cos\left(\frac{n_1\pi}{L_1}x_1\right)\sin\left(\frac{n_2\pi}{L_2}x_2\right)\sin\left(\frac{\pi}{L_3}x_3\right)\vec{e}_1$. However, the requirement of uniform deposition in an industrial reactor means that n_e is independent of x_1 and x_2, and therefore, the value of n_{e0} calculated by (2) is independent of the spatial distribution of the electric field along x_1 and x_2. Thus, equation (2) simplifies to give:

$$n_{e0} = \frac{\int_0^{L_3} n_e(x_3)\sin^2\left(\frac{\pi x_3}{L_3}\right)dx_3}{\int_0^{L_3} \sin^2\left(\frac{\pi x_3}{L_3}\right)dx_3} \tag{4}$$

which is the electron density averaged over its profile between the electrodes. This is the key to measuring n_e in a large, flat overmoded cavity by the microwave technique. Even if the signal intensity at a given frequency is a superposition of many resonating modes (which could well be the case since L_1 and L_2 are large compared to the wavelength), all these modes should shift by the same frequency, so that the measurement of n_{e0} is nevertheless well defined.

Measurement and identification of individual eigenmodes

A typical spectrum from a frequency sweep shows a certain number of discrete peaks with a repetitive structure. The spectral mode density is lower than calculated using equation (3). In fact, there is a strongly selective measurement of certain modes for three principal reasons: Firstly, the position of the launcher and of the detector preferentially excites and detects modes whose anti-nodes correspond to the position of the launcher and of the detector. Secondly, the walls corresponding to $x_1 = 0$ and $x_1 = L_1$ have both a very low Q-factor because of the fact that one wall is used for pumping and presents a large number of holes, and the other one is a grid (see Fig. 1). The reactor is therefore almost a tunnel-like cavity due to these poorly-defined boundaries. Consequently, modes with high n_1 are practically absent. The third reason explaining the selective observation of modes is that the position of the launcher and of the detector is at a wall where the would normally be zero (due to the wall boundary condition for a tangential E-field): for that reason, the modes with a high n_2 are preferentially excited because the electric field must vary rapidly along x_2 in order for some component to exist close to the waveguide apertures. In conclusion, the modes with small n_1, large n_2, and $n_3 = 1$ are preferentially observed. This was checked by laterally displacing the reactor walls $x_2 = 0$ and $x_1 = L_1$, with the launcher and detector fixed on the wall at $x_2 = L_2$: Displacing the wall $x_1 = L_1$ did not affect the global appearance of the spectrum, whereas displacing the wall $x_2 = 0$ displaced the peaks of the spectrum with a spatial period $\lambda = c/f \approx 3$ cm (at 10 GHz). From these considerations, we could identify the mode frequencies, as shown in figure 2.

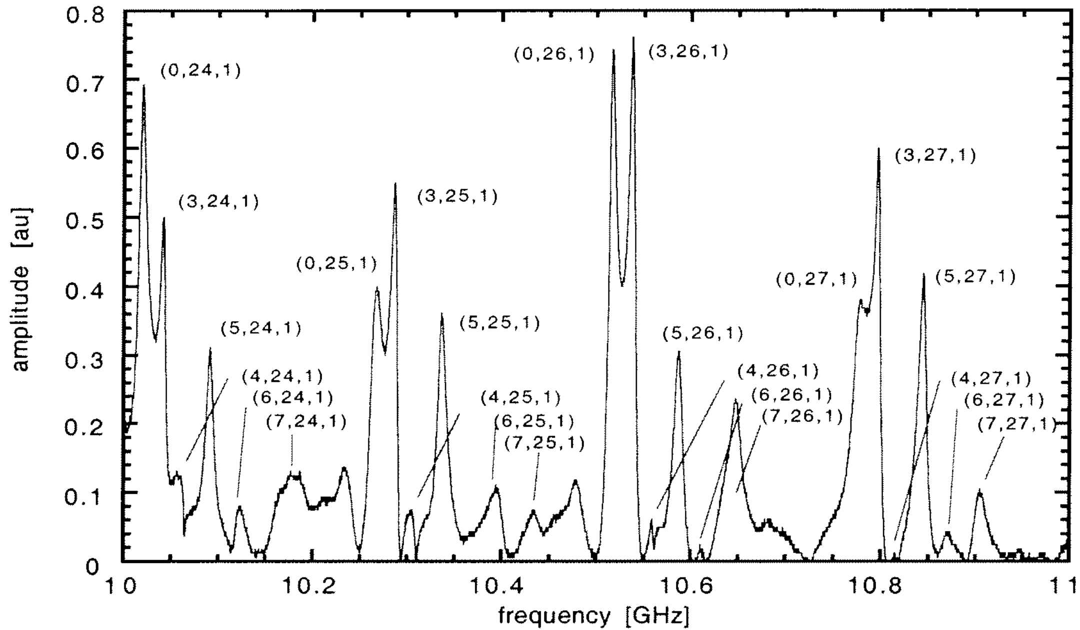

Figure 2: *Measured spectrum and calculated mode frequencies in the large area reactor (with no windows).*

Quality factor of the large area cavity

The quality factor of the cavity can be determined experimentally from the full-width-at-half maximum, $\Gamma = \omega/Q$ [1]. For an ideal cavity in aluminium, the theoretical value is $Q \approx V/A\delta$ where V is the cavity volume, A the wall area, and δ the skin-depth given by $\delta = (\pi\sigma f\mu_0)^{1/2}$ (σ is the wall conductivity, f the frequency, and μ_0 the vacuum permeability). One obtains for our cavity $\delta = 1.7 \cdot 10^{-6}$ m and $Q \approx 6'500$. To determine the real Q-factor of our cavity, we consider the double peak which is principally due to the modes (0,26,1) and (3,26,1) of figure 2. By fitting the sum of Lorentzian curves, corresponding to the modes in figure 2, we find $\Gamma = 9$ MHz, giving a quality factor of about 1150 comparable to that found by Stoffels *et al* [1]. This is largely under the calculated Q-factor because the cavity is not ideal.

The frequency spectrum in figure 3 shows a measurement, averaged over 50 acquisitions on a Lecroy digital oscilloscope, during a 60 W plasma in argon at 0.3 torr. The launcher and detector were placed oppositely in walls $x_2 = 0$ and $x_1 = L_1$. The double peaks in figure 2 are here convolved into a single, broader peak because the cavity Q-factor was further degraded by the window apertures used for other diagnostics as shown in figure 1.

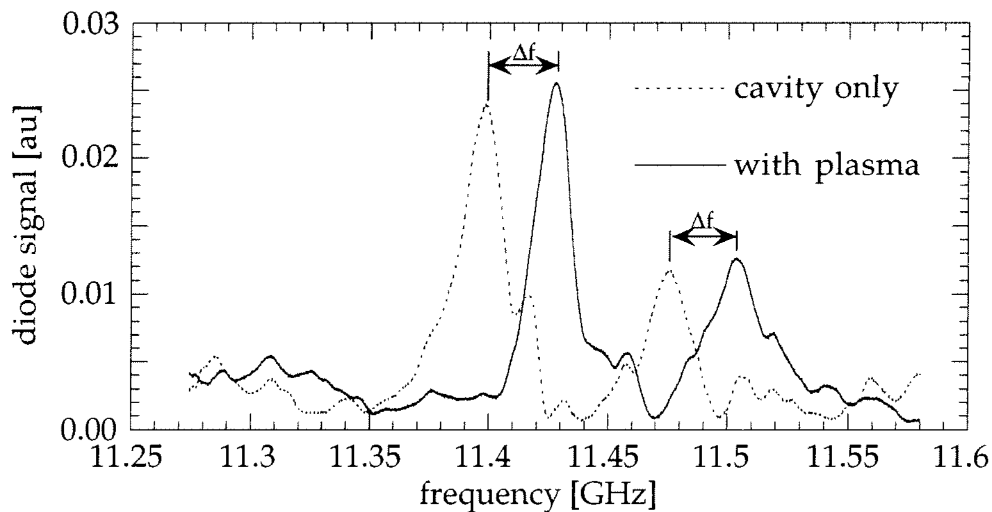

Figure 3: *A typical measurement, showing the spectrum shift with plasma (with window apertures).*

Conclusions

The microwave cavity technique for direct measurement of the free electron density has been demonstrated to be a convenient, inexpensive and reliable diagnostic even for large area industrial reactors. The method yields an absolute value for the electron density interelectrode profile weighted over the $\sin^2$ electric field distribution. Individual resonant modes can be identified, although the frequency shift of any part of the spectrum can be used. A sensitivity of better than 10^7 electrons$\cdot$m^{-3} can readily be obtained even without high precision equipment.

Acknowledgments

We thank Dr. S. Alberti for advice and discussions. This work was funded by Swiss Federal Research Grant BEW 9400051.

References

[1] E. Stoffels, W. W. Stoffels, D. Vender, M. Kando, G. M. W. Kroesen and F. J. de Hoog, Phys. Rev. E **51**, 2425 (1995).

[2] L. Sansonnens, A. Pletzer, D. Magni, A. A. Howling, Ch. Hollenstein and J. P. M Schmitt, Plasma Sources Sci. Technol. **6**, 170 (1997).

Toward a fully monitored Fourier Transform Infrared Spectroscopic Ellipsometry

J.-C. Cigal, G.M.W. Kroesen
Eindhoven University of Technology
The Netherlands

Introduction

Ellipsometry can be defined as the measurement of the state of polarization of a polarized light wave. Infrared (IR) ellipsometry has emerged few years ago as a powerful sensitive and non-intrusive optical instrument for characterizing of surfaces, interfaces and thin films. This technique is used in order to obtain information about an optical system that modifies the state of polarization. First applications were roughly limited by the performances of grating and prism spectrometers used at that time and also by the lack of good light sources and good polarizers. The recent improvement of Fourier transform techniques and of polarizers, like tandem wire grid polarizers which were developed in our group [1], helped to overcome such problems. In the next future, real time measurements will allow the unveil of plasma enhanced etching and deposition. This article reports the last advances in our set-up.

Interest of Spectroscopic ellipsometry

After a reflection on a sample surface, a linearly polarized light beam is generally elliptically polarized. This is due to the fact that the reflected light has phase changes that are different for electric field components polarized parallel (p) and perpendicular (s) to the plane of incidence.

A measure for this change of polarization ρ is usually written in polar form in terms of the two ellipsometric angles Ψ and Δ as follows:

$$\rho \equiv \tan \Psi \, e^{i\Delta} \equiv \frac{R_p}{R_s}$$

The tangent of the angle Ψ and the angle Δ are the relative amplitude change and the relative phase shift between the two polarization directions, respectively. R_p and R_s are the overall complex amplitude reflection coefficients of the optical system.

By assuming a modeling of stacked layers on the top of a substrate surrounded by an ambient, Rp and Rs are given by:

$$R_p = \frac{r_{01p} + r_{12p} e^{-2i\beta}}{1 + r_{01p} r_{12p} e^{-2i\beta}}$$

$$R_s = \frac{r_{01s} + r_{12s} e^{-2i\beta}}{1 + r_{01s} r_{12s} e^{-2i\beta}}$$

where $r_{..p}$ and $r_{..s}$ represent the local reflection coefficients at the interface between the media, and β denotes the phase thickness defined as :

$$\beta = \frac{2\pi d \left(n_1^2 - n_0^2 \sin^2 \phi_0\right)^{\frac{1}{2}}}{\lambda_0}.$$

Here ϕ_0 represents the angle of incidence, n_0 the refractive index of the incident or the ambient medium, n_1 the refractive index of the thin film 1, d the thickness of the layer and λ_0 the wavelength in the ambient medium (see Figure 1).

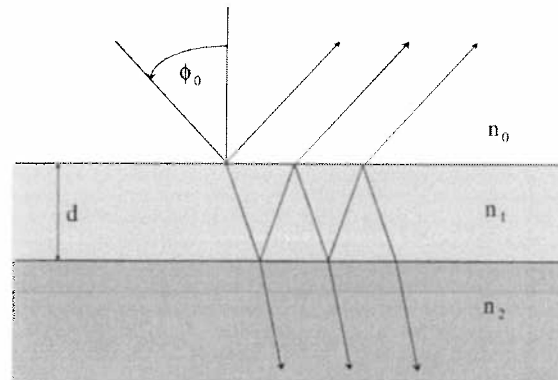

Figure 1: *A plane electromagnetic wave propagating in an ambient (index* n_0*) reflects at a system consisting of a substrate (*n_2*) covered by a layer (*n_1*).*

Hence, by performing ellipsometric measurement as a function of wavelength, one can deduce the different physical parameters of the complex surface sample, such as real and imaginary part of the refractive index, thickness, components of the layer, chemical bounds.
Furthermore, the development of Fourier transform spectrometers, consisting essentially of Michelson interferometers allowed an improvement in ellipsometric measure in a large part of the infrared spectrum (7000 cm^{-1} to 200 cm^{-1}), with an acquisition time remaining short enough to perform real-time measurements.
Thus, by combining the sensitivity of ellipsometry and the accuracy and the velocity of Fourier Transform Infrared (FTIR) spectrometer, one can bring to light processes of etching and deposition.

A spectroscopic rotating compensator ellipsometer

Among the different techniques in use in ellipsometry, we opted for a rotating compensator ellipsometer. This technique offers several advantages compared to other ellipsometry methods, like the non ambiguous determination of Δ, the insensivity to source and detector polarization, the self calibration of the compensator. However, one principal fact prevented a widespread application of rotating compensator ellipsometry for spectroscopic purposes. This fact was the absence of a good spectroscopic retarder. This problem was solved by den Boer *et al.* who developed a spectroscopic retarder [2]. An other limitation, to further application, was the time needed for data acquisition. The light leaving the Michelson interferometer enters the ellipsometer , passes the polarizer, reflects on the sample, passes the compensator, the analyzer and finally hits the detector. Compensator, for measurements, and polarizer and analyzer, for calibration, are driven by stepping motors. To combine the different types of instruments, it was necessary in the last set-up to temporarily stop the rest of them while one is moving. That means that during measurements, the compensator is only moving during time intervals the Michelson interferometer is not measuring, the rest of the time the compensator is held at a fixed position.

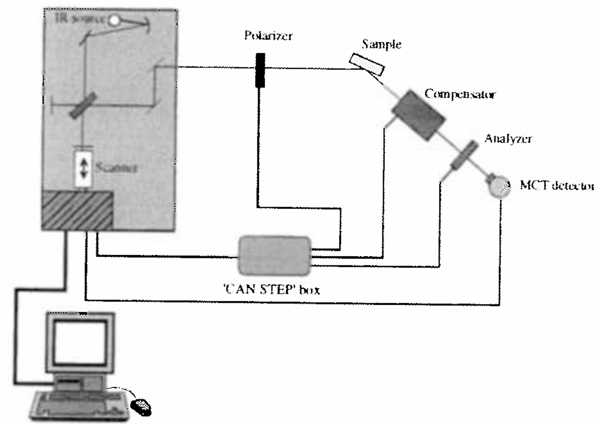

Figure 2: *Experimental set-up. By means of the 'CAN STEP" box, all the stepping motors are synchronized with the interferometer driver. The whole set is monitored by a PC.*

A tremendous improvement in measurement speed can be obtained, by an accurate synchronization between the scanner of the spectrometer and the stepping motors.
In order to improve the performance of the set-up, the interferometer has been modified and a 'CAN STEP' box was built to connect the stepping motors to the interferometer driver. Thus, data exchange is now performed only between a PC and the interferometer and stepping motors movements are synchronized with the scanner driver.
Preliminary results obtained with this setup will be discussed in detail.

References

[1] J.H.W.G. den Boer, G.M.W. Kroesen W. de Zeeuw, and F.J. de Hoog, Optics Letters **20**, 800-802 (1995)

[2] J.H.W.G. den Boer, G.M.W. Kroesen, and F.J. de Hoog, Meas. Sci. Technol. **8**, 484-492 (1997)

Diagnostics of Plasma Torch Fluctuations

J.-L. Dorier*, Ch. Hollenstein*, A. Salito°, M. Loch°, and G. Barbezat°
EPFL-Centre de Recherches en Physique des Plasmas, Switzerland
° Sulzer Metco AG, Wohlen, Switzerland

Introduction

Plasma spray coating is a well-established industrial technology which has achieved outstanding technological and commercial progress in the aeronautics, gas turbine, and biomedical industries [1]. In spite of this success, the underlying fundamentals are still poorly understood [2]. This leads to limitations not only for the reliability and reproducibility of the present techniques but also for further developments of new coatings. These limitations mainly come from the instabilities of the arc and the strong electrode erosion [2]. Up till now, improvements in torch stability and electrode wear reduction were based on empirical procedures, which have reached their limits. Further improvements of the processes need, amongst other things, a basic understanding of the arc physics and of the plasma jet dynamics [3].
The arc inside the torch nozzle experiences instabilities [4] which give rise to so-called "surging" and "whipping" motions of the plasma jet at the exit of the nozzle [3]. In addition, the arc tends to restrike upstream when it is lengthened due to the flow drag. A lot of R&D effort has been put into new torch designs to control arc fluctuations [5] and in process control and subsequent adjustment of the spraying parameters [6]. However, this has not yet convinced the manufacturers of plasma spraying systems, and the intrinsic performances of commercial plasma spraying guns can still be improved. The commercial plasma spraying systems usually control the spraying parameters only on the basis of experience in the form of recipes, or by successive testing until a good quality coating is obtained. Clearly, the measurement of the physical parameters of the plasma jet, and of their dependence on the operation conditions can significantly improve reliability and control of the spraying processes. Moreover the development of new coatings can also profit from this knowledge.
In this paper several diagnostics of the plasma torch are described. In particular, measurements of the temporal evolution and of the power spectra of the fluctuations in the torch voltage and current, the acoustic pressure and emission of the plasma jet evidence the instability of the arc, in connection with the electrode erosion and the working parameters. A time of flight technique has been set up which allows the estimation of the plasma jet velocity in the hottest regions.

Experimental arrangement

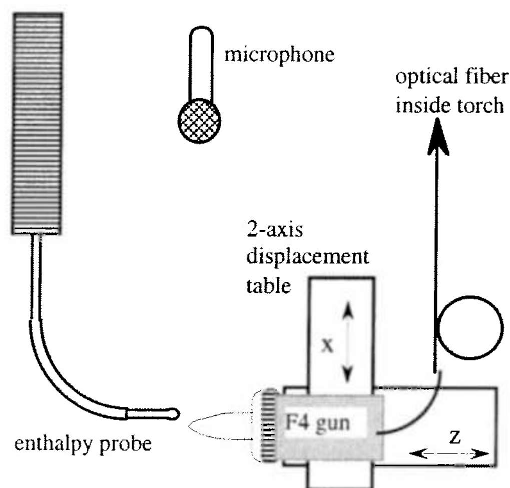

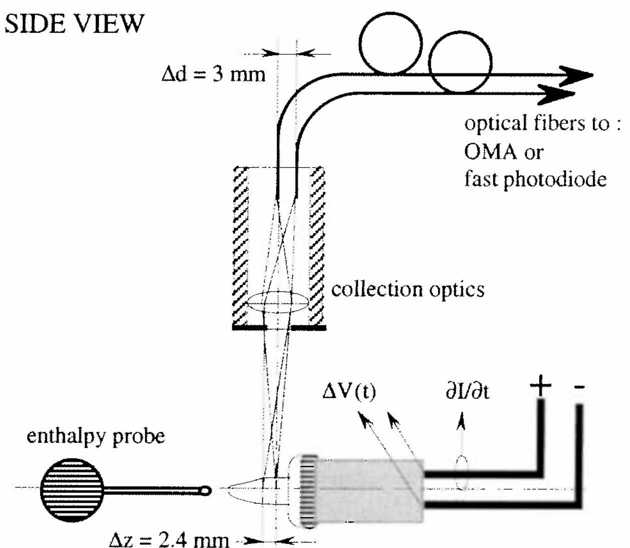

Figure 1 : *Top and side views of the experimental arrangement showing the F4 gun and various diagnostics*

The plasma torch investigated is a Sulzer Metco F4 gun equipped with a 6 mm diam. atmospheric anode nozzle, a thoriated tungsten cathode and a swirl gas injector. In this work the torch is operated at atmosphere without powder injection using a fully automated Multicoat™ control system. Typical operating parameters are: 500 A current, 50 SLM Ar alone or with 2 SLM H_2, up to 50 kW of electrical power with a torch efficiency of about 40-50%, depending on the gas mixture. The gun (Figure 1) is mounted on a 2 axis displacement table with the jet axis horizontal, and the various diagnostics are fastened on a static frame. The arc voltage is measured directly at the gun electrodes with a differential passive voltage probe (÷20, bandwidth DC-2 MHz). The time derivative of the torch current is measured with a Rogowsky coil (4.3 10^{-7} Vs/A, 50-10^5 Hz bandwidth) mounted around the anode current feed line. A microphone at 90° is positioned 1.2 m from the jet axis. An optical collection system, positioned 435 mm above the plasma jet, uses a lens (30 mm diam. aperture, 200 mm FL) which focuses the jet light emission onto 50 µm diam. optical fibers with a spatial resolution of about 0.08 mm. The collected light is either fed into a monochromator (OMA) for spectroscopy or detected by fast Si-PIN photodiodes with pre-amp for fluctuation measurements (bandwidth DC-1 MHz, adjustable gain). All the fluctuation signals are recorded by a digital oscilloscope and acquired on a PowerMacintosh via GPIB interface for further analysis. A commercial enthalpy probe system is also shown on figure 1.

Fluctuation measurements

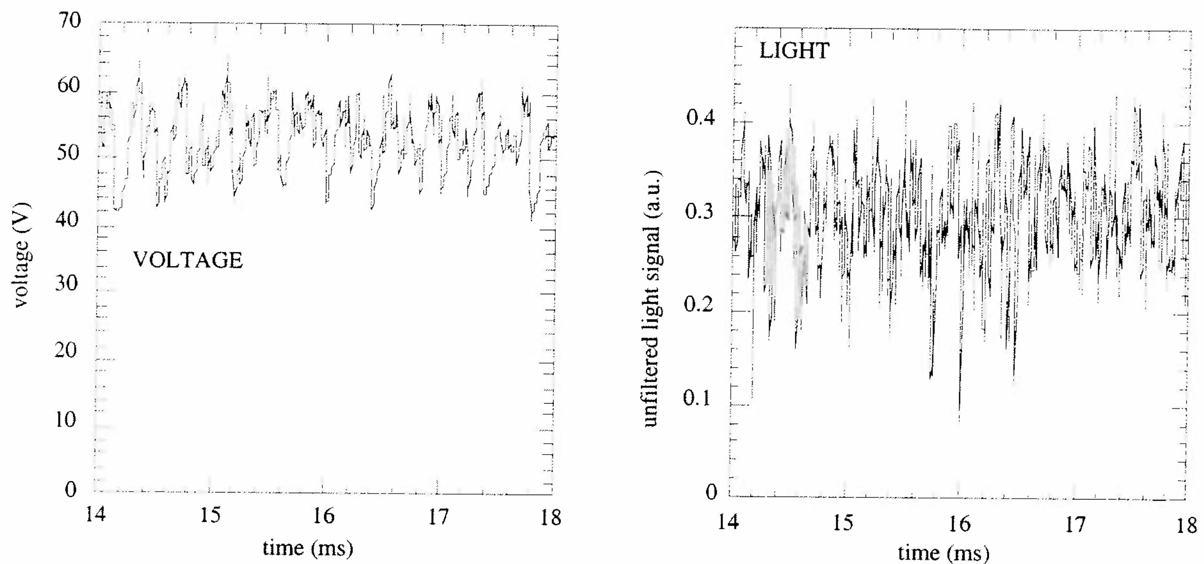

Figure 2 : *Time dependence of the torch voltage and jet light emission on axis at 5 mm from nozzle exit (H_2/Ar 2/50 SLM, 500 A).*

Figure 2 shows a typical time history of the fluctuating torch voltage and jet light emission for a H_2/Ar plasma at 500A. The unfiltered light emission is collected on the jet axis, at 5 mm from the nozzle exit. These signals show that the voltage fluctuation amplitude (peak-to-peak) represents about 45% of the mean level of 52 V, whereas the light fluctuation amplitude reaches 100% of the mean level. It should be noted that the plasma emission in the visible measured here is extremely sensitive to the local temperature variations for the temperature range considered here (10-15.10^3 K). On the voltage signal, one can find out a sawtooth pattern, which is typical of the restrike mode of the arc inside the torch [7]. The faster oscillations of smaller amplitude which are superimposed might be attributed to the orbital motion of the anode arc root induced by the swirl gas flow. Statistical analysis of the voltage and light signals has shown that the deepest voltage drops are correlated with the strongest emission reductions. This shows that the arc restrike is probably responsible for the strongest temperature transient drops. Other less important temperature oscillations evidenced by the emission fluctuations are associated with the cold air mixing and turbulence in the plasma jet. Measurements of the arc emission fluctuations using the optical fiber inside the torch exhibit much smaller amplitude variations. Since the arc temperature (above 20000K) is much higher than the jet temperature,

the line and continuum emission strengths are less sensitive to temperature variations of the arc, and therefore the light fluctuations are less important. It should be noted that, for a pure Ar plasma, the fluctuation amplitude is much smaller (several % for the voltage and less than 30% for the plume emission. Moreover, no sawtooth pattern is observed on the voltage signal in this latter case.

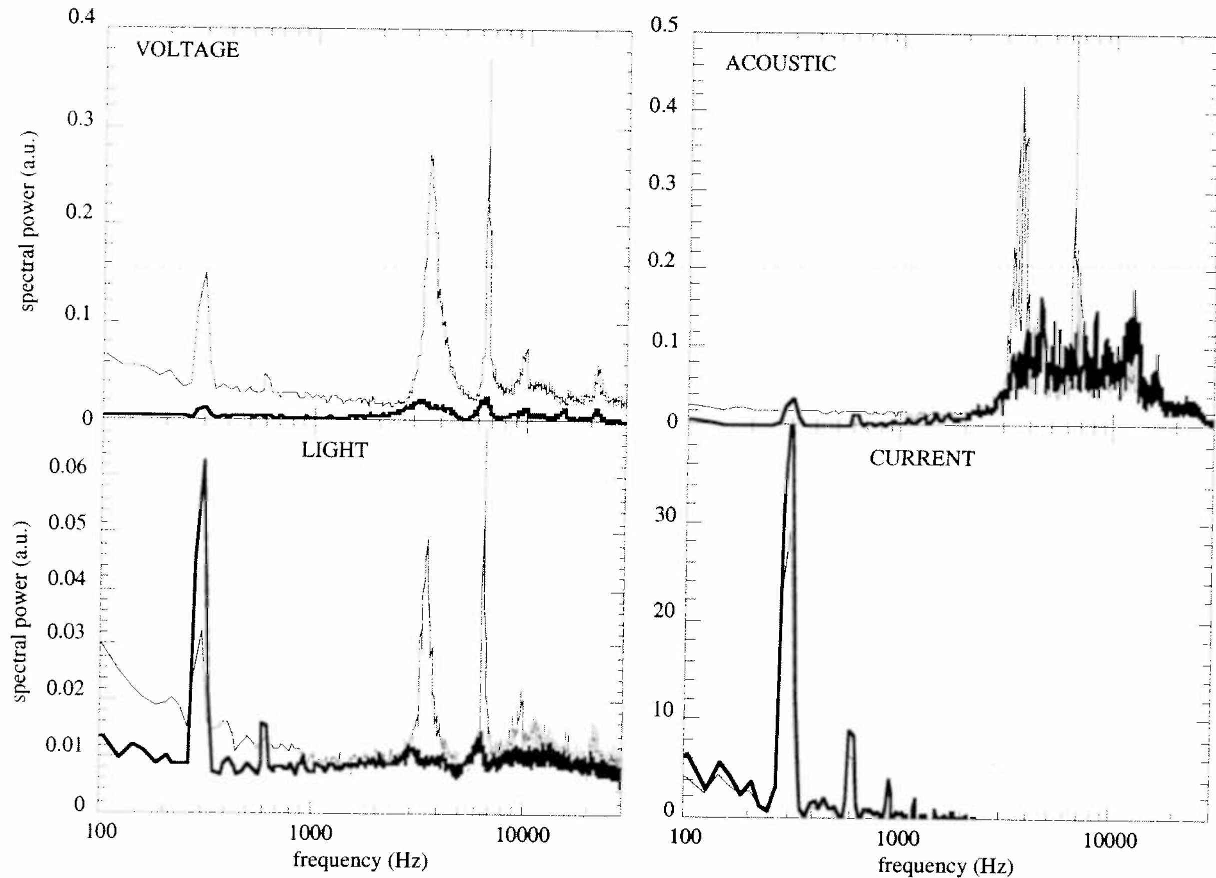

Figure 3 : *Power spectra of the torch voltage, current, the jet acoustic pressure and light emission on axis at 5 mm from the nozzle exit for two plasma conditions : 2/50 SLM H_2/Ar (plain) and 50 SLM pure Ar (**bold**) at 500 A.*

Figure 3 shows the power spectra of the voltage, light emission, acoustic pressure and current for pure Ar and Ar/H_2 plasmas. The power spectra are obtained numerically using a FFT algorithm on a record of 16384 data points sampled every 3 μs, corresponding to a 49.15 ms time history. The frequency resolution is therefore 20.35 Hz and the maximum theoretical frequency 166.67 kHz. The signals are band-pass filtered (10-10^5 Hz) and a Hanning window is applied prior to the FFT to avoid aliasing and to eliminate the large DC component. The above procedure is performed on a collection of 50 consecutive records, and the spectra are averaged. The power spectrum of the torch current is obtained by dividing the power spectrum of the current time-derivative by the frequency. It shows prominent peaks at 300 Hz and harmonics which come from imperfect rectification of the torch DC power supply. The 300 Hz is also clearly visible on the light power spectrum for the case of pure Ar and on the power spectrum of the voltage for the Ar/H_2 mixture. Except for the current, the pure Ar case shows much less fluctuations and no clearly-defined frequencies in comparison with the H_2 mixture for which the power spectra of voltage, light and acoustics are dominated by high frequencies in the range 3-30 kHz. The clearly-defined peaks in this frequency range are attributed to the arc motion and restrike inside the torch which is a quasi periodic phenomenon. These peaks change in amplitude and frequency with torch aging due to electrode wear. On the other hand, the light emission power spectrum shows a significant continuous background level which increases at low frequencies. This is attributed to the turbulence of the plasma jet, and the consecutive surrounding air entrainement.

Velocity estimation by TOF of light fluctuations

The time of flight (TOF) technique described in reference [8] has been used to estimate velocity profiles in the hottest regions of the plasma jet, where no kind of probe can survive. The technique is based on the assumption that local emission fluctuations of the plasma jet are due to successive plasma volumes of different temperatures which travel with the axial velocity of the jet (convective transport). The time of flight of these successive hot/cold puffs is measured by the cross-correlation of the light fluctuation signals collected by two optical fibers separated by a distance of Δd = 3 mm along the jet axis (Fig 1). The velocity is obtained from the ratio of the effective flight distance (Δz= 2.4 mm in Fig 1) with the time shift of the cross-correlation maximum. However the cross-correlation is strongly dependent on the frequency of the light fluctuations; namely, better cross-correlation is obtained if the signals are bandpass-filtered in the frequency range where the light fluctuations originate from arc movements and restrike, and not from the power supply or from the wide band turbulence fluctuations. Figure 4 shows a radial velocity profile obtained between 1 and 3.4 mm from the nozzle exit for two plasma conditions. The light fluctuation signals considered here have been bandpass-filtered between 3 and 12 kHz, where the most significant contributions to the power spectrum come from the arc instabilities (see Fig 3). One can see that a small amount of H_2 (4%) added to the plasma gas nearly doubles the axis velocity. Another striking feature is that the velocity profile is extremely peaked on the axis of the jet (the FWHM is only about 3 mm whereas the nozzle diameter is 6 mm). This has implications for the powder injection geometry for plasma spraying applications.

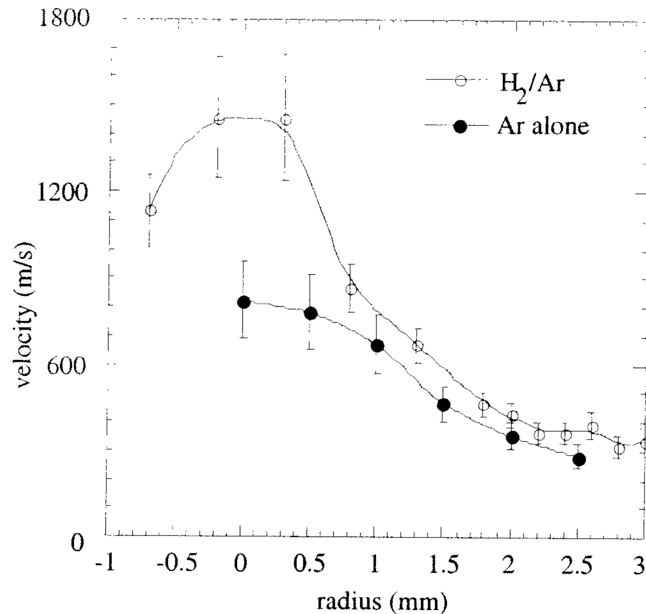

Figure 4 : *Plasma jet velocity profiles for two plasma conditions, estimated from the time of flight of light fluctuations (see text). plasma conditions : 2/50 SLM H2/Ar (o) and 50 SLM pure Ar (•) at 500A.*

References

[1] P. Fauchais and M. Vardelle, *"Plasma Spraying : Present and Future"*, Pure and Appl. Chem., Vol. **66**, No. 6, p. 1247-1258, (1994)

[2] J.-F. Brilhac, et al., *"Study of the Dynamical and Static Behavior of DC Vortex Plasma Torches"*, Plasma Chemistry and Plasma Processing, Vol. **15**, No. 2, p. 231, (1995)

[3] E. Pfender and C. H. Chang, *"Plasma Spray Jets and Plasma-Particulate Interaction : Modeling and Experiments"*, Proceedings of the 15th International Spray Conference, 25-29 May 1998, Nice, France, p. 315, (1998)

[4] S. A. Wutzke, E. Pfender, and E. R. G. Eckert, *"Study of Electric-arc Behavior with Superimposed Flow"* , AIAA Journal, Vol. **5**, No. 4, p. 707, (1967)

[5] T. Benecki, in *"Thermal Spray : Advances in Coating Technology"* (Pub.) ASM Int. Oh USA, p. 63 (1998)
S. Russ, E. Pfender, and J. Heberlein, in *"Thermal Spray Coatings : Research, Design and Applications"*, (Pub.) ASM Int. Oh USA, p. 97, (1993)

[6] L. Beall, et al, *"Controls for Plasma Spraying based on Plasma Jet Stability Analysis"*, Conference, 25-29 May 1998, Nice, France, p. 815

[7] J.F. Coudert, M.P. Planche, and P. Fauchais, High Temp. Chem. Processes, **3**, p. 639, (1994)

[8] M.P. Planche, J.F. Coudert, and P. Fauchais, Plasma Chemistry and Plasma Processing, **18** (2), p. 263, (1998)

Remote Silane Plasma Chemistry Studied By Mass Spectrometry and Langmuir Probes

W.M.M. Kessels, C.M. Leewis, M.C.M. van de Sanden, and D.C. Schram
Department of Applied Physics, Eindhoven University of Technology,
P.O. Box 513, 5600 MB Eindhoven, The Netherlands
w.m.m.kessels@phys.tue.nl

Introduction

An expanding Ar-H_2-SiH_4 plasma, used for deposition of solar grade a-Si:H at a growth rate of 10 nm/s [1], is studied by analyzing the plasma chemistry and the particles contributing to film growth. Langmuir probe measurements, ion mass spectrometry and appearance potential mass spectrometry have been used to study the electrons, ions and atomic hydrogen emanating from the plasma source and the products of silane dissociation. The relative contribution of SiH_3 radicals created by the interaction of H from the source and SiH_4 is shown to increase with H_2 admixture and the formation of large, hydrogen poor cationic silicon clusters is discussed. From Langmuir probe measurements the contribution of the ions to film growth is determined showing that the deposition is dominated by radicals.

Experimental setup and diagnostics

In a thermal plasma source, a cascaded arc, an Ar or Ar-H_2 plasma is created at a pressure of typically 400 mbar. This plasma is expanded in low pressure deposition chamber at 0.2 mbar (cf. Fig. 1). SiH_4 is admixed just behind the plasma source by ring injection. The gas flows used are 55 sccs Ar, 0 to 15 sccs H_2 and 10 sccs SiH_4 and the arc discharge is current controlled at 45 A. For the present study the substrate holder is replaced by a Hiden EPIC 300 mass spectrometer. Particles are extracted at the usual position of the substrate by a 50 μm orifice leading to a pressure in the mass spectrometer of about 10^{-6} mbar. Langmuir probe measurements have been performed by a cylindrical (ϕ = 0.2 mm, l = 3 mm) single and double tungsten probe at two axial positions (6 cm behind arc exit and 2 cm in front of mass spectrometer). The measurements have been analyzed by a probe theory valid in the transition zone between the thin sheath approximation and orbital motion limit and for a collisionless sheath [2]. Special attention is paid to probe measurements in the conditions with silane and it is shown that the ion saturation current is not suffering from the a-Si:H film formed on the probe surface for the conditions studied. For more information on these measurements as well as on the characteristics of the mass spectrometer (e.g, mass discrimination) the reader is referred to ref. 3.

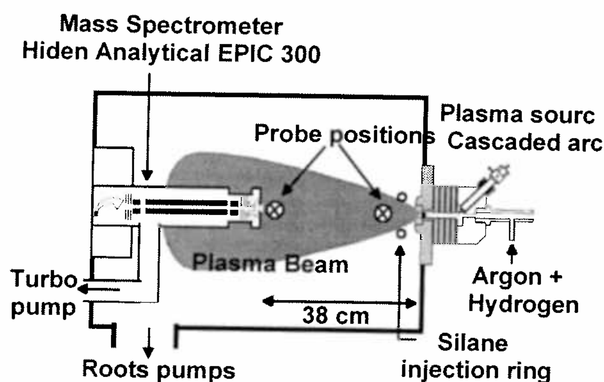

Fig. 1: Expanding thermal plasma for fast deposition of a-Si:H with mass spectrometer and Langmuir probe.

Plasma source: Ar-H_2 plasma

The Ar or Ar-H_2 plasma created in the cascaded arc is used to dissociate the downstream injected SiH_4 and therefore the reactive species emanating from the arc have been studied

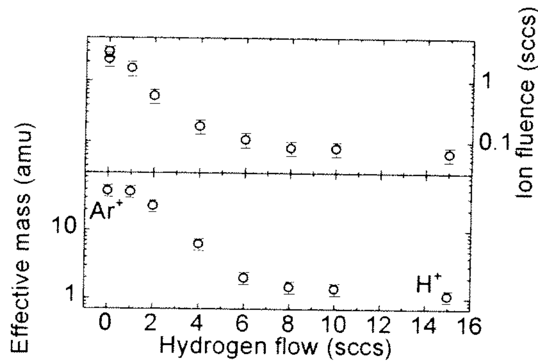

Fig. 2: Ion fluence emanating from the cascaded arc and effective ion mass.

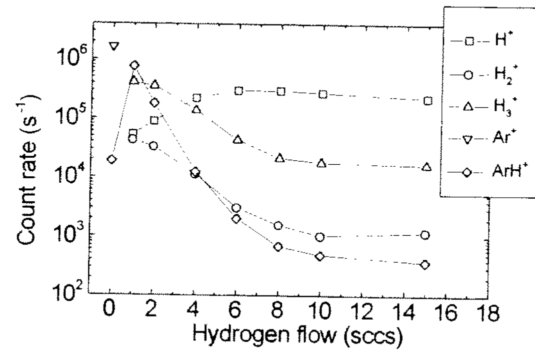

Fig. 3: Plasma ions as measured by mass spectrometry.

extensively [4,5,6]. In conformity with these earlier experiments, Langmuir probe measurements revealed an electron temperature in the range 0.1- 0.3 eV. This makes electron induced dissociation improbable. Therefore SiH_4 dissociation is mainly determined by the reactive heavy particles emanating from the source. The flow of ions, as possible candidates, has therefore been determined by radial probe measurements (as shown in Fig. 8a) directly behind the arc exit [3,7]. In Fig. 2 it is shown that the ion flow is heavily reduced when hydrogen is admixed by the reactions [5]:

$$Ar^{+} + H_2 \rightarrow ArH^{+} + H \tag{1}$$

$$ArH^{+} + e \rightarrow Ar + H \tag{2}$$

Furthermore, from the ratio of electron and ion saturation current the effective ion mass is determined [8] indicating that the dominant ion changes from Ar^{+} to H^{+} (cf. Fig 2). This is in agreement with the mass spectrometry data in Fig. 3. Another type of reactive particle that emanates from the plasma source when H_2 is admixed is atomic H. The flow of H is less easily quantified [6] but from appearance potential mass spectrometry it is observed that the flux increases with H_2 admixture for larger H_2 flows (cf. Fig. 4). The deviant behavior at low H_2 flows can probably be attributed to a combination of 1) a decreasing gas temperature for increasing hydrogen flow and 2) production of H by reactions (1) and (2) just in front of the mass spectrometer as for small hydrogen flows relatively more ions will recombine at this position.

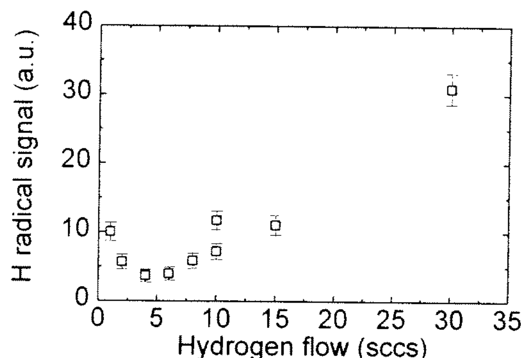

Fig. 4: H radical signal measured by appearance potential mass spectrometry.

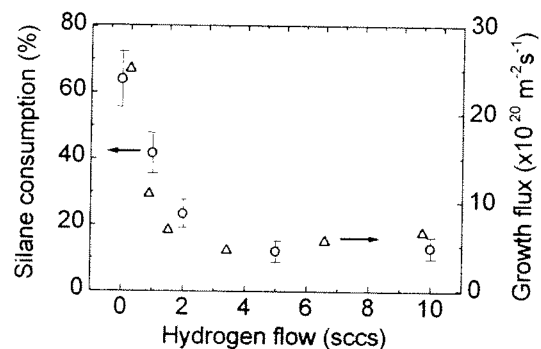

Fig. 5: Silane consumption and Si growth flux as a function of H_2 admixture.

$Ar\text{-}H_2\text{-}SiH_4$ plasma

The SiH_4 consumption and Si growth flux obtained when SiH_4 is admixed to the Ar-H_2 plasma is given in Fig. 5. From their dependence on H_2 flow and from the properties of the Ar-H_2 plasma as presented above it was concluded in previous studies [7,9] that for low H_2 flows silane dissociation is governed by ions:

$$Ar^+ (H^+) + SiH_4 \rightarrow Ar\,(H) + SiH_3^+ + H \qquad (3)$$

followed immediately by dissociative recombination with electrons when the electron density is high ($>10^{17}$ m^{-3}) leading presumably mainly to SiH_2 and SiH. Furthermore it was concluded that for higher H_2 flows mainly SiH_3 is created by the reaction:

$$H + SiH_4 \rightarrow H_2 + SiH_3 \qquad (4)$$

as mainly H emanates from the arc. In order to verify these reactions direct measurements of the created silicon products are carried out. First measurements of the SiH_3 flux by appearance potential mass spectrometry (cf. Fig. 6) indeed show the presence of SiH_3. After correcting for the amount of silane consumed it is clear that the contribution of SiH_3 to film growth increases with H_2 admixture. This is shown in Fig. 6, however still in arbitrary units. The fact that the deposition is not totally due to SiH_3 is indicated by the observation of large, hydrogen poor cationic silicon clusters with up to ten Si atoms [10] as shown in Fig. 7. This shows the ion spectrum for a H_2 flow of 10 sccs. In this case the electron density is sufficiently low such that sequential ion-silane reactions can compete with recombination reactions [10]:

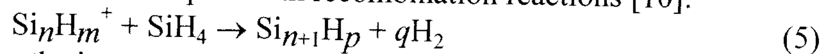

$$Si_nH_m^+ + SiH_4 \rightarrow Si_{n+1}H_p + qH_2 \qquad (5)$$

Very interesting is the fact that the ion mass spectra for low H_2 flows, where SiH_4 dissociation is dominated by ions, show a similar distribution and magnitude of the cluster ions. This has also been confirmed by Langmuir probe measurements in the SiH_4 plasma just in front of the mass spectrometer (cf. Fig. 8b): no strong dependence on the H_2 flow is observed (cf. Fig. 9) while the flow of ions emanating from the arc is strongly dependent on the H_2 flow [3]. This indicates a strong dissociative recombination of ions at the position where SiH_4 is admixed as long as the electron density is high:

$$Si_nH_m^+ + e \rightarrow Si_pH_q + ... \qquad (6)$$

At the point that the electron density is reduced in sufficient extent sequential ion-silane reactions (5) get again important. Furthermore, the maximum contribution (i.e., assuming unity sticking probability) of the cationic clusters to a-Si:H growth has been determined (cf. Fig. 9b) indicating that for low hydrogen flows the deposition is still dominated by radicals, which are not SiH_3.

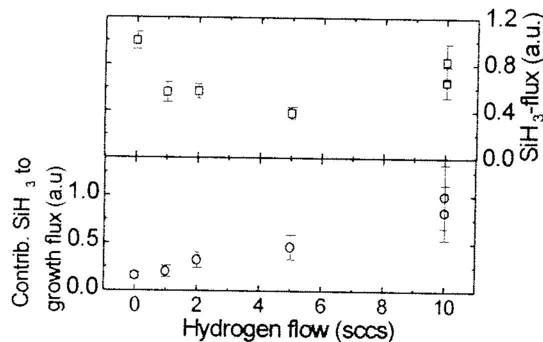

Fig. 6: SiH3 flux as determined by appearance potential mass spectrometry and contribution of SiH3 to growth flux, both in arbitrary units.

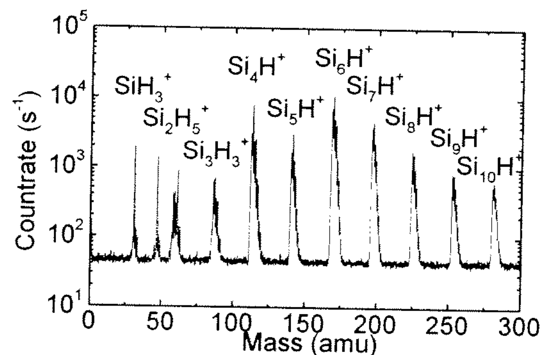

Fig.7: Ion mass spectrum in an argon-hydrogen-silane plasma with 10 sccs H_2. Dominant ions are indicated.

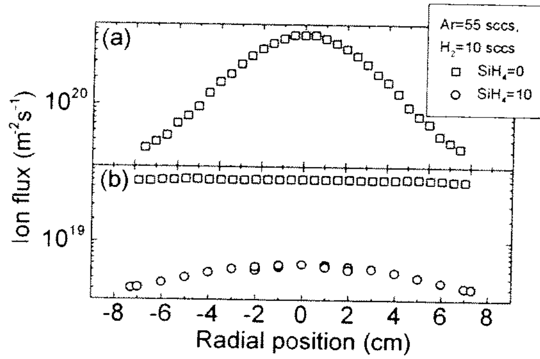

Fig. 8: Ion flux for a) just behind plasma source b) in front of the mass spectrometer.

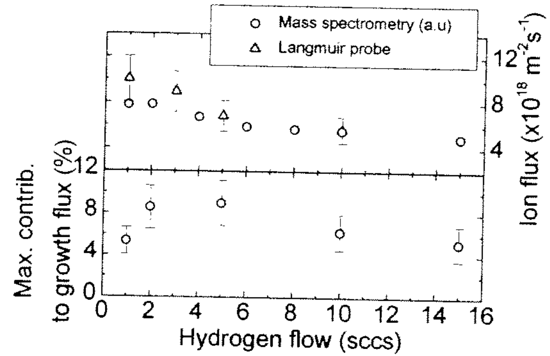

Fig.9: Ion flux in front of mass spectrometer as a function of hydrogen flow and maximum contribution ions to Si growth flux..

Conclusion

The combination of ion mass spectrometry and Langmuir probe measurements is very powerful in the study of the ion chemistry: the quantitative information on the ion flux obtained by the Langmuir probe is complimentary to the more qualitative information on the type of ions present in the plasma as obtained by mass spectrometry. Appearance potential mass spectrometry is a powerful technique to obtain information on the flux of radicals towards the surface of the mass spectrometer but its strength is mainly limited by a relative high detection limit (due to the necessity of ionization) and the reactivity of radicals with surfaces. The latter complicates quantification of the data drastically. Yet more insight in the SiH_4 dissociation process and the contribution of the created particles as cationic silicon clusters and SiH_3 radicals is obtained for the expanding Ar-H_2-SiH_4 plasma

References

[1] W.M.M. Kessels, R.J. Severens, M.C.M. van de Sanden, D.C. Schram, J. Non-Cryst. Solids **227-230**, 133 (1998).

[2] E.W. Peterson and L. Talbot, AIAA Journal **8**, 2215 (1970).

[3] W.M.M. Kessels, C.M. Leewis, M.C.M. van de Sanden, D.C. Schram, submitted for publication.

[4] M.C.M. van de Sanden, J.M. van de Regt, and D.C. Schram, Plasma Sources Sci. Technol. **3**, 501 (1994).

[5] R.F.G. Meulenbroeks, R.H.A. Engeln, M.N.A. Beurskens, R.M.J. Paffen, M.C.M. van der Sanden, J.A.M. van der Mullen, and D.C. Schram, Plasma Sources Sci. Technol. **4**, 74 (1995).

[6] S. Mazouffre, M.G.H. Boogaarts, J.A.M. van der Mullen, and D.C. Schram, somewhere in these proceedings.

[7] M.C.M. van de Sanden, R.J. Severens, W.M.M. Kessels, R.F.G. Meulenbroeks, and D.C. Schram, J. Appl. Phys. **84**, 2426 (1998).

[8] G.J.H. Brussaard, M.C.M. van de Sanden, and D.C. Schram, Phys. Plasmas **4**, 3077 (1997).

[9] W.M.M. Kessels, L. Gabella, J. Bastiaansen, R.J. Severens, M.C.M. van de Sanden and D.C. Schram, in 'Papers presented at the 2nd conference on low temperature plasma diagnostics', Bad Honnef (1997).

[10] W.M.M. Kessels, M.C.M. van de Sanden, and D.C. Schram, Appl. Phys. Lett. **72**, 2397 (1998).

Mie Scattering from Zirconia Evaporating in an Inductively Coupled Plasma

Günter Lins and David W. Branston
Siemens AG, Corporate Technology, Plasma Technology
Germany

Introduction

Inductively coupled high-power radio frequency plasmas generated at pressures of some hundred mbar reach temperatures of the order of 10,000 K. Besides applications such as radio frequency plasma spraying [1] they have been used in a process termed plasma flash evaporation to completely vaporise materials introduced as fine powders and to subsequently deposit films immediately out of the vapour phase. This technique which has been demonstrated successfully by the production of high-temperature superconducting films of $YBa_2Cu_3O_{7-x}$ [2], [3] takes advantage of the low streaming velocity of the induction plasma and the ensuing long residence time of the material to be evaporated. The feasibility of the process with high-melting substances such as zirconia crucially depends on whether the material can be completely vaporised and maintained in the vapour phase on its way to the substrate to be coated.

Evaporation time of zirconia particles in a thermal plasma

A zirconia particle immersed in a plasma of 10,000 K undergoes three stages of heating and three phase transitions. The particle is assumed to be heated sequentially to the transformation temperature where ZrO_2 changes from its α– to the β– phase, to its melting point, and finally to the boiling point, absorbing the latent heat of transformation, melting and evaporation at the respective temperatures.

The evaporation time was calculated considering spherical particles with radius R, temperature T, and infinite thermal conductivity exposed to a thermal plasma with a temperature $T_p > T$. The plasma was treated as constant in time and uninfluenced by the particles and their vapour. If constant average values are adopted for the specific heat c_p of the particle and the thermal conductivity λ_p of the plasma, the temperature of a particle evolves according to [4],

$$T(t) = T_p + (T_0 - T_p)\exp(\frac{3\lambda_p t}{\rho c_p R^2})$$

with the mass density ρ and the initial temperature T_0 of the particle. The time intervals for latent heat supply are readily obtained by equating the energy transferred from the plasma to the particle the enthalpy necessary for the respective phase transition. In the case of evaporation the decrease of the particle radius has to be taken into account.

Evaporation times of zirconia particles were calculated using the data listed in table 1, the thermal conductivity for an atmospheric argon plasma at a temperature of 10,000 K, λ_p = 1

transformation temperature	1478 K	transformation enthalpy	4.83×10^4 J/kg
melting point	2963 K	melting enthalpy	7.08×10^5 J/kg
boiling point	4573 K	evaporation enthalpy	$5{,}23 \times 10^6$ J/kg
mass density ρ	5560 kg/m³		

Table 1 - Thermophysical data of zirconia [5]

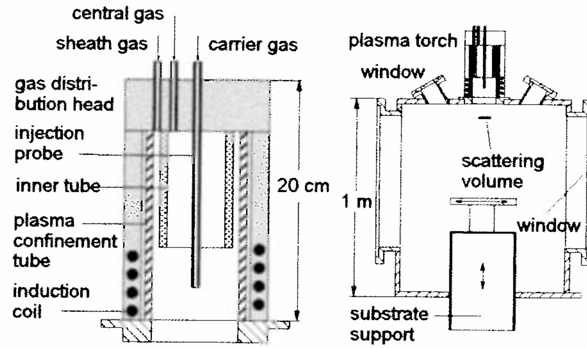

Figure 1: *Plasma torch and reaction chamber*

W/Km [6], and an average value c_p = 623 J/kgK as calculated from data of [7]. Heating a particle from room temperature to complete vaporisation takes 130 and 560 μs, for particle diameters of 12 and 25 μm, respectively. The plasma streaming velocity in inductively coupled plasmas is of the order of 10 m/s [8]. Hence the residence time of the particle within the hot induction coil region amounts to milliseconds and should be sufficient to warrant complete vaporisation of particles less than 25 μm in diameter.

Experiment

The plasma source (figure 1) was a high-power induction torch as described in [9]. An induction coil which was powered by an r.f. generator delivering up to 30 kW at a frequency of 4 MHz coaxially surrounds two coaxial tubes. Between the outer ceramic plasma confinement tube and the inner quartz glass tube argon with an addition of hydrogen was introduced as a sheath gas. Pure argon was used as the central gas, flowing through the inner tube with a swirl velocity component. A third argon stream carried the powder to be evaporated through an axially mounted injection probe into the plasma. Gas flow rates used in the experiments were 70 slm for the sheath gas, 25 slm for the central gas and 2 to 4 slm for the carrier gas at a chamber pressure of 450 mbar. The plasma emerging from the source entered a reaction chamber where it was observed through a number of windows. Most of the experiments were done with a -12 + 2 μm yttria-stabilised zirconia powder.

A necessary condition for the evaporation of ZrO_2 and the existence of its vapour in the plasma over a period of time sufficient to reach the substrate without condensation is a plasma temperature well above the temperature at which the vapour pressure equals the plasma pressure of, typically, 450 mbar. From the vapour pressure curve of ZrO_2 the corresponding temperature amounts to 4360 K [10]. The plasma temperature was determined from optical spectra of singly ionised Zr taken at wavelengths around 435 nm. Assuming local thermodynamic equilibrium the temperature was inferred from Boltzmann plots of 10 lines. The temperature as shown in figure 2 lies well in a range where ZrO_2 vapour can exist.

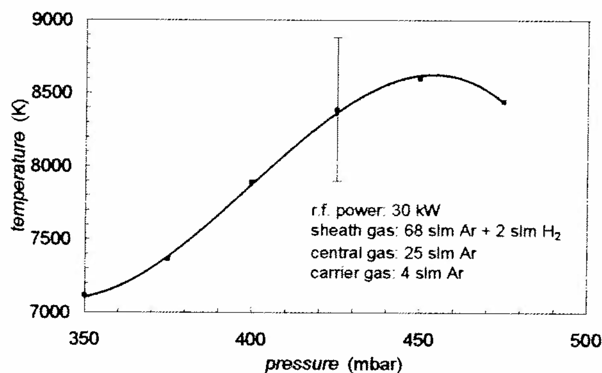

Figure 2: *Plasma temperature 6 cm off the torch exit as inferred from spectra of singly ionised Zr. The plasma was generated with an r.f. power of 30 kW, with 2 slm of H_2 added to the sheath gas.*

The evaporation times estimated in the preceding section and the temperature measured spectroscopically both suggest that it should be possible to completely evaporate zirconia under the prevailing experimental conditions. To give evidence to complete evaporation and to know the maximum powder feed rate up to which it can be achieved a laser light scattering experiment was carried out. The beam of a frequency-doubled Nd:YAG laser was directed through the reaction chamber such as to intersect the z-axis of the plasma torch at a distance of 6 cm from its exit. The laser was operated at a repetition

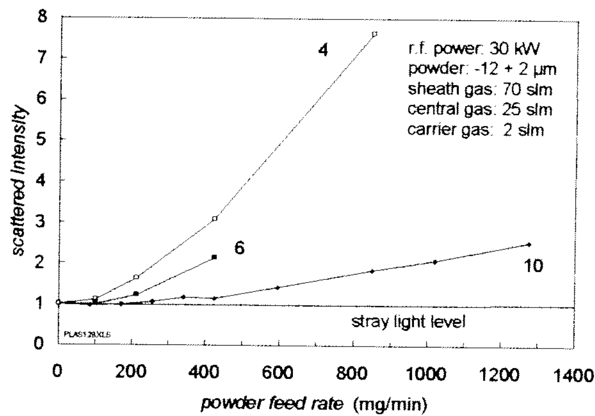

Figure 3: *Scattered intensity normalised to the stray light level, as a function of the powder feed rate. Hydrogen flow rates are indicated in units of slm by numerals on the curves.*

rate of 10 Hz, producing pulses of 10 ns duration and 6 MW peak power. Scattered light was discriminated in a 1m monochromator and detected in a photomultiplier. The signals so obtained were processed in a boxcar averager where they were normalised to the signal of a photodiode serving as a monitor for the laser intensity and finally averaged over 100 laser pulses. The laser beam was directed through the reaction chamber via Brewster windows and a baffle system containing three apertures both on the entrance and exit sides to reduce the stray light. The observation volume was a rectangle of $8x10x0.25\ mm^3$. If particles are continuously introduced into the plasma at a rate of 100 mg/min and if none of these evaporate, there are about 10 particles present in the observation volume at any time with a residence time of an individual particle of the order of 2 µs.

For a given kind of particles the scattered intensity depends on their number density, their size, and their shape [11] all of which are badly known before and completely unknown during the evaporation process. Hence no attempt was made to put the results on an absolute scale. Instead, the stray light level was used as a reference all intensities were normalised to. (In future work Rayleigh scattering from a well-defined source will be used as a reference.) The evaporation of particles results in a decrease of the scattered intensity, owing to their reduction in size as well as in number. The scattered signal produced by feeding powder in the absence of a plasma is several orders of magnitude higher than the intensity measured with a plasma present.

Figure 3 shows the scattered intensity as a function of the powder feed rate. The sheath gas composition was varied by changing the flow rate of hydrogen keeping the total flow rate constant at 70 slm. With an addition of 4 slm H_2, the scattered intensity is always greater than the stray light level, and rises steeply upon increase of the powder feed rate. When the H_2 fraction is increased the slope of the scattered intensity decreases, again indicating that the fraction of evaporated material rises due to an improved thermal conductivity of the plasma. With an addition of 10 slm H_2 there is no scattered intensity above the stray light level up to a powder feed rate of 200 mg/min. When the hydrogen flow rate is further increased to 12 slm the amount of evaporated material decreases, owing possibly to an unfavourable change in the streaming properties of the plasma. The results are summarised in figure 4 which gives the maximum evaporation rate as a function of the hydrogen flow rate.

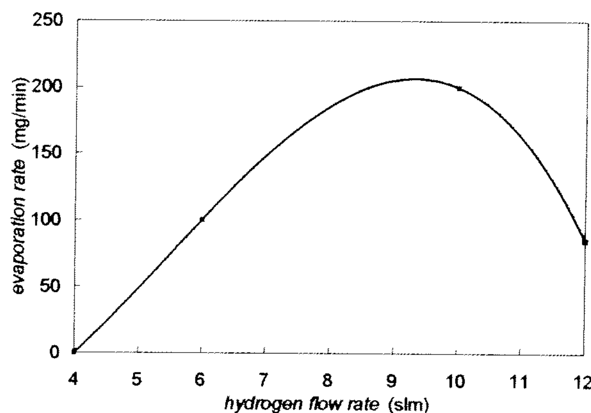

Figure 4: *Maximum evaporation rate as a function of the hydrogen flow rate in the sheath gas.*

Conclusions

Threefold evidence has been given to the feasibility of complete evaporation of zirconia powder introduced into a 30 kW inductively

coupled argon-hydrogen plasma. Firstly, a theoretical estimate shows that evaporation of particles less than 25 μm in diameter should be possible within the residence time of the particles inside the plasma. Secondly, the plasma temperature is well above the boiling point of zirconia, and, finally, a laser scattering experiment revealed that zirconia powder could be evaporated at a rate of 200 mg/min under plasma conditions appropriately chosen. Further work will have to concentrate on keeping the zirconia in the vapour phase on its way to the substrate and to investigate the processes occurring in the immediate neighbourhood of its surface.

Acknowledgments

The contributions of Kai Griesenbrock and Jobst Verleger to the experimental work are gratefully acknowledged.

References

[1] T. Okada, H. Hamatani, T. Yoshida, *J. Am. Ceram. Soc.*, **72**, 2111-2116 (1989)
[2] K. Terashima, H. Komaki, T. Yoshida, *IEEE Trans. Plasma Sci.*, **18**, 980-984 (1990)
[3] G. Lins, B. Michelt, R. Seeböck, *VDI-Berichte*, **1166**, 379-386 (1995)
[4] E. Bourdin, P. Fauchais, M. Boulos, *Int. J. Heat Mass Transfer*, **26**, 567-582 (1983)
[5] G.V. Samsonov, *The Oxide Handbook*, New York 1973
[6] M.I. Boulos, P. Fauchais, E. Pfender, *Thermal Plasmas*, vol. 1, New York, 1994
[7] O. Kubaschewski, C.B. Alcock, *Metallurgical Thermochemistry*, Oxford 1979
[8] T. Yoshida, *Mater. Trans. JIM*, **31**, 1- 11 (1990)
[9] M.I. Boulos, *Pure & Appl. Chem.*, **57**, 1321-1352 (1985)
[10] Y.S. Touloukian, Ed., *Thermophysical Properties of High Temperature Solid Materials*, vol. 4, part I: *Simple Oxygen Compounds and Their Mixtures*, New York 1967
[11] C.F. Bohren and D.R. Huffman, *Absorption and Scattering of Light by Small Particles*, Wiley, New York 1983

Characteristics of a Pulsed Microwave Oxygen Plasma

M. Baeva, X. Luo, J. Uhlenbusch
Institute für Laser- und Plasmaphysik, Heinrich-Heine-Universität-Düsseldorf
Universitätsstr. 1 , 40225 Düsseldorf, Germany

1. Introduction

Chemical reactive plasma discharges are widely used to modify the surface properties of materials. Most of the processing plasmas are oxygen containing, as they are used in the semiconductor industries. Though its concentration is not necessarily high, oxygen has crucial influences on the properties of the plasma due to its relatively low ionization potential, low threshold of dissociation, and the formation of negative ions.

In the present work a pulsed microwave excited low pressure oxygen plasma is investigated. The characteristics are studied with help of various plasma diagnostic techniques. The electron density is determined using an HCN laser interferometer and a Langmuir probe. The detection of negative ions is made by combining laser interferometry with the photodetachment technique. CARS spectroscopy is applied to determine the vibrational temperature.

A kinetic model predicting the temporal behavior of the densities of oxygen atoms and molecules, metastable singlets, negative and positive ions, ozone and the electron density has been developed. A set of 60 reactions for the production and destruction of the species has been considered.

2. Experimental

2.1 Apparatus

Fig. 1 illustrates schematically the experimental arrangement. Pulsed microwave power generated by a 6 kW magnetron at 2.45 GHz is coupled to a cylindrical cavity of 45 mm radius through a quartz glass window of 10 mm thickness, which provides the separation from the atmospheric pressure. The length of the chamber is $\sim$ 80 mm. Four

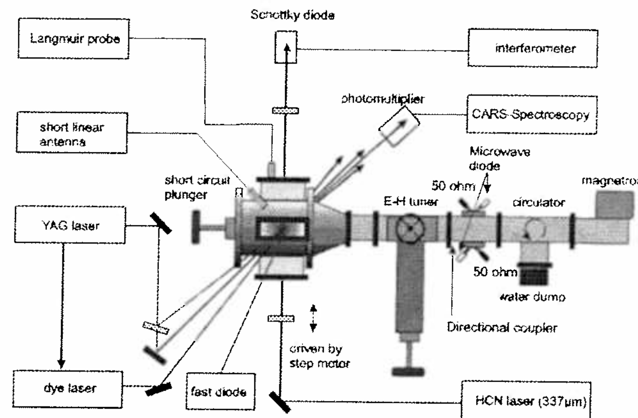

Figure 1. Experimental setup.

lateral ports are fixed for diagnostic purposes. Using a home-made switched power supply, the pulse duration can be changed from 50 μs to cw, the repetition frequency from DC up to 10 kHz, and the peak power from 0 up to 6 kW with a rise time of 20 μs. An E-H tuner matches the impedance. The power absorbed in the discharge is monitored by a simultaneous measurement of the forwardly directed and the reflected power using

two HP423B crystal detectors connected with the directional couplers. By alignment of the plunger the maximum electric field, and hence ignition of the discharge occurs in the center of the discharge vessel.

2.2 Temporal behavior of the discharge

The electron density changes the index of refraction n in the interfeometer cavity. For our conditions (p=1~10 $mbar$, n_e ~$10^{11} cm^{-3}$ and HCN laser angular frequency of 5.6 THz), the collisionless plasma approximation can be used to give:

$$n = 1 - \frac{1}{2}\left(\frac{\omega_p}{\omega}\right)^2 = 1 - \frac{n_e}{2n_c} \tag{1}$$

with the plasma frequency ω_p and the cut-off density $n_c = m_e \varepsilon_0 \omega^2 / e^2$. If the working point of the interferometer is chosen near the inflection point of the transmission curve, a nearly linear relation between the change of optical path Δl_{opt} and the transmitted HCN laser intensity ΔI is valid. The intensity ΔI_D that reaches the detector follows from integration over the entire diameter of the plasma:

$$\Delta I_D = \int_{-R_{pl}}^{R_{pl}} \Delta I dl, \qquad with \qquad \Delta I = \left(\frac{dI}{dl_{opt}}\right)_{wp} \Delta l_{opt}, \tag{2}$$

where the slope of the transmission curve at the working point $\left(\frac{dI}{dl_{opt}}\right)_{wp}$ can be determined experimentally and R_{pl} is the radius of the discharge.

In Fig. 2 temporally resolved measurements of the electron density, the electric field, the forwardly directed and reflected microwave power, and the power absorbed in the discharge derived from these signals are plotted. The experimental conditions are as follows: pressure 10 mbar, gas temperature about 500 K, repetition rate 10 Hz. At the instant of breakdown, the E-field sharply drops due to the dissipation of the microwave power into the discharge volume.

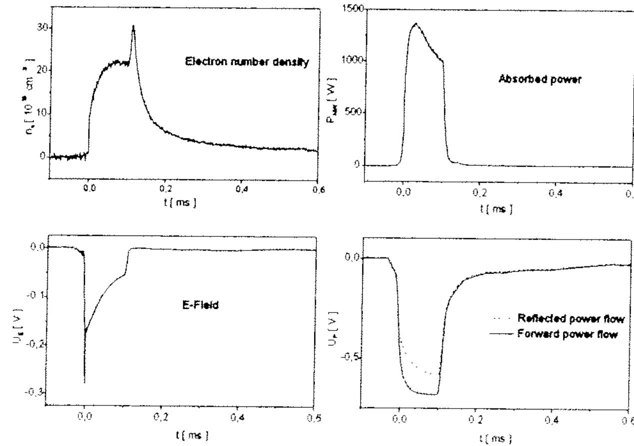

Figure 2. Measured discharge charakteristics.

It is interesting to see, that the electron density shows a spike at the end of the pulse. This is considered to be a contribution of negative ions in the discharge, where electrons are released from O^- by the collisions immidiately after the pulse.

2.3 Photodettachment technique

Negative O^- ions are detected by the photodetachment technique. Illumination of the plasma by a short laser pulse with a photon energy exceeding the binding energy of the electrons wrenches the electrons away from the negative ion according to the reaction

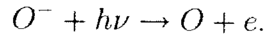

$$O^- + h\nu \rightarrow O + e.$$

If a laser beam of frequency ν and radius R_{YAG} passes the plasma with negative ions, the relative number of detached atoms can be written as

$$\frac{n_-^{\det}}{n_-} = 1 - \exp\left(-\frac{W\sigma}{h\nu A}\right) \tag{3}$$

where σ is the cross section for photodetachment. For O^- at the used wavelength of 532 nm of the frequency doubled YAG laser one finds[1] $\sigma = 6.4 \times 10^{-22} m^2$. The cross section of the YAG laser beam is $A = \pi R_{YAG}^2$. With the pulse energy of over 150 mJ and a radius of 5 mm of the YAG laser beam used in our experiment, it is ensured that nearly total detachment (over 96 %) of the O^- negative ion within the YAG laser beam can be achieved. The change in the electron density due to photodetachment can be measured by the HCN laser interferometer technique mentioned in the previous section (see also [2]). Fig. 3 shows the time resolved electron density in the plasma together with the excess electrons due to the photodetachment at the moment when the YAG laser passes through the discharge. The density of the negative ion O^- can be determined taking into account the ratio of the plasma radius to radius of the YAG laser beam. In our case, the measured change in the electron density multiplied by the factor of 2.5 of the ratio $\frac{R_{pl}}{R_{YAG}}$ gives the O^- density of $10^{11} cm^{-3}$.

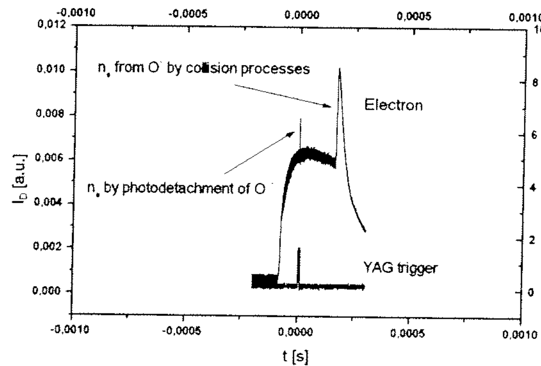

Figure 3. Interferometer signal

3. Kinetic model

The kinetic model developed determines the main production and destruction processes for the principal active species O_2, O, $O_2(a^1\Delta)$, $O_2(b^1\Sigma)$, O^-, O_2^-, O^+, O_2^+, O_3 and e. A set of 60 processes are taken into account. The rate coefficients with electron participation are obtained by solving the Boltzman equation for the electrons. The respective rates for reactions involving atoms, molecules and ions are taken from the literature [3]-[5].

A system of rate equations for the ten species is written down. The electric field needed to obtain the rate coefficients by solving the Boltzmann equation for the electrons follows from the energy balance:

$$W_a = en_e v_{dr} E_{eff}, \tag{4}$$

where W_a is the microwave power absorbed in the plasma, v_{dr} is the electron drift velocity and E_{eff} is the effective electric field. The time evolution of the absorbed power is known from the experiment. The electron drift velocity is calculated as function of E_{eff}/N. The electric field is derived implicitly from Eq. (4). An iterative procedure is employed to obtain the self-consistent solution of the system of the rate equations and Eq. (4). Starting at t=0 and assuming that only oxygen molecules are present and that the electron density has an initial value of several 10 cm^{-3} the equations are solved numerically until a quasi steady-state is achieved. The calculated temporal behavior of the species considered in the model shows that the neutrals are substantially present in the afterglow discharge phase while the charged particles appear when the discharge burns. The experimental and theoretical results for the electron density agree very well (see Fig. 4). Both of them show a characteristic peak just after the microwave pulse. This effect results from the detachment processes of O^- with species like O, $O_2(a^1\Delta)$, O_2.

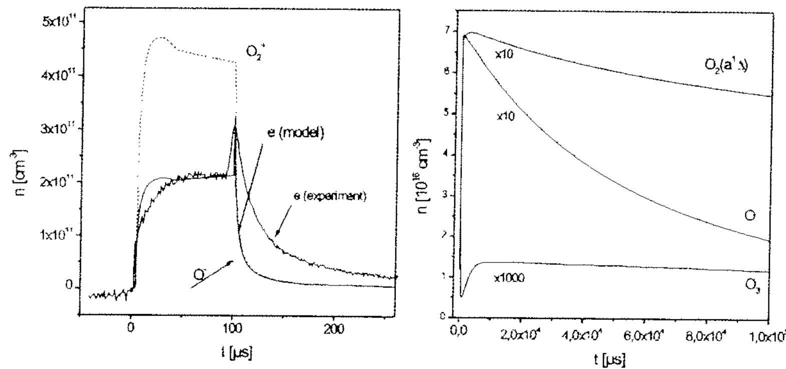

Figure 4. Densities of the main species in the plasma.

References

[1] D. S. Burch, S. J. Smith, L. M. Branscomb, " Photodetachment of O_2^-", *Phys. Rev.* **112**, 171-175 (1958)

[2] C. Schiffer, J. Uhlenbusch, "Negative-oxygen-ion detection by cross-beam photodetachment technique", *Plasma Sources Sci. Technol.* **4**, 345-352 (1995)

[3] B. Eliasson, "Electrical discharge in oxygen, Part1: Basic data and rate coefficients", *Brown Bovery Res. Rep.* KLR 83-40 C (1983)

[4] O. E. Krivinosova, S. A. Losev et al., "Recomended data on the rate constants of chemical reactions among molecules consisting of N and O atoms", in *Reviews of Plasma Chemistry*, B. M. Smirnov, ed., 1-29 (1991)

[5] I. A. Kossyi, A. Yu. Kostynski et al., "Kinetic scheme of the non-equilibrium discharge in nitrogen-oxygen mixtures", *Plasma Sources Sci. Technol.* **1**, 207-220 (1992)

Complementarity of in-situ IR absorption spectroscopy and mass spectrometry for diagnostics in organosilicon plasmas.

D.Magni, Ch. Deschenaux, C. Courteille, Ch. Hollenstein, P.Fayet*
Centre de Recherches en Physique des Plasmas EPFL 1015 Lausanne Switzerland
** Tetra Pak Suisse SA, Plasma Processing, 1680 Romont Switzerland*

Introduction

Chemical vapour deposition of silicon oxide enhanced by plasma (PECVD) is commonly used in semiconductor technology for the production of insulators or in the packaging industry to produce ecological oxygen barrier. The trend is actually going to non toxic precursors like HMDSO[1] (hexamethyldisiloxane) which do not require costly installation. Diagnostics in this environment should be non- intrusive, inexpensive, easy to use and to handle, and measure in a simple and correct way process relevant parameters. In the following we will concentrate on the application of the FTIR spectrometry to the diagnostic of plasmas using hexamethydisiloxane (HMDSO) and its complementarity with mass spectrometry.
Besides translational energy, the energy of the molecules (and in plasma polymerisation more and more complex precursors are used), consists in rotational, vibrational and electronic excitation energy[2]. Since all molecular species, with exception of the homonuclear diatomic are infrared active, IR absorption spectroscopy has wide applicability. However whether a particular molecular species will be actually detected in the plasma depends upon the species concentration, the strength of the infrared absorption and the sensitivity of the spectrometer used. The species that cannot be detected readily by IR absorption technique (atoms, short-lived radicals) are the most easily detected by mass spectrometry[3]. But ionisation mass spectrometry cannot distinguish between isomers and in addition the ionisation process leads to a cracking pattern, which very often prohibits unique interpretation of the mass spectrum. Therefore the observation of heavy neutral compounds formed in these reactive plasmas is difficult to perform. Consequently simultaneous application of these two methods allow a by far better identification of the most abundant neutral plasma components and the determination of their chemical structure. In this contribution we would like to present results of IR absorption spectroscopy and mass spectrometry in particular applied to the detection of species produced in HMDSO plasmas diluted with oxygen, argon and/or helium.

Result and discussion

With the help of IR absorption measurements, access to many important process parameters are possible[4]. Monomer depletion partial pressure, detection of plasma created species, and rotational and vibrational temperatures[5] can be obtained. In addition, under certain conditions, valuable information on the powder composition, particle size and particle number density can also be estimated.
Fig 1 shows the absorbance spectra of plasma produced components of a HMDSO plasma diluted with helium and oxygen. The absorbance is obtained from the measured transmittance spectra of the feeding gas and the plasma. In this representation negative going peaks indicate a consumption, where as a positive going contribution indicated formation of solid and/or gaseous matter. The strong negative narrow band peaks originate from different infrared active

vibrations (Si-O-Si, Si-(CH_3)n, CH_3) of the HMDSO molecule. The overlap between the negative narrow gas peak at 1070 cm-1 and a positive broad feature indicates the formation of SiO_x powder within the plasma. In Fig 2 the spectrum is corrected for the HMDSO gas depletion (67 % in this particular case). In this case the HMDSO molecule absorption lines are completely eliminated and the remaining Si-(CH_3)n and CH_3 absorption suggest the presence of carbon compounds within the SiO_x particles. The lines at 2140 cm-1 and 2340 cm-1 represent the gas phase stretch vibration of CO and CO_2 respectively, whereas the absorption lines at 1725 and 1783 cm^{-1} are most probably due to the C=O stretching in an aldehyde-type and carboxilic acid molecule respectively. These measurements show that in the deposition of SiO_x with HMDSO, a fraction of the excess carbon is transported out of the reactor by infrared active species CO, CO_2 and by aldehyde and acid formation, which correspond to all the steps of combustion reactions from methyl groups (CH_3). Creation of these molecules could be either in the plasma via carbon-oxygen reactions, which suppose a fairly high fragmentation of the HMDSO molecule or from plasma-surface reactions such as oxygen etching of carbon in the deposited film. Traces of hydrocarbone are also detected as acetylene at 730 cm^{-1} and methane at 3018 cm^{-1}.
Particle contamination of reactive plasmas is at present a very important item and widespread research is going on to understand the powder formation. The infrared absorption technique can also contribute to the comprehension of this interesting phenomenon. In the absorbance spectra shown in Fig 3a the large deviation from the base line is due to elastic scattering on the nanometer sized particles suspended in the plasma. The measured absorbance is the sum of two contributions: The absorption part due to the Si-O-Si vibrations at 1000 cm^{-1} and the light scattering part from the particles. The scattering and absorption cross section can be calculated from Mie theory using optical constants for appropriate materials. Fig 3a shows together the calculated absorbance including absorption, assuming a-SiO particles and scattering at particles with an size of 300 nm and the measured spectra. Light scattering shows an R^{-6} dependence, whereas the absorption follows a R^{-3} dependence. These different dependencies on the particle size allows the determination of the particle size and particle number density (Fig 3b).
In addition it turns out that the width of the Si-O absorption at 1000 cm^{-1} gives interesting information[6] on the status of the agglomeration of the particles in the plasma (Fig 4). In a modulated HMDSO discharge (80 ms plasmas on, 1600 ms plasma off time) small, unagglomerated particles have been obtained. The in-situ infrared absorption spectra in these conditions shows well two separated peaks due to the longitudinal (LO) and transverse (TO) mode. Large agglomerations, as typically obtained in a continuously running discharge tends to broaden these peaks, and leading finally to the LO mode being completely overlapped by the TO mode. Moreover it was found that the breath of the TO mode does not allow to distinguish between agglomerates constituted of very large or small particles.

However the interpretation of IR absorption spectroscopy is not always unambiguous. Not all possible plasma gas components are infrared active, furthermore the diagnostic only delivers information about the presence of bonding elements. Often a unique identification of the plasma components on the basis of IR spectra is often not at all possible. Mass spectrometry suffers from similar drawbacks. The attribution of different masses is often not unique and the complex cracking pattern also does not help to make life easier. But the complementarity can be exploited. For example the C=O vibration at 1730 cm-1 can be

attributed to many kind of aldehyde. Due to chemical evidences and mass spectrometry on neutrals, formaldehyde (COH_2) is found to be the most possible one.
Fig. 5 shows the mass spectra on neutrals of HMDSO diluted with oxygen, helium and argon in its gas and plasma phase. The plasma parameters are similar to those chosen for the results presented in figure 1. In the gas phase, argon, helium, oxygen and the cracking pattern of HMDSO (m=162) distinguish clearly themselves. We notice that the mass 147 is the most representative one and corresponds to the HMDSO molecule substracted by one methyl group, which in turn reacts to form compounds such as formaldehyde, formic acid, CO and finally CO_2. The spectrum of the plasma phase indicates a depletion of the monomer (around 60%), visible through the decrease of the masses which come from the cracking pattern (m=59, 66, 73, 147). The consumption of oxygen (infrared inactive) proves aslo that oxydation products and SiO_x particles, with x bigger than one, can exist. On the other hand we can see that species like H (m=1), H_2 (m=2), methane (m=16), water (m=18), formaldehyde (CH_2O, m=30), formic acid (CH_2O_2, m=46), CO or/and Si (m=28) and CO_2 (m=44) are detected and confirm the IR absorption results, subject to these masses correspond to the infrared-active species. The problem is obviously the attribution of the masses to some elements.

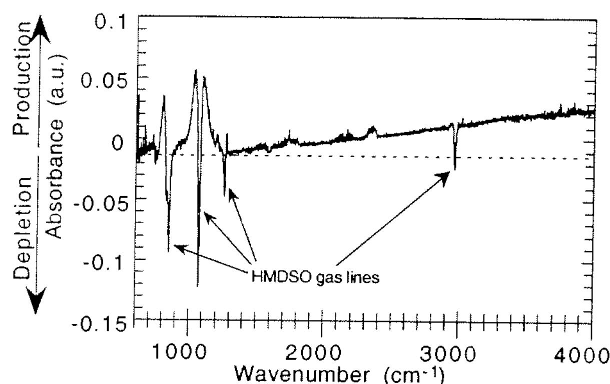

Figure 1: IR absorption spectrum of a diluted HMDSO plasma. 5.5 sccm HMDSO 13 sccm O_2, pressure 0.1 mbar, rf power 100 W.

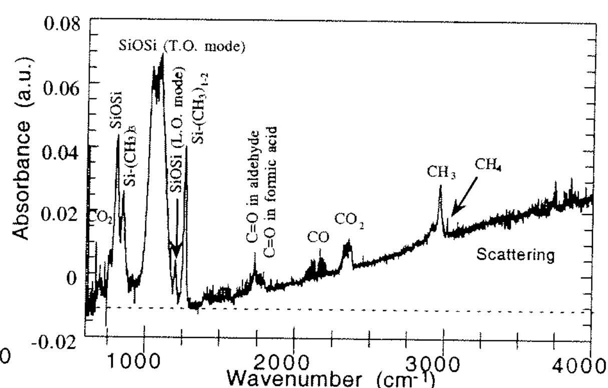

Figure 2: Absorbance spectrum of diluted HMDSO plasma (fig1) corrected for 67% depletion of the monomer vapour.

Typically the mass 44 is commonly attributed to carbon dioxide (CO_2), but it could be also the fingerprint of silicon oxide (SiO, not IR-active) and methaldeyde (C_2H_4O), and also probably present in the discharge. We can make similar considerations between the atomic oxygen and the methane and between carbon oxide and silicon. These simple examples show well that only both diagnostics together can give a realistic picture of the plasma composition of a discharge with HMDSO diluted in oxygen, argon and/or helium.
Future plasma process reactors in research or in production should be equipped, besides basic parameter measurements, with several complementary plasma diagnostics. Their interplay of different diagnostic methods is a necessity for the advance of plasma processing and towards a better understanding of its physics and chemistry.

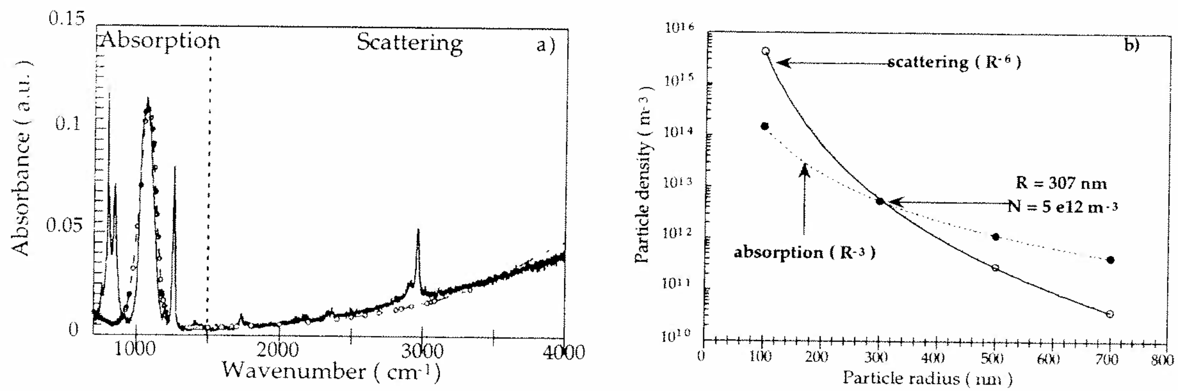

Figure 3: a) Measured absorbance spectrum and calculated absorption and scattering contributions of a diluted HMDSO plasma. 10 sccm HMDSO, O2 and helium at a pressure of 0.1 mbar. b) Determination of the size and particle number density from the absorbance spectra in fig. 3a.

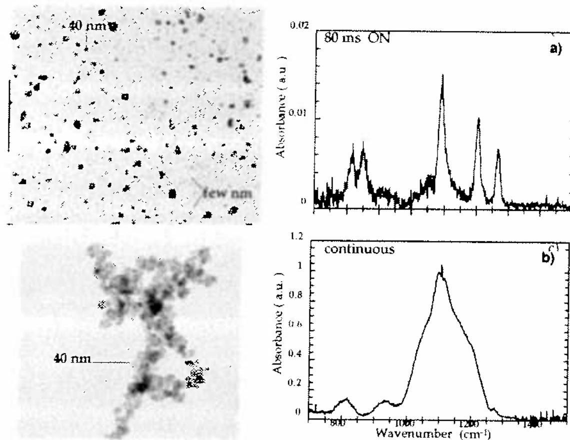

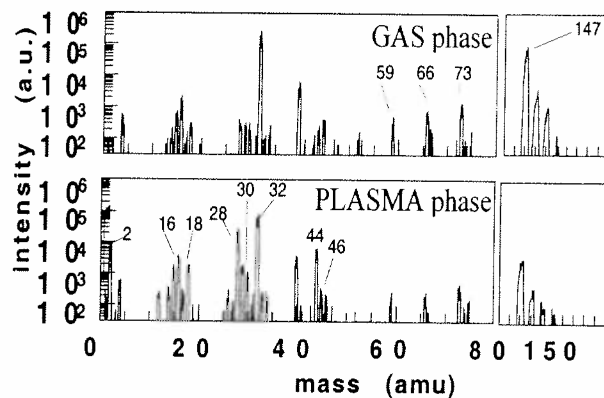

Figure 4: Comparison of absorbance spectra of a RF power modulated and of a continous plasma with TEM pictures produced in these discharges.
a) modulated (80 ms ON, 1600 ms OFF)
b) continous RF power discharge

Figure 5: Mass spectra of a diluted HMDSO in gas and plasma phase. 1.5 sccm HMDSO, 14.5 sccm O_2, 1 sccm Ar and He.

References

[1] C.Rau, W. Kulisch; Thin.Solid.Films, **249**, 28-37 (1994)

[2] N.B. Colthup, L.H. Daly and S.E. Wiberley, *Introduction to infrared and Raman Spectroscopy* (Academic Press, San Diego, 1990)

[3] G. Socrates, *Infrared characteristic group frequencies*, Sec. Ed (John Wiley, Chichester,1994)

[4] Y. Segui and P. Raynaud, "Plasma diagnostic by Infrared Absorption Spectroscopy", in Plasma Processing of Polymers. Vol. NATO ASI Series E: Applied Science- Vol. 346, pp 81-100.

[5] T.A. Cleland and D.W. Hess, J. Appl.Phys. **64** (3), 1068-1077 (1988).

[6] C. Courteille, D. Magni, Ch. Deschenaux, P. Fayet, A.A. Howling and Ch. Hollenstein. 41th Annual Technical Conference Proceedings of the Society of Vacuum Coaters, 327-332 (1998).

TDL Absorption Diagnostics and Chemical Modelling of Microwave Plasmas Containing Hydrocarbons

L. Mechold[1], J. Röpcke[1], M. Käning[1], D. Loffhagen[1] and P.B. Davies[2]

[1] *Institut für Niedertemperatur-Plasmaphysik, 17489 Greifswald, F.-L.-Jahn-Str. 19, Germany*

[2] *Department of Chemistry, Univ. of Cambridge, Lensfield Road, Cambridge CB2 1EW, U.K.*

Introduction

Low pressure, non-equilibrium, molecular microwave plasmas are of growing interest in the field of plasma processing and technology due to their favourable properties, such as their high chemical reactivity caused by the large concentrations of transient or stable chemically active neutral species present. The investigation of plasma chemistry and kinetics *in situ* requires detailed knowledge of the main plasma parameters, which can be obtained by appropriate diagnostic techniques. Tunable infrared diode laser absorption spectroscopy (TDLAS) has been applied to determine the ground state concentrations of many molecular plasma species. These experiments are accompanied by model calculations and the corresponding results are presented in this paper.

Experiment

Planar microwave (2.45 GHz) plasma reactors have been used extensively for plasma chemical applications [1]. The experimental arrangement for the present studies has been described in detail in [2] so that only a short summary is given here. The infrared diode laser beam from the TDL source assembly entered the plasma chamber via a KBr window. The measurements reported here were made at a fixed position in the reaction chamber with the laser beam making two passes through the plasma. After leaving the plasma reactor the diode laser beam passed first through a mode selection monochromator before detection with a HgCdTe detector. The plasma vessel was filled with 1.5 mbar of H_2-Ar-O_2-CH_4 (or -CH_3OH) mixtures by means of a mass flow controller system. For all experiments shown here the partial pressures of Ar and CH_4 (or CH_3OH) were 10.8 % and 7.2 %, respectively. The hydrocarbon content was selected to represent typical flows used in practical CVD reactors. TDLAS has been used to measure under static conditions (sc) the methyl radical and ten other significant stable molecules with concentrations varying over more than six orders of magnitude. The static condition was chosen to avoid flow effects and to be sure that no further temporal changes of the concentration appeared.

Modelling of the Plasma

In order to obtain a deeper understanding of the main kinetic processes in microwave plasmas containing hydrocarbons, model calculations for the chemical kinetics of H_2-Ar-O_2-CH_4 mixtures have been performed. The model is based on a set of rate equations for 21 components and about 90 of their reactions have been taken into account. The rate coefficients for the various chemical reactions are averaged over space and time and have mainly been taken from the literature [3-9]. The rate coefficients for the electron collision processes have been determined by solving the time-dependent Boltzmann equation for given values of the reduced electric field, the microwave frequency and the mixture composition up to the establishment of the periodic state, followed by averaging the results over the microwave cycle. The calculations have been performed using a multi-term approximation for the

electron velocity distribution function expanded in Legendre polynomials and solved using the solution technique described in [10]. The model does not include an electron rate equation. The electron density has been assumed to be constant and its value has been chosen to give the measured power input. The rate equations form a system of stiff ordinary differential equations which has been solved using the programming package KINEL [11]. Starting from different mixture compositions the concentrations of the species under static conditions have been determined by means of a time-dependent relaxation procedure. The static condition is reached if all species concentrations become time-independent.

Results

The present studies have been performed for a total pressure of 1.5 mbar and a microwave power of 1.5 kW. The concentrations of eleven species measured at different H_2/O_2 ratios are shown in Fig. 1 for methane and Fig. 2 for methanol, where the total H_2+O_2 content is constant and corresponds to a value of 455 sccm. The right-hand panels of each figure show the most noticeable oxygen-dependent changes that occurred for C-2 hydrocarbons. The figures also give an overview of the mass balance and the degree of dissociation. The major products at high oxygen content are water, carbon monoxide and carbon dioxide. By comparing the concentrations of CO and CO_2 formed with the concentration of hydrocarbons removed, it became obvious that about 50% of the available methane and up to 80% of the available methanol appear as CO and CO_2.

As shown in Fig. 1 the methyl radical concentration was found to be in the range of 10^{10}-10^{12} molecules cm^{-3} and the degree of dissociation of methane increased up to slightly more than 90%. The concentration of the methyl radical decayed exponentially in the case of

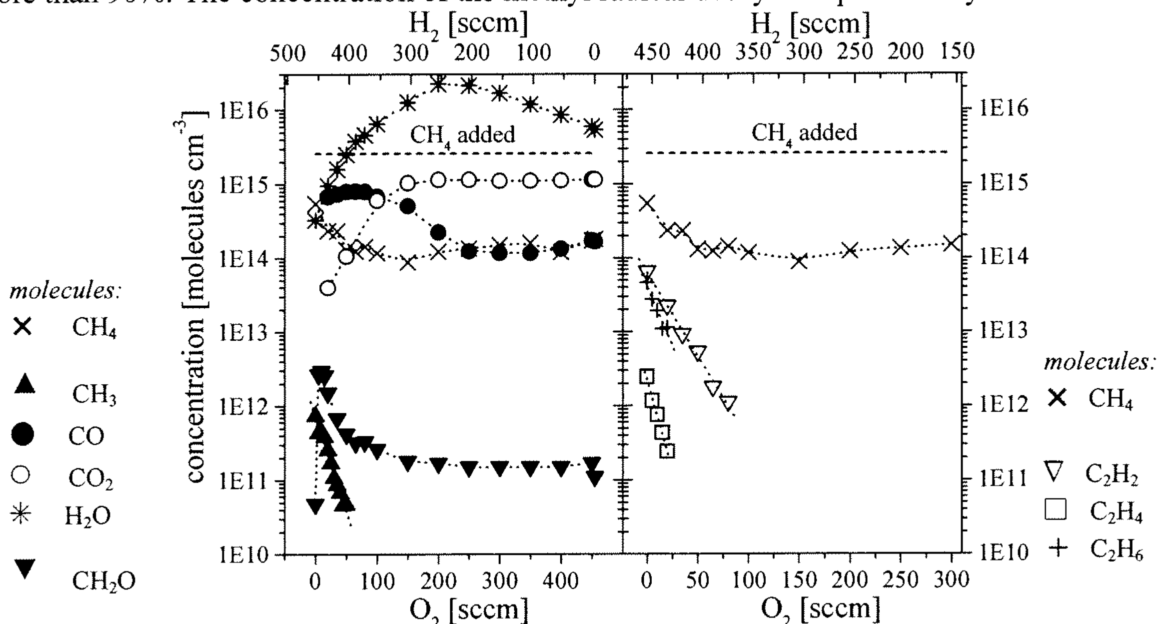

Figure 1: *Molecular concentrations in methane plasmas as a function of the H_2/O_2 ratio*

increasing oxygen content. The same behaviour was observed for all product hydrocarbons like C_2H_6, C_2H_4 and C_2H_2. Oxidation products like CH_2O, CO and CO_2 appeared when oxygen was added. The CO and CO_2 concentrations show their characteristic behaviour: at lower oxygen content the concentration of CO is higher than that of CO_2, but with increasing oxygen content the CO_2 concentration finally exceeds that of CO. The water concentration is mainly governed by the ratio of hydrogen to oxygen. It rises steeply to a maximum at a H_2/O_2 ratio of about 1:1.

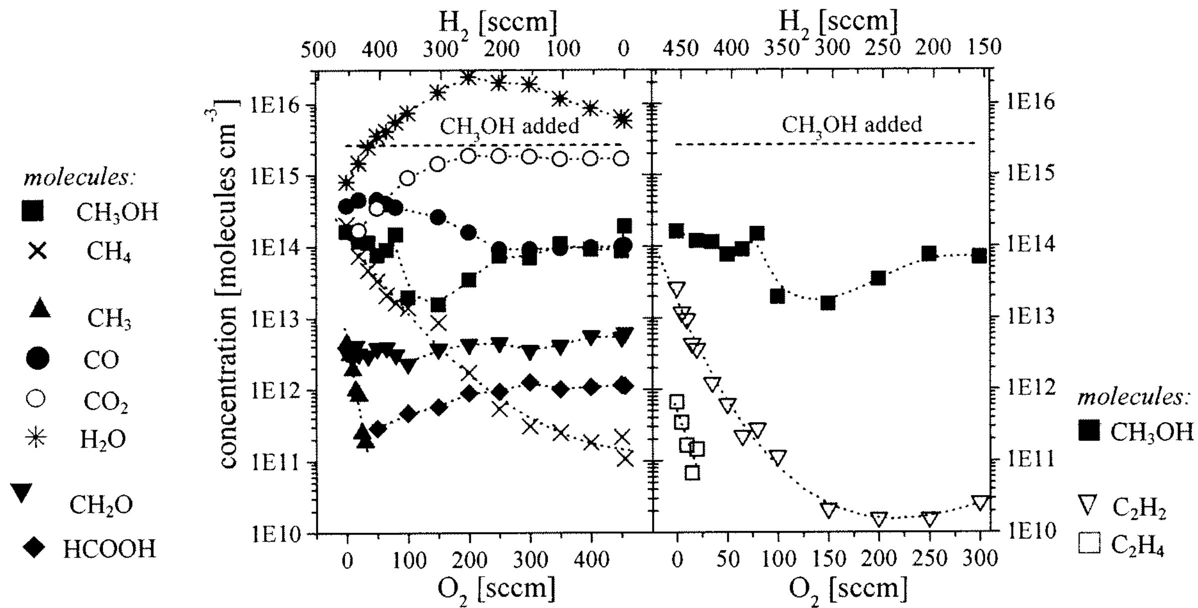

Figure 2: *Molecular concentrations in methanol plasmas as a function of the H_2/O_2 ratio*

Figure 2 shows the experimental results in H_2-Ar-O_2 plasmas containing methanol. It can be seen that increasing oxygen content has a more marked effect for methanol than for methane plasmas. The degree of dissociation is higher and reaches about 99% for methanol. The methyl radical was also formed and decayed exponentially with increasing oxygen content. The same products are not always found for both precursor hydrocarbons. Thus, methane was detected in methanol plasmas, but methanol was not detected in methane plasmas. Formaldehyde was detected in both types of hydrocarbon plasmas containing oxygen and its concentration was always considerably higher in methanol than in methane plasmas. Formic acid was only detected in methanol plasmas. Its concentration behaviour roughly followed that of formaldehyde. This suggests that it was produced from CH_2O.

Model calculations have been performed for plasmas containing methane. Figure 3 shows the measured and calculated results for the oxygen-free H_2-Ar-CH_4 mixture with a composition of 82/10.8/7.2 % at a total pressure of 1.5 mbar and a gas temperature of 1000 K. The theoretical and experimental results for the species produced in the plasma match within an order of magnitude.

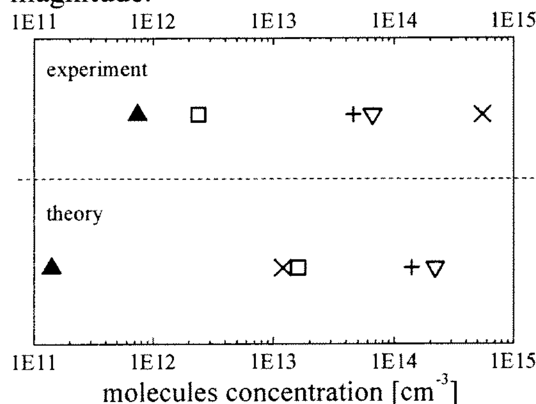

Figure 3: *Measured and calculated species concentrations in a H_2-Ar-CH_4 plasma.*

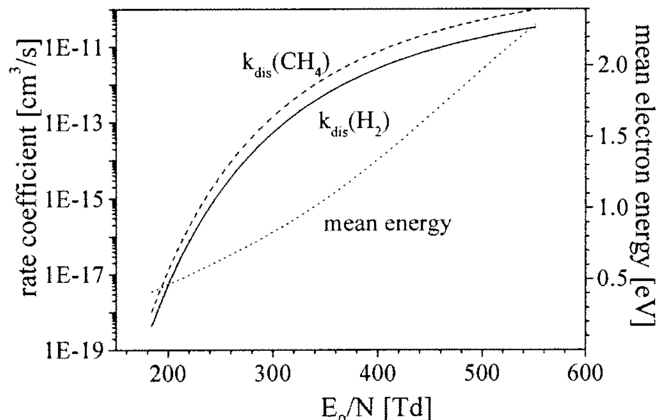

Figure 4: *Calculated dissociation rate coefficients and mean electron energy as a function of the reduced field strength*

× - CH_4; ∇ - C_2H_2; □ - C_2H_4; + - C_2H_6; ▲ - CH_3

Electron collisions can be assumed to be the initiating processes which dissociate the source gas [3,9]. The corresponding rate coefficients for the electron collision dissociation of H_2 and of CH_4 as a function of the amplitude of the reduced microwave electric (E_0/N) field are presented in Fig. 4. In addition, the mean electron energy is shown in this figure. These time-averaged quantities have been determined using the above-mentioned procedure for the solution of the electron Boltzmann equation. The relevant electron collision cross sections for H_2, Ar and CH_4 have been taken from [12], [13] and [14], respectively. The calculated results presented in Fig. 3 have been obtained using the rate coefficients for an E_0/N of about 280 Td.

Conclusion

The concentrations of eleven different species in microwave plasmas containing hydrocarbons have been measured by infrared diode laser spectroscopy. The experimental results show the versatility of this technique, which has enabled progress to be made in determining which species are present. The concentrations of these species has been measured a wide range of oxidising conditions. The experiments are accompanied by model calculations. First results match with the experimental data to within one order of magnitude for the plasma produced species and hence the main reaction paths have been established.

Literature

1. A. Ohl, Large Area Planar Microwave Discharges, in *Microwave Discharges: Fundamentals and Applications*, C.M. Ferreira (Ed.), Plenum, New York, 205 (1993).
2. J. Röpcke, L. Mechold, M. Käning, W.Y. Fan and P.B. Davies, *Plasma Chemistry and Plasma Processing*, (1999), in press.
3. L. E. Kline, W. D. Partlow and W. E. Bies, *J. Appl. Phys.* **65**, 70 (1989).
4. K. Tachibana, M. Nishida, H. Harima and Y. Urano, *J. Phys. D: Appl. Phys.* **17**, 1727 (1984).
5. M. Frenklach and H. Wang, *Phys. Rev. B* **43**, 1520 (1991).
6. L. S. Zelson, D. F. Davidson and R. K. Hanson, *J. Quant. Spectrosc. Radiat. Transfer* **52**, 31 (1994).
7. D. L. Baulch et al., *J. Phys. Chem. Ref. Data* **21**, 411 (1992).
8. W.L. Hsu, *J. Appl. Phys.* **72**, 7, 3102-3109 (1992).
9. W.Y. Fan, P.F. Knewstubb, M. Käning, L. Mechold, J. Röpcke and P.B. Davies, *J. Phys. Chem.*, submitted.
10. D. Loffhagen and R. Winkler, *J. Phys. D: Appl. Phys.* **29**, 618 (1996).
11. A. Levchenko and G. Alexeev, KINEL Manual, Moscow (1994).
12. S. J. Buckman and A. V. Phelps, *JILA Information Center Report* **27**, University of Colorado, Boulder, Colorado (1985).
13. M. Hayashi, Electron Collision Cross Sections, in: *Plasma Material Science Handbook*, Japan Society for the Promotion of Science (Ed.), Ohmsha, Ltd, Tokyo, 748 (1992).
14. D. K. Davies, L. E. Kline and W. E. Bies, *J. Appl. Phys.* **65**, 3311 (1989).

Optical Emission Study of Plasma-Surface Interaction in Reactive Plasmas

S.A.Moshkalyov
School of Mathematics and Physics, Queen's University of Belfast, Belfast, Northern Ireland, UK

Introduction
Plasma processing of materials often involves bombardment of surfaces with energetic ions. In this work, spatially-resolved optical emission spectroscopy was employed for experimental study of material sputtering in reactive plasmas containing chlorine. Sputtering-induced optical emission from the target (Si, Al) was found to be strongly localized near the surface. Both atomic (Si, Al) and molecular (SiCl, AlCl) sputtering-induced emission was observed. Velocities of sputtered excited atoms and molecules were found from the emission spatial decay ($>10^6$ cm/s and $\sim 10^5$ cm/s, respectively), and mechanisms of excitation were shown to be different for atoms and molecules. Fast excited atoms can be produced only in the first collisions of incident ion in the surface layer, and slow excited molecules are knocked off by secondary atoms originated from a collision cascade inside the solid.

Experimental
Experiments on reactive ion etching were performed with a RF discharge (13.56 MHz) in a diode type etcher with the operational parameters varied in the ranges of 0.1-1 Pa, 3-50 sccm, 10-400 W, respectively [1,2]. Cl_2 or $SiCl_4$ mixtures with Ar were used. An Al_2O_3 powered electrode was partly covered by Si wafer (10 and 15 cm in diameter, respectively). Plasma emission was collected through the quartz window by use of the quartz lens. Two diaphragms were utilized for selecting of emission only from the narrow area above the electrode. A small scanning monochromator (1 nm spectral resolution) was employed for spectra recording. The detection system was mounted on a platform, which can be scanned in vertical direction with precision better than 1 mm.

Results and discussion
It has been found that emission of species, originating from the processed material (Si, Al, SiCl, AlCl) is localized typically within several mm from the surface, in the sheath region. For the most cases, this emission peaks not exactly at the surface as it could be expected, but at some distance (2-3 mm) apart. The distance at which the Si line emission peaks, differs for different lines.

In the bulk plasma (both for Cl_2 and $SiCl_4$ discharges) SiCl molecules were found to emit basically at 280.9 and 282.3 nm ($B'^2\Delta \rightarrow X^2\Pi_r$ transition), while near the wafer surface (within 1-2 mm) the maximum of emission was shifted to 280 nm with the smaller peak

appeared at 285 nm and with a relatively weak emission observed at 282.3 nm. This is likely due to rotational (vibrational) excitation of sputtered molecules, which can be in either $B'^2\Delta$ or $B\ ^2\Sigma^+$ electronic state [3]. Another species existing in plasma, are unlikely to emit at these wavelengths.

Several mechanisms which may produce excited species near the surface have been considered [1,2], and sputtering-induced excitation has been shown to be responsible for the observed localized emission of sputtered particles in plasma sheath. For low-pressure plasmas, excitation by secondary electrons, accelerated in the sheath, could be important. However, in this case the local emission peaks should exist also for main plasma species, like Ar, in contrast to that observed.

Excitation of sputtered atoms and molecules under bombardment by energetic ions was studied earlier in beam experiments [4]. The process of surface sputtering in reactive plasma environment has several distinctive features. Two factors can affect substantially the characteristics of sputtering-induced emission in plasma environment: strong coverage of the surface by chemisorbed reactants and collisions of sputtered excited particles in the sheath. Like a sputtering yield, an atomic excitation yield also can be strongly enhanced under high coverage conditions since a large part of atoms, sputtered from the surface top layer, may be primarily in a molecular form [4]. Further, in plasma environment the population of excited levels of sputtered atoms can be perturbed by electric field and collisions in a sheath, which can lead to enhanced non-radiative relaxation of highly excited levels, and eventually, to increased intensity of the emission from the lower ones. The observed non-monotonical spatial behavior of the sputtered-induced emission $I^*(x)$ gives the evidence that excitation of a large number of upper-lying levels does take place under present plasma conditions. This results in the cascade feeding of the lower-lying levels, from which the observed transitions occurs.

To take into account the cascade feeding, a simplified level scheme can be considered [1]. In this scheme the upper levels are grouped into one level (3), decaying with some average relaxation rate through the lower ones and resulting in the observed transition $2 \rightarrow 1$. Assuming only radiative transitions between the levels under consideration, one can get the following solution for population of level 2 at 3-level scheme :

$$N_2(t) = \frac{N_3(0)\tau_{2,1}}{\tau_{3,2} - \tau_{2,1}}\left[\exp\left(-\frac{t}{\tau_{3,2}}\right) - \exp\left(-\frac{t}{\tau_{2,1}}\right)\right] \qquad (1),$$

where $\tau^{-1}_{i,k}$ are the rates of radiative decay from *i*- to *k*-level, and $\tau^{-1}_{2,1} >> \tau^{-1}_{3,2}$. This solution shows a non-monotonical behavior of the emission (in time and in space), with a fast rise and slow decay with the effective decay time $\tau_{3,2}$, depending on the actual level scheme.

Further, from Eq.(1) the time of peak emission can also be estimated:

$$t_{peak} = \frac{x_{peak}}{v_{\perp}} \approx \frac{\tau_{2,1}\tau_{3,2}}{\tau_{3,2} - \tau_{2,1}} \ln \frac{\tau_{3,2}}{\tau_{2,1}} \qquad (2).$$

From the measured distance of the emission peak from the surface ($x_{peak} = t_{peak}\, v_{\perp}$) and the decay lenght, values of both τ_{eff} and $v_{\perp}$ can be estimated, if τ_{l} is known. From the experimental data, velocities of sputtered excited Al and Si atoms have been estimated to be in the range (2-7)x 10^6 cm/s, with the corresponding kinetic energies of 50-700 eV.

Unlike atoms, excited molecules do not show clear evidence of the cascade feeding from the upper electronic states, since a monotonical decay with distance from the surface is observed for molecular sputtering-induced emission. The origin of excited molecules is different from that of atoms (most probably, a knock-off by slow (~10^5 cm/s) secondary atoms, produced during a collision cascade of the energetic ion in the target). Collisions with fast ions likely cause dissociation of surface molecules rather than their internal excitation.

The observed spectral features of SiCl emission in the region of 280-290 nm are of particular interest. In bulk plasma SiCl transitions in this spectral region (from $B\,^2\Sigma^+$ and $B'\,^2\Delta$ excited states) have doublet structure, since the lower state $X\,^2\Pi_r$ has a considerable spin-orbital doublet splitting. The change of the SiCl spectra in the vicinity of the surface, can be explained by the strong rotational excitation of sputtered molecules. With the increasing rotation, transition between the Hund's case (a) to (b) can occur, with the corresponding shift of the wavelength and gradual reducing of the doublet splitting (spin uncoupling) [5].

Sputtering of diatomic molecules from the surface top layer has been considered within the frame of an impulsive collision model developed in Ref.6. This model describes the process of sputtering as a single correlated collision between an energetic subsurface particle and two atoms of a molecule, weakly bound to the surface. The molecule obtains translational and internal energy during the collision as a result of a direct inter-nuclear momentum transfer between projectile and the constituent atoms of the molecule. The results of calculations [2] are in qualitative agreement with the experimental data, showing that strong rotational excitation is possible for this type of collision.

References

[1] S.A.Moshkalyov, M.Machida, D.Campos, A.Dulkin; J. Va. Sci. Technol., B **16**, 514 (1998)

[2] S.A.Moshkalyov, M.Machida, D.Campos; Jpn. J. Appl. Phys., **36**, 4675 (1997)

[3] J.B.Jeffries; J. Chem. Phys., **95**, 1628 (1991)

[4] R.B.Wright and D.M.Gruen; J. Chem. Phys., **73**, 664 (1980)

[5] G.Herzberg: Spectra of Diatomic Molecules (Van Nostrand Reinhold, New York, 1950)

[6] R.de Jonge, J.Los and A.E.de Vries; Nucl. Instrum. & Methods, B **30**, 159 (1988)

DIAGNOSTICS OF A PLANAR MAGNETRON SPUTTER SOURCE BY LANGMUIR PROBE AND OPTICAL EMISSION SPECTROSCOPY

A. Neuffer and A. Lunk

Institut für Plasmaforschung, Universität Stuttgart, Pfaffenwaldring 31, D-70569 Stuttgart

Introduction

In a planar magnetron sputter device plasma parameters were measured by plane and cylindrical Langmuir probes and emission spectroscopy. The sputter gases used were helium, neon and argon. Following parameters were measured by Langmuir probes in dependence on the distance r to the cathode: $n_e(r)$, $k_BT_e(r)$, $U_{pl}(r)$ and the electron energy distribution function (EEDF(r)). The measurement of the electron temperature by emission spectroscopy were performed by adding a small amount of helium into argon [1]. A two fluid model based on [2] was developed with ions and electrons as the two components of the magnetron discharge.

Experimental setup

The magnetron is located in the center of the vacuum chamber with a titanium target which is 160 mm in diameter. A cylindrical and a plane Langmuir probe were used for the measurements of the plasma parameters. These probes are driven by computer controlled stepper motors for an exact positioning. The light emitted from the plasma were measured by an 1m B&M spectrometer. For noise reduction the signal from the photo multiplier was amplified with the lock-in technique. Fig. 1 shows the experimental setup.

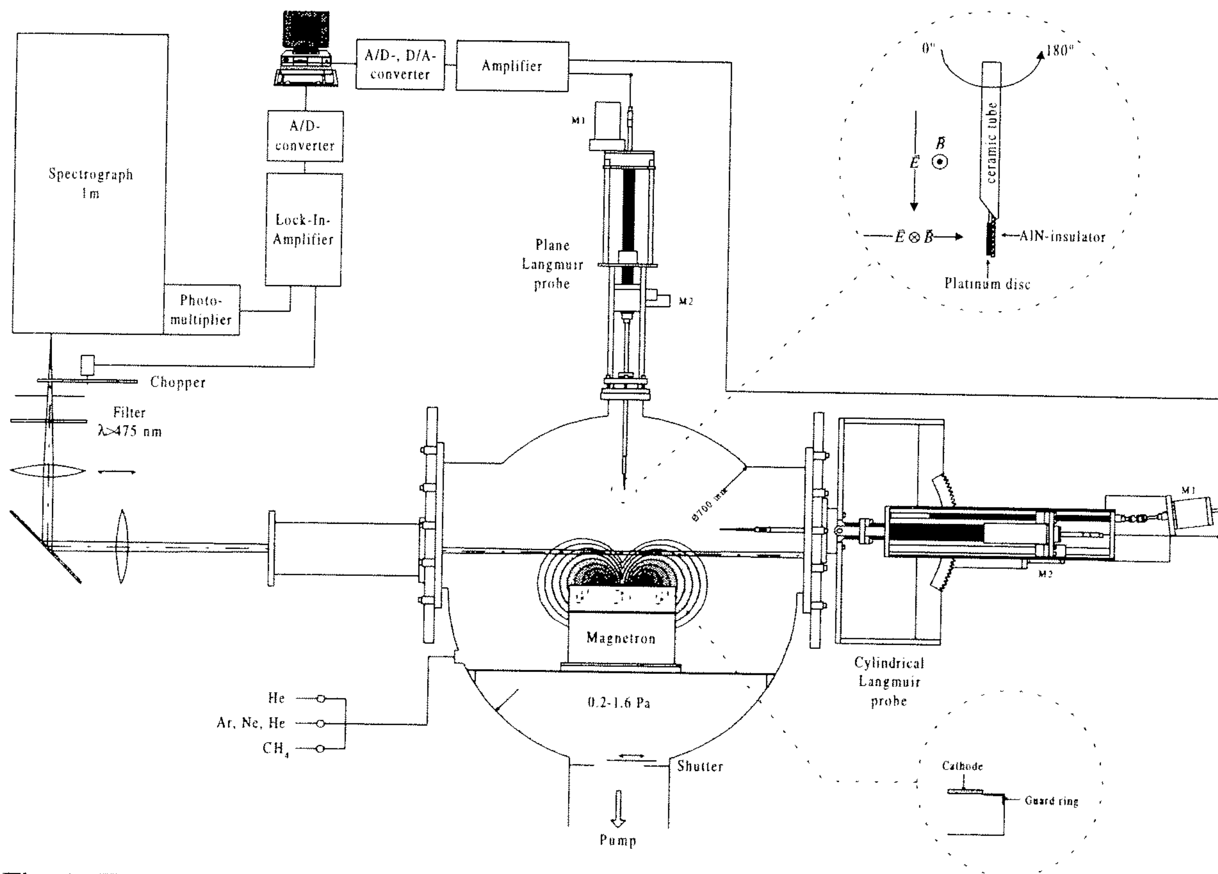

Fig. 1 Experimental setup.

Results and discussion

The spatially resolved measurements of the plasma parameters with the Langmuir probe show a constant plasma density, average electron energy and plasma potential along magnetic field lines. Fig. 2 shows the electron density in dependence on the radial and axial distance to the cathode.

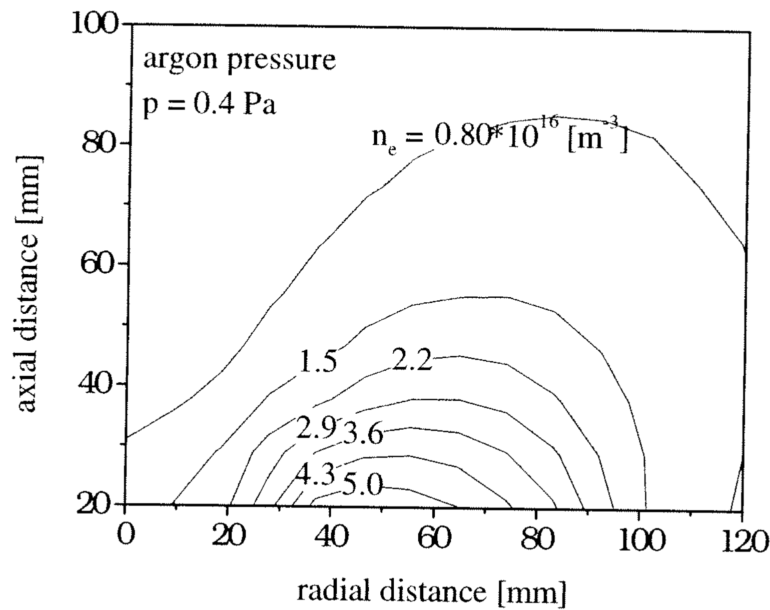

Fig. 2 Electron density in dependence on the axial and radial distance to the target.

Perpendicular to the magnetic field lines both plasma density and average electron energy decrease exponentially with increasing distance to the cathode. The measured and the modelled electron densities are shown in fig. 3.

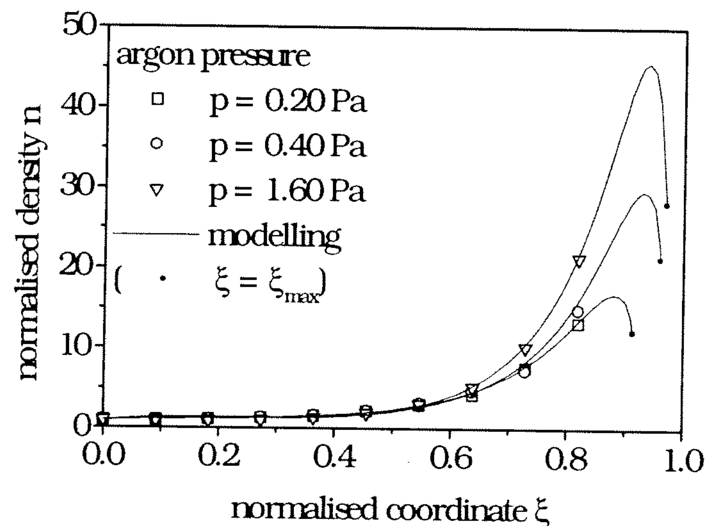

Fig. 3 Measured and modelled normalised electron density perpendicular to the magnetic field lines.

Here $\xi = 1$ marks the position of the cathode and $\xi = 0$ corresponds to a distance r of 130 mm

to the cathode: $\xi = 1 - \frac{r}{130mm}$. The electron density n is normalised to the density at r = 130 mm so that n = n(ξ)/n(r = 130 mm). The measurements were done at that points with distance to the cathode where the component of the magnetic field perpendicular to the cathode surface vanishes. With increasing pressure the average electron energy decreases and the electron density increases. The emission spectroscopy shows significant differences of the electron temperatures $k_B T_e$ for larger distances to the cathode in contrast to the measurements with the Langmuir probes. Also a minimum was detected in the spatially resolved electron temperature measurements by emission spectroscopy. The results of these measurements are shown in fig. 4.

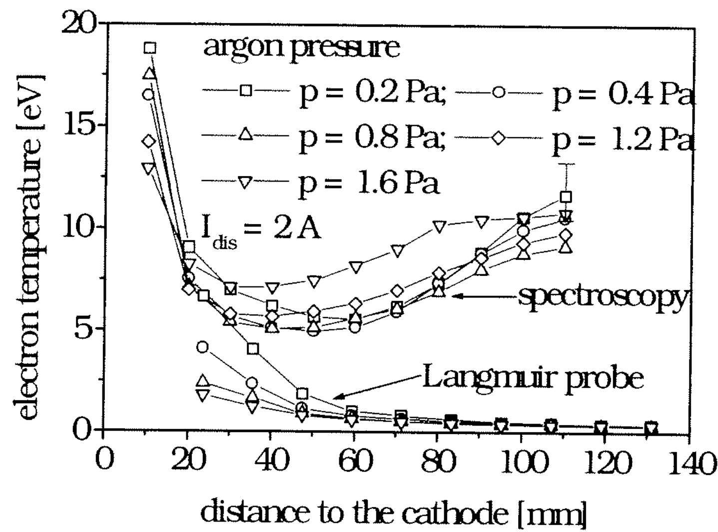

Fig. 4 Electron temperature measured by Langmuir probes and emission spectroscopy.

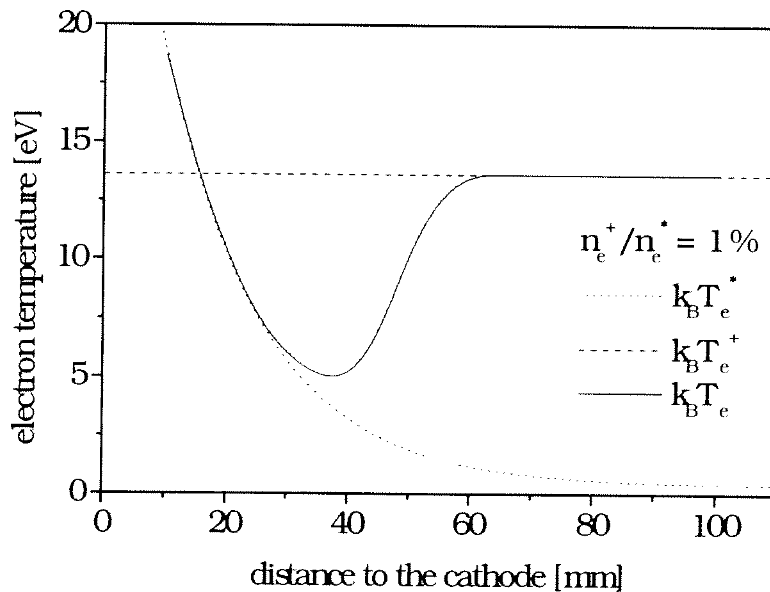

Fig. 5 Electron temperature $k_B T_e$ calculated from the line intensity ratio of Ar/He for two

electron groups with temperature $k_BT_e^*$ and $k_BT_e^+$. Fig. 5 shows the electron temperature calculated from the line intensity ratio of argon and helium (667.73 nm/667.82 nm) with the assumption of bulk electrons with a temperature $k_BT_e^*$ and density n_e^* and a high energetic electron group with a constant temperature $k_BT_e^+$ = 13.6 eV and density n_e^+:

$$\frac{I_{Ar}}{I_{He}} = \frac{n_{Ar} X_{Em,Ar}(k_B T_e)}{n_{He} X_{Em,He}(k_B T_e)} = \frac{n_{Ar}\left(n_e^* X_{Em,Ar}(k_B T_e^*) + n_e^+ X_{Em,Ar}(k_B T_e^+)\right)}{n_{He}\left(n_e^* X_{Em,He}(k_B T_e^*) + n_e^+ X_{Em,He}(k_B T_e^+)\right)} \frac{I_{Ar}}{I_{He}}.$$

We concluded from the discrepancy in the measured electron temperatures, obtained by Langmuir probes and emission spectroscopy, that in the magnetron discharge additional electrons with a high temperature $k_BT_e^+$ and low density n_e^+ (≤ 1 % of the density of the bulk electrons) exist. The temperature $k_BT_e^+$ of these high energy electrons were derived from the measurements by emission spectroscopy at a distance of 110 mm to the cathode. In this region the bulk electrons with a temperature $k_BT_e^*$ of 0.3 eV make no significant contribution to the excitation and ionisation processes. With decreasing distance to the cathode the temperature of the bulk electrons increases (derived from the Langmuir probe measurements) and their contribution to the excitation becomes important.
The modelling of the discharge was only possible with the existence of electrons with high temperature $k_BT_e^+$. Fig. 6 shows the resultant ionisation frequency ν_{ion} from the modelling, which is the sum of the ionisation frequencies of the hot component (ν_{ion}^+) and the bulk electrons (ν_{ion}^*): $\nu_{ion} = (1-c)\nu_{ion}^* + c\nu_{ion}^+$. The relative concentration $c = n_e^+/n_e^*$ is 0.51 % and $k_BT_e^+$ = 12.7 eV.

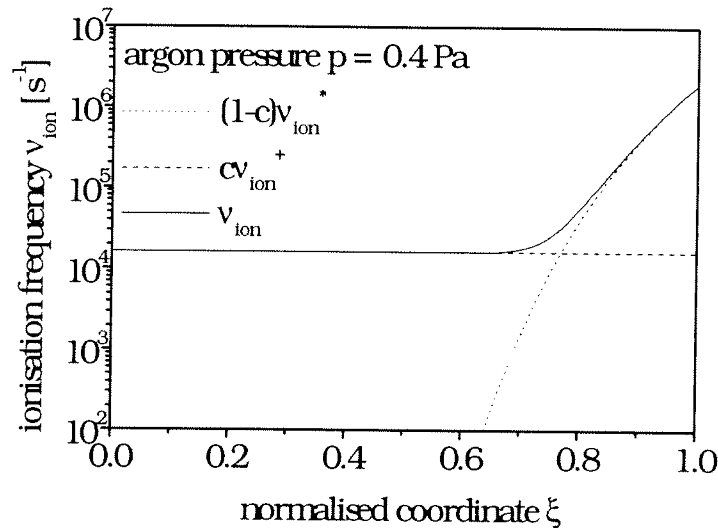

Fig. 6 Resultant ionisation frequency ν_{ion} from the modelling

References
[1] K. Behringer, Plasma Phys. Contr. Fusion **33** (1991) 997
[2] J. W. Bradley, Plasma Sources Sci. Technol. **5** (1996) 622

Modeling of the Composition of the Ion Flux Emanating from a Methane Electron Cyclotron Resonance Plasma

P. Pecher
Max-Planck-Institut für Plasmaphysik, EURATOM Association,
POB 1533, D-85740 Garching, Germany

Introduction

Having interesting properties and a wide range of applications carbon and hydrogen containing (C:H) films are widely used in technology [1]. However, the microscopic growth processes of the films during plasma deposition are mostly unknown. Besides cross sections of growth reactions, the particle fluxes emanating from the plasma onto the growing film/substrate are of predominant importance for improving the knowledge of the film growth. Recently, a simple plasma model was proposed describing the flux of particles towards and from the surface by taking into account electron-induced ionization and dissociation of the neutral gas and reactions at the growing film surface [2-5]. Chemical reactions in the plasma are neglected, according to the low pressure in electron cyclotron resonance (ECR) plasmas.

In this paper the measured composition of the ion flux emanating from ECR methane plasmas is presented, which cannot be described, not even qualitatively, by the recent plasma model. A plasma model based on ion-molecule reactions using the measured neutral gas partial pressures is developed and compared with the measured composition of the ion flux.

Experimental

The experiments were performed in an ECR apparatus which was used previously to measure ion-energy distributions with a retarding field analyzer (RFA) [6] and CH radical densities [7]. The system consists of a stainless steel vacuum chamber with a volume of 15 l, which is pumped to a base pressure of about $3 \cdot 10^{-5}$ Pa by a turbomolecular pump. Methane (99.5% purity) is introduced via commercial mass flow controllers into the chamber, while the pressure is controlled independently using a throttle valve between chamber and pump. The magnetic field is provided by a set of external solenoids and the microwave (HF) power at 2.45 GHz is introduced through an aluminum oxide window from the high-field side ($B > B_{res}$). The flux of particles is measured by a differentially pumped commercial energy mass analyzer (HIDEN EQP HAL 301 S/2) immersed into the plasma for line of sight measurements through a 50 μm sampling orifice. This analyzer is magnetically shielded an consists of an ion transfer optics, an ionizer for detection of neutral components, an electrostatic 45° energy analyzer, and a quadrupole mass spectrometer with a channeltron detector [8]. With this analyzer neutral gas densities [9] and methyl radical fluxes [10] were measured in ECR methane plasmas. The transmission of the HIDEN EQP was determined by comparing its results with absolute RFA measurements for noble gas plasmas under identical plasma conditions.

Model

The measured composition of the ion flux shows high abundances of hydrocarbon ions, which cannot be formed by electron impact ionization in the plasma, e.g. H_3^+, CH_5^+, $C_2H_3^+$, $C_2H_5^+$, $C_3H_3^+$ or $C_3H_5^+$ (see figures 1, 2). These high abundances cannot be explained by the recent ECR plasma model [2-5] which take into account only electron-induced ionization, thus producing CH_4^+ as the heaviest ion in methane plasmas. The recent ECR plasma model do also neglect chemical reactions in the plasma, since the pressure is low. This is true for most reactions between neutral particles, but rate coefficients for ion-molecule reactions reported in literature [11] are often much higher. To explain the composition of the ion flux a simple plasma model based on ion-molecule reactions was developed. Basic idea is the stationarity of the plasma ion densities in the plasma in equilibrium. The loss of the ions due to the ion flux has to be balanced by the primary electron-induced ionization of the neutral gas and the change of ion densities due to ion-molecule reactions. The ion flux is determined by the ion residence time, which was calculated for the used reactor [2,3]. The influence of the ion-molecule reactions is described using the rate coefficients from literature [11] and the measured neutral gas densities in the plasma [9]. The production rate of ions due to primary electron-induced ionization of neutral gas is calculated like in the recent plasma model [2,3], but the electron temperature is assumed to have a fixed, pressure dependent value. Note that the presented model is not a self-consistent calculation.

Results

Figure 1 shows the measured composition of the ion flux emanating from pure hydrogen ECR plasmas for various pressures as symbols. The lines are model results. In hydrogen plasmas three ions are present: H^+, H_2^+ and H_3^+. The first two ions are primary ions, i. e. they are produced by electron impact ionization of neutral gas (hydrogen). H^+ ions have a small abundance of about 2%, since the rate coefficient for primary ionization

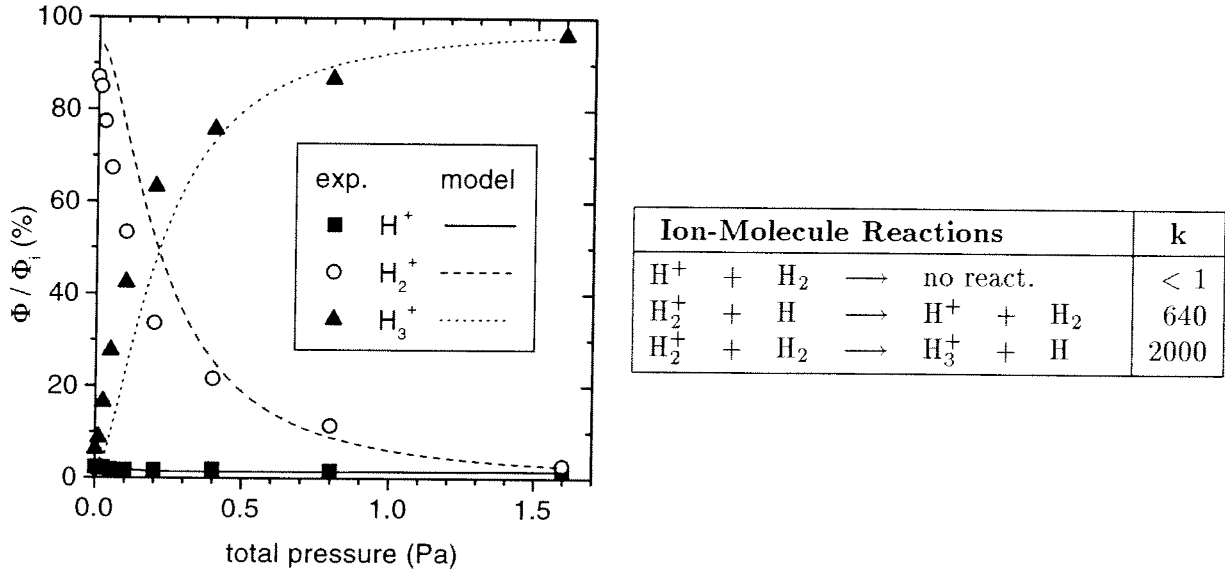

Ion-Molecule Reactions							k
H^+	+	H_2	$\longrightarrow$	no react.			< 1
H_2^+	+	H	$\longrightarrow$	H^+	+	H_2	640
H_2^+	+	H_2	$\longrightarrow$	H_3^+	+	H	2000

Figure 1: *The composition of the ion flux for* H_2 *plasmas at a HF power of 100 W at various pressures. Symbols are experimental, lines are modeling results. On the right hand side ion-molecule reactions with the corresponding rate coefficient* k *in* 10^{12} cm^3 s^{-1} *are listed.*

of H_2 to H^+ is much smaller than to H_2^+. But the abundance of H_2^+ ions decreases with increasing pressure. This is due to ion-molecule reactions. On the right hand side in fig. 1 ion-molecule reactions with reaction rate coefficients [11] in hydrogen plasmas are shown. H^+ and H_3^+ undergo no ion-molecule reaction. H_2^+ reacts with atomic and molecular hydrogen. The model neglects reactions with atomic hydrogen, which is only a minor process here. (The flux/density of atomic hydrogen was under the detection limit of the presented setup [10]). Therefore in the case of hydrogen plasmas there is only one ion-molecule reaction of importance: $H_2^+ + H_2 \longrightarrow H_3^+ + H$. At low pressure the reaction rate for ion-molecule reactions is small, since the molecular hydrogen density is low, and so the ion flux consists mainly of H^+ and H_2^+ ions. With increasing pressure and thus increasing molecular hydrogen density not only the reaction rate for ion-molecule reactions increases, but also the residence times of the ions increase, since the transport becomes more diffusive with increasing gas density. Both effects lead to the fast decrease of the H_2^+ abundance with increasing pressure, while H_3^+ ions are produced. At pressures above 0.1 Pa H_3^+ is the most abundant ion. The model results show a very good agreement with the pressure dependence of the measured abundances.

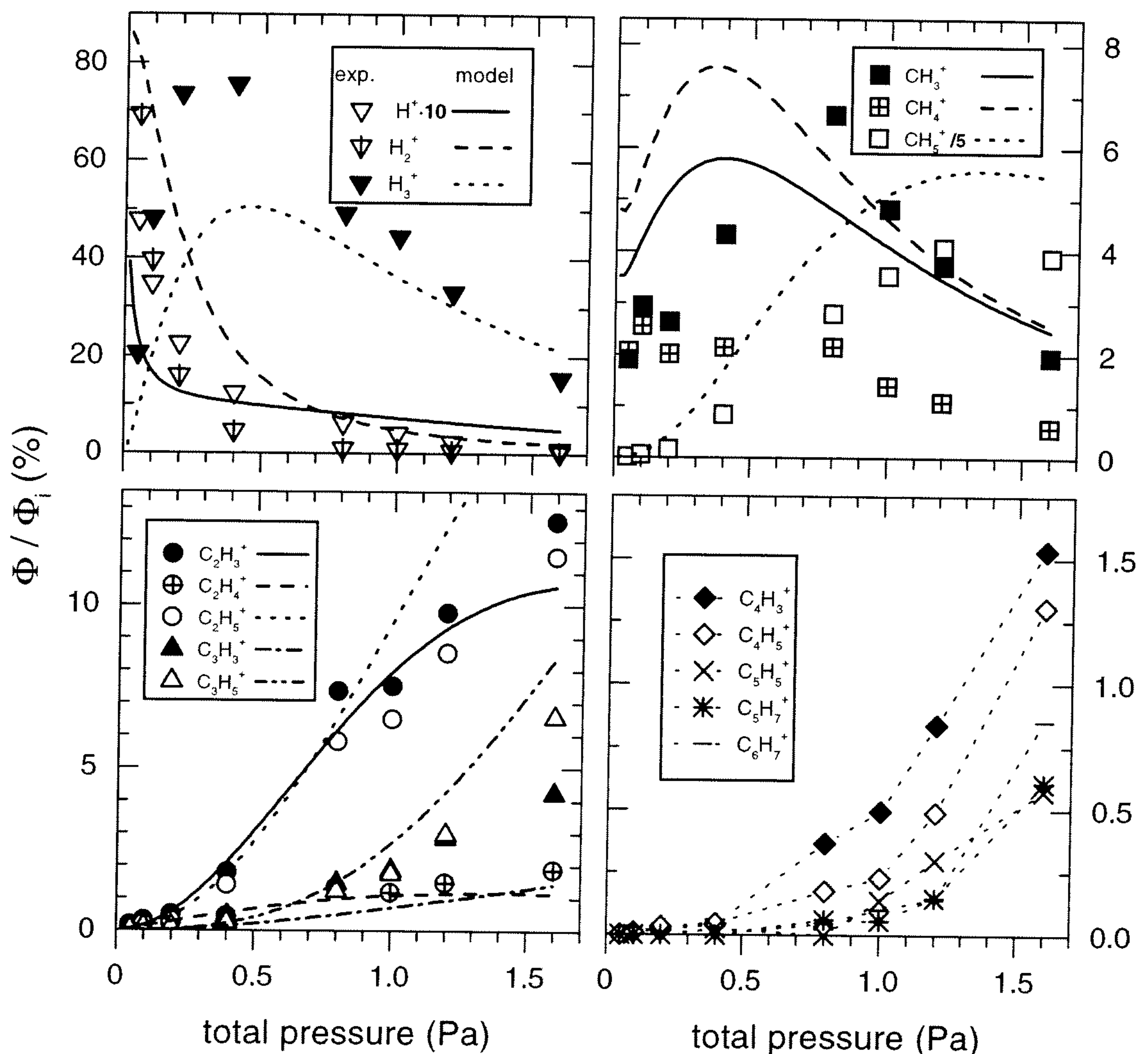

Figure 2: *The abundances of various plasma ions at different pressures. The methane gas flow was 2 sccm, the HF power 100 W. Symbols are experimental, lines are modeling results, except in the graph on the lower right, where only measured results are shown.*

In figure 2 the measured abundances of different ion species for methane plasmas with a gas flow of 2 sccm and various pressures are plotted as symbols. The lines are model results, except for the graph to the lower right. In the case of methane plasmas the model deals with 83 ion-molecule reactions. Therefore, the system is much more complicated than in hydrogen plasmas. With increasing pressure the abundance of light ions decreases while the abundance of heavy ions increases. There is only very rare data for ion-molecule reactions of ions containing more than 2 carbon atoms, so that these reactions are not included in the model. In this case the model describes the dependence of pressure of the abundance of the different ions very good and also the absolute values agree quite well.

Conclusion

The ion flux from hydrogen and methane electron cyclotron resonance plasmas was measured absolutely. The recent plasma model for ECR plasmas, which neglect chemical reactions with reference to the low pressure, is not able, not even qualitatively, to describe the composition of the ion flux. A plasma model based on ion-molecule reactions with rate coefficients from literature and the measured neutral gas densities was developed. The model describes the composition of the ion flux and especially the dependence on the plasma parameter quite well.

References

[1] J. Robertson, Surf. Coat. Technol. **50**, 185 (1992).

[2] M. Engelhard, IPP Report 4/262, IPP, Garching (1993).

[3] W. Möller, Appl. Phys. A **56**, 527 (1993).

[4] A. v. Keudell and W. Möller, J. Appl. Phys. **75**, 7718 (1994).

[5] W. Möller, W. Fukarek, K. Lange, A. v. Keudell, and W. Jacob, Jpn. J. Appl. Phys., Part 1 **34**, 2163 (1995).

[6] P. Reinke, W. Jacob, and W. Möller, J. Appl. Phys. **74**, 1354 (1993).

[7] W. Jacob, M. Engelhard, W. Möller, and A. Koch, Appl. Phys. Lett. **64**, 971 (1994).

[8] I. D. Neale and T. H. Russel, EQP/EQS Operating Manual (Hiden Analytical Ldt., Warrington, England, 1993).

[9] W. Jacob and P. Pecher, in Proceedings of the Frontiers in Low Temperature Plasma Diagnostics II, edited by H. F. Doebele, W. G. Graham, G. Hancock, G. Kroesen, J. Perrin, and N. Sadeghi, (APP, Bochum 1997), pp. 155–158.

[10] P. Pecher and W. Jacob, Appl. Phys. Lett. **73**, 31 (1998).

[11] V. K. Anicich, J. Chem. Phys. Ref. Data **22**, 1469 (1993).

Diagnostics and modelling of an ICP discharge

P. Scheubert, P. Awakowicz, R. Schwefel, G. Wachutka
Lehrstuhl f. Technische Elektrophysik, Technische Universität München, Arcisstr. 21, D-80290 München

Abstract: A 2D-fluid model consisting of balance equations for ion mass and momentum and electron mass and energy was used to calculate electron density and temperature profiles in an ICP. By self-consistent coupling with an electrodynamic model, the power dissipation in dependence of coil positions and currents was taken into account.

The influence of gas pressure and different coil configurations is discussed and compared with experimental results obtained by Langmuir probe measurements. Theory and experiment are in excellent agreement over a wide pressure range.

1 Introduction

In order to calculate transport processes in low temperature plasmas fluid models [1], [2], [3] are widely used. The various models differ in the degree of self-consistency and the number of conservation equations.

In this paper, a model is presented which considers the mass and momentum conservation for ions in the whole simulation domain, i.e. the plasma bulk and the sheath regions. Therefore realistic setups like biased wafers or electric probes can be simulated with this approach.

For the electrons conservation of mass, a drift diffusion approximation and an energy balance equation were used. An electrodynamic model is coupled self-consistently with the plasma model to take into account the heating by the externally applied RF-current .

Calculated density distributions are compared with Langmuir probe measurements. Experiments in an inductivley coupled argon discharge over a wide pressure range (0.5 - 50 Pa) and for different coil configurations were carried out in order to validate the model and the model parameters. For low pressures the agreement of simulation and experiment is excellent, while for higher pressures slight differences might indicate that the thermal conductivity for electrons is overestimated by the simulation.

2 Model

Hydrodynamic balance equations derived from Boltzmann's equation [4], [5] were used. For the ions, conservation of mass (1) and momentum (2) were considered:

$$\frac{\partial n_i}{\partial t} + \nabla \cdot (n_i \vec{v}_i) = n_e \cdot \nu_{iz}(T_e), \qquad (1)$$

$$\frac{\partial(n_i m_i \vec{v}_i)}{\partial t} + \nabla \cdot (n_i m_i \vec{v}_i \vec{v}_i) = e n_i \vec{E} - n_i m_i \nu_i \vec{v}_i. \tag{2}$$

Here, n_i, $\vec{v}_i$ denote ion number density and velocity, respectively. Particle generation is given by $n_e \cdot \nu_{iz}(T_e)$, where n_e is the electron number density and ν_{iz} the ionisation frequency which is a function of the electron temperature T_e. The ion mass is m_i, the electric field is $\vec{E}$ and ν_i is the frequency of inelastic collisions with neutral atoms. Each ion is charged with the elementary charge e.

For electrons, conservation of mass (3) and energy (4) are considered:

$$\frac{\partial n_e}{\partial t} + \nabla \cdot \vec{j}_e = n_e \cdot \nu_{iz}(T_e), \tag{3}$$

$$\frac{\partial n_e \epsilon}{\partial t} + \nabla \cdot \vec{\Gamma}_e = -e\vec{E} \cdot \vec{j}_e - P_c + P_h. \tag{4}$$

The electron particle flux density $\vec{j}_e$ is calculated by a drift-diffusion approximation:

$$\vec{j}_e = \frac{n_e e}{m_e \nu_e} \vec{E} - \frac{1}{m_e \nu_e} \nabla n_e k T_e, \tag{5}$$

where k denotes the Boltzmann constant, m_e the electron mass and ν_e the elastic electron neutral collision frequency. Energy loss caused by collisions with neutral particles and heating by an externally applied RF-field are given by P_c and P_h, respectively. The mean electron energy is ϵ and the electron energy flux density $\vec{\Gamma}_e$ consists of a convective and thermal conductivity term:

$$\vec{\Gamma}_e = \frac{5}{2} k T_e \vec{j}_e - \frac{5}{2} \frac{k T_e}{m_e \nu_e} \nabla k T_e. \tag{6}$$

Electric interaction between electrons and ions is given by Poisson's equation:

$$\Delta \Phi = \frac{e}{\varepsilon_0}(n_e - n_i), \tag{7}$$

here, ε_0 is the permittivity of the vacuum. The electric field $\vec{E}$ is derived from a scalar electrostatic potential Φ by

$$\vec{E} = -\nabla \Phi. \tag{8}$$

It is assumed that the RF-field $\underline{\vec{E}}$ induced by coil currents is orthogonal to the electrostatic field $\vec{E}$ and can be therefore treated separately.

2.1 Electrodynamic Model

To calculate the energy transfer from the RF-field to the plasma, an electrodynamic model [6] is used. Assuming time harmonic dependence for all quantities of the form $\exp(i\omega t)$, the differential equation describing the RF-induced field $\underline{\vec{E}}$ is:

$$\Delta \underline{\vec{E}} + \underline{k} \underline{\vec{E}} = i\omega \mu_0 \underline{\vec{j}} \tag{9}$$

with

$$\underline{k} = \varepsilon_r \frac{\omega^2}{c_0^2} - i\omega \mu_0 \underline{\sigma} \tag{10}$$

The current density in the coils is given by $\underline{\vec{j}}$. Infinite electrical conductivity $\underline{\sigma}$ is assumed for the conducting walls. For the plasma, the following approximation [5] was used:

$$\underline{\sigma} = \nu_e \frac{n_e e^2}{m_e \left(\nu_e^2 + \omega^2\right)} - i\omega \frac{n_e e^2}{m_e \left(\nu_e^2 + \omega^2\right)} \tag{11}$$

Assuming cylindrical symmetry of the problem, only the azimuthal component E_Θ of the electric RF-field has a nonzero value. The resulting scalar differential equation for the RF-field then reads:

$$\Delta \underline{E}_\Theta + \underline{k}\underline{E}_\Theta = i\omega\mu_0 \underline{j}_\Theta. \tag{12}$$

The power transferred to the plasma is then given by:

$$P_c = \Re\left\{\underline{\sigma}\right\} \left|\underline{E}_\Theta\right|^2. \tag{13}$$

3 Results

Simulation and experiment were carried out for a planar ICP discharge as shown in Fig. 1. The chamber had a radius of $R = 10$ cm and a height of $H = 4$ cm. On top of the chamber three cylindrical coils were mounted. Argon was used as process gas, the RF-frequency was 27 MHz. Results are presented for a gas pressure of 10 Pa and for the case that only one coil was powered. Measurements were carried out using an automatic Langmuir probe system (APS3). The probe was moved in radial direction in order to measure an electron density profile at a vertical position $z = H/2$.

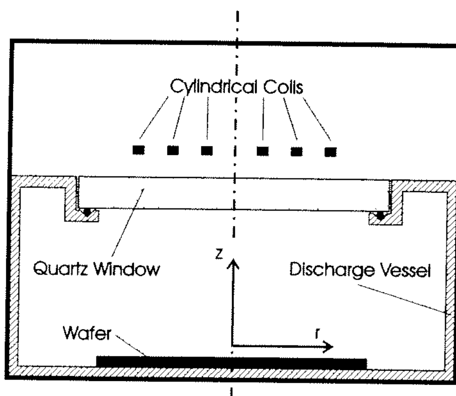

Fig. 1: Simulation Geometry

In Fig. 2a - Fig. 2c theoretical and experimental results are shown for the three different coil configurations. The coil positions are marked near the r-axis in the diagrams. Generally simulation and experiment agree quite well. A correlation between coil position and the maximum of the electron density can be observed. This is on one hand caused by the electric field of the RF-antenna which causes a maximum of heating in vicinity of the coils.

On the other hand, for increasing neutral gas pressure the thermal conductivity of the electrons decreases significantly. The discharge becomes therfore more localised, which is in agreement with a number of other simulations and experiments.

For the case the outermost coil "3" is powered (Fig. 2C) in the middle of the chamber, (r=0) simulation and experiment differ slightly.

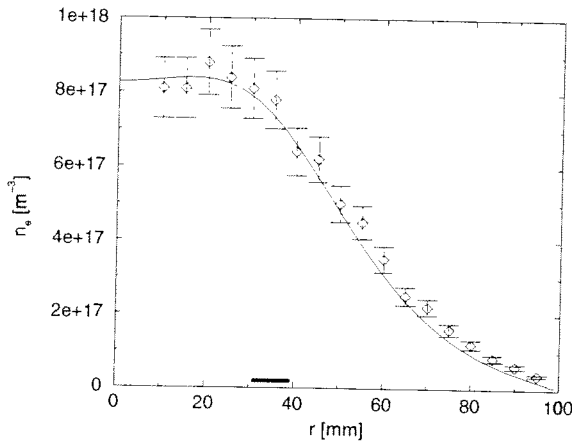

Fig 2a: Electron density (Coil "1")

The calculated value for the electron density is higher than the measured value. Comparisons with other simulations at higher pressure show, that this effect can be correlated with the thermal conductivity of electrons which depends on the electron-neutral collision frequency ν_e. The values used for the simulation were obtained from mobility measurements and might not be applicable for the conditions in low pressure discharges.

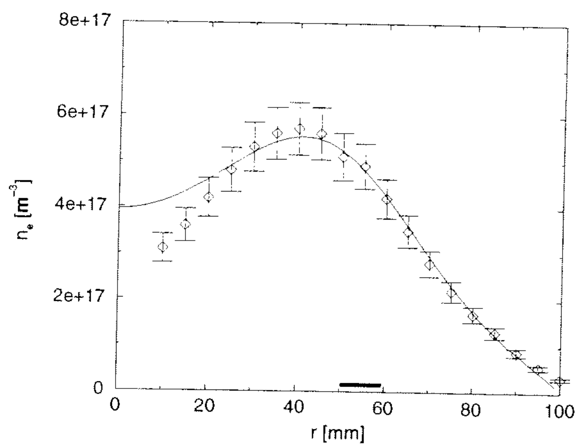

Fig 2b: Electron density (Coil "2")

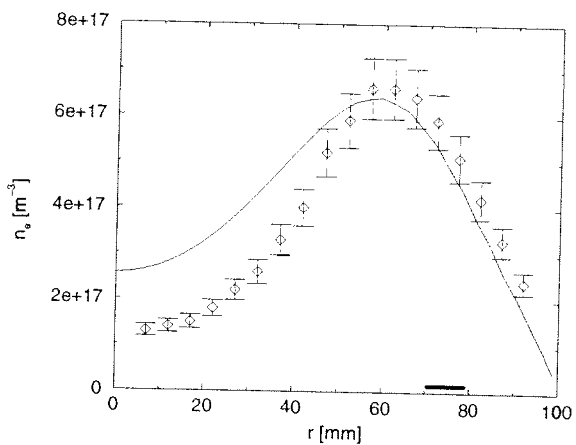

Fig 2c: Electron density (Coil "3")

References

[1] M. Meyyappan and J. P. Kreskovsky, "Glow discharge simulation through solutions to the moments of the Boltzmann transport equation," *J. Appl. Phys.*, vol. 68, no. 4, pp. 1506, 15 August 1990.

[2] J.D.P. Passchier and W.J. Goedheer, "A two-dimensional fluid model for an argon rf discharge," *J.Appl.Phys.*, vol. 74, no. 6, pp. 3744, 1993.

[3] R.A. Stewart, P. Vitello, and D.B. Graves, "A two-dimensional fluid model of high density inductively coupled plasma sources," *J.Vac.Sci.Technol.B*, vol. 12, pp. 478, 1994.

[4] V.E. Golant, A.B. Zhilinsky, I.E. Sakharov, and S.C. Brown, *Fundamentals of plasma physics*, John Wiley and Sons, 1980.

[5] I.P. Shkarofsky, T.W. Johnston, and M.P. Bachynski, *The particle kinetics of plasmas*, Addison-Wesley, 1996.

[6] J.S. Tolliver E.F. Jaeger, L.A. Berry and D.B. Batchelor, "Power deposition in high-density inductively coupled plasma tools for semiconductor processing," *Phys. Plasmas*, vol. 2, no. 6, pp. 2597, June 1995.

Determination of the absolute density of F_2 formed in a CF_4 plasma by time-resolved threshold-ionization mass spectrometry

W. Schwarzenbach, J. Derouard and N. Sadeghi
Laboratoire de Spectrométrie Physique, UMR CNRS 5588,
Université Joseph-Fourier - Grenoble 1, B. P. 87, F-38402 Saint Martin d'Hères Cedex

Introduction

CF_4 plasmas have a number of industrial applications. To improve our understanding of the elementary processes taking place in the plasma volume or on a surface in contact with the plasma, the knowledge of the absolute concentrations of different plasma produced radicals is of great interest. In our previous works, we used threshold ionization mass spectrometric technique to determine the absolute density of atomic fluorine [1] and of CF_x radicals [2] in a CF_4 plasma.

The detection of molecular fluorine using optical absorption spectroscopy is reported by Corbin *et al* [3] in the range 210 - 450 nm. However, the corresponding absorption coefficient is very weak, particularly at micro-bar partial pressure range. Using mass spectrometry, the lack of informations about the ionization cross section and the apparatus function for F_2 seems often to prevent the obtention of the absolute F_2 density. In this work, a method based on the comparison of the mass spectrometer signal from the direct ionization of F atoms and from the dissociative ionization of F_2 is presented.

Experimental Apparatus

The flowing afterglow reactor used in our experiments was extensively presented in [1] and is schematically shown in Fig. 1. The 2.45 GHz microwave plasma was generated (with power from 15 to 75 W) in a pyrex tube open downstream to a reaction chamber. A low CF_4 flow rate (1.25 sccm) was used and the pressure was adjusted to 15 mTorr by a throttle valve separating the reactor from a mechanical pump.

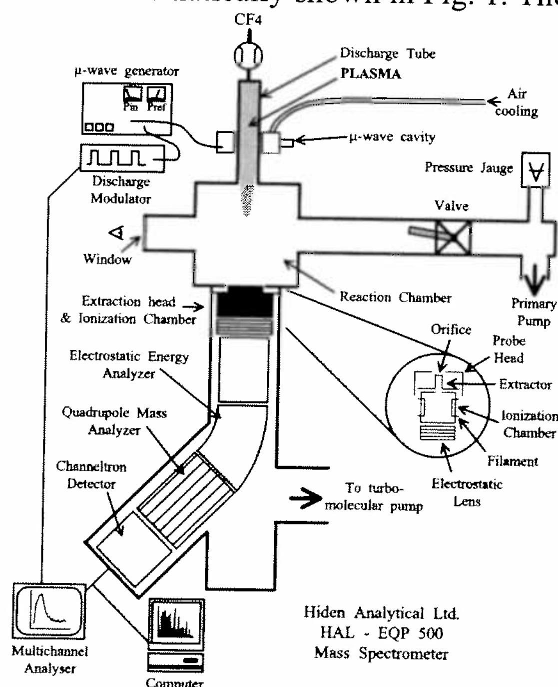

Figure 1 : *Schematic view of the flowing afterglow reactor and of the mass spectrometer*

Detection of neutral particles in the reaction chamber was achieved by a Hiden HAL-EQP 500 quadrupole mass spectrometer (QMS). Differentially pumped, it collects the radicals from the reaction chamber via a 150 µm extraction orifice located opposite to the discharge tube. The electron ionization energy was varied within 10 to 70 eV.

For time-resolved experiments, the µ-wave discharge was pulsed (plasma on 30 ms, plasma off 98 ms). The ion counting pulses provided by the QMS were supplied to a multichannel counter to acquire time resolved signals.

Mass spectrometric detection of F atoms

F atoms detection using threshold ionization mass spectrometry technique has been detailled extensively in [4]. The m/e = 19 signal detected by the QMS, namely the F^+ ions created in its ionization chamber, can results from several reactions. Some of these reactions and their threshold energies are detailled in the following :

- The dissociative ionization of CF_4 takes place already without the plasma :

$$CF_4 + e \rightarrow F^+ + CF_3 + 2e \qquad E_{CF4,F^+} = 36 \text{ eV [5]} \qquad (1)$$

- The dissociative ionization of CF_x radicals, of F_2 molecule and the direct ionization of F atoms. These reactions take place only with the plasma produced species :

$$CF_3 + e \rightarrow F^+ + CF_2 + 2e \qquad E_{CF3,F^+} = 30 \text{ eV [6]} \qquad (2)$$

$$CF_2 + e \rightarrow F^+ + CF + 2e \qquad E_{CF2,F^+} = 30 \text{ eV [6]} \qquad (3)$$

$$CF + e \rightarrow F^+ + C + 2e \qquad E_{CF,F^+} \approx 24 \text{ eV [7]} \qquad (4)$$

$$F_2 + e \rightarrow F^+ + F + 2e \qquad E_{F2,F^+} = 21 \text{ eV [7]} \qquad (5)$$

$$F + e \rightarrow F^+ + 2e \qquad E_{F,F^+} = 18 \text{ eV [8]} \qquad (6)$$

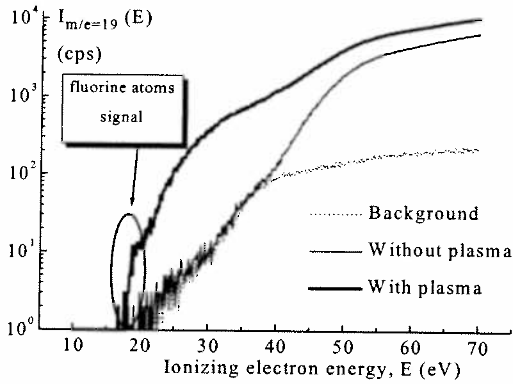

Fig. 2 : *QMS signal for m/e = 19 vs E with any gas in the reaction chamber (dot), 15 mTorr CF_4 without plasma (thin line) and a 50 W plasma (thick line).*

The mass spectrometer signal $I_{m/e\,=\,19}$ *versus* the ionizing electron energy E is presented on figure 2. The backgound signal is collected without any gas introduced in the reaction chamber. The signal without plasma for E > 36 eV is due to the dissociative ionization of the CF_4 parent molecule in the ionization chamber of the QMS. The signal with plasma can be related to the F atoms only if E is between 18 and 21 eV. Above this last value, the signal includes contributions from the other radicals and especially from F_2.

Relation between the mass spectrometric signal and the radical concentration

Let consider the dissociative ionization of the radical AB in the reaction chamber of the QMS to produce A^+ ions. The I_{AB,A^+} (E) collected signal can be expressed as :

$$I_{AB,A^+}(E) = [AB] \,.\, \delta_{AB} \,.\, \varepsilon_{AB} \,.\, I \,.\, \sigma_{AB,A^+}(E) \,.\, \beta_{A^+} \qquad (7)$$

with : - δ_{AB} the conductance of the extractor of the QMS for the radicals AB,

- ε_{AB} the residence time of the radicals AB in the ionization chamber,
- I the ionizing electron beam current,
- σ_{AB,A^+} (E) the cross section for the ionization of AB into A^+,
- β_{A^+} the mass-dependant transmission of the mass spectrometer filters for A^+ ions.
- [AB] the radical concentration.

Relation (7) can be used to relate the $I_{m/e\,=\,19}$ QMS signal to the F atoms absolute density [1], with the condition 18 < E < 21 eV. To determine this concentration, we used CF_4 as a calibration gas to get ride of the apparatus function. In the case of the fluorine molecule

F_2 detection, an equation similar to (7) could be writen for the F_2^+ signal. However, CF_4 can not be used to calibrate the $I_{m/e\,=\,38}$ signal. Therefore, to have access to the F_2 density, we propose to use the signal of F^+ ions formed from F_2 following reaction (5) inside the ionization chamber of the QMS. To distinguish this signal from that produced by direct ionization of F atoms, the CF_4 plasma is modulated and kinetics measurements are performed.

Kinetics of the F atoms and F_2 molecules

Figure 3 presents a typical time resolved m/e = 19 signal along the modulation period of a 15 mTorr, 30 W CF_4 plasma. The electron energy E is set to 27 eV. t = 0 refers to the plasma extinction.

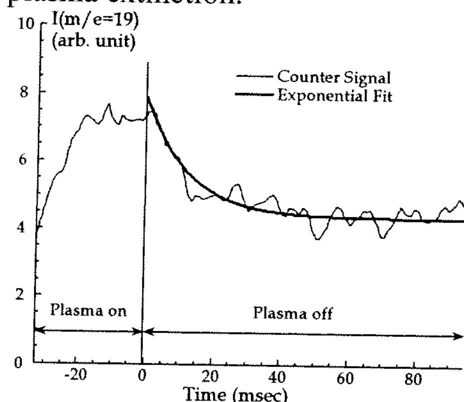

Figure 3 : Typical time resolved m/e = 19 signal along a modulation period with an exponential fit of the decay of [F] in the afterglow. 15 mTorr, 30 W CF_4 plasma.

With E = 27 eV, this signal presents several contributions : one due to the direct ionization of F atoms, a second due to the dissociative ionization of F_2 and a third due to the background of the QMS. According to figure 1, the background contribution with E = 27 eV is less than 3 % of the collected signal with the plasma. This contribution can then be neglected. More precisely, the dissociative ionization of CF following (4) could also contribute to this signal. However, due to the low CF concentration [2] and the low cross section for (4) at E = 27 eV, we can also neglect this contribution.

In a precedent paper [1] we have demonstrated that the modulated part of the m/e = 19 signal represents the F atoms contribution. This signal decays exponentially during the afterglow, with a time constant of about 50 s^{-1}. The non-modulated part of the signal presented on figure 3 is attributed to F^+ ions issued from the dissociative ionization of F_2. F_2 density decreases in the afterglow with a time constant which corresponds to the pumping speed of the reaction chamber, *i. e.* around 1 s^{-1}. So F_2 concentration can be considered as a constant. Following (7), the time resolved $I_{m/e\,=\,19}$ signal can be detailled as :

$$I_{m/e=19}(E=27,t) = I_{F,F^+}(E=27,t) + I_{F_2,F^+}(E=27) \qquad (8)$$

$$I_{m/e=19}(E=27,t) = [F]_o.\delta_F.\varepsilon_F.I.\sigma_{F,F^+}(E=27).\beta_{F^+}.e^{-\Gamma t} + [F_2].\delta_{F_2}.\varepsilon_{F_2}.I.\sigma_{F_2,F^+}(E=27).\beta_{F^+} \qquad (9)$$

At t = 0, the ratio between the modulated and the non-modulated part of the time-resolved signal gives :

$$\frac{I_{F,F^+}(E=27,t=0)}{I_{F2,F^+}(E=27)} = \frac{\sigma_{F,F^+}(E=27)}{\sigma_{F2,F^+}(E=27)}\frac{[F]_o}{[F_2]} \qquad (10)$$

From figure 3, the ratio I_{F,F^+} (E = 27 eV, t = 0)/I_{F2,F^+} (E = 27 eV) is around 2/3. Hayes *et al* [8] gives σ_{F,F^+} (E = 27) = 0.24 Å^2. Cross section for the dissociative ionization of F_2 following (5) has been given by Rao and Srivastava as σ_{F2,F^+} (E = 27) ≈ 0.025 Å^2 [9]. F atoms concentration in our plasma conditions has been measured to be 3.10^{18} m^{-3} [1].

Following (10), the F_2 concentration in the reaction chamber can then be estimated to about 4.10^{19} m^{-3} (CF_4 plasma, 15 mTorr, 30 W).

Another, indirect, estimation of F_2 density

An other way to obtain this result is to consider that F_2 molecules are produced by surface recombination of F atoms on the reactor walls, while they are eliminated only by the pumping out of the reaction chamber. Hence, their concentration follow (11) :

$$\frac{d[F_2]}{dt} = \frac{1}{2} \alpha_F \phi_F \frac{A}{V} - \frac{[F_2]}{\tau_{pump}} \qquad (11)$$

with : - α_F the sticking coefficient of F atoms on the stainless steel reactor walls ≈ 0.003 [1],

- $\phi_F = v[F]/4$ the F atoms flux to the reactor walls,
- $A/V = 0.849$ cm^{-1} the surface to volume ratio of our reaction chamber,
- τ_{pump} the residence time of a non-sticking molecules in the reaction chamber, related to the pumping speed. In our experimental conditions, τ_{pump} is estimated to 0.7 s.

In steady-state conditions, F_2 concentration would be :

$$[F_2] = \frac{1}{8} \alpha_F \, v \, [F] \frac{A}{V} \tau_{pump} \qquad (12)$$

Following (12), in our plasmas conditions (CF_4, 15 mTorr, 30 W μ-wave power) the absolute concentration of molecular fluorine can again be estimated to 4.10^{19} m^{-3}.

Conclusion

The absolute concentration of molecular fluorine F_2 is estimated in our 15 mTorr CF_4 plasma : $[F_2] \approx 4.10^{19}$ m^{-3}. Our two different approaches give similar results. In comparison with our previous estimations of the F and CF_x ($x = 1 - 3$) radicals density [2], F_2 seems to be one of the main plasma produced species in the reaction chamber. Its high concentration could be explained considering two different factors : F_2 molecules are formed with a high efficiency from fluorine atoms recombination on the reactor walls but due to their low reactivity in the gas phase and with the reactor walls, they are slowly eliminated by only the pumping out of the reaction chamber.

References

[1] A. Tserepi, W. Schwarzenbach, J. Derouard, N. Sadeghi, J. Vac. Sci. Technol. A **15**, 3120 (1997)

[2] W. Schwarzenbach, A. Tserepi, J. Derouard, N. Sadeghi, Jpn. J. Appl. Phys. **36**, 4644 (1997)

[3] G. A. Corbin, R. E. Cohen, R. F. Baddour, *Macromolecules* **18**, 98 (1985)

[4] W. Schwarzenbach, J. Derouard, N. Sadeghi, Proc. 13th Int. Symp. Pl. Chem., Beijing (1997)

[5] K. Stephan, H. Deutsch, T. D. Märk, *J. Chem. Phys.* **83**, 5712 (1985)

[6] R. A. Bonham, *Jpn. J. Appl. Phys.* **33**, 4157 (1994)

[7] K. P. Huber, G. Herzberg, *Molecular Spectra and Molecular Structure, IV. Constants of diatomic molecules*, Ed. Van Nostrand Reinhold Company, New York (1979)

[8] T. R. Hayes, R. C. Wetzel, R. S. Freund, *Phys. Rev. A* **35**, 578 (1987)

[9] M. V. V. S. Rao, S. K. Srivastava, *Proc. 8th Int. Conf. Pl. Enhanced At. Collisions,* Aarhus, Danemark (1993)

Charged Particles Fluxes and Energy Distributions Diagnostics in PECVD-Reactor During the Growth of Silicon- and Carbon-Based Films

A.S.Smirnov, A.I.Kosarev*, M.V.Shutov*, K.E.Orlov, T.V.Chernoiziumskaya.
St.Petersburg State Technical University, Polytechnicheskaya 29, St.Petersburg 195251
**A.F.Ioffe Physico-Technical Institute, Polytechnicheskaya 26, St.Petersburg 194021*
Russia

Introduction

Charge particle bombardment of the substrate surface is one of the most important factor in plasma technology. It affects on particle deposition, atom mobility on the surface and surface chemical reactions. So particle bombardment determines anisotropy of plasma etching and structure of deposited films. Otherwise, strong ion bombardment may generate defects in the substrate and in the growing film. Effect of the bombardment depends on particle energy and current. Measurements of these parameters give an important information about plasma and sheathes and provide a possibility to compare growth (or etching) conditions in different discharges [1-3]. In this paper we present results of charged particles flux and energy distribution measurements by multy-grid retarding field energy analyzer. This technique is quite simple and can be used in various discharges, including PECVD reactor during the film growth.

Experimental setup

The experimental PE CVD reactor equipped with an energy analyzer is shown in Fig.1 [3]. Substrates were mounted in the center of the grounded electrode (230x230 mm^2) occupying the central area (80 mm in diameter). The powered electrode was 220 mm in diameter, interelectrode spacing was 25 mm. Measurements were performed in DCOS-regime, when electrodes were isolated, DCSC-regime, when electrodes were connected by inductive coil and dc current flow between electrodes and regimes with varied bias applied to the powered electrode. The substrate temperature was 250° C. Discharge frequency was 13.56 MHz and 58 MHz.

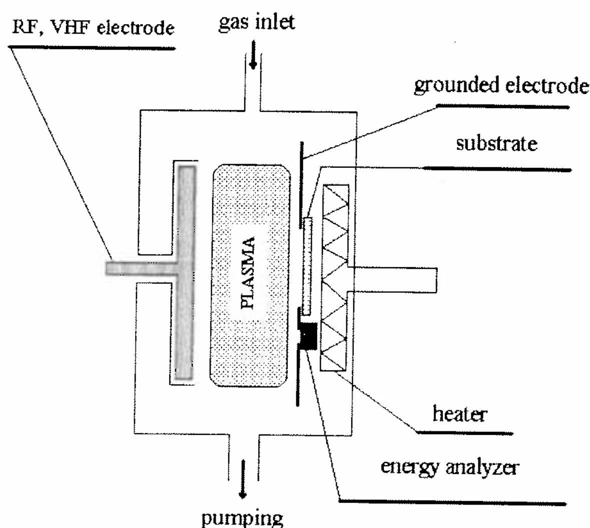

Figure 1 : *The experimental reactor.*

Flat retarding field energy analyzer was placed on the grounded electrode as close as possible to the substrate. The input orifice of the energy analyzer was 5 mm in diameter. Analyzer was covered by the shutter which was moved out for shot time needed for spectra measurements. It was necessary to prevent film growth on the grids. All grids and elements of the energy analyzer were made of nickel, the only exception was stainless steel shield. Grids had the cells with the dimensions 140x140 mkm^2 , and the grid transparency was about 80%. The first grid of the analyzer

was connected to the grounded electrode to minimize plasma perturbation. For ion flux measurements in silan discharge potentials applied to the grids were as follows. Potential at second grid was -100 V, which was fairly sufficient to reject electrons. Analyzing potential was applied to the 3-d grid and swept from 0 to +300 V. The 4-th grid had -18V potential to reject secondary electrons emitted from the collector. The collector potential was zero. For electron flux measurements the 2-nd grid was kept at +300V potential to reject ions, potential of the 3-rd grid was swept from 0 to -100V. Potential of the 4-th grid was zero, collector potential was +18V. Time scan over the energy range took about 5 sec. The similar analyzers was used in capacitively coupled noble gas discharges, inductively coupled and ECR discharges. Potentials of the second and third grid were tuned to reject high energy particles and to cover a whole range of particles energy.

Inductively coupled discharge was burned in the same vacuum vessel as capacitively coupled one. Electric field was induced by flat four turn spiral inductive coil 10 cm in outer diameter. Coil was mounted in reactor instead of powered electrode and separated from discharge by quartz glass plate.

ECR discharge was burned in 30 cm diameter 10 cm high vessel. 2.45 GHz power from magnetron generator through bi-directional coupler and $\lambda/4$ plate polarizer pass to 9.4 mm cylindrical waveguide and injected into the discharge vessel through the cylindrical quartz glass window. Polarizer was used to turn wave polarization from linear to right-hand and left-hand circular. Magnetron generates pulsed power with 100 Hz frequency and 4 msec pulse duration.

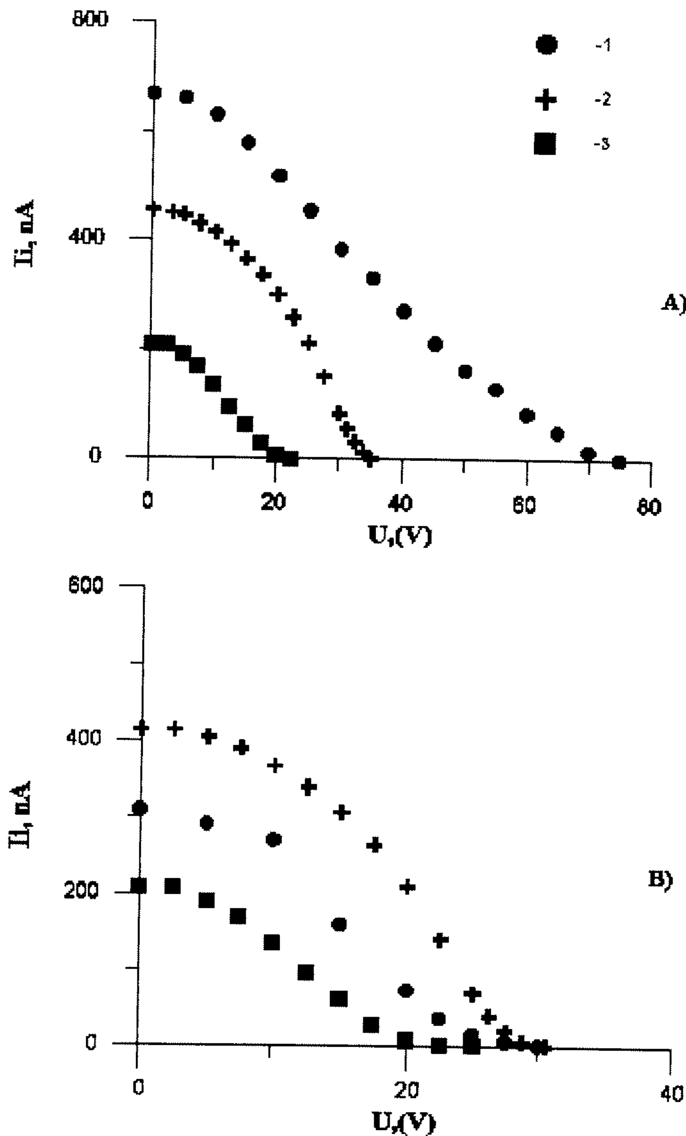

Figure 2 : *Collector current I versus retarding voltage V, I-V characteristics in Ar, H_2, SiH_4, discharges in DC SC (A) and DC OC (B) regimes. 1- Ar discharge f=13.56 MHz, P=0.12 Torr, W=14 W, 2- SiH_4 discharge, f=58 MHz, P=56 mTorr, W=17 W, 3- H_2 discharge, f=58 MHz, P=0.36 Torr, W=10 W.*

Results and discussion

Typical ion retarding curves for different gases in capacitively coupled discharge are presented in fig.2. Generally, secondary electron currents from the second grid is comparable with the ion current and gives negative collector current for high retarding voltage [1], but in low power discharge this effect is

unimportant. Ion energy distribution function can be obtained from these curves by differentiating on retarding voltage, but it is more convenient to determine ion flux and maximal energy directly from retarding curves. These values together with the power loaded to ion acceleration can be used as a ion bombardment characteristics. In fig.3 deposition rate of silicon film dependence on ion bombardment power is presented for 13.56 and 58 MHz discharges. Ion power was varied by discharge power and electrode bias variation. Deposition rate increases with ion power in both regimes. For a given ion power deposition rate is independent of frequency. More complicated dependence is observed for defect density fig.4. Two branches of N_d (W_i) can be distinguished in the plot. The upper branch corresponds to high ion energy regimes. In this case defect density increases with the ion power. Lower branch corresponds to low ion energy modes. In this case defect density decreases with ion power increase. So one can conclude that to decrease defect density ion power should be increased by increasing ion flux. It can be easily achieved in VHF discharge, but not automatically, because in VHF discharge upper branch of dependence is observed.

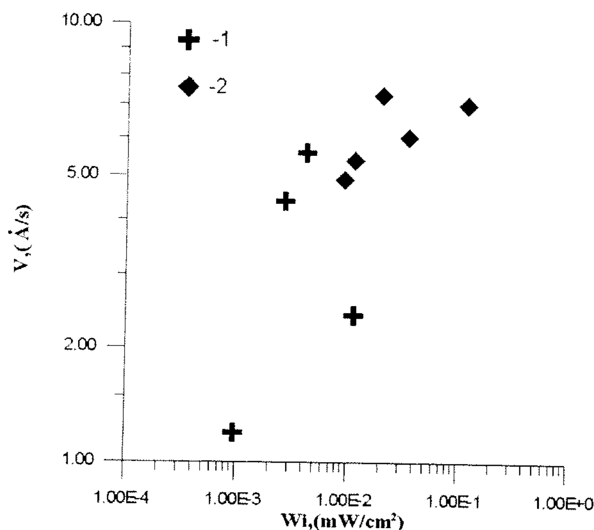

Figure 3 : *Deposition rate (V) of SiH_x films versus density of ion loaded power (W_i) for silane discharge. 1-13.56 MHz, 2-58 MHz.*

Effective electron temperature T_e of the high energy EDF tail can be obtained from the electron retarding curves. In RF discharge T_e was about 3.25 eV, in VHF discharge T_e was about 2.5 eV [3].

In low pressure high power discharges fast gamma electrons emitted from the power electrode were observed [2]. Electron current was of the same order of magnitude as ion current and electron energy was about two applied to electrodes voltage amplitudes (300-1000 V). Thus in such regimes electron bombardment power is much higher than ion one and can determine surface processes. Effective ion-electron secondary emission coefficient can be obtained from these measurements [1].

Measurements performed in inductively coupled discharge demonstrate that ion bombardment energy is close to one observed in capacitively coupled discharge in similar regimes, though ion current was higher by the order of magnitude. So we can believe that films deposited in inductive discharge would have better electronic properties.

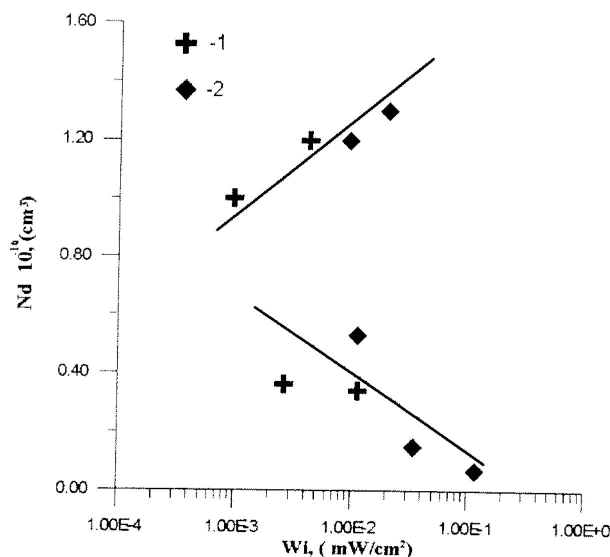

Figure 4 : *Defect density (N_d) in SiH_x films versus density of ion loaded power (W_i) for silane discharge. 1-13.56 MHz, 2-58 MHz.*

Ion current dependence on electromagnetic wave polarization in ECR discharge presented in fig.5. Pure right-hand polarization corresponds to polarizer angles -45° and +135°, left-hand polarization corresponds to angles +45° and -135°. One can see that plasma is efficiently generated when right hand polarization mode has a sufficient amplitude. Left-hand polarization mode does not generate plasma. Reflected power, measured by bi-directional coupler is practically independent of polarization and does not exceed 10% of the incident power in all cases. In the absence of discharge power is probably absorbed in vessel walls. No polarization dependence was observed in pressures higher than $4 \bullet 10^{-4}$ Torr. Thus we can conclude that electron cyclotron absorption of the electromagnetic wave is important only in low pressure discharges ($p<4 \bullet 10^{-4}$ Torr). In higher pressures collisional wave damping prevails.

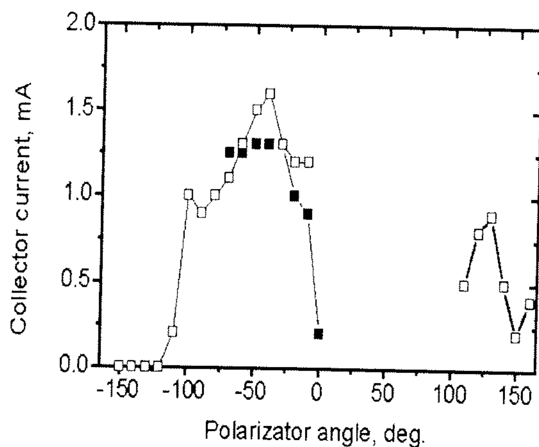

Figure 5: *Polarization dependence of ion current in ECR discharge. Ar, $p=2.2 \bullet 10^{-4}$ Torr, B=1200 G, W≈400 W*

Conclusion remarks

Results presented demonstrate that multy-grid retarding field analyzer is a useful tool for charged particle impinging on substrate diagnostics. It gives information about particles fluxes and energy distribution functions. This information can be useful in interpretation of external discharge parameters (frequency, power, pressure, etc.) influence on film growth or deposition process. Value of particle current on substrate characterize power absorption in discharge independently of power losses in matching network and other elements of experimental setup. Multy-grid analyzer is less convenient than deflection analyzers for EDF measurements or time-resolved measurements [4], but this tool is simple, does not disturb plasma and can be used in discharges of different types, including PECVD reactors.

Acknowledgments

This work was supported by INTAS grant N 96-0235, RBRF grant N 96-02-16918, Naval Research Laboratory Contract N 68171-97-M-5379, International Atomic Energy Agency Contract N 9238/R1.

References

[1] A.Smirnov, A.Ustavschikov, K.Frolov. Sov.Phys., Technical Phys., **40**, 627-636, (1995)

[2] C.Bohm, J.Perrin. Rev. Sci. Instr., **64**, 31-44, (1993)

[3] A.Kosarev, A.Smirnov, A.Abramov, A.Vinogradov, A.Ustavschikov, M.Shutov. J.Vac.Sci.Technol., **15**, 298-306, (1997)

[4] A.Smirnov, K.Orlov. Electron Kinetics and Applications of Glow Discharges. NATO ASI Series. Series B: Physics, **367**, 525-530, Plenum Press 1997

Application of triple probe for volume-resolved monitoring of internal plasma parameters during industrial plasma polymerization process

P. Špatenka[a), *J. Krumeich*[b), *J. Blažek*[c), *H.-J. Endres*[b),, *R. W. Cook*[b)

[a) University of South Bohemia, Faculty of Biological Sciences, Department of Mathematics, Physics and Chemistry, Branišovská 31, CZ-37001 České Budějovice, Czech Republic.

[b) Buck-Werke GmbH & Co., Technologiezentrum Fronau, D-83426 Bad Reichenhall, Germany

[c) University of South Bohemia, College of Education, Department of Physics, Jeronýmova 10, CZ-371 15 České Budějovice, Czech Republic.

Introduction

Plasma polymerization has been used in many areas for modification of surface properties of conventional materials, e.g. to improve biocompatibility in surgery or as barrier coating in food industry. Although the plasma polymerization is a complex process involving both the processes on the surface and in the bulk of plasma, it is generally accepted that the primary step of plasma polymerization is the radical formation in the bulk of plasma by electron collisions. Thus the electron density and electron energy play crutial role in the plasma polymerization processes.

In large-scale applications volume inhomogenities of the plasma may occur which results in inhomogenities of the film properties. Volume resolved measurements of the electron (or ion) density yield essential information for control of large-scale deposition process and provides more accurate information of the process conditions than the external power measurements.

The aim of this paper is to demonstrate the potential of the triple probe method for characterization of an industrial-scale plasma polymerization process.

Experimental

For the plasma characterization we used the plasma monitor system based on the triple probe method [1]. The system consists of measuring electronics, multiplexor and triple probe sensors with removable probe heads. The measuring heads contain rf

filters and three hairpin probes of the same diameter (0.05mm) and length (10 mm). The cable connections of the measuring heads with the multiplexor allow the simple and flexible placing of the probes at any position in a reactor. To avoid the influence of the covering of the probe by a polymer film all probes were heated to high temperature prior to data collection.

During the measurement one of the probes is held at the floating potential, between the other two a constant voltage is applied. Assuming the Maxwellian electron energy distribution the electron temperature is calculated from the voltage shift of the positive biased probe with respect to the floating probe, the ion concentration from the measured ion current using the radial motion model by Allen Boyd, Reynolds [2].

Measurements were performed in a system for plasma deposition of barrier coatings on the inner wall of plastic bottles. Six bottles were deposited simultaneously using an asymmetrical rf-discharge. The plasma was excited with two parallel electrodes connected to the rf generator (13.56 MHz) via a matching unit. The bottles were placed in a line between these electrodes. The external power was calculated as the difference between the forward and reflected power measured by a BIRD Thruline Wattmeter. The triple-probe sensors were placed in the center of each bottle. The bottles and the both electrodes, the vacuum and the gas feed manifolds were mounted in a movable stand which was inserted into the vacuum vessel.

Results and discussion

To determine the limits of our resolution caused by the spread of the impedance of the blocking filters we measured parameters of argon plasma in every bottle with all probes and we calculated for every position the average value, the standard deviation and the relative variability from the data. The typical results are summarized in Fig. 2. The highest relative variability of the electron temperature was 20%, the relative variability of the ion current reached 10%. For further considerations we took these values as the limits of our resolution. Higher uncertainty in determination of electron temperature is due to higher sensitivity of the probe method to differences in the impedance of the rf filters in the probe sensor.

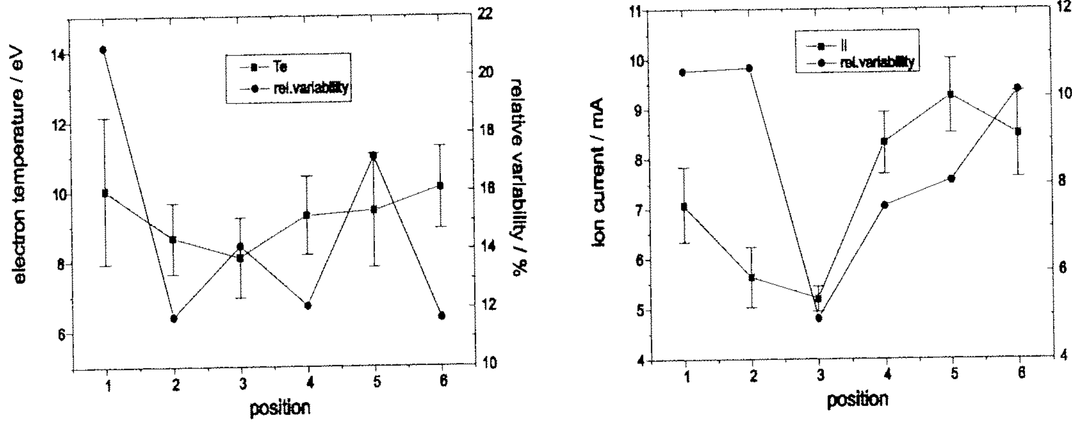

Fig. 1: *Ion current and electron temperature averaged for every position from values measured with all probes*

A typical result of electron temperature and ion density averaged from 8 deposition processes is shown in Fig. 2. The electron temperature varies between 4 and 5 eV, which is slightly above the limits of our resolution. The ion density differed between particular position which indicates different power absorption in particular bottles. This difference increases with pressure enhancement. In this series the highest power absorption was found in the position 5, followed by position 1, the minimum absorption occured in the position 4. The ratio between the highest and lowest ion density was about 2. We believe that this effect is due to small inhomogenities in the rf-field between the electrodes. A change in the maximum distribution to another position after small modification of the electrodes confirms this hypotheses. The calculated relative variability indicated the 94% reproducibility of the process.

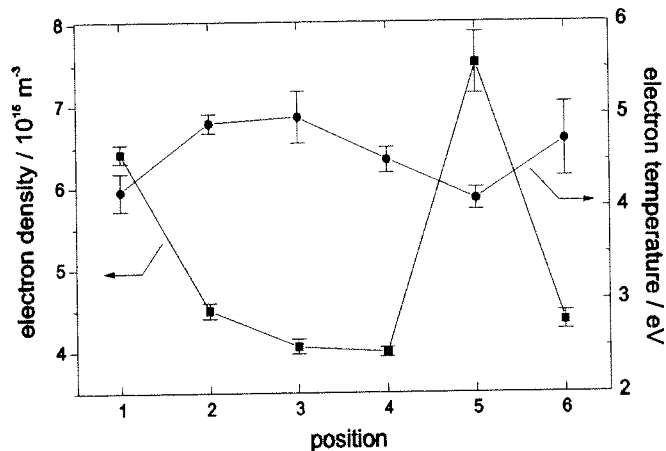

Fig. 2: *The distribution of the ion density and electron temperature in the particular bottles.*

In the another experimental series the influence of the internal process parameters such as power, pressure and gas composition on the barrier properties of

the film were investigated The triple probe diagnostic was routine applied during this series. To reduce the number of experiments statistical methods were used for their specification and evaluation [3]. The difference between the particular position was confirmed but the barrier properties of the corresponding bottles varied only insignificantly. Long time measurement of the solvent losses from sealed bottles showed only slow dependence of the barrier properties of the film on the measured plasma parameters. This indicates relatively large "process window" which is convenient for industrial application because of low sensitivity of the process to e.g. plasma inhomogenity and thus its simple adaptation to various substrate geometry.

Conclusions

The triple probe method is convenient for characterization of the industrial plasma polymerization process. The limits of the volume resolution were 20% in the electron temperature and 10% in the ion current, respectively. The reproducibility of the investigated process was better then 94%.
Statistical evaluation of large number of experiments with various external parameters deduced low sensitivity of the process to electron density and temperature which is convenient for process adaptation to various substrate geometry.

Acknowledgement

This work was partly supported by the grant of Grant Agency of the Czech Republic No 202/98/0116.

References

[1] S. Chen, T. Sekiguchi: J. AZppl. Phys. 36 (1965) 2363

[2] J. E. Allen, R. L. F. Boyd, P. Reynolds: Proc. Phys. Soc. B 70 (1957) 297

[3] J. Krumeich: Statistische Versuchsplanung. Buck Technologien GmbH – internal report, Fronau 1998.

Test function for detection of parameters in electropositive and electronegative plasmas

E. Stamate, G. Popa[*] and K. Ohe

Department of Systems Engineering, Nagoya Institute of Technology
Showa-ku, Nagoya 466-8555, Japan
[*] *Faculty of Physics, "Al.I.Cuza" University, Iasi 6600, Romania*

Introduction

While logarithmic plots of the second derivative of probe current show a linear slope for a Maxwellian electron energy distribution function (EEDF), the EEDFs detected in this way deviate from the linearity by including double slopes, depletion and double-humps. Such a nonlinear dependence increases with the deviation of EEDF from the Maxwellian, so that, a semi-logarithmic representation cannot resolve the fine structure of the bulk EEDF. Moreover, the inevitable noise included in the EEDF's tail makes it difficult to distinguish the positive ions from the energetic electron contributions.

In the present work, we use the test function, which is highly sensitive to plasma constituents that contribute to the total probe current, to examine Maxwellian and bi-Maxwellian electrons as well as positive and negative ions [1]. A characteristic potential correlated with plasma parameters is also introduced.

Theoretical considerations

Let us assume $y=y(x)$ to be an exponential function of x and its first derivative, $y'(x)$ and second one, $y''(x)$. Thus one can introduce a test function $F(y)$ as

$$F(y) = yy'' - y'^2 , \tag{1}$$

which provides information as to whether $y(x)$ is exponential or not by testing if $F(y)=0$ or not.

Many plasmas may be composed of bulk Maxwellian electrons with their temperature T_e, cold ions with the temperature T_i, and other components due to negative charges (energetic electrons or negative ions). Then the total current $I_p(V)$ of a Langmuir probe can be expressed with respect to its probe bias V as,

$$I_p(V) = I_e(V) + I_{nc}(V) + I_i(V), \tag{2}$$

where $I_e(V)$, $I_{nc}(V)$ and $I_i(V)$ are the currents of bulk electrons, energetic electrons or negative ions, and positive ions, respectively. If the distributions of all species are regarded as Maxwellian, and $I_i(V)$ is expressed in the orbital motion limited (OML) model [2], their corresponding currents are given for $V \le V_{pl}$ as,

$$I_{e,nc} = en_{e,nc} S \lambda_{e,nc} \sqrt{\frac{k}{2\pi}} \exp \phi_{e,nc}(V) \tag{3a}$$

$$I_i = -en_i S \lambda_i \sqrt{\frac{k}{2\pi}} \alpha (1 - \phi_i(V))^{\beta} \tag{3b}$$

where $\phi_j(V) = e(V - V_{pl}) / kT_j$ and $\lambda_j = \sqrt{T_j / M_j}$ with $j=e$, nc, or i and S the probe surface area, and M_j the mass of each charged particle. I_{nc} can be divided into I_{eh} and I_{ni} where I_{eh} is the current

due to hot electrons (of density n_{eh} and temperature T_{eh}) as distinct from bulk electrons, and I_{ni} the current due to the negative ions with density n_{ni} and temperature T_{ni}. In Eq. (3b), α and β are coefficients dependent on the probe geometry and the Debye length [3].

If $I(V)$ is a combination of Eqs. (3a) and (3b) one may distinguish the following situations:

(a) if $I=I_{e.nc}$, then $F(I_{e.nc})=0$, corresponding to Maxwellian distributions for bulk electrons and hot electrons or negative ions.

(b) if $I=I_e+I_i$, $F(I)<0$ and it is reduced to,

$$F(I) = -\frac{e^4 S^2 \alpha}{2\pi k T_e} n_{i,F} \left[\frac{n_e A(V_k)}{\sqrt{m_e M_i}} \exp \Phi_e(V_k) - \frac{n_{i,F}}{M_i} \alpha\beta(1-\Phi_i(V_k))^{2(\beta-1)} \right], \quad (4)$$

where $A(V_k) = \beta(\beta-1)(1-\Phi_i(V_k))^{\beta-2} + 2\beta(1-\Phi_i(V_k))^{\beta-1} + (1-\Phi_i(V_k))^{\beta}$.

Then the positive ion density $n_{i,F}$, can be computed by Eq. (4) for $V_k<V_{pl}$.

(c) if $I=I_e+I_{nc}$, $F(I)>0$, in which $\ln(F(I))$ is linearly dependent on $(V-V_{pl})$, [4] of slope,

$$\tan\theta = \frac{e}{k}\left(\frac{1}{T_{nc}} + \frac{1}{T_e}\right) \quad (5)$$

Another function $W(V)$ has also been introduced [4],

$$W(V) = \frac{I'\tan\theta - I''}{I} = \frac{e}{k}\frac{1}{T_{nc}T_e} = const. \quad (6)$$

Thus, the temperatures T_{nc} and T_e can be determined from Eqs. (5) and (6) as,

$$T_{nc,e} = \frac{e}{k}\frac{\tan\theta \mp \sqrt{(\tan\theta)^2 - 4W}}{2W}. \quad (7)$$

(d) if $I=I_e+I_{nc}+I_i$, $F<0$ for $V<V_{ch}$ and $F\geq 0$ for $V_{ch}\leq V\leq V_{pl}$, where V_{ch} is the characteristic potential defined as $F(V_{ch})=0$. V_{ch} profiles for various $\xi_{eh}=n_e/n_{eh}$ are presented in Fig. 1. Notice that V_{ch} ranges from 0 to –7 V depending on ξ_{eh}, T_{eh} and the probe geometry, and it appears even for $n_{eh}<2\%\ n_e$. This fact shows that V_{ch} can be used as a sensitive method for hot-electron group detection. If $\xi=n_e/n_{nc}$, for $F(I_p(V_{ch}))=0$ one can deduce the following relation,

$$\xi^2(A_4 - A_2) + \xi(A_1 - A_2 - A_3 + 2A_4) + A_4 - A_3 = 0, \quad (8)$$

where the coefficients $A_{1\text{-}4}$ (which depend on V_{ch}, $T_{e,nc,i}$, α and β) were defined elsewhere [1].

From the floating potential V_f ($I_p(V_f=0)$) we have,

$$\xi = \frac{n_e}{n_{nc}} = \frac{\lambda_i \alpha(1-\phi_i(V_f))^{\beta} - \lambda_{nc}\exp\phi_{nc}(V_f)}{\lambda_e \exp\phi_e(V_f) - \lambda_i\alpha(1-\phi_i(V_f))^{\beta}}. \quad (9)$$

The plasma potential reduces to,

$$I(V_{pl}) = en_{nc}S\sqrt{\frac{k}{2\pi}}[\xi(\lambda_e - \lambda_i) + \lambda_{nc} - \lambda_i]. \quad (10)$$

All plasma parameters can be computed from Eqs. (7,8-10).

Application of test function to detection of plasma parameters

A multipolar magnetically-confined device of cylindrical geometry was used to produce an Ar plasma. The details of the experiments are referred to elsewhere [5]. The function F emphasizes the contribution of the hot electrons to the EEDF due to its high sensitivity to the EEDF shape. $F(I_p)$ for 10^{-4}, $3x10^{-3}$ and $9x10^{-3}$ Torr and I_d=250 mA detected by the cylindrical probe is presented in Fig. 2. F turns to negative values for $p=9x10^{-3}$ Torr from the large positive with V_{ch}<-6 V for $p=10^{-4}$ Torr and V_{ch}>-2 V at $p=3x10^{-3}$ Torr, suggesting the strong thermalization of hot electrons. Since, $I_e \to 0$, and thus $I_p \to I_i$ for $V<<V_{pl}$, one can compute $n_{i,OML}$ [2]. The coefficients α and β were fitted to the practical probe characteristics in order to achieve a complete I_i subtraction. As an example, $F(I_p-I_i-I_{eh})$ for I_d=100 mA is presented in Fig. 3, where solid curves are Fs with full I_{eh} and I_i, and dashed ones are those with a reduction of I_{eh} and I_i to 95 and 90% from their full values; zooms of $F(I_p-I_{eh})$ and $F(I_p-I_i)$ are also included. While a complete subtraction of I_{eh} and I_i reduces $F(I_p-I_i-I_{eh})$ over ΔU to a noise level, the incomplete subtraction produces a legible $F(I_p-I_i-I_{eh})$. Such high sensitivity of F makes possible a very accurate determination of plasma parameters for the bi-Maxwellian. The sharp decrease in F for $V_H<V<V_{pl}$ is due to the experimental evolutions of I_p' and I_p" which deviate from a bi-exponential distribution as $V \to V_{pl}$.

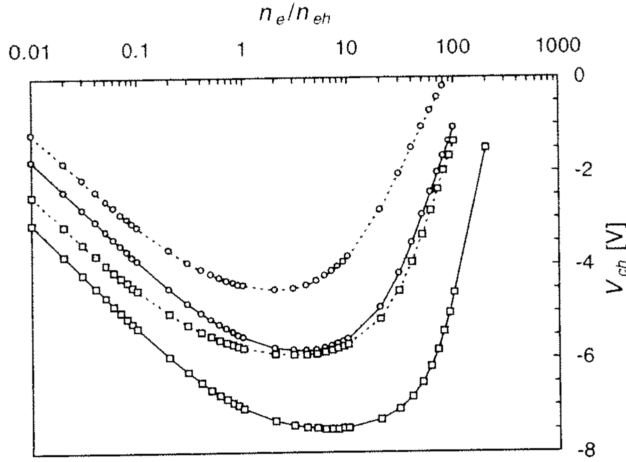

Fig. 1. V_{ch} profiles for a cylindrical (solid curves) and a spherical probe (dashed curves) as a function of ξ_{eh}, where $n_e=10^{15}$ m^{-3}, T_e=1 eV, V_{pl}=0 V, T_{eh}=4 and 8 eV.

Since F is negative for $p=9x10^{-3}$ Torr (see Fig. 2), the EEDF seems to be Maxwellian, and Eq. (4) can be used to obtain $n_{i,F}$. However, the subtraction of I_i yields $F(I_p-I_i)>0$, a fact corresponding to a hot electron population of only 1.7% n_e. The influence of n_{eh} on $n_{i,F}$ profiles is illustrated in Fig. 4. The non-subtraction of I_{eh} results in a large underestimation of $n_{i,F}$, while the subtraction results in $n_{i,F}$ within a limit of 20% error with respect to $n_{i,OML}$. Because $n_{i,OML}$ is obtained for $V<<V_{pl}$ and $n_{i,F}$ and $n_{i,fitt}$ for V slightly below V_{pl}, it is difficult to predict which one of these values is a better approach compared with the real n_i. However, a good agreement has been found between $n_{i,OML}$, $n_{i,F}$ and $n_{i,fitt}$.

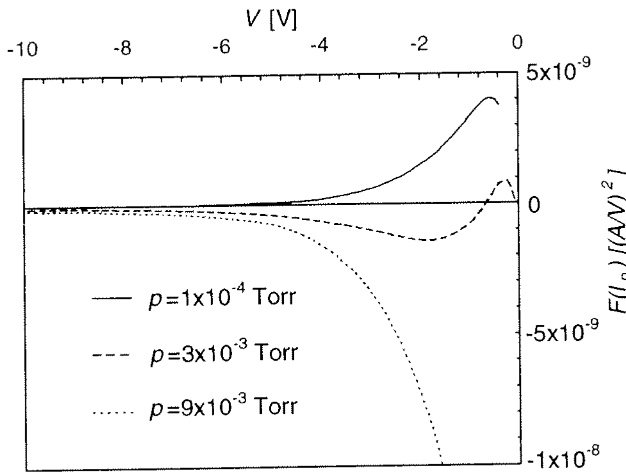

Fig. 2. $F(I_p)$ for a cylindrical probe for various values of p with I_d=250 mA.

Determination of negative-ion plasma parameters by this test-function method in the

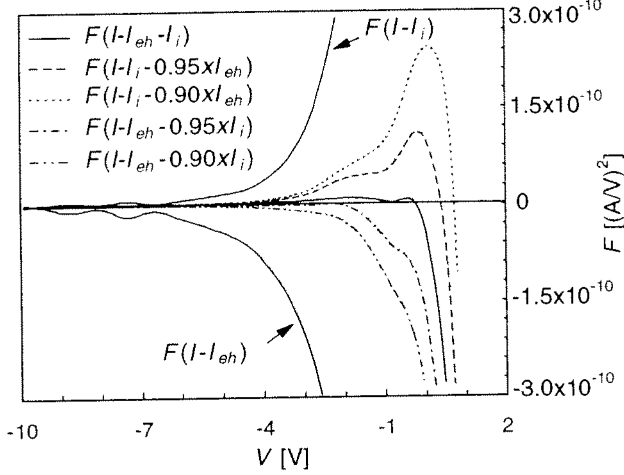

Fig. 3. $F(I_p-I_i-I_{eh})$, $F(I_p-I_{eh})$ *and* $F(I_p-I_i)$ *for* I_d=*100 mA and p=3x10*$^{-3}$ *Torr, where the best fits correspond to the solid curves.*

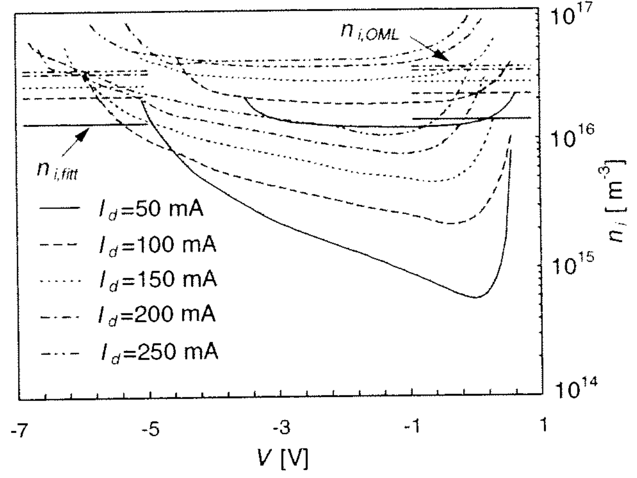

Fig. 4. $n_{i,F}$ *profiles, where low* $n_{i,F}$ *is a case without subtracting* I_{eh}*, and high* $n_{i,F}$ *is one with subtraction.* $n_{i,OML}$ *(right-hand-side) and* $n_{i,fitt}$ *(left-hand-side) are also shown as a reference.*

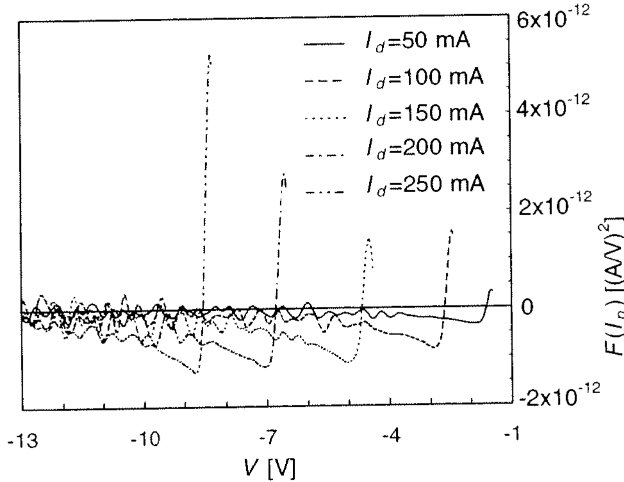

Fig. 5. $F(I_p)$ *from the spherical probe in Ar/SF*$_6$ *plasma for various values of* I_d*, where p=5x10*$^{-4}$ *Torr and, Ar and SF*$_6$ *flows were 2.0 CCM and 0.1 CCM, respectively.*

Ar/SF_6 plasma has been described elsewhere [5]. Some examples of $F(I_p)$ by the spherical probe in the target plasma for various I_d are shown in Fig. 5. For $V \ll V_{pl}$, $F(I_p)$ showed negative values dependent on the positive-ion contribution, while showing positive values with a sharp increase after crossing zero at V_{ch}. This change in $F(I_p)$ by introducing SF_6 was correlated with the drastic decreasing of $I_p(V_{pl})$, which was attributed to the negative ions. Moreover, $\ln F(I_p-I_i)$, where I_i was subtracted by the OML model with T_i=0.3 eV, showed a linear dependence on V, making it possible to compute $\tan\theta$ over ΔU. Thus, provided that both bulk-electron and negative-ion distribution functions are Maxwellian, the plasma parameters T_e, T_{ni}, n_e and n_{ni} can be obtained from Eqs. (7) and (8-10) for $I_{nc}=I_{ni}$, as presented in ref [5].

References

[1] E. Stamate and G. Popa and K. Ohe, Rev. Sci. Instrum. **70**(1) (1999)

[2] J. G. Laframboise, Report No. 100, Univ. of Toronto, Institute of Aerospace Studies (1966)

[3] I. D. Sudit and R. C. Woods, J. Appl. Phys. **76**, 4488 (1994)

[4] D. Ruscanu, G. Popa and E. Stamate, Proc. of the ICPP, Innsbruck, Vol. 2, p. 1179 (1992)

[5] E. Stamate and K. Ohe, J. Appl. Phys. **84**, 2450 (1998)

Pulsed Discharge at High Overvoltages: Diagnostic, Basic Features and Possibility of Applications

N.B. Anikin, S.V. Pancheshnyi, S.M. Starikovskaia, A.Yu. Starikovskii
Moscow Institute of Physics and Technology,
Institutskii lane 9, Dolgoprudny, Moscow region, 141700 RUSSIA

1 Introduction

High-voltage nanosecond discharge in gases develops in the form of so called fast ionization wave (FIW) propagating at a velocity of $10^9 - 10^{10}$ cm/s. High electric fields in the FIW front existing only a few nanoseconds lead to an appearance of the the fast electrons, responsible for the uniform pre-ionization of the discharge volume, and for the high reproducibility of the discharge. Then electric fields drop to values efficient for the excitation of electronic degrees of freedom. In some respects, the FIW combines a characteristic features of electron beam and gas discharge. Present paper describes complex investigation of FIW by time-resolved electric measurements and absolute emission spectroscopy, results of self-consistent measurements of electric field, electron density, excited particles concentration behavior and the analysis of possibility of this discharge applications.

2 Experimental Setup

Negative voltage pulses with a U=15.5 kV amplitude, 40 Hz repetitive frequency, and a 25 ns duration with a 3 ns rise time were used to initiate the FIW. The pulses were transmitted from the generator (1) through the coaxial cable to the high voltage electrode of the discharge tube. The glass discharge tube (3) of 60 cm length and 1.75 cm inner diameter with the plate electrodes at the ends was surrounded by a coaxial metallic screen (4) of diameter 6 cm. The low voltage electrode was connected to the screen by a coaxial cable with a matching resistance (6). The tube was pumped and filled with air by means of the vacuum system (5).

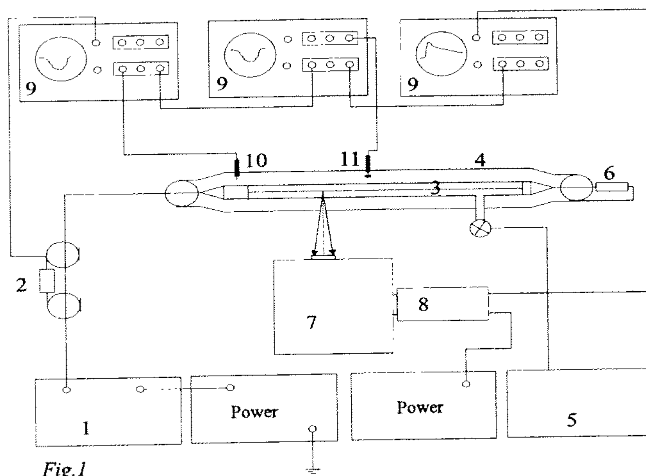

Fig.1

Pulse amplitude was controlled by the low-inductive calibrated current shunt (2) that was included into cable shield break. A modification of the electrical signal along the tube was registered with the aid of a calibrated broadband capacitive detector (11) which yields a voltage signal related to the presence of a charge density in the discharge cell. The probe was moved in the slit of the screen along the tube axis at intervals of 3 mm.

The radiation produced by separate transitions was recorded by an optical system that consists of a set of diaphragms, monochromator MDR-12 (7) and photomultiplier (8) 14ELY-FT.

The radiation was selected in the direction perpendicular to the discharge device axis at a distance of 20 cm from the high-voltage electrode. Measurements were performed in air and spectrally pure nitrogen for 0–0 transition of the 2^+ (λ=337.1 nm) and 0–0 transition of the 1^- system (λ=391.4 nm) for the pressure range 0.1–20 Torr. The width of each electron-vibration transition was experimentally determined with a spectral step of 0.25 Å. To obtain absolute characteristics the optical system was calibrated with the use of light sources with known absolute radiation densities: deuterium calibrated DDS-30 and tungsten TRY-1100.

The signals were registered on the oscillographs S9-4A (9) with synchro-signal taken from the gauge (10). Oscillographs were positioned in a shielded room and all cables were additionally screened to prevent high - frequency electrical noise.

3 Results and Discussion

The method of reconstruction of longitudinal component of the electric field includes a charge - dynamics registration taking into account a space sensitivity function of the detector. The registration is coupled with computational procedure of inverse problem solving to obtain the real charge distribution and electric field value.

It was established that the electric field profiles rise to a peak value during 3-4 ns and then drop during ~2 ns, after that, a decrease down to zero is observed. Peak electric field values increase slightly with pressure: from 4.5 kV/cm when $P = 1$ Torr to 8 kV/cm at 16 Torr. At the same time, peak values of the reduced electric field, represented in Figure 2, curve (1), change by an order of magnitude within the investigated pressure range.

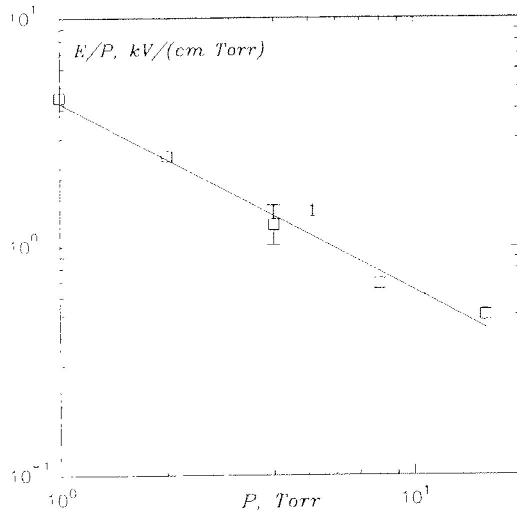

Fig.2

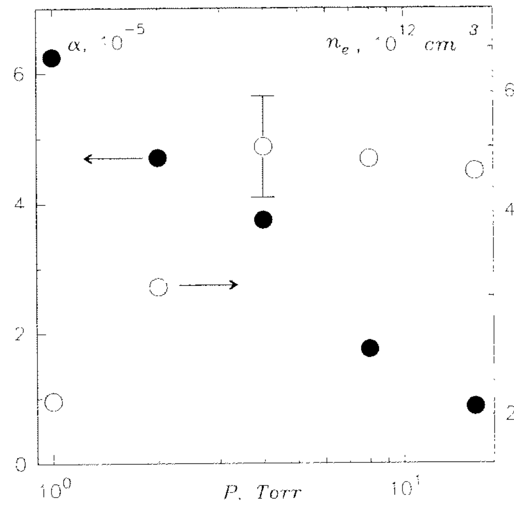

Fig.3

The electron concentration behind the ionization wave front was found from the drift approximation on the basis of the charge per unit length q and the longitudinal electric field E data determined previously. The degree of ionization behind the FIW front represented in the form $\alpha = n_e/N$, where N is neutral gas density, is shown in Figure 3 together with the electron density n_e. The degree of ionization diminishes with pressure, whereas electron density dependence $n_e(P)$ has the form of a smooth curve with maximum value $n_e = 5 \cdot 10^{12}$ cm^{-3} at the pressure $P = 4$ Torr.

The peak values of $N_2(C^3\Pi_u, v'=0)$ and $N_2^+(B^2\Sigma_u^+, v'=0)$ states concentration at

various pressures are shown in Figure 4, curves 1 and 2, respectively. The excited states population is determined by processes of excitation, radiative depopulation and quenching during collisions with heavy particles.

The $Q(t)$ rate of excitation of the certain electronic level may be reconstructed for any time t from excited states particle concentration $[N^*]$ and $d[N^*]/dt$ values measured in the experiment. On the other hand the population rate is determined by concentrations of electrons n_e and nitrogen molecules in the ground state $[N_2]$, excitation process section σ and electron energy distribution function $f(\varepsilon)$: $Q = n_e[N_2] \int_{\varepsilon_k}^{+\infty} \sigma(\varepsilon)\sqrt{2\varepsilon/m_e}\sqrt{\varepsilon}f(\varepsilon)d\varepsilon$, where ε_k – energy threshold of the state excitation.

To analyze the EEDF in the nanosecond discharge the numerical solution of Boltzman stationary equation in two-term approximation and three different analytical dependences were used: Maxwell distribution, Druivestein distribution and EEDF characterized by the slower than Maxwell and Druivestein functions decrease of the number of electrons in the distribution "tail": $f_{1/2}(\varepsilon) = 6\sqrt{3}\varepsilon_e^{-3/2} \exp\left(-2\sqrt{3}\,(\varepsilon/\varepsilon_e)^{1/2}\right)$. The distribution function $f_{1/2}$ represents an intermediate version between the spectrum of the relaxing impulsed beam and stationary distribution in the external electric field.

Independent measurements of FIW electron concentration and electric fields by means of an electrical make it possible to analyze usability of EEDFs of various types at conditions of discharge under high overvoltage at earlier stages.

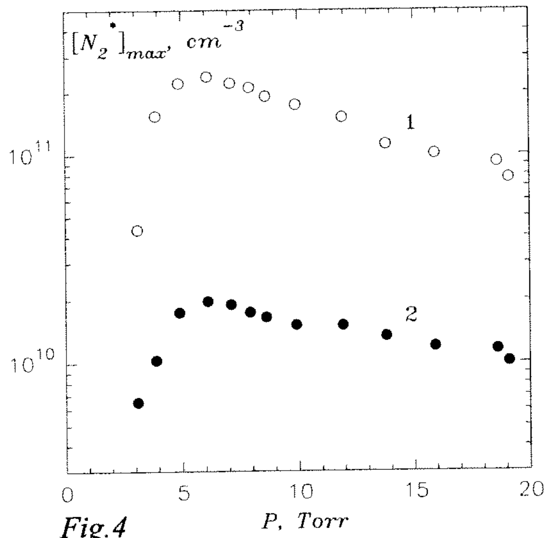

Fig.4

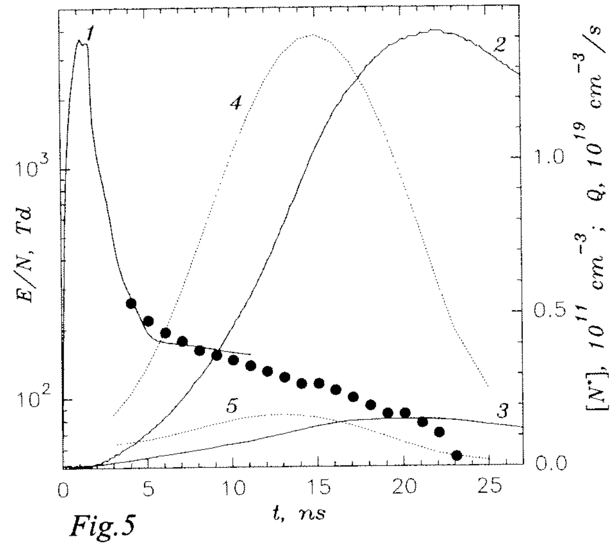

Fig.5

Electron recombination processes for the period of time compared with nanosecond breakdown can be disregarded, and the decrease of the level excitation rate is caused by decrease of the electron energy. Hence, electron concentration is to be monotonically built up during the impulse and become stationary. We adopted this behavior of electron concentration as one of criteria of the actual EEDF approximation accuracy. Conformity of the absolute value of maximum electron concentration to the n_e values experimentally obtained serves as the second criterion.

As a result, it was shown that in a region of relatively low electric fields behind the ionization wave front the average energy, drift velocity of electrons and low-level electron state excitation rate constants can be calculated with a good accuracy using the two-term approximation of Boltzman stationary equation.

Meanwhile, the non-stationary degrading spectrum formed by runaway electrons in

the FIW front essentially affects the EEDF formation at high energies. Therewith, the gas ionization rate and high level population essentially increase. The proposed modeling EEDF $f_{1/2}$ llustrates the stated effect and makes it possible to qualitatively describe the prime lows of the discharge development in the form of FIW in the whole range of parameters under studies.

It was proved that the generation of the required electron concentration as well as upper electron level population take place behind the FIW front in residual fields and sections corresponding to the "electric" and "luminous" FIW fronts are essentially separated in the space. This fact is illustrated in Figure 5, where temporal evolution of electric field (curve 1 – measurement by electric gauge, filled circles - data restored from the spectral measurement), $N_2(C^3\Pi_u, v'=0)$ and $N_2^+(B^2\Sigma_u^+, v'=0)$ level concentrations (curves 2, 3 respectively) and population rates (curves 4, 5) in nitrogen at $P = 4$ Torr are represented in the same time scale.

4 Conclusions

Thus, main regularities of the development of discharge at high overvoltages are derived for complex measurements of electrical and spectral characteristics of the nanosecond breakdown. Nanosecond breakdown is useful in the case when typical concentration of excited and dissociated particles of $\sim 10^{11} - 10^{13}$ cm^{-3} has to be created during a short time (tens of nanosecond). Due to specific conditions of development, mainly to high spatial uniformity and repetiatibility this type of discharge is applicable in understanding the basic features of development of any breakdown at high overvoltages, for example of streamer one.

These studies were partially supported by grants *96-03-32746*, *96-02-18297* of the RBRF and *96-2120* INTAS.

Monitoring a single micrometer size particle by angle resolved light scattering

W.W. Stoffels*, E. Stoffels*, G.H.P.M. Swinkels, G.M.W. Kroesen
Eindhoven University of Technology
PO Box 513, 5600 MB Eindhoven, The Netherlands.
**e-mail: stoffels@discharge.phys.tue.nl*

Introduction

In the last decade dusty plasmas have grown into an extensive research field. Numerous aspects of the formation, interactions and consequences of dust particles in plasmas have been investigated, ranging from dust dynamics in the interstellar space [1] to the dust contamination problem in industrial surface processing plasma reactors [2,3]. In many cases the global properties of the particle plasma interaction are studied. In this contribution we study the treatment of a single micrometer size dust particle in a low-pressure radio frequency plasma. This is expected to give insight in the basic phenomena of plasma particle interaction, from the material-science point of view. The aim of the work is to derive knowledge on particle etching and deposition from a single particle study, which can be generalized to particle clouds. At that stage plasma processing of particles can become an industrially relevant process with a large potential for various applications.

Experimental setup

A schematic overview of the experiment is shown in Figure 1. A single, well-defined particle is introduced into the plasma and pinpointed it in a specially constructed potential well. We demonstrate that we can accurately determine the particle properties and influence them in a controlled way by means of plasma processing. In particular, we employ angle-resolved Mie scattering to monitor the particle radius and we control the particle size by means of etching in a low-power radio-frequency oxygen discharge. We use commercial melamine-formaldehyde particles with a diameter of about 12 μm and a refractive index of 1.68. For the particle injection, we use a particle-filled sieve, which is mounted on a manipulator arm. The measurements are performed in a GEC reference cell: a parallel-plate capacitively coupled 13.56 MHz radio-frequency reactor. An aluminum ring (diameter: 2 cm, thickness: 1.5 mm) is placed on the lower powered electrode in order to create a potential trap, so the particles shed from the sieve are immediately "caught" at the glow-sheath edge above the metal ring. In this way it is possible to prepare a Coulomb crystal, but also to "freeze" a single particle in a fixed position. Angle-resolved Mie scattering is applied to monitor the particle size and refractive index as a function of time during plasma processing. The light source is an argon ion laser, linearly polarized in the direction perpendicular to the detection plane (see Fig. 1). The scattered light is collected by an optical fiber, passed through an interference filter and fed to a photo-multiplier. The optical fiber is mounted on a moveable stage. This allows continuous scanning of the detection angle in the range of 1 to 15 degrees for forward scattering. The maximum detection angle is limited only by the geometry of the optical ports of the GEC reactor. The angular resolution depends on the entrance opening of the optical fiber and its distance to the particle. In our case the square opening is 1 mm^2 and the distance is 90 cm, which results in an angular resolution of 0.06 degree. The angle-resolved scattering intensities are fitted to a numerical model for Mie scattering using the particle radius and refractive index as tuning parameters. A typical angle-resolved measurement and its fit to the data are shown in Figure 2. As can be seen, there is a good

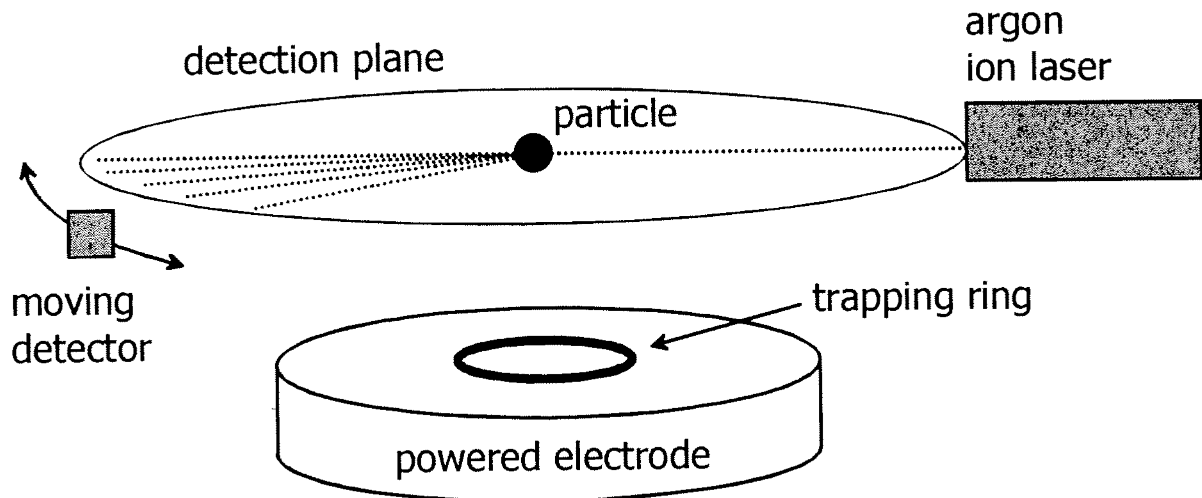

Figure 1. A schematic view of the set-up. A metal ring, placed on the electrode creates a circular disturbance of the sheath above the ring. The potential well created this way is used to trap a single particle at the plasma sheath boundary. Mie scattering measurements are performed using argon ion laser light (λ = 488 nm), polarized perpendicularly to the detection plane. An optical fiber mounted on a moveable stage collects the scattered intensity in the forward direction. This allows a continuous angle-resolved detection of the scattered light between 1 and 15 degrees with an angular resolution of 0.06 degrees

agreement between the measured data and the fit. The fitted particle radius (a = 5.90 μm) and refractive index (n = 1.68) agree with the size determination using SEM pictures and the data provided by the particle manufacturer. The particle size can be determined with accuracy better than 1 % by the angle-resolved scattering technique.

Experimental results

In order to demonstrate a good control of the particle radius and the sensitivity of the diagnostics, we use a low power discharge to etch the particle material in a controlled way. It should be noted that there is a large difference between the standard etching of a substrate placed on the electrode and the etching of a free floating particle in a plasma. In the sheath of the powered electrode a high potential in the order of 1 kV accelerates positive ions towards the surface. High-energy ions, reaching the electrode surface are responsible for sputtering and etching of the material. In contrast, the potential difference between the plasma and a floating particle is much lower, in the order of 10 V. Therefore, plasma chemical effects due to low-energy ions and radicals are expected to be most important for microscopic particle etching. In order to prove that there is no physical ion sputtering, we monitored time changes in the angle-resolved scattering signals of single particles trapped in argon and oxygen plasmas. In argon, where no chemical etching can occur, no remarkable changes were observed even after hours of plasma operation, while substantial variations of the scattering signal were recorded already after a few minutes of processing in oxygen. Oxygen is a well-known etching gas suitable for etching of organic polymer materials. Ion and radical chemistry in radio-frequency oxygen discharges was extensively studied in the past [3,4]. Free oxygen radicals and oxygen ions provide an ideal composition of active species to etch organic polymer particles trapped in the discharge.

Figure 3 shows the time evolution of the angle-resolved intensity scattered by a single particle in a 5 W, 0.2 mbar oxygen plasma. The characteristic Mie fringes are clearly visible, and it is evident that the maxima shift towards higher angles as the etching proceeds. In terms of the Mie theory, this implies that the particle size decreases in time. Using the numerical

model the time dependent particle size is deduced, as shown in Figure 4. The corresponding etch rate for a single particle is 0.1 nm/s. The etching process is determined by various plasma parameters. Tuning of these parameters provides a means to obtain a good control of the etch rate and consequently of the particle radius.

Conclusions

We have shown that a single particle can be efficiently trapped in a discharge, and its size can be accurately regulated. We discuss etching as an example of such controlled particle treatment, but the presented technique opens many other possibilities. Particle size can be increased in deposition plasmas, e.g. using silane or methane [6]. Fine tuning of the particle size, at a well-defined rate, has undeniable benefits. For example, particle modification process can be studied on a relative simple, single particle system, and extended to the situation of particle clouds. Moreover, the forces acting on a particle are size-dependent, so an accurate determination and modification of particle size can prove extremely helpful in a study of the force balance and particle motion in the plasma.

Acknowledgments

This work is supported by the "Stichting voor Fundamenteel Onderzoek der Materie" (FOM) and by the Dutch Technology Foundation (STW). The research of Dr. W.W. Stoffels has been made possible by a fellowship of the Royal Netherlands Academy of Arts and Sciences (KNAW).

References

[1] *The physics of dusty plasmas.* ed. P.K. Shukla. World Scientific, Singapore (1996). ISBN 981-02-2644-6

[2] *Dusty plasmas.* ed. A. Bouchoule, to be published by John Wiley & Sons, (1999).

[3] E. Stoffels, W.W. Stoffels, G.M.W. Kroesen, F.J. De Hoog, Electron Technology, 31(2), p. 255-274 (1998).

[4] E.Stoffels, W.W. Stoffels, D. Vender, M. Kando, G.M.W. Kroesen, F.J. De Hoog, Phys Rev. **E 51**, 2425 (1995).

[5] D. Vender, W.W. Stoffels, E. Stoffels, G.M.W. Kroesen, F.J. de Hoog, Phys. Rev. **E 51**, 2436 (1995).

[6] K. Tachibana, Y. Hayashi, T. Okuno, T. Tatsuta, Plasma Sources Sci. Technol. **3**, 314 (1994).

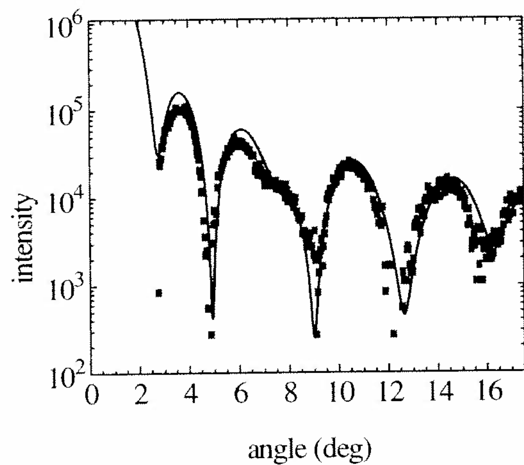

Figure 2. Angle-resolved Mie scattering data of a single melamine-formaldehyde particle (squares), trapped in a radio-frequency oxygen plasma. The data are fitted by a theoretical scattering curve for a particle of 5.90 μm radius and 1.68 refractive index.

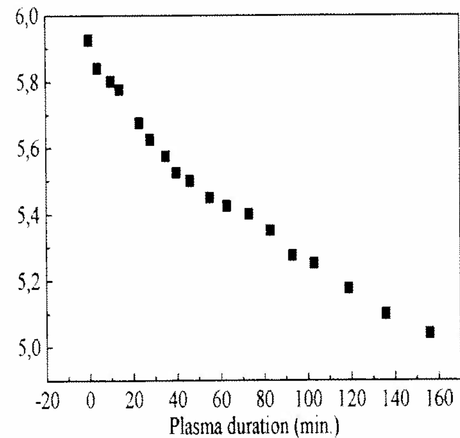

Figure 4. Particle radius as a function of the treatment time in a radio-frequency oxygen plasma. The particle radius is determined by fitting the experimental data of Figure 3 with theoretical Mie scattering intensities using the particle radius and refractive index as fitting parameters. Best fits are obtained by keeping the refractive index constant in time (n = 1.68) and allowing the radius to decrease.

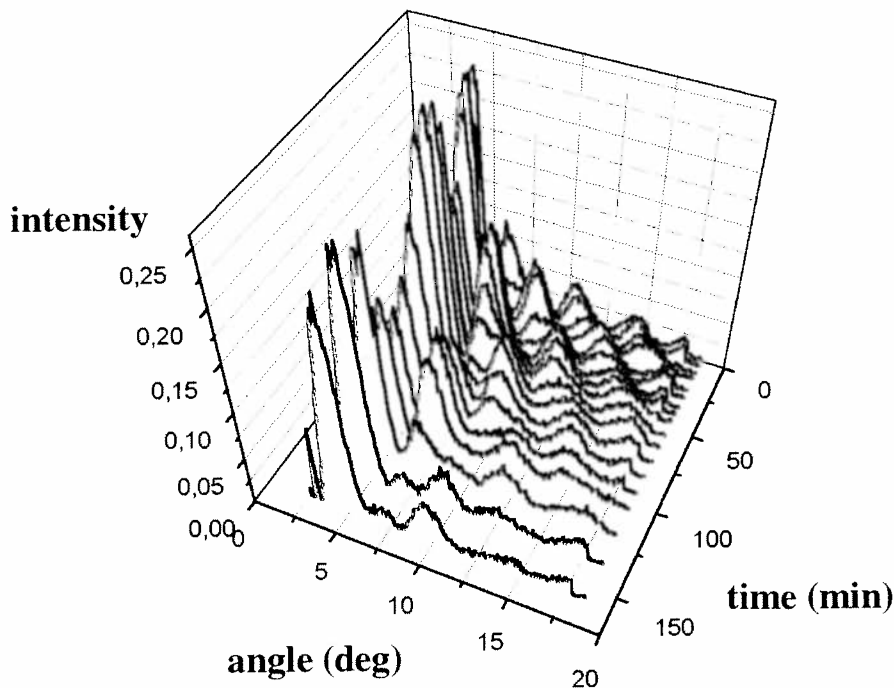

Figure 3. Time-dependent angle-resolved scattering intensity of a single melamine-formaldehyde particle treated in a 0.200 mbar, 5 W oxygen plasma. The position of the maxima and minima moves to larger scattering angles with time, indicating that the particle size continuously decreases in time.

Measuring the Temperature of Dyed Dust Particles in RF Plasmas.

Geert Swinkels and Gerrit Kroesen

Department of Physics, Eindhoven University of Technology, PO Box 513, 5600 MB Eindhoven, The Netherlands.

Dusty plasmas have attracted a lot of attention in the last decade. In semiconductor processing plasmas it appeared that the formation and the trapping of dust particles was a serious source of surface contamination and the reason for defects in fabricated components. Therefore the semiconductor community initiated an extensive research effort to understand dusty plasmas. Nowadays, the increased knowledge is used in a new line of research: the production of particles with unique and desired qualities.

The particles are trapped in the plasma and there they are subjected to all kind of different processes that occur in the plasma. These processes influence the internal particle temperature that is governed by the thermal balance:

$$\frac{4}{3}\pi r_p^3 \rho C \frac{\partial T_p}{\partial t} = Q_h + \pi r_p^2 I_{abs} - 4\pi r_p^2 (\Phi_{con} + \Phi_{rad} + \Phi_{chem}). \quad (1)$$

In the thermal balance, r_p is the particle radius, ρ the specific mass density, C the specific heat capacity, I_{abs} the absorbed laser energy per unit surface, and Q_h is the incoming heat flow rate. There are three heat fluxes leaving the particle and these are represented by Φ_{con}, Φ_{rad}, and Φ_{chem}: conductive cooling due to the neutral gas, a radiative cooling term (Stefan-Boltzmann), and the loss of volatile energetic species produced in chemical reactions respectively. The incoming heat flow rate Q_h is determined by different processes in the plasmas like ion recombination at the particle surface, radical association, and absorption of plasma radiation. The internal temperature of the particle thus yields valuable information about these different processes.

Daugherty[1] has performed measurements on the internal temperature of dust particles. Recording the phosphorescent radiation of manganese activated magnesium fluorogermanate particles in the afterglow of an argon plasma, he was able to measure an internal particle temperature. The phosphorescent radiation has a temperature dependent decay time. Measurement of this decay time resulted in a temperature of 410 K.

In the literature it has been shown that one can also use dyes to measure temperatures, e.g. thermal plumes[2]. We have used melamine formaldehyde powders, which are volume dyed with Rhodamine B (MF/RhB) to measure the temperature of particles in radio frequency plasmas. The particles allow for a real time and in-situ measurement of the internal temperature.

Our measurements have been performed in a GEC reference cell. A top view of the reactor is depicted in Fig. 1.

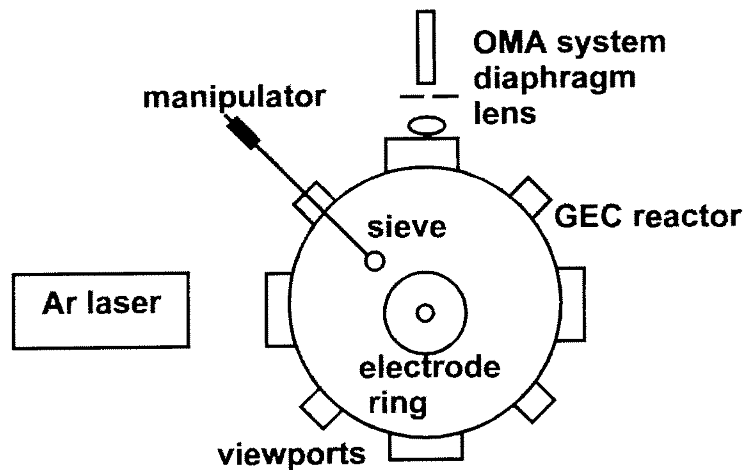

FIG. 1. Top view of the GEC cell. The sieve is used to inject the particles into the plasma.

The OMA system depicted in Fig. 1 is used to record the spectral profile of the fluorescent emission. In order to record the spectrum the dye has been excited using a argon ion laser operated at 514nm and 25 mW. A manipulator arm with a sieve attached allows for the injection of the particles ($2r_p$ = 1.2 μm) into the plasma. The spectral behavior of the particles has been calibrated as a function of temperature after mixing the particles with oil. This is shown in Fig. 2.

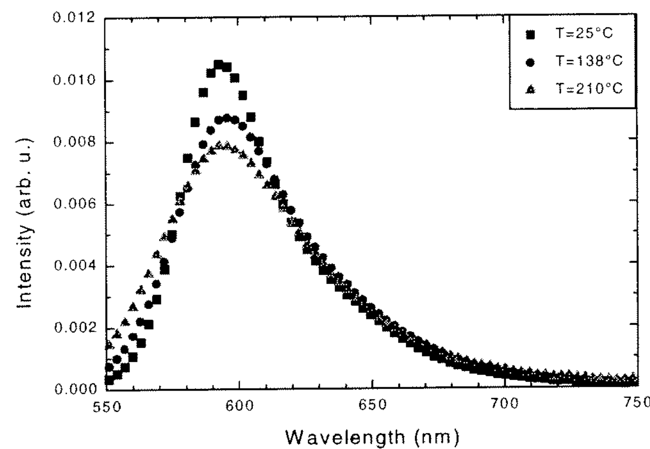

Fig. 2. The spectral behavior of the MF/RhB particles recorded in oil. The squares, circles, and triangles represent temperatures of 25°C, 138°C, and 210°C.

These curves are used to determine the particle temperature in the plasma without making use of the absolute intensity. This is a big advantage. Several processes can obstruct in performing reliable measurements of the absolute intensity: the density of trapped particles is not constant, laser radiation can photo bleach the dye, plasma emission can degrade the dye, and plasma processes like etching and sputtering can be of influence.

In Fig. 3 a typical fluorescent emission spectrum is shown. This spectrum is measured in an argon plasma at a pressure of 0.4 mbar, 17W, and a gas flow rate of 1 sccm.

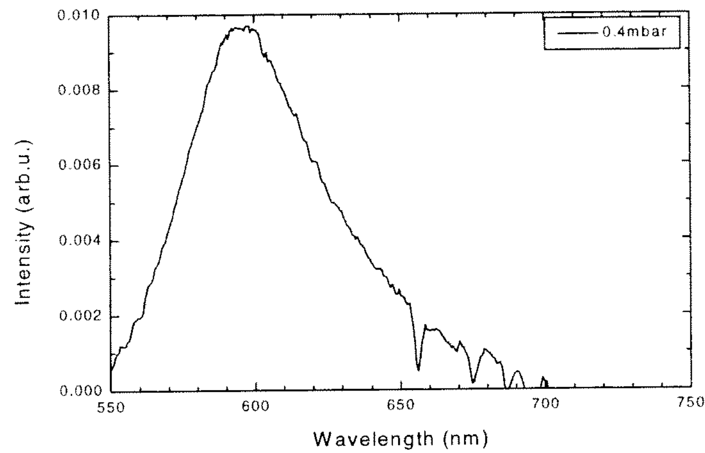

Fig. 3. The fluorescent emission in an argon plasma (0.4 mbar, 17W and 1sccm).

Above wavelengths of 650nm interference of plasma emission lines are visible. With the aid of the calibration curves a temperature of 138°C can be attributed to the measured spectrum.

References

[1]J. E. Daugherty and D. B. Graves, J. Vac. Sci. Technol. A **11**,1126 (1993).
[2]J. Coppeta and C. Rogers, Experiments in Fluids **48**, 1 (1998).

Time resolved Langmuir probe measurements in medium pressure Ar-H_2 microwave plasma

E.Teboul, A;Rousseau, P.Leprince

Laboratoire de Physique des Gaz at des Plasmas, (URA 73 CNRS), Bat 212
Université Paris Sud 91405 Orsay Cedex France

Abstract :

In this contribution we aim at presenting charged particles density and electron temperature measurements determined from a Langmuir probe using theoritical model from Tichy and al. [1] which takes into account collisions of charged particles in the sheath.. Measurements in a continuous and pulsed microwave Ar have been performed. The pressure ranges from 1 to 10 Torr. Time resolved densities and temperature measurements have been carried out during the pulse and the temporal post discharge.

1. Introduction:

The major advantage of probe measurements is that they can make local measurements rather than giving results averaged over a large volume of plasma.
The number of collisions in this sheath determines which theory describe the collection of charged particles by a Langmuir probe.The working regime of the probe is described by three parameters namely by the Knudsen number for both ions and electrons $K_{i,e} = \lambda_{i,e} / R$ ($\lambda_{i,e}$ is the mean free path for ions and electron and R is the probe radius), by the Debye number $D_\lambda = R / \lambda_D$ with $\lambda_D = (\varepsilon_0 kT_e / n_e q^2)^{1/2}$ is the Debye length and $\tau = T_e/T_i$. Which is called the anisothermocity parameter. Because $K_{i,e}$ characterizes the magnitude of the ion and electron mean free path, the product ($K_{i,e}*D_\lambda$) is proportional to the number of collisions of these particles with neutrals across the sheath.

2. Collisional Theories of Ions and Electrons Collection

The collisionless case has been treated by Laframboise [2], Chen [3]. In collisional case the determination of charged particles densities from directly measures probe characteristic become impossible. One of the most known collisional theory of Langmuir probe has been developed by Chou, Talbot and Willis [4,5] for an arbitrary Knudsen numbers $0 \leq K_i \leq \infty$. In this theory, the collisional current is calculated from the Laframboise collisionless current with a correction factor which take into account reduction of ions and electrons current due to scattering of these charged particles in collisions with neutrals in the sheath. A second collisional theory probe has been treated by Zakrzewski and Kopiczynski [6] where they take into account not only the decreasing of ions and electrons currents due to scattering but also the increasing of these currents due to destruction of ions and electrons orbital motion by collisions with neutrals in the sheath. However, this theory is not applicable at high pressure (i.e. $K_i \leq 1$) due to approximation formulae used for description of the effect of scattering. Thus, in order to extend the validity of Zakrzewski and Kopiczynski [5] to arbitrary K_i, Tichy and Sicha [1] suggest to apply the Talbot and Chou theory [4,5] to determine the correction factor which describe the effect of scattering and keep the correction factor from Zakrzewski and Kopiczynski [6] theory in order to describe orbital motion

destruction due to collisions of ions with neutrals in the sheath. Then, the normalized ion probe current I^*_+ can be written as :

$$I^*_+ = \gamma_1 \gamma_2 I^*_L$$

where γ_1 describes the rate of increase of ion current due to destruction of orbital motion and calculated according the Zakrzewski and Kopiczynski [6] theory, and γ_2 corresponds to the rate of reduction of ion current due to scattering and given by the Chou, Talbot and Willis [4,5] theory. I^*_L is the normalized collisionless ion probe current predicted by Laframboise [2].

3. Experimental Arrangement

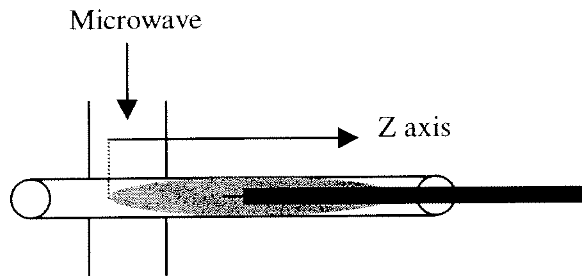

Figure 1: *Experimental setup*

A schematic representation of the experimental setup is given Fig.1. The microwave power is transferred via a surfaguide [7]. The plasma is created by a surface wave in a quartz tube where the electron density decrease along the tube axis (z direction). The experiments have been done in argon at pressure range between 1 and 10 Torr. The cylindrical Langmuir probe consist of a 50 μm radius tungsten wire and 5 mm length. The body of the probe is alumna. Cleaning by electron bombardment is necessary in order to avoid contamination phenomenon. The probe is. longitudinally movable on the axis of the discharge tube. In order to achieve time resolved measurements, acquisition facilities from Jobin Yvon Digiprobe has been used. The pulse duration was set equal to 1 ms and the repetition rate equal to 500 Hz. With such an acquisition system, it has been possible to reach a time resolution of 20 μs.

4. Results in continuous plasma

Figures 2 and 3 show electron density and temperature respectively, versus pressure. The incident power ranges from 50 W to 150 W.

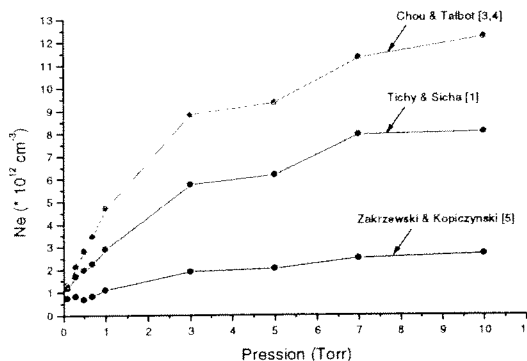

Fig. 2 : *Electron density calculated from three theories in Ar plasma*

The electron density is determined by three different methods. In our case we choose the theory from Tichy and Sicha because they take into account the two effects mentioned above. Electron density found by this theory are in quite good agreement with microwave interferometry measurements [8].

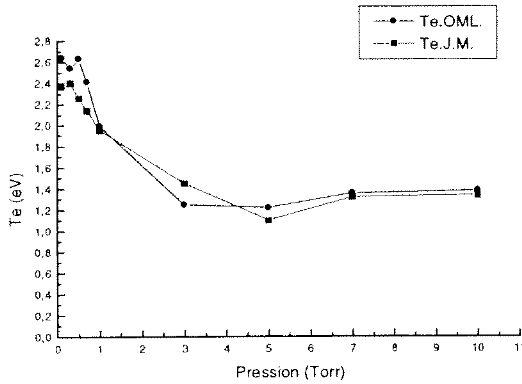

Fig.3: *Values of electron temperature*

The electron temperature was determined both with simple and double probe. For the single probe we use the semilogarithmic plot method, whereas for the double probe, we used the theory developed by Johnson & Malter [9]. From the plot, one can see the good agreement between the two collisionless theory. Moreover Kirchhoff, Peterson and Talbot [10] showed that the correction factor for collisions effect on electron temperature does not exceed few percent.

4.1. Results in pulsed plasma

Figures 4 and 5 show the electron density and Figures 6 and 7 show the electron temperature, both for 1 Torr and 10 Torr. In order to ignite the plasma at every pulse, a continuous background of power equal to 40 Watt has been kept when the pulse off. During the pulse, the power is set equal to 125 Watt.

We can see from these plot the effect of pressure on creation time [11] of electron. One can see that for 1 Torr this time is close to 200 μm whereas for 10 Torr is quite longer

We can also noticed that as we said before, in this kind of plasma, the density decreasing from the gap to the end of the plasma.

In the beginning of the pulse, the electron temperature reach a maximum value due to the breakdown electromagnetic field. Then, when the discharge is stable, the value of electron temperature stay quite constant. We can also noticed as for the electron density that the electron temperature decrease along the axis of the discharge.

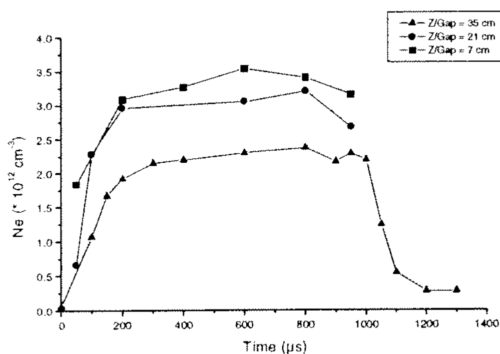

Fig 4 : *Value of electron density in Ar plasma at 1 Torr versus different times and positions*

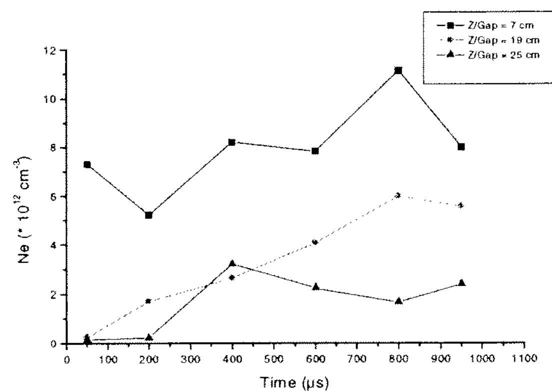

Fig 5 : *Value of electron density in Ar plasma at 10 Torr versus different times and positions*

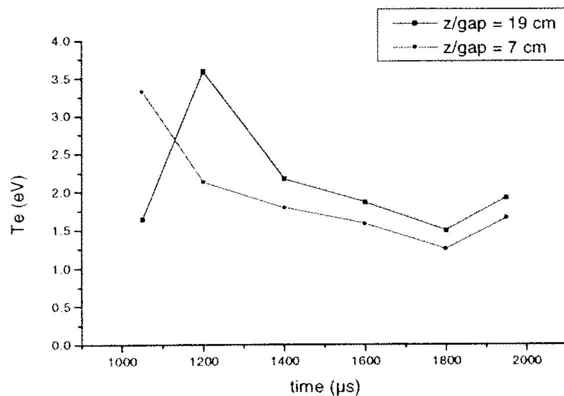

Fig 6 : *Value of electron temperature in Ar plasma at 1 Torr at different times and positions*

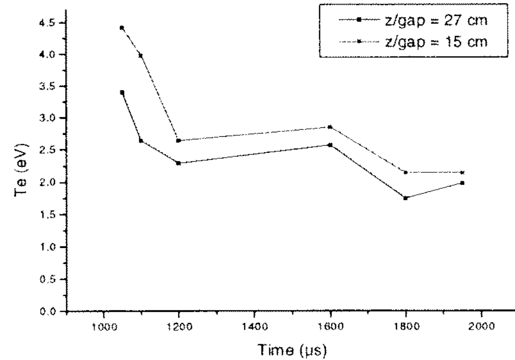

Fig 7 : *Value of electron temperature in Ar plasma at 10 Torr at different times and positions*

5. Conclusion :

Results of a new positive ion collection by a cylindrical probe at medium pressure have been presented. In the near future measurements on hydrogen at higher pressure (30 Torr) in pulsed plasma will be investigate. However this model has been developed for one component plasma. At higher pressure there is a real possibility of the presence of complex ions.

Acknowledgements

The authors wish to acknowledge the helpful discussion with professor M.Tichy on the subject.

References

[1] Tichy. M, Sicha. M, David. P, David.,T. Contrib. Plasma Phys. **34** (1994) 1, 59-68.
[2] Laframboise. J. G., Univ. of Toronto. UTIAS Rept. N° 100 (1966).
[3] Chen. F. F., Plasma Phys. **7** (1965) 64.
[4] Chou. Y. S., Talbot. L.; Willis. D. R., Phys. Fluids **9** (1966) 2150.
[5] Talbot. L, Chou. Y. S., Rarefied Gas Dynamics. Ac. Press (1966) 1723.
[6] Zakrzewski. Z., Kopiczynski. T., Plasma Phys. **16** (1974) 1195.
[7] Rousseau. A., Tomasini. L., Gousset. G., Boisse-Laporte. C., Leprince. P., J. Phys. **D 27**, 2439 (1994).
[8] Bloyet. E., Llamas. Blasco. M., Marec. J., Phys. Letters, **83A** 391 (1981)
[9] Johnson. E. O., Malter. L., Phys. Rev., Vol **80**, N° 1 (1950), 58-68.
[10] Kirchhoff. R. H., Peterson. E. W., Talbot. L., AIAA Journal **9** (1971) 1686-1694.
[11] Granier. A., Boisse-Laporte. C., Leprince. P., Marec. J., Nghiem. P., J.Phys. **D 20**, 204 (1987).

Poster Session II

Thomson scattering in fluorescent lamps

L.P. Bakker, and G.M.W. Kroesen
Eindhoven University of Technology
The Netherlands

Introduction

From the application point of view, it would be convenient if the colour temperature of a fluorescent lamp could be changed during operation. This colour variation can be achieved in a fluorescent lamp, filled with neon and mercury. In a normal fluorescent lamp, the neon atoms only act as a buffer gas. The discharge is basically running on mercury. However, when the electron temperature in the positive column is high then the neon atoms can be excited by the electrons. These neon excitations result in the production of red light which is mixed with the white light produced by the mercury atoms in combination with the fluorescent powder on the inner tube wall. In order to measure the electron temperature for several discharge configurations and for different electrical signals, a Thomson scattering set-up will be built.

Thomson scattering

In the Thomson scattering set-up, the reduction of stray light coming from the glass tube is very important. Because of the high intensity, the stray light reduction has to be more than 10 orders of magnitude. This reduction can be achieved by using a dye laser at the sodium D1 wavelength and a sodium vapour absorption cell that absorbs resonant radiation. A schematic drawing of the set-up is shown in figure 1.

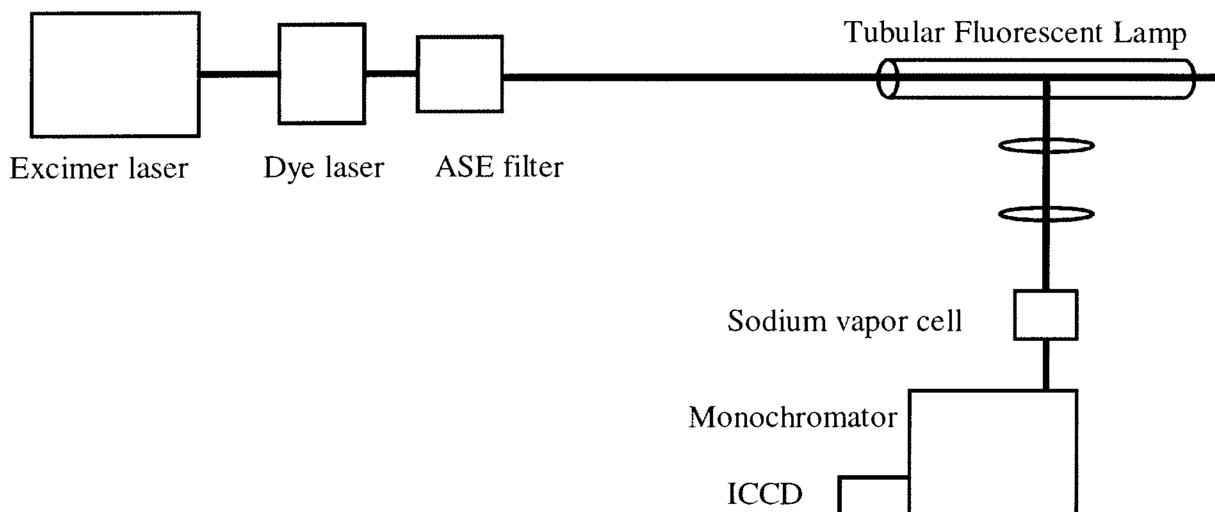

Figure 1: Schematic drawing of the Thomson scattering set-up.

Since the D-lines are resonant, the stray light will be absorbed in the absorption cell. The Thomson signal is broad enough to be transmitted through the cell, without being absorbed.
In order to make this set-up feasible the Amplified Spontaneous Emission of the dye laser has to be filtered out because of the fact that it is broader than the Thomson signal. This can be done with a spatial filter. Because of the high intensity during the laser pulse we will have to use a prism as the dispersive component in the filter. However, the dispersion of one prism is too small to obtain a sufficiently narrow spatial filter. Therefore, we designed a spatial filter with 20 prisms in order to have a much higher dispersion in the filter.

The ideal situation is achieved when the width of the spatial filter is narrower than the width of the absorption line of the sodium vapour absorption line. Then all the light scattered in the glass tube, except for the Thomson scattered photons will be absorbed by the sodium vapour. This situation can be achieved in two ways: (1) narrowing the filter or (2) broadening the absorption line. The narrowing of the filter can be achieved by using twenty prisms as described above. The broadening of the absorption line can be achieved by adding argon to the sodium vapour, this will result in the pressure-broadening of the sodium line.
The transmission of the ASE filter and the transmission of the absorption cell are measured with a ring dye laser. Figure 2 shows the results of these measurements.

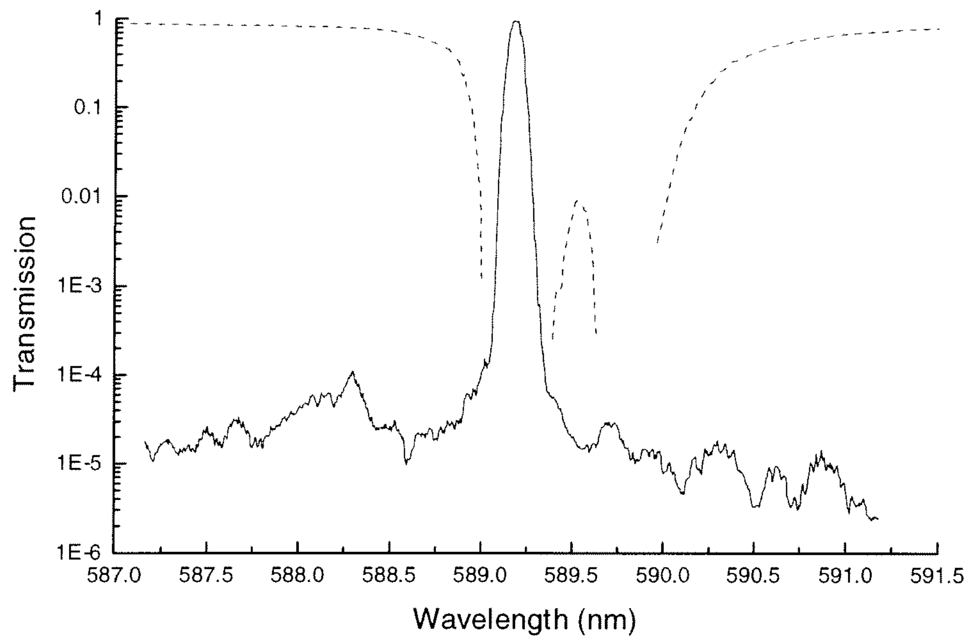

Figure 2: The transmission of the ASE filter and the vapour cell.

The transmission of the ASE filter for radiation with the selected wavelength is higher than 80%. The transmission of the vapour cell is around 70% for radiation with a non-resonant wavelength. In figure 2 these transmission are normalized to unity.
The ASE level of the dye laser is 10^{-4} of the power in the laser line. The ASE filter reduces this level with a factor 10^{-5}, see figure 2. In conclusion, we will have a stray light reduction of 10^{-9}, this reduction is high compared to 10^{-3} to 10^{-5} with a Nd:Yag laser. By allowing the laser beam to pass the ASE filter twice, we can square the ASE reduction to 10^{-10}, which gives a stray light reduction of 10^{-14}. The performance of the ASE filter and the sodium vapour absorption cell will be discussed in detail.

Acknowledgements
This research is supported by the Technology Foundation STW and by Philips Lighting Eindhoven.

Atomic Lithium Beam Spectroscopy for N_e and T_e in Reactive Plasmas

M. Böke[1], G. Himmel[1], B. Schweer[2] and J. Winter[1]

[1]*Institut für Experimentalphysik II, Ruhr-Universität Bochum, D-44780 Bochum, Germany*
[2]*Institut für Plasmaphysik, Forschungszentrum Jülich, D-52425 Jülich, Germany*

1. Introduction

In a reactive plasma the species composition and the flows of particles to a substrate depend upon the electron energy distribution and its spatial variation and time dependence. The electron density has a large influence on the growth rate of thin films deposited from the discharge gas. To control plasma assisted processes it is important to have a detailed knowledge of these quantities during every phase of a process, preferably with high spatial and time resolution. A disturbing factor of conventional invasive diagnostics such as Langmuir probes is the film deposition on this probes. This makes the measurements non reproducible and difficult to interpret. The aim of this work is to develop atomic lithium beam supported emission spectroscopy for reactive plasmas. It is insensitive to film deposition, provides local and time resolved data and does not change the plasma properties. To prove and to characterize this diagnostics first investigations are made in rare gases in a GEC reference cell.

2. Atomic Lithium Beam supported Emission Spectroscopy

Atomic beam supported Li emission spectroscopy is based on the measurement of line intensities and intensity ratios of electron excited states of the neutral Li- atom. These are in particular the 2S-2P transition at 670.8nm, the 2P-3S transition at 812.6nm, and the 2P-3D transition at 610.4nm, see fig.1. Li-beam spectroscopy has already been used successfully for the diagnostics of the edge region of fusion plasmas [1].

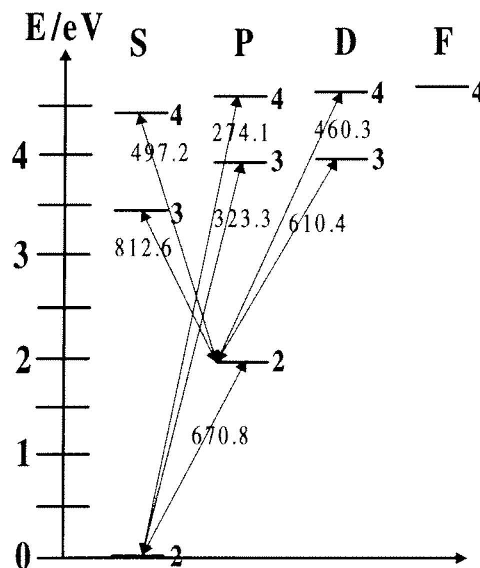

Figure 1: *Term scheme of lithium*

In the case of reactive low pressure plasmas several factors impede the application. One main obstacle comes from the fact that these plasmas are usually operated in the 0.1-10Pa range and have a low degree of ionisation. Thus a large fraction of neutrals has to be accounted for. At low pressure (0.1Pa) one obtains a well defined narrow lithium beam because the mean free path of lithium atoms is in the range of 10 centimeters and it is possible to reach high

spatial resolution in the measurement of the plasma parameters. At higher pressure (a few

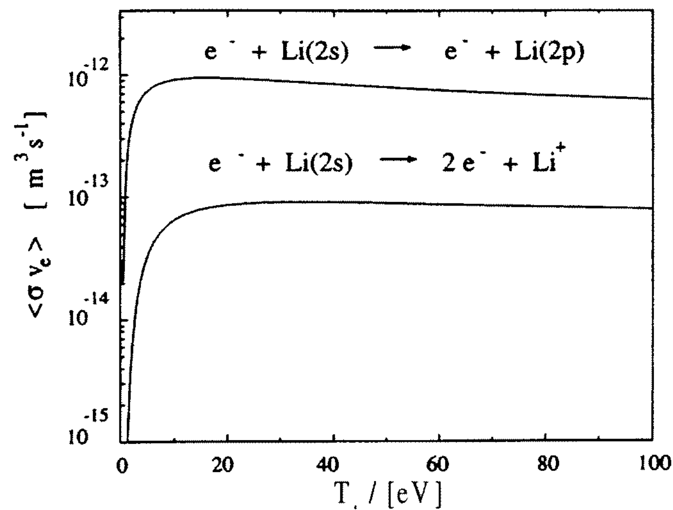

Figure 2: *Crosssections for e⁻-excitation and ionization*

10Pa) the situation changes: The beam becomes broader and degenerates to a lithium cloud due to collisions with the discharge gas. The discolouration of the discharge stays usable but the spatial resolution is limited and the modelling effort becomes higher.

The other problem is due to the low electron temperature in the reactive plasmas. Whereas for fusion edge conditions with T_e values above 10eV energy independent constant cross sections may be used (see fig. 2), the threshold region with significant dependence on energy applies for reactive plamas with T_e of about 1eV.

3. Experimental Setup and First Measurements

Using a CCD-camera, optionally in combination with a spectrographical system or with interference filters for the observed lithium lines, the spectral line emission from a beam of neutral lithium atoms after collisional excitation is investigated perpendicularly to the beam direction with spatial and temporal resolution. The atomic beam is produced by a lithium oven which consists in a Knudsen cell - filled with an alloy of copper and lithium (2% lithium) - and an aperture system in order to collimate the beam. By indirect resistive heating of the Knudsen cell up to 950°C one receives a dynamic balance between diffusion from lithium atoms to the surface of the Cu-Li-alloy and evaporation of atoms controlled by vapour pressure in the cell. The advantage of this solid state source in comparison to fluid sources and ion beam sources is a simple construction, its high operating time, optional orientation of mounting and its insensitiveness to unexpected air leakage. The outlet velocity is in the range of 10^3 ms^{-1} and the flux of lithium atoms out of the oven at about 10^{17}-$10^{18}m^{-2}s^{-1}$. The diagnostics is installed on a GEC reference cell which provides between its

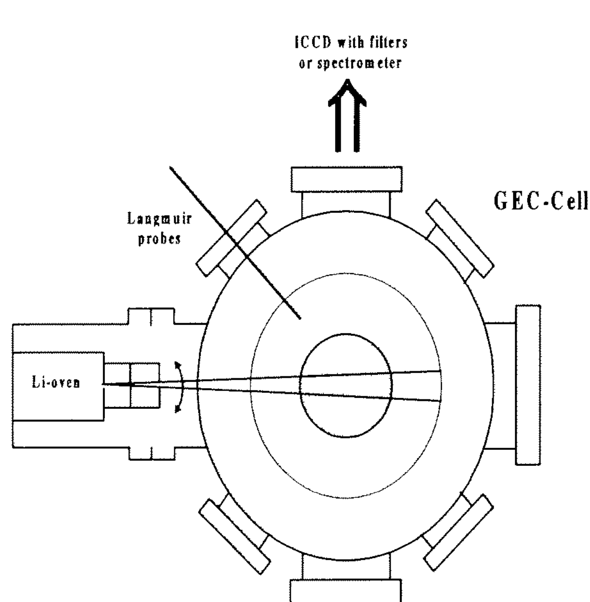

Figure 3: *Experimental Setup*

parallel electrodes a capacitively coupled rf-discharge (electrode diameter: 10cm, distance between electrodes: 4cm, pressure: 0.1-10Pa, T_e~ eV, N_e~ $10^{17}m^{-3}$, frequency: 13.56MHz). Figure 5 shows the intensity variation of the Li line at 670.8nm integrated over a volume of about 1 cm^2 x beam width at a location close to the discharge center in hydrogen and argon. Whereas in the case of Ar an increase of the intensity is found with increasing pressure, the H_2 plasma yield saturating Li intensities. Figure 6 shows the variation of the Li line intensity for the same geometrical conditions as in figure 5 as a function of the rf-power coupled to the plasma. Because the excitation occurs in the threshold regime no direct relation to the electron density can be made. A collisional radiative model is required for further analysis.

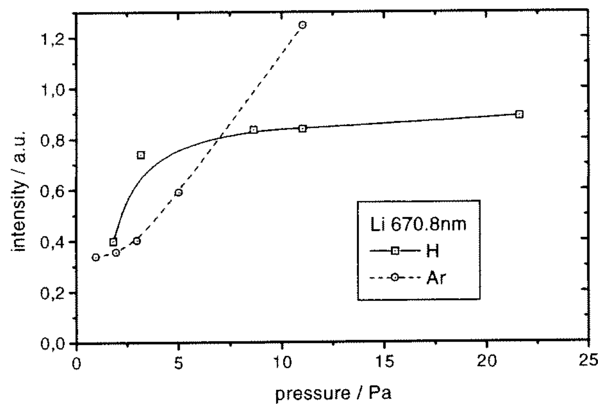

Figure 4: *Pressure dependence of overall lithium line emission*

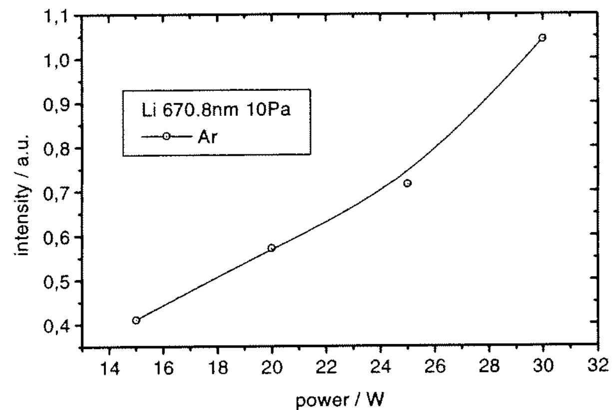

Figure 5: *Power dependence of overall lithium line emission*

4. Résumé and Further Developments

From the measured line intensities it is possible to obtain locally the electron energy and density at low pressure. But at higher pressure the spatial resolution of the diagnostics is reduced due to beam broadening and degeneration to a cloud of lithium atoms. In addition in this case the density reduction of the neutral lithium atoms by collisional ionization has to be taken into account and it is necessary to measure the spatial development of this neutral Li-atom density using a diode laser.

In order to enlarge the efficiency of the diagnostics and to reach a sufficient beam collimation and penetration depth even at higher pressures the transition to pulsed and fast atomic beams (also with heavier atoms, e.g. potassium) provided by laser ablation [2] is in preparation. Also a comparison to Thomson scattering at the same discharge geometry is planned.

This work is supported by Deutsche Forschungsgemeinschaft within SFB 191 (B8).

5. References

[1] A. Dinklage, T. Lokajczyk, H.J. Kunze, B. Schweer and I.E. Olivares; Rev. Sci. Instrum., **69** **(1)**, 321-322 (1998)

[2] Y.T. Lie, A. Pospieszczyk and J.A. Tagle; Fusion Technology, **6**, 447-452 (1984)

Cavity Ring Down detection of neutral hydrogen atoms and negative hydrogen ions in plasmas

M.G.H. Boogaarts, A.H.M. Smets, M.C.M. van de Sanden, and D.C. Schram

Department of Applied Physics, Eindhoven University of Technology, P.O. Box 513, 5600 MB Eindhoven, The Netherlands.

The Cavity Ring Down (CRD) technique has been applied for the absolute detection of low density species in two different hydrogen containing plasmas. CRD measurements have been performed in a 10 Hz pulsed capacitively coupled RF H_2-plasma to detect negative hydrogen ions (H^-) as well as atomic hydrogen in the n=2 state (H(n=2)). A broadband absorption of 3.5×10^{-6} per pass due to photo-detachment of H^- was observed, which corresponds to a H^- density of 10^{16} m^{-3}. In addition, CRD measurements on H(n=2) have been performed in the expanding plasma of a cascaded arc, in which H_2 or C_2H_2 is injected. Densities of H(n=2) down to 10^{12} m^{-3} have been measured. In both plasmas a severe decrease of the reflectivity of the cavity mirrors over time was observed, which is possibly caused by diffusion of atomic hydrogen into the reflective coating.

Introduction

In many low-temperature plasma applications, low density (i.e. short lived) species are expected to play a key role, but often their role is not established in detail. The study of low density species in plasmas calls for a sensitive technique that is applicable in the hostile environment of a plasma. In this contribution two experiments will be presented that demonstrate the high potential of the 'cavity ring down (CRD)' technique for this purpose. The CRD technique [1], which is first demonstrated by O'Keefe and Deacon in 1988 [2], is based on the measurement of the rate of absorption of a light pulse confined in a closed optical cavity. The cavity usually consists of two highly reflective mirrors with a reflectivity R and a separation d around the sample medium with density n, absorption cross section σ, and absorption pathlength L. With monochromatic light, the rate of absorption, which is characterized by the 'ring-down time' τ, is directly related to the absolute absorption $n\sigma L$, via the expression $1/\tau = (1-R+n\sigma L)c/d$ (1).

In the first experiment the CRD technique has been applied to measure the absolute density of excited hydrogen atoms in the n=2 state (H(n=2)) in the expanding plasma of a cascaded arc under conditions that are used for the fast deposition of hydrogenated amorphous carbon (a-C:H) films. In the second experiment the possibility is explored to use CRD for the detection of negative hydrogen ions (H^-). Negative ions can be measured via absorption of a photon which results in photo-detachment of the extra electron. Thus far, negative ion measurements relied in nearly all cases on the detection of the detached electrons, usually by means of a Langmuir probe. Only very recently, Döbele and coworkers reported negative ion measurements via the detection of optical absorption [3,4]. Here we report on CRD measurements on H^- as well as on H(n=2) in a 10 Hz pulsed capacitively coupled RF H_2-plasma.

Cavity Ring Down set-up

The ring-down cavity was implemented on both plasma reactors in a very similar way. Fig. 1a gives the experimental set-up for the CRD measurements in the expanding plasma beam, while Fig. 1b gives the set-up for the measurements in the capacitively coupled RF-reactor. In both cases a stable optical cavity is set up by two highly reflective dielectric mirrors (Laseroptik GmbH) with a 1 inch diameter, a radius of curvature r = -500 mm, and a specified reflectivity $R \geq 0.999$ at 656 nm, that are a distance d = 756 mm apart. The mirrors are mounted on flexible bellows and directly seal the low-pressure plasma reactor. To protect the mirrors from the hostile plasma environment, gas is purged contineously from the mirrors into the plasma through 5 mm diameter diaphragms that are positioned in front of the mirrors on the axis of the cavity.

The light pulse that is coupled into the cavity via the mirror on the left, is generated by a pulsed tunable dye-laser (Spectra-Physics/Quanta-Ray PDL-2) that is pumped with a 10 Hz Nd:YAG-laser (Spectra-Physics/Quanta-Ray DCR-11). The light leaking out from the second mirror on the right, is detected with a PMT. A broadband Balmer-α filter is mounted behind the second mirror to reduce the exposure of the PMT to continuous plasma and background light. The PMT signal is sampled by a digital 1 Gs/s, 100 MHz oscilloscope (Tektronix TDS340), averaged on board over several laser pulses, and the resulting transient is processed by a PC, where the characteristic 'ring-down time' τ is determined from a weighed least-squares fitting of the logarithm of the data.

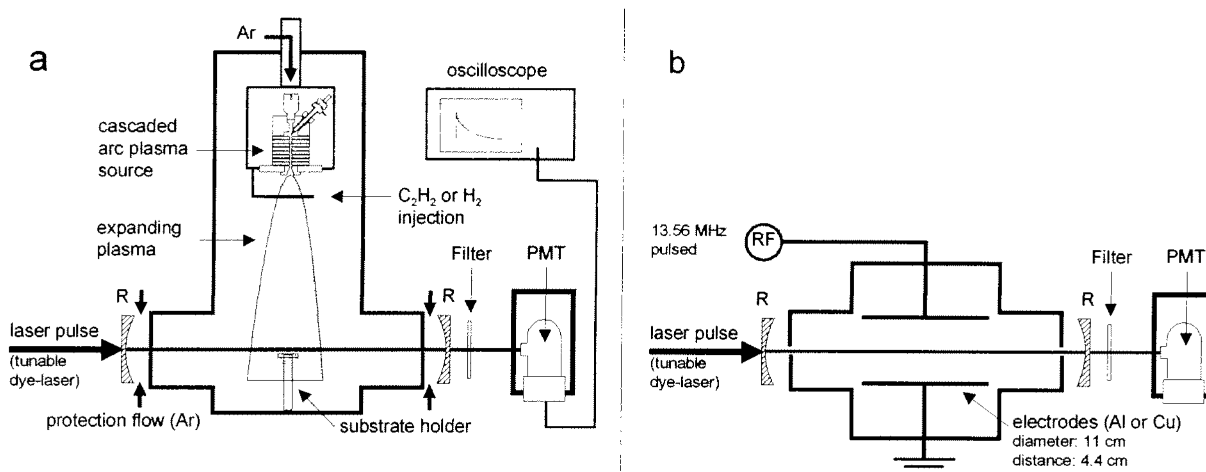

Fig. 1: *Experimental CRD set-up implemented on the expanding cascaded arc plasma, used for the fast deposition of a-C:H (a, left panel), and implemented on the capacitively coupled RF reactor (b, right panel).*

Detection of excited hydrogen atoms in an expanding plasma beam

Part of the research in our group focuses on the fast deposition of hydrogenated amorphous carbon (a-C:H) layers using an expanding plasma created by a cascaded arc (Fig 1a), where growth rates well above 10 nm/s are easily obtained [5]. The plasma is generated in pure Ar and expands from a nozzle at the end of the cascaded arc channel into a low-pressure (sub-mbar) vessel. Precursor gases (in our case H_2 or C_2H_2) are injected into the plasma beam via a ring that is mounted a few cm downstream from the nozzle. During a-C:H growth, C_2H_2 is injected into the plasma beam, where charge exchange with Ar^+ occurs. The dissociative recombination: $C_2H_2^+ + e^- \rightarrow C_2H + H(n=2,3,...)$ is then considered to be the main reaction channel. Consequently C_2H is believed to be the dominant radical for a-C:H growth.

To test this hypothesis, a CRD experiment was set up to sample the plasma beam 6 cm above the substrate holder, in order to detect H(n=2), which is one of the products of the above reaction. H(n=2) is detected by measuring the absorption of Balmer-α radiation at 656.3 nm in the transition to the n=3 state. The absorption spectrum is derived from a recording of the ring-down time τ as a function of wavelength, using the above expression (1). In the left panel of Fig. 2, spectral absorption profiles of H(n=2) are shown for various settings of the cascaded arc source. The profile for 69.3 A is plotted both in units of cavity loss ($1/c\tau$, right axis), as well as in units of absolute absorption per pass ($n\sigma L = d/c\tau - (1-R)$, left axis). From the baseline cavity loss, a mirror reflectivity R of 0.9989 can be deduced. Notice that the absolute absorption due to H(n=2) can only be determined by measuring the difference in cavity loss of the cavity with and without the absorbing species. In the case of a narrowband absorption this is automatically accounted for by recording a spectral scan, where the loss of the empty cavity determines the baseline. A comparison between the various absorption profiles can only be made in units of absolute absorption per pass.

Knowing the absorption strength or cross section σ and estimating the absorption path length L, the absolute H(n=2) density can be determined from a spectral integration of the absorption profiles. This allows to study the density as a function of experimental parameters. The right panel in Fig. 2 gives

for instance the H(n=2) density, determined from the profiles in the left panel, as a function of the cascaded arc current, which is a measure of the power input into the plasma. The physical consequences of this measurement will be treated elsewhere, but it should be noted that from this measurement a noise equivalent detection limit for H(n=2) of 10^{12} m^{-3} can be inferred.

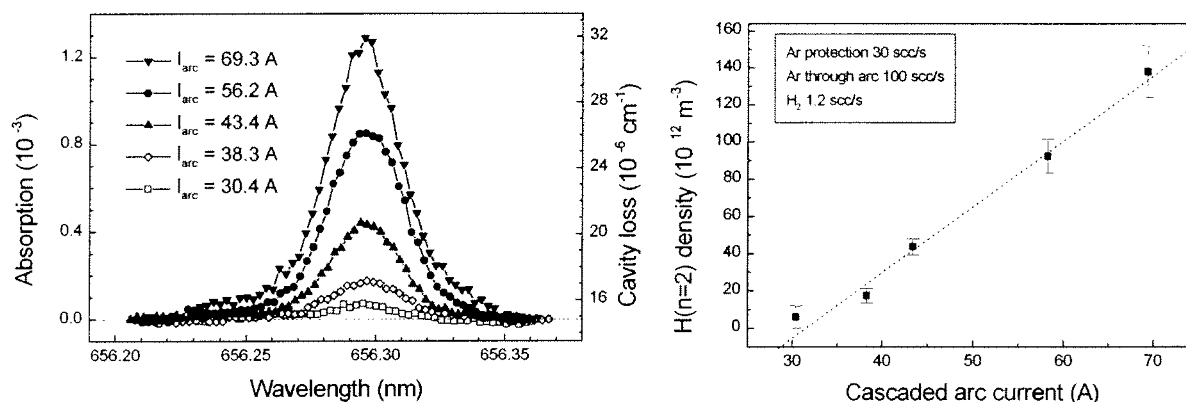

Fig. 2. *Left panel: Balmer-α spectral absorption profiles of the expanding plasma beam for various settings of the cascaded arc source. Right panel: Absolute H(n=2) density versus the current through the cascaded arc. The data points are obtained by spectral integration of the profiles in the left panel.*

Detection of negative hydrogen ions in a pulsed RF plasma

The CRD technique has also been applied to perform measurements in a conventional capacitively coupled 13.56 MHz RF reactor with two parallel electrodes of 11 cm diameter at a 4.4 cm distance and with a pressure in the sub-mbar range. The cavity axis is centred between the electrodes, and a pure H_2 gas flow enters the reactor near the mirrors and through the diaphragms. The negative hydrogen ions produced in the reactor can be detected by measuring the absorption due to photo-detachment. The absorption cross-section for photo-detachment of H^- is spectrally broadband, with a threshold at 0.75 eV and a value of 3.5×10^{-21} m^2 around 650 nm [6].

Now one should realize that a broadband absorption can only be detected by measuring the difference in cavity loss with the plasma on and with the plasma off. This simple procedure, however, inflicts some experimental difficulties unless a puled plasma is used, where τ is measured alternately in the on- and off-period. Just switching the plasma on and off causes the ring-down time to change already quite substantially, partly due to changes in experimental parameters like temperature and/or pressure, but more importantly due to the influence of reactive plasma particles on the reflectivity of the mirrors. This is clearly illustrated in the left panel of Fig. 3, which shows the result of a non-stop recording of τ for over an hour. The dramatic decrease in ring-down time after starting the plasma, is not due to disalignment or contamination of the mirrors. After switching off the plasma, τ recovers slowly but completely to the original value. Using a pulsed plasma enables to reach a quasi-stationary state, where the experimental set-up is stable and the reflectivity of the mirrors does not change any more. By properly choosing the exact moments where τ is measured in the on- and the off-period, respectively, absorption differences can be measured within the residence time of the reactor. In addition, by scanning the time at which the light pulse arrives over the on- and off-period of the pulsed plasma, the time evolution of the plasma particles can be studied.

The right panel of Fig. 3 shows a measurement in a 10 Hz pulsed plasma (0.71 sccm H_2-flow, 15 Pa, 100 W RF power, 50% duty cycle), where for every wavelength value both the ring-down time during the on-period (solid circles) as well as during the off-period (open squares) is measured. From the measurement both a narrowband and a broadband absorption can be seen. The narrowband absorption is again due to H(n=2). The broadband absorption of 3.5×10^{-6} per pass, that is derived from the baseline difference of the 'plasma on' and the 'plasma off' spectrum, corresponds to a H^- density of 10^{16} m^{-3}, which is in agreement with the expected negative ion density in this type of plasma.

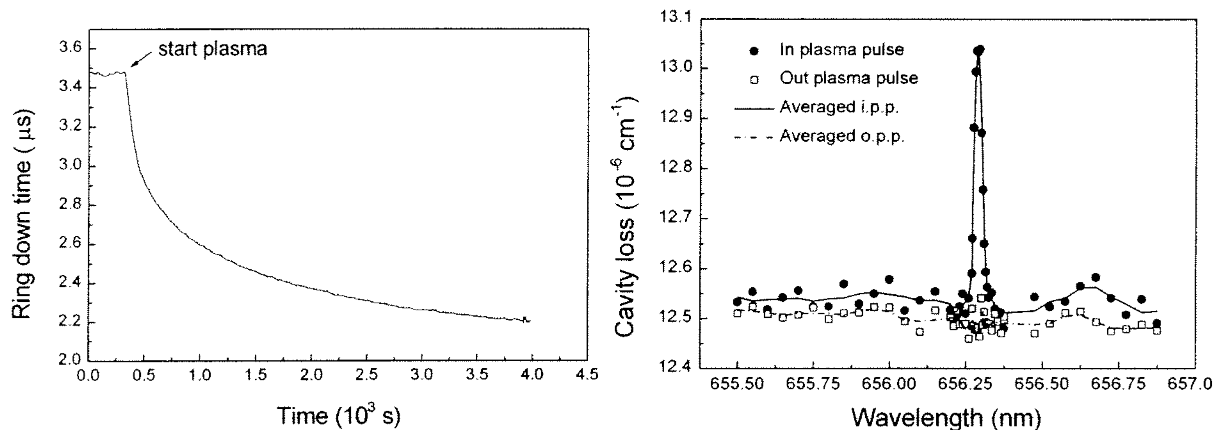

Fig. 3. *Left panel: Evolution in time of the ring down time under the influence of a hydrogen containing plasma. Right panel: Cavity loss spectrum of a 10 Hz pulsed capacitively coupled RF plasma in H_2, measured both in the 'plasma on' period (solid circles) and in the 'plasma off' period (open squares). The solid and dashed lines give the 3 point running averages of the 'plasma on' and 'plasma off' data points, respectively.*

Discussion and outlook

The CRD technique combines all advantages of direct optical absorption measurement techniques with a high sensitivity. It therefore has a high potential for application in hostile environments as for instance encountered in plasma and in combustion research. The two presented experiments that demonstrate this applicability, give both an example of a narrowband (H(n=2)) and of a broadband absorption (H^-). The detection limit for H(n=2) in our set-up is 10^{12} m^{-3}, while that for H^- is 3×10^{15} m^{-3}, the difference being completely accounted for by the difference in absorption cross section. The measurement of a broadband absorption, however, puts extra requirements on the experimental procedures. To prove unambiguously that the broadband absorption in Fig.3 for instance is caused by negative ions, at least the following conditions should be met. First of all, a spectral scan should be recorded to show the broadband nature of the absorption and to exclude spectral coincidences with other absorptions. Even then, the absolute value of the absorption can only be determined by comparing the 'plasma on' case with the 'plasma off' case. For this a pulsed plasma should be used to enable to reach a quasi-stationary state, where the experimental set-up is stable and the reflectivity of the mirrors does not change. In addition it should be shown that the absorption depends on experimental parameters (e.g. pressure, flow, and wall material) as expected, and that the absorption is absent in for instance an Ar plasma. Experiments are currently being performed to fulfill this last requirement.

Acknowledgement

This work is financially supported by the STW, FOM Rolling Grant, and NOVEM. The authors would like to thank Dr. G.M.W. Kroesen and coworkers at the Eindhoven University of Technology for using their parallel plate RF reactor, and H.M.M. de Jong, M.J.F. van de Sande and A.B.M. Hüsken for their skillful technical assistance.

References

[1] A full account of the CRD literature will not be given here. For further reading about CRD one is referred to: *Cavity Ring Down Spectroscopy - a new technique for trace absorption measurements*, eds. K.W. Busch and M.A. Busch, American Chemical Society, Washington (1998).
[2] A. O'Keefe and D.A.G. Deacon, Rev. Sci. Instrum. **59**, 2544 (1988).
[3] E. Quandt, H.F. Döbele, and W.G. Graham, Appl. Phys. Lett. **72**, 2394 (1998).
[4] E. Quandt, I. Kraemer, and H.F. Döbele, Europhysics Lett., accepted.
[5] M.C.M. v.d. Sanden, R.J. Severens, J.W.A.M. Gielen, R.M.J. Paffen, and D.C. Schram, Plasma Sources Sci. Technol. **5** (1996), 268.
[6] S.J. Smith and D.S. Burch, Phys. Rev. **116**, 1125 (1959).

Absolute Concentrations of Reactive Species in Etching Plasmas by High-Sensitivity UV Absorption Spectroscopy

J.P.Booth, D.Romanini, A.Katchanov, L.Biennier and G.Cunge
Laboratoire de Spectrométrie Physique, Université Joseph Fourier-Grenoble, France

Introduction

Many of the reactive species of interest in etching plasmas (for example, CF_x radicals and SiF_x etch products in fluorocarbon plasmas) absorb light in the UV spectral region (200 – 300 nm). Measurement of these weak absorbances (10^{-2} – 10^{-4} for a single pass) allows their absolute concentration to be determined. Low-resolution spectra have recently been obtained by broad-band absorption spectroscopy, using a Xe arc lamp as the light source and a small monochromator equipped with a CCD or diode array detector(1). With relatively long integration times excellent sensitivity can be achieved. The recently developed Cavity Ring-Down Spectroscopy (CRDS) technique has much higher spectral resolution, and (potentially) higher sensitivity. In this technique, the pulsed tunable output of an excimer pumped doubled dye laser is injected into a high-Q optical cavity in which the plasma is included. The absorbance as a function of wavelength is then deduced from the lifetime of the light pulse in the cavity. This technique offers the possibility of real-time (1 second) absolute concentration measurements. Initial results have been obtained for the detection of CF and CF_2 radicals in capacitively-coupled radio-frequency plasmas in fluorocarbon gases.

Broad-band UV absorption spectroscopy

The time-honoured technique of broad-band UV absorption spectroscopy offers the possibility of detecting many reactive species in plasmas using rather simple equipment, but in the past has lacked the necessary sensitivity top be of use in low pressure plasma systems. This has changed due to the current availability of sensitive multi-channel detectors, which allow the effect of lamp intensity fluctuations to be minimised, so that fractional absorptions in the range 10^{-3} or less can be readily observed(1,2). Whereas the spectral resolution cannot match that of tuneable lasers, it has the advantage that the whole absorption band is recorded simultaneously. Not only does this eliminate temperature sensitivity from the density measurement, but it also allows the determination of vibrational and rotational temperatures without the drift problems associated with long laser wavelength scans.

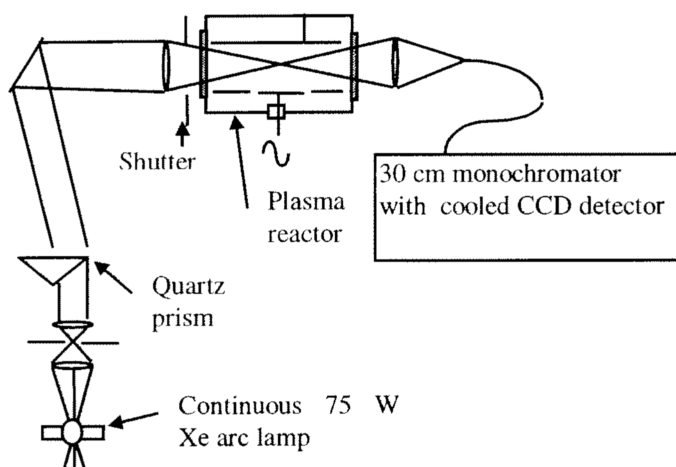

Figure 1. *Experimental setup for the broad-band UV absorption experiment*

The experimental equipment is shown schematically in Fig. 1. The plasma reactor is of conventional capacitively-coupled radio-frequency type. Light from a Xe arc lamp is spectrally filtered with a crude monochromator arrangement (to eliminate the intense unwanted visible light) and passed once through the reactor. The transmitted light is focussed into an optical fibre and

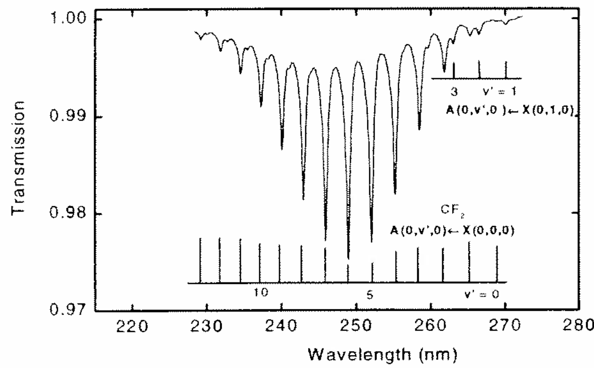

Figure 2. *Transmission spectrum of a 100 mT 100 W C_2F_6 plasma, showing the A-X transition of the CF_2 molecule.*

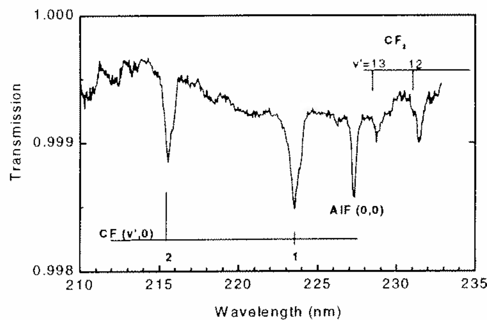

Figure 3. *Transmission spectrum of a 200 mT CF_4 plasma, showing transitions of CF_2, CF and AlF radicals sputtered from the reactor walls.*

transmitted to a small monochromator equipped with a cooled CCD detector. Spectra are taken sequentially with and without plasma, (and also with the shutter open or closed, to allow for plasma emission and background noise), and integrated for up to 40 minutes. An example of the transmission spectra obtained is shown in Fig. 2. This shows the relatively strong absorption due to the A-X transition of the CF_2 molecule. From the absorbed intensity, the optical path length and the published value of the absorption cross-section (3) the absolute concentration can be estimated to be $4x10^{13}$ cm^{-3}. Another example is shown in Fig. 3, which shows the (somewhat weaker) absorbances due to CF and AlF radicals in the same reactor (but with CF_4 feedstock gas). Further radicals that can can be detected by this technique include SiF_2 etch products, and S_2 dimers.

Cavity Ring-down Spectroscopy

In the novel technique of Laser cavity ring-down spectroscopy (4), a narrow-band tunable laser beam is injected into a high-Q optical cavity, consisting of high reflectivity spherical mirrors, and containing the plasma (or other sample to be analysed).

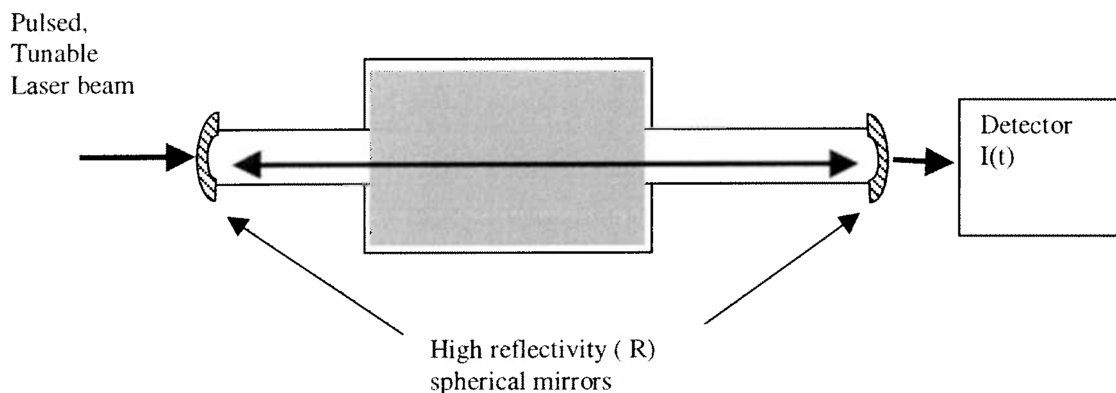

Figure 4. *Principle of Laser Cavity ring Down Spectroscopy of plasmas*

The injected fraction of the intense laser pulse remains trapped inside the cavity and then decays exponentially in time due to cavity losses, including mirror transmission, T. This corresponds to light re-transmitted outside the cavity at each round trip, which is detected and allows to measure the photon lifetime in the cavity. This "ringdown time" τ is monitored while the laser wavelength is tuned across each absorption line of the sample. Considering the surface and diffraction losses L of the mirrors and the absorption coefficient of the sample, α, the decay rate of the trapped photons is

$$1/\tau = (T+L+\alpha l)/(l/c) = 1/\tau_0 + c\alpha, \qquad (1)$$

where c is the speed of light and l the cavity length. $1/\tau_0$ is a broadband smooth baseline which can be easily distinguished from the rapidly varying spectral features of the sample. Thus the sample absorption α is obtained directly in units of 1/cm. An equivalent absorption path-length may be defined as the interaction time τ of the trapped photons with the sample: $l_{eq}=c\tau$. Recently the technique has been extended to CW lasers (5), allowing extremely weak absorbances to be observed in the visible region of the spectrum. However, for the electronic transitions of interest here, the necessary wavelength is in the UV region, and only pulsed dye lasers with frequency doubling are available. Furthermore, the mirrors available in this region have relatively poor reflectivities (99.5%, compared to 99.98% or better in the visible region.).

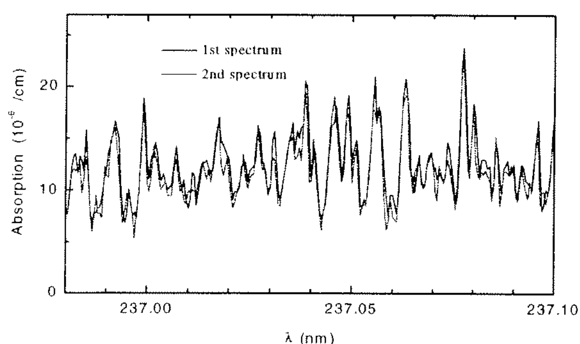

Figure 5 *Cavity ring Down Spectrum of a part of the CF_2 A(0,10,0) ← X(0,0,0) spectrum, in a C_2F_6 plasma.*

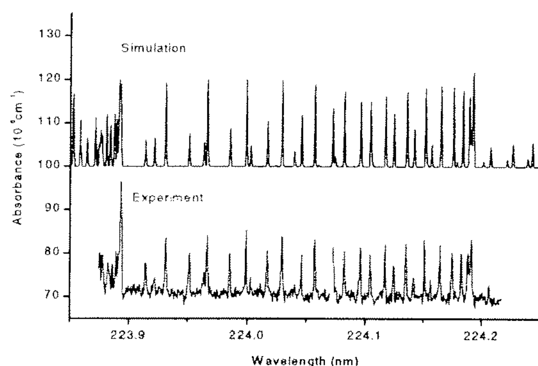

Figure 6. *CRDS spectrum of the CF A-X (1,0) band in a CF_4 plasma. Also shown is a simulated spectrum.*

The first CRDS spectrum we obtained in a plasma is shown in Fig. 5. This shows a small part of the CF_2 A(0,10,0) ← X(0,0,0) spectrum. This rather weak band (see Fig. 2) was chosen simply because of the availability of mirrors for this spectral region. The ragged appearance of this spectrum is not noise (as it would appear), but is the reproducible complex rotational structure of this transition. Unfortunately, the rotational constants for the CF_2 A-state are not known for $\nu_2'' > 5$, so this structure has not been analysed. Fig. 6 shows a CRDS spectrum of the CF A-X (1,0) band. This band is much "cleaner" than the (0,0) band (which we also observed), as it does not suffer from background absorption due to the last (weak) bands of CF_2 (see Fig. 3). These spectra were taken with signal averaging over 10 laser shots, which leads to an equivalent noise of about 10^{-4} per passage through the plasma, or an uncertainty of 2% in the determination of the ring-down time, τ. Current work is in progress to reduce this noise, and therefore improve the ultimate sensitivity of the technique.

Comparison of the two techniques

The two UV absorption techniques both have their advantages, and are complementary for plasma diagnostics applications. The broad-band technique has the obvious advantage of using relatively simple (and inexpensive) equipment, and is relatively easy to align compared to the laser technique. The whole spectrum is recorded simultaneously, eliminating drift problems, and making it attractive for gas rotational and vibrational temperature measurements. However, the broad-band technique requires relatively long signal integration times (10's of minutes) compared to CRDS, which offers the possibility of real-time (second time-scale) absolute concentration measurements during wafer processing. The sensitivity of the two techniques is comparable (single-pass absorbances of about 10^{-3} can be observed with a signal-to-noise ratio of 10 to 1), although the higher spectral resolution of CRDS may allow lower concentrations to be detected in some circumstances. The detectivity is expected to improve for both techniques. For broad-band absorption, use of a newer CCD camera with greatly improved read-out rate and dynamic range should dramatically improve the sensitivity/integration time trade-off. Improved analysis of the CDRS decay signal (which in practice is not single exponential, due to cavity mode effects) should also lead to improvements.

References

(1) J. P. Booth, G. Cunge, F. Neuilly, and N. Sadeghi, Plasma Sources, Sci. Technol. **7,** 423 (1998).

(2) M. A. Childs, K. L. Menningen, P. Chevako, N. W. Spellmeyer, L. W. Anderson, and J. E. Lawler, Phys. Lett. **A171,** 87 (1992).

(3) S. Sharpe, B. Hartnett, H. S. Sethi, and D. S. Sethi, J. Photochem. **38,** 1 (1987).

(4) D. Romanini and K. K. Lehmann, J. Chem. Phys. **99,** 6287 (1993).

(5) A. Campargue, D. Romanini, and N. Sadeghi, J. Phys. D **31,** 1168 (1998).

PHOTO–DETACHMENT TECHNIQUE APPLIED TO HIGH–FREQUENCY PRODUCED PLASMAS

F M Dias and E Tatarova

Centro de Física dos Plasmas, Instituto Superior Técnico, 1049-001 Lisboa, Portugal

1. Introduction

Laser photo-detachment is a widely used technique for the measurement of the number density of negative ions. Yet, the application of this technique to plasmas produced by HF fields presents some difficulties, partly unresolved so far, concerning the measurement of the photo-detachment signal because: i) the spectral content of this signal is very close to frequency of the sustaining field; ii) all probe measurements must always be carried out using high-frequency compensation; iii) the probe must only be biased positively during the time required to perform the measurements in order to prevent a rise in temperature up to electron-emission conditions; iv) the probe sheath impedance must be measured simultaneously since it belongs to the measuring circuit. We present H^- density measurements in a surface wave (SW) sustained discharge using a photo-detachment system which was developed in order to circumvent the above problems.

2. The Measuring System

We stand by the principle, fully justified by our previous experience, that any measurements involving an electrical probe must be carried out with probe compensation for all the actually present potential fluctuations. Yet, as shown below, to do so while using the photo-detachment technique in a HF sustained discharge is complicated and introduces some limitations.

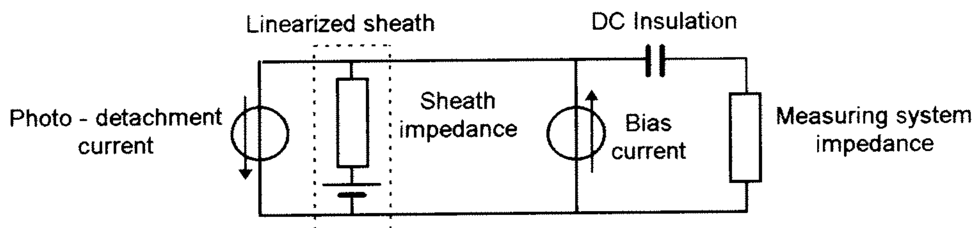

Figure 1. *Ideal basic photo-detachment arrangement.*

The standard photo-detachment arrangement, as depicted in Figure 1, shows that the photo-detachment current will flow not only in the measuring system but also through the sheath impedance of the probe. The relative importance of the latter depends, of course, on the relative value of the impedances but, although usually forgotten in previous works, its value can often be non-negligible. Note that, due to the unsteady phenomena produced by the laser pulse, the sheath impedance is actually time-dependent and its exact evaluation is time-consuming. Due to this limitation we currently measure the steady-state impedance only.
In addition, the value of the probe bias, referred to the plasma potential, is required in order to relate accurately the measured quantities with the actual negative ion density.

So, as simultaneously as possible with the measurement of the photo-detachment current, we trace the probe I-V characteristic in a region at least extending from the point at which the probe is biased for the photo-detachment measurements (above the plasma potential) until well below the plasma potential, so that we may get an idea of the electron mean energy.
The main part of the spectral content of the photo-detachment signal lays above a few MHz, which makes its detection in HF discharges virtually impossible using standard experimental arrangements. To overcome this problem in the 13.56 MHz range may require using active techniques, but above 100 MHz we suggest the use of high-Q passive filters. Currently we work in a 500 MHz SW sustained discharge so the latter is the most convenient solution for our case.
The filtering is threefold because it must simultaneously: i) prevent the microwave signal from disturbing the measuring system; ii) uncouple the input impedance of the measuring system from the probe HF compensation, since this is achieved in our case by passive devices only [1]; iii) uncouple the reactive compensating impedance from loading the measuring line. To this end, we use a two-section, quarter-wavelength ($\lambda/4$) coaxial lines (see Figure 2), the last ending in open-circuit. In this way, we ensure a short-circuit at $\lambda/4$ from the end of the line, precisely where the connection to the measuring system is made (zero electric field), and a virtual open-circuit (zero current) will be present at the input of this line to which the compensation circuit is connected. In addition, a *resonant capacitor* tuned at the SW frequency enables an undisturbed operation of the probe compensation circuit (see Figure 2) and simultaneously avoids the loading of the measuring line.

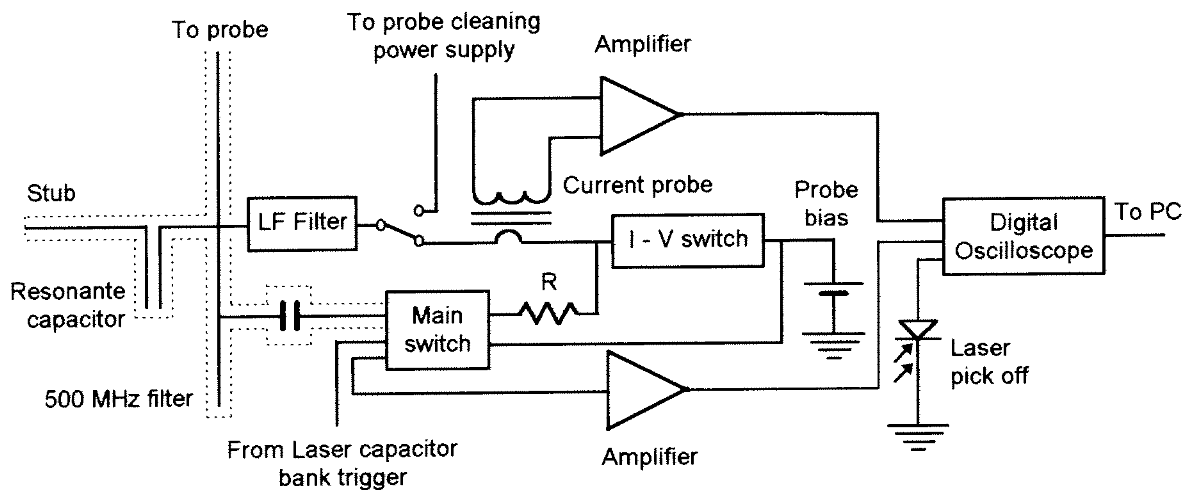

Figure 2. *Block diagram of the measuring system.*

The presence of the stub, used to achieve the HF compensation of the probe, produces a notch filtering of the signal we want to measure. The notch frequencies occur roughly when the electrical length between the *resonant capacitor* and the short-circuit of the stub equals an odd multiple of $\lambda/4$. If the stub could be connected directly to the capacitor, the lowest of the above frequencies would be higher than half of the SW frequency but we have to use an interconnecting cable which brings the lowest notch frequency to above 75 MHz. Anyway, the -3 dB band-rejection is $\approx$ 0.4 MHz only, which means that there is no noticeable distortion on the measured signals (the whole measuring system has a useful bandwidth up to 200 MHz).
High density, high temperature plasmas present an extra problem to the use of probes: probe heating. As a result, our probe becomes hot enough for thermoionic emission when biased in steady-state close to the plasma potential in a hydrogen plasma sustained by a 500 MHz SW.

For the time being, we preferred to keep the probe cool in order to avoid the extra burden that otherwise should be added to the theoretical formulation.
Keeping the probe cool, in a photo-detachment technique, implies switching on the bias voltage during only a short time centred around the arrival of the laser pulse. Yet, switching voltages up to 60 V at the entrance of a measuring device with a sensivity of about 10^{-7} of that value is definitely not the wiser choice! This means the detection circuitry can be switched to the measuring line only when the transients have vanished. We actually use separated devices to measure the low and the high-frequency content of the signal. We solved the problem with a diode gate, biased ON with 5 mA, which enables a dynamic range of about 5×10^4 for the high-frequency measuring system (5 kHz – 100 MHz). The low-frequency measuring system (30 Hz – 20 MHz) is intended to measure the steady-state bias current and does not need to have its input gated.
The timing of the above switching systems is the following: i) the probe is biased when the capacitor bank of the laser is fired ($t = 0$); ii) the diode gate is opened 50 μs later; iii) the laser is *Q-switched* at $100 < t < 180$ μs; iv) the diode gate is closed at $t = 250$ μs; v) the probe is grounded at about $t = 300$ μs.
As we already mentioned, we need to trace a I-V probe characteristic in the neighbourhood of the plasma potential. To do so, we added a self-triggered switching system which senses the falling edge of the probe voltage at $t = 300$ μs and then bias again the probe, but this time through a capacitor. In this way we produce a near-exponential voltage pulse to sweep the probe characteristic. The time sequence is completed by the switching of another device that discharges the above capacitor 1 ms later.
In this way we achieved our goal of biasing, measuring, and tracing the probe characteristic fast enough so that the probe remains cool (≈1% duty-cycle).
The circuitry includes a low-pass filter, using our standard distributed-coil, 4th-order topology [2], and a resistor (R in figure 2) intended to improve the LF response of the high-frequency measuring system. Nevertheless, a system of 5th-order integro-differential equations needs to be solved and the low frequency measured current needs to be deconvoluted in order to evaluate the photo-detachment current and the probe characteristics.
Though a low frequency compensation of the probe is possible in the above described system, we only foresee practical solutions that imply some bandwidth reduction. Since our plasma proved to be stable (no striations), only the microwave generator can be a main source of low frequency noise. Indeed the EPSCO EP250C is extremely noisy: highly insufficient mains filtering and ultra-spiking, switching HV power supply. We chose to filter the generator instead of daring to reduce the bandwidth. To do so, we added a second-order 35 kHz passive filter to the generator's HV line, we increased AC feedback of its power supply in order to bring the ripple down to below 5 V and then we added an active AC filtering to the HV line. In this way, the presence of a remaining 50 Hz noise can be detected in the probe when it is located at the end of the plasma column only.
The response of the measuring system to a fast pulse produced by a charged line and a coaxial, mercury-wetted relay pulse generator was recorded, thus enabling us to deconvolute the measured signals whenever the rise-time gets close to 5 ns.

3. Experimental Results

We are currently using the following detection equipment: A Tektronics TDS220 digital real-time oscilloscope stores the photo-detachment signal; channel 1 receives the high-frequency part which is pre-amplified by a Stanford Research Systems SR445 amplifier; channel 2

receives the low-frequency part which is detected and amplified by a Tektronic P6021 AC current probe and a 7A14 current probe amplifier; the trigger is fed by a Thorlabs DET2-SI high-speed silicon detector which receives a sample of the laser beam at the rear of one of the mirrors on the optical path.
We used the same probe, probe arrangement and discharge tube as in Ref. 1. The laser is a Continuum Surelite I (532 nm) operating at 10 Hz repetition rate, and it illuminates the probe axially, *i.e.*, radially to the discharge tube.

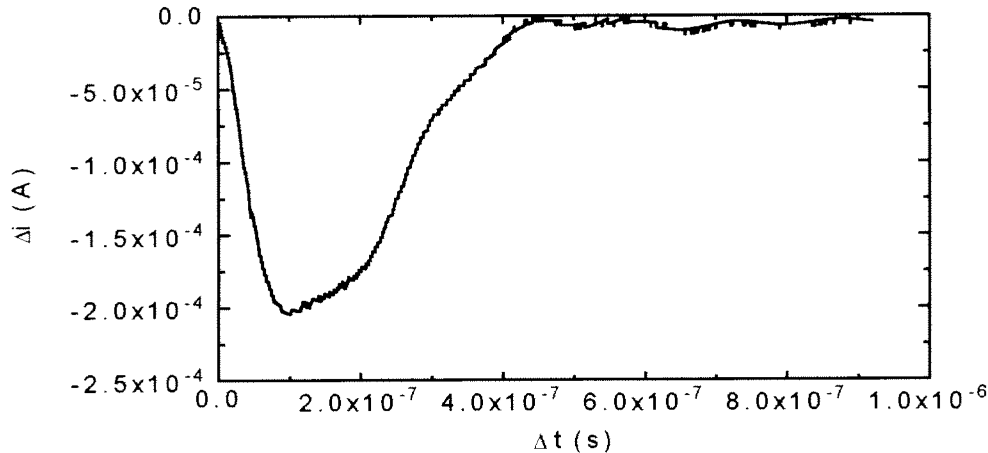

Figure 3. *Probe current variation following the arrival of the laser pulse.*

In figure 3 we show a typical probe current variation following the arrival of the laser pulse (at $t = 0$ in the figure) evaluated from the signal detected by the high-frequency measuring system. The experimental conditions were: flowing hydrogen at 0.2 Torr, 24 mJ laser energy, probe biased 4 V above the plasma potential, 1.88 mA steady-state probe current, 6 cm from the plasma end (8.7×10^{15} m^{-3} electron density).
A simple glance at the above relative probe current variation reveals that a considerable H^- concentration is present in plasmas produced by surface waves. In order to determine accurately the H^- density the peculiarities of the photo-detachment method, namely, the potential well around the illuminated probe and the non-maxwellian energy distribution of the detached electrons, should be taken into account. Detailed results will be presented elsewhere.

Acknowledgments: The authors wish to express their appreciation to Helder Crespo for making available to us a fully operational Nd:YAG laser.

References

[1] F. M. Dias, E. Tatarova, and C. M. Ferreira 1998 *J. Appl. Phys.* **83** 4602-4609
[2] F. M. Dias 1995 *Plasma Sources Sci. Technol.* **4** 86-93

Time-resolved absorption and emission measurements of rotational temperatures and concentrations of C_2 and CH in a H_2/CH_4 microwave pulsed plasma.

Xavier Duten[0], Antoine Rousseau *, Alix Gicquel[0], Philippe Leprince *.

[0]*Laboratoire d'Ingéniérie des Matériaux et des Hautes Pressions*
CNRS - Université Paris 13
Avenue J.-B. Clément
F 93430 Villetaneuse - France.

**Laboratoire de Physique des Gaz et des Plasmas,*
Université Paris Sud
CNRS, Bât 210, UPS
F 91405 Orsay - France.

Abstract

The results of spectroscopic studies of absorption and emission rotational temperatures and concentrations of the radicals C_2 (Swan Band: (0,0) at 516,5 nm) and CH ((0,0) at 431 nm) as present in a pulsed H_2/CH_4 microwave plasma used for diamond deposition, are presented. The absolute concentrations of C_2 in the $a^3\Pi_u$ state and CH in the $X^2\Pi$ state, measured during the pulse and the post-discharge as a function of pressure and microwave power, are compared with optical emission spectroscopy of excited states of C_2 ($d^3\Pi_g$ state) and CH ($A^2\Delta$ state). The rotational temperature of excited state of C_2 is found to be higher than the ground state's one (equal to the gas temperature), indicating that excitation of C_2 is the result of chemical reactions rather than of inelastic non-reactive collisions, i.e. is chemiluminescent to a large extent, whereas CH ground and excited states rotational temperatures are close to the gas temperature.

Introduction

Microwave plasmas are very efficient sources of active species (radicals, excited neutrals, ions) and their applications increase continuously (thin film deposition and etching, polymer treatments, environmental applications). In the case of diamond deposition, H, CH_3 and C_2H_2 concentrations and spatial distributions at the surface and in the plasma are crucial for optimizing the whole process, and appear to be key parameters for diamond deposition, together with the plasma temperature, the substrate temperature, the crystallographic orientation and other surface characteristics [1,2,3]. Based on a $H_2 + CH_4$ 1D plasma model developed in the Laboratoire d'Ingéniérie des Matériaux et des Hautes Pressions, we establish relationships between CH_3 and CH mole fractions, and C_2H_2 and C_2 ones respectively. As no experimental detection facilities of CH_3 and C_2H_2 (i.e. IR or UV absorption techniques) were still available in our laboratory, we suggest to use CH and C_2 as "tracers" for CH_3 and C_2H_2 respectively. As a matter of fact, these latter are detectable by OES and may be interesting species for analyzing and monitoring the plasma. Probing C_2 and CH species in their ground electronic states requires the use of techniques based on laser-induced fluorescence or absorption techniques. Owning to the fact that laser induced fluorescence technique is not suitable to determine absolute densities, absorption techniques are necessary for such measurements. Although optical emission spectroscopy (OES) provides

measurements of species only in electronic excited states, the simplicity of OES makes it a popular plasma diagnostic as well in the research laboratories as in industry. We propose here a study which aims to correlate C_2 and CH ground state concentrations with emission intensities ratios $I_{C2*(0,0)}/I_{Ar}$ and $I_{CH(0,0)}/I_{Ar}$ measured by OES, while changing the coupled action of the total pressure (from 10 to 70 mbar) and microwave power.

The determination of the temperature of the neutrals, very important for the understanding of the energy deposition in the plasma, is made difficult by the fact that the plasma is not in thermodynamic equilibrium. The simultaneous determination by optical emission spectroscopy, of kinetic, rotational and vibrational temperatures gives helpful informations about complex plasma processes. In principle, the gas (kinetic) temperature can be determined, by optical spectroscopy by considering the Doppler broadening of the spectral lines. However, the Doppler broadening related to typical gas temperature in low pressure plasmas is often very weak, so that numerous work have reported the possibility of considering the rotational temperature as the gas temperature. In a previous work devoted to a low pressure (1 mbar) plasma set in a small diameter tube comparison between H_2 rotational and translational temperature of both H_2 and H was reported in a pure hydrogen plasma[4] showing that the rotational distribution of hydrogen is not in equilibrium with the gas temperature in this pressure range.

Experiment

In this study the plasma is activated by a 915 Mhz microwave generator (pulsed or continuous mode) in a 5 cm large diameter tube. The microwave radiation initiate a discharge in the centre of the tube. Adjustment of a tunable backshort in the waveguide optimizes the power coupling. The plasma is composed by a mixture of CH_4 (0-6%), Ar (3% - actinometer) and H_2. The pressure ranges from 5 to 80 mbar, the microwave power from 3 to 30 kW and the gas velocity does from 0 to 40 ms^{-1} (at 300K). The power density, ratio of the power to the volume of the plasma, extends from a few W/cm^3 up to 70 W/cm^3 (70 mbar - 30 kW). In pulsed mode, the duty cycle ranges from 10 to 90%.

After being evacuated down to the order of 10^{-3} Torr by a roots pump, the system is isolated from the latter, and the gas mixture is introduced up to the desired pressure, 10 to 70 mbar. During the experiment, gas is recycled into a loop; its velocity is controlled by a pump.

White light absorption spectroscopy is performed with an OSRAM high pressure ultra-stable Xenon arc lamp as a continuum source. The light from the lamp is focused at the center of the plasma and re-imaged onto the entrance slit of a Jobin-Yvon HR1000 spectrometer coupled with a EG&G CCD detector. The resolving power of the system, in first order at 5000 Å, is about 0,3 Å, which is enough to resolve rotational structure of emission and absorption spectra, and obtain enough intensity in order to increase the signal/noise ratio. Absorption path length varies from 5 to 2.5 cm as the pressure ranges from 10 to 70 mbar.

Experimental results

Rotational temperatures of C_2 ground and excited states are determined by the Bolzmann plot method applied to the P1(40) -> P1(47) lines [5]. The P1(31) line was selected for measurements of C_2 concentration in the plasma [6]. Both emission and absorption rotational spectra of C_2(0,0) Swan Band at 516.5 nm are shown in figure 1.

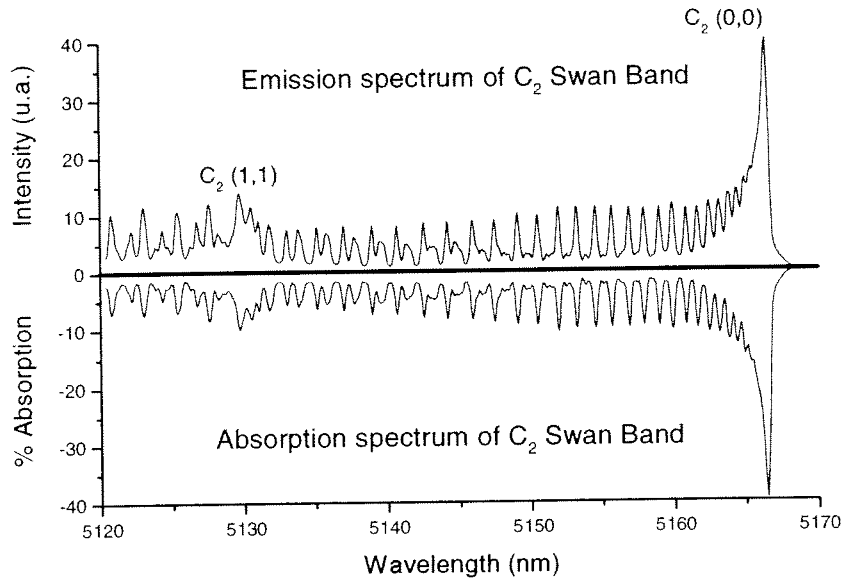

Figure 1: *Emission and absorption spectra of $C_2(0,0)$ Swan Band.*

1> H_2 / CH_4 continuous plasma.

Rotational temperatures and concentrations of C_2 in a continuous plasma are presented (figure 2) as a function of microwave power. The total pressure is set at 40 mbar (H_2 + 3% CH_4).

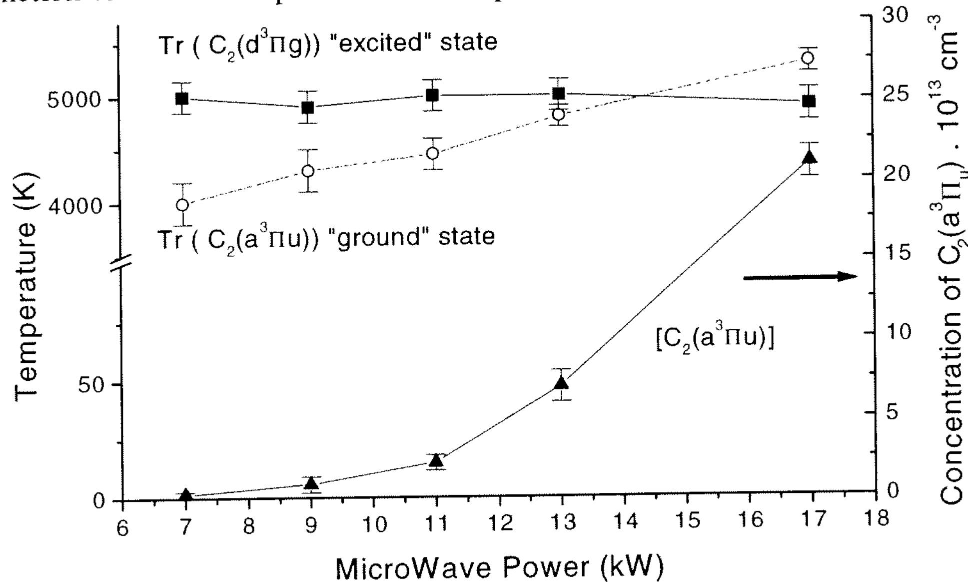

Figure 2:. *Rotational temperatures and concentrations of C_2* as a function of Microwave Power (kW).

We clearly show that rotational temperature of ground and excited states are different, whatever the power. The excited state rotational temperature is not sensitive to the microwave power, whereas the ground state ones (equal to the gas temperature) increases linearly with the power. The evolution of the concentration of C_2 with the power is quadratic (the color of the plasma changes from pink (P = 7kW) to green (P> 13 kW)), indicating a high mole fraction value of C_2 at high power).

2> H_2/ CH_4 Pulsed/ Plasma

We present here "time-resolved" measurements of rotational temperatures and concentrations of C_2 in the H_2/CH_4 pulsed plasma. The microwave power is 15kW during the pulse; the duty

cycle is set to 50%. The frequency of the pulse is 8.5 Hz (Pulse time = 56 ms) The total pressure is equal to 50 mbar (H_2 + 3% CH_4).

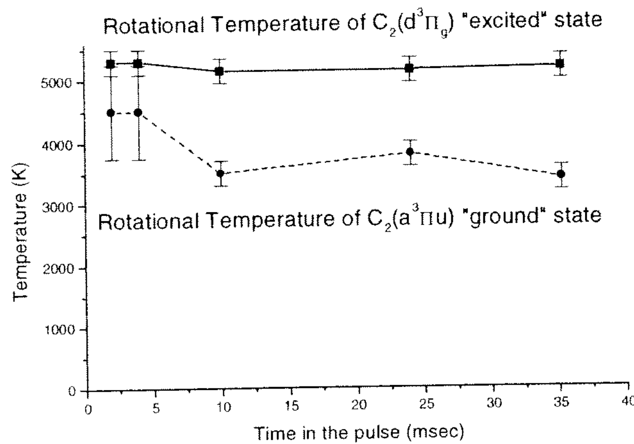

Figure 3: *Rotational temperatures of excited and ground states of C_2 Swan Band.*

Variations of rotational temperature of ground and excited states are ploted figure 3 as a function of the time in the pulse. Rotational temperature of excited state is 2000 K higher than ground state one, leading to a chemiluminescent formation of $C_2^*(d^3\Pi g)$, rather than thermal or electronic excitation. The rotational temperature of ground state (which is close to the gas temperature) is still high 2 msec after the beginning of the pulse. Both excited and ground states temperatures keep constant values during the pulse.

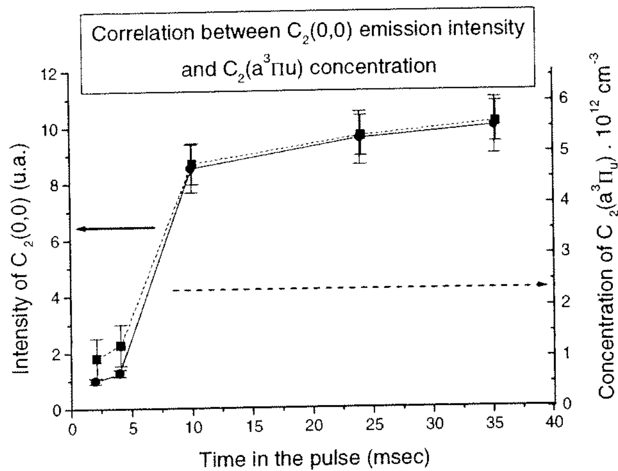

Figure 4: *Emission intensity of C_2(0,0) head band and C_2 ground state concentration as a function of the time in the pulse.*

We present here the concentration of C_2 $a^3\Pi u$ state (dash lines) and the emission intensity of the C_2(0,0) head band (solid line) as a function of the time in the pulse. Both emission intensity and concentration of ground state present the same behavior during the pulse, so that C_2(0,0) head band intensity looks to be a good "tracer" for the C_2 concentration. The C_2 concentration reaches a constant value 10 msec after the beginning of the pulse.

Conclusion

Good agreement was found between emission intensity of C_2(0,0) head band and C_2 ground state concentration. The rotational temperature of excited state is higher than ground state one (except for the continuous mode at 17 kW) , indicating that excitation of C_2 is mainly chemiluminescent. In the pulsed mode, heating of the gas is very short (<2msec), but C_2 concentrations reach a stationary value 10 msec after the beginning of the pulse.

References

[1] J. Harris and A. M. Weiner, *J. Appl. Phys.* **74,** 1022 (1993).
[2] E. A. Evans and J. Angus et al *Diamond and Related Materials* **5,** 200 (1996).
[3] D. G. Goodwin, *J. Appl. Phys.* **74** (11) 6895 (1993).
[4] P Chabert, A Rousseau, G Gousset, P Leprince ,*J. Appl. Phys*, 84, 161-167.(1998).
[5] R. Bleekrode, *Philips Research Reports Suppl*, **n°7** (1967).
[6] Q. Ngoc, M. VanPee, *Combustion and Flames*, **62,** 193-210 (1985).

Detection of atomic fluorine concentrations in discharges by two-photon absorption laser induced fluorescence spectroscopy (TALIF)

A.Francis, U.Czarnetzki, and H.F.Döbele
Institut für Laser- und Plasmaphysik, Universität GH Essen
Germany

Introduction

The detection of radicals like atomic fluorine in reactive plasma discharges is of great importance for the understanding of the chemical processes involved in discharge applications such as etching and plasma-enhanced chemical vapour deposition. In 1980 first measurements of the atomic fluorine concentrations in discharges by the actinometric technique were performed by Coburn and Chen [1]. Using this technique e. g. Booth and Sadeghi investigated the oxygen and fluorine atomic kinetics in ECR-plasmas [2]. The detection of atomic fluorine by resonantly enhanced multiphoton ionization (REMPI) was demonstrated in the following years [3]. For absolute concentration measurements the technique of vacuum ultraviolet absorption spectroscopy (VUVAS) [4] was developed. The detection of atomic fluorine in a flow tube system was also demonstrated by two-photon absorbed laser-induced fluorescence spectroscopy (TALIF) with excitation wavelengths in the VUV region [5].
In this project the quantitative measurement of atomic fluorine concentrations and of the spatial and temporal distributions is attempted by TALIF to investigate a fluorine containing capacitively coupled RF-discharge.

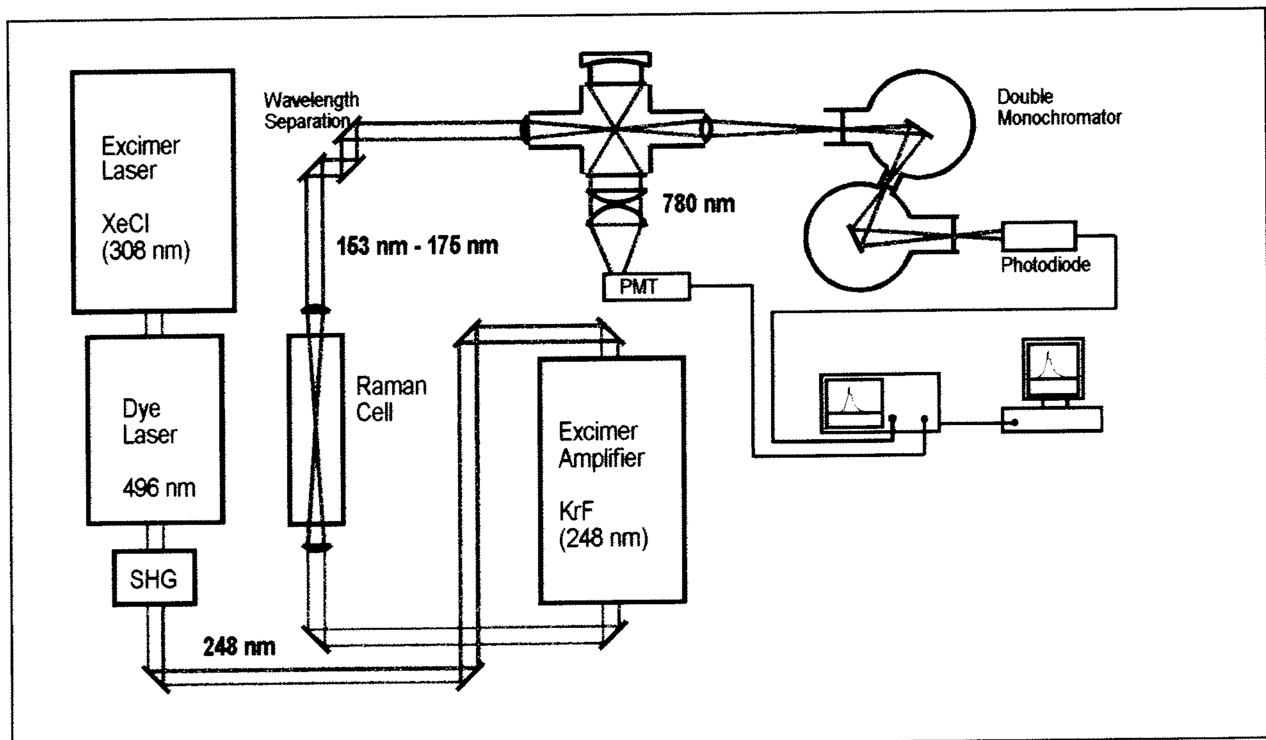

Figure 1: *Experimental Setup*

Experimental

TALIF has been applied to concentration measurements of several atomic species like H, O, N and Cl. Two photons of the radiation field of appropriate wavelengths excite the atom from its groundstate to an excited state. In the present application two different excitation schemes are considered: The first scheme uses two photons at $\lambda = 153$ nm. The fluorescence emission is then at $\lambda = 394$ nm. The second scheme takes advantage of two photons of different wavelengths: $\lambda_1 = 163$ nm and $\lambda_2 = 175$ nm. In this case the fluorescence is at $\lambda = 780$ nm.

The two schemes are compatible with VUV generation by stimulated Raman scattering in H_2 using radiation at $\lambda \approx 248$ nm. In the first scheme the radiation field corresponds to the 6th anti-Stokes order whereas the second scheme uses the radiation of the 4th and 5th anti-Stokes orders, [Fig.1]: An excimer laser pumped dye laser is doubled to deliver radiation at $\lambda = 248$ nm. This radiation is then amplified in a KrF excimer unit whereby up to 80 mJ [Fig.2] of narrow bandwidth output radiation is obtained [6]. The UV laser beam is focused into a H_2 filled Raman cell, whereby the active volume is cooled down to 77 K by liquid nitrogen [7]. The anti-Stokes orders contain energies in the µJ range.

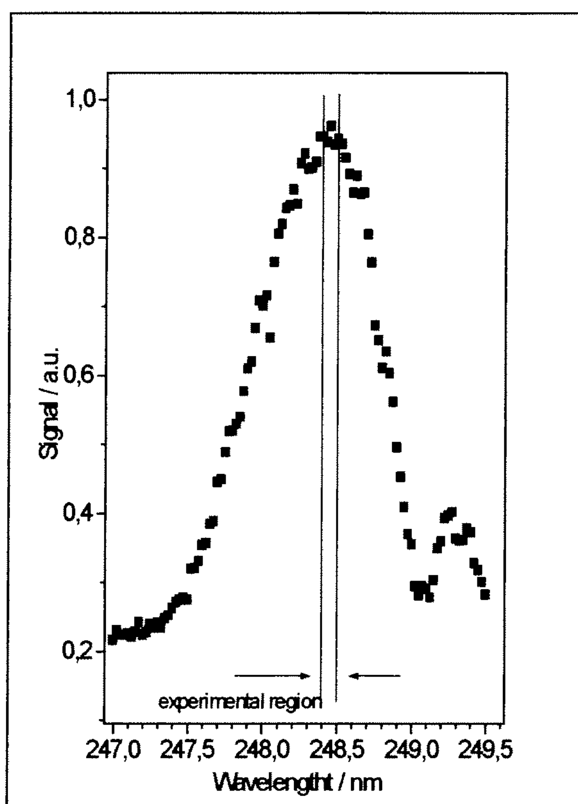

Figure2: *Tuning curve of KrF*

The anti-Stokes radiation fields are filtered out and reflected by a dielectric mirror system. A f = 11 cm lens focuses the beam into the center of the plasma chamber. A second lens is placed at the output to image the beam onto the entrance slit of a double monochromator equipped with a vacuum photodiode to monitor the energy of the excitation beam. The fluorescence light is imaged perpendicular to the laser beam by a f = 10 cm lens onto a photomultiplier.

In the first experimental phase the atomic fluorine is produced in a microwave flow tube reactor. This allows the absolute calibration of the fluorescence detection system by a titration method with chlorine [8].

The TALIF technique described will be applied later to the investigation of a capacitively coupled RF-discharge. Possible plasma gases will be CF_4 or SF_6.

References

[1] J.W.Coburn, M.Chen; J.Appl.Phys., **51**, 3134 (1980)

[2] J.P.Booth, N.Sadeghi, J.Appl.Phys., **70** (2), 611 (1991)

[3] W.K.Bischel, L.E.Jusinski, Chem.Phys.Lett., **120** (4,5), 337 (1985)

[4] K.Sasaki, et al., J.Appl.Phys., **82** (12), 5938 (1997)

[5] G.C.Herring, et al., Opt.Lett., **13** (5), (1988)

[6] H.F.Döbele., M.Hörl, M.Röwekamp, Appl.Phys.B, **42**, 67-72 (1987)

[7] M.Spaan, et al., Appl.Opt., **33**, 3865, (1994)

[8] D.W.Setser, ed.: M.A.A.Clyne, W.S.Nip in:"Reaction Intermediates in the Gas Phase, Generation and Monitoring", Academic Press, 1979

Investigation of Pulsed Reactive Microwave Plasmas by Time-resolved Laser-induced Fluorescence

A. Georg, Ch. Soll, St. Behle, A.Brockhaus, and J. Engemann
Forschungszentrum für Mikrostrukturtechnik-fmt, University of Wuppertal
Germany

Introduction

Pulsed low-pressure microwave and rf plasmas have found widespread interest in many topics of actual plasma research, since they have the potential to improve controlling of many plasma processes of industrial relevance. As reported by Samukawa et al. [1] pulsing of reactive plasmas shows a significant effect on the production of reactive species. Pulse frequency and duty ratio are used as additional control parameters. Nevertheless there remains a lack of knowledge about the mechanism responsible for the change in plasma-surface interaction if the plasma is pulsed. Most studies concentrated either on the investigation of basic plasma parameters like electron density and temperature without consideration of surface effects, or they are empirical studies based on the optimization of surface properties.
To get a deeper insight into the control mechanism of pulsed plasmas we assume that it is necessary to combine the diagnostic of plasma composition with the investigation of deposited films, seeking out for relationships. For this purpose we use two separated experimental set-ups of similar geometry and plasma generation. One was used as a deposition experiment to create SiO_2-films from $Ar:O_2$:HMDSO(hexamethyldisiloxane) gas-mixtures. The other one served as diagnostical facility for various techniques including time-resolved optical emission spectroscopy [2], time-resolved Langmuir probe and microwave interferometry measurements [3], and two-photon allowed laser-induced fluorescence (TALIF). This method is of great importance because it allows time-resolved measurements of atomic oxygen in the ground state ($2p^3P$) which cannot be performed by other common techniques like actinometry since dissociative excitation of oxygen has to be taken into account. Atomic oxygen itself is supposed to play an important role in the formation of precursors needed for the polymerization of HMDSO-fragments.
The present work describes the influence of pulse frequency and argon content on the density of atomic oxygen and demonstrates the effect on the surface morphology of deposited films.

Experimental set-up

The plasma is generated in a 2.45 GHz SLAN (slotted antennae) microwave plasma source, which has been described in detail elsewhere [4], powered by a 2 kW microwave generator. In pulsed operation the generator output power is modulated at a rectangular waveform with pulse frequencies in the range from 10 Hz to 10 kHz at a constant duty ratio of 50 %. This plasma source is connected to a cubic vacuum chamber of 30 cm side length as shown in Figure 1. Several quartz windows guarantee a good optical access. Feedstock gases used in this experiment are oxygen and mixtures of argon and oxygen at a total flow rate of 50 sccm. Best results are obtained for pressures about 50 Pa, where the quenching rates are considerably low.
Our laser system consists of a Nd:YAG laser with a repetition rate of 10 Hz which is frequency tripled to 355 nm. This laser pumps a tunable dye laser operated with Coumarin 47 to produce radiation at 452 nm. Because of a Littrow configuration the laser bandwidth reaches 0.08 cm^{-1}. The radiation at 452 nm is frequency doubled by a BBO-crystal and the

resulting radiation at 226 nm is focussed 25 cm downstream of the plasma source by a quartz lens of 30 cm focal length.

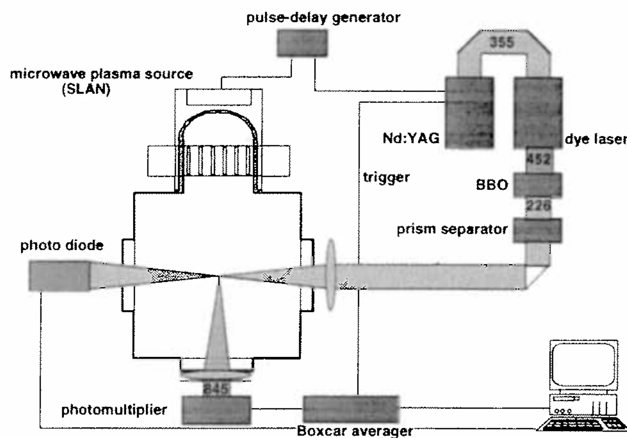

Figure 1: *Schematical drawing of the experimental set-up*

In a two photon absorption process ($2p^3P \rightarrow 3p^3P$) atomic oxygen is excited and relaxes down to the $3s^3S^0$ state by emission of radiation at 845 nm. The fluorescence radiation was detected perpendicularly to the incident laser beam by a fast photomultiplier restricted to 845 nm by an interference filter. Signals are integrated over 400 laser shots by a digitized oscilloscope to assure a sufficient signal to noise ratio. To avoide side effects like ASE, photodissociation and three-photon ionization we checked the signal dependency on the laser pulse energy. It has been proven to be quadratic up to 250 µJ, thus we restricted all experiments to energies of about 150 µJ. This allows the correction of the TALIF-signal to compensate power fluctuations of the dye laser. For this purpose the beam intensity transmitted through the vacuum chamber is monitored by a photodiode. The temporal position of the laser shots with respect to the discharge pulses is controlled by a programmable pulse-delay generator.

Results and discussion

As mentioned in the introduction we are interested in the influence of the pulse frequency on the temporal development of the atomic oxygen density in pulsed plasmas. Figure 2 shows typical measurements for two different pulse frequencies, which show that a significant

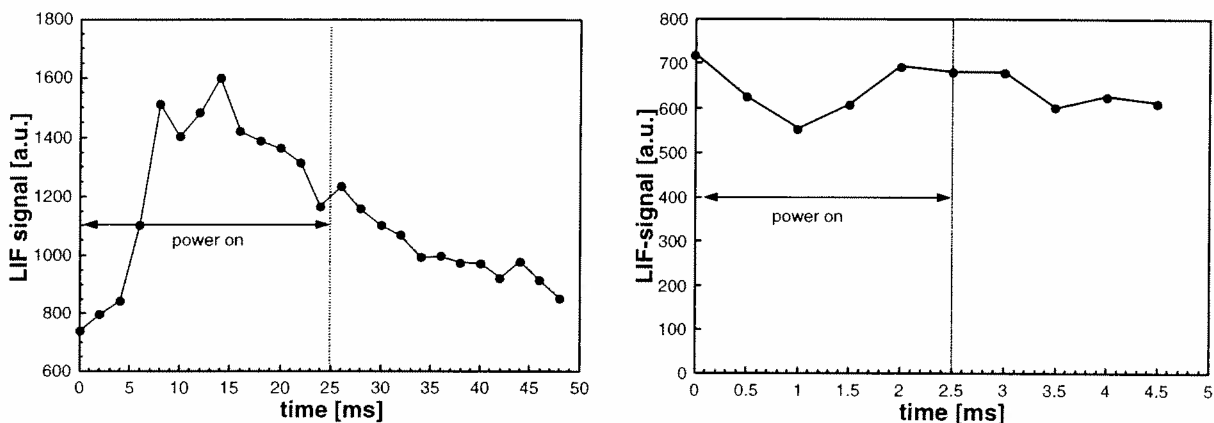

Figure 2: *Comparison of $N_O(t)$ for 20 Hz (left) and 200 Hz (right). The left diagram also shows the effect of correcting fluctuations of laser power*

variation during a pulse is only observed for frequencies below 200 Hz. It has to be pointed out that the rise time of about 13 ms is in good agreement with the rise time of the electron density measured by Langmuir probes [3]. The decay of atomic oxygen on the other hand is determined by diffusional transport of atomic oxygen to the walls, since other loss reactions can be neglected for the pressure range we investigated. In Figure 3 the temporally averaged atomic oxygen density as function of the pulse frequency is presented. A maximum density is

observed at a pulse frequency of about 50 Hz. This maximum coincides with a maximum of the temporally averaged electron density. This behaviour can be understood in terms of a global model of pulsed plasmas developed by Lieberman et al. [5]. Due to the different characteristic time scales of gain and loss reactions one gets an optimal pulse frequency for the temporally averaged density of electrons and other species. Because diffusion to the walls is the main loss for both electrons and atomic oxygen in our experiment, this optimum pulse frequency depends only on the geometry of the plasma volume. Absolute densities of atomic oxygen have not been measured yet, but earlier measurements in cw plasmas yielded a degree of dissociation in the range of a few percent [6]. All these measurements have been carried out in pure oxygen plasmas. To investigate the effect of argon onto the average density of atomic oxygen, argon is added to the feedstock gas up to amounts of 50 %. It can be easily seen from Figure 4 that a maximum atomic oxygen density is reached for admixtures of 30 % argon. The increase of the degree of dissociation is explained by the influence of Ar metastables which lead to a better energy transfer to molecular oxygen according to reaction (1)

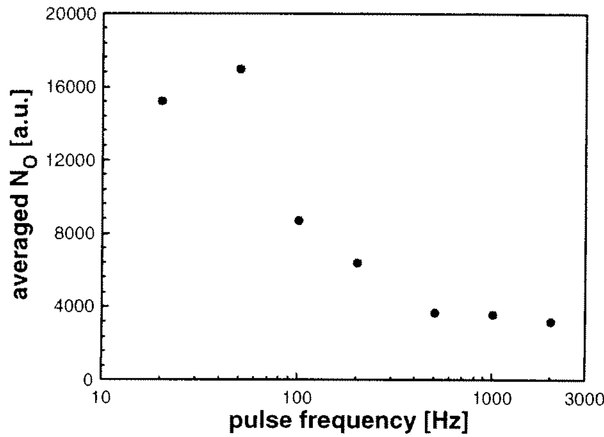

Figure 3: *Average N_O as function of pulse frequency*

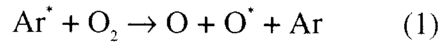

$$Ar^* + O_2 \rightarrow O + O^* + Ar \qquad (1)$$

Because of the decreased density of molecular oxygen in discharges of high argon contents, reaction (1) becomes less efficient as can be seen in Figure 4.

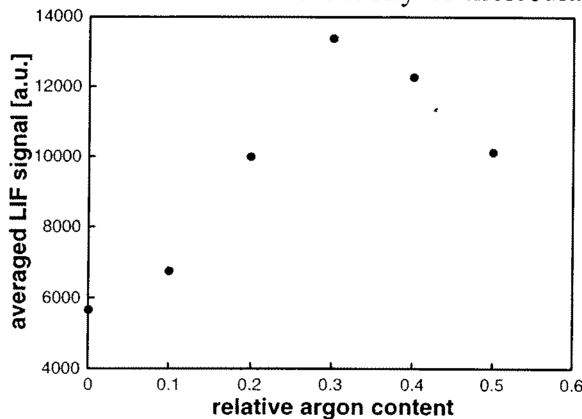

Figure 4: *Influence of argon admixtures on LIF-signal (pulse frequency 20 Hz)*

We now will compare these results with surface measurements of SiO_2-films deposited by pulsed plasmas of similar geometry. One major application of these films is coating of optical components, therefore these surfaces have to be very homogeneous with a minimal roughness. In Figure 5 the results of atomic-force microscopy measurements (AFM) for cw plasmas and pulsed plasmas of various pulse frequencies are shown. Compared to films deposited in cw plasmas an improvement of roughness is possible which can be tuned by the pulse frequency. Best film quality is obtained for 100 Hz which is near the optimum pulse frequency of the temporally averaged density of both electrons and atomic oxygen. Atomic oxygen is able to reduce the amount of hydrocarbon compounds in the gas phase which could otherwise form clusters. If these clusters get to the substrate the surface becomes rough and powdery, which is unwanted, because such films can easily be removed.

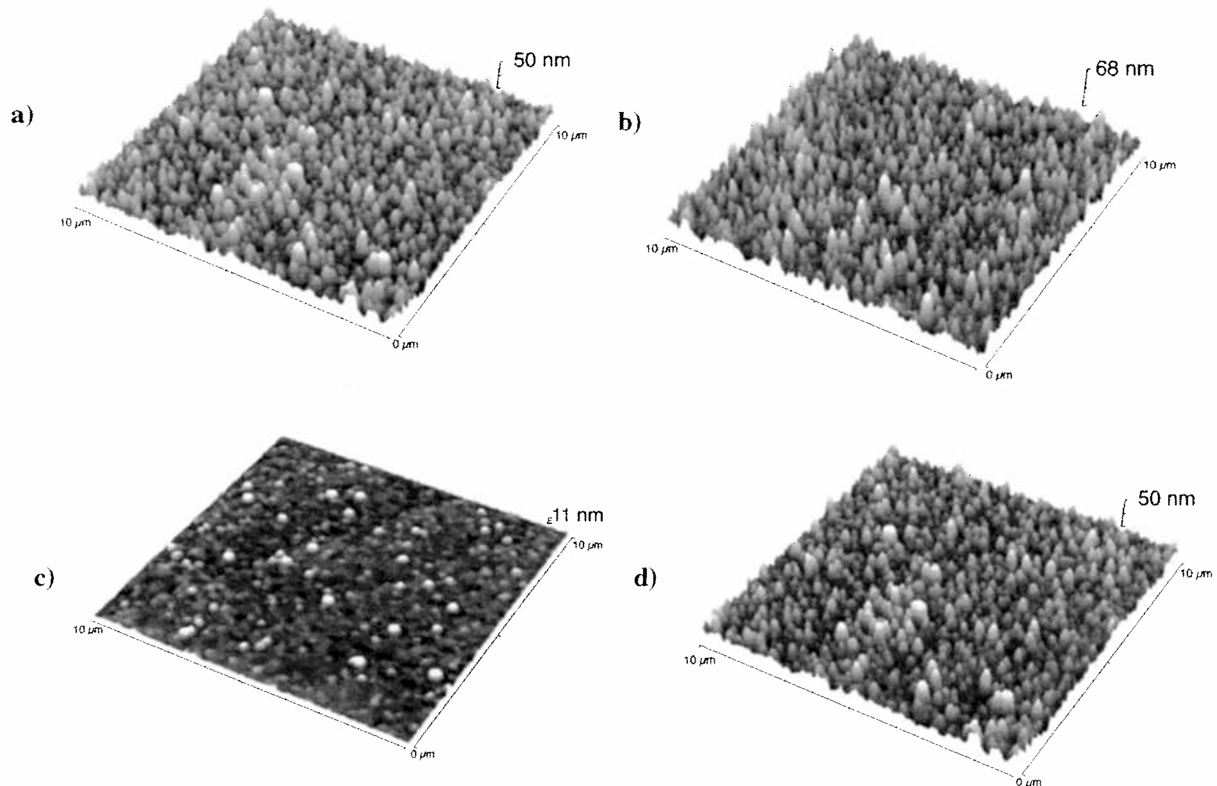

Figure 5: *AFM pictures of deposited SiO_2-films for a) cw, b) 10 Hz, c) 100 Hz, d) 200 Hz at a pressure of 50 Pa and an average microwave power of 1 kW*

Conclusion

The time-resolved relative density of atomic oxygen has been measured in a pulsed microwave discharge by TALIF for a wide range of parameters. Besides studies of the influence of pulse frequency and argon content we performed deposition experiments to investigate changes in surface morphology of deposited films. As a result the pulse frequency turned out to be a significant control parameter, because tuning pulse frequency leads to films with minimal roughness and a quality which cannot be reached by cw plasmas. To quantify the TALIF results calibration measurements are necessary. Based on the experimental data a deeper insight into the deposition process itself is also possible.

References

[1] Seiji Samukawa and S. Furuoya; Appl.Phys Lett., **63**, 2044-2046 (1993)

[2] St. Behle, A. Georg, Y. Yuan, J. Engemann, A. Brockhaus; Surf. Coat. Technol., **97**, 734-741 (1997)

[3] St. Behle, A. Brockhaus, J. Engemann; to be published in J. Vac. Sci. Technol. A

[4] D. Korzec, F. Werner, A. Brockhaus, T.P. Schneider, R. Nemanich, J. Engemann; J. Vac. Sci. Technol. A,**13**,(1995)

[5] S. Ashida and M.A. Lieberman; Jpn. J. Appl. Phys., **36**, 854-861 (1997)

[6] A. Brockhaus, Y. Yuan, St. Behle, J. Engemann; J. Vac. Sci. Technol. A, **14**, (1996)

Acknowledgement

The AFM-pictures have been taken by L.J. Balk et al., University of Wuppertal.
This work has been supported by the Bundesministerium für Bildung und Forschung (BMBF) under contract no. 13N6720.

Applications of the Cavity Ring-Down Technique to a Large Area RF-Plasma Reactor

F. Grangeon, C. Monard, J.-L. Dorier, A.A. Howling, Ch. Hollenstein
Ecole Polytechnique Fédérale de Lausanne - Centre de Recherches en Physique des plasmas
1015 Lausanne, Switzerland
D. Romanini, N. Sadeghi
Laboratoire de Spectrometrie Physique (UMR 5588)
Université Joseph Fourier de Grenoble, BP87, 38402 Saint Martin d'Hères Cedex, France

Introduction

The understanding of phenomena occurring in industrial rf plasmas is of great interest for the improvement of these processes and the resulting materials. A few years ago, the Cavity Ring-Down (CRD) technique was presented by O'Keefe and Deacon [1]. This diagnostic is based on the observation of the intensity decay of a laser light pulse trapped in a cavity formed by two high-reflectivity mirrors. One of the main advantages of this technique is its high sensitivity due to the multipass optical path; very low extinction coefficients (10^{-8}-10^{-5} cm^{-1}) can be measured, and therefore allowing detection of species at trace concentration [2, 3]. Due to its high sensitivity, the CRD technique could be employed to determine additional characteristics such as negative ion density by photodetachment [4] or trapped nano-particles in rf plasmas by light absorption [5]. This paper shows the feasibility of using the cavity ring down technique in an industrial plasma reactor for the determination of the negative ion density in pure oxygen and hydrogen plasmas, the observation of nano-particles trapped in silane plasmas and results concerning an observed long-term plasma-induced drift of the ring down decay time.

Experimental set-up

The rf plasma box reactor is a Balzers Kai1 [6] which is formed by two rectangular electrodes (47 x 57 cm), with a gap of 24 mm. The reactor pressure was varied from 0.075 to 0.4 Torr. The excitation frequency is 13.56 MHz, and the power dissipated in the plasma can be up to 120 W for these experiments. The ring down cavity consists of two high reflectivity dielectric mirrors (> 99.99%) in vacuum. The distance between the mirrors is 120 cm of which the plasma width occupies about 39% of the path length. A pulsed dye laser tuned at 566 nm is introduced into the back face of the entrance mirror. About 10^{-4} of the incident energy is coupled into the cavity. The output signal is measured behind the exit mirror. The output intensity I decays exponentially. A computer determines the exponential decay time τ (usually about 20 μs which corresponds to 4000 passes). The presence of absorbing species in the cavity causes a decrease in the decay time which is related to the absorption coefficient [3]. In practice, the ring-down time shown a plasma-induced drift. The cause is due to degassing of the reactor walls. Reducing this drift is thus of great importance in order to perform reproducible measurements.

Negative ion measurements

A discharge in oxygen causes a perfectly reproducible decrease in the decay time. This decrease is a function of the plasma power, but is independent of the laser wavelength. This effect was already observed in He-Ne laser multipass experiments in H_2 plasmas [4], and attributed to photodetachment of negative ions, leading to a measurable extinction coefficient. A vertical profile of the extinction was obtained by changing the position of the cavity between the electrodes. Figure 1 shows the variation of α_{ext} with the distance to the rf electrode, for different plasma powers. The profile exhibits a typical bell-shaped distribution for negative ions in rf plasmas with a maximum in the center of the plasma and a negligible density at the sheaths. This kind of distribution has already been observed [7] and shows unambiguously that the observed extinction is due to photodetachment of negative ions. It is known that the negative ions in pure O_2 rf discharges are mostly O^- ions (about 90%) [8]. Since the photodetachment cross-section of O^- ions is known [9], it is possible to determine the negative ion density. The measured density mid-way between the electrodes (12 mm) is about 10^{10}-10^{11} cm^{-3} and is shown as a function of the input plasma power for different pressures in figure 2. The density

increases quasi-linearly with the input power, but decreases when the pressure increases. These trends are in good agreement with experimental and numerical results dealing with negative ions in oxygen rf discharges [10].

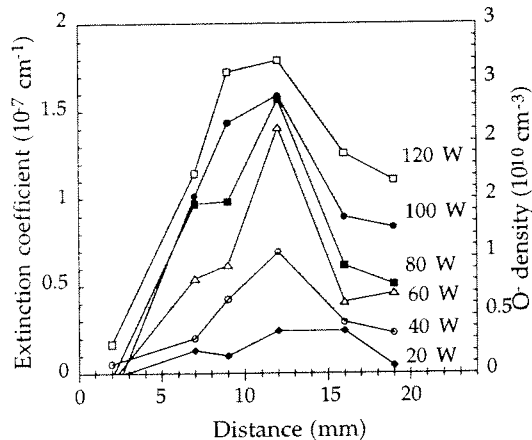

Figure 1: *Extinction coefficient profile/O⁻ density vs the distance between the electrodes for different rf plasma powers (0.1 Torr, 100 sccm O_2).*

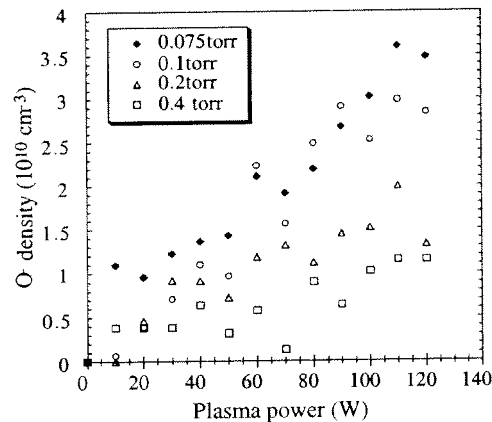

Figure 2: *O^- density vs rf plasma power at different pressures at a gas flow of 100 sccm.*

These experimental results were compared with numerical calculations from the Kinema SIGLO-RF software [11]. We have observed a good qualitative and quantitative agreement between experiments and calculations. This confirms that the observed decrease of the ring-down time is due to photodetachment on negative ions. The density of negative ions, for different plasma conditions, was also determined in pure hydrogen plasmas. The anion present in H_2 rf plasmas is the H^- ion [7]. Since the photodetachment cross-section is known [12], the negative ion density has been estimated to be about 10^9-10^{10} cm^{-3} in our plasma conditions. As in oxygen plasmas, the density increases when the power is increased or when the pressure is decreased. The preceding results show the validity of the cavity ring-down technique for the measurement of negative ion density by a photodetachment process for rf discharges in electronegative gases. The principal advantages of the CRD technique are that it is a highly sensitive and non-intrusive diagnostic.

Powder measurements

One of the main topics in the study of deposition plasmas is the characterisation of nanometer-size particles created and trapped in the plasma [13]. It appears that intermediate size particles (protopowders) are not easy to characterise by Rayleigh-Mie scattering due to their small cross-section, and other techniques such as photodetachment [14] and laser-induced particle heating [15] are intrusive. A new, non-intrusive technique allowing the study of these protopowders is therefore of great interest. It seems that the CRD technique is suitable for the study of powders in silane plasmas. With this aim, we have performed measurements of the extinction coefficient in Ar/SiH_4 plasmas. For these experiments, the reactor was heated at 200°C in order to reduce the powder formation rate. By fitting the exponential decay time in real time for each laser pulse, we obtain the time evolution of the extinction coefficient after plasma ignition for different plasma conditions. A decrease of the decay time was observed. At this stage, we cannot specify if the decrease is due to photodetachment on negative ions/clusters or scattering/absorption due to powder particles trapped in the plasma. In figure 3 the observed slow oscillations of the extinction coefficient indicate that the decrease of the decay time is due to solid particles created and trapped in the plasma. These oscillations are characteristic of powder creation/growth/elimination cycles in the reactor as already shown by other diagnostics [15]. At low silane dilution, as on figure 4, the extinction coefficient rapidly reaches 5.10^{-5} cm^{-1}, after which the ring-down signal is lost and measurements are no longer possible. These results can be used to determine the measurable range of extinction coefficient in our system: the lower limit, about 10^{-8} cm^{-1} (10^{-7} cm^{-1} for real-time measurements) is determined by the shot-to-shot

reproducibility of the laser, the dark noise of the detector, and other noise sources; the upper limit is about 5.10^{-5} cm^{-1}, when the decay time is shorter than the response time of our detection system. It is important to notice that the CRD diagnostic presents

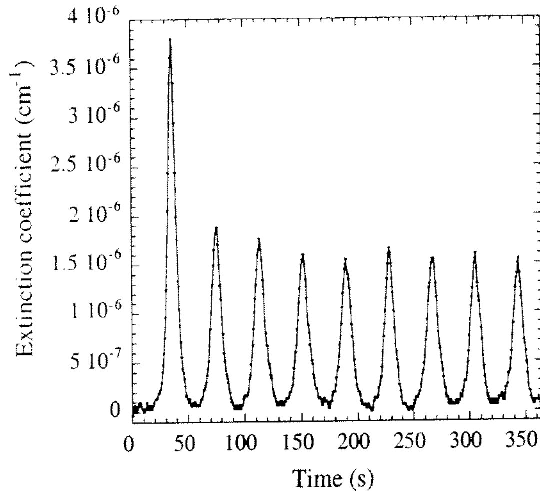

Figure 3: *Time evolution of the extinction coefficient due to powder particles in an Ar-SiH_4 plasma (0.2 Torr, 500 sccm Ar, 50 sccm SiH_4, 12 W)*

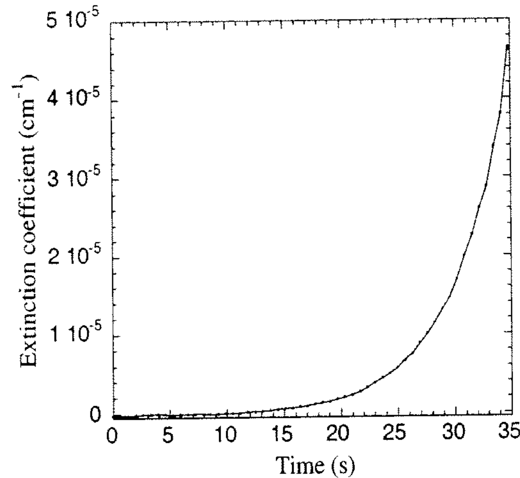

Figure 4: *Time evolution of the extinction coefficient due to powder particles in an Ar-SiH_4 plasma (0.2 Torr, 500 sccm Ar, 15.4 sccm SiH_4, 10 W)*

a sensitivity of several orders of magnitude higher than a single pass absorption diagnostic. In the case of the cavity ring-down technique, we have observed extinction coefficients in the range 10^{-8}-5.10^{-5} cm^{-1}. A single path absorption arrangement allowing to detect transmitted relative intensity variations of about 10^{-3}, which represents a good signal/noise ratio, could not measure extinction coefficients less than about 10^{-4} cm^{-1} for our large reactor. The extinction observed in our argon/silane experiments is probably due to small size particles (clusters or powders smaller than 30 nm). Since the detection of particles begins soon after plasma ignition, it is likely that the extinction of the signal intensity is due to a high density of these small particles. In the case of powder particles trapped in the reactor, the cavity ring-down technique allows to determine the volume fraction of the plasma occupied by solid-state particles [16] . In the range of our extinction measurements (10^{-8}-5.10^{-5} cm^{-1}), the volume fraction occupied by powder is about 7.10^{-12} – $3.5.10^{-8}$. These values are much lower than the volume fractions measured in dusty plasmas by single-pass Mie scattering diagnostic (about 10^{-8} - 10^{-7}) [16]. It is important to note that the CRD technique complements the Rayleigh scattering technique, difficult to use when the volume fraction of solid powder within the plasma is small ($<10^{-8}$). To summarise, these results show that the CRD technique is a powerful, non-intrusive diagnostic for nanometric particles detection in dusty plasmas and can be used to investigate the early phases of powder formation and the coagulation of the protoparticles. Moreover, the cavity ring-down diagnostic could be of great interest as a monitor in industrial processes which require conditions free of nanometric particles to avoid contamination of sub-micron features.

Observation of drift in the ring-down time

During these experiments, we frequently observed a spurious drift of the ring-down time induced by the presence of a plasma in the reactor. Several observations support the view that the degradation of the cavity ring-down time is in fact due to plasma desorption of water adsorbed on the reactor electrodes and walls, which then recondense on other surfaces, such as the mirrors. This would reduce the mirror reflectivity and lead to the observed decrease of the decay time τ. This hypothesis is confirmed by the following observations. The drift is minimised when the base pressure in the reactor is low ($< 1.10^{-6}$ Torr), after prolonged pumping and heating at 200°C, i.e. after a thorough degassing of the reactor. The plasma-induced drift decreases with time. But the drift reappears immediately if the reactor is opened to atmosphere and then evacuated. It appeared that a silane plasma running for 15 minutes reduces

the ring-down time drift induced by the argon plasma. Moreover without silane plasma, it takes several hours to recover the initial cavity quality. But after silane plasma, the cavity recovers its initial state about 500 seconds after the argon plasma extinction. Reducing the drift is of great importance for CRD experiments. A deposition plasma (silane, for example) seems to limit or avoid the drift by passivating the reactor walls. The drift effect would appear to be a major limitation of the CRD technique, but it is merely a consequence of the diagnostic's high sensitivity to the presence of a thin film on the mirror surface. In fact, the CRD technique could be employed to study the optical/spectral characteristics of very thin films deposited on the mirror surface, for example at the early stages of a deposition process.

Conclusion

We have investigated the practicability of the cavity ring-down technique as a diagnostic for negative ions and powder particle detection in large area rf-plasma reactors. The negative ion densities found in pure oxygen and hydrogen plasmas are respectively about 10^{10}-10^{11} and 10^{9}–10^{10} cm^{-3}. The cavity ring-down technique is a powerful technique for the characterisation of nano-scale particles created and trapped in dusty plasmas. The observed extinction due to the particles (10^{-7} to 5.10^{-5} cm^{-1}) is several orders of magnitude smaller than with other non-intrusive techniques (about 10^{-4} cm^{-1}). The time evolution of very low volume fractions of solid particles in the plasma (10^{-12} – 10^{-8}) can be measured by this technique. One experimental difficulty is the plasma-induced drift of the decay time, probably due to water desorption, which can significantly perturb ring-down measurements. A thin film of silicon reduces this drift probably by trapping the water between the reactor walls and the silicon layer. The cavity ring-down technique is a powerful diagnostic for the characterisation of rf plasmas and could be extended to applications such as thin film characterisation or as industrial process control.

References

[1] A. O'Keefe and D. Deacon, Rev. Sci. Instrum. **59** (1988) 2544

[2] D. Romanini, «Cavity ring down and intracavity laser absorption» in «Cavity-RingDown Spectroscopy – a new technique for trace absorption measurements», 1-19, K.W. Busch and M.A. Busch eds., American Chemical Society, Washington, 1998

[3] D. Romanini and K.K. Lehmann, J. Chem. Phys. **99** (1993) 6287

[4] E. Quandt, H.F. Döbele and W.G. Graham, Appl. Phys. Lett. **72** (1998) 2394

[5] A. Campargue, D. Romanini and N. Sadeghi, J. of Phys. D, Appl. Phys. **31** (1998) 1168

[6] L. Sansonnens, A. Pletzer, D. Magni, A.A. Howling, Ch. Hollenstein and J.P.M. Schmitt, Plasma Sources Sci. Technol. **6** (1997) 170

[7] M.A. Lieberman and A.J. Lichtenberg «Principles of plasma discharges and materials processing» Wiley-Interscience Publications, New York, 1994

[8] T. Suzuki and T. Kasuya, Phys. Rev. A **36** (1987) 2129

[9] M. Shibata, N. Nakano and T. Makabe, J. of Phys. D Appl. Phys. **30** (1997) 1219

[10] E. Stoffels, W.W. Stoffels, D. Vender, M. Kando, G.M.W. Kroesen and F.J. de Hoog, Phys. Rev. E **51** (1995) 2425

[11] J.P. Boeuf and L.C. Pitchford, Phys. Rev. E **51** (1995) 1376 and Kinema Research Associates SIGLO-RF (Simulation of Glow Discharges RF-excited, capacitively-coupled) modeling software

[12] J.H. Fink, Fusion Technology, **6** (1984) 548

[13] K.G. Spears, T.J. Robinson and R.M. Roth, IEEE Trans. Plasma Sci. **14** (1986) 179

[14] T. Fukuzawa, K. Obata, H. Kawasaki, M. Shiratani and Y. Watanabe, J. Appl. Phys. **80** (1996) 3202

[15] A. Bouchoule, A. Plain, L. Boufendi, J.-Ph. Blondeau and C. Laure, J. Appl. Phys. **70** (1991) 1991

[16] C. Courteille, Ch. Hollenstein, J.-L. Dorier, P. Gay, W. Schwarzenbach, A.A. Howling, E. Bertran, G. Viera, R. Martins and A. Macarico, J. Appl. Phys. **80** (1996) 2069

Thomson scattering applied to a large volume ECR discharge

— D Hemmers[1], A Beck[1], S Brezinsek[1], S Meier[1], H Kempkens[1], H B Schweer[2], J Stańco[1], J Uhlenbusch[1] — [1]*Institut für Laser- und Plasmaphysik, Heinrich–Heine–Universität Düsseldorf,* — [2]*Institut für Plasmaphysik, Forschungszentrum Jülich*

Electron cyclotron resonance (ECR) discharges play increasingly an important role in industrial processes like etching or chemical vapour deposition. In order to optimize those processes reliable diagnostic techniques to determine important plasma parameters are necessary. In ECR plasmas often probes are used to determine the electron density and temperature although the interpretation of the probe characteristic is difficult due to the presence of the magnetic field, the microwave field and reactive species. Thomson scattering of laser light on the other hand offers the possiblity to determine these parameters non–intrusively and unambiguously but with a rather large experimental effort.

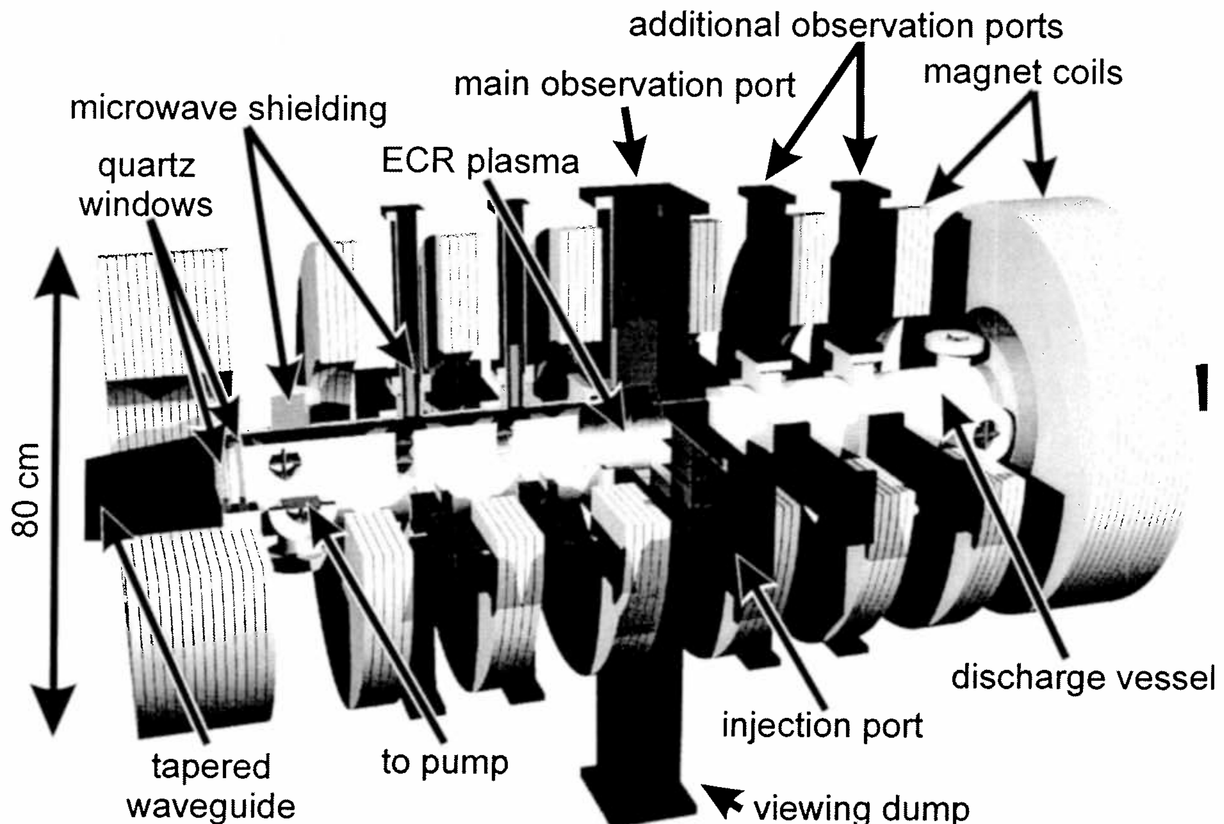

Figure 1: *Experimental set–up of the discharge*

The experimental set–up of the discharge is shown in figure 1. The discharge vessel, which is a stainless steel cylinder with a length of 1.6 m and a diameter of 18 cm, is immersed in a static magnetic field produced

by 58 water–cooled magnet coils. The resulting field is an asymmetrical magnetic mirror field with a mirror ratio of 1.7. The microwave (2.45 GHz, 0.6 kW .. 6.0 kW, rcp TE_{11}–Mode) is injected into the plasma from the high field side through a quartz window and propagates towards the central part of the vessel where the ECR condition (B=87.5 mT) is fulfilled. The main observation port provides diagnostic access to the whole plasma diameter. Measurements were performed on this port and on the additional observation ports to obtain radial and axial profiles.

The Thomson scattering experiment uses a pulsed frequency doubled Nd:YAG laser (532 nm) with a repetition rate of 10 Hz and a pulse energy of 400 mJ as a light source. The beam is focussed horizontally into the plasma through a Brewster window and a series of baffles to reduce stray light (equivalent to the Rayleigh signal of 0.5 Pa Ar). Using a solid angle of approximately $d\Omega$=0.018 the scattering volume (length 11 mm, diameter 0.4 mm) is imaged onto the entrance slit of a single monochromator with high efficiency for 532 nm. After spectral decomposition (resolution 0.5 nm) the entrance slit is imaged onto eleven parallel exit slits, which are each filled with separate fibre bundles guiding the scattered light to eleven photo multiplier tubes (R3896) with fast preamplifiers. The signal detection is done by a gated multichannel VME–ADC. To obtain a complete spectrum the signals are averaged over 1000 laser shots. The lowest detectable electron density is approximately $10^{17}\,m^{-3}$ at a temperature of 5 eV.

Figure 2 shows the electron temperature and density as a function of axial position for different Ar pressures and a microwave power of 600 W. The electron temperature, which is approximately constant along the discharge axis due to the large heat conductivity of the electrons parallel to the magnetic field, drops from $3.5 \cdot 10^4$ K at 0.05 Pa to $1.5 \cdot 10^4$ K at 2.0 Pa due to increasing collision frequencies. On the other hand, the electron density develops steeper gradients due to the slow ambipolar particle transport parallel to the magnetic field. The electron density, which is found to be overcritical, varies from $5 \cdot 10^{17}\,m^{-3}$ at 0.05 Pa to $7 \cdot 10^{18}\,m^{-3}$ at 2.0 Pa. Furthermore, it is observed that the maximum of the electron density constantly shifts towards the microwave source with increasing pressure. This is attributed to increasing collision frequencies and electron density, which broadens the resonance zone, so that microwave power becomes absorbed at a field strength much higher than the resonant field strength and thus closer to the microwave source. Radial profiles of the electron density (not shown here) are close to Bessel profiles while the

electron temperature shows slight hollow profiles or is constant over the diameter.

The dotted curves in figure 2 represent results obtained from a two–dimensional modelling of the discharge. In this model a particle and energy balance for the electrons are solved simultaneously with a wave equation for the electric field of the microwave. The material properties

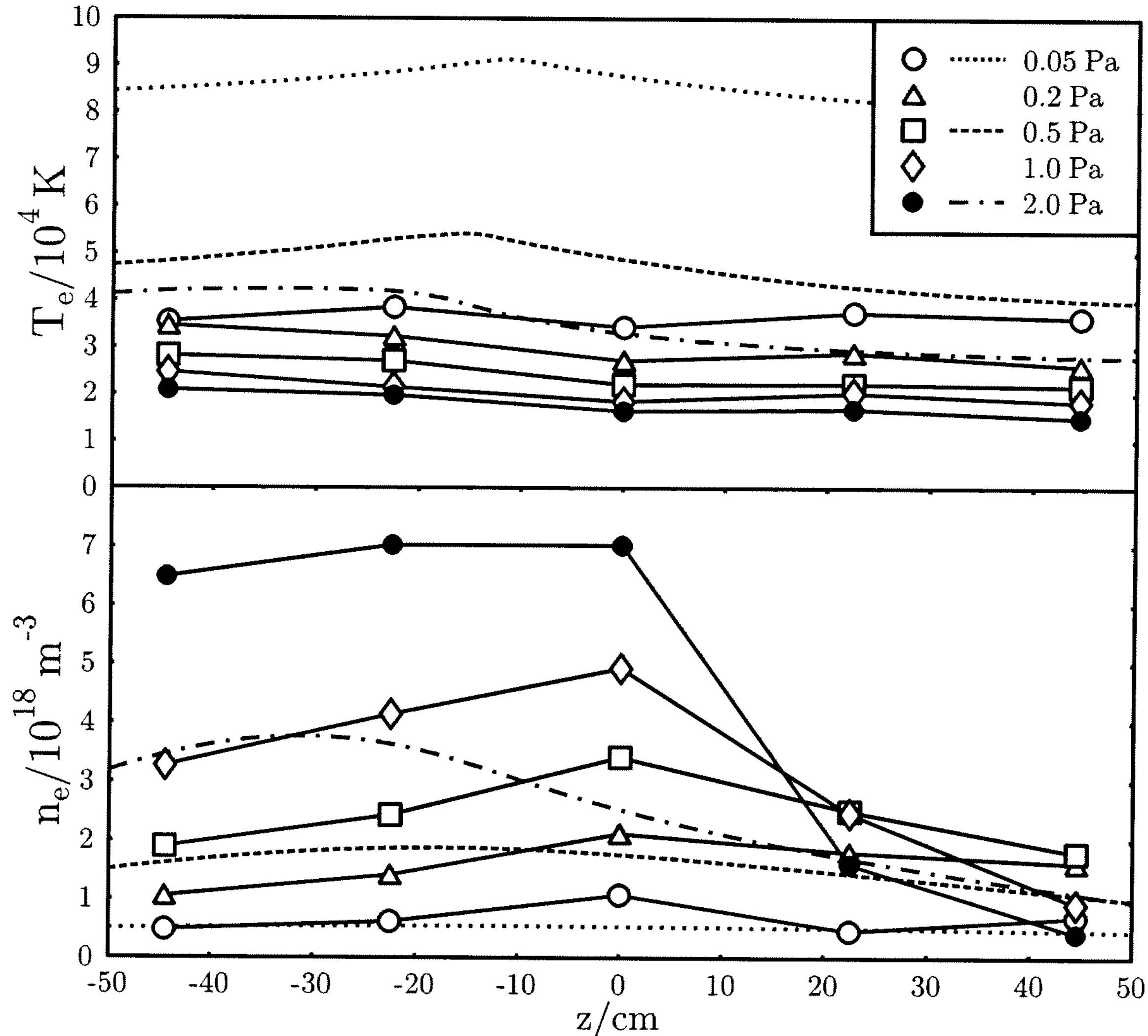

Figure 2: *Axial profiles of the electron temperature and density in argon for different pressures and a microwave power of 600 W. The dotted curves represent results obtained from the modelling. Microwave incident from the left.*

of the plasma are obtained self–consistently as a function of the plasma parameters from the dispersion relation of microwaves in hot plasmas, already simplified for the case of parallel propagation and right–handed polarization. We find that the general form of the profiles is in agreement with the measurements. The shift of the electron density towards the microwave source and the homogeneity of the electron temperature are predicted well. On the other hand the absolute values of T_e and n_e

show discrepancies. There are several possible reasons. First of all, there might be deviations of the electron energy distribution function (eedf) from a Maxwellian, which has been assumed to be valid in the model to calculate rate coefficients and transport coefficients. Figure 3 shows the eedf perpendicular to the magnetic field up to an energy of 11 eV as measured by Thomson scattering. Up to now we could not detect any

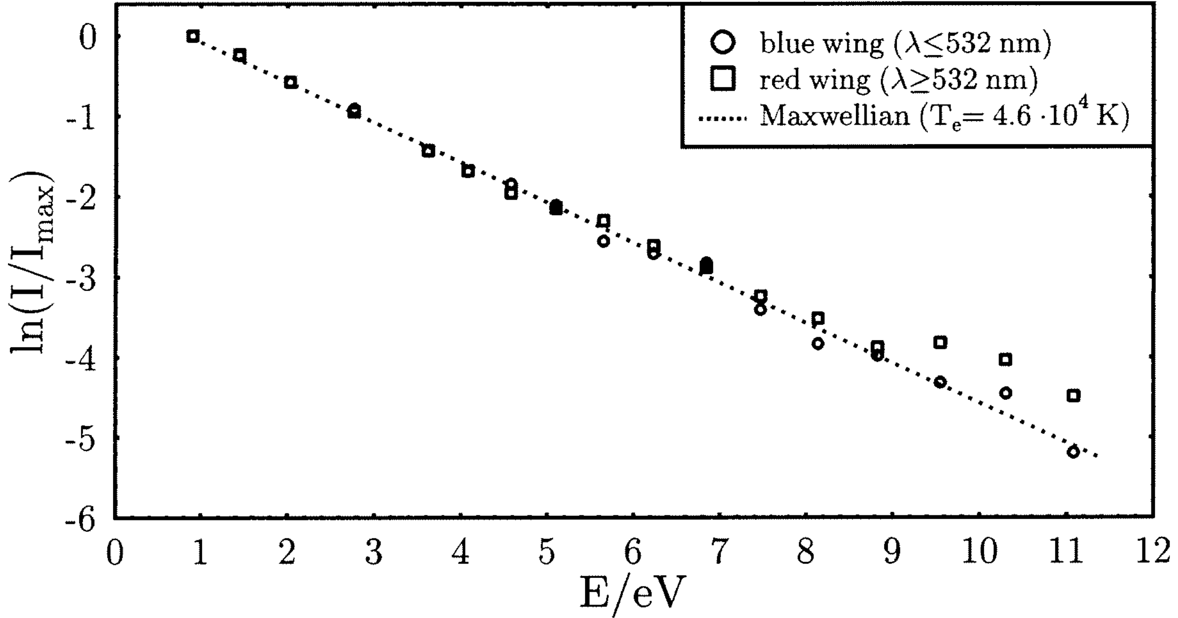

Figure 3: *Electron energy distribution function perpendicular to the magnetic field for an argon plasma at 0.05 Pa and 2400 W. The dotted line corresponds to a Maxwellian distribution with a temperature of* $4.6 \cdot 10^4$ *K.*

deviations from a Maxwellian. Secondly, a constant neutral density was assumed. Measurements by Rayleigh scattering indicate that the neutral density is depleted down to 50 % in the central region of the plasma for operating conditions with high pressure, which might affect the electron density by a changed ionization rate. Finally, the use of a scalar index of refraction in the computation of the electric field might oversimplify the problem since a magnetized plasma originally has a tensorial dielectricity. This could lead to a different power deposition profile, in which the energy is distributed over a larger volume resulting in a lower electron temperature.

Acknowledgement

This work was supported by the Deutsche Forschungsgemeinschaft, Sonderforschungsbereich 191 (Teilprojekt Niedertemperaturplasmen).

Diagnostics and modeling of SiH_2 density in $Ar/H_2/SiH_4$ deposition plasmas

M. Hertl, J. Jolly

Laboratoire PRIAM, CNRS-ONERA, Fort de Palaiseau, 91761 Palaiseau Cedex France

Introduction

Radio frequency (RF) discharges in $Ar/H_2/SiH_4$ gas mixtures are extensively used for amorphous hydrogenated silicon (a-Si:H) thin film deposition, and many efforts have been carried out to understand the deposition mechanism. Recently, powerful 2D models have been developed for such plasmas [1,2], and they have been validated by laser diagnostics [3]. The SiH_2 radical is supposed to have an important impact on the a-Si:H film quality, but its diagnostics under realistic deposition conditions remains difficult. Similarly, its modeling is affected by uncertainties about the main production and loss processes. In the present study, we present absolute SiH_2 densities measured by laser induced fluorescence (LIF) for a large variety of typical $Ar/H_2/SiH_4$ deposition plasmas. By means of a very simple model we demonstrate that SiH_2 is mainly produced by dissociation of SiH_4 by electron impact, and that the main loss processes are the reaction with SiH_4 and diffusion to the walls.

Experimental Set-up

The experimental set-up has been described in detail elsewhere [3,5]. Briefly, a RF plasma (13.56 MHz) is sustained between two parallel plate electrodes (d = 32 mm, Ø = 120 mm). RF power is applied to the upper electrode, which is shower like for gas injection. The grounded electrode is heated up to 573 K and is covered by a silicon substrate. In the LIF experiments, SiH_2 is excited via the $\tilde{A}^1B_1(v_1v_2v_3=020)J_{KaKc}=0_{00} \leftarrow \tilde{X}^1A_1(000)1_{10}$ transition by means of a Nd:YAG pumped dye laser (λ = 580 nm) [4]. The fluorescence signal is detected on the $\tilde{A}^1B_1(020) \rightarrow \tilde{X}^1A_1(010)$ branch around λ = 618 nm. The plasma is turned off for 40 µs during the LIF measurements and the laser pulse is set at 4 µs in the afterglow. The absolute density calibration is achieved by a Rayleigh scattering experiment in nitrogen using the same optical set-up. Simultaneously, a 1.5 m focal length monochromator is used to detect

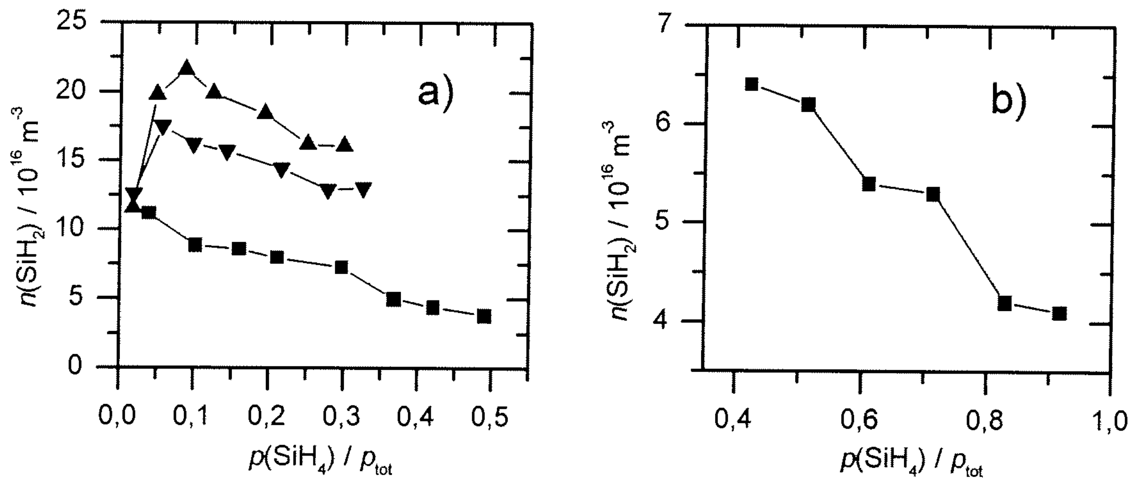

Figure 1 *SiH_2 density in Ar (a) and H_2 (b) diluted SiH_4 plasmas as function of the relative pressure of SiH_4 in the plasma. a) Fed gases: Ar (10 sccm) + SiH_4 (1-13 sccm), p = 9.3 Pa, V_{RF} = 620 V (▲), 520 V (▼), 270 V (■). b) H_2 + SiH_4 = 20 sccm, p = 9.3 Pa, V_{RF} = 400 V.*

plasma emission on the Si $5p^3D(J=3) \rightarrow 4s^3P°(2)$ line (λ = 579.79 nm) and on the Ar $4s_1'''' \rightarrow 2p_8$ line (λ = 666.41 nm). The integrated signal of these lines will be used to estimate relative electron densities. A HIDEN EQP 300 mass spectrometer is mounted under the grounded electrode [5]. Species in the vicinity of the substrate holder are sampled in the mass spectrometers ionization chamber via a Ø = 300 μm hole in the grounded electrode. In the present study we use mass spectrometry to measure the partial pressure of Ar, H_2 and SiH_4 in the plasma.

Results and discussion

The measured SiH_2 densities are represented in figure 1-a) and b) respectively for argon and hydrogen diluted silane plasmas as a function of silane concentration. In the Ar/SiH_4 plasmas at low RF power (V_{RF} = 270 V), the SiH_2 density decreases for increasing SiH_4 concentration, as has already been reported [6]. At higher RF power (V_{RF} = 520 V and 620 V), the SiH_2 density first increases before decreasing with increasing silane partial pressure. The SiH_2 peak density occurs at a SiH_4 concentration which increases with the RF power. In the case of H_2/SiH_4 plasmas, the SiH_2 density decreases when the SiH_4 concentration in the plasma increases from 50% to near 100% (figure 1-b)).

To interpret these results, we first suppose that SiH_2 is mainly created by dissociation of SiH_4 by electron impact, and that SiH_2 losses are mainly due to reactions with SiH_4 and diffusion to the walls:

$$\frac{\partial[\mathrm{SiH_2}]}{\partial t} = k_{\mathrm{SiH_2}}\, n_e\, [\mathrm{SiH_4}] - k_{\mathrm{reac}}\, [\mathrm{SiH_2}][\mathrm{SiH_4}] - \frac{D}{\Lambda^2}[\mathrm{SiH_2}], \quad (1)$$

where [X] is the density of the species X and n_e the electron density. k_{SiH2} and k_{reac} are the rate constants for respectively the creation of SiH_2 by dissociation of SiH_4 by electron impact and its loss by reactions with SiH_4. D is the diffusion coefficient, and Λ the diffusion length, which depends on the reactor dimensions as well as the SiH_2 loss probability β on the reactor walls [7]. We have estimated $k_{reac} = 2.3\times10^{-17}$ m^3s^{-1}molecule^{-1} and β = 0.6 from preliminary measurements of the SiH_2 density decay in the afterglow. The electron density is often deduced from the Ar* or the Si* emission intensity using the following equations:

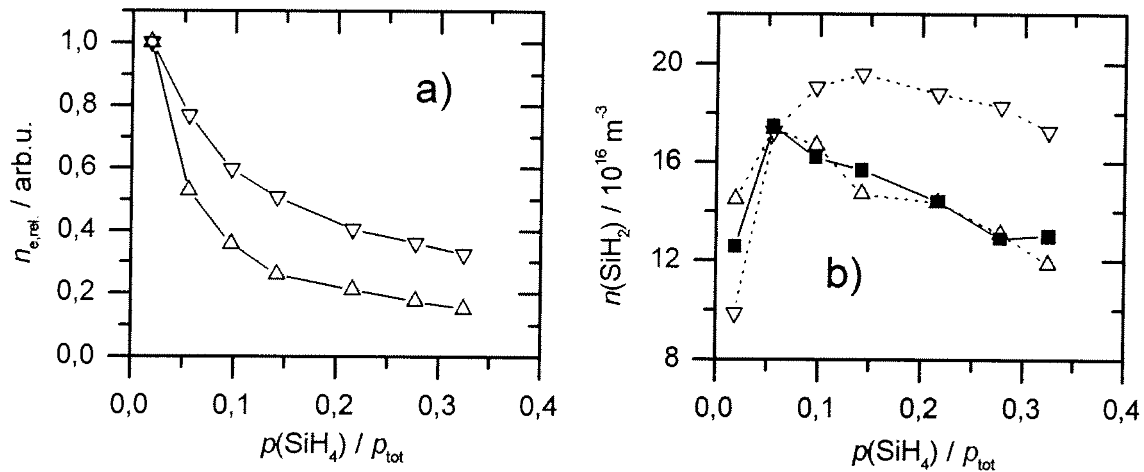

Figure 2 (a) Relative electron density in Ar diluted SiH_4 plasmas estimated by using Ar (∇) and Si* (Δ) emission. Fed gases: Ar(10 sccm) + SiH_4(1-10 sccm), p = 9.3 Pa, V_{RF} = 520 V. (b) Comparison of measured (■) SiH_2 densities and those calculated by using equations (4) (∇) and (5) (Δ) for the same plasma conditions as in (a).*

$$k_{\mathrm{Ar}^*}\, n_e\, [\mathrm{Ar}] = \frac{1}{\tau_{\mathrm{Ar}^*}} [\mathrm{Ar}^*] \qquad (2)$$

$$k_{\mathrm{Si}^*}\, n_e\, [\mathrm{SiH}_4] = \frac{1}{\tau_{\mathrm{Si}^*}} [\mathrm{Si}^*] \qquad (3)$$

In these relations one supposes that Ar* is created by electron impact with Ar ground state atoms, that Si* is created by dissociative excitation of SiH_4, and that losses are mainly due to radiative decay for both excited species. This approach neglects possible Ar* creation by electron impact with metastable argon atoms, as well as the creation of Si* by other excitation mechanisms. We will demonstrate that under our conditions only the Si* emission signal yields a good approximation for the electron density. In steady state conditions we may write $\partial/\partial t = 0$, and replacing n_e in equation (1) by using (2) and (3) yields

$$[\mathrm{SiH}_2] = \frac{k_{\mathrm{SiH}_2}}{\tau_{\mathrm{Ar}^*} k_{\mathrm{Ar}^*}} \frac{[\mathrm{Ar}^*]}{[\mathrm{Ar}]} [\mathrm{SiH}_4] \left\{ k_{\mathrm{reac}}\, [\mathrm{SiH}_4] + \frac{D}{\Lambda^2} \right\}^{-1} \qquad (4)$$

$$[\mathrm{SiH}_2] = \frac{k_{\mathrm{SiH}_2}}{\tau_{\mathrm{Si}^*} k_{\mathrm{Si}^*}} [\mathrm{Si}^*] \left\{ k_{\mathrm{reac}}\, [\mathrm{SiH}_4] + \frac{D}{\Lambda^2} \right\}^{-1} \qquad (5)$$

Absolute values for [Ar], [SiH_4] and [H_2], obtained by mass spectrometry, are used as input parameters in (4) and (5) as well as for the calculation of D. Relative densities of Ar* and Si* are deduced from the emission measurements. We now suppose that for a given RF power the electron temperature, and hence k_{SiH2}, k_{Ar^*} and k_{Si^*}, do not change significantly with the Ar/H_2/SiH_4 mixing ratio. Therefore we may simplify equation (4) and (5) with: $k_{\mathrm{SiH}_2}/(\tau_{\mathrm{Ar}^*} k_{\mathrm{Ar}^*}) = f$, and $k_{\mathrm{SiH}_2}/(\tau_{\mathrm{Si}^*} k_{\mathrm{Si}^*}) = f'$, where f and f' depend only on the RF power. The assumption of constant T_e is confirmed by Langmuir probe measurements applied to Ar/H_2 plasmas at p = 4.0 Pa, which show that T_e varies only slightly with the Ar partial pressure [8].

Figure 2-a) shows the relative electron density estimated as $n_e \propto [\mathrm{Ar}^*]/[\mathrm{Ar}]$ and $n_e \propto [\mathrm{Si}^*]/[\mathrm{SiH}_4]$ for the Ar/SiH_4 plasmas at V_{RF} = 520 V. Both curves show decreasing electron densities for increasing SiH_4 concentration. In figure 2-b) we present the SiH_2 density as a function of the silane concentration calculated from equations (4) and (5) for the same plasma conditions, as well as the experimental results. The only fitting parameters are the proportionality factors f and f'. The experimental curve is very well reproduced by equation (5), in which the Si* emission is used to substitute n_e. Using the Ar* signal through equation (4) leads to an error of up to 40% in the calculated SiH_2 density. The same observation is made for

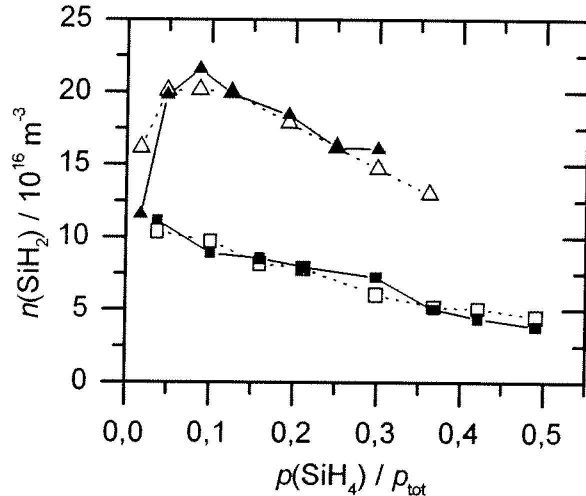

Figure 3 Comparison between measured (full symbols) and calculated (hollow) SiH_2 densities in Ar/SiH_4 plasmas. Fed gases: Ar (10 sccm) + SiH_4 (1-13 sccm), p = 9.3 Pa; triangle: V_{RF} = 620 V, square: V_{RF} = 270 V.

the other two curves obtained in Ar/SiH_4 plasmas, and we present only, in figure 3, the results obtained with the Si* values. The proportionality factor f' in equation (5) is set to 6.0×10^{18} s^{-1}, 5.8×10^{18} s^{-1} and 10.5×10^{18} s^{-1} respectively for the curves at V_{RF} = 620 V, 520 V and 270 V. Figure 4 represents the relative electron density in the case of H_2/SiH_4 plasmas, deduced from the Si* emission signal (a) and the comparison between the measured and calculated SiH_2 density (b). As in the Ar/SiH_4 plasmas the modeling result fits quite well the measurements. The numerical factor in this case is $f = 8.8\times10^{18}$ s^{-1}.

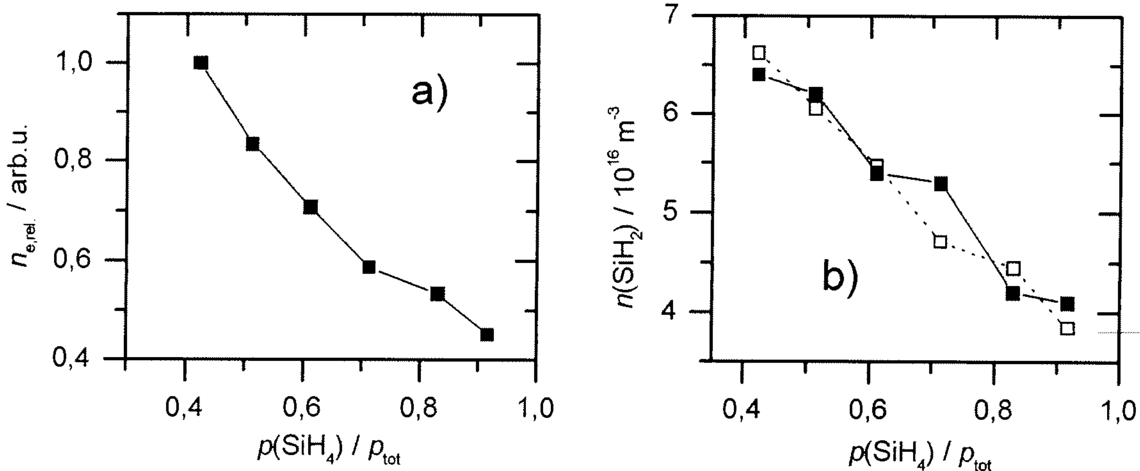

***Figure 4** (a) Relative electron density in H_2 diluted silane plasmas obtained from equation (5). Fed gases: H_2 + SiH_4 = 20 sccm, p = 9.3 Pa, V_{RF} = 400 V. (b) Comparison of measured (■) and calculated (□) SiH_2 densities for the same plasma conditions.*

In conclusion, we have demonstrated that relative SiH_2 densities can be calculated on the basis of some very simple assumptions for a large variety of low pressure $Ar/H_2/SiH_4$ plasmas. Due to the very good modeling results we may conclude that our assumptions represent well the physics of SiH_2 plasma processes: The only relevant SiH_2 creation process is direct dissociation of SiH_4 by electron impact, and SiH_2 losses are mainly due to reactions with SiH_4 and diffusion to the walls. Moreover, the relative electron density can be deduced from the normalized Si* emission signal: $n_e \propto [Si^*]/[SiH_4]$. On the other hand, normalized emission intensities from argon do not lead to a correct estimation of n_e in the simple way presented above. This is probably due to important creation of the excited argon level used in this study from the metastable argon states. If the relative density of metastable argon $[Ar^*_{meta}]/[Ar]$ increases with the SiH_4 concentration, this would lead to an overestimation of the electron density by the above described procedure.

References

[1] O.Leroy, G.Gousset, L.Alves, J.Perrin, J.Jolly, Plasma Sources Sci. Technol. 7, 348-58 (1998)
[2] G.Nienhuis, W.Goedheer, E.Hamers, W.van Sark, J.Bezemer, J. Appl. Phys. **82**, 2060-71 (1997)
[3] M.Hertl, N.Dorval, O.Leroy, J.Jolly, M.Péalat, Plasma Sources Sci. Technol. 7, 130-5 (1998)
[4] M.Hertl, J.Jolly, Proc. XIVth ESCAMPIG, Malahide (1998), 386-7
[5] P.Kae-Nune, J.Perrin, J.Jolly, J.Guillon, Surface Science **360**, L495-8 (1996)
[6] K.Tachibana, T.Shirafuji, Y.Matsui; Jpn. J. Appl. Phys. **31**, 2588-91 (1992)
[7] P.J.Chantry, J. Appl. Phys. **62**, 1141-8 (1987)
[8] J.T.Gudmundsson, Plasma Sources Sci. Technol. 7, 330-6 (1998)

Light Scattering Diagnostic System for Investigation of Reactive Plasmas in a Capacitively Coupled RF-Discharge

M. Kaczor, H. Soltwisch
Institut für Experimental Physik V, Ruhr-Universität Bochum
Germany

Introduction

The presented multi-channel light scattering diagnostic system is used at a capacitively coupled RF-discharge (ν_{RF} = 13.56 MHz). A tunable, frequency doubled (425nm-480nm), high repetition (1 kHz) Ti:S-Laser system (1mJ within 50 ns) is used as a light source for incoherent Thomson scattering. The tuning capability is essential for selecting a wavelength at the lowest possible plasma background and for avoiding the excitation of laser induced fluorescence (LIF). To reduce the time for the acquisition of a Thomson spectrum at typical electron densities of $10^{15}m^{-3}$ to $10^{17}m^{-3}$, eight optical fibers are used to map the spectrum onto eight channels which simultaneously perform time resolved photon counting. The temporal behaviour of the scattered light is registered to keep track of any low intensity laser induced fluorescence, which may be superimposed on the Thomson spectrum.

Concept of the experiment

Thomson scattering in low density reactive plasmas has to cope with several difficulties that are discussed in detail elsewhere in these proceedings. The major aspects that have to be considered when planing an experimental setup are as follows:

1) The large number of molecular species emit very complex spectra that depend on the chemical composition.
2) Depending on the plasma conditions (dominance of different species), the laser wavelength could be close to molecular bands, which would produce "broadband" laser induced fluorescence.
3) Due to the low electron density only a few Thomson photons per laser shot can be observed, even with high pulse energy. An effective stray light reduction is therefore essential for performing Thomson scattering.
4) Mie scattering on dust particles will give additional stray light.

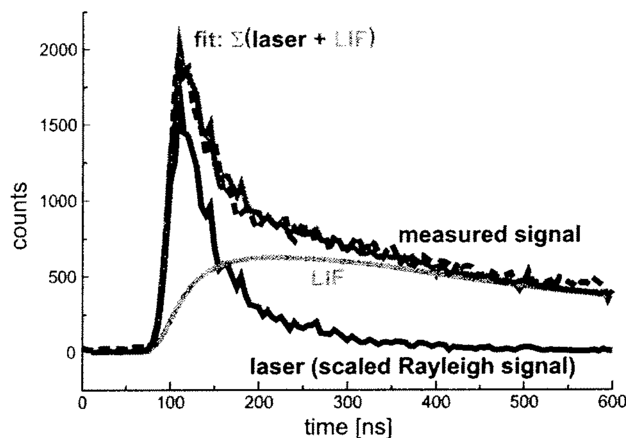

Figure 1: *the temporal behaviour of the scattered light shows laser induced fluorescence*

Conditions 1) and 2) require a tunable laser system to avoid regions with either high intensity of plasma emission or the occurrence of LIF from molecular species.

In order to detect residual broadband LIF with intensities comparable to the Thomson signal a time resolved recording of the detected light emission is necessary (see Figure 1). The two different types of emission can be distinguished by their different time behaviour: Thomson scattering follows the laser pulse, whereas LIF can be identified by a slow decay of the observed signal.

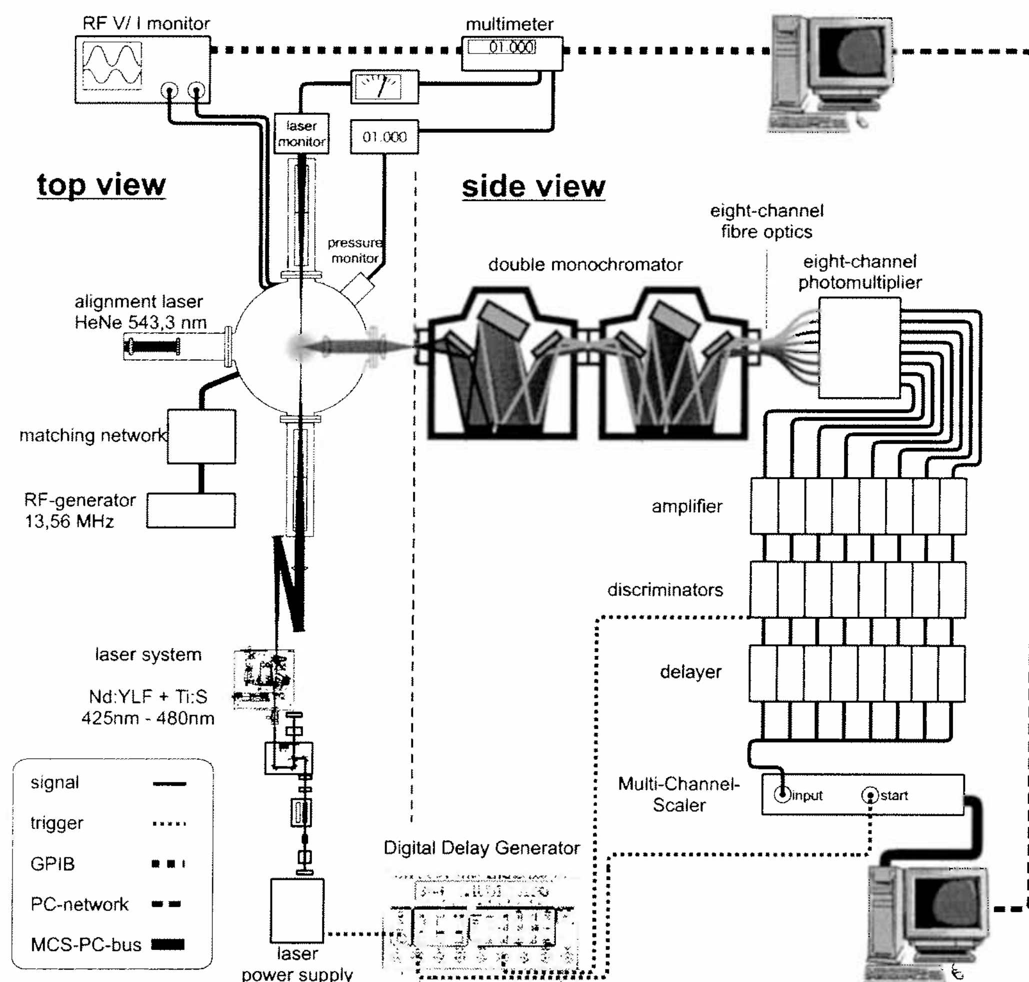

Figure 2: *Experimental setup*

Experimental Setup

Time resolved measurement of the scattered light is performed with photon counting techniques. Therefore the energy of the laser was chosen such that the detected number of Thomson photons is in the order of one per laser shot. The laser system (INTRA-Ti, LAS) runs at a high repetition rate (1 kHz) to obtain a sufficient number of counts within reasonable time. The range of tunability is from 425 nm to 480 nm, where our photomultiplier has its maximum quantum efficiency.

To reduce the stray light, the laser beam enters and exits the vacuum chamber through 0.8 m long tubes sealed by plane glass plates (see Figure 4). Inside each of these tubes the laser beam passes a system of 3 apertures. The intensity of the laser is measured by a monitor behind the output window. Inside the vacuum chamber black glass plates are positioned to further minimize the stray light (see Figure 3). The scattered light is observed under 90° with an optical system of two lenses. The first lens, an aspherical achromat with a focal length of f = 54 mm is positioned inside the reaction chamber so that the focal point coincides with the laser focus. The second lens which is placed behind a plane window focuses the scattered light onto the 6 mm wide entrance slit (0.3 mm height) of a double monochromator (HR250, Jobin Yvon) consisting of two ¼ m monochromators with holographic gratings (2400 grooves/mm). A viewing dump is positioned opposite to the first lens (see Figure 3). It consist of black glass plates, arranged such that their orientation towards the rays through the laser focus corresponds to the Brewster angle.

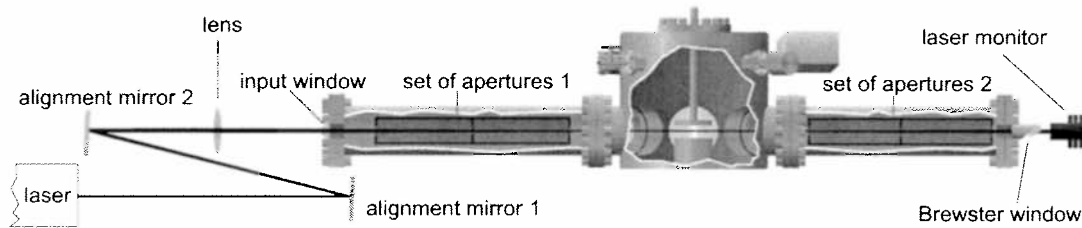

Figure 4: *Alignment of the laser through the discharge*

In order to permit the observation of the complete Thomson spectrum, the slit between the two monochromators has to be rather wide. Even under these conditions, the reduction of stray light is still much higher than that of a single monochromator of equivalent resolution.

The spectrally resolved photons are guided by eight optical fibres to an eight-channel photomultiplier (R6665, Hamamatsu).

The signal from each photomultipier channel is amplified by a separate 500 MHz amplifier and fed to a discriminator, that is gated to provide a better signal-to-noise ratio. It also acts as a filter to eliminate noise pulses (see Figure 5).

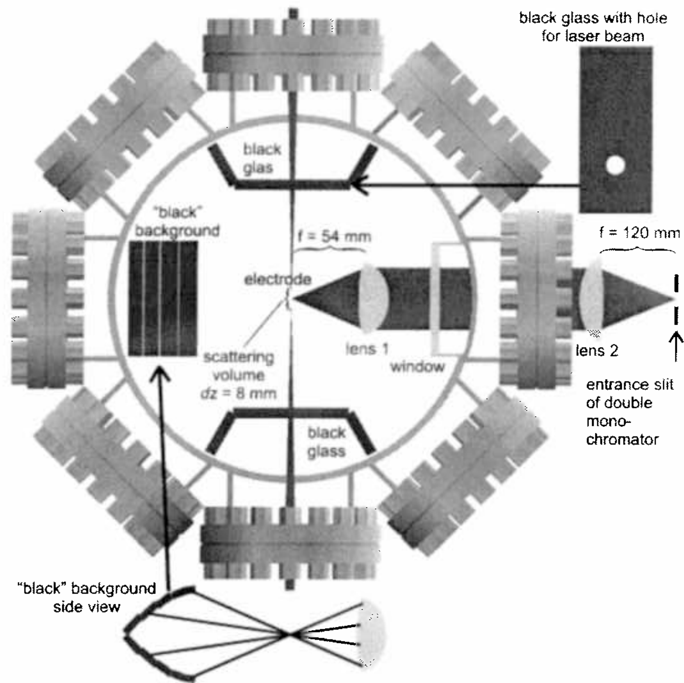

Figure 3: *Additional stray light reduction and detection optics*

The gate signal is produced with a Digital Delay Generator (DG535, Stanford Research), which is triggered by the Q-switch electronic of the pump-laser. The gate is opened 50 ns before pulses from scattered photons arrive at the discriminators and is typically open for 400 ns to permit the registration of the time behaviour of the scattered light during 350 ns. In order to facilitate further investigations of flourescence the gate times and delay times can be changed easily.

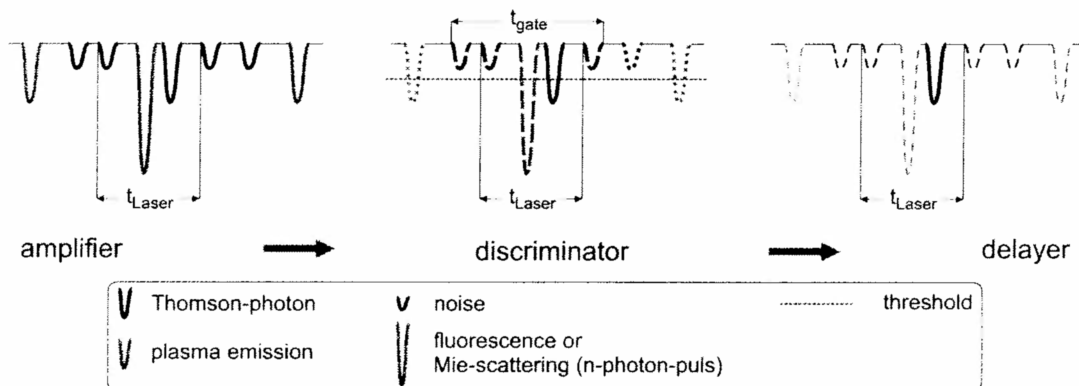

Figure 5: *Gating and noise reduction*

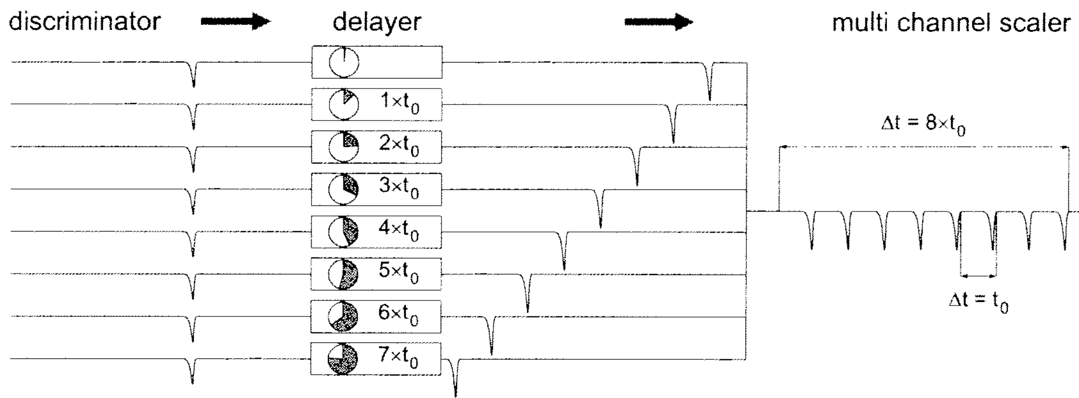

Figure 6: *Separation of pulses in time*

To utilize a single multi channel scaler (time resolution 5 ns) with its single input, the eight simultaneous photomultiplier signals have to be serialized in order to be recorded individually. For this purpose they are fed into individual delay units (see Figure 6). The delay time is set to $\Delta t_i = t_0 \times (i-1)$ with i = 1, ..., 8 being the channel number and t_0 = 500 ns, thereby separating the different channels by gaps of 100 ns. The multi channel scaler itself is again triggered by the Digital Delay Generator and records the serialized chain of photomultipier signals as a sequence of eight individual pulses.
After an integration time that ranges from 1 to 4 million laser shots sufficient pulses of the scattered light have added up in each channel for a significant analysis. The sum of the count rates in all channels yields the electron density (calibrated by Rayleigh scattering). The electron temperature is deduced from the spectral distribution, taking into account the finite width of the spectral channels as determined by the dimensions of the optical fibres.

Outlook

Within the next months the presented system will be set up at a GEC-cell. The scattered light will be observed under an angle of 140° which yields a broader Thomson profile. In this setup the first lens will be outside the discharge chamber to avoid coating.

Time Behaviour of Various Emissions in a Modulated Hydrogen Microwave Discharge

N. Lang(1), M. Kalatchev(2), M. Käning(1), B.P. Lavrov(2), J. Röpcke(1)
(1)Institut f. Niedertemperatur-Plasmaphysik, 17489 Greifswald, R.-Blum-Str. 8-10, Germany
(2)Faculty of Physics, St.-Petersburg State University, 198904 St.-Petersburg, Russia

Introduction

The production of H atoms in discharges plays an important role in many applications of plasmas, e.g. deposition processes or surface treatment. In particular pulsed microwave plasmas turned out to be very efficient for that purpose and are therefore of great interest, e.g. [1,2]. In this contribution the temporal behaviour of various emissions in a modulated hydrogen microwave discharge is studied by time-resolved optical emission spectroscopy (OES). The time-resolved evolution of atomic emission of H and Ar atoms is compared with the emission of the radiative dissociation continuum of the hydrogen molecule ($a^3\Sigma_g^+ \rightarrow b^3\Sigma_u^+$ electronic transition) and with the emission of Q-branch lines of (2-2) band of the Fulcher-α band system ($d^3\Pi_u^- \rightarrow a^3\Sigma_g^+$). Various methods have been used for the determination of translational, rotational, vibrational and Balmer lines excitation temperatures. The experimental results were analysed in relation to the dissociation of molecular hydrogen in the discharge.

Experiment

The measurements were performed in a planar type of microwave discharge [3], modulated by rectangular pulses with a frequency of 500 Hz at 50% duty cycle (gas flow: 50 sccm, H_2+Ar (0.3%), pressure: 50 Pa). The small amount of Ar was added to work as a probe for the temporal development of the electronic parameters. The power coupled into the discharge was 3.6 kW in the active phase and 600 W in the afterglow. The spectrometric system provided necessary spectral (0.006 nm) and time (10 μs) resolution. In addition to the optical multi-channel analyser (OMA) with a gated intensifier a photomultiplier with several interference filters was used for the detection of the hydrogen dissociation continuum and as a reference of atomic hydrogen lines (H_α, H_β).

Results and Discussion

We measured the intensities of the first five Q-branch lines of (2-2) Fulcher-α band, the dissociation continuum (at 214, 239 and 265 nm) and the first five Balmer lines. In the experiment a principle difference in the behaviour of H_2 molecular lines and of the dissociation continuum (Fig. 1b) on one side and of H atomic lines on the other side was observed. As an example the H_β emission intensity is shown in Fig. 1a which does not reach a complete saturation within the pulse width of 1 ms. The signals of the photomultiplier and of the OMA system are in relatively good accordance. In contrast to Fig. 1a the emissions in Fig. 1b follow the shape of the microwave power pulse and have a maximum in the first part of the pulse. The phenomenon is analogous to that observed in [4,5]. Within about the first 250 μs the emissions reached a plateau, which is connected to a steady state of the discharge.

In order to get in addition to the power input also an optical reference signal, which is connected to the density and the energy of the electrons a small admixture of Ar (0.3%) was used. The intensity changes of this rare gas reflect the changes in excitation only because its concentration is constant. The object of observation was one of the brightest Ar lines

(750.387 nm) which is usually supposed to be excited by direct electron impact and therefore commonly used in actinometry. In Fig. 1b the behaviour of the Ar line intensity is compared with those of the molecular lines and the dissociation continuum. This proves that the population of excited molecular levels is mainly governed by direct electron impact. In the case of the H atoms obviously other processes are involved (Fig. 1a). Most probably it is the manifestation of the competition between direct and dissociative electron impact excitations [6].

For the determination of the gas temperature three well known optical methods have been used, namely: 1) determination of the rotational temperature in the molecular ground $X^1\Sigma_g^+$, v=0 vibronic state from the rotational intensity distributions in several vibronic bands of Fulcher-α band system (v'=v"=0 - 4) and $j^3\Delta_g^- \rightarrow c^3\Pi_u$ (v'=v"=0 - 2) bands according to the scheme proposed in [7] (see also [8,9]); 2) Doppler broadening of molecular lines, and 3) Doppler broadening of H_α line, taking into account the fine structure [10]. A comparison of the values obtained by these different methods shows a good accordance within the errors of the measurement (Tab. 1). One may see that in contradiction with recent work [11] we have rather good ability to get the gas temperature.

The temperature variations in time derived from the Doppler broadening and from rotational line intensity distributions as well as the excitation temperature corresponding to populations of level n=6 and 7 of atomic hydrogen are presented in Fig. 2a. One may see that in the active phase it grows from 600K to 1100K. Again the translational temperature of the molecules is in good accordance with the rotational temperature of the ground state. Doppler broadening of the H_α line shows slightly higher translational temperature probably due to the dissociative excitation.

Fig. 2b presents the variation in time of the vibrational temperature derived from measured ratio of Q1 line intensities in (0-0) and (2-2) Fulcher-α bands proposed in [12]. One may see that in our conditions T_{vib} is growing up to 4000 K during the active phase of the discharge. Because of low intensities of the molecular lines T_{vib} could not be measured in the afterglow.

The populations of the atomic hydrogen levels n=3 - 7 (Fig. 3), divided by their degeneracy, show a decrease of the excitation temperature derived for two adjacent levels. The lowest measured values obtained for the levels with n=6,7 are close to the gas temperature, which can be seen in Fig. 2a. This is an evidence of the important role of collisions of excited atoms with heavy particles in our conditions (see also recent calculations [13]).

The method of estimation of the dissociation degree of hydrogen from measured ratio of certain atomic and molecular emissions has been proposed in [14]. In the present work the method was extended to use the intensity of a Balmer line and only one rotational line of the Fulcher-α bands (we used Q1 in (2-2) band). An additional correction term has to be introduced to describe the temperature dependence of the population of the selected rotational level. Fig. 4a shows the time behaviour of the results for H_α and H_β. The error bars reflect only random errors of the intensity measurements. The dissociation degree, as defined in [14], increases during the pulse period and reaches a value of ≈16%. The normalised intensity ratio of Balmer lines to the argon line shows qualitatively the same shape in the active phase, Fig. 4b.

The data presented in the contribution will be used in further *quantitative* analyses of excitation and relaxation kinetics in the plasmachemical reactor under the study.

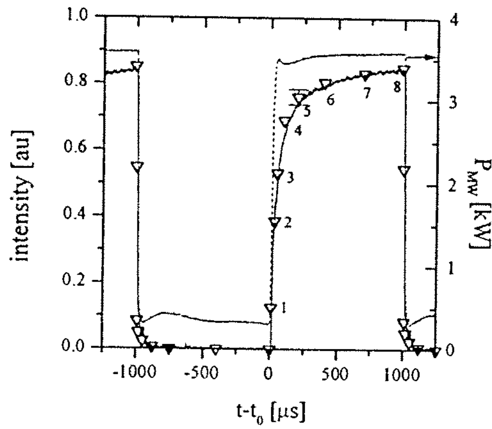

Figure 1a: *Time evolution of H_β emission with microwave power as a reference (- - photo multiplier with interference filter, ∇- OMA system)).*

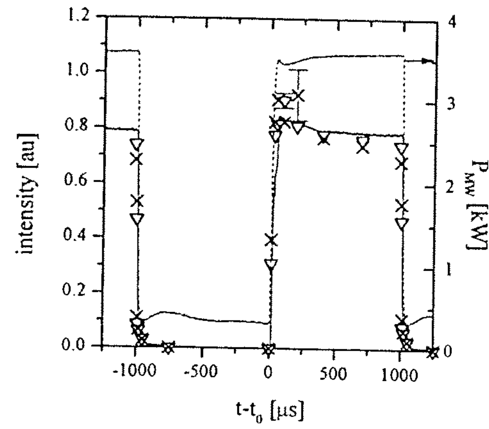

Figure 1b: *Time evolution of H_2 emission: (∇) $d^3\Pi_u^- \rightarrow a^3\Sigma_g^+$, v'=v''=2, (—) $a^3\Sigma_g^+ \rightarrow b^3\Sigma_u^+$ transitions and Ar emission (×) (750.387nm, 4p'-4s' transition) with microwave power as a reference.*

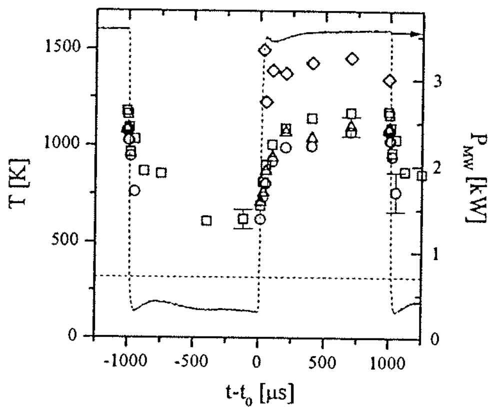

Figure 2a: *Variation in time of the gas temperature derived from H_α (□) and H_2 (o) line Doppler broadening and from rotational line intensity distribution of $d^3\Pi_u^- \rightarrow a^3\Sigma_g^+$, v'=v''=2 transition (Δ) as well as the excitation temperature defined on H atomic level population density (◊).*

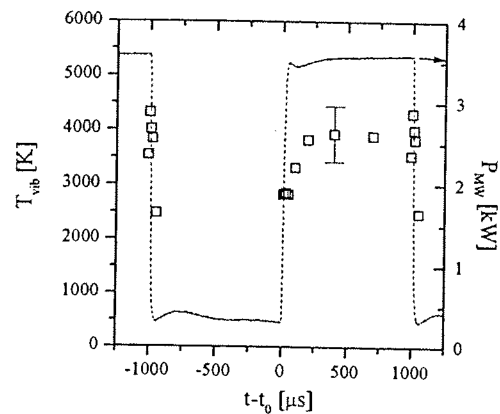

Figure 2b: *Variation in time of the vibrational temperature derived from lines of $d^3\Pi_u^- \rightarrow a^3\Sigma_g^+$ transition.*

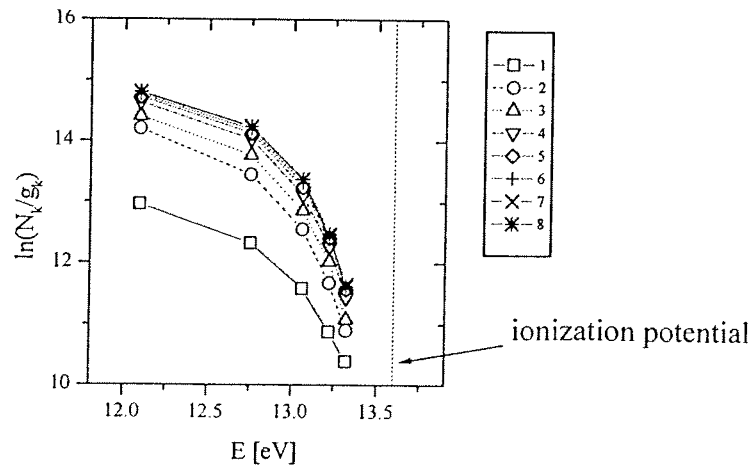

Figure 3: *Population of atomic hydrogen levels (n= 3-7) divided by degeneracy in dependence of level energy (1-8 corresponds to the time points of Fig. 1a).*

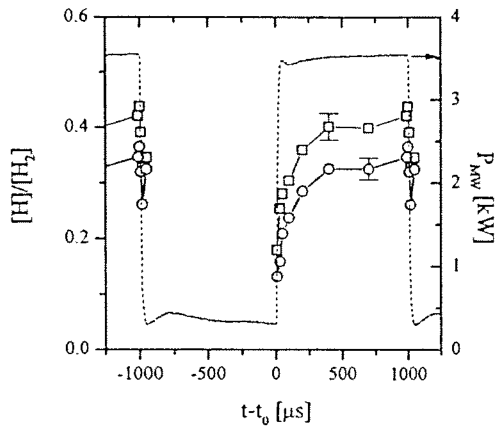

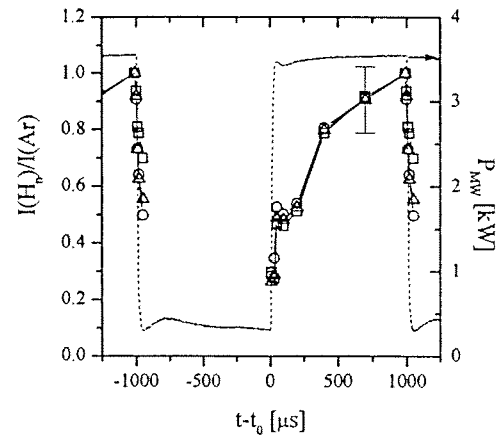

Figure 4a: *Ratio of atomic to molecular hydrogen concentrations derived from intensity ratios of Balmer H_α (□), H_β (o) lines to Q1 line of (2-2) Fulcher-α band.*

Figure 4b: *Normalised ratios of Balmer H_α (o), H_β (Δ), H_γ (□) lines to the intensity of the Ar 750.387 nm line.*

Method	Transition	Lines	Gas Temperature T_g, K					mean value
			(0-0)	(1-1)	(2-2)	(3-3)	(4-4)	
Rotational line Intensities	$d^3\Pi_u^- \rightarrow a^3\Sigma_g^+$	Q-branch	1310 (30)	1190 (90)	1060 (30)	780 (40)	1060 (70)	1060(150)
	$j^3\Delta_g^- \rightarrow c^3\Pi_u$		1120 (50)	1000 (40)	890 (50)	-	-	
Doppler Broadening	$d^3\Pi_u^- \rightarrow a^3\Sigma_g$	Q1	1030(100)	1020	1100	970	1010	1070 (80)
		Q2	1050	1090	1040	1080	1100	
		Q3	980	1110	1030	1120	1180	
		Q4	1060	1050	1280	-	-	
		Q5	1240	1000	1000	-	-	
	H(3→2)	H_α	1170 (50)					

Table: *Survey about gas temperature in the active phase of the microwave discharge derived from Doppler broadening of H_2 and H_α lines and from rotational line intensity distributions in different H_2 band systems.*

References

[1] H. Chatei et al., *Diamond Relat. Mater.* **6**, 1997, pp. 505.
[2] A. Hatta et al., *Plasma Sources Sci Technol.* **5**, 1996, pp. 235.
[3] A. Ohl in Microwave Discharges, C.M. Ferreira & M. Moisan, Plenum Press, 1993.
[4] A. Gamero et al., *J. Appl. Phys.* **65** (6), 1989, pp. 2199.
[5] G. Himmel et al., *J. Phys. IV France* **8**, 1998, pp. 327.
[6] B.P. Lavrov, *Opt. Spectrosc.* **42** (3), 1977, pp. 250.
[7] B.P. Lavrov, *Opt. Spectrosc.* **48** (4), 1980, pp. 375.
[8] S.A. Astashkevich et al., *J. Quant. Spectrosc. Radiat. Transfer* **56** (5),1996, pp. 725.
[9] M. Käning et al., XIV. ESCAMPIG 1998, Europhys. Conf. Abstr. **22H**, pp. 506.
[10] B.P. Lavrov et al., Frontiers in Low Temperature Plasma Diagnostics II., 1997, pp. 169.
[11] L. Tomasini et al., *J. Phys. D: Appl. Phys.* **29**, 1996, pp. 1006.
[12] B.P. Lavrov and V.P. Prosikhin, *Opt. Spectrosc.* **58** (3), 1985, pp. 317.
[13] A.V. Cheboratev et al., XXIII ICPIG (Toulouse, France) 1997.
[14] A.M. Devyatov et al., *Opt. Spectrosc.* **71** (6), 1991, pp. 910.

Diagnostic studies of a capacitively coupled RF plasma containing CH_4-H_2-Ar

Part II: On CH_4 dissociation and hydrocarbon plasma chemistry

M. Käning[(1)], J. Röpcke[(1)], C. Lukas[(2)], T. Kawetzki[(2)],
V. Schulz-von der Gathen[(2)], H.F. Döbele [(2)]

[(1)] *Institut f. Niedertemperatur-Plasmaphysik, 17489 Greifswald, R.-Blum-Str. 8-10, Germany*
[(2)] *Institut für Laser- und Plasmaphysik, Universität GH Essen, 45117 Essen, Germany*

Introduction

The decomposition of methane in a variety of Plasma Enhanced Chemical Vapor Deposition processes is of interest, because of its role for the deposition of thin carbon films. A prerequisite for the understanding of the ongoing plasma chemistry and kinetics *in situ* is a detailed knowledge of the main plasma parameters. In particular, electron induced dissociation processes of hydrocarbon source gases in relation to parameters of the electron gas are still not satisfactorily investigated. In this contribution the dissociation of CH_4 and the production of the methyl radical and of stable hydrocarbons (C_2H_2, C_2H_6) has been studied for the first time at a capacitively coupled RF discharge containing CH_4-H_2-Ar with tunable infrared diode laser absorption spectroscopy (TDLAS), 1mm microwave interferometry and emission spectroscopy simultaneously. In addition to the concentration of hydrocarbons the electron density, the gas temperature and emission line intensities have been monitored. On the basis of these measurements a model has been developed that describes the chemical processes and allows to identify the main plasma chemical reaction paths.

Experimental

The infrared absorption spectroscopy in the spectral region between 3 and 20 μm with tuneable diode laser (TDLAS) is a modern promising technique to measure number densities of molecules and radicals in the electronic ground state directly, as well as neutral gas temperatures [1] and to investigate dissociation processes of molecular low-temperature plasmas [2-5]. The infrared TDLAS technique has proven to be the most useful technique because it can also measure the concentrations of related species provided they are IR active. World-wide TDLAS is still at the beginning of utilisation for plasma diagnostics.

For TDLAS diagnostics reported here a new compact and transportable tunable infrared multi-component acquisition system, "IRMA" has been used. The IRMA system contains 4 independent laser stations which can be temporally multiplexed. Based on rapid scan software using direct absorption with sweep integration, the absolute concentrations of several molecular species could be measured simultaneously (For more details: J. Röpcke et al, '"*IRMA" a Tunable Infrared Multi-Component Acquisition System for Plasma Diagnostics*', in the same issue). The infrared diode laser beam from the IRMA system entered the plasma chamber via KBr windows making two passes through the plasma. After leaving the plasma reactor the infrared laser beam was focused on a HgCdTe detector.

A 1mm microwave heterodyne interferometer allows the measurement of electron densities down to some 10^9 cm^{-3}. Emission spectroscopy is used to determine the gas temperature. The discharge chamber with a movable electrode system is typically at pressures of about 100 Pa at gas flows of 66 sccm.The complete experimental set-up is decribed in detail in Part I of this contribution (C. Lukas et al, '*Diagnostic Studies of a Capacitively Coupled RF Plasma Containing CH_4-H_2-Ar, Part I: On the Species Concentrations and Temperature*

Distributions', in the same issue). The peak height of the second derivative signal was calibrated against the R(19) line of N_2O at 606.146 cm^{-1} which has a known line strength. The concentration of the methyl radical was then calculated using the method described earlier [7].

Results and Discussion

In Fig.1 the degree of dissociation of methane in Ar or H_2 as the power was increased is shown. The degree of dissociation of CH_4 depends nearly lineraly, while the electron density seems to part into two linear dependences from power (Fig. 2). At the maximum of power a degree of dissociation of methane of about 15 % was achieved. The electron density had a value of about $4x10^{10}$ cm^{-3}.

The hypothesis that the methyl free radical is the most likely precursor for forming carbon films is now gaining acceptance. In the RF plasma under study the methyl radical density increased with power (Fig. 3), but shows a less pronounced dependence compared to the degree of dissociation. There were noticeable differences of about 25 % of the methyl radical densities in Ar and in H_2. At a power of 100 W a CH_3 density of about $5x10^{12}$ molecules cm^{-3} was found in H_2. The ethane density (not shown here) showed a similar behaviour compared to the methyl radical density: increasing with power up to about $3x10^{14}$ molecules cm^{-3} in the hydrogen case and significant lower densities in argon. For the density of acetylene also an increasing with power was obtained (Fig. 4). But the behaviour in Ar or H_2 was just opposite to CH_3 and C_2H_6: higher acetylene densities were measured in Ar.

To study further the influence of the Ar or H_2 on the dissociation of methane their content was varied in the plasma. The electron density showed a maximum at about 1:1 of Ar and H_2 (Fig. 5). In contrast the degree of dissociation of methane has lower values at a higher electron density. Unfortunately it is very difficult to monitor the electron energy distribution function (EEDF) in layer forming plasmas. It is known that the rate for electron impact dissociation depends strongly on the EEDF [8]. As a result of a changed plasma mixture a modified EEDF can be expected leading to different conditions and therefore to changed contributions of channels for electron impact dissociation of methane (comp. Fig. 7). The variation of the concentration of the methyl radical as a function of Ar content is comparable to the variation of the electron density. But it should be noted, that for the acetylene production and also for the relative emission intensity of the CH radical, measured by OES, a qualitatively different behaviour could be observed: a maximum at about 80 % Ar content (Fig. 6).

In addition to a changed electron density and most probably also a modification of the EEDF a variation of the Ar and H_2 content leads to modified chemical conditions in the plasma. At high hydrogen partial pressure the chemical reaction of methane with hydrogen atoms forming methyl is of importance [9]. The dominant reaction forming ethane is recombination of methyl radicals. The abstraction of hydrogen atoms from ethane to produce the ethyl radical and then ethylene is most probably too slow to be important under the conditions of study. An alternative source of C_2H_4 is the rapid reaction of the CH radical with methane which has a relatively high rate coefficient. According to the model presented in ref. [6] the largest source of acetylene is electron impact dissociation of ethylene. In [6] it was experimentally checked that acetylene does not arise from ethane. In Fig.7 a reaction scheme showing the major contributing steps in CH_4- H_2-Ar plasmas is presented.

A detailed chemical modelling of plasmas containing hydrocarbons can be found in: L. Mechold et al *„TDL Absorption Diagnostics and Chemical Modelling of Microwave Plasmas Containing Hydrocarbons"* in the same issue.

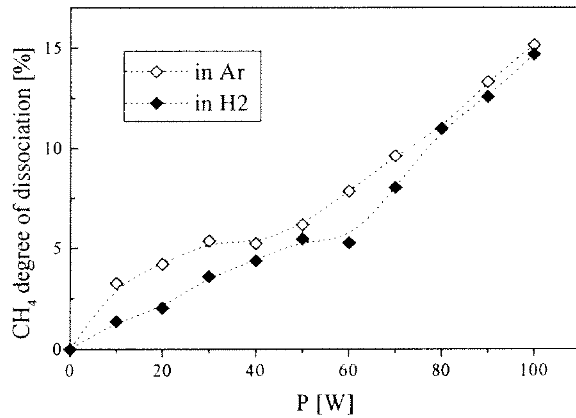

Figure 1: *The degree of dissociation of methane in Ar or H_2 as the power was increased. (p= 100 Pa, 50% CH_4)*

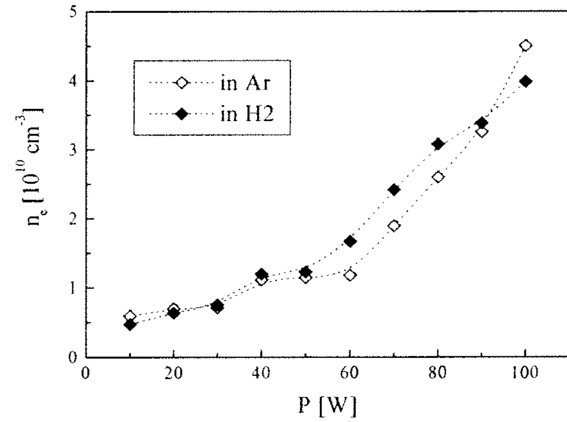

Figure 2: *Electron density as a function of power. (p= 100 Pa, 50% CH_4 in Ar or H_2)*

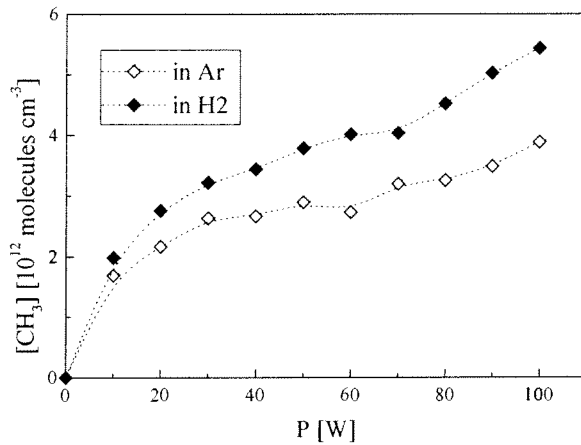

Figure 3: *Variation of the concentration of the methyl radical as a function of power. (p= 100 Pa, 50% CH_4 in Ar or H_2)*

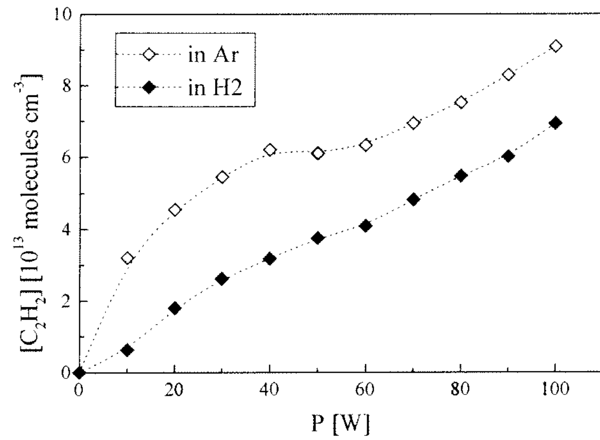

Figure 4: *Variation of the concentration of acetylene as a function of power. (p= 100 Pa, 50% CH_4 in Ar or H_2)*

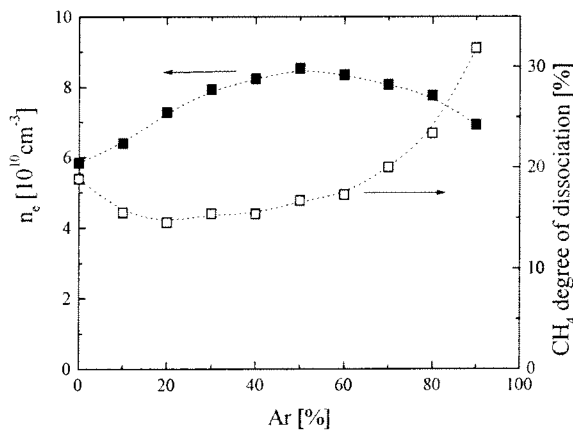

Figure 5: Electron density *and degree of dissociation of methane as a function of Ar content (P= 100 W, p= 100 Pa, 10% CH_4, Ar+H_2: 90%).*

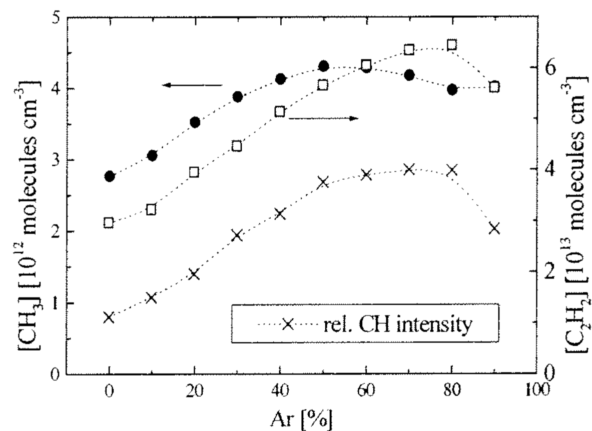

Figure 6: *Variation of the concentration of the methyl radical and acetylene and of the relative CH band intensity as a function of Ar content (P= 100 W, p= 100 Pa, 10% CH_4, Ar+H_2: 90%).*

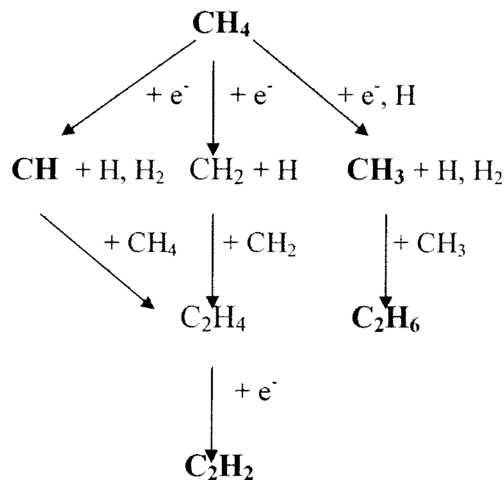

Figure 7: *Reaction scheme showing the major contributing steps in CH_4- H_2-Ar plasmas. Several minor steps have been omitted for clarity.*

Acknowledgement

This work is a collaboration performed in the frame of the Sonderforschungsbereich 191 „Physik der Niedertemperaturplasmen" and of the Sonderforschungsbereich 198 „Kinetik partiell ionisierter Plasmen"

References

[1] M. Haverlag, Stoffels E., Stoffels W. W., Kroesen G. M. W. and De Hoog F.J. , J. Vac. Sci Technol. *A* **14**, 380 (1996)

[2] P. B. Davies and P. M. Martineau, Adv Mater. **4**, 729 (1992)

[3] S. Naito, N. Ito, T. Hattori, and T. Goto, Jpn. J. Appl. Phys. **34**, 302 (1995)

[4] Haverlag M., Stoffels E., Stoffels W. W., Kroesen G. M. W. and De Hoog F.J. , J. Vac. Sci Technol. A **12**, 3102 (1994)

[5] J. Röpcke, L. Mechold, M. Käning, W.Y. Fan, P.B. Davies, Plasma Chem. Plasma Process., in print.

[6] W.Y. Fan, P.F. Knewstubb, M. Käning, L. Mechold, J. Röpcke, P.B. Davies, J. Phys. Chem. A, submitted.

[7] W.Y. Fan, J. Röpcke, P.B. Davies, J. Vac. Sci. Technol. A **14**(1996) 2970-2972

[8] T. Nakano, H. Toyoda, H. Sugai, Jap. J. Appl. Phys. **30**, 2912-2915 (1991).

[9] W. L. Hsu, J. Appl. Phys. **72**, 3102-3109 (1992).

Diagnostic Studies of a Capacitively Coupled RF Plasma Containing CH_4-H_2-Ar

Part I: On radial species concentrations and temperature distributions

C. Lukas(1), T. Kawetzki(1), V. Schulz-von der Gathen(1), H.F. Döbele (1),
M. Käning(2), J. Röpcke(2)
(1) *Institut für Laser- und Plasmaphysik, Universität GH Essen, 45117 Essen, Germany*
(2) *Institut für Niedertemperatur-Plasmaphysik, 17489 Greifswald, R.-Blum-Str. 8-10, Germany*

Introduction

CH_4 and H_2 containing plasmas are finding widespread application for the deposition of thin carbon layers. Admixture of noble gases like argon results in an enhanced film growth rate [1]. Both the spatial structures in these discharges and the plasma chemical processes determine the film homogeneity. Neither of these influences is understood satisfactorily. Here, a combination of diagnostic methods is applied for the first time simultaneously to a capacitively coupled RF discharge with CH_4-H_2-Ar mixtures to achieve detailed spatially resolved information on basic plasma parameters and an insight into the ongoing plasma chemistry. A movable electrode system and the Abel inversion technique allow the determination of radial distributions of plasma parameters. We report on the measurements of gas temperatures, line intensities and electron densities based on emission spectroscopy and 1-mm microwave interferometry. The concentration of the methyl radical, the most likely precursor for forming carbon films, was measured by tunable infrared laser absorption spectroscopy.

Experimental

Capacitively coupled RF discharges are in industrial use for surface modication techniques like coating, cleaning or etching of microstructures. The GEC reference cell was introduced as a standard device allowing the comparison between different research groups and industrial devices. Here a device was set up with dimensions and other parameters typical for the GEC reference cell but allowing spatially resolved measurements between its stainless steel electrodes. This is achieved by mounting the electrodes (diameter= 100mm, distance= 25mm) in a supporting frame that can be moved over a range of 100 mm within a cuboid vacuum vessel [1]. The output power of a commercial transceiver (10 - 100W) is coupled through a matching box to the electrodes. The difference between supplied and reflected power is measured with a SWR and is termed here as 'power'. During the experiments the gas flow is controlled by mass flow controllers for Ar, H_2 and CH_4. Throughout all experiments presented here the gas flow was set to 66 sccm. Three sets of windows were mounted on opposing sides of the chamber to allow the optical pathes of the three installed diagnostic techniques to overlap in the center of the chamber (Fig.1). The first of these is a 1 mm microwave heterodyne interferometer (MWI). It allows after Abel inversion to determine radial profiles of the electron densities at different positions between the electrodes with a transverse spatial resolution of about 6 mm. The detection limit amounts to several 10^9 cm^{-3} [2]. The second diagnostic is tunable infrared diode laser absorption spectroscopy (TDLAS). The system installed here incorporates 4 laser stations allowing the simultaneous measurement of the absolute concentrations of several molecular species with absorption bands between 3 and 20µm (described in more detail elsewhere in this issue: „*J.Röpcke et al: 'IRMA' A Tunable*

Infrared Multi-Component Acquisition System for Plasma Diagnostics"). The last diagnostic technique overlapping at the same position with the other ones is optical emission spectroscopy (OES). The radiation from the discharge is linked via an optical fiber to a 2 m grating spectrograph. The resolution of about 0.03 nm is mainly determined by the installed intensified CCD camera. From spectra taken near a wavelength of 600 nm the gas temperature was measured as rather commonly done from rotational lines of Fulcher diagonal bands [4]. Another spectral interval at 434 nm was observed where emission lines from hydrogen, argon, argon ions and CH bands with excitation energies between 2 and 25 eV can be detected simultaneously. From these lines at least information on changes of the electron energy distribution function (EEDF) can be derived. It would be very valuable to get information on the EEDF - determining all electron driven plasma processes - from emission spectroscopy since the typical method to measure an EEDF by Langmuir probes is difficult to incorporrate in layer forming plasmas.

Results and Discussion

Since the admixture of argon is claimed to change the production rate of hard carbon layers drastically [1], the discharge was examined for different admixtures of argon, methane and hydrogen. Furthermore, the influence of the input power was analyzed. Fig. 2 shows the power dependence of the electron density for a 50% admixture of argon and of hydrogen to methane. The increase is for both cases overlinear with power from about $n_e = 5 \cdot 10^9\,cm^{-3}$ to $4 \cdot 10^{10}\,cm^{-3}$. This changes totally for argon fractions of more than 90% where the measured electron densities are a factor of 4 higher [3]. This can be attributed to the energies transfered into the ro-vibrational states of the molecules at only a few eV of excitation energy. Especially for the argon admixture a change in the slope of the increase is observed for a power of 50 W. At this point the discharge probably changes from the α to the γ mode. The effects on the dissociation of methane are presented in part II of this contribution.

A second series of experiments was performed with various admixtures of methane to hydrogen or argon at constant power. The resulting gas temperatures are presented in figs. 3 and 4. While the gas temperature decreases with increasing methane content in argon it nearly stays constant for the H_2-CH_4 variation. This again reflects that in the pure molecular gas mixtures the number of energy consuming ro-vibrational states does not change significantly while with increasing argon content the energy can heat the gas. At the same time the number of 'hot' electrons with energies sufficient to dissociate the molecules increases. This results in a drastic increase of the degree of dissociation of methane for low methane fractions in argon (Fig.5). This is in contrast to the behaviour in hydrogen where the hydrogen dissociation probably is more energy effective. For admixtures of more than 20% of CH_4 the discharge is determined by the methane resulting in equal degrees of dissociation.

The figures are based on present line-integrated measurements. The electron densities were calculated assuming a homogeneous distribution in the volume between the electrodes. Since the diagnostics chords overlap at the same position in the center plane of the discharge chamber spatially resolved parameters can be calculated from the line-integrated measurements by Abel inversion from a series of measurements for different displacements of the electrode system. Fig. 6 shows symmetrized radial profiles for the gas temperature, the electron density and the methyl radical concentration. The profiles show very significant differences that are yet not completely understood. The electron density displays a characteristic maximum just inside the electrode edge and a dip in the center of the discharge. This behaviour was also observed in pure gases [3], with probes [5] and in computer models [6]. The gas temperature and the CH_3 concentration, however, show a main maximum in the

center of the discharge and a secondary maximum at a distance of 25 (CH_3) and 50 (T_g) mm from the discharge axis. On the basis of the temperature profile shown in figure 6 the increase of the CH_3 concentration in the center could be explained by additional thermally activated chemical processes.

Acknowledgement

This work is a collaboration performed in the frame of the Sonderforschungsbereich 191 „Physik der Niedertemperaturplasmen" and of the Sonderforschungsbereich 198 „Kinetik partiell ionisierter Plasmen"

References

[1] D.M.Gruen, C.D.Zuiker, A.R.Krauss and X. Pan; J.Vac.Sci.Technol. A; **13** (1995) 1628

[2] N.Niemöller, V.Schulz-von der Gathen, A.Stampa, H.F.Döbele: Plasma Sources Sci.Technol. **6** (1997) 478

[3] C.Lukas, M.Müller, V.Schulz-von der Gathen, H.F.Döbele, Plasma Sources Sci.Techn. (accepted for publication)

[4] S.A.Astashkevich, M.Käning, E.Käning, N.V.Kokina, B.P.Lavrov, A.Ohl. and J.Röpcke; JQSRT; **56** (1996) 725

[5] L.J.Overzet and M.B.Hopkins; J.Appl.Phys.; **74** (1993) 4323

[6] D.P. Lymberopoulos, D.J. Economou; Appl.Phys. Lett.; **63** (1993) 2478

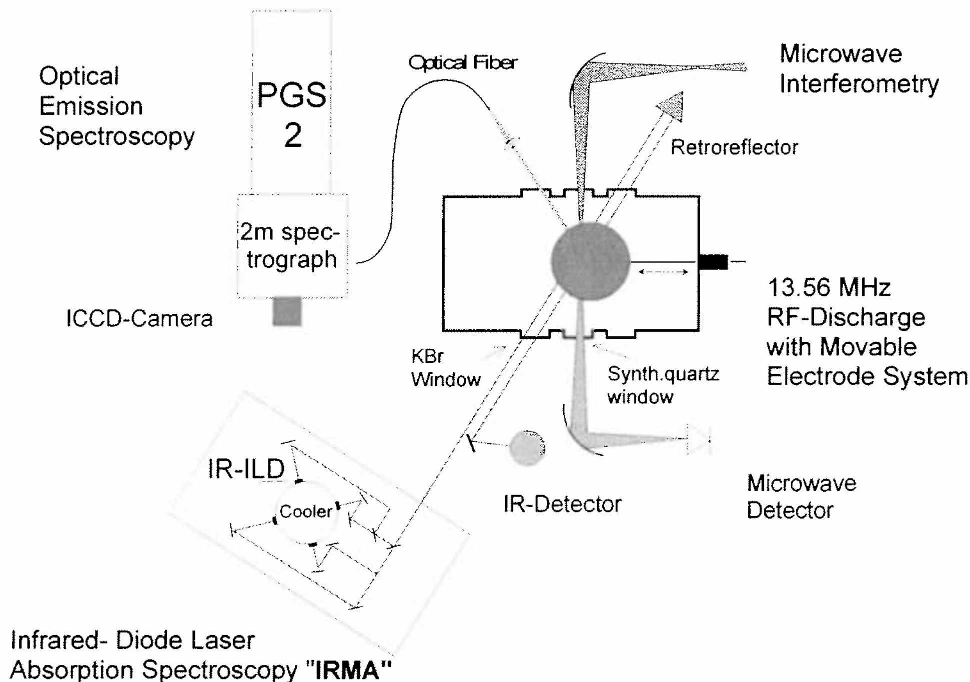

Fig.1: *Sketch of the experimental set-up showing the overlap of the optical chords of the applied diagnostics in the center of the movable electrode assembly*

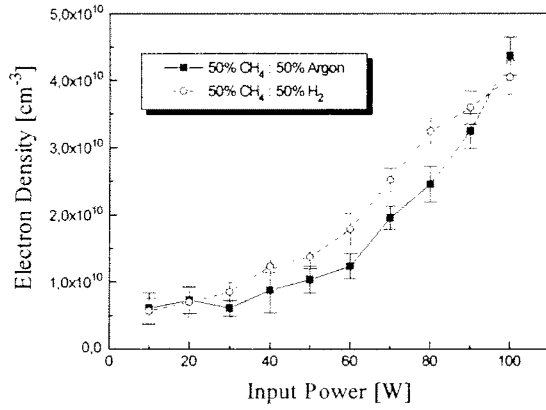

Fig.2: *Electron density from microwave interferometry for a 1: 1 mixture of CH_4 and hydrogen resp. argon (p=100 Pa, total flow 66 sccm)*

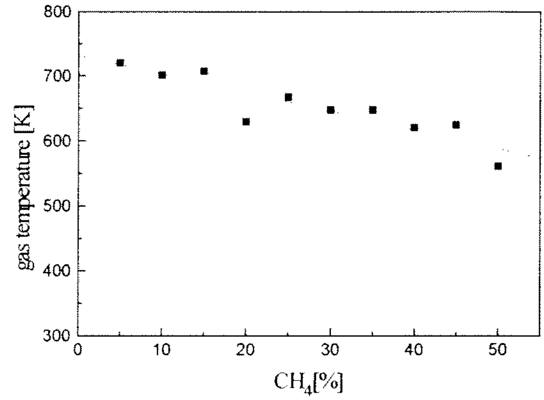

Fig.3: *Gas temperature from OES as function of the methane admixture to argon (p=100 Pa, P=100 W, total flow 66 sccm)*

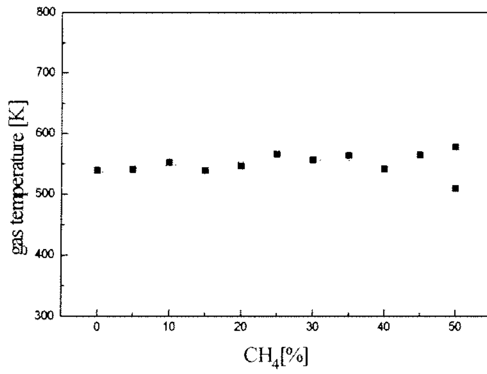

Fig.4: *Gas temperature from OES as function of the methane admixture to hydrogen (p=100 Pa, P=100 W, total flow 66 sccm)*

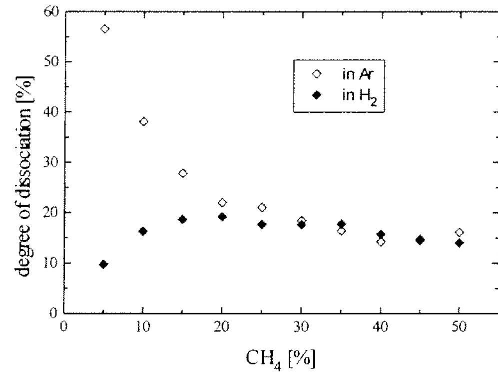

Fig.5: *Degree of dissociation of methane as function of the admixture of methane to argon and hydrogen respectively (p= 100 Pa, P=100W, ϕ =66 sccm)*

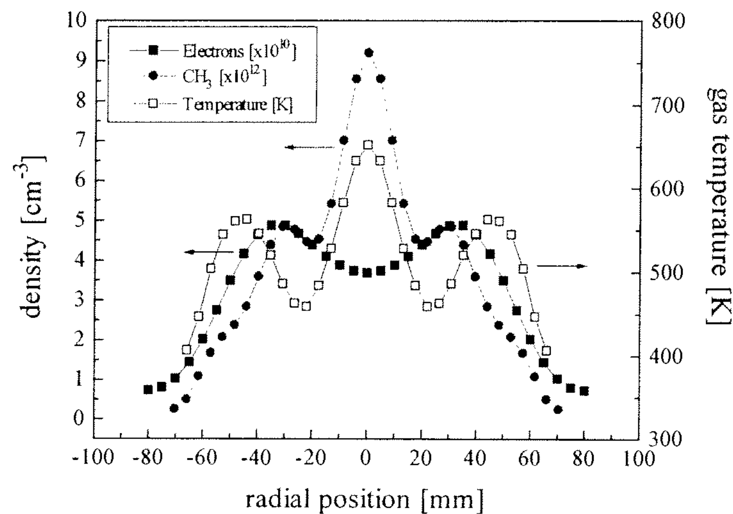

Fig.6: *Radial distribution of gas temperature, CH_3 concentration and electron density (p= 100 Pa, P=100 W, 25% CH_4: 75% H_2)*

A 2-photon LIF study on the expansion behaviour of a plasma beam generated from a mixture of Ar and H_2.

S. Mazouffre, M.G.H. Boogaarts, I.S.J. Bakker, J.A.M. van der Mullen, and D.C. Schram.

Department of Applied Physics, Eindhoven University of Technology, P.O. Box 513, 5600 MB Eindhoven, The Netherlands.

In an expanding plasma created by a cascaded arc from a Ar-H_2 mixture, spatially resolved densities, temperatures, and velocities of ground state atomic hydrogen are obtained by applying two-photon excitation laser induced fluorescence. The axial velocity profile of H indicates a strong coupling between Ar and H atoms. However, the atomic hydrogen density and temperature profiles can not be fully described in terms of a supersonic expansion model in contrast with the profiles of Ar. There are several indications that hydrogen atoms can escape the supersonic domain by a scattering process.

1 Introduction

When a cascaded arc[1] created plasma is expanded into a vacuum vessel, a versatile high quality particle beam is obtained. Such an expanding plasma beam has many applications[2] like fast deposition of thin layers, etching of microstructures, and atom or ion source in the field of nuclear fusion. In all these applications atomic species, and especially atomic hydrogen, play a key role. Moreover, these atomic species are often transported from the plasma source to a downstream region using argon as a carrier gas. Thus from a technological point of view, but also from a fundamental perspective, it is of interest to study the properties of a beam generated from a mixture of Ar and H_2 and to understand them in terms of transport of hydrogen atoms from a reservoir to a processed surface.

2 Experimental

The experimental 2-photon excitation laser induced fluorescence (TALIF) method has already been described in detail elsewhere[3,4,5]. A simplified scheme of the experimental set-up is depicted in figure 1.

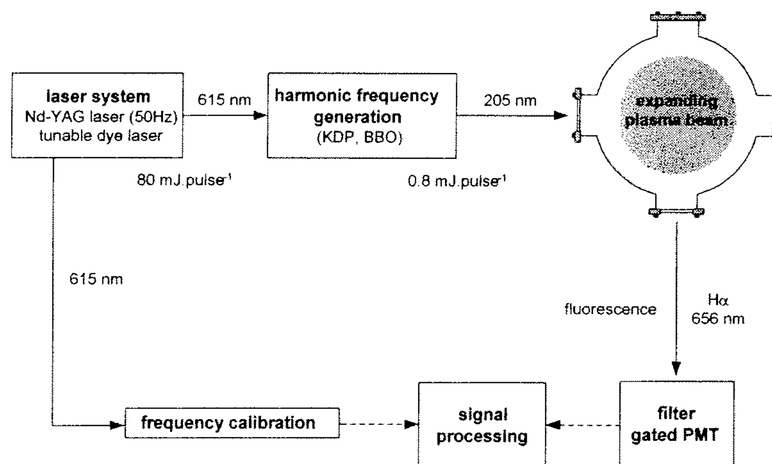

Fig. 1: *Scheme of the TALIF set-up.*

In this experiment the cascaded arc is operated on 40 A dc current and with a cathode voltage of 100 V. A gas flow of 3.0 slm Ar and 0.5 slm H_2 is used.

A tunable 50 Hz Nd:YAG pumped dye laser delivers radiation around 615 nm. The output of the dye laser is frequency-tripled using non-linear optical crystals resulting in 0.8 mJ of tunable UV light around 205 nm with an estimated bandwidth of 0.15 cm^{-1}. The UV beam is focused into the plasma jet and the resulting fluorescence photons at the Balmer-α line are detected with a gated photo-multiplier tube. The PMT signal is then processed using a computer. The laser frequency is calibrated by simultaneous recording of the absorption spectrum of molecular iodine[6,7].
From a spectral scan over the two-photon transition several quantities are obtained. Integration of the line profile allows the determination of the relative local H density. In order to obtain absolute number densities the LIF set-up has to be calibrated. This is accomplished via a titration with NO_2 in a flow tube reactor[8]. Assuming Doppler broadening to be the main broadening mechanism, the local H temperature can be determined from the full width at half maximum. In addition, the velocity component in the direction of the laser beam is obtained from the absolute Doppler shift of the peak.

3 Results and discussion

3.1 On-axis transport

When a 3:1 Ar-H mixture at a temperature of 1 eV expands into vacuum, a value of 3800 $m.s^{-1}$ is obtained from adiabatic supersonic expansion theory[9,10], for the maximum axial velocity. Figure 2 shows a measured axial velocity profile of H atoms at 20 Pa background pressure, where the measured maximum speed is about 3800 ms^{-1}. This implies a complete coupling of Ar and H atoms at the beginning of the expansion. From the measured translational temperature the speed of sound is calculated. The Mach number ahead the stationary shock front equals 5. Axial temperature profiles depicted in figure 3 show that both position and thickness of the shock front depend on the background pressure as expected[11]. The cooling effect due to the adiabatic expansion can clearly be seen. Using Rankine-Hugoniot[12] relations, a Mach number of 3 is deduced from the temperature jump at 20 Pa.

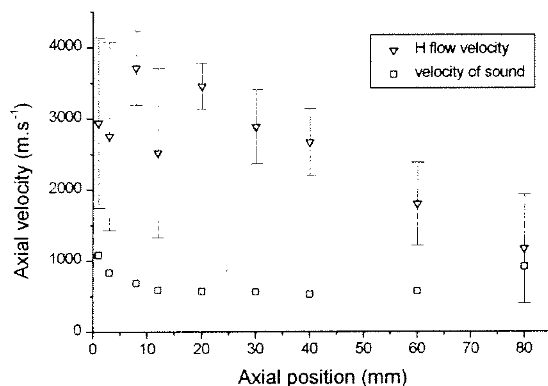

Fig. 2: *Axial velocity profile of H atoms and local velocity of sound at P_{back} = 20 Pa.*

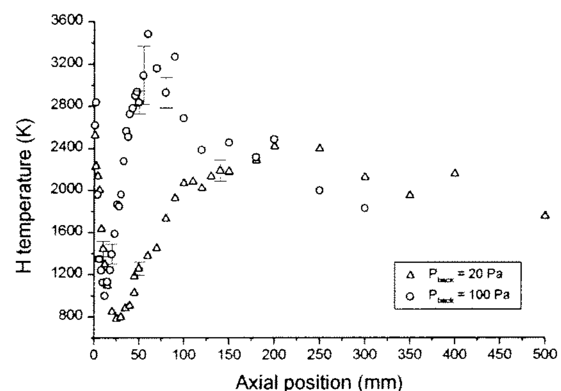

Fig. 3: *Axial temperature profile of H atoms for 2 different background pressures.*

As shown in figure 4, there is no density jump for H (only a weak structure appears at high pressure) whereas Ar density profiles, as measured by Rayleigh scattering[13], clearly show a density jump. At 20 Pa, using a Mach number equal to 5, Rankine-Hugoniot relations give a value of 3.6 for the density ratio ahead and behind the shock. This disagreement can be

explained by the fact that the H mean free path for momentum exchange[14] increases with the decreasing Ar density along the beam axis, as it is shown in figure 5. Ahead the shock front, the mean free path is already larger than the shock thickness. Thus the argon stationary shock front is transparent to H atoms. When increasing the background pressure, the mean free path decreases, but is still in the order of the shock thickness.
The fact that at the outlet of the source, the steepness of the density decay depends on the background pressure means that H atoms in the plasma jet core receive information from the background, which is impossible in a supersonic expansion. The only way to explain such a phenomenon is to allow for diffusion of H atoms out of the supersonic domain meaning that H is not perfectly confined inside the argon jet.

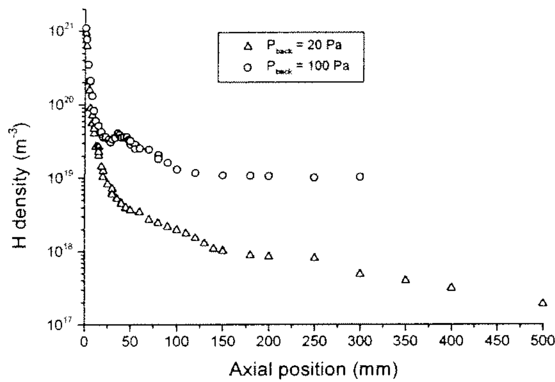

Fig. 4: *Axial density profile of H atoms for 2 different background pressures.*

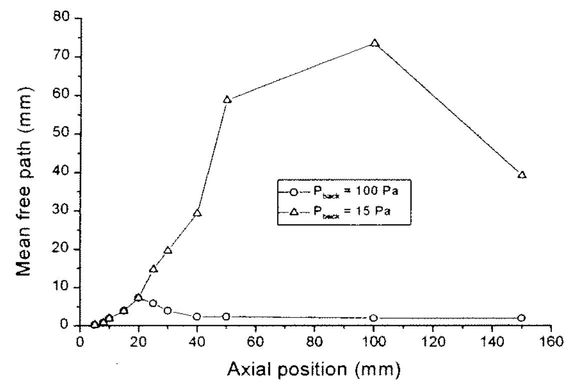

Fig. 5: *H-Ar momentum exchange mean free path for 2 background pressures.*

3.2 Confinement

Figure 6 shows radial profiles of the density, temperature and radial velocity of atomic hydrogen at a distance z = 8 mm from the arc nozzle for two different background pressures. The peaks in the temperature profiles are associated with the argon barrel shock structure[10,11] where H atoms collide with Ar atoms and then transfer there kinetic energy, i.e. there directed velocity, into thermal motion. Therefore the radial velocity decreases across the barrel shock. When the plasma jet radius is defined to be the distance between the two temperature peaks, the jet radius is found to decrease with increasing background pressure. The temperature profiles clearly show an adiabatic cooling effect inside the plasma jet, depending on the distance traveled from the nozzle. The low background gas temperature outside the plasma jet core, can be either explained by the close presence of a wall, or may be a sign for the existence of an independent structure like a vortex which prevents this cold gas to mix with the hot gas from the downstream region of the vessel.
Looking at the shape of the radial density profiles one might conclude from the broader and less explicit structure at 100 Pa background pressure, that the confinement of H atoms inside the argon beam is less at higher background pressure. The proof for the opposite comes from a comparison of the absolute on-axis H density for the two background pressures. The lower absolute H density in the 20 Pa case can only mean that in between the nozzle and the measurement position already more H is lost from the plasma jet than in 100 Pa case. The high density in the wings of the 100 Pa profile can then be explained by a slow outward diffusion of H. It just takes more time for H to pass the Ar barrel shock. This is consistent with the much lower radial velocity observed in the high background pressure case.

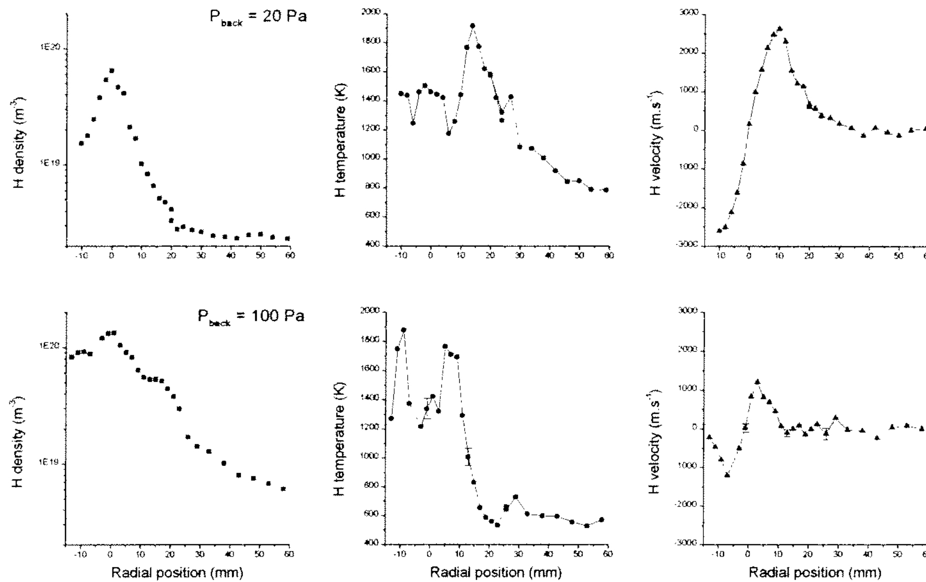

Fig. 6: *Radial profiles of the density, temperature and radial velocity of H atoms at z = 8 mm for two different background pressures.*

4. Conclusion

Two-photon excitation LIF of ground-state atomic hydrogen has been used to study the supersonic expansion of a Ar-H mixture. From the axial profiles it is concluded that the Rankine-Hugoniot relations are not obeyed for atomic H: no H density jump across the Ar shock front is observed. This can be explained by the large mean free path of H. Because of the mass difference between argon and hydrogen, H atoms can easily escape the supersonic domain of the plasma beam in radial direction by a scattering process. This is confirmed by the radial profiles of density, temperature and radial velocity of H, as well as by a comparison for different background pressures.

Acknowledgments

This work is financially supported by the Netherlands Technology Foundation (STW) and by the Netherlands Fundamental Research on Matter Foundation (FOM).

References

[1] G.M.W. Kroesen, D.C. Schram, and J.C.M. de Haas, *Plasma Chem. Plasma Proc.* **10**, 531 (1990).
[2] R.F.G. Meulenbroeks et al., *Plasma Sources Sci. Technol.* **4**, 74 (1995).
[3] J.R. Dunlop et al., *Plasma Chem. Plasma Proc.* **12** (1), 157 (1992).
[4] U. Czarnetzki et al., *J. Opt. Soc. Am. B.* **11**, 2155 (1994).
[5] M.G.H. Boogaarts et al., *Proc. 8 Int. Symp. Laser-aided Plasma Diagnostics* (LAPD-8), 109 (1997).
[6] S. Gerstenkorn and P. Luc, Atlas de spectroscopie d'absorption de la molecule d'iode, CNRS, Paris, 1978.
[7] S. Gerstenkorn and P. Luc, *Rev. Phys. Appl.* **14**, 791 (1979).
[8] D.W. Setser, *Reactive Intermediates in the Gas Phase*, Academic press, New York, 1979.
[9] H. Ashkenas and F.S. Sherman, *Proc. Rarefied Gasdynamics*, **4**, Academic press, New York, 1966.
[10] G. Scoles, ed., *Atomic and Molecular Beam Methods*, Oxford University press, 1988.
[11] H. C. W. Beijerinck et al., *Chem. Phys.* **96**, 153 (1985).
[12] L. Landau and E. *Liftshitz, Fluid Mechanics*, Pergamon, London, 1989.
[13] M.C.M. van de Sanden, Ph.D Thesis Eindhoven university of Technology, 1991.
[14] A.V. Phelps, *J. Phys. Chem. Ref. Data* **21**, 883 (1992).

Concentrations of molecular species in a CH_4/O_2-plasma: a simple numerical model and measurements by infrared absorption spectroscopy

C. Busch, I. Möller, H. Soltwisch
Institut für Experimentalphysik V, Ruhr-Universität Bochum, Germany

1. Introduction

Methane plasmas with varying admixtures of hydrogen and oxygen are used for the deposition of hydrogenated carbon films. Oxygen is employed as a source gas in order to influence the properties of the deposited films. In addition to directly changing the plasma-surface interactions, it also has a large effect on the discharge properties by expanding the plasma bulk chemistry as well as being a source of negative ions.

Measurements of molecular parameters are performed using absorption spectroscopy with diode lasers [1]. Due to the large number of molecular species and the complexity of the discharge processes, these measurements can provide only incomplete information on the molecular plasma properties. Therefore the experiments have to be complemented by numerical modeling as an additional "diagnostic" tool aiding in the interpretation of the experimental data and providing predictions for further experimental investigations.

2. Experiment

The discharge reactor set-up together with the absorption spectrometer is shown schematically in figure 1. We are studying a capacitively coupled RF (13.56 MHz) discharge operated at typical pressures of 0.1-10 mbar and input powers of 5-100 W. Methane and oxygen are used as source gases with flow rates of a few sccm.

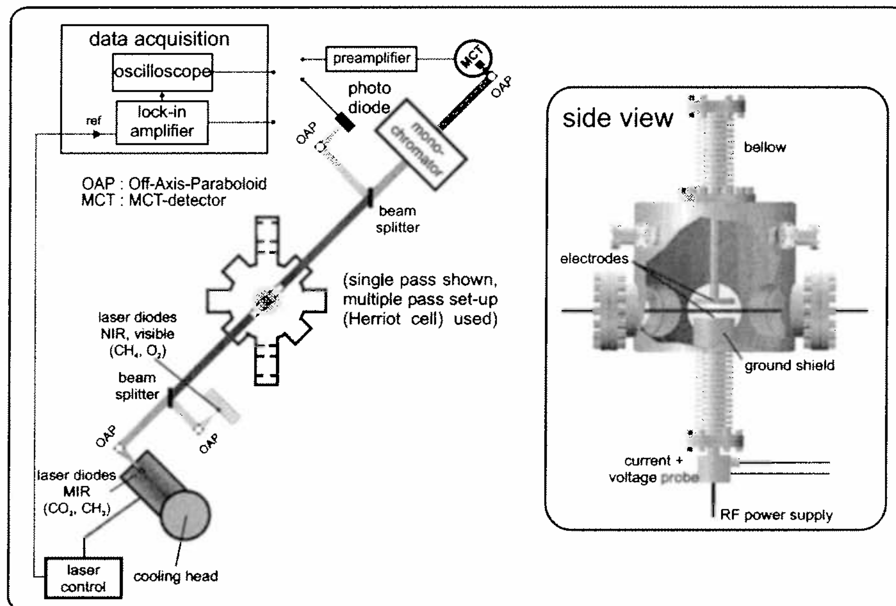

Figure 1. *Set-up of the absorption spectrometer*

In the visible and the near infrared we use single mode laser diodes operating at or close to room temperature, whereas for larger wavelengths we employ multimode lead salt laser diodes requiring cryogenic cooling.

To be able to measure molecular densities of species that have small absorption line strengths or exist only in minute concentrations, an optical multipass set-up (Herriott

design) has been implemented which increases the absorption path length by a factor of forty.

In the case of saturation-free absorption, the transmitted intensity is given by the Beer-Lambert law which can be linearized for absorptions of less than ten percent according to

$$I(L) = I_0 \exp(-Sn\, g(\tilde{\nu})L) \approx I_0(1 - Sn\, g(\tilde{\nu})L) \tag{1}$$

(with the line strength S, the particle density n, the line profile function $g(\tilde{\nu})$ and the absorption length L).

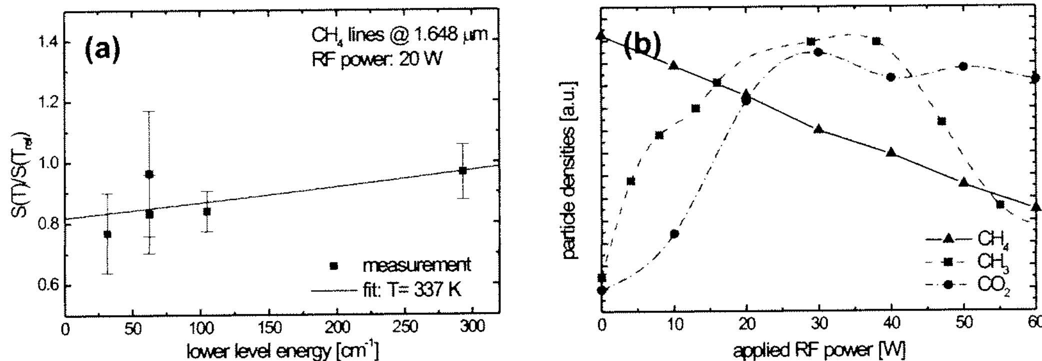

Figure 2. *(a) Determination of the vibrational temperature, (b) Normalized molecular densities as a function of applied RF power*

By use of equation (1), the determination of several molecular quantities is possible. Due to the small spectral width of the laser lines, the Doppler broadened absorption line profile is resolved and from its half-width the translational molecular temperature can be determined directly. The area under the line profile is proportional to the product of line strength S and molecular density n. The former depends on the population distribution of the energy levels and therefore on the rovibrational temperature. Because of this, the rovibrational temperature and molecular density have to be determined simultaneously unless the temperature is known a priori. This can be done by considering the normalized quantity $n \times S(T)/S(T_{ref})$ for different lines as a function of the lower level energy, resulting in a curve with a form determined by the temperature and absolute values depending on the density. Both quantities can then be obtained by a numerical fit of the theoretical function. As can be seen in figure 2(a), the vibrational temperature of methane for a RF power of 20 W is only slightly higher than room temperature.

For peak absorptions down to a few percent, the absorption profile can be measured directly by scanning the laser wavenumber and detecting the transmitted intensity. To increase sensitivity we employ the technique of derivative spectroscopy, where the laser wavelength is modulated sinusoidally at a high frequency and harmonic components of the transmitted signal are detected.

Presently we have laser diodes for the detection of the feed gases methane and oxygen, for the reactive methyl radical and for carbon dioxide as a stable product. Some measured molecular densities as a function of the applied RF power are shown in figure 2(b). Obviously, the functional dependence of the different species on RF power differs greatly, and the identification of chemical reaction pathways and the influence of species that have not been measured is difficult to deduce from these data.

To help in the interpretation of the measured quantities' dependence on external plasma parameters, a comparatively simple, one-dimensional, time independent numerical model is being developed.

3. Modeling

There exist some very elaborate numerical models (e.g. [2]) that try to achieve an accurate numerical representation of the complete plasma discharge. However, due to their numerical complexity and computational demands, they are not well suited for an "everyday" use. For this reason we have started to develop a simplified plasma model with an emphasis on the description of the gas phase plasma chemistry, allowing us to treat the discharge electron and ion kinetics in a rather crude approximation.

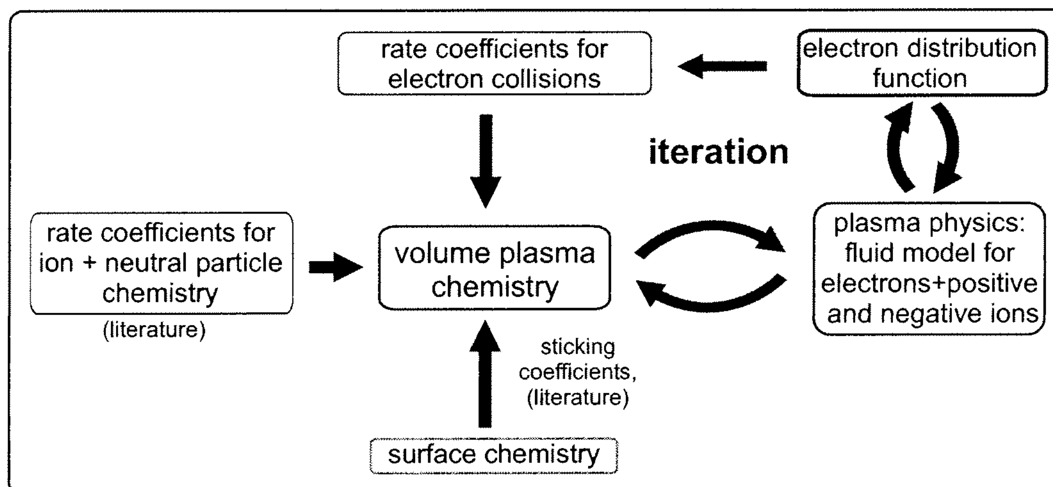

Figure 3. *Set-up of the numerical model*

The complex problem is subdivided into three separate parts: a module for the solution of the volume plasma chemistry, a fluid model describing the interaction of the charged particles and a Boltzmann equation solver. These modules iterate until self-consistency is achieved (figure 3). By using this approach, the model becomes easily modifiable and extendable and can be run on a desktop computer. Although in practice plasma-surface interactions play an important role, their detailed numerical description is rather difficult, since so far little experimental data on surface processes is available. For this reason surface reactions are taken into account very crudely by the use of sticking coefficients in the boundary conditions for the molecular fluxes at the electrodes. The only spatial dimension considered is the axis perpendicular to the electrodes.

The chemistry in the plasma volume is described by a system of rate equations with free and ambipolar diffusive transport for neutrals and ions, respectively. In figure 4(a) the results of a test calculation for a simplified hydrocarbon system with CH_4 as the source gas are shown. The position at zero cm corresponds to the discharge center.

The rate coefficients for reactions induced by electron collisions have to be calculated by averaging the energy-dependent cross sections with the electron distribution function (EDF) which is expected to be non-Maxwellian for the small degree of ionization found in our discharge. In the model, the EDF is calculated from the two-term Boltzmann equation using the approximations of "local approach" and "effective RF heating field". Some calculated EDFs showing strong deviations from Maxwellian or Druyvesteyn distributions and a sensitive dependence on the plasma composition are plotted in figure 4(b).

The main purpose of the fluid model is to derive the ambipolar electric field needed for the calculation of the EDF and the ambipolar diffusion coefficients of the ions. Instead of dealing with the full variety of charged species, positive and negative ions are combined into one positive and one negative representative "species", respectively, resulting in a three component fluid model. Quasineutrality, time independence and the

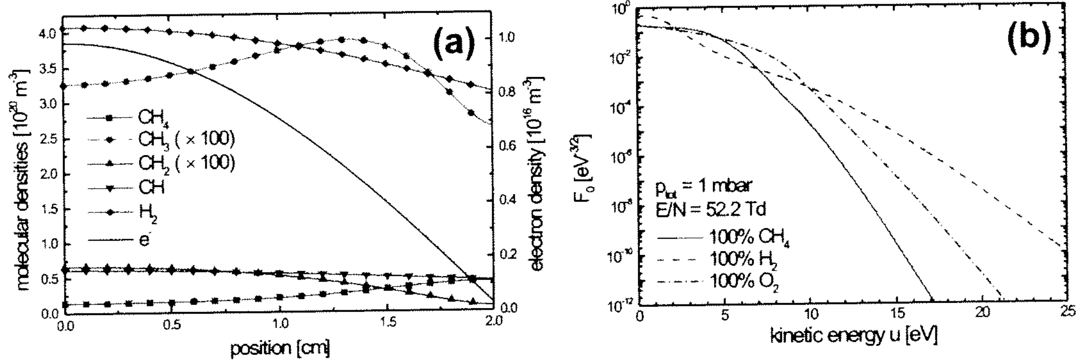

Figure 4. (a) Axial molecular density profiles, (b) Calculated EDFs for different gases

absence of stationary currents are assumed. Together with the flux and particle continuity equations, a differential system of seven unknowns $(n_{i+}, n_{i-}, n_e, \Gamma_{i+}, \Gamma_{i-}, \Gamma_e, E_{amb})$ and seven equations is obtained that is solved with appropriate boundary conditions for the fluxes at the center and the plasma-sheath interface.

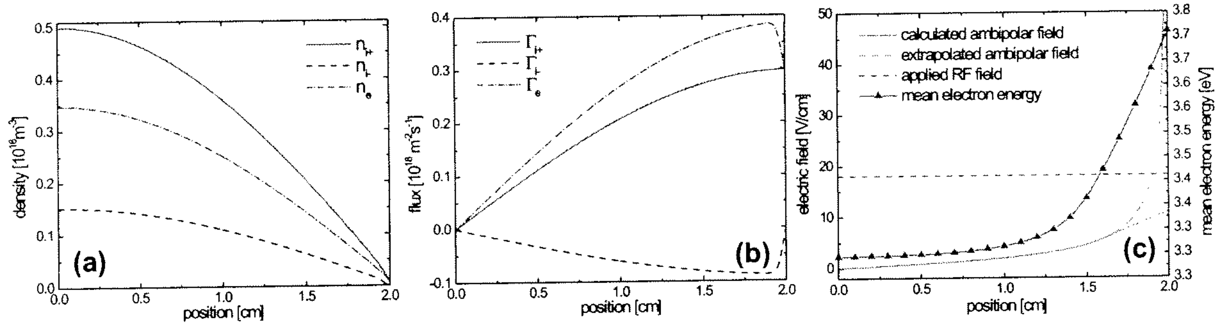

Figure 5. Calculated self-consistent set of plasma quantities

The results of a self-consistent calculation of the plasma physics modules are shown in figure 5. Figures 5 (a) and 5 (b) show the axial distribution of charged particle densities and fluxes for a mixture of CH_4, H_2 and O_2. A significant content of negative ions formed in the discharge can be seen. In figure 5(c) the corresponding ambipolar and RF electric fields together with the mean electron energy are plotted.

In the present stage of development, self-consistency between the calculated electron distribution function and the fluid module has been achieved. The next step is the inclusion of the chemistry module in the iteration process.

4. Conclusions

Numerical modeling and experimental investigations will be used interactively to obtain a better understanding of the complex plasma environment. We expect the numerical plasma description to be accurate enough to predict and identify the important discharge processes, thus aiding the interpretation of measurements made by absorption spectroscopy and Thomson scattering (see the contribution of M. Kaczor in these proceedings).

This work was supported by the SFB 191 of the "Deutsche Forschungsgemeinschaft".

[1] P. B. Davies and P. M. Martineau. Infrared laser diagnostics in methane chemical-vapor-deposition plasmas. *J. Appl. Phys.*, 71:6125–6135, 1992.

[2] E. Gogolides. A synthetic approach to rf plasma modeling verified by experiments: Demonstration of a predictive and complete plasma simulator. *Jpn. J. Appl. Phys.*, 36(4B):2435–2442, 1997.

Thomson Scattering Using ICCD Detectors in Photon Counting Mode for Low-temperature , Low-density Plasma Diagnostics

S.A.Moshkalyov, C.Thompson, T.Morrow and W.G.Graham
School of Mathematics and Physics, Queen's University of Belfast, Belfast, Northern Ireland, UK

Introduction

Thomson scattering (TS) with high-repetition rate lasers has been recently introduced as a diagnostic of electron parameters in low-density, low-temperature gas discharge plasmas [1]. This method has some distinct advantages over other techniques (like electric probes) which are commonly used to measure electron parameters in gas discharges. The interpretation of incoherent Thomson scattering data is straightforward, in most cases it can be considered as a non-intrusive technique, and high spatial and temporal resolution in measurements can be achieved.

However, due to the small cross-section of light scattering by free electrons (~ 10^{-24} cm^2) the intensity of the scattered light is extremely low. In this case, noise characterization of the detector is essential. To improve signal-to-noise ratios, measurements are typically made by accumulating the signals over 10^3 – 10^4 laser pulses. In most TS experiments single-channel low-noise photomultiplier tubes are used for light detection. A further development of the diagnostic is to the use of novel multichannel detectors such as gated intensified CCD's which record the entire TS spectrum and thus reduce considerably the time needed for measurements of the electron parameters.

Experimental

In our laboratory, a Thomson scattering diagnostic system using 10 Hz YAG laser (0.5 J at 532 nm) and ICCD detector (Andor Technology Ltd, with intensifier diameter of 25 mm, maximum gain of ~500, CCD size of 378x585 pixels, effective pixel size of ~28 μm) is under development. It will be used as a diagnostic for the gas discharge plasma in the GEC reference cell, which can operate in both inductive and capacitive modes. The scattered light is collected at a right angle to the probing laser beam. In this case, the total number of photo-electrons generated in a photocathode by scattered light is given by

$$N_{TS} = \frac{E_l}{h\nu_l} L N_e \sigma_T \Delta\Omega T \eta$$

where E_L is the laser energy, $h\nu_L$ is the energy of laser photon, L is the length of scattering volume, N_e is the plasma density, σ_T is the TS cross section, $\Delta\Omega$ the solid angle of light detection, T is the transmission of the optical system and η is the quantum efficiency of the photocathode. For the conditions of our experiment (second harmonic of YAG laser, laser wavelength = 532 nm, E_L=0.5 J, L = 1 cm, $\Delta\Omega$ ~ 0.1 srad, T ~ 0.3, η ~ 0.1) the total TS signal is as low as ~10-20 photo-electrons per laser pulse for a plasma electron density of 10^{11} cm^{-3}.

The signal-to-noise ratio is determined by photon statistics and the noise of detector, i.e.:

$$SNR = \frac{N_{TS}}{\sqrt{N_{TS} + N_n}}$$

where N_n is a sum of background light signals (plasma emission and stray light) and detector dark signal (readout noise is negligible for ICCD's). Dark noise can be considerably reduced by cooling of the detector (three stage thermoelectric cooling system provides temperatures as low as - 20^0 C or - 40^0 C with air or water assisted cooling, respectively). Fast gating of the ICCD (minimum gate width is ~ 4 ns) makes it possible to eliminate practically the contribution of plasma background emission.

At very low light levels, photon counting technique may be utilized to improve signal-to-noise ratios. This method of detection is based on the fact that light signals (i.e., signals generated by the photo-electrons) generally have higher amplitudes than dark signals. Hence, by setting an appropriate threshold, reliable detection of single photo-electron events can be achieved. However, cross-talk between adjacent channels in ICCD (spreading of the signal generated by a single photo-electron into several pixels of CCD) causes an uncertainty in the appropriate threshold level. This problem can be solved by binning of groups of adjacent pixels into super-pixels with area larger than the area of a signal cross-talk (about 3 pixels). It should be noted that the binning is also helpful in terms of the readout time reduction. The readout process for a fully resolved image (378x585 pixels) takes about 3 seconds, i.e., is much slower than the minimum period between laser pulses (0.1 seconds). On the other hand, dark noise rises in proportion with the number of pixels. Therefore, the optimum size of super-pixels (M_{sp}) is determined by a trade-off between the image readout speed and dark noise which will allow a reliable detection of single photo-electron events.

The statistics of signals under high cross-talk conditions have been experimentally studied using a dc light source, to determine suitable algorithms for accurate measurements of low-light level signals. It turned out that at - 20^0 C (air assisted cooling) an accurate setting of threshold for photon-counting is possible for number of pixels M_{sp} ~10, with the readout time of about 1 second. With deeper cooling (water assisted) dark current is expected to be reduced in ~10 times, to reach the level which allows to increase M_{sp} to about 100, with the image readout speed corresponding to the maximum available frequency of the laser pulses (10 Hz).

References

[1] K.Muraoka, K.Uchino and M.D.Bowden, Plasma Phys. Control. Fusion , **40**, 1221-1239 (1998)

Reactive Species densities measured by optical emission and absorption spectroscopy in a chlorine inductively coupled plasma

F. Neuilly*, J.P. Booth, N. Sadeghi and L. Vallier**
Laboratoire de Spectrométrie Physique, Univ. J. Fourier- Grenoble I, (France)
*Centre Commun CNET-STMicroelectronics, 38926 Crolles Cedex
** CNET 28 Chemin du vieux chêne, 38243 Meylan Cedex

Introduction

Plasma processing is widely used by semiconductor manufacturers. As the minimum feature size has shrunk, anisotropic etching has become necessary to transfer the photoresist pattern into the substrate. Si or Al etching processes are mainly based on chlorine chemistry (Cl_2, BCl_3). For metal interconnect etching, argon or nitrogen are added to stabilize the plasma. In Si processing, the etch rate in chlorine plasmas is lower than with fluorine, but the anisotropy is much more controlled. Furthermore, the selectivity to SiO_2 is improved with HBr addition. Measurement of plasma parameters such as reactive species densities is very important to identify dominant chemical mechanisms. Reactive species concentration variations while discharge parameters are changed can show changes in their production and loss processes. Optical emission is a simple method to monitor species density. This in-situ technique is non-perturbing but plasma changes can modify measurements. A small amount of non-reactive gas (e.g. Argon) permits the emission intensities to be correlated with concentrations. This method only gives relative concentration variations. Another method to measure concentration is UV/visible absorption spectroscopy. Absolute concentrations can be determined, provided that the radial density profile and the absorption coefficients are known [1].

Experimental procedure

The actinometry experiments were performed in an industrial helicon source. The 13.56MHz-RF power in the source can vary from 0 to 2000 W. This source generates a high density plasma (10^{12} cm^{-3}) at low pressure (until 2 mTorr). The substrate can be RF-biased using a 600 W power supply at 13.56 MHz. In these experiments, a silicon wafer was placed on the substrate holder, but without polarization ; so that there were negligible amounts of etch products in the plasma. The absorption experiments were performed in an ICP source (RF power 0 to 600 W), which has lower plasma density (10^{11} cm^{-3}). The working pressure was 3 mTorr for the actinometry experiments but the absorption experiments couldn't be done at such a low pressure due to the weak absorption coefficient of Cl_2. The typical range of pressure for our absorption experiment was from 10 to 50 mTorr.

Results

In order to estimate the Cl_2 dissociation fraction, the 310 nm continuum for Cl_2 and the Argon 750.4 nm emission were monitored [2]. A simple gas-phase and surface reaction set was used.

Gas-phase Reaction	Surface Reaction
$Cl_2 + e^- \rightarrow 2\,Cl + e^-$ (k_1)	$2\,Cl + S \rightarrow Cl_2 + S$ ($\beta1$)
$Cl_2 + e^- \rightarrow Cl_2^+ + 2\,e^-$ (k_2)	$Cl_2^+ + e^- + S \rightarrow Cl_2 + S$ ($\beta2$)
$Cl + e^- \rightarrow Cl^+ + 2\,e^-$ (k_3)	$Cl^+ + e^- + S \rightarrow Cl + S$ ($\beta3$)
$Cl_2^+ + e^- \rightarrow Cl^+ + Cl + e^-$ (k_4) High energies	$Cl_2^+ + e^- + S \rightarrow 2\,Cl + S$ ($\beta4$)
$Cl_2 + e^- \rightarrow Cl^+ + Cl + e^-$ (k_5)	

The rate of change of the Cl_2 concentration is given by

$$\frac{\partial[Cl_2]}{\partial t} = \text{Input } Cl_2 \text{ Flux} - k_1 n_e[Cl_2] - k_2\, n_e[Cl_2] - k_5 n_e[Cl_2] - D_{Cl2}[Cl_2] + \beta_1[Cl]^2$$

Where D_{Cl2} is the diffusion coefficient of Cl_2.

Dissociation and recombination are very fast reactions compare to the resident time so the $\beta_1[Cl]^2$ and $k_1 n_e[Cl_2]$ terms canceled themselves. Thus, at the steady state, the Chlorine concentration is proportional to $1/(n_e\text{+constant})$. So we can write

$$\frac{1}{[Cl_2]} = \frac{1}{[Cl_2]_0} + C' n_e \qquad (1)$$

Where $[Cl_2]_0$ is the chlorine concentration with no discharge.

The observed emission intensities are only due to electron impact excitation of the ground state species, $X + e^- \rightarrow X^* + e^-$, (8-9 eV for Cl_2 and 13.5 eV for Argon), so the intensities are proportional to the electron density and the ground state concentrations :

$$I_{Cl2^*} = C'\, n_e[Cl_2] \qquad (2)$$

$$I_{Ar^*} = C'\, n_e[Ar] \qquad (3)$$

As the excitation energy level is not the same for Cl_2 and Ar, but we shall assume that the electronic temperature is only function of the Pressure and the geometry of the system, and the electron density is proportional to the input power [3]. In our experiments, the electron temperature is considered to be constant. Therefore, from eq. (3), we can deduce that the Argon emission intensity is directly proportional to the electron density. Then Dividing (3)/(2) and substituting (1) into (2) we get :

$$\frac{I_{Ar}}{I_{Cl_2}} \propto \frac{n_e}{I_{Cl_2}} \propto \frac{1}{[Cl_2]} \propto \frac{1}{[Cl_2]_0} + \alpha I_{Ar} \qquad (4)$$

Figure 1 shows that If we plot the Argon to Chlorine intensity ratio versus the argon intensity, we obtain a straight line as expected with the eq. (4).

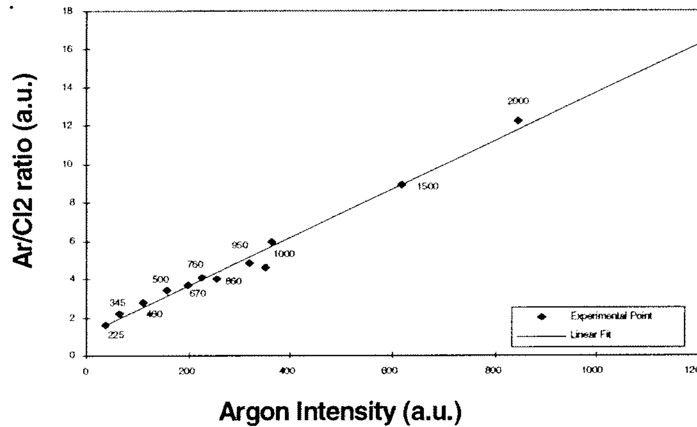

Figure 1 : Ar to Cl_2 emission ratio versus Argon intensity. Values on the plot represent the equivalent RF power.

By extrapolating the line to zero, $[Cl_2]_0$ is determined and the dissociation rate can be calculated. As shown in Fig. 2, the Cl_2 dissociation is high even at low RF power, and increases further at high RF power.

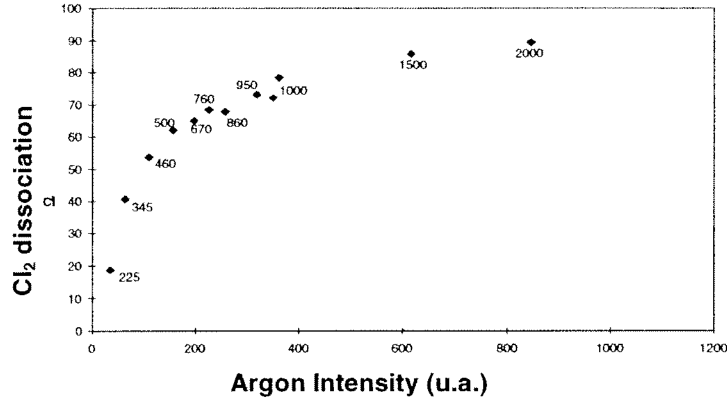

Figure 2 : Dissociation rate of Cl_2 versus the Argon intensity. Values on the plot represent the RF power source.

Whereas the actinometry technique only gives relative concentrations, absolute values can be obtained by absorption spectroscopy. With the development of the multi-channel detectors (CCD, diode array), the whole spectrum can be recorded simultaneously, greatly reducing the uncertainty coming from the lamp intensity fluctuations, and approaching the shot-noise limit in sensitivity. As10^8 photons can be counted in 1 acquisition, the signal-to-noise ratio which varies as the square-root of the number of counts is about 10^4. Hence one can easily detect 0.1% of absorption.

We have used the UV absorption technique to determine the absolute density of Cl_2 molecules in the plasma, using the Cl_2 absorption spectrum around 280-370 nm with a maximum at 320 nm [4] and thus deduce the fractional dissociation. Our experimental setup is composed of a UV beam from a 75 W Xe arc lamp that is collimated onto a UV mirror and focused by a lens into the reactor chamber. At the exit of the reactor, a lens focuses the light into a 19-cm-spectrometer . The light was dispersed on a 600 grooves/mm grating and analyzed by a 1024*256 CCD camera.

The spectrometer is controlled by a computer that can operate a shutter in front of the light beam and can also switch the RF power. Thus 4 kinds of acquisitions can be made :

$L_{off}P_{on}$: Plasma emission (Lamp OFF – Plasma ON)
$L_{on}P_{on}$: Plasma Transmission (Lamp ON – Plasma ON)
$L_{off}P_{off}$: Background (Lamp OFF – Plasma OFF) - but Gas is ON
$L_{on}P_{off}$: Lamp spectrum (Lamp ON – Plasma OFF) - ibid.

From Beer-Lambert's Law, the transmitted light is related to the cross-section σ, and the average density n along the optical path L by $I_t=I_0\exp(-\sigma nL)$.

The transmission trough the plasma is the transmitted light through the plasma divided by the light spectrum without any gas in the reactor.

$$tr(plasma) = \frac{L_{on}P_{on} - L_{off}P_{on}}{L_{on}G_{off} - L_{off}G_{off}}$$

Ideally, the transmitted spectrum of the plasma should be compared to the spectrum of the lamp without plasma and *without Cl_2 gas*. However, as the gas pressure takes a long time to stabilise, it is not practical to modulate the gas concentration. Instead, we chose to use the spectrum of the lamp transmitted through the reactor containing the Cl_2 gas as the reference spectrum. As the absorption spectrum of the gas alone can be measured with high accuracy, it is a simple matter then to correct this spectrum to obtain the lamp spectrum that would have

been obtained without gas. This was achieved in the following way. We first measured the gas transmission, defined by :

$$tr(gas) = \frac{L_{on}G_{on} - L_{off}G_{on}}{L_{on}G_{off} - L_{off}G_{off}}$$

The plasma transmission was then measured :

$$tr*(plasma) = \frac{L_{on}P_{on} - L_{off}P_{on}}{L_{on}P_{off} - L_{off}P_{off}}$$

Finally the true transmission spectrum of the plasma was determined from :
tr(plasma)=tr★(plasma)*tr(gas)

Typical spectra are shown on figure 3. They were obtained for a 30 mTorr chlorine plasma with 300 W RF power source. The Cl_2 absorption spectrum around 280-370 nm with a maximum at 320 nm [4]
The partial pressure of Cl_2 calculated from the spectrum gives around 15 mTorr.

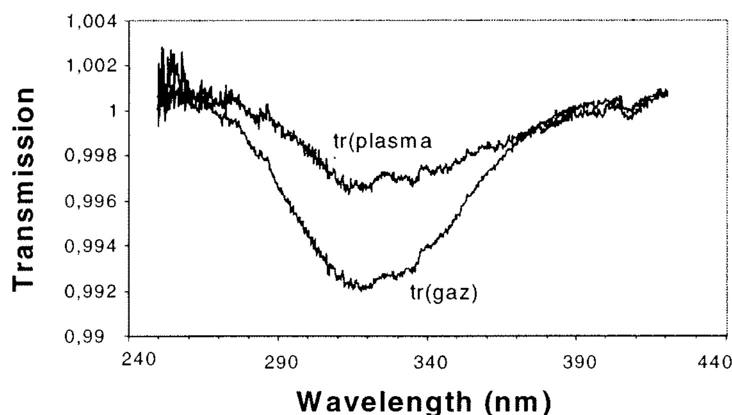

Figure3 : 30mTorr Chlorine Gas absorption (tr(gas)) compared with the 300W Chlorine plasma absorption (tr(plasma)).

Comparison with the absorption spectrum of a well-known quantity of Chlorine gas permits the degree of dissociation of Cl_2 to be determined as function of the RF source power. Differences in the shape of spectra may be explained by a modification of the rotational and vibrational excitation of Cl_2, and possibly by absorption from $SiCl_x$ etch products.

Conclusion

Two methods were used to measure the degree of dissociation of Cl_2 in different reactors. Actinometry is faster (seconds compared to tens of minutes) so that real time measurement can be made. Absorption spectroscopy gives the absolute concentration directly, can also detect other species, such as etch products imcluding SiCl, $SiCl_2$, AlCl... These methods are simple to perform compared to laser spectroscopy, although they don't have their spatial resolution.

References

[1] J.P. Booth, G. Cunge, F. Neuilly & N. Sadeghi, Plasma Source Sci. Technol. **7**, 423 (98)
[2] Donelly, J. Vac. Sci. Technol. A **14**(3), 1076 (96)
[3] C. Lee, M. A. Lieberman, J. Vac. Sci. Technol. A **13**(2), 368 (95)
[4] G. E. Gibson, O. K. Rice & N. S. Bayliss, Phys. Rev. **14**, 193 (33)

On Use of Rotational Intensity Distribution in $GK^1\Sigma_g^+ \rightarrow B^1\Sigma_u^+$ bands of H_2 for Diagnostics of Non-equilibrium Plasmas.

S.A.Astashkevich, M.V.Kalachev, B.P.Lavrov, V.L.Ovtchinnikov
Institute of Physics, St.-Petersburg State University, 198904 Russia
E-mail: lavrov@pobox.spbu.ru, http://lavserv.phys.spbu.ru

Introduction. In recent publications [1-5] the opportunity was proposed and analysed to use intensities of R-branch lines of (0-0) band in $GK^1\Sigma_g^+ \rightarrow B^1\Sigma_u^+$ electronic transitions of H_2 for the determination of the gas temperature T of low pressure non-equilibrium plasma of gaseous discharges in pure hydrogen and mixtures H_2+CH_4, H_2+N_2. The results of different works are controversial. The effective rotational temperatures of $G^1\Sigma_g^+$,v=0 vibronic state T_{rot}(G,0R) are in good [1,2,5] and in poor [3,4] agreement with gas temperatures obtained independently. In [5] this method gave acceptable results only for pressures p>20 Torr and temperatures T>800 K, while in [2] reasonable values were obtained for p≤0.3 Torr and T≈300 K. Two main assumptions common for all the works [1-5] are:

1) Honl-London factors (adiabatic rotational line strengths for Hund's cases "a,b") were used as the line strengths although it is well known that the $G^1\Sigma_g^+$ state is strongly perturbed due to the electronic-rotation coupling with several electronic states (better call it $GK^1\Sigma_g^+$) [6];

2) It is assumed that in the $GK^1\Sigma_g^+$,v=0 vibronic state there exist Boltzmann distribution of rotational level populations with the gas temperature. The knowledge of the rate coefficients for excitation-deactivation processes nowadays is not sufficient to be able to make correct estimation of an applicability of the last assumption. Most probably it doesn't work in the conditions studied in [1-5].

The first assumption should lead to an overestimation, the second one - to an underestimation of the effective rotational temperature thus obtained. In every particular case the value of the temperature determined by the method of [1-5] is the result of the competition of two (or more) opposite tendencies playing different roles under different conditions in plasma.

It should be mentioned, that abnormal intensity distributions in R-branches of (0-0), (1-0) and (2-1) bands of $GK \rightarrow B$ transition have been observed in experiments with positive column of glow discharge cooled by liquid nitrogen [7]. Under extremely low gas temperature T=(145±20) K rather bright R-lines were detected starting from too high rotational levels (up to J=11). After that work it should be quite evident that one has to be careful with those bands.

The authors of [1-5] mentioned that they tried to use the emission of other band systems of H_2, in particular Fulcher-α bands ($d^3\Pi_u \rightarrow a^3\Sigma_g^+$). They also used Honl-London factors and got non-Boltzmann rotational population distributions and/or unreasonable values of effective rotational temperature (lower than the room temperature, for example). It looks like they are not familiar with our papers published since 1978 (see references in [8,9]). Our experimental studies and appropriate modeling show that the rotational population distributions in low pressure plasma have usually non-Boltzmann character. But correct methodology [8] and use of semiempirical transition probabilities [9] made it possible to obtain rather good agreement

between the gas temperatures determined in DC, RF, and microwave plasmas from: 1) various bands of H_2 ($e^3\Sigma_u^+$, $d^3\Pi_u^\pm$, $k^3\Pi_u^- \to a^3\Sigma_g^+$, $j^3\Delta_g^- \to c^3\Pi_u^-$, $J^1\Delta_g^- \to C^1\Pi_u^-$, $D^1\Pi_u^- \to E^1\Sigma_g^+$), 2) Q-branches of Fulcher-α bands ($d^3\Pi_u^- \to a^3\Sigma_g^+$) of various isotopic species H_2, HD, D_2; and 3) Doppler broadening of H, D, H_2, D_2, Ne lines (see refs. in [8,9]).

The goal of present work was the investigation of the possibility to use $GK^1\Sigma_g^+,v',J' \to B^1\Sigma_u^+,v'',J''$ rovibronic line intensities in non-equilibrium plasma diagnostics. In contrast with previous works [1-5] we didn't restrict ourselves in studies of only one (0-0)R branch (what would lead to only one experimental value of T for each plasma condition). Therefore we measured: 1) the intensities of several vibronic bands of GK → B transition (the results for (0-0), (0-1), (0-2) and (0-3) bands presented herein); 2) both R and P branch lines (they start from the same upper levels and in principle should give the same values of the populations); 3) Q-branchs of Fulcher-α diagonal bands (known to be unperturbed); and 4) Doppler broadening of H_α line for the determination of the translational temperature [10].

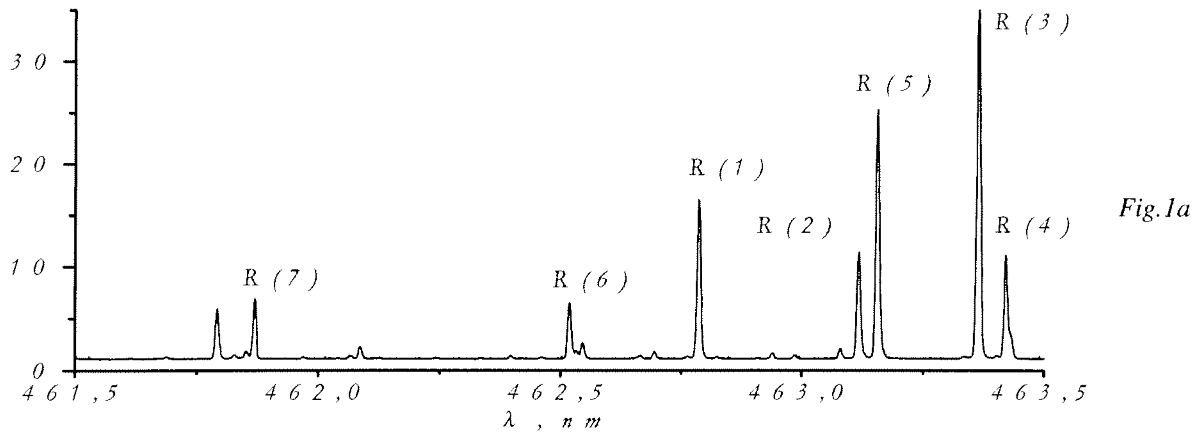

Fig.1a

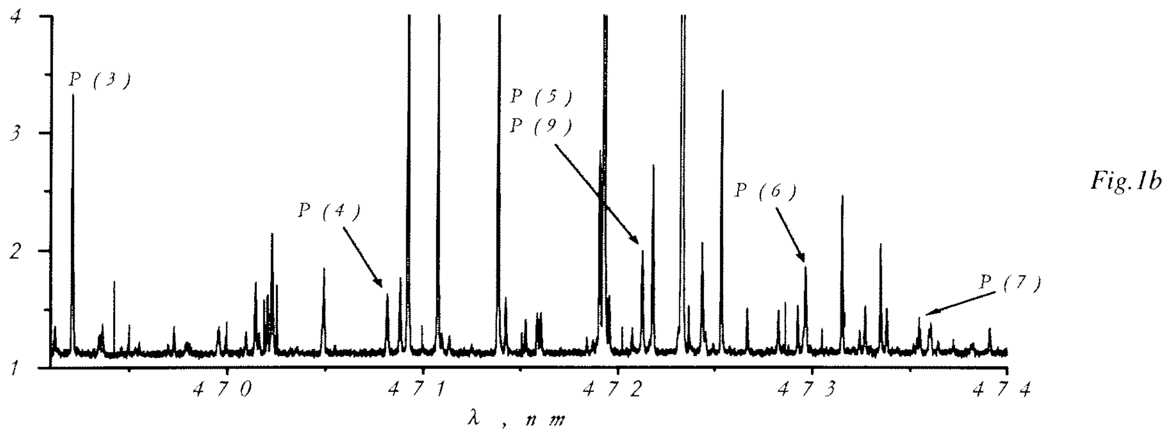

Fig.1b

The experiments were performed with pure hydrogen plasma of hot cathode arc discharge through 2 mm capillary under the pressure p≈5 Torr and currents i=20–300 mA. Two fragments of the emission spectrum corresponding to R and P branches of (0-0) band for i=20 mA are shown in Fig. 1. One may see that lines of (0-0)R branch are very convenient for the detection. They are bright, can be easily distinguished in the spectrum even by low-resolution spectrometer, located in the wavelength range suitable for intensity measurements and therefore in principle looks like prospective for plasma diagnostics especially *in situ* control of chemical processes in industrial plasmas. It is much more difficult to work with P-branch lines because their intensities are one-two orders of magnitude lower (pay attention to scales in Fig. 1a and 1b). Newertheless high enough spectral resolution and signal to noise

ratio of our spectrometer made it possible to measure intensities of most of P-lines identified in [11] (Illustrative spectra of Fig. 1 are much compressed along λ axes).

The results and discussion. For plasma diagnostics line intensities themselves are not so interesting as population densities of upper rovibronic levels which are determined by plasma parameters (*i.e.* by gas temperature [8]). Those two magnitudes are related by radiative transition probabilities which are unknown for $GK \rightarrow B$ transitions (First attempt to study the branching ratios has been performed very recently [12]). Therefore the only way is to use existing adiabatic Honl-London factors instead of real (perturbed) line strengths and to see what consequences it will lead to. The $GK^1\Sigma_g^+$,v',J' rovibronic level populations (divided by their degeneracy) obtained under that assumption have been plotted as a function of the rotational energy $E_{X0J'}$ of the ground $X^1\Sigma_g^+$,v=0 vibronic state of H_2. Typical result obtained with i=20 mA is shown in Fig. 2 (1 - R-branch, 2 - P-branch). In the framework of simple excitation-deactivation model [8,9], they should represent relative population distribution over rotational levels of the ground $X^1\Sigma_g^+$,v=0 state. The same plot for Q-branch of Fulcher-α (2-2) band is also presented in Fig. 2 (points 3). One may see that line intensities of R and P branches give sufficiently (10 times and more) different values of the populations of the same $GK^1\Sigma_g^+$,0,J' rovibronic levels. It is obvious that the contradiction is caused by our use of Honl-London factors. Previous investigators were not able to see this fact because they measured the intensities of only (0-0)R branch. Moreover the ratio of the intensities of R and P lines starting from the same upper level is directly connected with relative line strength S_R/S_P (so-called rotational branching ratio). The results of our measurements of branching ratios averaged over entire range of currents are presented in Fig. 3 (points 1, 2, 3 and 4 corresponds to (0-0), (0-1), (0-2) and (0-3) bands) together with ratios of Honl-London factors (points 5).

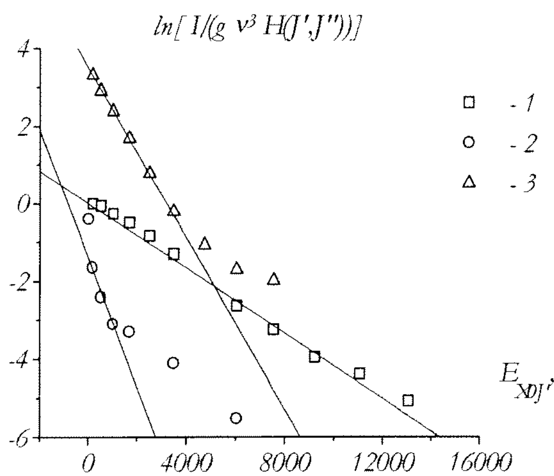

Fig.2

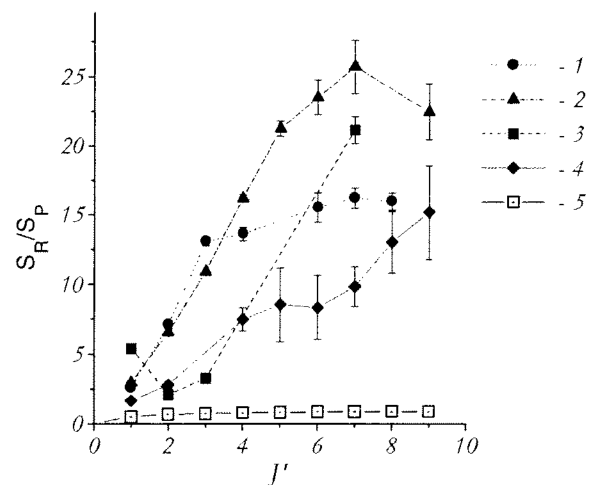

Fig.3

One may see that 1) experimental branching ratios are in remarkable disaccordance with those calculated by Honl-London formulas; 2) they are different for different vibrational bands what is direct manifestation of the breakdown of an adiabatic approximation in the case of $GK \rightarrow B$ transition.

It can be seen from Fig. 2 that the scaled intensities of R and P branches have sufficiently different dependencies on the energy $E_{X,0,J'}$ and therefore sufficiently different effective

temperatures (in the case of P branch it is not so easy to introduce a temperature at all because of non-Boltzmann character of the plot). Nevertheless we introduced some effective temperatures corresponding to the beginning parts of the curves [8] (see straight lines in Fig. 2) and listed the results thus obtained in the Table. One may see that values of the temperature obtained from R and P branches are in dramatic contradiction. The same is true for all other investigated (v'-v") bands of GK → B transition. On the other hand, the effective temperatures associated with GK → B transition are sufficiently different from those, obtained with Q branches of Fulcher-α bands. At the same time the later ones are in rather good accordance with the values of the translational temperature determined from Doppler broadening of H_α line of hydrogen atom. It means that both methods works quite good in our conditions.

i, mA	H_2				H_α
	$GK^1\Sigma_g^+ \rightarrow B^1\Sigma_u^+$ transition		$d^3\Pi_u^- \rightarrow a^3\Sigma_g^+$ transition		Doppler broadening
	(0-0)		(0-0)	(2-2)	
	R-branch	P-branch	Q-branch	Q-branch	
20	1780(70)	580(70)	580(20)	540(20)	600(70)
50	2390(70)	590(110)	920(20)	910(20)	950(100)
100	2600(100)	590(120)	1050(20)	990(20)	1150(150)
300	3000(200)	620(120)	1400(40)	1280(30)	1350(200)

Conclusion. The results of our work show that the agreement between rotational T_{rot}(G,0R) and gas temperatures observed in [1-5] is most likely just an occasional coincidence. To be able to use the emission of GK → B bands in plasma diagnostics it is necessary to have spontaneous emission transition probabilities (or line strengths), radiative lifetimes of upper rovibronic levels and rate coefficients of electron impact excitation of $GK^1\Sigma_g^+$ state for various values of vibrational and rotational quantum numbers. Without these data even simple diagnostic task - determination of gas temperature - looks like almost meaningless and premature.

References.

[1] Chu H.N. et al. Phys.Rev.A. .**44**, 3796 (1991).
[2] Barbeau C. et al. ISPC-10, Bochum, Germany, **2**, 1 (1991).
[3] Giequel A. et al. Diamond Relat. Matter. **3**, 581 (1994).
[4] Goyette A.N. et al. J.Phys.D: Appl. Phys. **29**, 1197 (1996).
[5] Laimer J. et al. J.Phys.D: Appl.Phys. **29**, 1197 (1996).
[6] Ross R.S. et al. Phys.Rev.A. **50**, 4618 (1994).
[7] Otorbaev D.K. et al , *Electron-excited Molecules in Non-equilibrium Plasma*, Nova Science Publishers, New York (1989).
[8] Lavrov B.P, in *Plasma Chemistry*, B.M.Smirnov (ed.), Energoatomizdat, Moscow (1984), pp.45-92.
[9] Astashkevich S.A. et al. J.Quant.Spectrosc.Radiat.Transfer. **50**, 725 (1996).
[10] Lavrov B.P. et al. Abstracts of "Frontiers II" Bad Honnef, Germany, 169-172 (1997).
[11] Crosswhite H.M.(ed.), *The Hydrogen Molecule Wavelength Tables of Gerhard Heinrich Dieke*, Wiley-Interscience, New York (1972).
[12] Astashkevich S.A. et al. Optics and Spectroscopy, (1999, in print).

Measurement of Quenching Rates for Short-Lived States in the Afterglow of Nanosecond Discharge

S.V. Pancheshnyi, S.M. Starikovskaia, A.Yu. Starikovskii
Moscow Institute of Physics and Technology,
Institutskii lane 9, Dolgoprudny, Moscow region, 141700 RUSSIA

In this paper the dynamics of the nitrogen electron state relaxation is investigated by the emission spectroscopy of high time resolution in afterglow of the nanosecond pulse repetitive high-voltage discharge in the form of fast ionization wave (FIW). From the viewpoint of elementary process studies, the most promising features of such a breakdown are the spatial uniformity, good reproducibility. and short periods of time required for gas excitation.

FIW was initiated by negative polarity voltage impulses of 15.5 kV amplitude, 25 ns duration at half maximum, 3 ns rise time and 40 Hz repetition frequency. The pulses were transported from a high-voltage generator to the high-voltage electrode of the discharge tube through a coaxial cable with a wave impedance of 50 Ω. The discharge device comprised a glass tube of 17.5 mm inner diameter, 21.5 mm outer diameter and 600 mm length at which ends electrodes of stainless steel were located. The tube was surrounded by a metal shield of 60 mm diameter. Radiation was recorded by the optical system that consists of a condenser, a set of diaphragms, a monochromator and a photomultiplier (the spectral sensitivity range of the photocathode was 250–600 nm). The radiation was selected in the direction perpendicular to the discharge device axis at a distance of 20 cm from the high-voltage electrode. We was able to pump down the vacuum system to a pressure of $\sim 10^{-4}$ Torr with the help of the forevacuum and diffusion pumps. Pressure of the gas studied was measured by a U-tube oil pressure gauge.

Measurements were performed in pure nitrogen, N_2:O_2(1:4), N_2:CO (1:2), N_2:H_2(9:1) and N_2:H_2:O_2 (4:2:1) mixtures at pressures ranged from 0.1 to 20 Torr. The spectrally pure nitrogen, hydrogen, carbon monoxide and industrial oxygen were used in mixture composition. The measurements were performed for $0 \rightarrow 0$ transitions of the second positive nitrogen system ($\lambda = 337.1$ nm) and the first negative nitrogen system ($\lambda = 391.4$ nm).

In fast ionization wave when propagating the electric field peak along the discharge tube the internal degrees of gas freedom are being excited for a short period of time ($\sim 10^{-8}$ s). In this event both the gas dissociation degree and the relative concentration of excited particles in a single impulse make up value $\alpha \sim 10^{-4}$ which makes it possible to disregard quenching of levels investigated in collisions with excited particles.

Specific times of gas relaxation make up $10^{-3} - 10^{-5}$ s, as resulted from the analysis of the kinetic scheme with the process rate constants taken from [1]. Therewith, the excited particles accumulation from one impulse to another is negligible in the case the mixture is not chemically-reactive.

There are somewhat different conditions for mixture N_2 - H_2 - O_2. A mixture of nitrogen with water vapor (at pressures no over the saturation pressure) is the thermodynamic equilibrium state of this mixture at the ambient temperature. The investigations performed have demonstrated that the complete hydrogen conversion under FIW conditions which is observed by radiation continuum (H_2, $a^3\Sigma_g^+ \rightarrow b^3\Sigma_u^+$) in UV spectral band (250–400 nm) takes place under our conditions in the period of time about 3–5 min which makes it possible to consider the discharge gas composition be close to equilibrium one. In doing so, the H_2O vapor pressure was recalculated with the use of stoichiometric relations.

The radiation intensity decrease in the both lines in the pressure range investigated in this paper can be described by exponential time dependence $I = I_0 \exp(-t/\tau)$ with a good accuracy.

At the stage of earlier afterglow (prior to 100 ns) the electron excited state relaxation in N_2-M mixtures takes place due to collisional deactivation and radiative depopulation. The dynamics of the $[N^*]$ upper excited level depopulation is described by the kinetic equation (1) with a solution in the form of (2).

$$\frac{d[N^*]}{dt} = -\frac{1}{\tau_0}[N^*] - k_{q(i)}^{N_2}[N_2][N^*] - k_{q(i)}^{M}[M][N^*] \tag{1}$$

$$\ln\left\{\frac{[N^*]}{[N^*]_0}\right\} = -t\left(\frac{1}{\tau_0} + k_{q(i)}^{N_2}[N_2] + k_{q(i)}^{M}[M]\right) = -\frac{t}{\tau} \tag{2}$$

Herein τ – the time of the radiation decrease in e times which was observed in the experiment and caused by all the processes in total. If there is no reabsorption the radiation intensity $I(t)$ of the associated band is proportional to $[N^*](t)$ upper level population which makes it possible to determine the gas pressure dependence of $1/\tau$ for the investigated levels in various mixtures in accordance with equation (2). This dependence is represented in Figure A for $N_2(C^3\Pi_u, v'=0)$ and in Figure B for $N_2^+(B^2\Sigma_u^+, v'=0)$ - state of nitrogen. Lines marked with figures from 1 to 5 correspond to differet mixtures: 1 - pure N_2, 2 – 20% N_2 and 80% O_2, 3 – 90% N_2 and 10% H_2, 4 – 33% N_2 and 67% CO, 5 – 57.1% N_2, 28.6% H_2 and 14.3% O_2. The values of the radiative lifetime were obtained by extrapolation to the zero pressure. The quenching rates were determined from the inclination angle of the straight line $1/\tau(P)$.

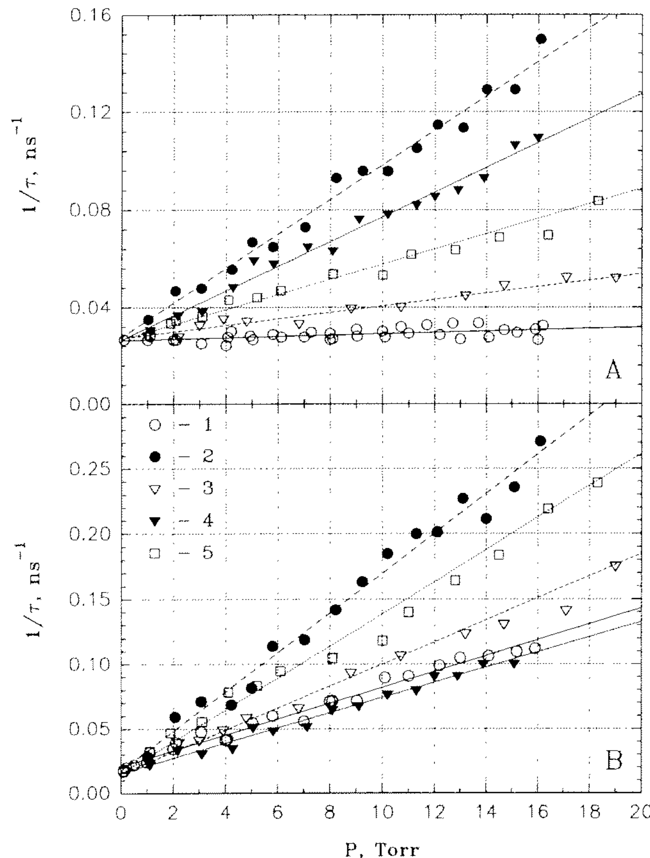

The rate constants and electron excited state lifetimes found are summarized in Tables 1, 2. A comparison with the results of other authors is given therein. As far as we know, the experimental data on the rates of quenching of the nitrogen molecule and ion by hydrogen and carbon monoxide, as well as one of the ion by water vapor are being published for the first time.

Thereby, the $N_2(C^3\Pi_u, v'=0)$ and $N_2^+(B^2\Sigma_u^+, v'=0)$ electron excited state radiation lifetimes and rate constants of deactivation by N_2, O_2, H_2, CO and H_2O molecules have been measured in the early afterglow of the nanosecond impulsed repetitive discharge developing in the form of fast ionization wave. This measurement method is characterized by simplicity, universality and may be applied to obtain deactivation sections in other gases or gas mixtures.

Table 1: $N_2(C^3\Pi_u, v'=0)$ level lifetime and deactivation rate constants

τ_0^{2+}	$k_q^{N_2}$	$k_q^{O_2}$	$k_q^{H_2}$	k_q^{CO}	$k_q^{H_2O}$	Ref.
37±6	0.12±0.02	3.4±0.7	—	—	—	[2]
37±3	0.15±0.02	1.35±0.13	—	—	—	[3]
30±2	0.11±0.01	2.85±0.18	—	—	—	[4]
46.3	0.12	—	—	—	—	[5]
40.5±1.3	0.13	—	—	—	—	[6]
—	0.1–0.2	2.6	—	—	—	[7]
29	0.11	2.73	—	—	4.12	[8]
—	0.11	3.12	—	—	—	[9]
37±4	0.09±0.03	2.7±0.3	3.2±0.3	2.4±0.2	3.0±0.3	PW*

Table 2: $N_2^+(B^2\Sigma_u^+, v'=0)$ level lifetime and deactivation rate constants

τ_0^{1-}	$k_{qi}^{N_2}$	$k_{qi}^{O_2}$	$k_{qi}^{H_2}$	k_{qi}^{CO}	$k_{qi}^{H_2O}$	Ref.
—	4.53	7.36	—	—	—	[9]
66	2.2–8.2	—	—	—	—	[10]
64±6	8.2±1.6	—	—	—	—	[11]
—	7.5	—	—	—	—	[12]
62±6	2.1±0.2	5.1±0.5	6.8±0.7	1.9±0.2	8.6±0.9	PW*

PW* – present work; τ_0 values are given in 10^{-9} s and k_q^i – in 10^{-10} cm^3/s.

References

[1] V. Guerra and J. Loureiro, Plasma Sources Sci. Technol., 6 (1997) 373.

[2] E.I. Asinovskii, L.M. Vasilyak, Yu.M. Tokunov, Tepl. Vys. Temp., 17 (1979) 858.

[3] H. Anton, Ann.Phys. 18 (1966) 178.

[4] P. Millet, Y. Salamero, H. Brunet et al. J.Chem.Phys. 58 (1973) 5839.

[5] L.L. Nichols and W.E. Wilson, Appl.Optics. 7 (1968) 167.

[6] J.M. Calo and R.C. Axtmann, J.Chem.Phys. 54 (1971) 1332.

[7] G.K. Vinogradov, D.I. Slovetskii, T.B. Fedoseeva, Tepl. Vys. Temp., 21 (1983) 655.

[8] F. Albugues and all, J.Chem.Phys. 61 (1974) 2695.

[9] K.B. Mitchell, J.Chem.Phys. 53 (1970) 1795.

[10] A.E. Belikov, O.V. Kusnetsov, R.G. Sharafutdinov, J.Chem.Phys. 102 (1995) 2792.

[11] A. Plain and J. Jolly, Chem.Phys.Let. 111 (1984) 133.

[12] S.H. Neff, J.Chem.Phys. 75 (1981) 4897.

LIF diagnostic of NO removal in a high pressure photo-triggered discharge

F. Fresnet, G. Baravian, S. Pasquiers, C. Postel, V. Puech, A. Rousseau, M. Rozoy
Laboratoire de Physique des Gaz et des Plasmas URA 073,Bat 210, Université Paris XI
91405 ORSAY Cedex - France

Introduction

Pulsed discharges are amongst the considered techniques for atmospheric pollutant removal [1]. The non-equilibrium plasma initiates the appropriate chemistry by creating key radicals which react with pollutants during the post-discharge. The radical creation mechanisms, and of the following reaction pathways, are key steps to be studied for the understanding of the cleaning process [2]. Numerous works have been performed using dielectric barrier or corona discharges [1-4]. However, these filamentary discharges are strongly non-homogeneous so that temporally resolved diagnostics can be hardly compared to the predictions of 0D kinetics model on a large time scale. In order to overcome this problem, we have used an homogeneous photo-triggered discharge [5]. In this study, the Laser Induced Fluorescence (LIF) diagnostic is used to detect the ground state NO population during the post-discharge in binary N_2/NO mixtures. We discuss the influence of both the electrical energy deposited in the discharge and the initially applied reduced electric field, on the NO removal efficiency.

Experimental set-up and LIF diagnostic

The photo-triggered discharge has been previously demonstrated to be very efficient for the NO removal [6-7]. The set-up used consists of an energy storage unit (C=17.44 nF), the discharge chamber, and the pre-ionisation circuit. The electrodes, 50 cm long, have a gap of 1 cm and a flat profile over 1 cm. As a result, a volume V_{dis}=50 cm^3 can be homogeneously excited at each shot. The value of the applied voltage, V_o, can be chosen from 19 up to 38 kV. The current pulse duration is about 50 ns. A gas flow is achieved in a loop, and the discharge repetition rate (0.625 Hz) is such that the whole reactor volume, 500 cm^3, is renewed between two shots. The whole volume of the experimental device, reactor plus loop, is V_{tot}=6.5 liters. The deposited energy in the plasma, $E_{dep}=CV_o^2/2$, ranges from 3 up to 12 J per pulse. It corresponds to values of the specific energy, $E^V_{dep}=E_{dep}/V_{dis}$, between 60 and 240 J/l. The total pressure of the N_2/NO mixtures ranges from 345 up to 600 Torr, with an initial NO concentration, i.e. before discharges have been made, η_o, between 500 and 4000 ppm.

A Datachrome 5000 Quantel frequency doubled YAG/Nd laser pumps a Rh 590/610 dye, and the resulting 574 nm wavelength is frequency doubled and mixed to the 1064 nm radiation to produce a tunable laser emission around 226 nm corresponding to the $A^2\Sigma \rightarrow X^2\Pi$ excitation transition. Fluorescence is observed at 248 nm, 200 µs after the current pulse, and in the middle of the 50 cm long homogeneous post-discharge volume. In order to avoid absorption, we choose to detect weak intensity rotational lines in the blue part of the spectrum, figure 1A. The output signal of a photo-multiplier is recorded by a Boxcar synchronized with the laser shot. Comparison between LIF-signals measured from the initial mixture, i.e. without discharge, and from the temporal post-discharge, i.e. with the discharge working in the volume V_{dis} , gives the NO removal efficiency for one discharge, τ_{NO}. This efficiency is defined as: $\tau_{NO}=1-[NO]_d/[NO]_o$, where $[NO]_d$ is the remaining density 200 µs after the discharge, and $[NO]_o$ is the initial density of the mixture. A typical example of LIF measurements is given in figure 1B.

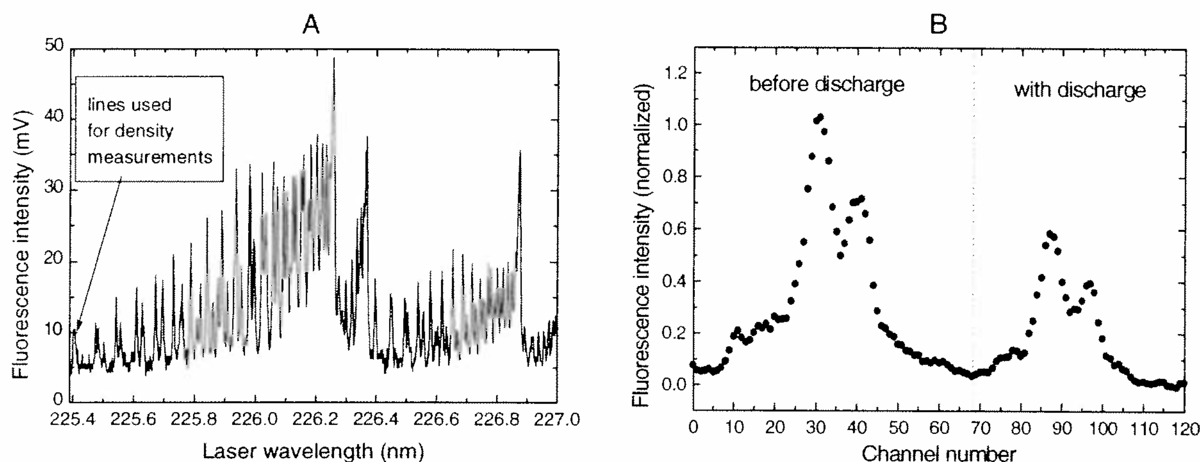

Figure 1: *LIF diagnostic to detect NO molecules in the temporal post-discharge. A: Central part of the experimental NO A-X LIF spectrum. B: LIF-signals measured at 450 Torr, for an initial NO concentration of 767 ppm (partial pressure: 0.345 Torr), and V_o=25 kV, E^V_{dep}=109 J/l.*

Results

Influence of the initial NO concentration

In figure 2 is displayed the evolution of τ_{NO} against V_o at a total pressure of 345 Torr. $[NO]_o$ is set equal to 5.5 10^{15}cm^{-3} (η_o=500 ppm), or to 1.1 10^{16} cm^{-3} (η_o=1000 ppm).

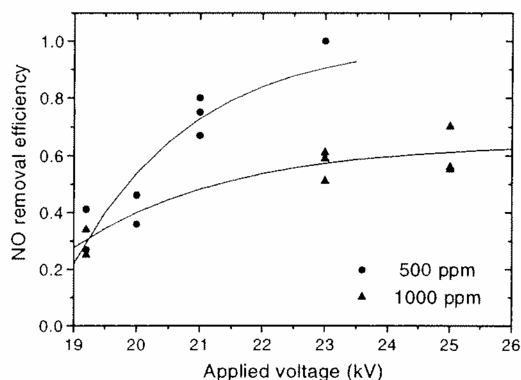

Figure 2: *Evolution of the NO removal efficiency for one discharge, at 345 Torr, against the applied voltage. Initial NO concentration values are given on the figure.*

It is worth to notice that the absolute amount of NO molecules reduced is about equal for both η_o values, and depends only on the voltage for the conditions of the figure. For example, at Vo=23 kV, one discharge removes 100 % of 500 ppm and 55 % of 1000 ppm of NO, which corresponds to the same number of molecules (5.5x10^{15} cm^{-3}). In that conditions, the absolute efficiency of the discharge does not significantly depend on the initial NO density.

Figure 2 also emphasized that the applied voltage has a strong influence on the NO removal, since τ_{NO} increases from 30 % at Vo=19 kV up to 100 % at 23 kV, for η_o=500 ppm. At a constant pressure value, increasing V_o like in figure 2, increase altogether the values of the deposited energy, E^V_{dep}, and of the initial reduced electric field, $(E/N)_o=V_o(dN_{tot})^{-1}$, where N_{tot} is the total density and d is the electrode gap. However E^V_{dep} and $(E/N)_o$ should have different effects on NO removal, since $(E/N)_o$ influences directly the electron energy distribution function and, therefore, the electron-neutral reaction rates, and E^V_{dep} is related to the electron density.

Influence of the deposited energy during the discharge

In order to check the dependence of the NO removal efficiency with respect to the deposited energy, the applied voltage and the total pressure were increased so that the value of $(E/N)_o$ remains constant, equal to 205 Td, whereas E^V_{dep} increases proportionally to V_o^2. $[NO]_o$ was set to 1.1 10^{16}cm^{-3} for measurement of τ_{NO} in that conditions. The results obtained are

displayed in figure 3. The pressure, V_o, and E^V_{dep} values corresponding to the experimental points plotted in this figure are given in table 1.

Pressure (Torr)	285	345	375	400	450	500
V_o (kV)	19	23	25	26.8	30	33.4
E^V_{dep} (J/l)	62	92	108	124	156	194

Table 1: Experimental conditions investigated for the study of the NO removal efficiency with respect to the deposited energy, at a constant applied electric field.

It appears that the NO removal efficiency rapidly increases by a factor of 3, from 20% up to 60%, when the deposited energy increases by less than a factor of 2, from 60 up to 100 J/l. However τ_{NO} saturates to about 75% for energy values higher than 100 J/l.

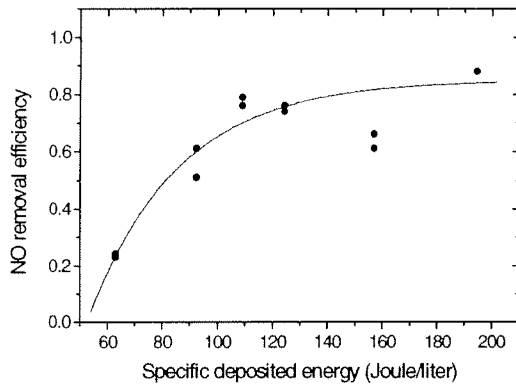

Figure 3: *Evolution of the NO removal efficiency for one discharge, at $(E/N)_o$=205 Td, against the deposited energy. Initial NO density value is 1.1 10^{16} cm^{-3}.*

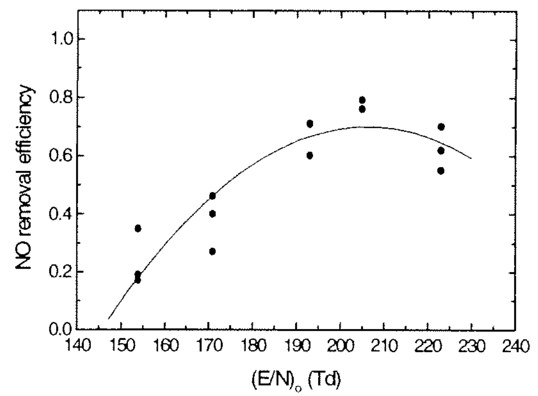

Figure 4: *Evolution of the NO removal efficiency for one discharge, at E^v_{dep}=109 J/l, against the applied reduced electric field. . Initial NO density value is 1.1 10^{16} cm^{-3}.*

Influence of the applied electric field

The influence of the $(E/N)_o$ value on τ_{NO} has been checked by fixing the voltage value, V_o=25 kV, and by varying the mixture pressure. The deposited energy is E^V_{dep}=109 J/l in this case. $[NO]_o$ is fixed to 1.1 10^{16} cm^{-3}. Table 2 gives the experimental conditions investigated, and the results are displayed in figure 4.

Pressure (Torr)	500	450	400	375	345
$(E/N)_o$ (Td)	154	171	192	205	223

Table 2: Pressure values investigated for the study of the NO removal efficiency with respect to the applied reduced electric field, at a constant deposited energy.

Figure 4 shows that the NO removal efficiency increases by near a factor of 4, from 20% up to 75%, when the applied electric field increases by 25%, from 150 up to 205 Td. This emphasizes that the cleaning process of the N_2/NO mixture is greatly improved by a small increase of the $(E/N)_o$ value, keeping constant the electrical energy consumption. In conditions of figure 4, the energy cost decreases from 310 eV/molecule at 150Td, down to 80 eV/molecule at 205 Td.

Discussion

In the N_2/NO mixture, it is known that the most important reactive species, for the reduction of NO, is atomic nitrogen N [1]. N is produced following electron collisions on N_2. In the post-discharge, a very simplified set of reactions involved in the NO removal process is:
(1) N + NO -> N_2 + O , (2) 2O + N_2 -> O_2 + N_2 , (3) O + NO + N_2 -> NO_2 + N_2 . However the formation of NO_2 remains at a very low level, so that (3) can be neglected [6,7]. Therefore, in a first approximation, the NO removal efficiency of the photo-triggered reactor can be directly related to its ability to create N atoms during the current pulse. Figure 4 emphasizes that N atom production is very sensible to the $(E/N)_o$ value, between 150 and 200 Td.

Reaction (1) shows that the number of NO molecules destroyed should be proportional to the number of N atoms produced during each shot provided this reaction is complete. This can be achieved in a mixture with a large excess of NO.

In order to check this, we have recorded the evolution of the concentration of NO in the whole volume (V_{tot} =6.5 liters) as a function of the number of shots, n_S. Typical results are plotted in figure 5 for V_o=23 kV and 345 Torr, i.e. $(E/N)_o$=205 Td and E^V_{dep}=92 J/l, and η_o=4000 ppm. NO concentration decreases first linearly with n_S, which shows that reaction 1 is complete when this concentration is higher than 1500 ppm. It is easy to show that NO density, [NO], verify :

$$d[NO]/dn = - [N] V_{dis} / V_{tot}$$

where $V_{dis} / V_{tot} = 7.6 \times 10^{-3}$.

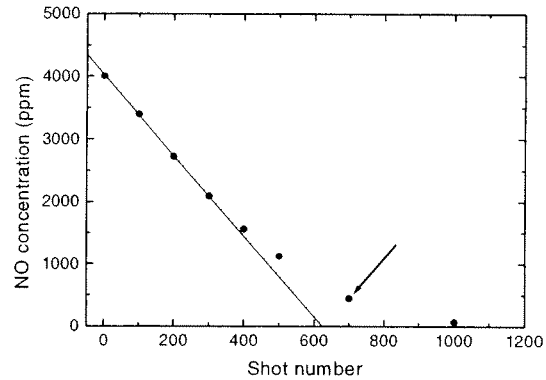

Figure 5: Evolution of the NO concentration against the number of discharges in the whole volume. 345 Torr at an initial concentration of 4000 ppm. $(E/N)_o$=205 Td and E^V_{dep}=92 J/l.

This simple approach gives an estimation of the N atom density, [N], created during each shot. We obtain $[N]=9.3\ 10^{15}$ cm^{-3} in conditions of figure 5. For low NO concentration values (< 1500 ppm), other reactions than (1) should be responsible for the disappearance of N atoms and the amount of NO removed per shot decreases. As a result the evolution of the NO concentration against the number of shots is no longer linear (arrow in figure 5).

References

[1] - Non-Thermal Plasma Techniques for Pollution Control, NATO ASI Series G, Vol. 34, Ed. B. Penetrante et S. Schultheis (1993)

[2] - B. Penetrante, J. Bardsley, M. Hsiao; Jpn. J. Appl. Phys., **36**, 5007-5017 (1997)

[3] - W. Niessen, O. Wolf, R. Schruft, M. Neiger; J. Phys. D, **31**, 534-550 (1998)

[4] - M. Spaan, D. Luggenhölsher, V. Schulz-Von der Gathen, H-F. Döbele; Bull. Am. Phys. Soc., **42**, 1710 (1997)

[5] - B. Lacour, C. Vannier; J. Appl. Phys., **62**, 754-758 (1987)

[6] - M. Rozoy, *Etude d'une décharge photo-déclenchée dans l'air. Application au traitement des effluents gazeux*, Thèse de doctorat, Université Paris-Sud, Orsay.

[7] - M. Rozoy, M-P. Monin, C. Postel, V. Puech, Proc. XXIII ICPIG, 270-271 (1997)

This work was partly performed in the frame of the french ECODEV program (CNRS), with financial support of the Groupement d'Intérêt Economique de Recherches et d'Etudes PSA-Renault. One of us (FF) acknowledges also the Agence de l'Environnement et de la Maîtrise de l'Energie for its financial support.

Time and Space Resolved LIF-Spectroscopy of O- and N-Atoms in a Dielectric Barrier Discharge

M. Spaan, Ch. Lukas, V. Schulz-von der Gathen, H.F. Döbele

Institut für Laser- und Plasmaphysik, Universität GH Essen, 45117 Essen Germany

Introduction

The Dielectric Barrier discharge (DBD) is finding application for a variety of plasmachemical processes like ozone production, the generation of UV and VUV light and for surface treatment. It is also considered for cleaning of automobile exhaust gases. The motivation for this application results from the strongly non-thermal character of the discharge which allows an efficient energy coupling to the electron component whereas the residual gas in which the subsequent chemical reactions take place is cold and in general at atmospheric pressure. The discharge in the reactor consists of a multitude of tiny filaments that are distributed in the interelectrode gap and ignite independently during the phase of steep changes of the electric field.

Our activities aim at measurements by methods of laser spectroscopy of concentrations of reactive species of importance to the decomposition of the toxic molecules. In this context the plasma generated atomic radicals N and O are of central concern. Our objective is therefore the space and time resolved relative concentration measurements of these atoms in the immediate vicinity of single narrow discharge filaments in order to allow the comparison with simulation calculations (performed by other groups) so that an improved understanding of the DBD will result.

Experimental

Our model reactor is operated with steeply rising voltages (15 kV/90 ns). The consequence is that all discharge filaments in a half cycle appear within a well defined time interval. This ignition interval has a typical duration of 10 ns. An important side effect is that these steep voltage ramps lead to a larger number of filaments in the discharge volume and allow, at the same time, the application of laser based spectroscopy with high temporal resolution. The home-made semiconductor based HV power supply allows repetition frequencies up to 50 kHz. The measurements reported here were taken at a repetition frequency of 20 kHz.

Atomic nitrogen is detected by TALIF whereby N atoms are excited by two photons of wavelength λ = 206 nm from their ground state into the 3p(3/2) level. The subsequent fluorescence occurs at λ = 743 nm. Reduction of the laser energy to 20 - 100 µJ (duration 8 ns, focal spot diameter 50 µm) exclude perturbations by photodissociation caused by the diagnosing laser beam. Two dimensional relative distributions of the N radical were measured at a single discharge filament which develops on a stainless steel pin. The interelectrode gap is 1.5 mm in these measurements.

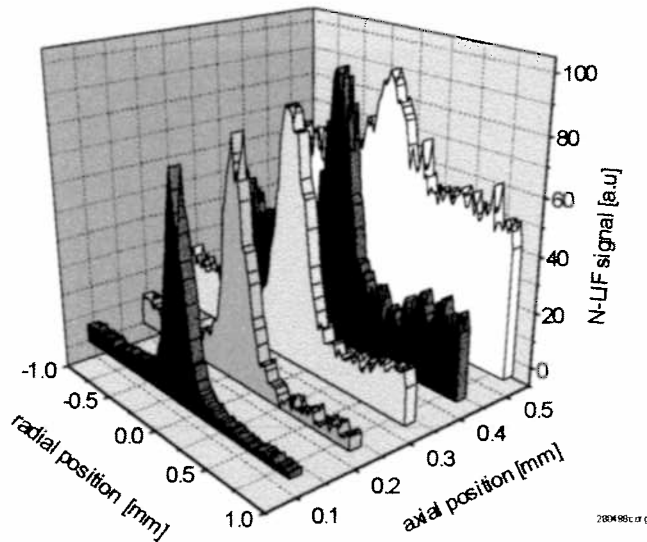

Figure 1: *Radial profiles of the N-density for different heights above the pin electrode in pure N_2*

Fig. 1 shows five radial profiles obtained at different heights above the pin (position x=0, y=0) at 2 µs after ignition for the case of an anodic dielectric in pure nitrogen at a pressure of 950 mbar. The radius of the discharge channel - inferred from the distribution of atomic nitrogen - amounts to 200 µm. Besides a slight widening of the channel a strong increase of the N density with approximation to the dielectric is observed. The nature of this intense source of radicals which exists possibly also in the intervals between the ignitions is unclear so far.

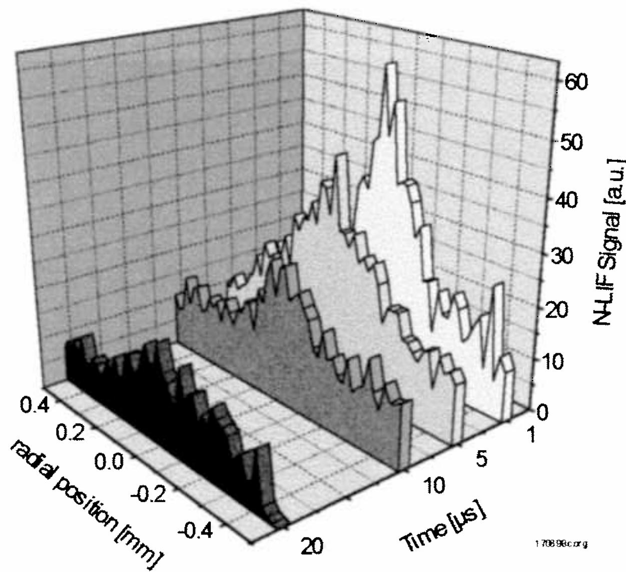

Figure 2: *N-density profiles for different times after streamer ignition in a mixture of 10% O_2 in N_2*

Spatial resolution – 50 µm - is obtained by displacement of the entire reactor. The temporal resolution of the TALIF measurements is limited by the duration of the ignition intervals within the voltage ramps during which the filaments ignite. With the present mode of excitation of the DBD the time resolution is approx. 10 ns. The addition of oxygen to a nitrogen discharge reduces the intensity of the TALIF signal to approx. 1/50 of the initial amplitude. Possible causes are "cooling" of the EEDF and attachment of O_2. Despite the strong quenching N radicals can still be detected in oxygen containing discharges by TALIF. Fig. 2 shows the temporal decay of the nitrogen density after the extinction of the discharge channel. The measurements were taken at a height of 0.1 mm above the metal tip. It is obvious that the N atoms disappear on a time scale of 20 µs and that diffusion which leads to a broadening of the channel plays only a minor role.

The time dependence of the N concentration was investigated for various gas mixtures by changing the delay between the laser shot and the plasma ignition. Fig. 3 shows the relative density distributions of the N radicals for pure nitrogen and for a mixture of 10 % oxygen in nitrogen. The two curves are normalised to the relative maximum in both cases. The presence of O_2 also results in a reduction of the N lifetime by almost an order of magnitude.

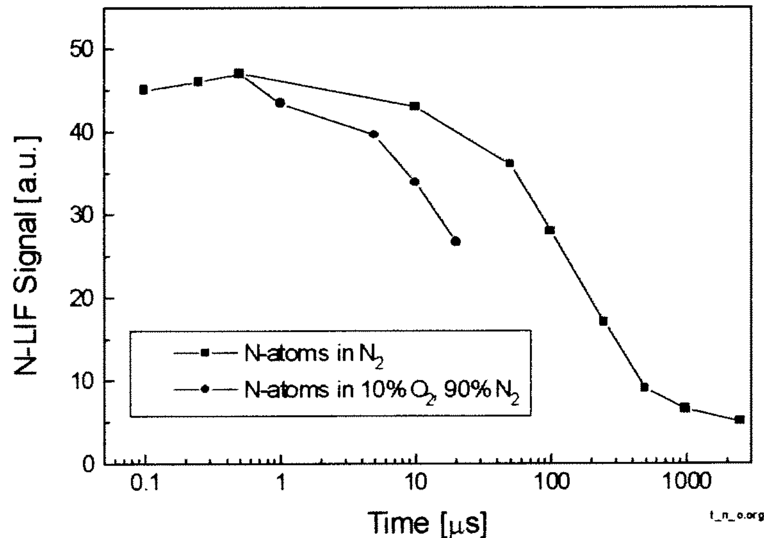

Figure 3: *Temporal behavior of the N-density in different gas mixtures*

Atomic oxygen is also of great importance for the ongoing chemical reactions after the plasma phase. It was detected by TALIF in a similar manner. The O atoms are excited by 2 x 226 nm; the fluorescence light is emitted at λ = 844 nm. Fig. 4 shows a comparison of radial profiles obtained for comparable conditions. The measurements refer to a plane 0.4 mm above metal electrode at 1 µs after ignition of the filament. We attribute the clearly broader radial profile in case of oxygen to the dissociation energy of molecular oxygen which is 4.7 eV lower than the corresponding value for N_2.

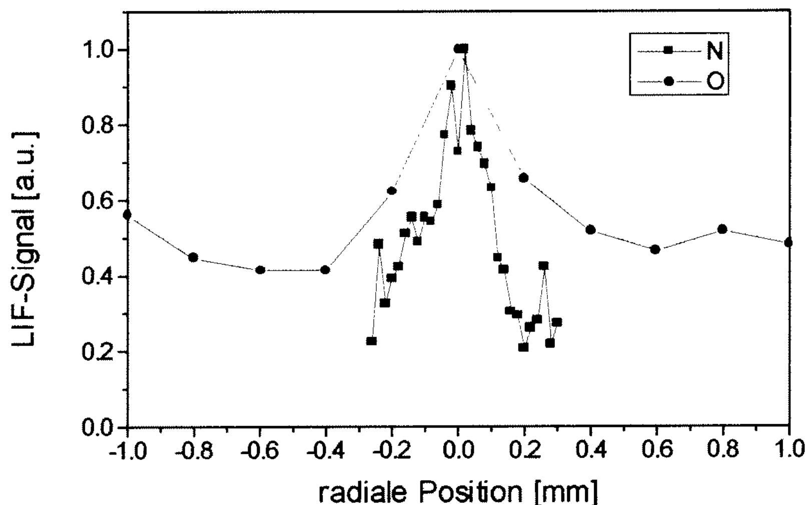

Figure 4: *Comparison of the radial profiles of N- and O-atoms*

In addition to the measurements reported here LIF spectroscopy was also applied to measure NO γ-band transitions which yield further information on the gas temperature and NO concentration. Emission spectroscopy of N_2- and O provides information on the longitudinal filament structure. The gas composition inside the plasma region and at the reactor outlet is monitored by FTIR spectroscopy. These measurements will be described in detail elsewhere.
(Funding by the "Bundesministerium für Bildung, Wissenschaft, Forschung und Technologie" is acknowledged, Project Number 13 N 7195)

Contributions without Presentations

The RF electric field and current density measured in an inductive discharge with a B-dot probe : anomalous skin effect and collisionless power absorption

G.CUNGE*, B.CROWLEY++, D.VENDER++ and M.M.TURNER++

*Laboratoire de Spectrométrie Physique,
Université Joseph Fourier Grenoble-1, BP 87, 38402 Saint Martin d'Hères, France

++Plasma research group, School of Physical Sciences,
Dublin City University, Glasnevin Dublin9, Ireland

Introduction

In inductively coupled discharges, the power is transferred from the inductive RF electric field to the plasma electrons within a skin depth layer near the plasma boundary by «ohmic» dissipation, and by a collisionless heating process in which plasma electrons «collide» with the oscillating electric field. In the real world of microelectronic device processing, the etching of anisotropic sub-micron patterns requires a collisionless pre-sheath that can only be obtained for pressures below 10 mTorr. For such plasmas, the mean free path of the electrons can become larger than the plasma chamber and it is expected that most of the power will be absorbed by a collisionless heating mechanism [1]. Because it is necessary to understand precisely how the power is coupled in industrial plasmas, the exact nature of collisionless power absorption in inductively coupled plasmas has been recently the subject of much theoretical work and experiment.

The normal skin effect, accompanied by ohmic (collisional) electron heating, occurs when the electron thermal motion is negligible. In such a case, the coupling between the RF current density J and the electric field E is *local* and given by $J = \sigma E$ where

$$\sigma = \frac{e^2 n}{m(\upsilon_m + j\omega)} \qquad \text{eq.1}$$

is the complex conductivity of a *cold* plasma (ω is the RF frequency and ν_m the electron collision frequency). In this case, electron neutral collisions break the regularity of the motion of the electrons (phase mixing) leading to ohmic heating.

If we now consider a *cold collisionless* plasma, the electron samples the field at a single location in space, and since the field has a harmonic time variation it averages to zero everywhere, so that no energy can be transferred. However, if the electrons are in thermal motion, they sample the field along some trajectory and in general the field does not average to zero along a trajectory. Since the electric field is confined to a skin depth, if an electron can transverse the skin depth in a time that is short compared to the period of the field, then it should gain net energy from the field. This collisionless power absorption mechanism is known as a "warm plasma effect", and an immediate consequence of the non negligible thermal motion of electrons is that an electric field applied to one part of the plasma at some time can affect the current everywhere in the plasma at all later times, so we can no longer write $J = \sigma E$, but instead we must now consider:

$$J = \int_r \int_t \Sigma(r) E \, dr \, dt \qquad \text{eq.2}$$

where $\Sigma(r)$ is a distributed conductivity and can be determined by a suitable linearization of the Vlasov-Maxwell equation.
This phenomenon of RF current diffusion due to electron thermal motion that results in spatial dispersion of the conductivity is responsible for the so-called *anomalous skin effect* described below. Measurements and calculations of the field distribution under such conditions have indeed demonstrated anomalous penetration and non-monotonic decay of the RF field in warm plasmas. Liebermann and Godyak [2] give a complete historical revue of those papers.
In the present work, we have obtained experimental evidence of the warm plasma effect in a cylindrical inductive discharge by accurately measuring the B_r and B_z field components as a function of radial position.

Experiments

The discharge chamber consists of a cylindrical stainless steel vacuum vessel of internal diameter 20 cm and length 80 cm mounted on a steel ground plate. One end of the cylinder is sealed with a Pyrex glass window 1.5 cm thick, the other end is sealed with a steel flange in the middle of which there is a 5 cm diameter port into which is inserted a quartz tube 30 cm long with wall thickness 3 mm, which houses the antenna. This "re-entrant" geometry is similar to that used for fluorescent RF lamps, and is promising for the production of negative hydrogen ion beams. Typical plasma operation parameters are between 0.4 and 10 mTorr for 100-300 Watts.

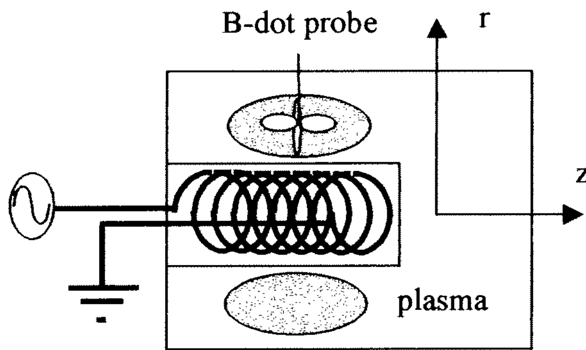

Figure 1: Experimental set-up.

The magnetic flux can be measured with so-called B-dot probes. Following Piejak *et al* [3], we have constructed a two dimensional "immersed" B-dot probe that is less perturbative than encapsulated probes. The probe consist of one loop (3mm diameter) measuring the $B_z(r)$ component of B and of a second loop in figure-8 form providing a direct measurement of $dB_r/d_z(r)$. The common mode noise can be removed to a large extend by using optimised balun transformers, and the measurement can be performed over several orders of magnitude of the B-dot signals. Thanks to those measurements, it is possible to determine the penetration of the azimuthal electric field $E_\theta(r)$ and that of the current density J(r) through the plasma by:

$$E_\theta(r) = -\frac{j\omega}{r}\int_0^r r'B_z(r')dr' \quad \text{eq.3}$$

$$J(r) = \mu_0^{-1}\left(\frac{dB_r}{dz} - \frac{dB_z}{dr}\right) \quad \text{eq.4}$$

The spatial dispersion of the plasma conductivity resulting from the «warm plasma effect» can then be determined. It should be noted here that the B-dot probe data are in polar form (amplitude and phase relative to electric field in vacuum), and that it is necessary to transform them into real and imaginary parts to perform the spatial integration and differentiation leading to E and J.

The radial distribution of the B_z field, the RF electric field and the current density, together with the corresponding phases are shown in fig.2 for a 5 mTorr, 300 W argon discharge.

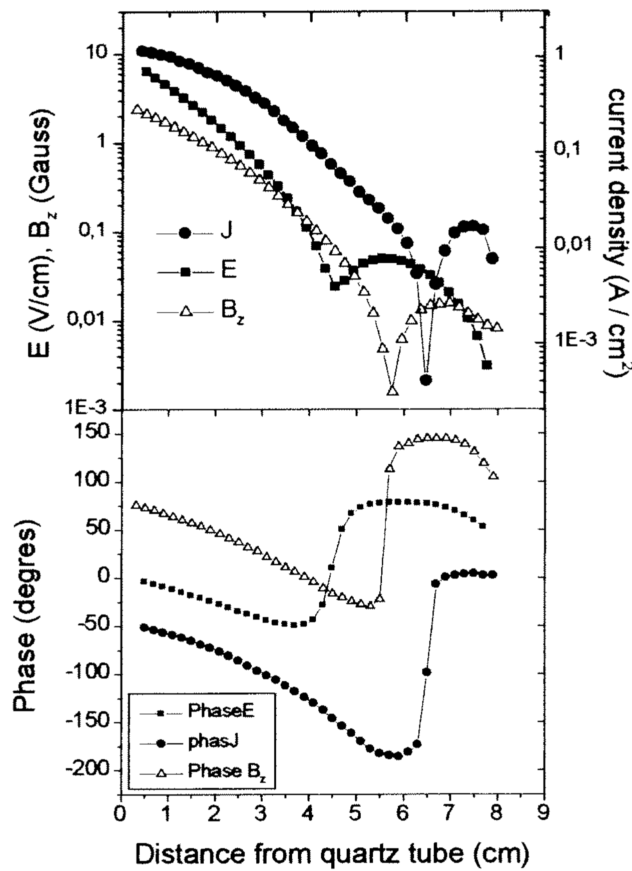

Figure 2: *Radial distribution of the Amplitude and Phase of the measured RF magnetic field electric field and current density.*

The non-monotonic distributions shown in fig.2 exhibit some typical features of the anomalous skin effect. The spatial decay of E and B are not exponential (as in the classical skin effect) and exhibit local maxima and minima in the plasma. This has also been seen by several other workers [3],[4]. Another essential feature of the anomalous skin effect resulting from the non-local interaction of electrons with the electromagnetic field due to their thermal motion is that the penetration length of the electric field and that of the magnetic field are different. The less rapid decay of the magnetic field and current density is due to ballistic transport of RF current due to thermal electron motion, as expected from the warm plasma theory. Another indication of the collisionless heating of electrons is that the phase distribution of E and J are significantly different, suggesting different propagation mechanisms for the current and the electric field. For *a cold* plasma, this phase difference should be almost constant and given by $\Delta\phi = \phi_E - \phi_J = \arctan(\omega\backslash\nu)$. In a cold plasma, $\Delta\phi$ should always be less than 90°, such that the power absorbed $P = E*J*\cos(\Delta\phi)$ is always positive. However, in our experiment, $\Delta\phi$ is clearly more than 90° at some radial positions indicating the presence of negative power absorption. Such negative power absorption was first demonstrated experimentally in a completely different plasma reactor (planar coil inductive discharge) by Godyak and Kolobov [5] and interpreted in terms of current diffusion. Following those authors, we show, in Fig.3, the distribution of the RF power density absorbed along

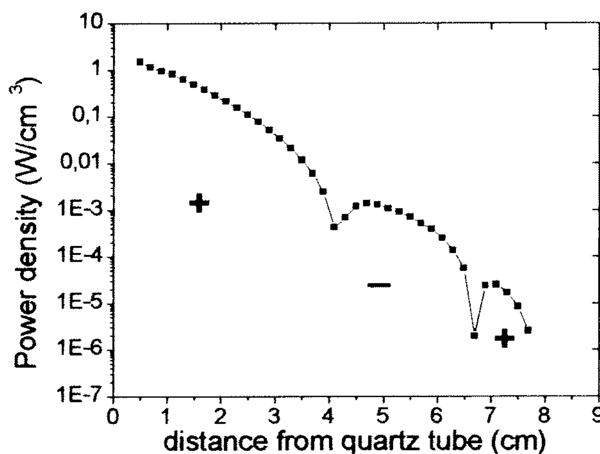

Figure 3: Absolute value of the *radial distribution of the power absorption profile (regions of negative power absorption are noted by the sign -)*.

the radial direction calculated as P = E*J*cos($\Delta\phi$) for a 200 W and 5 mTorr plasma. It can be seen in this figure that most of the power is absorbed in the skin layer near the window. However, outside the skin layer, the power absorbed changes sign and becomes negative for radial distance between 4 and 6.7 cm before becoming positive again. The power absorbed becomes negative when the phase of the electron current transferred from the skin layer by the electron thermal motion differs from the local electric field phase by more than 90° . At this point, the electrons begin to return a part of the energy they acquired in the skin layer back to the RF field (deceleration)[5][6]. This is characteristic of the warm plasma effect where the currents circulating near the walls (e.g. far away from the skin depth) are translated from the skin layer so that the current phase is defined by the electron mean velocity, although the electric field phase at this position is defined by the phase velocity that depends on the plasma density [2]. This can result in phase bifurcation when the electron thermal velocity equals the phase velocity of the RF field [7], and will lead, in general to a variety of patterns for P depending on the plasma chamber, and operating conditions. However, it is particularly interesting to see the similarity of our results from fig.2-3 to that of the experimental work of Piejak *et al* and Godyak *et al* [3][5], and with the analytical calculation of RF power absorption of Kolobov [6]. This is somewhat surprising since the chamber is completely different, leading to a different electric field distribution, but demonstrates that similar effects due to collisionless heating occur in different types of ICP.

Finally, we should mention here that it is possible to quantitatively observe collisionless electron heating by comparing the measured power absorption with that calculated using cold plasma theory [8]. This can be achieved in several ways which are beyond the scope of this paper, but we found, again in good agreement with Godyak *et all*, that collisionless power absorption dominates collisional power absorption for pressures below 10 mTorr.

References

[1] M.M.Turner; Phys.Rev.Letters, **71**, (1993)

[2] M.A. Lieberman and V.A. Godyak; memorendum No. UCB/ERL M97/65, (1997)

[3] R. Piejak, V.Godyak and B.Alexandrovich.; J.Appl.Phys, **81**,(8), (1997)

[4] B.Joye and H.Schneider; Helvetica Physica Acta, **51**, (1978)

[5] V.Godyak and V.I.Kolobov; Phys.Rev.Letters, (1998)

[6] V.Kolobov, electron Kinetics and application of glow discharge, Plenum press, NewYork, (1998)

[7] V.A.Godyak, electron Kinetics and application of glow discharge, Plenum press, NewYork, (1998)

[8] V.A.Godyak, R.B. Piejak, M.B.Alexandrovich and V.Kolobov, Phys.Rev.Letters, **80**, (1998)

Spectroscopy Diagnostics of the Multicomponent Arc Plasma in Metal Vapours

A.N.Veklich, I.L.Babich
Radiophys. Dept., Taras Shevchenko Kyiv University, 64, Volodymyrs`ka Str., Kyiv 252033, Ukraine

Introduction

The free-burning electric arcs between evaporated metal electrodes are very suitable devices as sources of dense plasma. Characteristic of such arcs is determining influence of electrode vapour on properties of arc plasma. Having a low ionization energy in comparison with atoms of ambient gas (as a rule noble, air, etc.), metal atoms make basic contribution to the established electron density. In a result it plays a key role in the processes of a heat, mass and charge transfer in plasma. Even the insignificant vapour impurity (about 1 %) appreciably changes in a wide temperature interval an electrical conductivity of plasma. Thus, the basic parameters of electric arc plasma are wholly determined by "polluting" impurity. Besides their presence has an effect for spatial distribution and absolute values of other basic plasma parameters: temperature, density of heavy components and etc.

Naturally, the multicomponent electrode compound as well as the plasmaformed gas mixture makes the investigation of electric arc plasma more difficult. Additional problem in the diagnostics is pulsing properties of plasma in ms temporal scale due to chaos change of arc position on electrodes.

This paper deals with the experimental spectroscopy investigation of the dense multicomponent plasma of the free-burning electric arc in the metal vapour by fast scanning techniques.

Experimental Setup

The arc was ignited between the end surfaces of the non-cooled metal electrodes in the gas mixture (air or air + CO_2). The multicomponent compound as well as pure copper electrodes were used. The electrode diameter was of 2 or 6 mm and the interelectrode gap ranged from 4 to 8 mm. To avoid the metal droplets appearing a pulsing mode was used: the current pulse up to 100 A was put on the "duty" weak-current discharge. The pulse interval ranged up to 30 ms. The quasi-steady mode was investigated.

Because of the discharge spatial and temporal instability the method of the single tomographic recording of the spectral line emission as well as the absorption was used. The copper vapour laser in the absorption spectroscopy was applied. Fast scanning of spatial distributions of radiation intensity was accomplished by an image dissector tube of electrostatic type. It allows to carry out the recording of radial distributions of nonstationary arc radiation intensity in arbitrary spatial sections simultaneously [1,2].

Results and Discussions

As a spectroscopy element the copper was used, which injects into a discharge gap as a result of electrodes' erosion.

The radial profile of temperature T(r) was determined from the ratio of local emission coefficients of spectral lines CuI 510.5 and 521.8 nm. The radial profile of electron density $N_e(r)$ was calculated from the experimentally obtained appropriate distribution of the intensity of the spectral line CuI 465.1 nm [2].

In the first stage of the investigations the influence of ambient gas on the radial distribution of arc plasma parameters was studied. The 6 mm copper electrodes in air atmosphere were flowed by CO_2 tangent stream. In Fig. 1 radial profiles of electron density and temperature determined in the average cross section of the interelectrode gap l_{ak} = 8 mm for several currents are given. The curves 1 and 2 correspond respectively to the arc discharge in the air and in the air + CO_2.

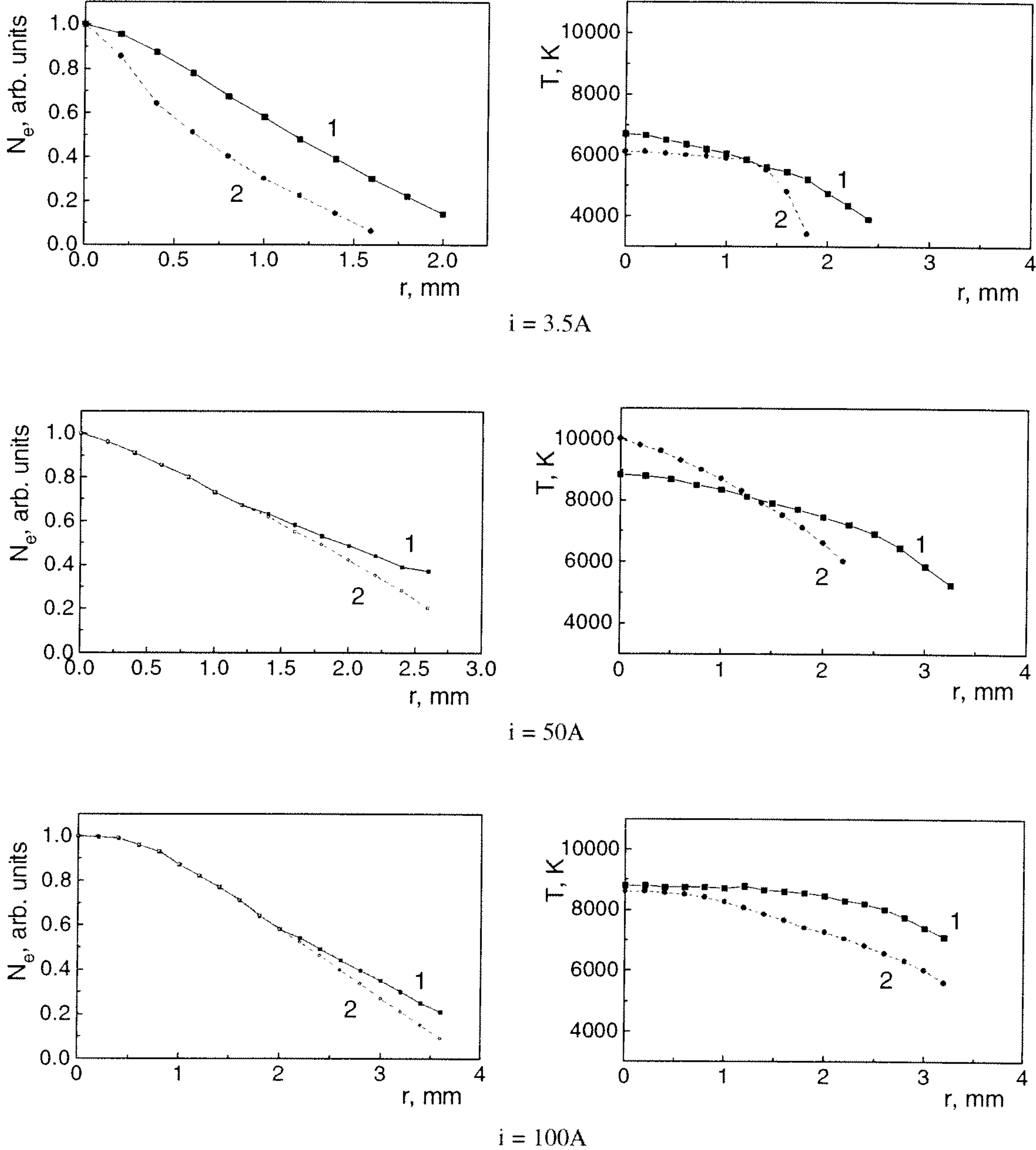

Figure 1

One can see that the CO_2 flow in all investigated arc modes causes the discharge channel to narrow. The hydrodynamics effect and plasma transport phenomena can probably serve as the reason in this case. We can suppose that as soon as the thermal conductivity of the CO_2 in accordance with data in [3] is much better in comparison to air components (for example, nitrogen) the CO_2 flow provides more efficiently the heat output from the arc column plasma. As the result of this mechanism the discharge channel tends to be narrow. We plan to carry out the additionally investigations of such kind arc plasma.

In the next stage the influence of the electrode composition on arc plasma parameters was investigated. The 2 mm "pencil"-shape iron electrodes with an axial copper insert were used. In this case the radial profile of electron density $N_e(r)$ and the factor of absorption κ_o in center of spectral line CuI $\lambda = 510.5$ nm were measured. It is possible to derive the spatial distribution of copper atoms from these profiles κ_o. In Fig. 2 radial profiles of electron density and the factor of absorption determined in the average cross section of the interelectrode gap $l_{ak} = 4$ mm at the current of 30 A are given. The curves 1 and 2 correspond respectively to the arc between pure copper and "pencil"-shape electrodes in the air.

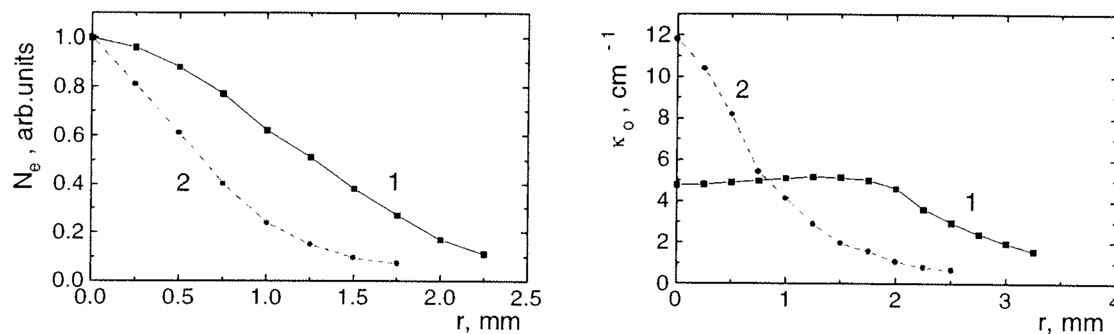

i=30A

Figure 2

As can be seen from the figure the discharge channel is more narrow in case of complex Fe+Cu electrodes. It is interesting to note that the radial distribution of copper atoms is significantly changed in this case (see profile $\kappa_o(r)$). The copper vapour in plasma tends to be located at the arc axis. As soon as values of the ionization potential of iron and copper are not too different the reason of such effect probably can be caused by difference of vapourisation temperatures and melting points as well. In accordance to the data in [4] the vapourisation of liquid copper is more efficient in comparison to liquid iron. Therefore the influence of copper atoms on plasma phenomena is more significant at the arc axis.

Conclusions

The preliminary results of investigation of the dense multicomponent plasma of the free-burning electric arc are obtained. The influence of the ambient gas and the electrode composition on the radial distribution of arc plasma parameters are shown.

We can conclude that transport phenomena such as the thermal conductivity of the plasmaformed gas mixture plays an important role in electric arc discharges. That is why in the

industrial applications of such type arc (for example, arc welding) complex gas mixtures more often are used.

The choice of the electrode composition in the arc technology is very important too. Namely, in the arc plasma the kind of metal atoms in the vapour phase depends on the vapourisation ability of melting electrode's components. Therefore the developing of special electrode compositions has a significant place in the switching device industry.

References

[1] A.N.Veklich, V.A.Zhovtyansky; J. Appl. Spectroscopy (translated from Russian), **50,** 359-363 (1989).

[2] I.L.Babich, A.N.Veklich, V.A.Zhovtyansky; J. Appl. Spectroscopy (translated from Russian), **51,** 1028-1031 (1989).

[3] The Mathematics Modelling of the Electric Arc. Ed. by V.S.Engelsht. Ilim. 1983 (in Russian).

[4] The Physics of Welding. Ed. by J.F.Lancaster. Pergamon Press. 1984.

Post-Deadline Papers

Diagnostics of Thermal Plasmas

Maher I. Boulos
Plasma Technology Research Centre (CRTP)
Université de Sherbrooke, Department of Chemical Engineering
2500 blvd. Université, Sherbrooke (Québec) Canada J1K 2R1

1. Introduction

Thermal plasmas are characterized by their high particle densities, high specific enthalpies and high flow velocities. These are often combined with the presence of steep property gradients and the simultaneous presence of particulate matter. Plasma diagnostic under these conditions offers quite a challenge which has been at the center of systematic study for the past two or three decades. Numerous techniques have been developed and are used on a regular basis for the measurements of the plasma and/or particulate parameters for the purpose of fundamental research, model validation, and process on-line controls. In the following, a brief over-view is given of the principal plasma and particulate diagnostics techniques currently used in thermal plasma studies giving for each; their potential, limitations and areas of applications. A number of general review papers have been published in the field [1-5]. Details about the individual techniques can be found in the vast literature on the subject.

2. Thermal plasma sources

A critical discussion of diagnostic techniques require a clear identification of the different plasma sources which would be the subject of study using these techniques. These can be classified for the purpose of the present review as direct current (d.c.), or inductively coupled, radio frequency (r.f.) discharges. The basic energy coupling mechanism and plasma flow configuration for each of these types of thermal plasma generators are presented schematically in Figure 1. These are discussed in the following.

2.1 D.C. plasma torches

As shown in Figure 1a, standard, plasma-spraying type, d.c. plasma torches operate with a central Thoriated Tungsten cathode and a water-cooled annular copper anode. The plasma gas is injected into the gap between the two electrodes and serves to keep the arc root in a continuous motion over the surface of the anode. Typical torch currents are in the range of a few hundred amps up to 1000 A or more. The torch voltage depends largely on the nature of the plasma gas and can vary between 25 to 30 V for pure argon operation up to 80 or 100 V when operating with molecular gases (Ar/H_2), N_2, ... As the gases pass around the arc through the anode nozzle constriction, they are heated and partially ionized emerging from the anode nozzle as a high velocity plasma jet with mean temperature of the order of 12 000 K and centerline plasma velocities that can be as high as 1000 m/s. Higher velocities can also be reached when discharging the plasma jet at low pressures 6.6 - 13.4 kPa (50 to 100 torr). The anode nozzle discharge diameter is typically of the order of 5 to 8 mm giving rise to steep property gradients in the fringes of the plasma jet. These can reach as high as a (10^3 K/mm) or hundreds ((m/s)/mm). The fringes of the plasma jet are also characterized by a rather complex turbulence structure which results from the interaction of the plasma jet with the cold ambient gas (air) surrounding it. When used for materials processing and thermal spraying applications, powders ($5 < d_p < 100$ µm) are injected into the plasma jet either internally into

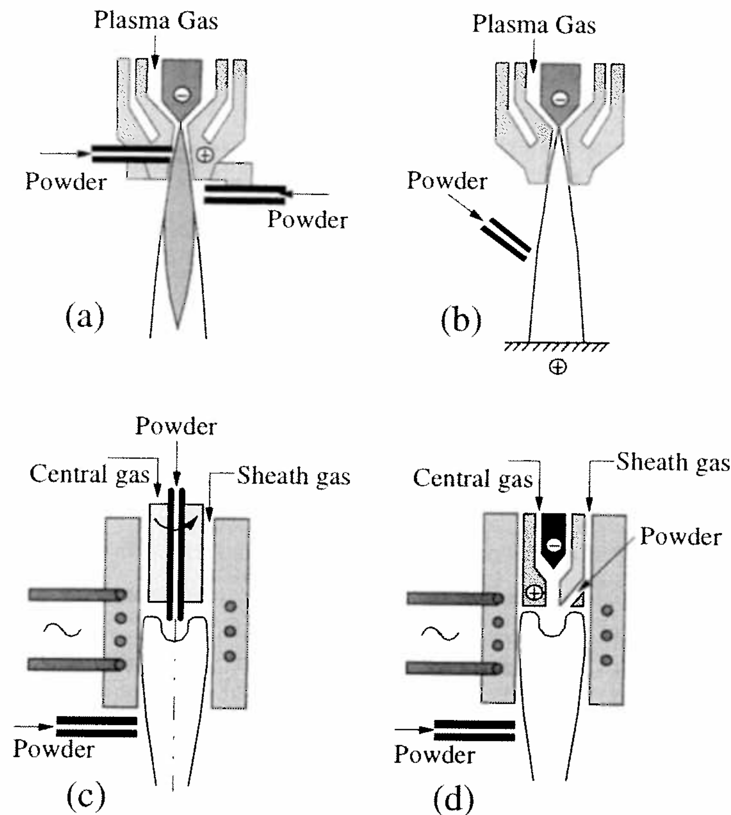

Figure 1: *Schematic of thermal plasma generation devices (a) d.c. plasma torch (b) d.c. transferred arc (c) r.f. induction plasma torch (d) d.c./r.f. hybrid plasma torch.*:

the anode nozzle, or externally as shown on either sides of Figure 1a. Typical material residence time in the plasma is less than one ms.

2.2 D.C. transferred arc plasmas

As shown in Figure 1b, transferred arcs differ from the standard d.c. plasma torches by the fact that they operate with an external anode which can be at a distance of a few centimeters up to 30 or 40 cm from the cathode. Typical arc currents are of the order of a few hundred amperes up to 1000 A or more. Arc voltages can vary between 20 to 30 V up to a few hundred volts depending on the arc length and the nature of the plasma gas. The plasma gas is injected in this case into the annular region between the cathode and an auxiliary nozzle which is usually kept at a floating potential. Typical conditions in the arc column are temperatures in the range of 12 000 K to 20 000 K though temperatures up to 26 000 K have been reported near the cathode tip. Gas velocities are of the order of a few tens of m/s. When used for material processing, transferred arcs are often used with a molten metal pool as anode in which the material in powder or chuck form is injected.

2.3 R.F. inductively coupled plasma torches

In this case (Figure 1c), the plasma is generated through the inductive coupling of the energy into the plasmas. The induction coil is typically formed of a three (3) to eight (8) turns, water-cooled, copper coil, surrounding a gas or water-cooled quartz or ceramic wall plasma confinement tube. Induction plasma discharges have been operated at power levels ranging from a few kW to 400 or 500 kW with plasma confinement tube diameters ranging from 18 mm up to 100 mm respectively. Induction plasma torches with a, water-cooled, segmented

metal, plasma confinement tubes have also been operated at power levels up to 800 or 1000 kW. The operating frequency varies with the power range and the diameter of the plasma confinement tube. These are typically in the MHz range (3 - 40 MHz) for operation at power levels up to 200 kW. Operation at higher power levels are usually associated with a drop of frequency to the 300 to 400 kHz range. Induction plasma sources have been operated at atmospheric pressure and soft vacuum conditions 13.4 - 40.1 kPa (100-300 torr) with a wide range of gases including Ar, Ar/H_2, Ar/He, N_2, O_2, Air,... Typical conditions prevailing in the discharge and at the exit of the torch nozzle are temperatures of the order of 8 000 – 10 000 K, and plasma velocities in the range of 40 to 50 m/s up to 1000 m/s or more. The latter was achieved through the use of a supersonic Laval nozzle attachment with a chamber pressure downstream of the torch of the order of 50 torr. Property gradients are less important in this type of device in the core of the plasma flow. Steep temperature and velocity gradients (10^3 K/mm and 10 to 50 (m/s)/mm) are still observed in the fringes of the discharge. When used for materials processing, the material to be treated is typically injected in powder form ($5 < d_p <$ 100-500 µm) either axially into the center of the discharge, or radically into the plasma jet at the exit of the plasma torch. Typical materials residence time in the plasma is of the order of 10 to 20 ms depending on the discharge conditions.

2.4 Hybrid d.c./r.f. torches

These are hybrid combinations of both d.c. and r.f. plasma generating techniques (Figure 1d) with approximately 5 to 10 % of the total plasma power supplied to the discharge by a central d.c. plasma torch. The balance of the power is coupled inductively in the emerging d.c. plasma jet. Though the technique is presently of limited use, it has its merits in allowing for the better control of the energy density distribution in the discharge and for the increase of the centerline plasma velocities. Operation of this type of discharge has been reported at powers up to a few hundred kW with a wide range of conditions for plasma synthesis and materials processing applications.

3. Diagnostic techniques available

A broad spectrum of diagnostic techniques have been successfully developed and used for the characterization of different plasma generating devices for a wide range of applications. These vary depending whether the measurement target is the plasma itself or the particulate matter being processed in-flight.

3.1 Plasma diagnostic techniques

These can be classified as follows according to the basic sensing technique used.

a) Optical methods

These are by far the most commonly used diagnostic techniques.

- *Emission/Absorption spectroscopy* using absolute intensity line techniques, Boltzman plots, Stark broadening, and two-point light emission correlation analysis.

- *Laser techniques* including Laser Induced Fluorescence (LIF), Thomson and Rayleigh Scattering and Coherent Antistokes Raman Spectroscopy (CARS).
- *Flow visualization* using high speed photography, laser interferometry and schelieren techniques.

b) Probe techniques

Although probe techniques have been available for many year for plasma diagnostics, they have been getting a wider acceptance over the past ten years. The most important of these are the langmuir and enthalpy probes. The latter can be used for the simultaneous measurement of the local specific enthalpy, velocity and composition of the plasma. Their main advantage is the simplicity of the technique, and its possible use for the simultaneous measurement of multiple plasma parameters with a generally acceptable spacial resolution. Its main limitation is that it is an intrusive technique, with the probe inevitably causing a local perturbation of the flow. Enthalpy probe techniques can not be used either for time-resolved measurements.

c) Acoustic and electrical signal analysis techniques

Increasing attention has been given over the past ten years to the relatively important information that can be obtained about the dynamics of the discharge through a simple spectrum analysis of the acoustic noise emitted and/or the arc voltage fluctuations associated with d.c. discharges (torches and transferred arcs).

3.2 Particulate diagnostic techniques

These are mainly optical techniques aiming at the measurement of the in-flight particle velocity, surface temperature, diameter and number flux density. The most common of these techniques are:

a) Laser Doppler anemometry (or velocimetry)

These are based on the observation of laser light scattered by the particles as they cross the measuring volume defined by the point of intersection of two laser beams. The techniques gives essentially information about the particle velocity. When combined with phase-shift analysis at two different observation angles, the technique can be used to obtain information about the particle diameter as well.

b) Laser strobe technique

When combined with high speed photography and image analysis, laser strobe techniques can be used for particle trajectory and particle velocity measurement.

c) Two-wave length pyrometry

Assuming gray body radiation, this technique can provide information about the in-flight surface temperature of the particles. When combined with time-of-flight measurement through the use of a well defined observation window, this technique can be used for the simultaneous measurement of the particle velocity and surface temperature.

4. Examples of enthalpy probe measurements in d.c. and r.f. induction plasma discharges

In the following, typical results are presented for enthalpy probe measurements in d.c. and r.f. inductively coupled plasma discharges. Details of the experimental techniques and measurement setup used can be found in the publication by Fincke *et al.* [6-8] for the d.c. work, and Rahmane *et al.* [9-12] for the r.f. induction plasma results respectively.

Figure 2 shows typical enthalpy probe measurements of the radical temperature, velocity and concentration profiles for a standard d.c. plasma torch in an open discharge in air [8]. These were obtained using a commercial d.c. plasma torch (Miller SG-100) operated with standard anode and cathode arrangements. The torch nozzle exit diameter is 8 mm. The operating conditions were 35.4 slpm (Ar), atmospheric pressure of 85 kPa (635 torr), torch current 900 A and torch voltage of 25V, with a corresponding torch power of 22.9 kW. The profiles given in Figure 2 were obtained at an axial location of 2.0 mm downstream of the torch exit. Superposed on Figure 2 are the results of laser scattering measurements, of the plasma temperature and velocity profiles. These are in good agreement with the enthalpy probe measurements.

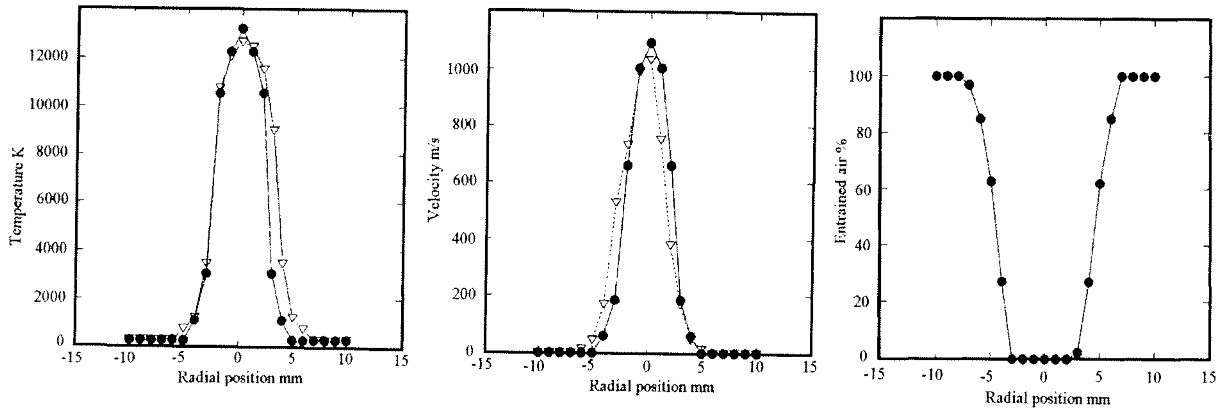

Figure 2: *Temperature, velocity and concentration profiles for a d.c. plasma jet discharge in air.* ● *Laser scattering* ∇ *Enthalpy probe (After Fincke et al. [8]).*

Figure 3 shows corresponding enthalpy probe measurements carried out within an induction plasma torch/reactor system [11]. These were obtained with a commercial induction plasma torch (Tekna model PL-50) with a 50 mm i.d. ceramic plasma confinement tube and a 43 mm i.d. torch exit nozzle. The torch was mounted in this case on the top of a 200 mm i.d. water-cooled chamber maintained at on absolute pressure of 33.4 kPa (250 torr). The operating conditions are: Sheath gas composed of an Ar/H_2 mixture (71 slpm Ar + 4 slpm H_2); central gas, 33 slpm (Ar); measurements are given for two situations in the absence (a) and presence (b) of probe injected gas, 8 slpm N_2. The plate power of the r.f. power supply was 20 kW (about 13 kW coupled into the discharge), and the oscillator frequency was 4 MHz. The results are presented in terms of radial profiles of the plasma temperature, velocity and composition (expressed in mole fraction of N_2), at different axial locations in the torch and downstream chamber (z = -22, +23, +77 and +122 mm) with the z = 0 level coinciding with the torch nozzle exit plane. The results are compared with the predictions of a 2-dimensional turbulent flow mathematical model with which they are in good agreement.

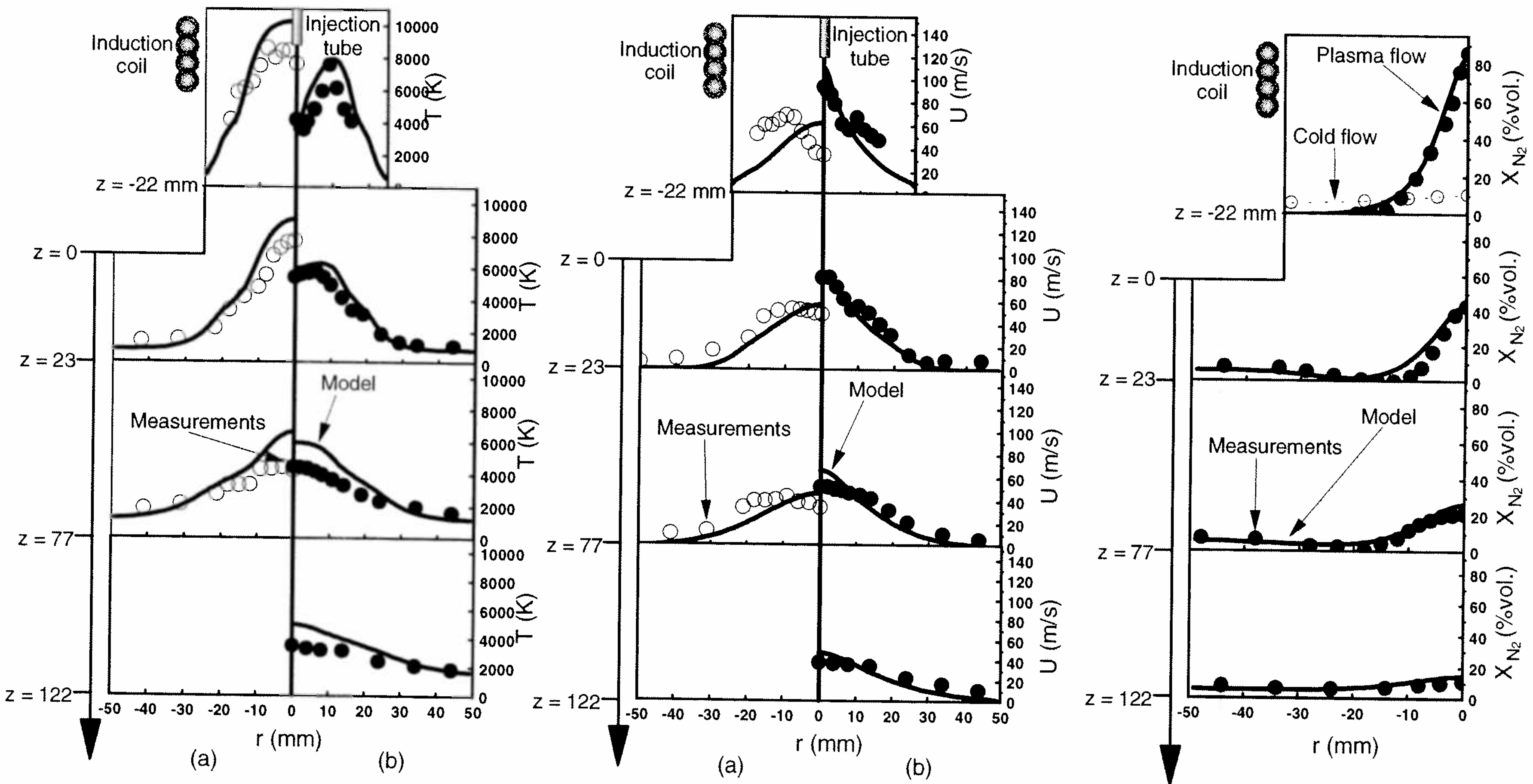

Figure 3: *Typical radial profiles of the plasma temperature, velocity and concentration at different axial locations in the absence (a) and presence (b) of axial injection of nitrogen in the centre of the discharge (After Rahmane et al. [11]).*

5. Summary and conclusions

Diagnostic techniques to be used for fundamental studies and on-line control of thermal plasma processes have to be well adapted to the high energy density and high velocity normally prevailing in such sources. A number of tools are available for such measurements base on optical, probes or acoustic and electrical signal analysis techniques. These can generally be used, however, for the measurement of either the plasma parameters in the absence of the particulates or the in-flight particulate parameters alone. Very few techniques can be used, however, for the measurements of the plasma parameters in the presence of the particulates. Further work is needed for the development and integration of simple and robust plasma and particulate diagnostic techniques in comprehension on-line process control schemes.

References

[1] M. Boulos, P. Fauchais, and E. Ffender. "Diagnostic Techniques in Thermal plasma Processing ", DOE report, no. DOE/ER-0270, **1-2** (1986)

[2] P. Fauchais, J.F. Coudert and M. Vardelle. In Plasma Diagnostics, Academic Press, N.Y. 349-446 (1989)

[3] P. Fauchais, J.F. Coudert, M. Vardelle, A. Vardelle and A. Denoirjean. "Diagnostics of Thermal Spraying Plasma Jets", J. Thermal Spray Technology, **1**, 117-128 (1992)

[4] K. Landers, "Diagnostics and On-line Control of a Plasma Spray Process», High Temp. Materials Processes, **1**, 315-326 (1997)

[5] C. Moreau. "Towards a Better Control of Thermal Spray Process», Proceedings ITSC-98, Nice France, 1681-1693 (1998)

[6] Swank, W. D., Fincke, J. R. and D.C. Haggard. "Modular Enthalpy Probe and Gas Analyzer for Thermal Plasma Measurements", Rev.Sci.Instrum., **64**, 56-62 (1993)

[7] Fincke, J. R., Swank, W. D., Snyder, S. C. and D.C. Haggard. "Enthalpy Probe Performance in Compressible Thermal Plasma Jets", Rev.Sci.Instrum., **64**, 3585-3593 (1993)

[8] Fincke, J. R., Snyder, S. C. and W.D. Swank. "Comparison of Enthalpy Probe and Laser Light Scattering Measurement of Thermal Plasma Temperatures and Velocities", Rev.Sci.Instrum., **64**, 711-718 (1993)

[9] Rahmane, M., Soucy, G. and M.I. Boulos "Analysis of Enthalpy Probe Technique for Thermal Plasma Diagnostics", Rev.Sci.Instrum., **66**, 3424-3431 (1995)

[10] Rahmane, M., Soucy, G., and M.I. Boulos. "Mass Transfer in Induction Plasma Reactors", Int.J.Heat Mass Transfer, **37**, 2035-2046 (1994)

[11] Rahmane, M., Soucy, G. and M.I. Boulos. "Diffusion Phenomena of a Cold Gas in Thermal Plasma Stream", Plasma Chem.Plasma Proces., **16**, 169S-189S (1996)

[12] Rahmane, M., Soucy, G. and M.I. Boulos. "Similarity Analysis and Scale-up Criteria for Thermal Plasma Jets", High Temp.Material Processes, **2**, 177-193 (1998)

DIAGNOSTIC STUDIES OF PROCESSING PLASMAS INVOLVING ELECTRONEGATIVE GASES

Read P.A., Rees J.A., Greenwood C.L.

Hiden Analytical Ltd
420 Europa Boulevard
Warrington
WA5 5UN

Introduction

A wide variety of electrical discharges are now used to modify the surfaces of materials ranging from semi-conductors to super-conductors. The processes include the deposition of wear-resistant coatings of TiN for machine tools and other hard films, such as diamond-like carbon, and the etching of subnano-meter features in a variety of semi-conductor materials. In many applications the gas mixture used includes at least one electronegative gas such as methane, silane, carbon tetrafluoride, sulphur hexafluoride or oxygen. In developing a particular process it is essential to characterise the wide range of physical and chemical processes taking place, both in the body of the plasma and at the plasma surface interface, and including both charged and neutral particles. For these reasons we have recently studied, using a Quadrupole Mass Spectrometer fitted with an electrostatic energy filter, capacitive RF plasmas in sulphur hexafluoride.

Main text

Experimental Conditions

The experiments were carried out in sulphur hexafluoride at a gas pressure of 6mTorr. The 13.56MHz r.f. signal to the 5 cm diameter, driven electrode (figure 1) was superimposed on a d.c. bias potential set using a 0-100V power unit. The driven electrode was 8 cm from the grounded entrance plane of a Hiden EQP instrument (figure 2). The discharge formed between the driven electrode and the front of the EQP was partially confined by a 5 cm diameter, 6 cm long glass tube sitting on the horizontal, driven electrode, which also partially shielded the discharge from the influence of the grounded metal walls of the discharge chamber.

Measurements

MASS SPECTRA

(a) Positive Spectra

The neutral gas sampled from the plasma chamber, with the RF plasma turned off was analysed using the EQP's internal electron impact source. The positive ion spectrum generated by the source shows all the expected components, described by the formula SF_x^+ with $1 \leq x \leq 5$ with additional peaks due to impurities such as nitrogen and oxygen. Doubly-charged ions of the same fragments (e.g. SF_3^{++}) were also produced. With the plasma turned on, the relative abundances of the various fragment ions were a function of the plasma conditions. With a plasma self-bias potential of -100V no SF_4^+ or SF_5^+ ions were observed, nor any doubly-charged fragments.

(b) Negative Spectra

With the EQP's source arranged to generate negative ions from the neutral gas sampled from the plasma, the mass spectra were considerably simpler than the corresponding positive ion spectra. Only F^-, SF_5^- and SF_6^- ions were observed, at any of the plasma conditions examined. Their relative abundances were a function of the plasma conditions.

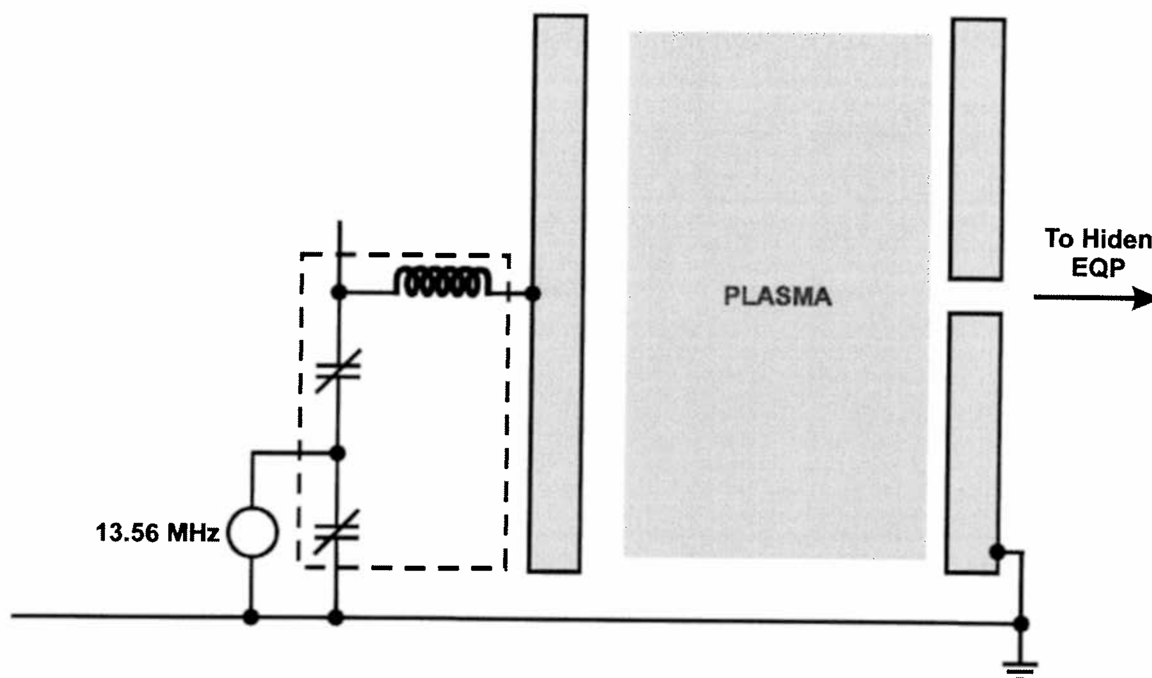

Figure 1

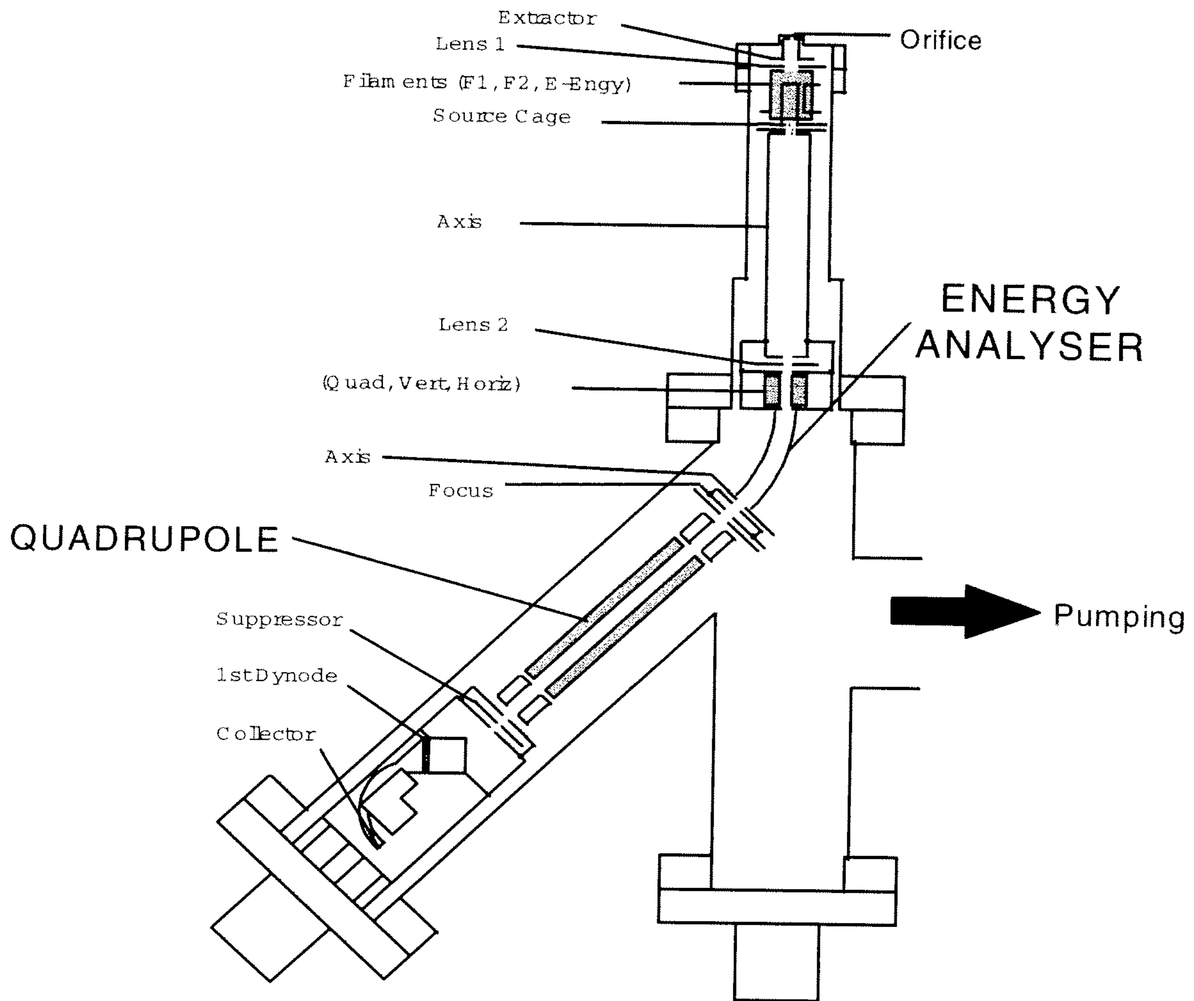

Fig 2

CONCLUSIONS

The positive and negative ion spectra obtained for the neutral gas sampled from an RF plasma in SF_6 were quite different. The negative ion spectra showed only F^-, SF_5^- and SF_6^- ions and may be easier to interpret in terms of the neutral fragments produced by the plasma.

The relative intensities of the F^-, SF_5^- and SF_6^- ions were dependent on the gas pressure and the plasma's electrical conditions. The energy spectra for the SF_5^- and SF_6^- ions showed two peaks at around 2.25 and 7eV for both species for both "plasma on" and "plasma off" conditions. The 7eV ions were only obtained for electron energies of below 8eV.

For the F^- ions, the peak observed in the ion energy distribution at around 8eV was only obtained for "plasma on" conditions. It may be concluded that the parent neutral species leading to these high energy ions is not ground-state SF_6 but either an excited, long-lived, state of SF_6 or a neutral fragment of SF_6. Since the peak for 6eV electrons at an ion energy of 8eV

increased with increasing gas pressure, if the parent neutral species produced by the plasma is in an excited state this would need to be collision-stabilised rather than de-excited.

Negative ion studies of the type described here may prove a useful way of investigating processing plasmas which involve electro-negative gases. Their interpretation requires extensive data for the reaction rates etc. of negative ion formation processes.

List of Participants

AWAKOWICZ
Peter
Lehrstuhl für Technische Elektrophysik
Arcisstr. 21
80290 München
Germany
Tel. +49 89 289 23125
Fax.+49 89 289 23141
awa@tep.ei.tum.de

BABOROWSKI
Jacek
EPFL
DMX-Laboratoire céramiques
1015 Ecublens
Switzerland
Tel. +41 21 693 29 44
Fax.+41 21 693 58 10
jacek.baborowski@epfl.ch

BAKKER
Leon
Eindhoven University of Technology
P.O. Box 513
5600 MB Eindhoven
The Netherlands
Tel. +31 40 2474091
Fax.+31 40 2456050
l.p.bakker@phys.tue.nl

BOEKE
Marc
Inst. für Experimentalphysik II
Ruhr Universität Bochum
Universitätsstr. 150
44780 Bochum
Germany
Tel. +49 - 234 700 45 76
Fax.+49 - 234 709 41 71
marc.boeke@ruhr-uni-bochum.de

BOOGAARTS
Maarten
Eindhoven University
PO Box 513
5600 MB Eindhoven
The Netherlands
Tel. +31 40 24 75 770
Fax.+31 40 24 56 442
maarten@etpserver.phys.tue.nl

BOOTH
Jean-Paul
Laboratoire de Spectrométrie Physique
P.O. Box 87
38402 St Martin d'Hères
France
Tel. +33 476 51 47 50
Fax.+33 476 51 45 44
jean-paul.booth@ujf-grenoble.fr

BOULOS
Maher
University of Sherbrooke
J1K2R1 Sherbrooke, Quebec
Canada
Tel. +1 819 821 71 68
Fax.+1 819 821 79 55
boulos@plasma.gcm.usherb.ca

BROCKHAUS
Albrecht
Forschungszentrum für Mikrostrukturtechnik - fmt
University of Wuppertal
Obere Lichtenplatzer Str. 336
42287 Wuppertal
Germany
Tel. +49 202 595096
Fax.+49 202 595098
bro@fmt.uni-wuppertal.de

BUCKLEY
Mark
Hiden Analytical Ltd
420 Europa Boulevard
WA5 5UN Warrington
UK
Tel. +44 1925 445225
Fax.+44 1925 416518
info@hiden.demon.co.uk

CARTRY
Gilles
Lab. de Physique des Gaz et des Plasmas
91405 Orsay
France
Tel. +33 1 69157752
Fax.+33 1 69157844
gilles.cartry@lpgp.u-psud.fr

CIGAL
Jean-Charles
Eindhoven University of Technology
P.O. Box 513
5600 MB Eindhoven
The Netherlands
Tel. +31 40 247 40 91
Fax.+31 40 245 60 50
cigal@discharge.phys.tue.nl

DESCHENAUX
Christian
EPFL-CRPP
Bat PPB
1015 Lausanne
Switzerland
Tel. +41 21 693 65 41
Fax.+41 21 693 51 76
christian.deschenaux@epfl.ch

DIAS
F.M.
Centro de Fisica dos Plasmas
Instituto Superior Tecnico
Av. Rouisco Pais
1096 Lisboa
Portugal
Tel. +351 1 8419326
Fax.+351 1 8464455
fjcmd@hotmail.com

DORIER
Jean-Luc
EPFL-CRPP
Bat PPB
1015 Lausanne
Switzerland
Tel. +41 21 693 34 61
Fax.+41 21 693 51 76
jean-luc.dorier@epfl.ch

DUTEN
Xavier
Lab. d'Ingéniérie des Matériaux et des Hautes Pressions
Université Paris Nord
Av. J.B. Clément
93430 Villetaneuse
France
Tel. +33 1 69 15 65 27
Fax.+33 1 69 15 78 44
xavier.duten@lpgp.u-psud.fr

ENGELN
Richard
Eindhoven University of Technology
PO Box 513
5600 MB Eindhoven
The Netherlands
Tel. +31 40 247 5770
Fax.+31 40 245 6442
r.engeln@phys.tue.nl

ENGEMANN
Jürgen
Forschungszentrum für Mikrostrukturtechnik FMT
Obere Lichtenplatzer Str. 336
42287 Wuppertal
Germany
Tel. +49 202 59 50 96
Fax.+49 202 59 50 98
engemann@fmt.uni-wuppertal.de

FRANCIS
Anne
Inst. für Laser- und Plasmaphysik
AG Prof. Doebele
Universitaetsstr. 5
45117 Essen
Germany
Tel. +49 - 201 - 1833027
Fax.+49 - 201 - 183 30 29
af@ilp.physik.uni-essen.de

GEORG
Axel
Forschungszentrum für Mikrostrukturtechnik - fmt
University of Wuppertal
Obere Lichtenplatzer Str. 336
42287 Wuppertal
Germany
Tel. +49 202 595096
Fax.+49 202 595098
georg@fmt.uni-wuppertal.de

GOEHLICH
Andreas
University of Essen
Universitätstrasse 2-5
45117 Essen
Germany
Tel. +49 201 183 3175
Fax.+49 201 183 2120
andreas.goehlich@uni-essen.de

GOTTSCHO
Richard
Lam Research
4650 Cushing Pkwy
94538 Fremont CA
USA
Tel. +1 510 572 8555
Fax.+1 510 572 8523
richard.gottscho@lamrc.com

GRAHAM
Bill
Queen's University
Physics department
BT71NN Belfast
Northern Ireland
Tel. +44 1232 27 35 64
Fax.+44 1232 43 89 18
B.Graham@qub.ac.uk

GRANGEON
Frederic
EPFL-CRPP
Bat PPB
1015 Lausanne
Switzerland
Tel. +41 21 693 65 86
Fax.+41 21 693 51 76
frederic.grangeon@epfl.ch

HAMERS
Edward
Lab. de Physique des Interfaces et des
Couches Minces - Ecole Polytechnique
91129 Palaiseau
France
Tel. +33 1 69 33 32 11
Fax.+33 1 69 33 30 06
hamers@poly.polytechnique.fr

HEMMERS
Dirk
Inst. für Laser- und Plasmaphysik
HHU-Düsseldorf
Universitätsstr. 1
40225 Düsseldorf
Germany
Tel. +49 - 211 81 12869
Fax.+49 - 211 81 13718
hemmers@uni-duesseldorf.de

HERNBERG
Rolf
Tampere University of Technology
Dept of Physics
PO box 692
33101 Tampere
Finland
Tel. +358 3 365 2364
Fax.+358 3 365 2090
hernberg@cc.tut.fi

HERTL
Michael
CNRS-ONERA
Laboratoire PRIAM
Fort de Palaiseau, Bât. S
91761 Palaiseau Cedex
France
Tel. +33 - 1 69 93 61 73
Fax.+33 - 1 69 93 61 82
hertl@onera.fr

HOLLENSTEIN
Christoph
EPFL-CRPP
Bat PPB
1015 Lausanne
Switzerland
Tel. +41 21 693 34 71
Fax.+41 21 693 51 76
christophe.hollenstein@epfl.ch

HOWLING
Alan
EPFL-CRPP
Bat PPB
1015 Lausanne
Switzerland
Tel. +41 21 693 34 96
Fax.+41 21 693 51 76
alan.howling@epfl.ch

KACZOR
Markus
Experimental Physics V
Ruhr-University Bochum
Universitätsstr. 150
44780 Bochum
Germany
Tel. +49 - 234 700 6216
Fax.+49 - 234 709 41 75
markus.kaczor@ep5.ruhr-uni-bochum.de

KALATCHEV
Michael
St. Petersburg State University
Ulyanovskaya 1
198904 St. Petersburg
Russia
Tel. +7 - 812 428 44 52
Fax.+7 - 812 428 46 77
mkalachev@usa.net

KAWETZKI
Timo
Inst. für Laser- und Plasma Physik, AG Döbele
Universität GH Essen
Universitätsstr. 5
45141 Essen
Germany
Tel. +49 - 201 1833125
Fax.+49 - 201 1833029
timo.kawetzki@uni-essen.de

KESSELS
Erwin
Eindhoven University of Technology
P.O. Box 513
5600 MB Eindhoven
The Netherlands
Tel. +31 - 40 - 247 34 77
Fax.+31 - 40 - 245 64 42
w.m.m.kessels@phys.tue.nl

KROESEN
Gerrit
Eindhoven University of Technology
PO Box 513
5600 MB Eindhoven
The Netherlands
Fax. +31 - 402 45 60 50
G.M.W.Kroesen@phys.tue.nl

LINS
Guenter
Siemens AG
ZT EN 3
P.O. Box 3220
91050 Erlangen
Germany
Tel. +49 9131 733087
Fax.+49 9131 724709
guenter.lins@erls.siemens.de

LUKAS
Christoph
Inst. für Laser- und Plasma Physik, AG Döbele
Universität GH Essen
Universitätsstr. 5
45141 Essen
Germany
Tel. +49 - 201 1833125
Fax.+49 - 201 1833029
christoph.lukas@uni-essen.de

LUO
Xiao
Inst. für Laser- und Plasmaphysik
Heinrich-Heine-Universität Düsseldorf
Universitätsstrasse 1, Geb. 25.33
40225 Düsseldorf
Germany
Tel. +49 211 8112157
Fax.+49 211 8113718
luo@uni-duesseldorf.de

MAGNI
David
EPFL-CRPP
Bat PPB
1015 Lausanne
Switzerland
Tel. +41 21 693 65 41
Fax.+41 21 693 51 76
david.magni@epfl.ch

MAURICE
Carole
Eindhoven University of Technology
P.O. Box 513
5600 MB Eindhoven
The Netherlands
Tel. +31 40 2474871
Fax.+31 40 2456050
maurice@discharge.phys.tue.nl

MAZOUFFRE
Stephane
Eindhoven Universtiy of Technology
P.O. Box 513
5600 MB Eindhoven
The Netherlands
Tel. +31 - 40 247 48 82
Fax.+31 - 40 245 64 42
s.mazouffre@phys.tue.nl

MECHOLD
Lars
Inst. für Niedertemperatur-Plasmaphysik
Robert-Blum-Str. 8-10
17489 Greifswald
Germany
Tel. +49 3834 515 224 or -229
Fax.+49 3834 554 301
mechold@inp-greifswald.de

MEIJER
Peter
Philips Research
Wag1
Prof. Holstlaan 4
5656 Eindhoven
The Netherlands
Tel. +31 40 274 27 73
Fax.+31 40 274 33 90
meijerp@natlab.research.philips.com

MERKULOV
Sergey
Institute of Microelectronics of the
Russian Academy of Sciences
Universitetskaya 21
150007 Yaroslavl
Russia
Tel. +7 - 0852 11 52 81
Fax.+7 - 0852 11 65 52
temper@postoff.ics.ac.ru

MOELLER
Ivonne
Experimental Physics V
Ruhr-University Bochum
Universitätsstr. 150
44780 Bochum
Germany
Tel. +49 - 234 700 66 75
Fax.+49 - 234 709 41 75
ivonne.moeller@ep5.ruhr-uni-bochum.de

MOSHKALYOV
Stanislav
Queen's University
Physics Department
BT71NN Belfast
Northern Ireland
Tel. +44 1232 273123
Fax.+44 1232 438918
s.moshkalyov@qub.ac.uk

NEUFFER
Andreas
Institute for plasma research
University of Stuttgart
70569 Stuttgart
Germany
Tel. +49 711 685 23 05
Fax.+49 711 685 31 02
neuffer@ipf.uni-stuttgart.de

NEUILLY
Francois
Centre National de Etudes et Communications
CNET, PO Box
850, Rue Jean Monnet
38926 Crolles
France
Tel. +33 4 76 76 43 95
Fax.+33 4 76 90 34
francois.neuilly@francetelecom.fr

NIESWAND
Christoph
EPFL-CRPP
Bat PPB
1015 Lausanne
Switzerland
Tel. +41 21 693 34 98
Fax.+41 21 693 51 76
christoph.nieswand@epfl.ch

OVTCHINNIKOV
Viatcheslav
St. Petersburg State University
Physical Faculty, Dept. of Optics
Ulianovskaya Str. 1
198904 St.-Petersburg
Russia
Tel. +7 - 812 428 4452
Fax.+7 - 812 428 4677
ovtchinnikov@usa.net

PANCHESHNYI
Sergey
Moscow Inst. of Physics and Technology
Institutskii lane 9
141700 Dolgoprudny Moscow Region
Russia
Tel. +7 - 095 408 63 47
Fax.+7 - 095 576 65 28
pon@physmech-gw.crec.mipt.ru

PECHER
Peter
Max-Planck-Institut für Plasmaphysik
P.O. Box 1533
85740 Garching
Germany
Tel. +49 89 3299 1157
Fax.+49 89 3299 1149
pecher@ipp.mpg.de

POPA
Gheorghe
"Al.I.Cuza" University
Faculty of Physics
Copou
6600 Iasi
Romania
Tel. +40 32 213300
Fax.+40 32 213330
ghpopa@uaic.ro

RÖPCKE
Juergen
Inst. für Niedertemperatur-Plasmaphysik
Robert-Blum-Str. 8-10
17489 Greifswald
Germany
Tel. +49 3834 515 227
Fax.+49 3834 554 301
roepcke@inp-greifswald.de

ROUSSEAU
Antoine
CNRS
P.O. Box 0210
Bat 210 LPGP-UPS
9140 Orsay
France
Tel. +33 1 69 15 65 27
Fax.+33 1 69 15 78 44
antoine.rousseau@lpgp.u-psud.fr

SADEGHI
Nader
Université Joseph Fourier
CNRS
PO Box 87
38402 Saint Martin d'Héres
France
Tel. +33 4 76 51 47 44
Fax.+33 4 76 51 45 44
Nader.Sadeghi@ujf-grenoble.fr

SCHEUBERT
Peter
Lehrstuhl für Technische Elektrophysik
Arcisstr. 21
80290 München
Germany
Tel. +49 89 289 23125
Fax.+49 89 289 23141
scheubert@tep.ei.tum.de

SCHMITT
JACQUES
Balzers Process Systems
5, Rue Leon Blum
91124 Palaiseau cedex
France
Tel. +33 1 69 19 12 80
Fax.+33 1 69 32 06 60
jschmitt@bfp.bps.balzers.net

SCHULZ-VON DER GATHEN
Volker
Inst. für Laser- und Plasmaphysik
Universitaet GH Essen
Universitaetsstrasse 5
45117 Essen
Germany
Tel. +49 201 1832476
Fax.+49 201 1833029
svdg@uni-essen.de

SCHWARZENBACH
Walter
Laboratoire de Spectrométrie Physique
P.O. Box 87
38402 St Martin d'Herès
France
Tel. +33 - 4 76 51 43 37
Fax.+33 - 4 76 51 95 44
walter.schwarzenbach@ujf-grenoble.fr

SIGNER
Hans
BALZERS AG, BPS
PO box 1000
9496 Balzers
Liechtenstein
Tel. +41-75 388 44 22
Fax.+41-75 388 54 03
sih@bps.balzers.net

SMIRNOV
Alexander
St. Petersburg State Technical University
Plasma Physics Department
Polytechnicheskaya 29
195251 St. Petersburg
Russia
Tel. +7-812 5526124
Fax.+7-812 5527954
smirnov@phtf.stu.neva.ru

SOLTWISCH
Henning
Ruhr-Universität Bochum
Exp.-Physik V
Universitätstr. 150
44780 Bochum
Germany
Tel. +49 - 234 - 700 6879
Fax.+49 - 234 - 709 4175
henning.soltwisch@ep5.ruhr-uni-bochum.de

SPATENKA
Petr
University of South Bohemia
Branisovska 31
37005 Ceske Budejovia
Czech Republic
Tel. +420 38 777 55 40
Fax.+420 38 45 985
spata@tix.bf.jcu.cz

STAMATE
Eugen
Dept. of Systems Engineering
Nagoya Institute of Technology
Gokiso-cho, Showa-ku
466 Nagoya
Japan
Tel. +81 - 52 732 2111 (5791)
Fax.+81 - 52 735 53 88
stamate@system.nitech.ac.jp

STARIKOVSKAIA
Svetlana
Moscow Inst. of Physics and Technology
Institutskii lane 9
141700 Dolgoprudny Moscow Region
Russia
Tel. +7 - 095 408 63 47
Fax.+7 - 095 576 65 28
sstar@physmech-gw.crec.mipt.ru

STEINBACH
Andreas
Siemens Microelectronics Center
Dresden
Königsbrückerstrasse 180
01099 Dresden
Germany
Tel. +49 351 886 22 63
Fax.+49 351 886 17 52
andreas.steinbach@siemens-scg.com

STOFFELS
Winfred
Eindhoven University of Technology
P.O. Box 513
5600 MB Eindhoven
The Netherlands
Tel. +31 402475753
Fax.+31 402456050
stoffels@discharge.phys.tue.nl

STOFFELS
Eva
Eindhoven University of Technology
P.O. Box 513
5600 MB Eindhoven
The Netherlands
Tel. +31 - 402 47 57 53
Fax.+31 - 402 45 60 50
stoffels@discharge.phys.tue.nl

SWINKELS
Geert
Eindhoven University of Technology
P.O. Box 513
5600 MB Eindhoven
The Netherlands
Tel. +31 40 2474340
Fax.+31 40 2456050
swinkels@discharge.phys.tue.nl

TEBOUL
Eric
Lab. de Physique des Gaz et des Plasmas
UPS Bât. 210
91405 Orsay
France
Tel. +33 - 1 - 69 15 81 92
Fax.+33 - 1 - 69 15 78 44
eric.teboul@lpgp.u-psud.fr

VALLEE
Christophe
Lab. des Plasmas et des Couches Minces - IMN
P.O. Box 32229
44322 Nantes
France
Tel. +33 - 2 - 40 37 39 64
Fax.+33 - 2 - 40 37 39 59
christophe.vallee@cnrs-imn.fr

VAN DE SANDEN
Richard
Eindhoven University of Technology
Dept. of Physics
P.O. Box 513
5600 MB Eindhoven
The Netherlands
Tel. +31 - 40 247 34 74
Fax.+31 - 40 245 64 42
m.c.m.v.d.sanden@phys.tue.nl

VARDELLE
Armelle
Ecole Nationale Superieure d'Ingenieurs de Limoge
16, Rue Atlantis Parc D'ESTER
87068 Limoges cedex
France
Tel. +33 5 5542 36 84
Fax.+33 5 5542 36 80
armelle@puce.ensil.unilim.fr

VON KEUDELL
Achim
Max-Planck-Institut für Plasmaphysik
Boltzmannstr. 2
P.O. Box 1533
85748 Garching
Germany
Tel. +49 89 3299 1631
Fax.+49 89 3299 1149
amk@ipp.mpg.de

WINTER
Jörg
Institut für Experimentalphysik II
Ruhr-Universität Bochum
Universitätstrasse 150
44780 Bochum
Germany
Tel. +49 243 700 3693
Fax.+49 234 7094 171
jw@plasma.ep2.ruhr-uni-bochum.de

Author Index

A

Abelson J.R. 109
Anders J. 113
Anikin N.B. 191
Astashkevich S.A. 279
Aumaille K. 105
Awakowicz P. 171

B

Babich I.L. 301
Baeva M. 147
Bakker L.P. 209
Bakker I.S.J. 265
Baravian G. 287
Barbezat G. 135
Beck A. 241
Behle St. 233
Berden G. 39
Bezemer J. 93
Biennier L. 219
Blazek J. 183
Böke M. 211
Boogaarts M.G.H. 215,265
Booth J.P. 117,219,275
Boulos M. 7
Braithwaite N.St.J. 117
Branston D.W. 143
Brezinsek S. 241
Brockhaus A. 89,233
Brussaard G.J.H. 73
Busch C. 269

C

Carty G. 123
Cernogora G. 123
Chernoiziumskaya T.V. 179
Chevalley L. 127
Cigal J.-C. 131
Cook R.W. 183
Cooperberg D. 61
Courteille C. 151
Crowley B. 297
Cunge G. 219,297
Czarnetzki U. 231

D

Davies P.B. 155
de Graaf A. 73
Derouard J. 175
Deschenaux Ch. 151
Dias F.M. 223
Döbele H.F. 17,231,257,261,291
Dorier J.-L. 135,237
Duten X. 227

E

Endres H.-J. 183
Engeln R. 39
Engemann J. 89,233

F

Fayet P. 151
Francis A. 231
Francou J.-M. 117
Fresnet F. 287

G

Georg A. 233
Gicquel A. 227
Goehlich A. 17
Gomez S. 97
Goodyear A. 117
Gottscho R.A. 61
Goullet A. 105
Graham W.G. 97,273
Grangeon F. 237
Granier A. 105

H

Hämäläinen E. 85
Hamers E.A.G. 93
Hemmers D. 241
Hernberg R. 85
Hertl M. 245
Himmel G. 211
Hollenstein Ch. 127,135,151,237
Howling A.A. 127,237

J

Jolly J. 245

K

Kaczor M. 9,249
Kalatchev M.V. 253,279
Käning M. 113,155,253,257,261
Katchanov A. 219
Kawetzki T. 257,261
Kempkens H. 241
Kessels W.M.M. 73,139
Korhonen T. 85
Kosarev A.I. 179
Kroesen G.M.W. 27,131,195,199,209
Krumeich J. 183

L

Lang N. 253
Lavrov B.P. 253,279
Leewis C.M. 139
Leprince Ph. 203,227

Letourneur K.G.Y. 73
Lins G. 143
Loch M. 135
Loffhagen D. 155
Lukas C. 257,261,291
Lunk A. 163
Luo X. 147

M
Magne L. 123
Magni D. 151
Magunov A.N. 101
Mahony C.M.O. 97
Mazouffre S. 265
Mechold L. 155
Meier S. 241
Meijer G. 39
Merkulov S.V. 101
Möller I. 269
Monard C. 127,237
Morrow T. 273
Moshkalyov S.A. 97,159,273

N
Nelson D. 113
Neuffer A. 163
Neuilly F. 117,275
Niemöller N. 17

O
Ohe K. 187
Orlov K.E. 179
Ovtchinnikov V.L. 279

P
Pancheshnyi S.V. 191,283
Pasquiers S. 287
Pecher P. 167
Peeters R. 39
Popa G. 187
Postel C. 287
Puech V. 287

R
Romanini D. 219,237
Röpcke J. 113,155,253,257,261
Rousseau A. 203,227,287
Rozoy M. 287

S
Sadeghi N. 175,237,275
Salito A. 135
Sansonnens L. 127
Scheubert P. 171
Schmitt J. 71
Schram D.C. 73,139,215,265
Schulz-von der Gathen V. 257,261,291
Schwabedissen A. 89
Schwarzenbach W. 175
Schweer H.B. 211,241
Schwefel R. 171
Shutov M.V. 179
Smets A.H.M. 215
Smirnov A.S. 179
Soll Ch. 89,233
Soltwisch H. 9,249,269
Spaan M. 291
Spatenka P. 183
Stamate E. 187
Stanco J. 241
Starikovskaia S.M. 191,283
Starikovskii A. Yu. 191,283
Steen P.G. 93
Steinbach A. 51
Stoffels E. 27,195
Stoffels W.W. 27,195
Swinkels G.H.P.M. 195,199

T
Tatarova E. 223
Teboul E. 203
Thompson C. 273
Turban G. 105
Turner M.M. 297

U
Uhlenbusch J. 147,241

V
Vahedi. V. 61
Vallée C. 105
Vallier L. 275
van der Mullen J.A.M. 265
van der Weg W.F. 93
van de Sanden M.C.M. 73,139,215
van Hest M.F.A.M. 73
Vardelle A. 37
Vattulainen J. 85
Veklich A.N. 301
Vender D. 297
von Keudell A. 109

W
Wachutka G. 171
Wienhold F.G. 113
Winter J. 211

Z
Zahniser M. 113